GL-TR-90-0306
ENVIRONMENTAL RESEARCH PAPERS, NO. 1071

AD-A229 915

Proceedings of the 7th Annual DARPA/AFGL Seismic
Research Symposium, 6-8 May 1985

Editor:
JAMES F. LEWKOWICZ

8 November 1990

EARTH SCIENCES DIVISION   PROJECT 2309
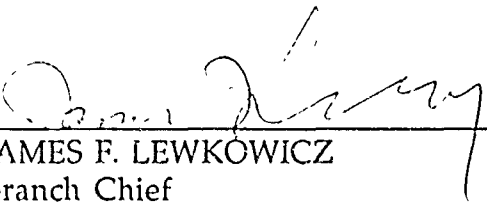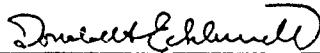# GEOPHYSICS LABORATORY
HANSCOM AFB, MA 01731-5000

90 12 3 015

"This technical report has been reviewed and is approved for publication."

FOR THE COMMANDER

JAMES F. LEWKOWICZ
Branch Chief
Solid Earth Geophysics Branch
Earth Sciences Division

DONALD H. ECKHARDT
Director
Earth Sciences Division

This report has been reviewed by the ESD Public Affairs Office (PA) and is releasable to the National Technical Information Service (NTIS).

Qualified requestors may obtain additional copies from the Defense Technical Information Center. All others should apply to the National Technical Information Service.

If your address has changed, or if you wish to be removed from the mailing list, or if the addressee is no longer employed by your organization, please notify GL/IMA, Hanscom AFB, MA 01731-5000. This will assist us in maintaining a current mailing list.

Do not return copies of this report unless contractual obligations or notices on a specific document requires that it be returned.

REPORT DOCUMENTATION PAGE

Public reporting burden for this collection of information is estimated to average 1 hour per response, including the time for reviewing instructions, searching existing data sources, gathering and maintaining the data needed, and completing and reviewing the collection of information. Send comments regarding this burden estimate or any other aspect of this collection of information, including suggestions for reducing this burden, to Washington headquarters Services, Directorate for Information Operations and Reports, 1215 Jefferson Davis Highway, Suite 1204, Arlington, VA 22202-4302, and to the Office of Management and Budget, Paperwork Reduction Project (0704-0188), Washington, DC 20503.

1. AGENCY USE ONLY (Leave blank)	2. REPORT DATE	3. REPORT TYPE AND DATES COVERED
	8 November 1990	Scientific, Interim

4. TITLE AND SUBTITLE

Proceedings of the 7th Annual DARPA/AFGL Seismic
Research Symposium, 6-8 May 1985

5. FUNDING NUMBERS

PE 61102F
PR 2309
TA G2
WU 04

6. AUTHOR(S)

Editor: James F. Lewkowicz

7. PERFORMING ORGANIZATION NAME(S) AND ADDRESS(ES)

Air Force Geophysics Laboratory, AFSC
AFGL/LWH
Hanscom AFB, MA 01731-5000

8. PERFORMING ORGANIZATION REPORT NUMBER

GL-TR-90-0306
ERP, No. 1071

9. SPONSORING/MONITORING AGENCY NAME(S) AND ADDRESS(ES)

DARPA/GSD
1400 Wilson Boulevard
Arlington, VA 22209-2308

10. SPONSORING/MONITORING AGENCY REPORT NUMBER

11. SUPPLEMENTARY NOTES

This research was supported by DARPA under PE 61101E and 62714E.

12a. DISTRIBUTION/AVAILABILITY STATEMENT

Approved for Public Release; distribution unlimited

12b. DISTRIBUTION CODE

13. ABSTRACT (Maximum 200 words)

These proceedings contain papers presented at the Seventh Annual Defense Advanced Research Projects Agency/Air Force Geophysics Laboratory (DARPA/AFGL) Seismic Research Symposium held 6-8 May 1985, in Colorado Springs, Colorado. In its capacity as a Technical Agent, the AFGL's Solid Earth Geophysics Branch (LWH) manages the DARPA Geophysical Sciences Division's (GSD) basic research program in seismology. The scientific objective of this program is to improve the Air Force's capability to seismically detect, locate, identify and estimate the yield of underground nuclear explosions. The purpose of this symposium, which is organized annually by LWH, is to provide the GSD staff an opportunity to review the research accomplished during the preceding year and outline areas of investigation for the coming year. For the researchers, it provides a forum for the exchange of scientific information, as well as occasions to meet personally with the GSD and LWH staff to discuss individual projects, ideas and results. In addition, the technical presentations serve as a means to

14. SUBJECT TERMS

underground nuclear explosion, seismic waves, regional
seismology arrays, yield estimation, source coupling. (JH)

15. NUMBER OF PAGES
454

16. PRICE CODE

17. SECURITY CLASSIFICATION OF REPORT	18. SECURITY CLASSIFICATION OF THIS PAGE	19. SECURITY CLASSIFICATION OF ABSTRACT	20. LIMITATION OF ABSTRACT
UNCLASSIFIED	UNCLASSIFIED	UNCLASSIFIED	UL

Standard Form 298 (Rev. 2-89)
Prescribed by ANSI Std Z39-18

inform representatives from other Government agencies about advances in seismic monitoring research, technologies and techniques as part of the important process of technology transition. The papers include studies on regional seismic wave propagation, attenuation and scattering, array processing and seismic techniques of yield estimation.

Accession For	
NTIS GRA&I	☒
DTIC TAB	☐
Unannounced	☐
Justification	

By	
Distribution/	
Availability Codes	

Dist	Avail and/or Special
A-1	

DTIC
COPY
INSPECTED
6

These Final Proceedings contain the papers that were presented at the DARPA/AFGL Seismic Research Symposium, held at the U.S. Air Force Academy 6-8 May 1985.

We thank all of the participants for their efforts in the preparation of the papers, and especially for the fine oral presentations.

Finally, we thank Professor Jack Oliver for taking time from his schedule to present the Keynote Address.

ROBERT A. GRAY
Solid Earth Geophysics Branch
Earth Sciences Division

JAMES F. LEWKOWICZ
Solid Earth Geophysics Branch
Earth Sciences Division

CONTENTS

YIELDS

MISCELLANEOUS

PAPER TITLE: TECTONIC RELEASE AT NTS AND ITS EFFECT ON
REGIONAL DISTANCE BODY WAVES

PAPER AUTHOR: Terry Wallace
Department of Geosciences
University of Arizona

CONTRACT NO.: SFRC F 19628-85-k-0014

SUMMARY: The tectonic release from Pahute Mesa, as constrained by SH wave-form modeling and the polarity of sP, has an average orientation that is a right lateral, srike-slip fault trending N15°W. The tectonic release orientation is very similar for all the events and varies in size depending on yield and proximity to previous explosions. The largest tectonic release event, BENHAM, has a seismic moment of 5.6×10^{24} dyne-cm. The tectonic release has a strong signature on the long-period regional distance seismograms. Since strike-slip orientations have the most dramatic influence on regional distance body waves it is possible to investigate tectonic release for small yields.

CONCLUSIONS AND RECOMMENDATIONS: It is clear that regional distance seismograms will play a major role in verifying compliance with a low yield threshold test ban, so the effects of tectonic release on the regional distance phases Pn and Pg must be better understood. The best procedure to investigate the frequency dependence of the tectonic release signature is to use broad band data. It is also important to model structural path complications. We are undertaking this task by modeling Pg that crosses a basin with generalized rays and finite difference.

Introduction

Most underground nuclear explosions are accompanied by some amount of non-isotopic seismic radiation which is usually interpreted in terms of tectonic release. This tectonic release has a distinct long-period signature on both the body and surface waves. For body waves, SH at teleseismic distances is a fairly common observation and for events with large F factors there can be a significant distortion of the long-period P wave (Wallace et al., 1983) and a phase reversal of SV. One of the most dramatic examples of the effect of tectonic release on surface waves is for certain events in the Shagan River region of the East Kazakh test site where Rayleigh waves are 180° out of phase when compared to low tectonic release explosions (Rygg, 1979).

The signature of tectonic release at short-periods is much less obvious. For most events tectonic release probably has only a very minor influence on the short-period, teleseismic P wave ab amplitude (Bache, 1976; Guta and Blandford, 1983). On the other hand, the P wave coda may show some systematic variation with tectonic release (Burger et al., 1985). Wallace et al. (1983) showed that there is a distortion of long-period P_{nl} waveforms by tectonic release, but Pomeroy et al. (1982) states that tectonic release has little affect on Lg amplitudes (at frequencies of 3 to 10 hz). These apparent discrepancies imply that the signature of tectonic release is frequency dependent. This is most likely the result of crustal structure effects; at short periods the tectonic release signature is dominated by scattering and propagation through laterally varying structure. Barker et al. (1981) have shown that near surface crustal structure at NTS has a large effect on Pg and Lg amplitude which amounts to an order of magnitude.

The best way to resolve the frequency dependence of the tectonic release signature is to window broadband data. The tectonic release for large events

2

at Pahute Mesa is now fairly well understood, so these events can be used to calibrate the trade off between tectonic release and propagation effects. In this paper we review the tectonic release from Pahute Mesa explosions and its signature on long-period regional body waves.

Tectonic Release at NTS

SH waveforms provide the most direct information about tectonic release size and orientation, but the number of events which have sufficient long-period data is limited to large yield explosions. Since 1966, there have been 21 Pahute Mesa explosions (see Table 1, Wallace et al., 1985) which produced teleseismic SH waves. These events provide an ideal data base to study tectonic release because they are spatially related (area of less than 300 km^2), structurally related (mostly in Silent Valley Caldera), and have yields which range over an order of magnitude. For most of these events the SH waveforms are remarkabley similar. Figure 1 shows a comparison of the SH waveforms for MUENSTER and GREELEY. (Note that there is a change in polarity in the MUENSTER waveform between FFC and LHC indicating that there is a node between N25°E and N45°E). The GREELEY and MUENSTER waveforms are essentially identical away from the node. The fact that there is a "characteristic" SH waveform associated with most Pahute Mesa events indicates that the mechanism for tectonic release for all the events is very similar. Wallace et al. (1985) showed that these SH waveforms are nearly identical to those observed for several shallow strike-slip earthquakes in the Basin and Range.

It is not possible to determine the orientation of the Pahute Mesa tectonic release on the basis of tectonic release alone. This is the same problem with the Love waves, the radiation pattern for a vertical strike-slip fault and 45° dip-slip fault (strike rotated 45° from the strike-slip fault)

are identical. Although the radiation pattern is the same for both fault orientations the seismic moments required to match the observed SH amplitudes is different by a factor of two. In addition, the two fault models represent significantly different amounts of P-wave excitation. Fortunately the ambiguity can be resolved with constraints provided by distortions to the P waves. Figure 2 shows the seismograms for several Pahute Mesa events recorded at SHA and SES. The sP phase from the tectonic release dominates the second swing in the P waveform. Both sP and SV are reversed at SES as compared to SHA for BENHAM and GREELEY (high tectonic release events). This node crossing, along with SH waveform modeling were used to constrain the average orientation for Pahute Mesa events. Figure 3 shows the range of fault plane solutions which are acceptable.

An observed SH waveform is a function both of the dislocation history on the fault and the structure of the travel path between source and receiver. If these quantities are known then the seismic moment can be determined on the basis of amplitude. Unfortunately, most of the observed SH waveforms for tectonic release are at upper mantle distances (14° to 30°) and, in general, the waveforms will change dramatically with distance due to the triplication. Further, the structure is dependent on azimuth. The use of a single earth structure to model all the upper mantle records would result in wide variation in the moments determined. In particular, it is very difficult to determine the attenuation, and the assumption of a constant t^* for the entire range in distances is undoubtedly poor. In an attempt to alleviate the problems of determining the complicated upper mantle velocity and Q structure we determined the moments for the tectonic release on the basis of comparison of amplitudes with two earthquakes. These earthquakes are shallow, strike-slip events with orientations similar to the Pahute Mesa tectonic release orientation. The moments are tabulated in Table 1.

4

In an attempt to isolate the dependency of the tectonic release on yield or explosion size the seismic moments were plotted against the average short-period P wave ab amplitude for all available WWSSN and CSN data (taken from Lay et al., 1984). Each ab amplitude has had the instrument gain equalized to unity at a period of one second and geometric spreading corrections were applied to equalize the data to a distance of 50°. The relative size or yield can be determined by using a master event and normalizing the average amplitudes by the master event amplitude. In figure 4 BOXCAR is the master event; HANDLEY has the largest ab amplitude average (1.41) while PIPKIN is the smallest (0.16). This measure of relative size is used instead of published values of yield because it does not require an explicit formulation relating yield to M_b or M_s.

From figure 4 it is clear that although the size of the tectonic release generally increases with yield there are significant exceptions. Most notably, events which are well separated from previous explosions have a larger amount of tectonic release than those close to a previous explosion (eg. BOXCAR and JORUM). In figure 4 those events which are isolated are marked with an H while those in the vicinity of a previous explosion are marked with an L. There is a fairly clear separation of the populations. A least-squares fit of seismic moment to event size shows that the two populations are parallel but offset. The fact that the trends remain separated even at small yields suggest that there is no "threshold" yield for tectonic release.

Assuming that the yield scales with the short-period ab amplitude, then the trends in figure 4 imply that tectonic release at Pahute Mesa scales like yield to the power 1.4. This suggests that at some point the tectonic release should dominate the explosion waveform.

Regional Distance Seismograms

Certain systematic effects emerge when a large number of regional distance seismograms from Pahute Mesa explosions are compared. For example, the P_{nl} waveforms records at ALQ and TUC appear much more like those produced by earthquakes than explosions. Figure 5 is a composite of different explosions recorded on the regional WWSSN network. ALQ and TUC are in the loop direction for the tectonic release orientation in figure 3, while LON, which is in good agreement with the explosion synthetic, is near a node. DUG, which is in the negative quadrant has a greatly reduced P amplitude. Although figure 5 is a composite, it is highly suggestive that there is a significant tectonic release signature on long-period regional waveforms. Strike-slip orientations have the largest effect on the P_{nl} waveforms from explosions. The displacement response from dip-slip faulting is higher frequency than that for strike-slip motion and generally adds or subtracts to the explosion waveform without substantially changing it.

Figure 6 shows the vertical component for 12 Pahute Mesa explosion waveforms at PAS, a long-period (30-90) station 5.5° from NTS. At these periods it is assumed that the travel paths are identical, and most of the differences in the waveform must be due to source. It is interesting to compare events which are spatially close, but separated in time. For example, GREELEY (12-20-66) and KASSERI (10-28-75) are less than 3 km apart and about the same yield, but GREELEY has a much higher tectonic release. In figure 6 the PAS records are very similar except that KASSERI is deficient in the long-periods. By adding a strike-slip source to the KASSERI record it is possible to produce a waveform very similar to GREELEY. This shows the strong long period signature of tectonic release at NTS.

Future Work

At the longer periods ($T \geq 5$ seconds) it is relatively easy to isolate structure and path effects, and there is a strong tectonic release signature for certain events. Once our knowledge of the long-periods is expanded we can attempt to model higher frequency data, such as Pg since we have prior information about the orientation and magnitude of the tectonic release. The use of large yield events to develop a characteristic signature is useful in that the effects of tectonic release may be subtle for small yields. We anticipate that by modeling the 21 events in the Pahute Mesa data set we will be able to extend the analysis to events with yields less than 200 kt.

References

Bache, T. (1982). Estimating the yield of underground nuclear explosions, Bull. Seism. Soc. Am., 72, 5131-5168.

Barker, B.W., Z.A. Der, and C.P. Mrazek (1981). The effect of crustal structure on the regional phases Pg and Lg at the Nevada Test Site, J. Geophy. Res., 86, 1686-1700.

Burger, R.W., T. Lay, C.G. Arveson, and L.J. Burdick (1985). Estimating seismic yield, pP parameters and tectonic release characteristics at the Novaya Zemlya Test Site, Final Technical Report WCCP-R-85-03.

Guta, I.N. and R.R. Blandford (1983). A mechanism for generation of short-period transverse motion from explosions, Bull. Seism. Soc. Am., 73, 571-590.

Pomeroy, P.W., W.J. Best, and T.V. McEvilly (1982). Test Ban Treaty verification with regional data -- a review, Bull. Seism. Soc. Am., 72, 5089-5130.

Rygg, E. (1979). Anomalous surface waves from underground explosions, Bull. Seism. Soc. Am., 69, 1995-2002.

Wallace, T.C., D.V. Helmberger, and G.R. Engen (1983). Evidence of tectonic release from underground nuclear explosions in long-period P waves, Bull. Seism. Soc. Am., 73, 593-613.

Wallace, T.C., D.V. Helmberger, and G.R. Engen (1985). Evidence of tectonic release from underground nuclear explosions in long-period S waves, Bull. Seism. Soc. Am., 75, 157-174.

Table 1.   Tectonic Release from Pahute Mesa Explosions

Name	Date	OT	Lat(N)	Long(W)	Depth(km)	m_b	Est. Yield(kt)	$M_o x 10^{24}$
Almendro	06-06-73	13:00	37.24	116.35	1.064	6.1	570	1.0
Benham	12-19-66	16:30	37.23	116.47	1.402	6.3	1000	5.6
Boxcar	04-26-68	15:00	37.29	116.46	1.158	6.2	1000	1.4
Camembert	06-26-75	12:30	37.28	116.37	1.311	6.1	750	1.4
Cheshire	02-14-76	11:30	37.24	116.42	1.167	5.8	350	0.7
Colby	:03-14-76	12:30	37.31	116.47	1.273	6.2	900	0.8
Estuary	03-09-76	14:00	37.31	116.36	0.869	5.8	350	0.7
Fontina	02-12-76	14:45	37.27	116.49	1.219	6.1	900	2.2
Greeley	12-20-66	15:30	37.30	116.41	1.215	6.3	830	3.1
Halfbeak	06-30-66	22:15	37.32	116.30	0.819	6.1	450	1.0
Handley	03-26-70	19:00	37.30	116.53	1.206	6.4	1900	2.4
Inlet	11-20-75	15:00	37.22	116.37	0.817	5.9	500	0.3
Jorum	09-16-69	14:30	37.31	116.46	1.158	6.1	700	0.5
Kasseri	10-28-75	14:30	37.29	116.41	1.265	6.2	1200	2.0
Mast	06-19-75	13:00	37.35	116.32	0.912	5.9	520	0.5
Muenster	01-03-76	19:15	37.30	116.33	1.451	6.2	600	3.2
Pipkin	10-08-69	14:30	37.26	116.44	0.617	5.6	82	0.2
Pool	03-17-76	14:15	37.26	116.31	0.879	6.0	500	0.2
Scotch	05-23-67	14:00	37.27	116.37	0.978	5.7	140	0.3
Stilton	06-03-75	14:20	37.34	116.52	0.731	5.8	275	0.1
Tybo	05-14-75	14:00	37.22	116.47	0.765	5.9	380	0.3

Figure Captions

Figure 1:   Comparison between the SH waveforms for GREELEY and MUENSTER (top trace).

Figure 2:   Long-period vertical component recordings of several Pahute Mesa events form WWSSN station SHA and CSN station SES. Note that at SHA the second upswing of the P wave increases with increasing SV amplitude. At SES the long-period P waves show a more complicated pattern; for the loarge tectonic release events (BENHAM and GREELEY) the SV and Rayleigh waves are actually reversed as compared to the low tectonic release events.

Figure 3:   The extreme focal mechanisms allowed for the average tectonic release from Pahute Mesa.

Figure 4:   The moment of the tectonic release for the Pahute Mesa events plotted against the average ab amplitude. The explosions have been divided into two populations: (1) those which are isolated and are predicted to have high tectonic release (labeled H), and (2) those which are close to a previous explosion and should have low tectonic release (labeled L).

Figure 5:   The P_{nl} waveforms for several Pahute Mesa explosions (top trace at each station) and synthetics for an explosion source (mieddle trace) and a double couple (bottom trace). Both the observations and synthetics are lightly filtered. The fault orientation for the double couple is strike-slip. The nodal planes are sketched on the location map.

Figure 6:   Vertical seismograms for 12 Pahute Mesa explosions at PAS (30-90). The station is 3.3° from NTS. Numbers to right of traces give the maximum amplitude in mm.

11

SHA $\Delta = 24°$, $\phi = 97°$

P   SV

COLBY

HANDLEY

GREELEY

BENHAM

SES $\Delta = 14°$, $\phi = 15°$

P   SV   R

JORUM

HANDLEY

BENHAM

GREELEY

sec
0   30   60

14

LON
Δ=10.2°
Az=340°
HANDLEY

DUG
Δ=4.1°
Az=45°
HANDLEY

COR
Δ=9°
Az=327°
BENHAM

ALQ
Δ=8.4°
Az=103°
BENHAM

BKS
Δ=4.7°, Az=280°
Obs
Syn. Ex.
Syn. Eq.
MUENSTER

TUC
Δ=6.8°
Az=135°
BOXCAR

LON
BOZ
COR
DUG
BKS
GOL
ALO
TUC

45 sec
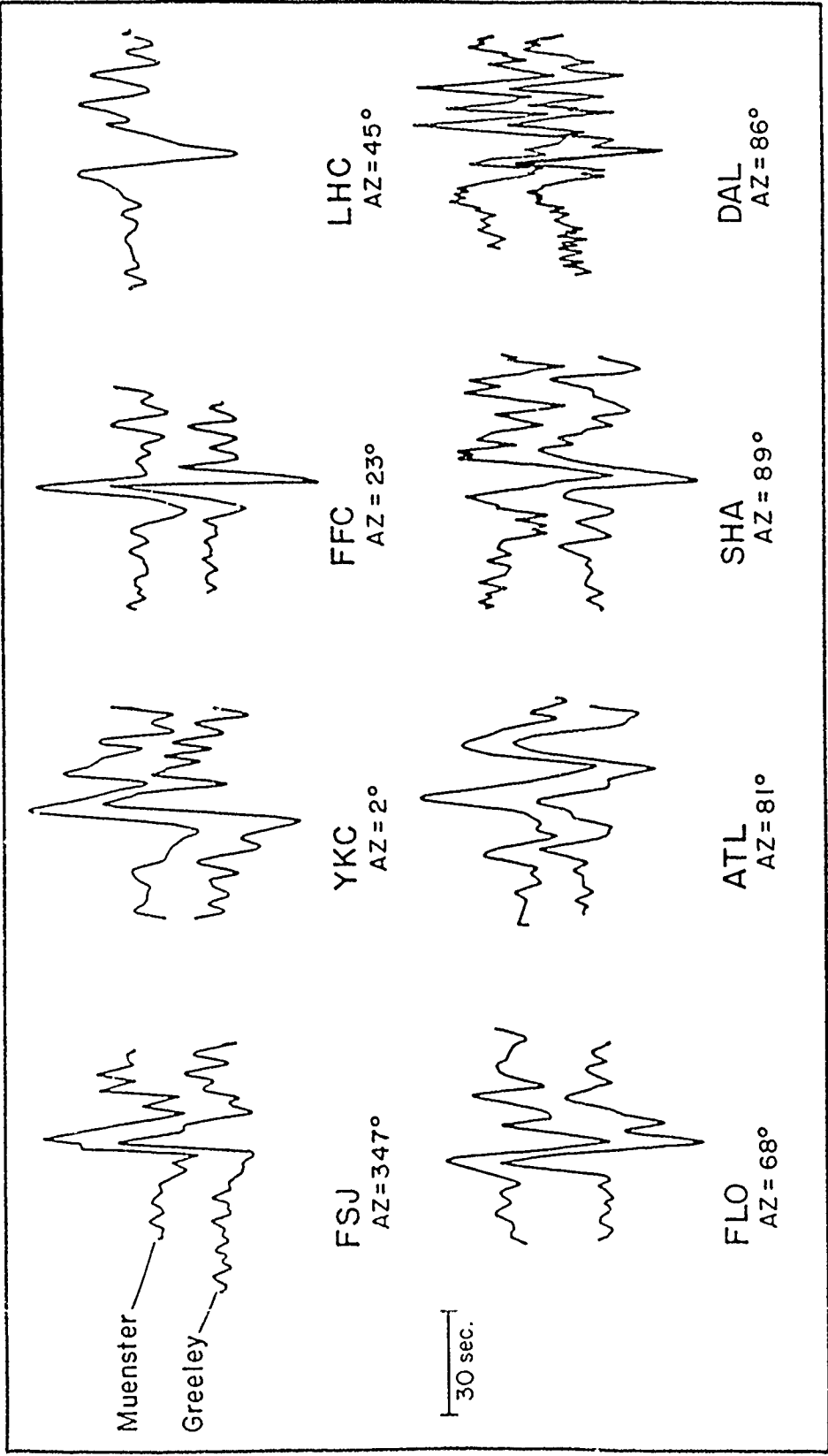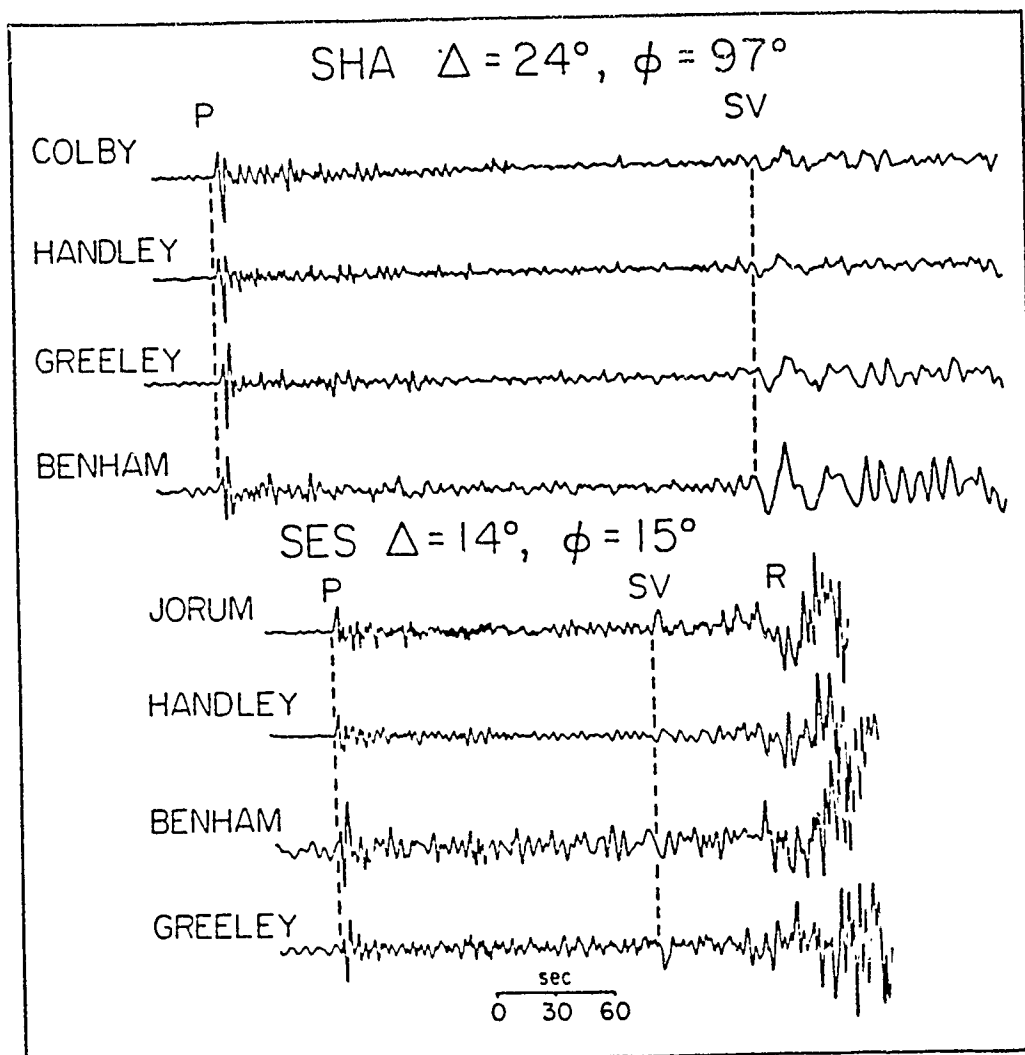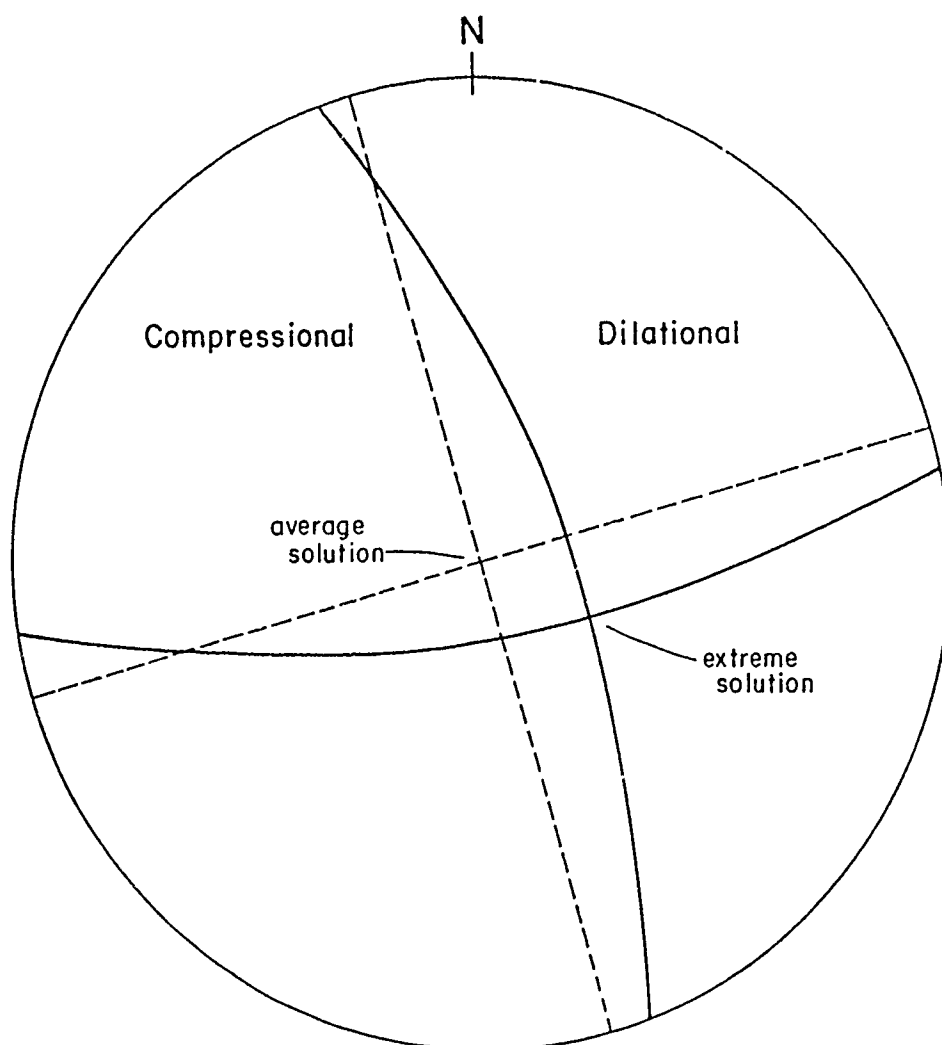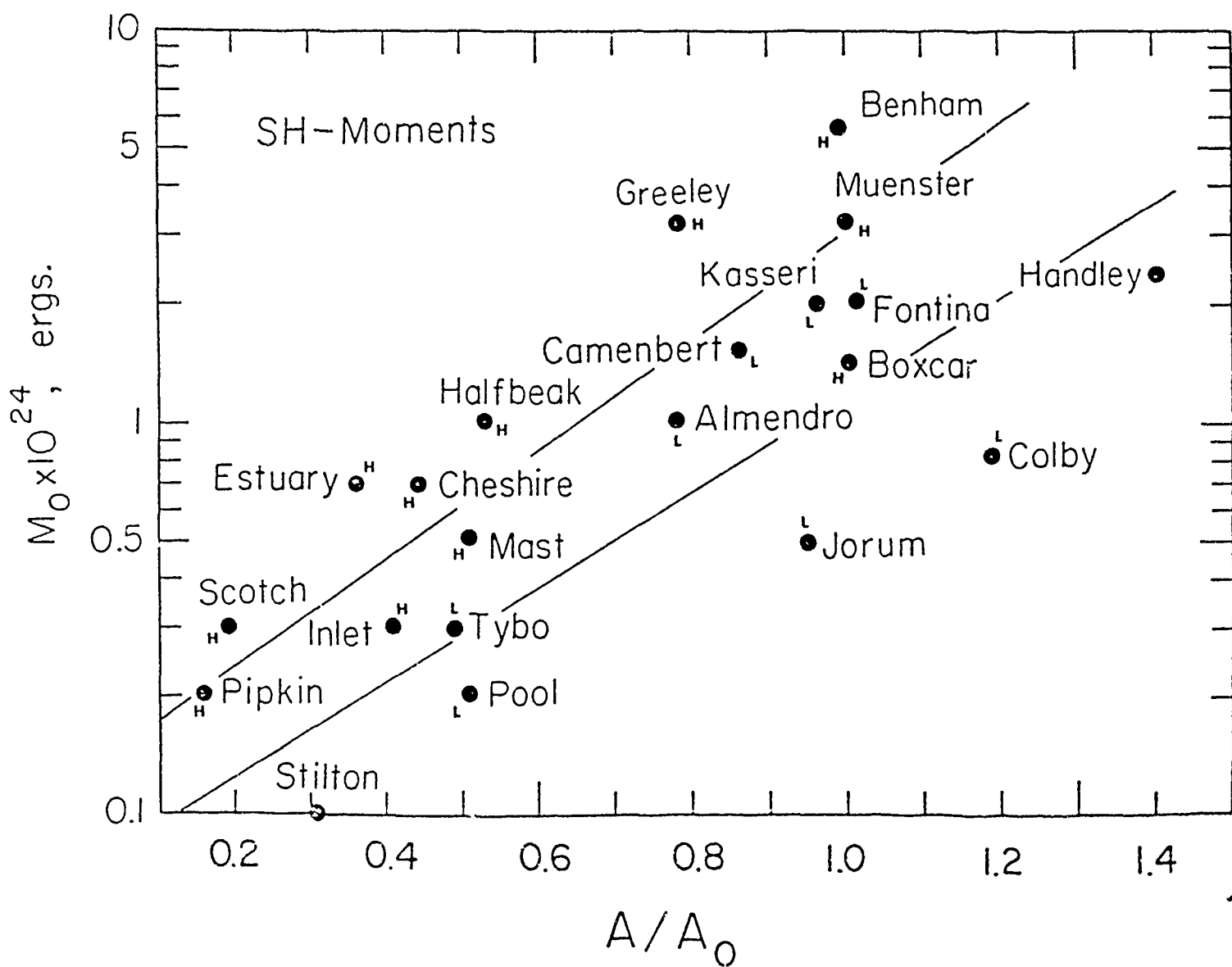
PAPER TITLE:

Modeling surface wave propagation in laterally heterogeneous media.

PAPER AUTHORS:

Janice Regan and Peter Glover
Seismological Laboratory, California Institute of Technology, Pasadena, California 91125

SUMMARY:

We have developed finite element forms of the seismic Representation Theorem (RT) to model Lg waves crossing continental margins and fundamental mode Rayleigh waves from explosions where the source region geology differs from the the propagation path. For the Lg case, we have verified the accuracy of this formulation using a layer-over-halfspace model for which a solution can be independently determined using conventional mode sum calculations. We also used this test case to illustrate the efficiency of an absorbing boundary condition designed to reduce computation time. In the modeling of transition regions, the decrease in crustal thickness from continents to oceans focuses seismic energy This results in surface amplitudes that are 50% larger in the oceanic crust at th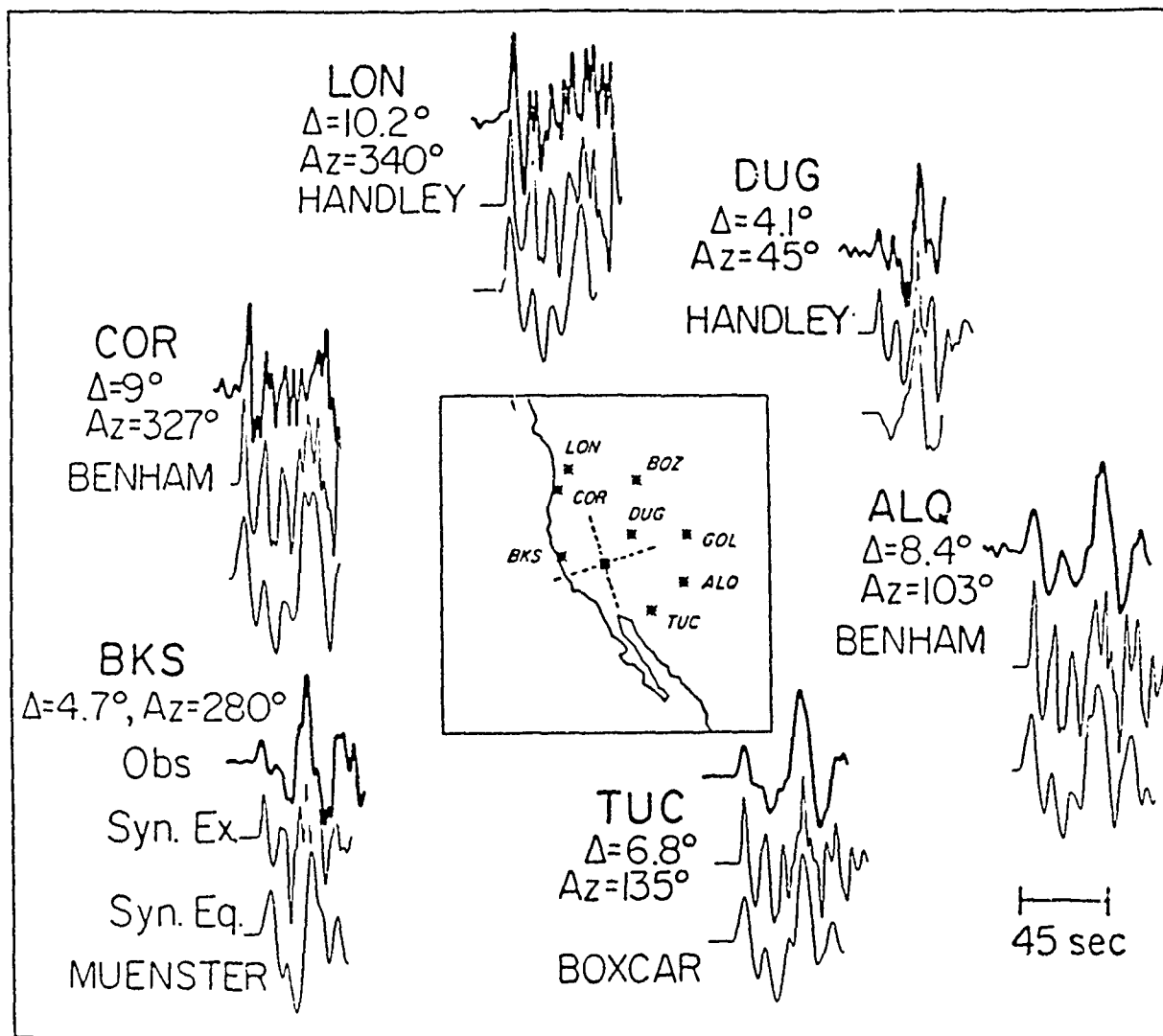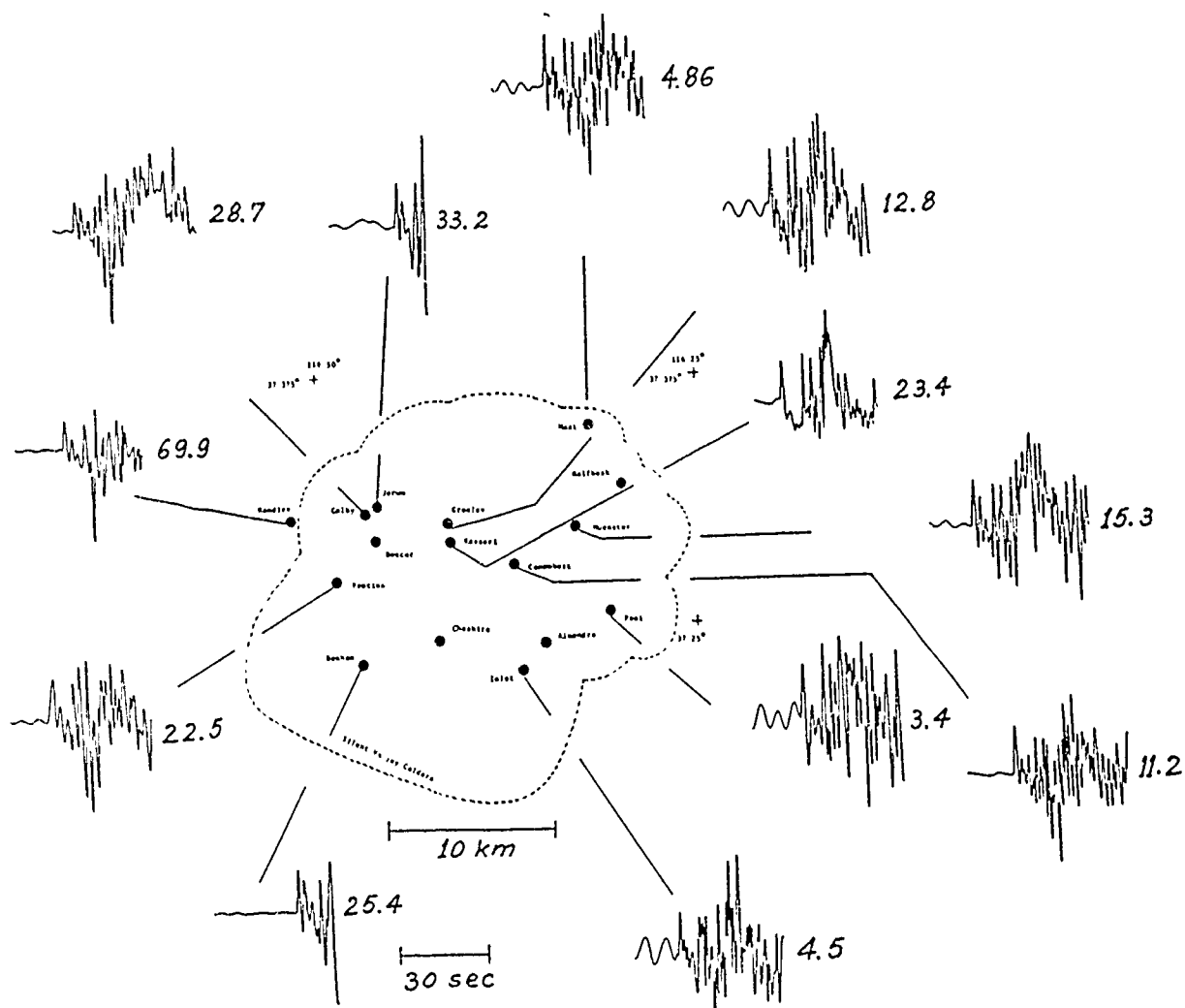e base of the continental than those in the adjacent continent. However, the amplitude of the Lg waves rapidly attenuates as they propagate to larger distances in the oceanic crust. Conversely, amplitudes are reduced when the Lg wavetrain passes through the transition from ocean to continent because energy disperses into the thickening crustal layer. For fundamental mode Rayleigh waves generated by simulated explosions with constant seismic moment, the amplitude of the wavetrain increases when the rigidity of the source material is decreased Amplification factors of 6 were found when the source material was an order of magnitude less rigid than the surrounding medium. These amplitudes were not predicted by the Conservation of Lateral Energy Flux (CLEF) approximation. However, when the impedance contrast is gradational across the boundary the CLEF results agree more closely with the RT calculations.

INTRODUCTION:

The principal advantage of our RT technique for propagating Lg waves is that it enables us to perform the calculations for mode sums. We are not restricted to mode by mode calculations through the transition region as in previous studies. In the results reported here, Lg is represented by the fundamental and first 5 higher SH modes. These 6 modes are then simultaneously propagated through the Finite Element (FE) grid representing the transition region of interest. A further advantage coupling is that the FE calculations are driven by specifying the displacement time histories at 2 adjacent columns of nodes which represent the boundary between the laterally homogeneous region and the transition zone. These time histories can be calculated using standard techniques when the source is separated from the margin by long continental paths. Alternatively, they can be input from other FE calculations, as in the case of the continent-ocean-continent transition discussed below. We should point out however that our technique is only valid for waves propagating at normal incidence.

Our applications of the RT method of modeling Rayleigh waves from explosions in laterally heterogeneous media are presently restricted to cases where the source region can be represented by a cylindrical plug of material embedded in an exterior medium. By modeling the source as a stress-glut of constant moment, we are able to model the effects of material properties on the partitioning of seismic energy

1 /

leaving the source region. Because the RT coupling is performed after the wavefield has propagated out of the source material, multiply reflected and converted phases are taken into account. We can then compare the RT results to calculations performed using CLEF which is widely used to calculate Rayleigh waves crossing vertical boundaries. The CLEF approximation has a similar basis to the vertical energy flux calculation in the Gaussian Beam method. Modifying our technique to include other geometries is quite feasible.

ACCOMPLISHMENTS

To understand the propagation of L_g waves across finite length transition zones the validity and accuracy of the RT method of coupling mode sum displacement histories into the Finite Element (FE) grid must be documented. The layer over a half-space grid used to verify the coupling method is illustrated in Figure 1a. The pair of vertical lines at the left end of the grid show the location of the nodes which are driven by the L_g mode sum displacement histories. These lines represent depth sections of receivers at epicentral distances of 1000 km and 1000.5 km from an 8 km deep source. The individual vertical lines R1 and R2 indicate the locations of the receivers used to monitor the wavefield. Mode sum and FE displacement histories of 55 second duration for the 2 surface nodes on R1 and R2 of Figure 1a are shown in Figure 1b. Those labeled FE were made in 2 steps using the hybrid technique. First, L_g mode sum displacement time histories were calculated for locations corresponding to each of the nodes in the first 2 columns of the grid. Then, the waves were propagated through the remaining portion of the path to the receivers using FE. The traces labeled synthetic were generated using the mode sum technique for the entire path of 1013.3 km or 1026.6 km. The synthetic and hybrid traces agree extremely well at all depths, showing that the hybrid method is valid and accurate.

The execution time of a FE calculation increases proportionally to the number of nodes used. Using reflecting or rigid boundary conditions (BC's), the length of the grid must be extended so that the two way travel time from the last receiver to the end of the grid is longer than the duration of the seismogram. To remove the additional calculation introduced by the increased number of nodes in such an extended grid an absorbing BC can be applied to a selected depth section of nodes near the last receiver. Seismograms can then be recorded near this depth section without being contaminated by reflected energy. The absorbing BC introduced is implemented by averaging a rigid boundary solution and a free boundary solution for the displacement at the end nodes at each time step. The bottom group of 3 pairs of traces in Figure 1b illustrate the efficiency of the absorbing BC. All traces in this group have a duration of 55 seconds. The large grid traces were generated using the hybrid method, with the FE portion of the path calculated in the long grid. The long grid was designed so that no reflections from the end of the grid would reach the receivers during the recording of the displacement history. The traces labeled large grid are identical to the traces in the first group labeled FE. The small grid traces were calculated using only the nodes to the right of the dotted vertical line in Figure 1a for the FE portion of the calculation. Reflections from the end of this short grid are clearly visible. The traces labeled small grid absorbing were also calculated using the short grid for the FE portion of the calculation. However, in this case the absorbing BC was imposed at the dotted vertical line in Figure 1a. The results show that the absorbing BC is very efficient for L_g mode sum input.

Reflections from the bottom edge of the grid should also be considered. In the case of an SH pulse propagating in a half-space reflections from the bottom of the grid also introduce difficulties. However, for the case of L_g mode sums propagating in a layer over a half-space, the L_g wave interacts predominantly with the real boundary between the layer and the half-space. Introducing absorbing BC's on the bottom of the grid makes no perceptible difference in the results. Since including the BC slightly increases the number of operations required at each boundary node at each time step, the bottom edge of

the grid is not constrained in any of the examples described here.

The FE grids used to study the propagation of an L_g wave along a continental to oceanic to continental path are shown in Figure 2a. The forward transition that takes the energy across a continental to oceanic transition region is modeled as a smooth thinning of the crustal layer and a gradual introduction of a water layer over a distance of twenty kilometers. The pair of vertical lines at the left end of the grid represent nodes constrained to move with the input L_g displacement histories. The 2 vertical lines labeled Fc1 and Fc2 show receiver sections used to determine the effect of the transition on the distribution of energy with depth. The pair of vertical lines labeled A are nodes for which displacement histories are recorded to use as input to the reverse transition. The reverse transition grid takes the wave across an oceanic to continental transition region. This transition is modeled as a smooth thickening of crust and thinning of the water layer over a distance of twenty kilometers. The pair of vertical lines at the left end of the grid are the nodes constrained to move with the L_g displacement histories recorded at the 2 columns marked A in the forward transition grid. The 2 vertical lines marked Rc1 and Rc2 show receiver sections used to determine the effect of the transition on the energy distribution with depth. Dots on Fc1, Fc2, Rc1, and Rc2 indicate positions of receivers for which displacement histories are illustrated in Figure 2b. Open circles refer to nodes for which displacement histories are plotted in Figure 2c.

The passage of the L_g wave through the transition region effects the distribution of energy with depth. The energy impinging on the crust/water sloping boundary is mostly reflected. Since no energy is transmitted into the water layer, the remaining energy is focussed along the sloping boundary into the oceanic crustal layer. This can be seen from Figures 1b and 2b. Comparing the seismograms in row Fc1 of Figure 2b and the synthetic traces for a layer over a half-space shown in Figure 1b, the difference in wave shape indicates interference of a reflected wave and the propagating L_g. Displacement histories at Fc2 in Figure 2b show larger amplitudes at than those at corresponding depths on Fc1 at all depths in the oceanic crustal layer. The difference is maximum at the surface of the oceanic crustal layer and decreases with depth, suggesting that some energy is traveling down the sloping surface into the oceanic crustal layer. The energy incident on the sloping crustal/half-space boundary seems to be primarily transmitted. Results indicate that the peak amplitude of the transmitted wave is about 2/3 that of the incident plus reflected wave. Conversely, for the reverse transition, the energy traveling in the oceanic crustal layer spreads into the entire continental crustal layer reducing the amplitudes at any particular depth. About 65% of the energy incident on the sloping half-space/crustal boundary is reflected.

The effects on the waveform and amplitude at the surface as an L_g wavetrain travels along a continental to oceanic to continental path have also been investigated. As the wavefront goes through the continental to oceanic transition surface displacement history amplitudes increase as the crustal thickness decreases. When the wavetrain propagates through the oceanic structure surface amplitudes decay rapidly with distance. Furthermore, as the wavefront passes through the oceanic to continental transition the decay in amplitude accelerates. After the L_g wave renters the continental structure a slow amplitude decay continues for a short distance while the waveform and amplitude stablize. These propagation effects on waveform are shown in Figure 2c.

We have extended our work with the RT modeling of Rayleigh waves in laterally heterogeneous media to incorporate finite-element calculations of a simple explosive source. The source is modeled by adding a stress-glut of constant moment to the dilatational stress at the centroids of 2 adjacent elements along the z-axis of the mesh. Geometrically, the source region is represented by a right cylinder with contrasting rigidity embedded in a plane-layered exterior propagation medium (See Figure 5). Stresses and displacements associated with the total wavefield propagating out of the source region are monitored at a series of surrounding nodes located on the source enclosure surface. The RT method then allows us to calculate the corresponding teleseismic Rayleigh waves by convolving these stress and displacement time

histories with the appropriate Green's functions for the exterior medium.

To establish the accuracy of this procedure we calculated the fundamental mode Rayleigh wave from an explosion in the same material as the upper layer of the propagation medium. Because there is no impedance contrast between the source and propagation media in this case, we can also calculate the solution using a direct method for comparison. We set the source moment at 5×10^{23} dyne-cm, the source depth at 0.4 km, and used the model CIT109 as the propagation medium. Synthetic seismograms were calculated for a long-period vertical component WWSSN seismometer at an epicentral distance of 3000 km. The effects of anelastic attenuation were incorporated. The bottom 2 traces in Figure 4 show the results. The maximum and minimum amplitudes, which occur in the Airy phase portion of the seismograms, agree to within 1.5%. The remaining portions of the 2 waveforms are essentially identical.

By changing the material within the source region cylinder we were able to investigate the effects of source region geology on the amplitudes of teleseismic Rayleigh waves. We selected 3 source media representative of NTS, Yucca tuff, Pahute Mesa volcanics, and Climax Stock granite. The seismic velocities and densities for the source media are given in the following table.

Material Properties of Source Region Models and Corresponding Teleseismic Rayleigh Wave Amplitude Ratios								
SOURCE MODEL (S)	α km/s	β km/s	ρ gm cm^{-3}	$\dfrac{\mu_{CIT}}{\mu_S}$	$\dfrac{(\lambda+2\mu)_{CIT}}{(\lambda+2\mu)_S}$	$\dfrac{A_S}{A_{CIT}}$	RT	CLEF
YUCCA	2.35	1.30	1.86	10.7	10.2	9.98	6.23	1.25
PAHUTE	4.00	1.90	2.30	4.06	2.86	2.64	1.38	0.95
CLIMAX	5.33	2.78	2.67	1.63	1.39	1.25	1.01	0.96
CIT109	6.20	3.51	2.74	1.00	1.00	1.00	1.00	1.00

The seismic moment of the explosion, source depth, propagation medium, attenuation coefficients, epicentral distance, and receiver type were as above. The upper traces to the left in Figure 4 are the resultant seismograms. The peak-to-peak amplitude ratio of the 24s phase of the wavetrain increased with respect to the CIT109 result (see column RT in the table above) as the rigidity contrast between the source and propagation media decreased. However, the magnitude of the observed increase cannot be predicted from the rigidity ratio. The rms amplitudes of the first 6 seconds of the forcing function time histories summed over Σ_{SES}, denoted A in the table, do scale inversely with $(\lambda+2\mu)$ as predicted. Therefore we believe that one effect of the sharp impedance contrast is to set up interference in the Rayleigh wavetrain. The Rayleigh wave amplitude ratios for the corresponding seismograms computed from CLEF are also listed in the table.

When the sharp boundaries of the source region are replaced by impedance gradients, the amplitude of the 24s phase is significantly reduced (see Figure 5). The RT results for the models GRADA and GRADB are in excellent agreement with the CLEF result for YUCCA at this period. However, for GRADC which has a sharp boundary on the side, gradient on bottom, some amplitude cancellation takes place at this period. The RT results all differ significantly from the CLEF approximation at the highest frequencies present in the seismograms. High frequencies differences are most apparent between the 24s and Airy phases.

RECOMMENDATIONS FOR FUTURE WORK:

We plan to extend our work with L_g propagation to include the following:

- develop an additional coupling method to permit modeling of propagation in laterally homogeneous media beyond the FE grid
- establish possible relationships between length of continent/ocean transition zone and attenuation rates.
- investigate the dependence of amplitude decay on the length of intermediate oceanic path in the continent/ocean/continent model.

For the Rayleigh waves from explosions in differing source media we propose to examine:
- effects on spectral M_s determinations by phase-match filtering the RT seismograms with the corresponding CLEF results.
- Other source region geometries, in particular sedimentary basins
- An example where the rigidity of the source region exceeds that of the uppermost layer of the propagation medium.

LG MODE SUM
LAYER OVER A HALFSPACE

a)   GRID GEOMETRY
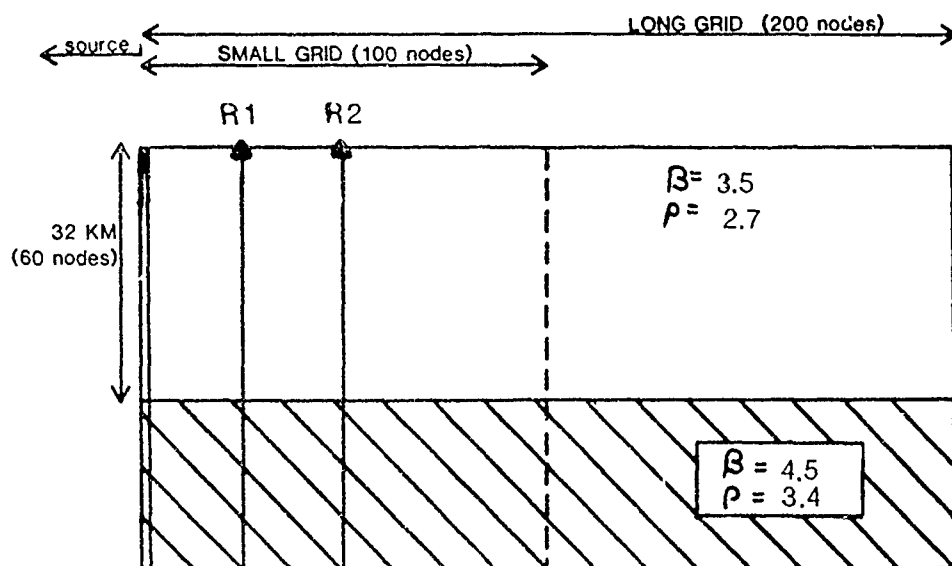
b)   SURFACE RECEIVERS

Figure 1   22

a)

forward transition

$\beta = 3.5$
$\rho = 27$

$\beta = 45$
$\rho = 3.4$

CONTINENTAL - OCEANIC   Fc1   Fc2

reverse transition

$\beta = 4.5$
$\rho = 3.4$

$\beta = 35$
$\rho = 2.7$
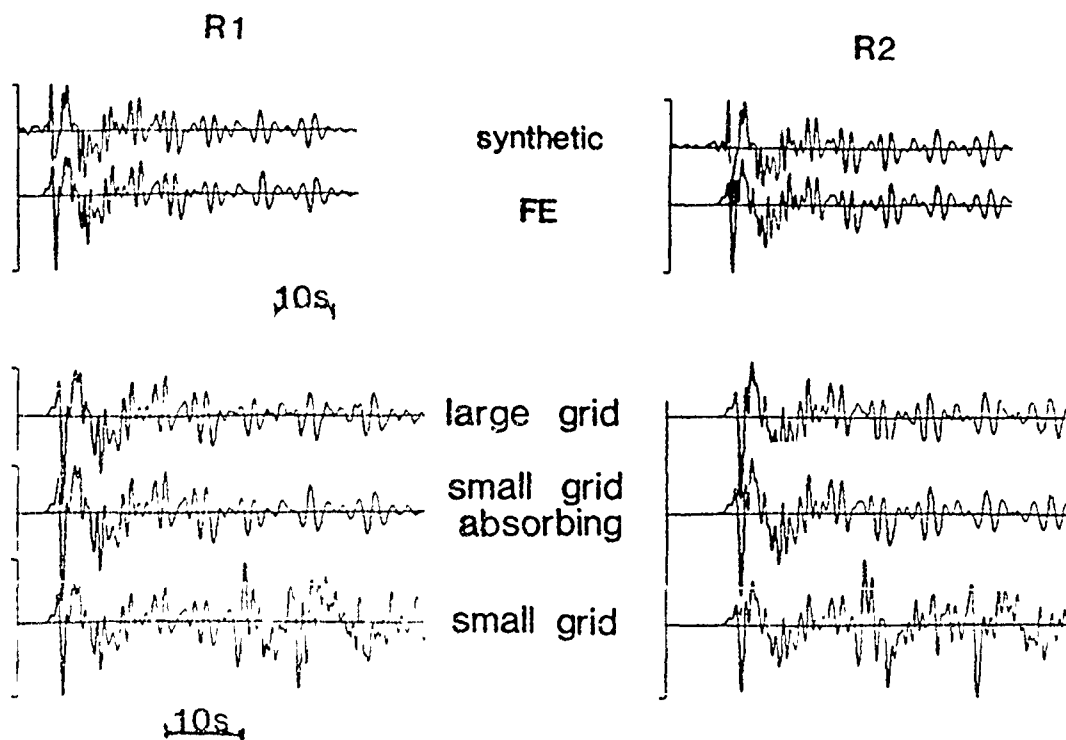
OCEANIC - CONTINENTAL   Rc1   Rc2
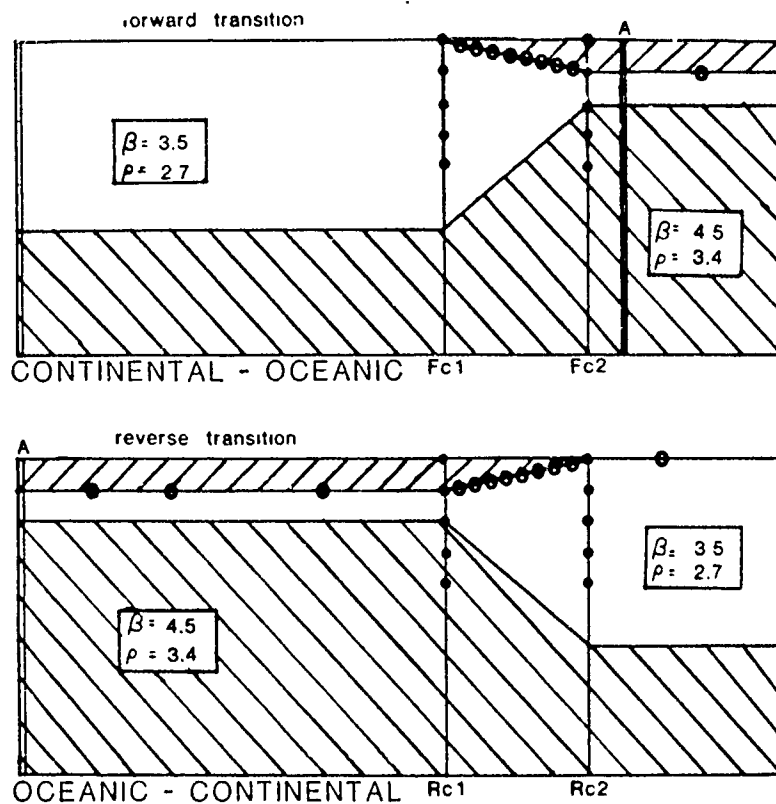
b)   depth sections of displacement histories

Fc1	Fc2	Rc1	Rc2
1320	00	00	1090
1100	1600	1590	724
1150	1080	737	711
969	745	535	653
917	596	433	497

10s

Figure 2

2.3
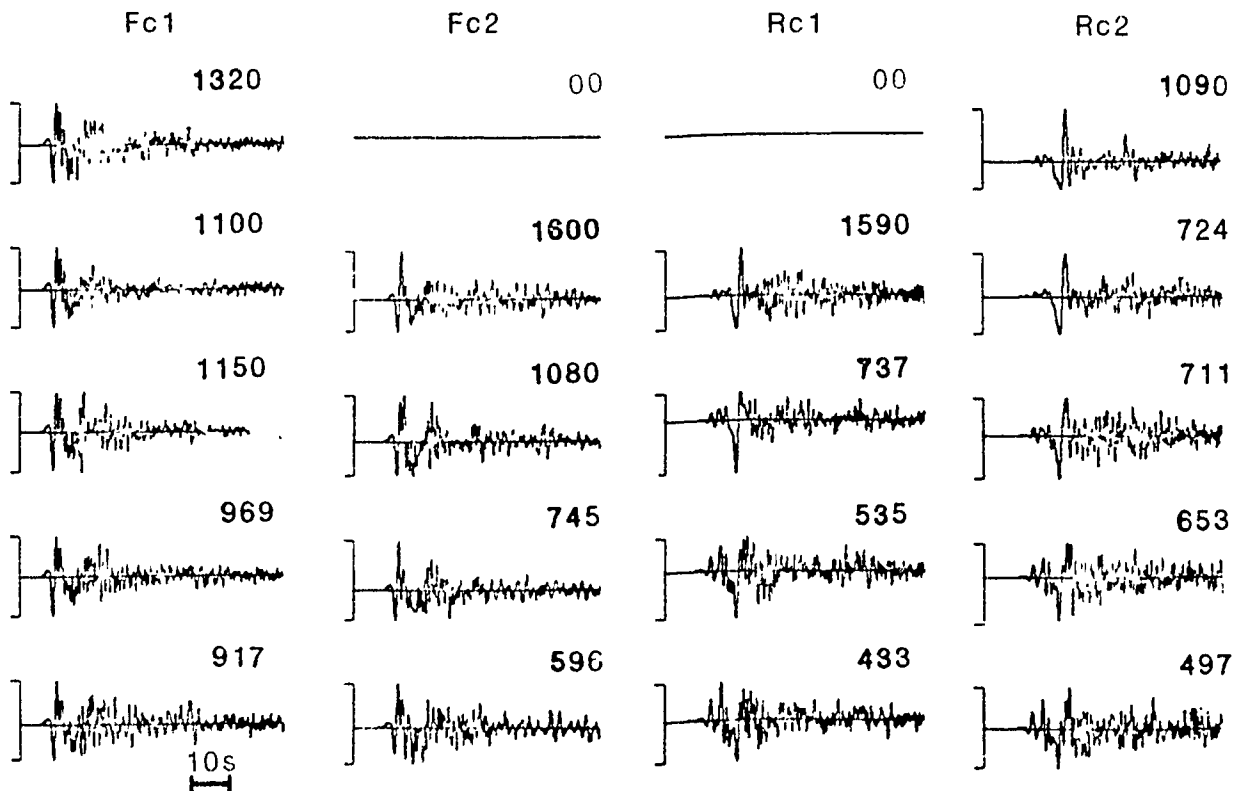
c)

SURFACE RECEIVERS

CONTINENTAL - OCEANIC - CONTINENTAL PATH
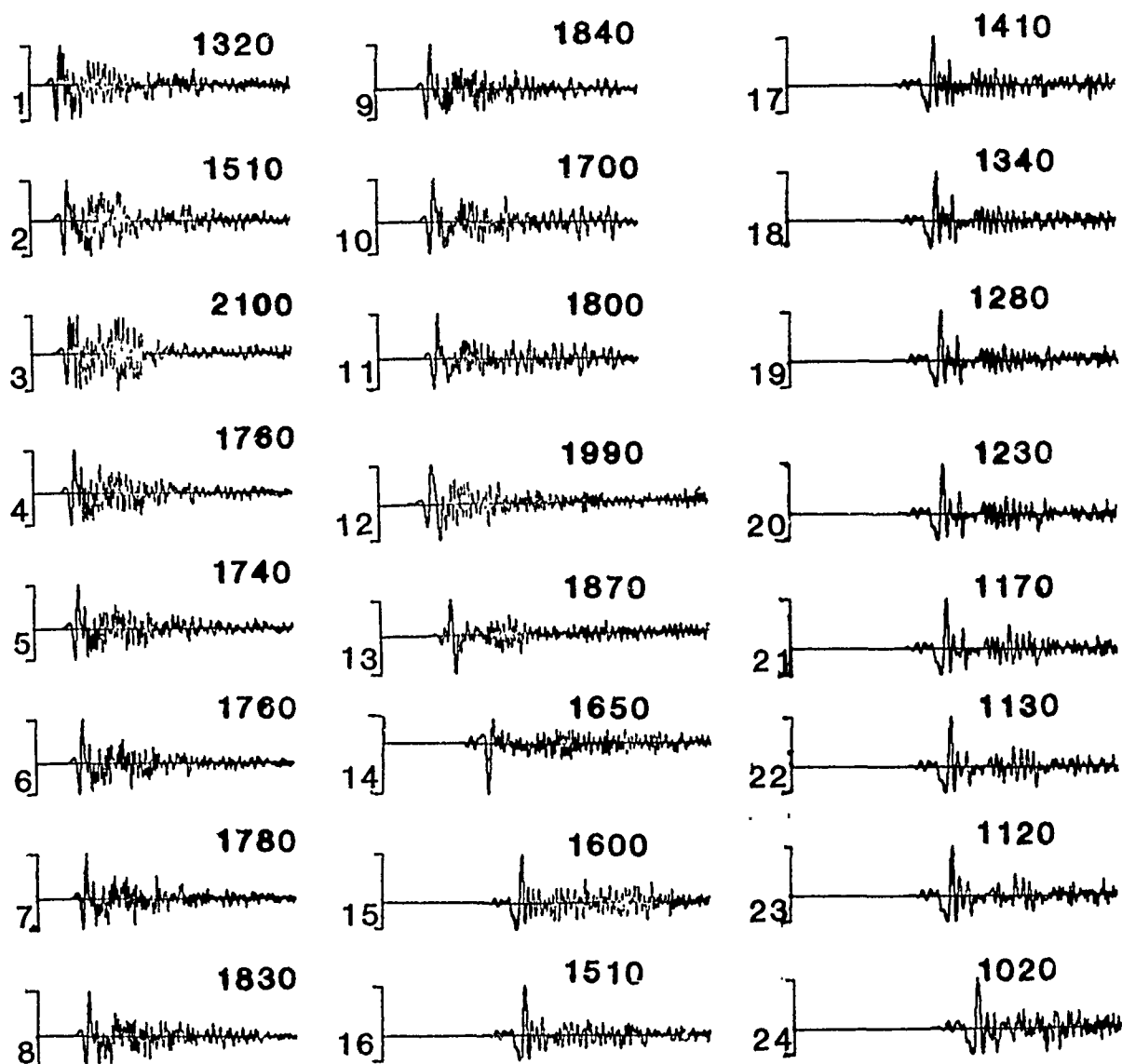
Figure 2: Grid geometries for a continental to oceanic transition and a oceanic to continental transition are shown in part a). The uppermost hatched layer in each grid is a water layer. The second layer is the oceanic crustal layer and the lower hatched layer is the half-space. The pair of lines marked A in the upper grid show the location where the input for the lower grid is recorded. The dots on vertical lines Fc1, Fc2, Rc1, and Rc2 show the locations of receivers for which displacement histories are illustrated in part. b) The open circles show the locations of the surface receivers for which displacement histories are illustrate in part c). The dots that fall on the surface are also included as surface receivers in part c). The numbers above each trace in parts b) and c) give the RMS amplitude for that trace. RMS amplitudes are calculated using a 30 second window. The numbers to the left of each trace in part c) indicate the order of receivers along the surface of the crustal layer starting with 1 at the begining of the forward transition and ending with 24 at the end of the reverse transition.
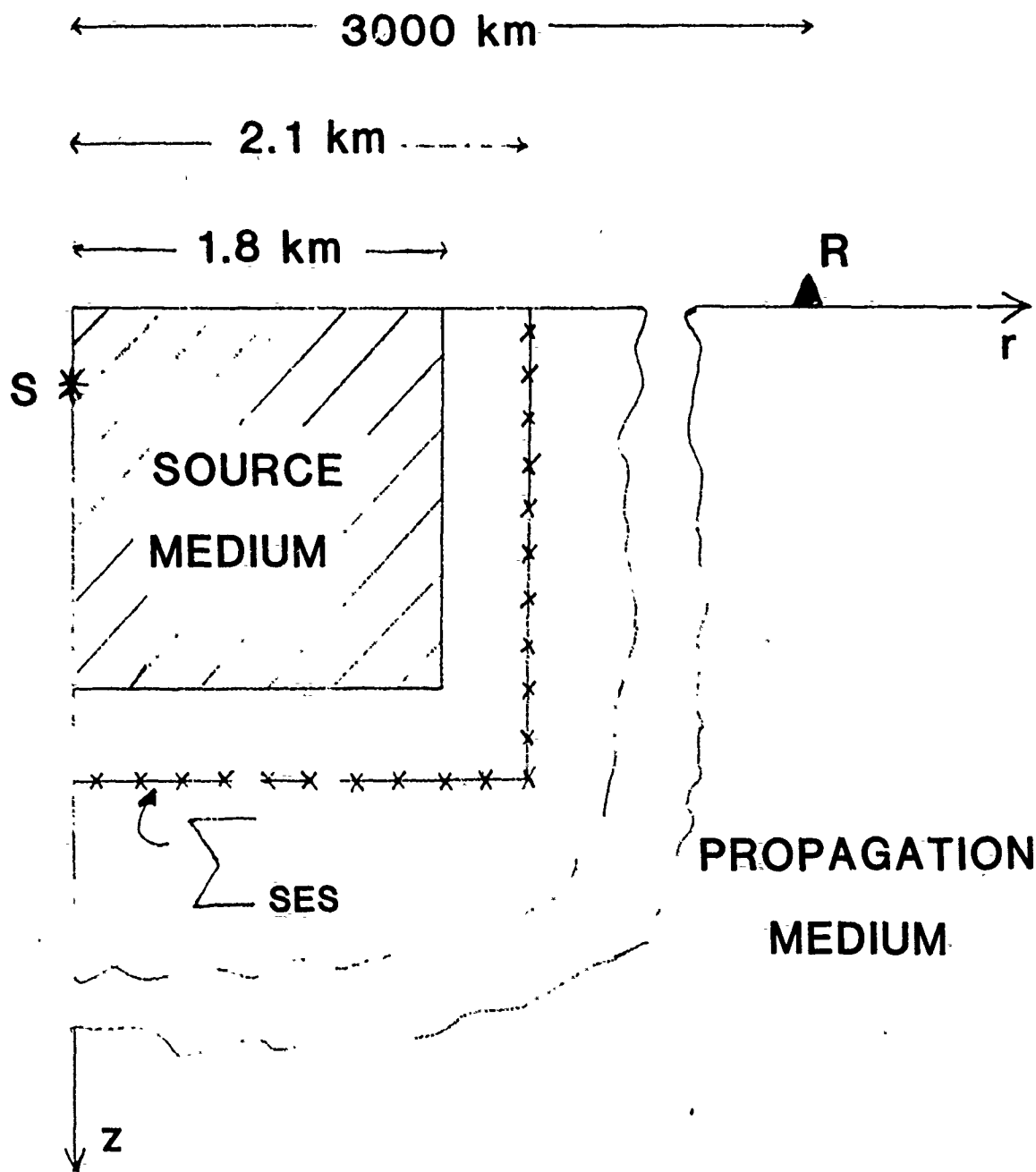
Figure 3: Geometry of the Finite Element grid of the source region and Source Enclosure Surface (Σ_{SES}) used in the Representation Theorem coupling to the propagation medium. Elements are 0.2×0.2 km, total grid size is 19.8×19.8 km. R denotes location of receiver, S location of source.
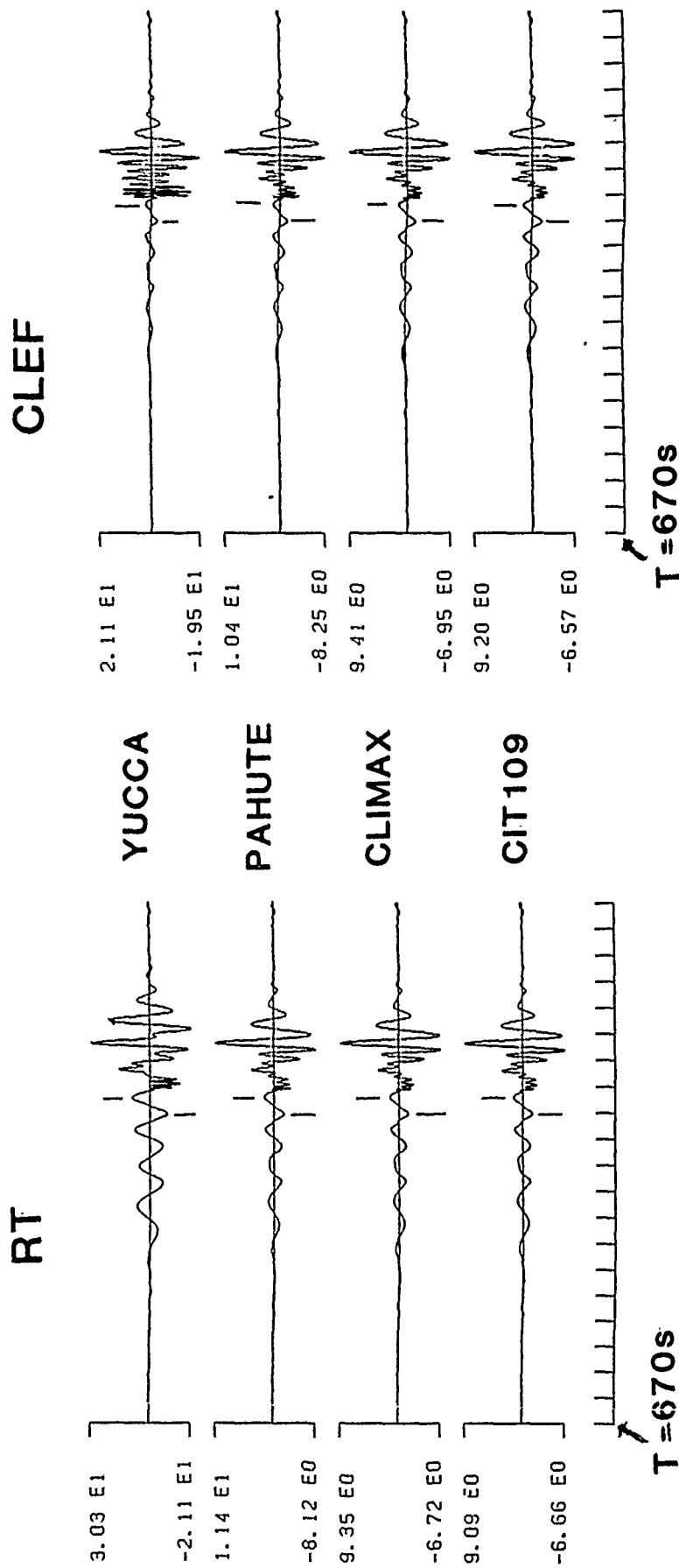
Figure 4: Synthetic fundamental mode Rayleigh waves from an explosion with seismic moment 5×10^{23} dyne-cm recorded by a vertical long-period WWSSN seismometer at 3000 km. Amplitudes are ground displacement in microns. Tick marks are at 20s intervals. Vertical bars indicate position of (p-p) amplitude ratios given in Table 1. LEFT, Representation Theorem (RT) calculations. RIGHT, Conservation of Lateral Energy (CLEF) approximations.

YUCCA
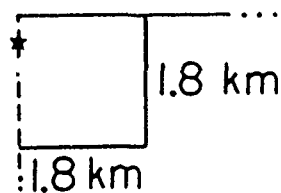
GRADA
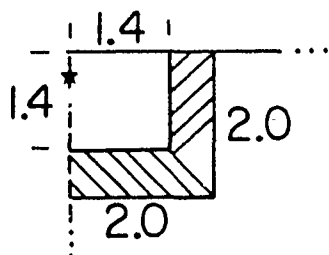
GRADB
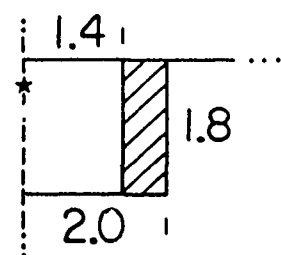
GRADC
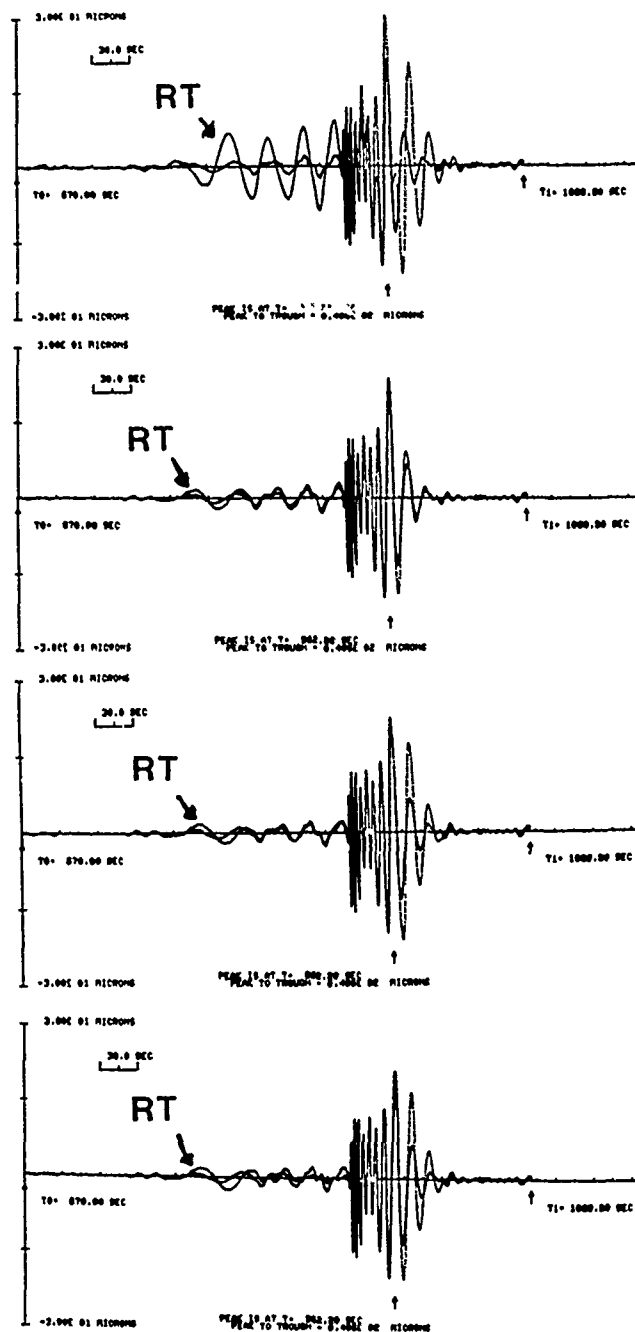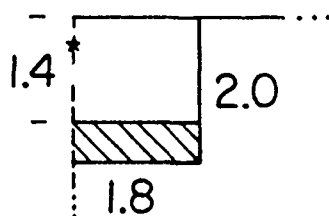
Figure 5: Synthetic seismograms showing effects of an impedance gradient between source material and propagation medium on amplitudes of Rayleigh wavetrain calculated using RT method. Dotted line represents RT result, solid line CLEF approximation to YUCCA model as reference. Hashed area of source region diagrams to left indicates location of gradient.

Long-period S Waves and Yield Estimation

Donald V. Helmberger, Stephen Grand and Gladys R. Engen

Seismological Laboratory

California Institute of Technology

Pasadena, California 91125

Summary

In a recent study by Wallace et al. (1985), the SH waves from 21 underground nuclear explosions at Pahute Mesa (NTS) were investigated with respect to tectonic release. The average orientation appears to be right lateral, strike-slip faulting with a N15° W trend. Seismic moments were determined on the basis of comparisons with two western strike-slip earthquakes near the test site. These two events produced SH-waveforms very similar to those associated with the GREELEY event. The average moments of the two earthquakes was 3.1 x 10^{24} dyne-cm and, thus, all remaining seismic moments were scaled accordingly. In this study we used our recently determined laterally varying upper-mantle structure, Helmberger et al. (1985), to model the SH-waveforms directly and obtained a slightly smaller moment of 1.9 for the GREELEY event.

In this brief report, we will review the GREELEY results and discuss the usefulness of the phase "pS" for yield estimation. Thus, since we can now obtain accurate upper-mantle structures for any region by remote sensing with multi-bounce S waves, we no longer require local earthquakes near foreign test sites for direct calibration.

Results

GREELEY has one of the most complete sets of SH observations and shows a clear node and polarity reversal. Figure 1 displays the most significant records along with synthetics which will be discussed later. Note that the polarity of stations FCC and RKON are reversed, indicating that the node is between N43°E and N25°E. Most of the Pahute Mesa explosions have SH waveforms remarkably similar to these displayed in Figure 1 with some evidence of changes at FCC. This probably means that FCC is near the node and some shifts in orientation are present. This is consistent with the work of Toksöz and Kehrer (1972) who inverted Love/Rayleigh amplitude ratios for six events and found strike-slip faulting with less than 10° of variation in strike.

Assuming that the orientation of the tectonic release is the same for all the Pahute Mesa events, then it is possible to compare the SH waveforms for many events at a single station and determine the relative size of the tectonic release. Figure 2 shows the two long period horizontal components at OXF ($\Delta = 22.40$) for eight different explosions. OXF is close to being naturally rotated (Back azimuth $= 274°$) so the N-S component is SH while the E-W is SV. All the records are at the same amplitude scale; CAMEMBERT has the largest SH amplitude while SLED has the smallest. The explosions are ordered on the basis of m_b as determined by Lay (1984). Although there is considerable uncertainty in relating yield to m_b, it is reasonable to assume that the records in Figure 2 are ordered on the basis of yield. Figure 2 shows that although the SH waveforms are similar for all the events, SH amplitude does not increase simply with explosion size. TYBO and CHESHIRE have nearly the same m_b, but the CHESHIRE SH wave is 3 times as large as the TYBO SH. In general, the SV amplitude is less influenced by the tectonic release. However, on the basis of a north-south, right lateral strike-slip model for the tectonic release it would be predicted that the SV from the explosion and tectonic release would constructively interfere at OXF although it is nearly nodal. This may explain the enhanced SV for CHESHIRE as compared to TYBO,
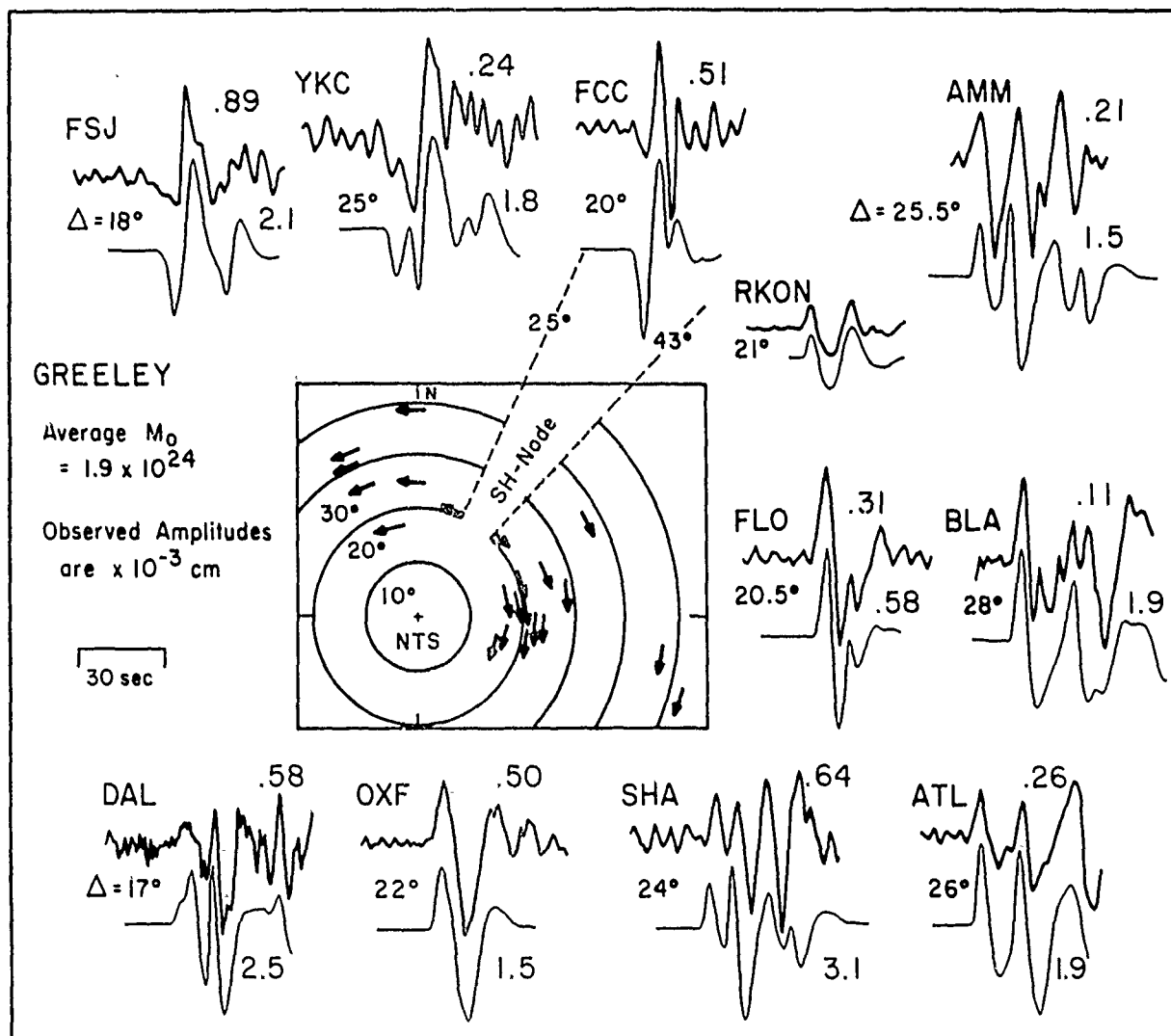
Figure 1: The observed long period SH waveforms for the event GREELEY. The arrows indicate polarities of SH, and are located to indicate the distance and azimuth from NTS (see Nuttli, 1969). Shown below the observed waveforms are synthetics for a strike-slip dislocation model with a source depth of 2.5 km, a trapezoidal time history of (.3, .3, .3 sec) and upper-mantle structure given in Figure 4. The numbers above each observed waveform indicates the amplitude in cm and the numbers next to the synthetics indicate the moment required to match the observed motions at that station. The t_β^*'s range from 2.6 at the nearest station (DAL) to 2.9 at the most distant station (BLA).
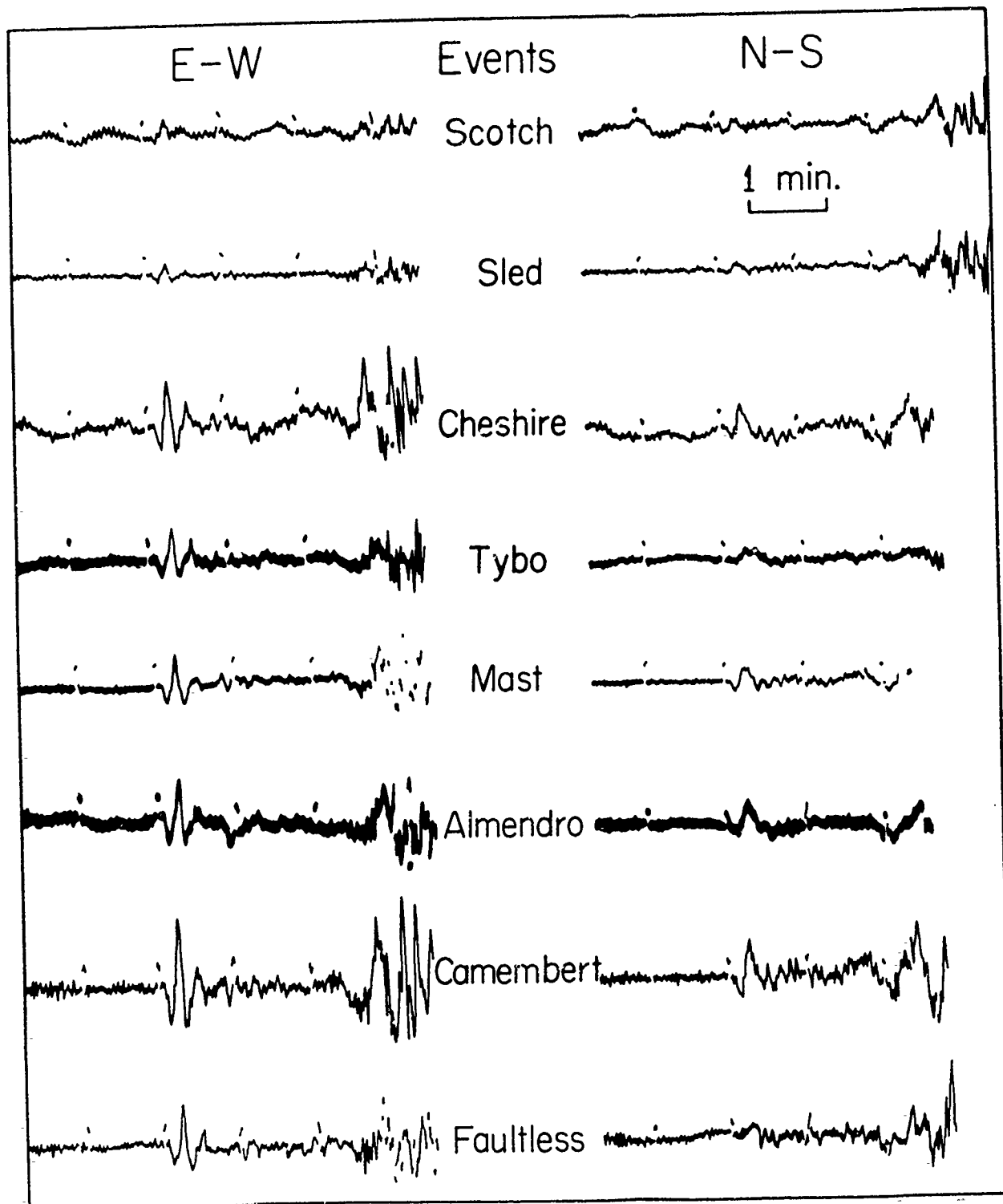
Figure 2: The long-period horizontal seismograms at OXF for several Pahute Mesa explosions. The station is nearly naturally rotated so that the E-W represents SV and N-S is SH. The explosions are ordered on the basis of increasing world-wide, short-period, ab P wave amplitude.

although CHESHIRE may have a larger Δm_b. The SV waveforms are very similar for all the events and it is difficult to identify a signature of tectonic release on the basis of SV alone at a single station.

Although there is some expected SV tectonic release accompanying the phase "pS" it is interesting to simply plot yield versus EW amplitude at OXF. Such a plot shows some scatter at the largest yields but looks quite good for yields less than a megaton. The relative yields for the Pahute shots studied by Lay (1985) are displayed in Figure 3. Also, plotted are the near-field estimates of Barker et al. (1984), the intercorrelation estimate from waveform inversion, Lay (1985), and the AFTAC m_b versus yield determinations. The phase "pS" values were calibrated to the released yields of BOXCAR (1300 kt) and SCOTCH (155 kt) as were the results of Lay (1985). The short period estimates from FAULTLESS exceed the yields of BOXCAR although it plots normal with respect to "pS" in Figure 3. Note that FAULTLESS is off the test site but intercorrelation measurements, Lay (1985), indicate that it's waveshapes are more compatible to say BOXCAR then those of ALMENDRO or CHESHIRE. This result suggests that the short-period excitation from FAULTLESS must be enhanced relative to long-periods when compared to Pahute MESA events. In fact, the errors usually have opposite sign, suggesting that it is the source excitation that is varying rather than coupling. Most of the m_b determinations are commensurable with the intercorrelation results.

Thus, the use of long-period shear seismic waves appears to be useful for improving the accuracy of yield estimations. The problem with using long-period waveforms is the need to account for the effects of tectonic release. This can be achieved by either utilizing waveforms that have no tectonic release signature, or by parameterizing the effects of tectonic release on the signal, (Intercorrelation of SH and SV using SH as a Green's function for SV, Burger and Helmberger (1985). The key is then in our ability to model the SH-waveforms in shape and absolute amplitude.

RELATIVE ERROR
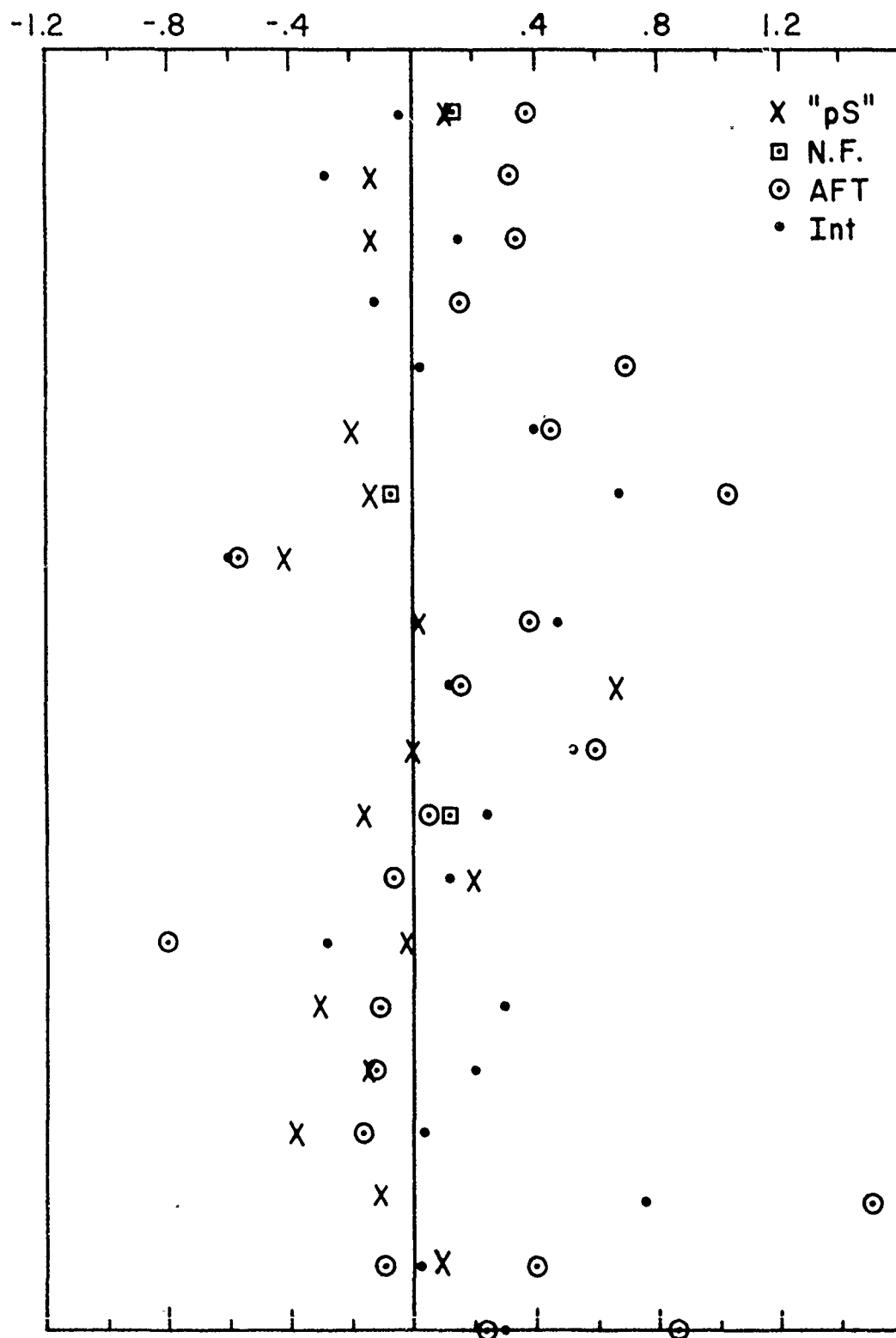
Figure 3: Plot of relative error in yield estimation using four different procedures.
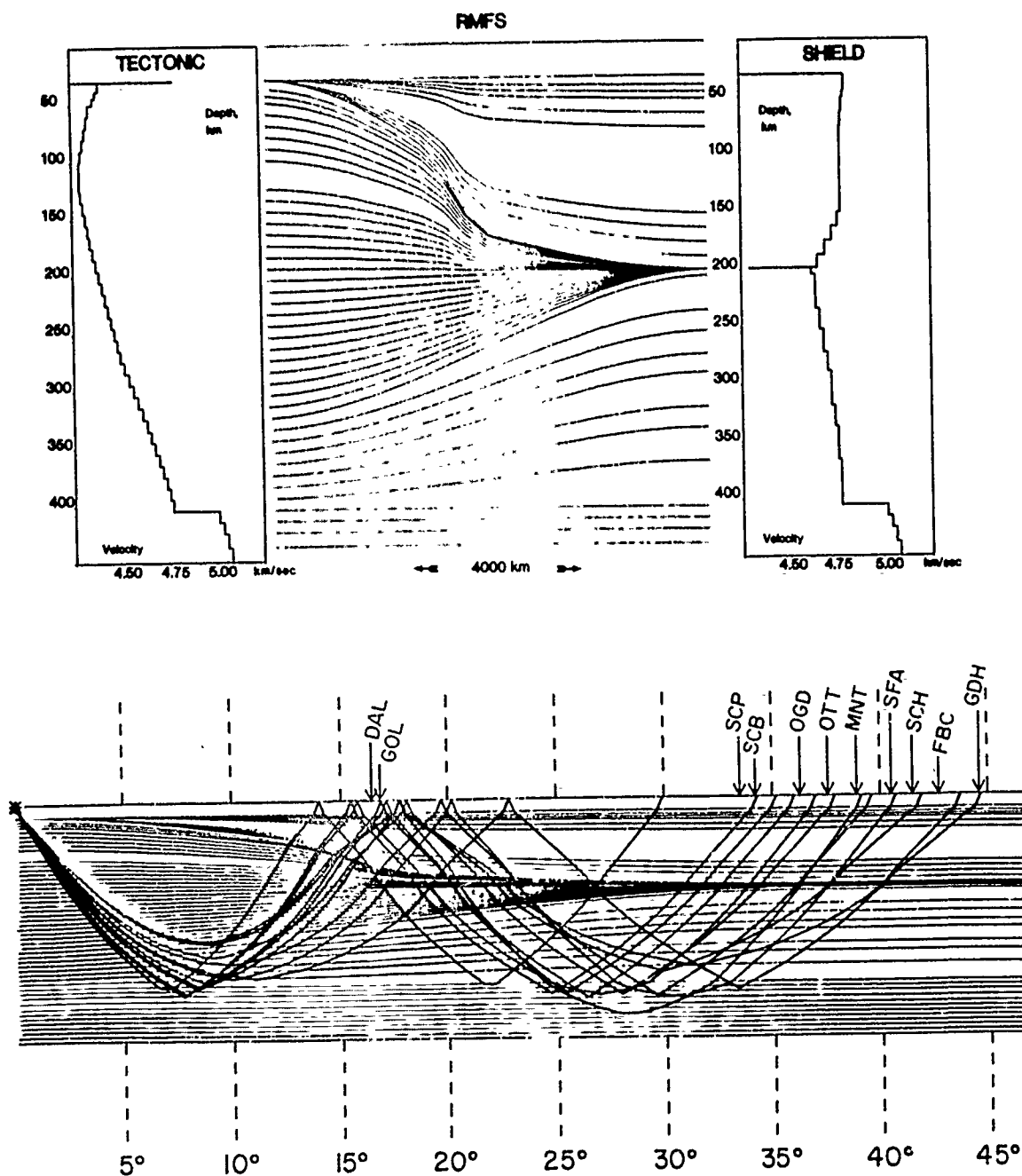
Figure 4: Upper panel displays model RMFS connecting TNA to SNA with a fast transition above the LVZ occurring at about 1500 km from the western edge. The lower panel displays ray paths sampling the upper 400 km velocity structure as a function of lateral position.

34

Some progress on mapping out the behavior of SH-waveforms has been reported on by Grand and Helmberger (1984, 85) with respect to pure path situations, paths in uniform structure. A cross-sectioned model running from California to Greenland is displayed in Figure 4. Note the large increase in lithospheric thickness near the Rocky Mountain Front, roughly an increase of 75 km in thickness over a horizontal distance of 400 km or less. The low velocity zone, with a velocity of 4.4 km/sec, is replaced by a much faster upper 300 km with velocities near 4.7 km/sec or a 7% overall increase. In constructing this model, we relied on the travel times of direct S over the range 10 to 30° and the synthetic modeling of S from 15 to 27°, SS-S from 36 to 52°, SSS-SS-S from 44 to 66°, see Helmberger, Engen and Grand (1985a and b).

Synthetics predicted by this model were displayed earlier in Figure 1. The number following each synthetic is the source strength (M_o) required to match the observed amplitude at that station. In general, the waveforms match quite well although there is some scatter in amplitude, for example FLO and OXF. The average moment estimate is 1.9×10^{24} dyne-cm. This is 40% smaller than the estimates based on calibrating to local earthquakes, see Wallace et al. (1985).

References

Barker, J., Hartzell, S., Burdick, L., and Helmberger, D. V., (1985). Determination of effective source functions and measurement of seismic yields, ARPA Final Report, WCCP-R-85.

Grand, S. P. and Helmberger, D. V., (1984). Upper-mantle shear structure of North America, Geophys. J. R. astr. Soc., 76, 399-438.

Grand, S. P. and Helmberger, D. V., (1984). Upper mantle shear structure beneath the Northwest Atlantic Ocean, J. Geoph. Res., 89, 11465-11475.

Grand, S. P. and Helmberger, D. V., (1985). Upper-mantle shear structure beneath Asia from multi-bounce S waves, submitted Phys. Earth Planet., Int.

Helmberger, D. V., Engen, G. R. and Grand S., (1985). Upper-mantle cross section from California to Greenland, submitted to Geophy. J..

Helmberger, D. V., Engen, G. R. and Grand, S., (1985). Long period wave propagation in laterally varying structure. Geophys. J., R. astr. Soc., in preparation.

Helmberger, D. V. and Engen, G. R. (1974). Upper mantle shear structure, J. Geophys. Res., 79, 4017-4028.

Lay, T. (1985). Estimating .plosion yield by analytical waveform comparison, submitted to Geophy. J..

Nuttli, O. W. (1969). Travel times and amplitudes of S waves from nuclear explosions in Nevada, Bull. Seism. Soc. Am., 59, 385-398.

Toksöz, M. N. and Kehrer, H. H. (1972). Tectonic strain release by underground nuclear explosions and its effect on seismic discrimination, Geophys. J., 31, 141-161.

Wallace, T. C., Helmberger, D. V. and Engen, G. R., (1983). Evidence for tectonic release from underground nuclear explosions in long-period P waves, Bull. Seism Soc. Am., 73, 326-346.

Wallace, T. C., Helmberger, D. V. and Engen, G. R., (1985). Evidence of tectonic release from underground nuclear explosions in long-period S waves, Bull. Seism. Soc. Am., 75, 157-174.

Effect of Lateral Heterogeneity on NTS Strong-Ground Motion

John Vidale, Donald V. Helmberger, and Robert W. Clayton

Seismological Laboratory, California Institute of Technology,

Pasadena, California 91125

INTRODUCTION

Due to the limitations of forward modeling techniques, most studies on sources and path effects at NTS use half-space or plane-layered structural models. We investigate the effect of a laterally varying velocity structure on profiles of strong-ground motions through finite-difference techniques. Synthetic acceleration profiles with a simple RDP source are presented. The agreement between the synthetics and observations is not yet satisfactory, but we have only begun to investigate the source and structure parameter space.

FINITE DIFFERENCE MODELING

A fourth-order finite-difference method is used to generate seismograms for double-couple and explosive sources in elastic media (Vidale and Helmberger, in prep, Vidale et al., submitted to BSSA). First, line sources running through the source area are aligned parallel to the long axis of a basin or geological structure which are idealized to be infinite in length. A "near-field" line excitation is applied such that it produces SH or P-SV vertical radiation patterns compatible with dislocation theory. Next, a line to point source transformation is applied to the F-D results which produces the familiar point source Green's functions. Synthetic seismograms generated by this procedure agree well with those generated by other methods for simple models.

NTS MODELING

The velocity structure shown in Figure 1 is taken from the cross-section in Orkild et al. (1969), and the velocities and densities are inferred from work summarized in Snyder and Carr (1984). Note the low-velocity Silent Canyon Caldera on the east. More vertical gradients are undoubtedly present, but we begin with a blocky model and look for gross features in the synthetics. The velocity structure is not well-known.

Figures 2a and 2b show synthetic profiles of the radial component of acceleration for an explosion and a strike-slip earthquake located within the caldera. The geometry is meant to mimic that of the blast Pipkin. Amplitude is arbitrary, although we know now how to scale the profiles to both seismic moment and Ψ. A modified RDP time function (Helmberger and Hadley, 1981) with K=6 and B=1 is used for both the explosive and earthquake time function. These parameters have been found from modeling the initial pulse in the strong motion records by Hartzell et al. (1981). Several phases may be identified in the profiles. Direct P is noticeably weaker, and S stronger in the earthquake profile. Reverberations in the caldera may be seen in both sections.

We have also generated synthetic seismograms for the reverse profile, which runs from the location of the blast Handley to the east into the caldera. Figure 3 shows the fall-off of peak amplitude for the horizontal component for these four cases. The explosions show roughly the same amplitude fall-off with distance as the earthquakes. The radial components show generally the same pattern as the horizontals. For a given moment, the accelerations from the Pipkin site are roughly five times as large as those from the Handley site, due to the slower velocities and shallower depth of the Pipkin site.

The synthetics do not match the data well. The data differs significantly between the Handley and Pipkin records. A single flat-layered model would have predicted only slight differences due to different source depths. In the presence of lateral velocity variations, source depth can make even less difference for the

seismic waveform (Vidale, 1985, in press). The model we have used may not accurately reflect the velocity structure of NTS. The transverse component of the acceleragram, however, is frequently as large as the radial and vertical components. This suggests that either structure is significantly 3-D or that tectonic release is important. Long-period tectonic release has been inferred from some teleseismic records (Wallace et al., 1983). Since we know how to model double-couple as well as explosive sources, the next area we intend to investigate is whether tectonic release can help us understand the observations without recourse to more complicated source time functions or 3-D structures.

REFERENCES

Hartzell, S.H., L.J. Burdick, and T. Lay, 1983. Effective source functions for Pahute Mesa nuclear tests; Final report WCCP-R-83-3, Woodward-Clyde consultants, Pasadena, Ca.

Helmberger, D.V. and D.M. Hadley, 1981. Seismic source functions and attenuation from local and teleseismic observations of the NTS events Jorum and Handley; Bull. Seism. Soc. Am., **71** : 51-67.

Orkild, P.P., K.A. Sargent, and R.P. Snyder, 1969. Geologic map of Pahute Mesa, Nevada Test Site and vicinity, USGS map 1-567.

Snyder, D.B., W.J. Carr, 1984. Interpretation of gravity data in a complex Volcano-Tectonic region, southwestern Nevada; J. Geophsy. Res., **89** : 10193-10206.

Stump, B.W., and L.R. Johnson, 1984. Near-field source characteristics of contained nuclear explosions in tuff; Bull. Seismo. Soc. Am., **74** : 1-26.

Vidale, J.E., D.V. Helmberger, 1985. Finite-difference seismograms for P-SV waves; manuscript in preparation.

Vidale, J.E., D.V. Helmberger, and R.W. Clayton, 1985. Finite-difference seismograms for SH waves; submitted to BSSA.

Wallace, T.C., D.V. Helmberger, G.R. Engen, 1983. Evidence of tectonic release from underground nuclear explosions in long-period P waves; Bull. Seism. Soc. am., **73** : 593-613.

Assumed Structure

West $\alpha = 2.5$ receivers   East

$\alpha = 3.5$ $\alpha = 2.5$

$\alpha = 4.0$ Pipkin   *

Handley * $\alpha = 5.5$

$\alpha = 3.5$

$\alpha = 6.0$

5 km

Figure 1. Assumed structure for the blasts Pipkin and Handley. Asterisks mark the blast locations. Nineteen stations are spaced 0.6 km apart on the surface. Only the P-wave velocities are labeled, note the range from 2.5 km/sec at the surface to 6.0 at depths greater than about 2 km. S-wave velocities are about half the P-wave velocities. Densities range from 2.0 at the surface to 2.7 at depth. The Silent Canyon caldera on the east side of the section is marked by low velocities. Profile is adapted from Orkild et al. (1969) and Snyder and Carr (1984).

Figure 2. Profile of the horizontal component of acceleration for a source at the site labeled Pipkin in Figure 1. Figure 2a shows an explosive source, while Figure 2b shows an earthquake source. The receiver sites are labeled in Figure 1 and range in distance from 0.6 to 11.4 km. Amplitudes are only relative.

Figure 3. Plot of the log (base ten) of peak horizontal acceleration against distance for four cases. The upper two lines represent explosive sources in the locations labeled Handley and Pipkin in Figure 1. The lower two lines represent strike-slip sources in the same locations.
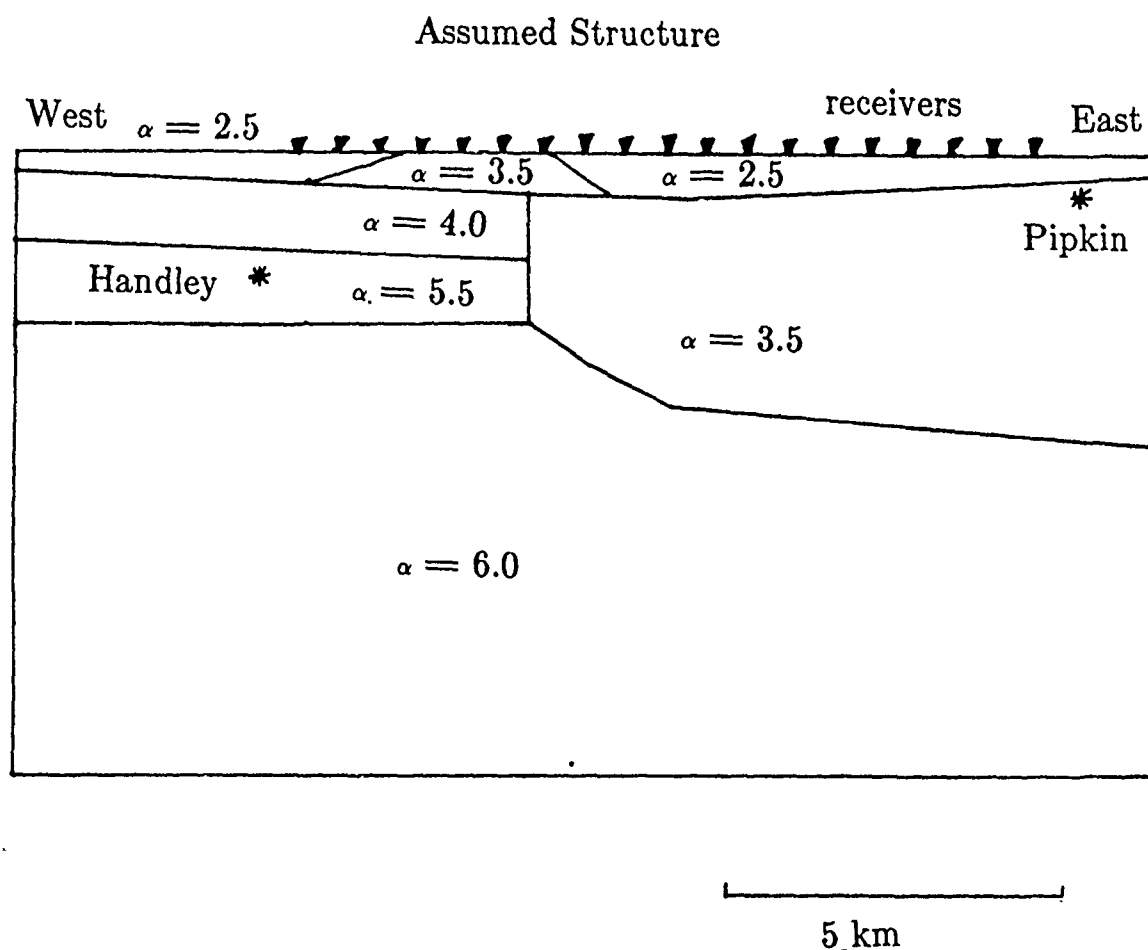
FIGURE CAPTIONS

Figure 1. Assumed structure for the blasts Pipkin and Handley. Asterisks mark the blast locations. Nineteen stations are spaced 0.6 km apart on the surface. Only the P-wave velocities are labeled, note the range from 2.5 km/sec at the surface to 6.0 at depths greater than about 2 km. S-wave velocities are about half the P-wave velocities. Densities range from 2.0 at the surface to 2.7 at depth. The Silent Canyon caldera on the east side of the section is marked by low velocities. Profile is adapted from Orkild et al. (1969) and Snyder and Carr (1984).
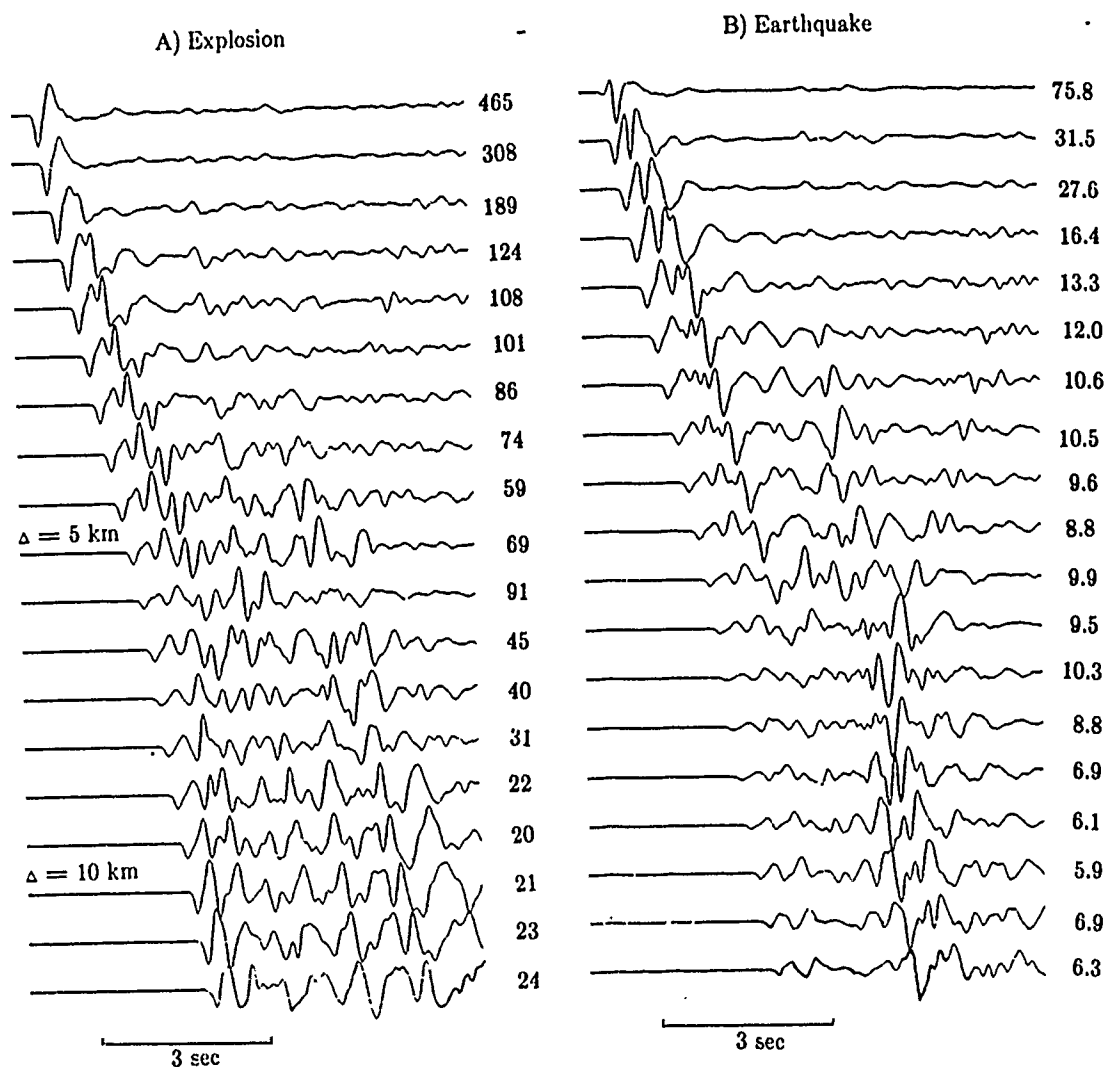
Figure 2. Profile of the horizontal component of acceleration for a source at the site labeled Pipkin in Figure 1. Figure 2a shows an explosive source, while Figure 2b shows an earthquake source. The receiver sites are labeled in Figure 1 and range in distance from 0.6 to 11.4 km. Amplitudes are only relative.
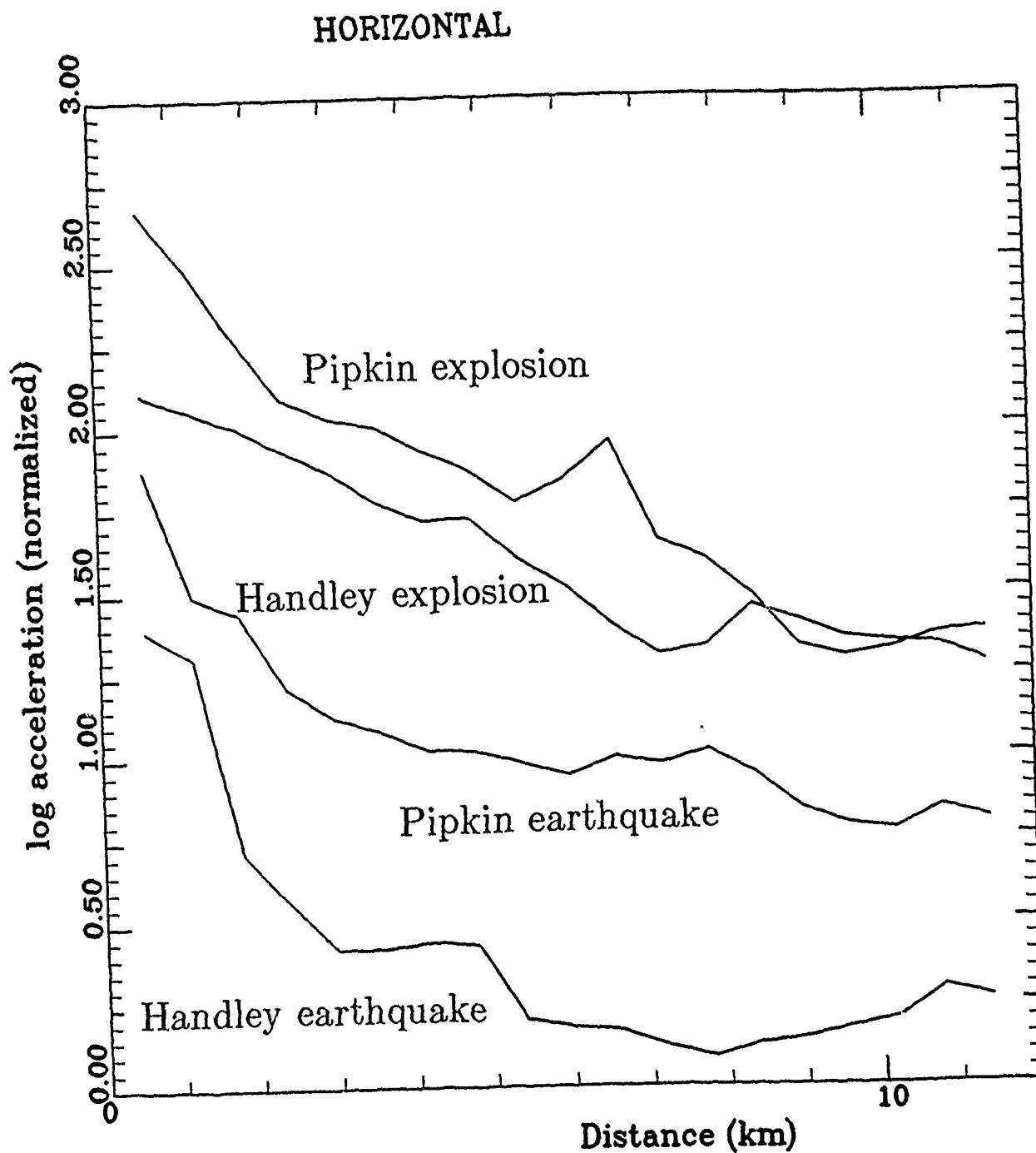
Figure 3. Plot of the log (base ten) of peak horizontal acceleration against distance for four cases. The upper two lines represent explosive sources in the locations labeled Handley and Pipkin in Figure 1. The lower two lines represent strike-slip sources in the same locations.

Geophysical Models of the Shallow Crustal
Structure at Pahute Mesa, Nevada

John F. Ferguson
Center for Lithospheric Studies
University of Texas at Dallas
Richardson, Texas 75080

The existence of regions of anomalous seismic velocity at depths near the base of the crust is well established. The effect of the deep structure on seismic waves is inadequate to explain the anomalous amplitudes and travel times of explosion signals observed teleseismically. If a reliable model of the shallow (< 5 km) crust at Pahute Mesa can be constructed from borehole, gravity and seismic exploration data, predictions of the effect of this shallow structure on teleseismic signals will be made. The model can have a significant effect on the discussion of tectonic stress release in seismic events due to the bias in source mechanism incurred by near source structure.

This study is in its initial phases. Logs of borehole gravity measurements in approximately 80 wells are being examined, and several hypotheses concerning the geologic history of the Pahute Mesa area are being considered. The stratigraphic units will be subdivided into four or five geophysically distinct units, which are mappable by gravity and seismic exploration methods.

Geophysical Models of the Shallow Crustal Structure at Pahute Mesa, Nevada

John F. Ferguson
Center for Lithospheric Studies
University of Texas at Dallas
Richardson, Texas 75080

Within the Nevada Test Site (NTS) there are local differences in the seismic response which cause a variation in the amplitudes of seismic waves observed at teleseismic distance. If body wave magnitudes are corrected for the known explosion yield, a residual of up to $\pm 0.2\ m_b$ unit remains (Alewine, personal communication). These magnitude residuals display a systematic variation and must correlate with zones of attenuation or scattering in the crust or upper mantle under the test site. Note that the magnitude estimates average over azimuth and take off angle and that studies of individual shot/station pairs may also show substantial amplitude variation (Lynnes and Lay, 1984).

Minster, et al (1981) have made a study of travel time residuals from NTS events in an effort to define the three dimensional structure of the test site down to depths of 150 km into the mantle. They have found a well defined velocity anomaly under Pahute Mesa in the upper mantle confirming an earlier prediction of Spence (1974). The data used in this study lacked resolution in the shallow (<10 km) portion of the crust. One conclusion of this investigation was that the magnitude residual pattern must be accounted for by shallow structure.

Ferguson (1983) studied the magnitude residuals at Yucca Flat, Nevada and found it possible to explain most of the observed variation by resonance and scattering effects in a two dimensional geophysical model of the Cenozoic basin at Yucca Flat. The geophysical model was very well constrained by boreholes, gravity and seismic data. The seismic response of this detailed model was evaluated by the Aki and Larner (1970; Bard and Bouchon, 1980a and 1980b) method with reasonable

accuracy.

It is proposed that shallow structure at Pahute Mesa has a similar effect that can be predicted and calculated. One must recognize, however, that Pahute Mesa is a more complicated geologic environment without the well defined geophysical contrasts known at Yucca Flat. In figure 1, the magnitude residuals are superimposed on the Bouguer gravity for Pahute Mesa and a very good correlation is observed. This suggests that structure can be mapped which will produce the necessary seismic response.

Pahute Mesa is underlain by a thick sequence of Tertiary volcanic rocks deposited in and around a sequence of calderas. No drill hole has ever penetrated the entire sequence into Paleozoic basement rocks. In addition there is a north-south trending basin and range structure overprinting the caldera structure. In spite of the lack of a well defined Paleozoic basement as at Yucca Flat there are recognized older volcanic rocks with lower porosity and higher density in many of the wells throughout and in outcrop in the southeastern portions of Pahute Mesa (Beyers, personal communication). These rocks may constitute the geophysical basement and provide the necessary variability in the shallow velocity structure to account for the magnitude residuals.

Existing data available for interpretation of geophysical structure consists of over one hundred boreholes as shown in figure 2 and about 400 gravity observations plotted in figure 3. The Bouguer anomaly is contoured in figure 4. Notice the well defined gravity low associated with Pahute Mesa.

Gravity logs are currently being examined in order to determine the densities of the various lithologic units. Two of these logs are presented in figure 5. In the PM-1 log the data are well represented by a linear density function as expected for a porous clastic rock. The oldest units have a constant density of about 2.5 gm/cc. In the shallow portions of UE20f a high density unit occurs within the

Rainer Mesa member. This unit is very uniform and well mapped by the boreholes. It can be accurately modelled and will not complicate the interpretation of the gravity data.

In order to illustrate the existance of a shallow, geophysically distinct layer at Pahute Mesa the profile located in figure 6 has been plotted in figure 7. The geologic cross section was simplified from Orkild et al (1969). The white patterned rocks are punger volcanic rocks characterized by the linear density function in figure 5. The stippled pattern indicates relatively high density Rainer Mesa rocks and the cross hatched pattern corresponds to dense (≥ 2.5 gm/cm^3) pre-silent Canyon rocks which seem to constitute a geophysical basement. The borehole control for this profile is indicated and density profiles for UE20f and PM-1 can be found in figure 5. The excellent correspondence of the gravity profile to the pre-silent Canyon interface indicates that this shallow structure can be mapped by conventional geophysical methods.

This study is in its initial phases. In the future the following work will be performed:

1) Lithologic units will be geophysically characterized based on geophysical logs.

2) Additional gravity data will be obtained at Pahute Mesa in selected areas to supplement the existing stations. (The coverage will be increased from 400 to 800 stations.)

3) A simplified four or five layer, three dimensional, shallow crustal model will be compiled using borehole and gravity data.

4) The feasibility of performing a seismic reflection/refraction experiment at Pahute Mesa to map the older volcanics will be investigated. The work of Hoffman and Mooney (1983) at Yucca Mt. lends some encouragement to this possibility.

5) Several seismic profiles would be run pending the results of 4. The geophysical model would then be refined using the seismic data.

6) An evaluation of the seismic response of the geophysical model will be made using an effective numerical technique, such as that of Aki and Larner (1970) and the results compared to teleseismic signals from Pahute Mesa explosions.

REFERENCES

Aki, K. and K. Larner, (1970), Surface motion of a layered medium having an
   irregular interface due to incident plane SH waves, J. Geophys. Res.,
   v. 75, p. 933-954.

Bard, P. and M. Bouchon, (1980), The seismic response of sediment filled
   valleys. Part 1 the case of incident SH waves, Bull. Seis. Soc. Am.,
   v. 70, p. 1263-1286.

Bard, P. and M. Bouchon, (1980), The seismic response of sediment filled
   valleys. Part 2 the case of incident P and SV waves, Bull. Seis. Soc.
   Am., v. 70, p. 1921-1941.

Ferguson, J., (1983), Body wave magnitude variation at Yucca Flat, Nevada, in
   Southern Methodist University Final Technical Report to Air Force Office
   of Scientific Research for contract #F49620-80-C-0010 covering Oct. 15,
   1981 to Oct. 14, 1982, E. Herrin and T. Goforth.

Hoffman, L. and W. Mooney, (1983), A seismic study of Yucca Mountain and
   vicinity, southern Nevada: Data report and preliminary results, U.S. Geol.
   Surv. Open File Rep., 83-588.

Lynnes, C. and T. Lay, (1984), Defocussing of short period P waves by a high
   velocity anomaly beneath Pahute Mesa, abstract for the Fall Annual Meeting
   of the American Geophysical Union, San Francisco, CA, Dec. 3-7, 1984.

Minster, J., J. Savino, W. Rodi, T. Jordan and J. Masso, (1981),

Three-dimensional velocity structure of the crust and upper mantle beneath

the Nevada Test Site, Systems, Science and Software report SSS-81-5138.

Orkild, P., K. Sargent, R. Snyder, (1969), Geologic map of Pahute Mesa, Nevada

Test Site and vicinity, Nye County, Nevada, USGS Miscellaneous Geologic

Investigations Map I-567.

Spence, W., (1974), P-wave residual differences and inferences on an upper

mantle source for the silent canyon volcanic centre, southern Great Basin,

Nevada, Geophys. J. R. Astr. Soc., v. 38, p. 505-523.

37° 22' 30"

37° 7' 30"

116° 30'

116° 15
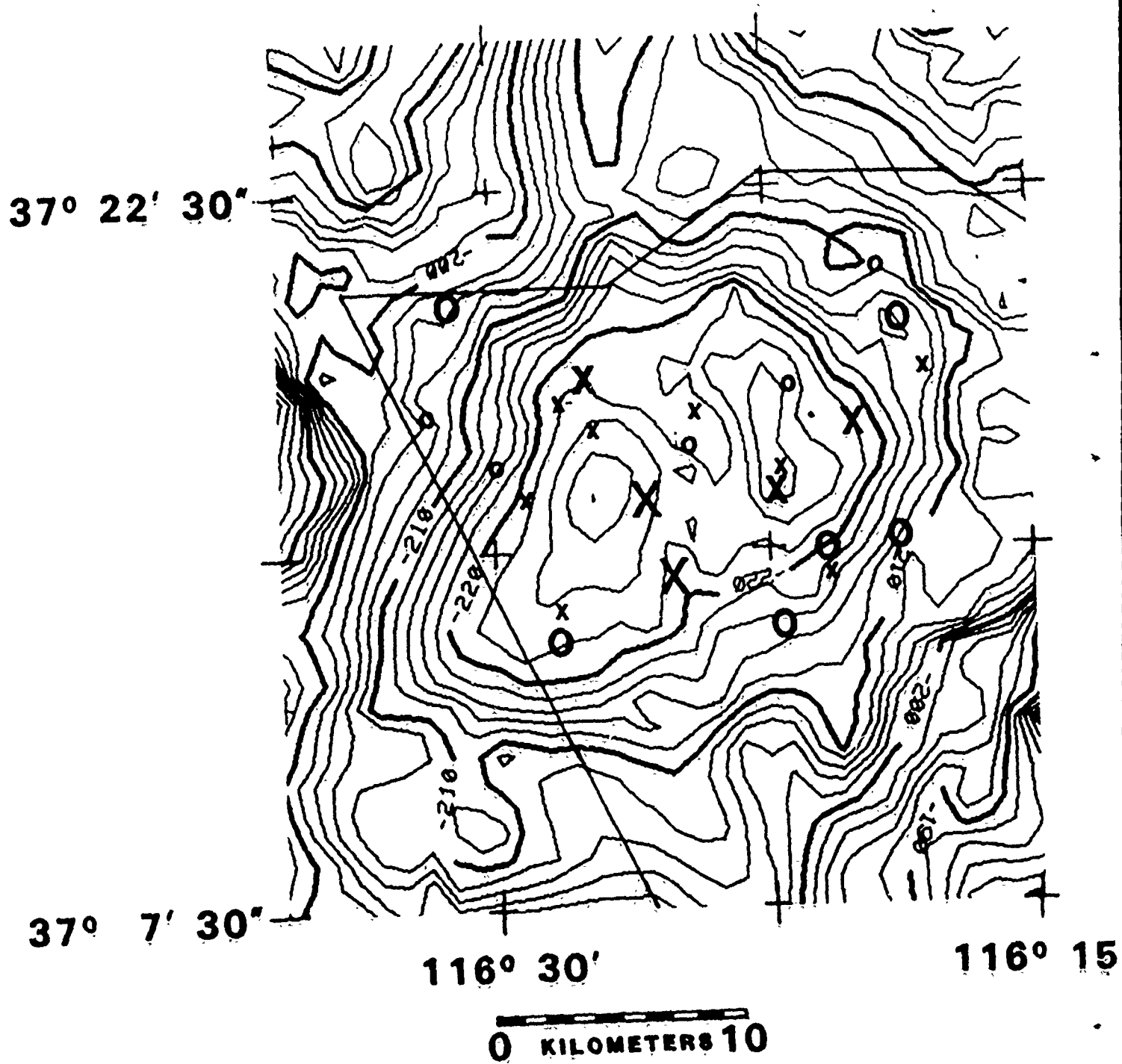
0 KILOMETERS 10

BOUGUER GRAVITY 2 mgal CONTOURS

Δmb

O		≥	0.2
O	0.1	—	0.2
o	0.0	—	0.1
x	−0.1	—	0.0
X	−0.2	—	−0.1
X		≤	−0.2

Figure 1

52

BOREHOLE LOCATIONS
PAHUTE MESA, NEVADA

Figure 2

53
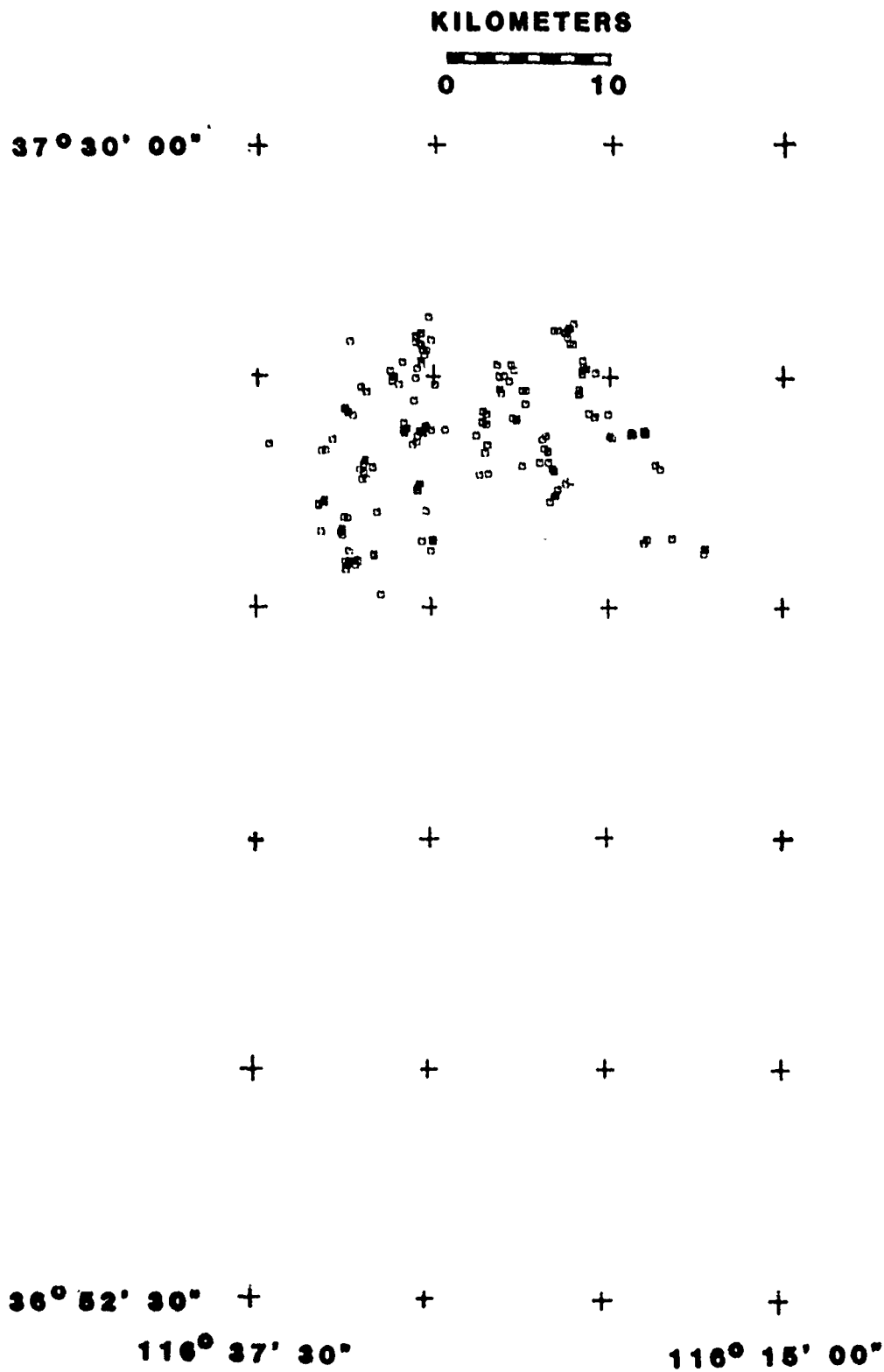
GRAVITY STATIONS
PAHUTE MESA, NEVADA
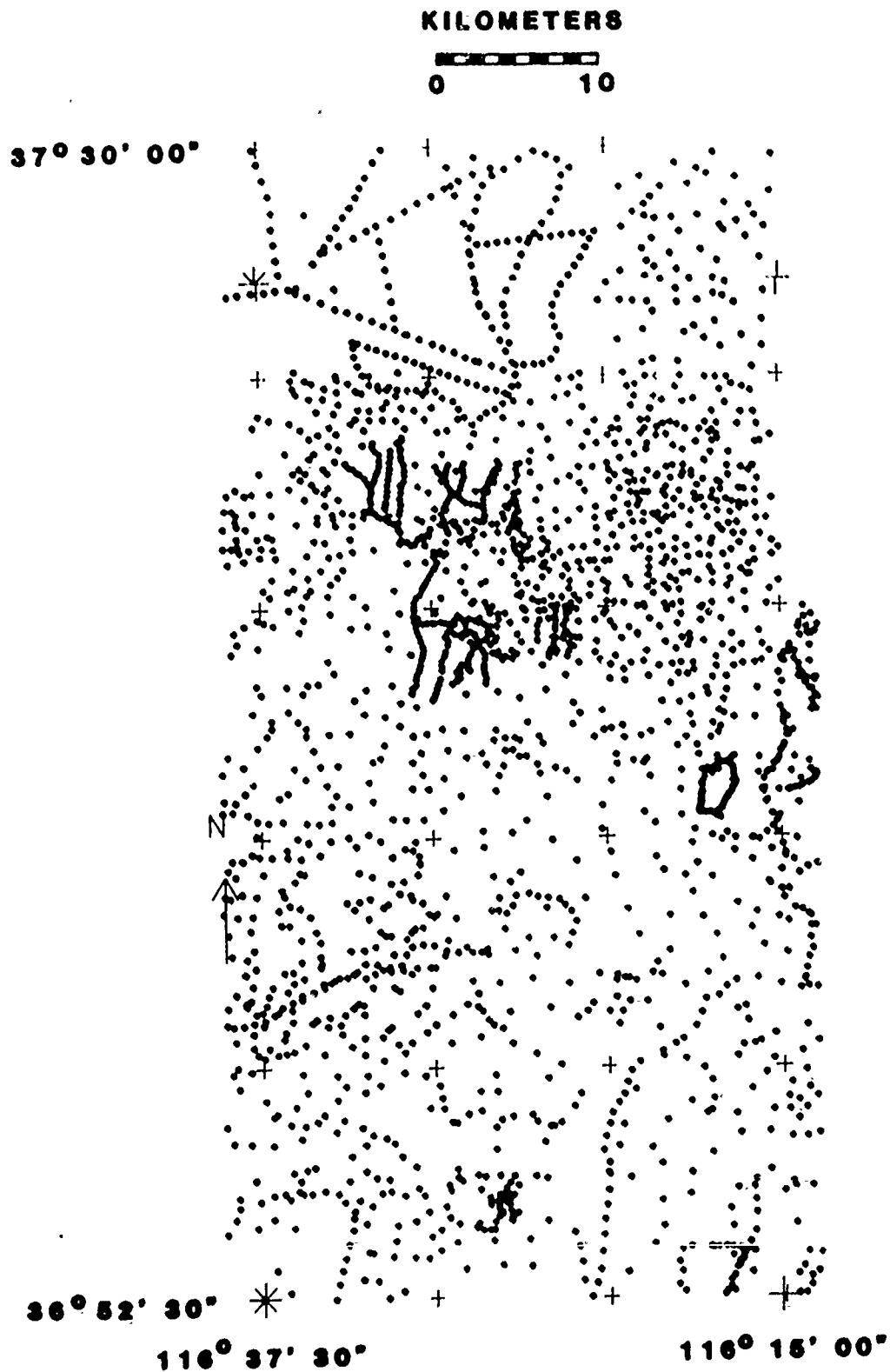
KILOMETERS

0   10

37° 30' 00"

N

36° 52' 30"

116° 37' 30"

116° 15' 00"

Figure 3

54

BOUGUER GRAVITY ANOMALY
PAHUTE MESA, NEVADA

KILOMETERS

0   10
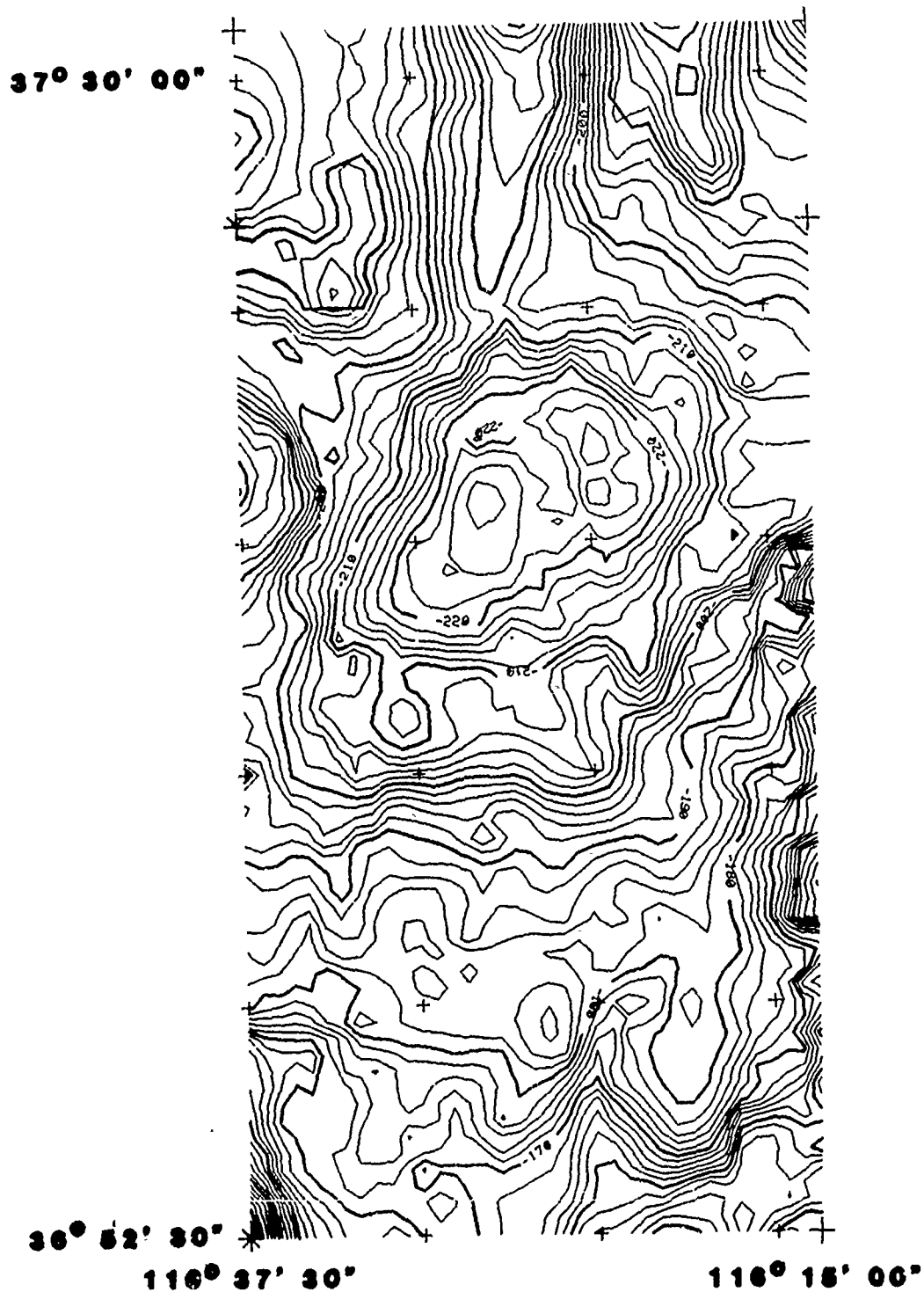
2 mgal CONTOUR INTERVAL

Figure 4

55
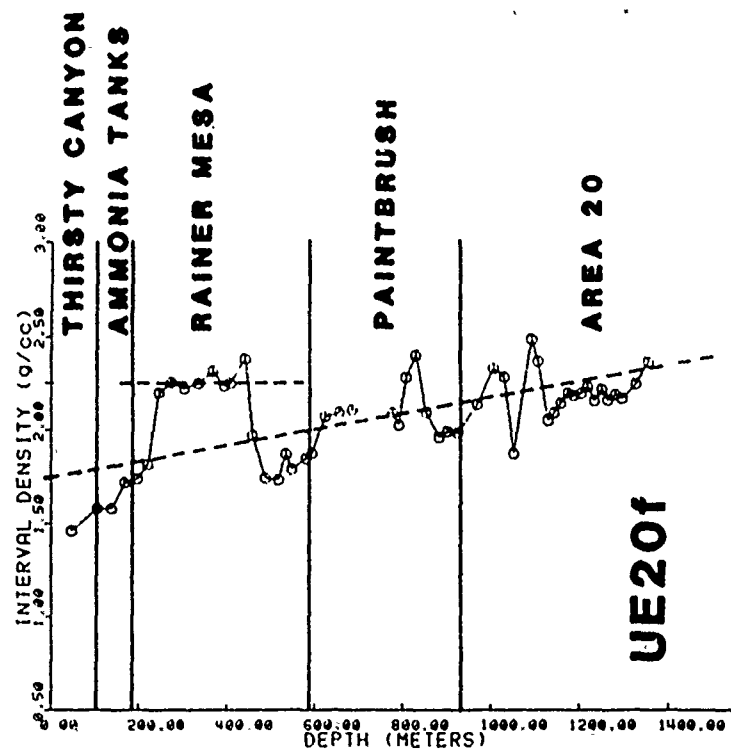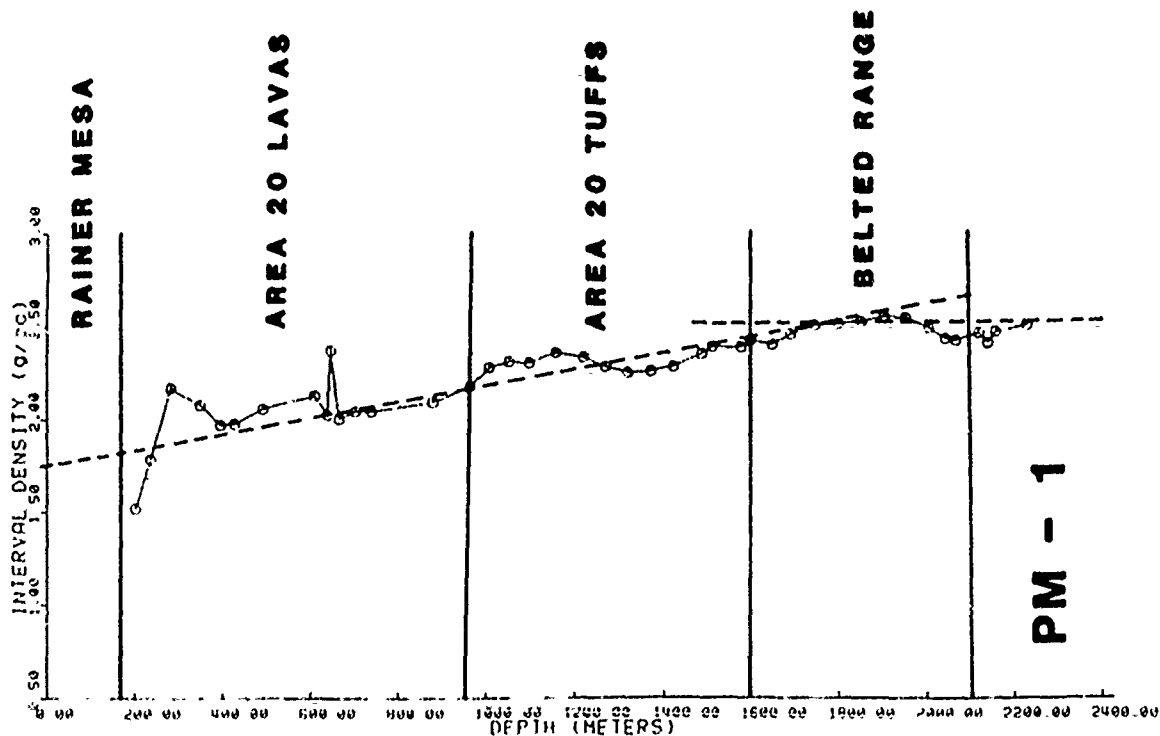
$$\rho(z) = 1.75 + 0.42z$$
$$z \text{ in km} \quad \rho \text{ in g/cc}$$

Figure 5

56

BOUGUER GRAVITY ANOMALY
PAHUTE MESA, NEVADA

KILOMETERS

0   10
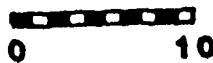
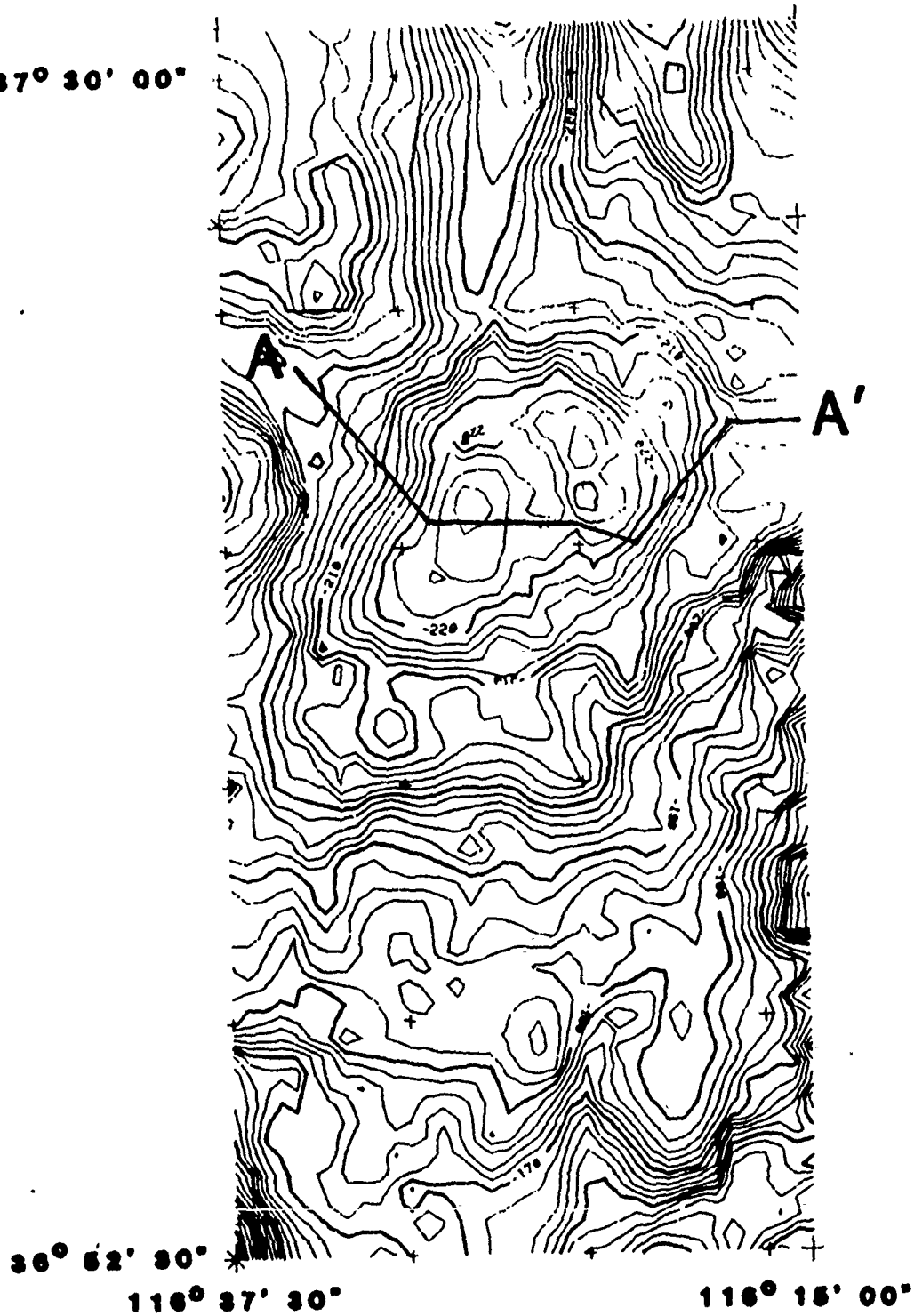

2 mgal CONTOUR INTERVAL

Figure 6

57

PAHUTE MESA, NEVADA
DENSITY CROSS SECTION

Figure 7

ρ = 1.75 + 0.42z
ρ = 2.25 gm/cc
ρ = 2.5 gm/cc

0   4
Kilometers
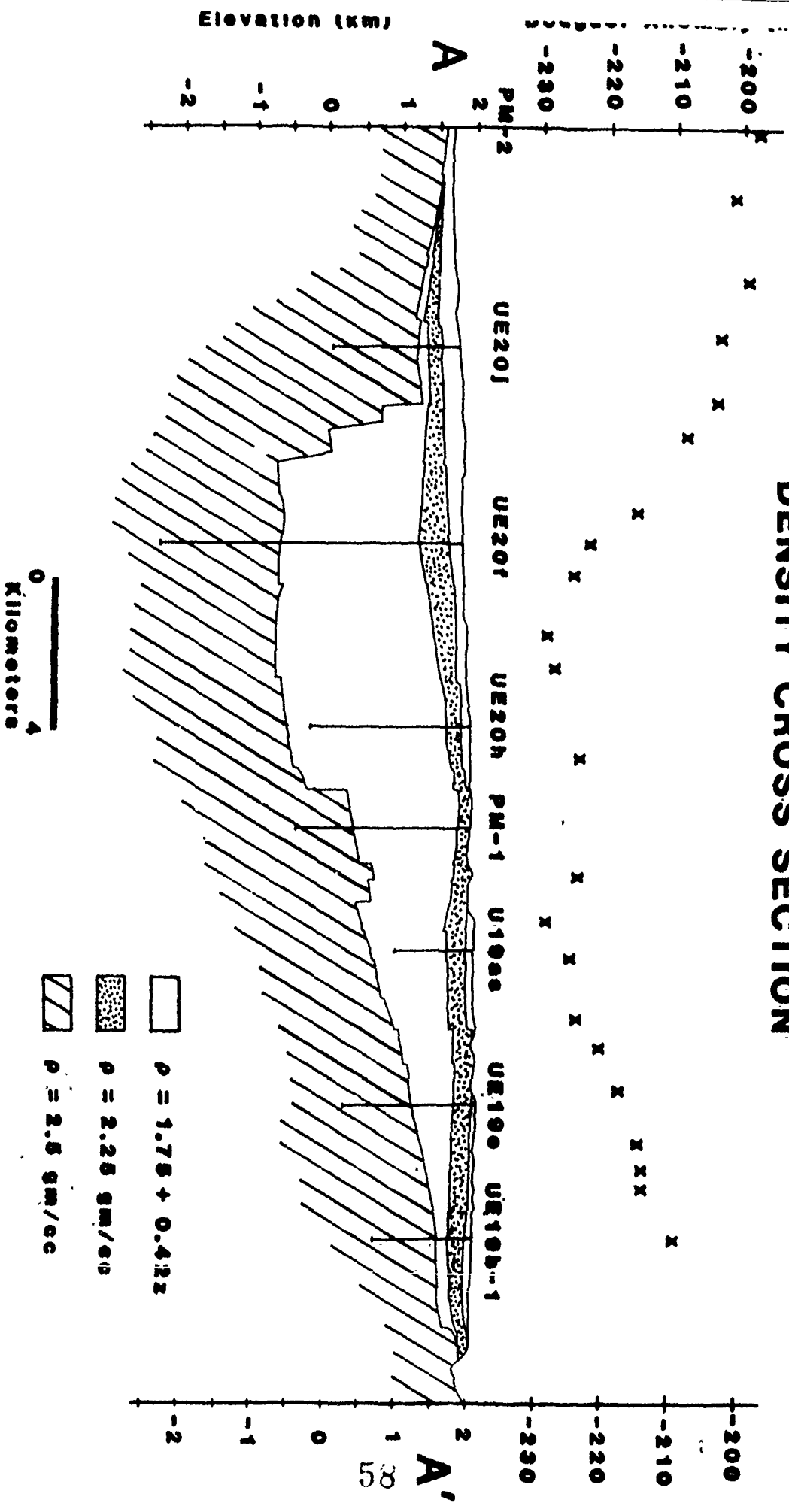
58

PAPER TITLE:

Direct Measurement of the Mantle Attenuation Operator from Broadband P and S waveforms

PAPER AUTHORS:

V.F. Cormier M.I.T. Department of Earth and Planetary Sciences

and

G.L. Choy U.S. Geological Survey, Golden Colorado

CONTRACT NUMBER:

SUMMARY:

Displacement and velocity records of P and S body waves with broadband frequency content from 0.01 to 5 Hz. are obtained either directly or through multi-channel deconvolution of earthquake waveforms from digitally recording stations of the GDSN and RSTN networks and the GRF array. Source parameters of deep focus earthquakes are determined by modeling P waveforms with a quasi-dynamic source model and an initial model of Q_α, which is based on the results of previous studies with bandlimited data. Using rupture models derived from the P waves, and neglecting the effects of scattering, a search is made for the minimum phase operators required to obtain matches to the observed S-waves. The variation in the inferred attenuation operator between S and ScS phases and its behavior with increasing distance and frequency are used to estimate a depth and frequency dependent model of intrinsic Q_β. Strong constraints on the frequency dependence of Q_β are given by fine details in the shape and dispersion of the broadband displacements of the S waves. Rise times are most sensitive to the higher end of the frequency band (0.2-1 Hz.), while the pulse width and tail are sensitive to the lower end of the frequency band (0.01-0.2 Hz). Although the frequency dependencies of the derived t_β^* 's are quite simple, having smooth decreases from 0.01 to 5 Hz., a relatively complex parameterization of the frequency and depth dependence of Q is required to match this frequency dependence. Either the power n in a Q-frequency dependence $Q = C f^n$ varies with depth, the high frequency cutoff in the relaxation spectrum varies with depth, or both. The mid- mantle between depths of 400 and 1600 km. contributes primarily to the attenuation of low frequencies (0.01 to 0.1 Hz.) of body waves. Below mantle depths of 1600-1800 km., the P and S waveforms for the paths investigated suggest little or no attenuation exists in the band of 0.01 to 5 Hz.

CONCLUSIONS AND RECOMMENDATIONS:

Broadband pulse modeling combined with the best possible source constraints offer a new means of determining the frequency dependence of attenuation in the Earth. Broadband pulses contain information on the dispersive property of intrinsic attenuation that can be used to retrieve the frequency dependence of t^*. The results reported here depended on a source analysis of earthquake P and S waves and on the existence of broadband digital, horizontal instruments. This configuration of instruments has, until quite recently, been rare. The GDSN network has not contained short period horizontal instruments until RSTN stations have been added to the day tapes. In the future, broadband records from Graefenburg type stations or multi-band records from RSTN type stations can be used to investigate the frequency dependence of attenuation observed over body wave paths sampling different tectonic regions.

Direct Measurement of the Mantle Attenuation Operator from Broadband P and S Waveforms

AUTHORS:

V.F. Cormier, Earth Resources Laboratory, Dept. of Earth, Atmos., and
Planet. Sci., Massachusetts Institute of Technology, 42 Carleton St.,
Cambridge, MA 02142

G.L. Choy, U.S. Geological Survey, MS 967, Box 25046, Denver Federal
Center, Denver, CO 80225

Abstract

Displacement and velocity records of P and S body waves with broadband frequency content from 0.01 to 5 Hz. are obtained either directly or through multi-channel deconvolution of earthquake waveforms from digitally recording stations of the GDSN and RSTN networks and the GRF array. Source parameters of deep focus earthquakes are determined by modeling P waveforms with a quasi-dynamic source model and an initial model of Q_α, which is based on the results of previous studies with bandlimited data. Using rupture models derived from the P waves, and neglecting the effects of scattering, a search is made for the minimum phase operators required to obtain matches to the observed S-waves. The variation in the inferred attenuation operator between S and ScS phases and its behavior with increasing distance and frequency are used to estimate a depth and frequency dependent model of intrinsic Q_β. Strong constraints on the frequency dependence of Q_β are given by fine details in the shape and dispersion of the broadband displacements of the S waves. Rise times are most sensitive to the higher end of the frequency band (0.2-1 Hz.), while the pulse width and tail are sensitive to the lower end of the frequency band (0.01-0.2 Hz). Although the frequency dependencies of the derived t_β^*'s are quite simple, having smooth decreases from 0.01 to 5 Hz., a relatively complex parameterization of the frequency and depth dependence of Q is required to match this frequency dependence. Either the power n in a Q-frequency dependence $Q = C f^n$ varies with depth, the high frequency cutoff in the relaxation spectrum varies with depth, or both. The mid-mantle between depths of 400 and 1600 km. contributes primarily to the attenuation of low frequencies (0.01 to 0.1 Hz.) of body waves. Below mantle depths of 1600-1800 km., the P and S waveforms for the paths investigated suggest little or no attenuation exists in the band of 0.01 to 5 Hz.

Introduction

The frequency dependence of the intrinsic anelasticity of the Earth complicates the estimation of the attenuation bias of a particular test site. With frequency dependence, it is possible that the attenuation bias measured in one frequency band may differ from that measured in another. Thus it is important to understand the behavior of intrinsic Q as a function of frequency

across the entire seismic band and how this behavior changes as the tectonic region sampled by a seismic wave changes.

Evidence for the frequency dependence of seismic Q until now has primarily come from experiments that match amplitude ratios and absolute amplitudes of body waves either in the frequency domain or time domain. In these experiments frequency dependence of Q is introduced to account for the differences in amplitudes measured on instruments having different pass bands in frequency. Other experiments, primarily in the high frequency band of body waves (0.1 - 10 Hz), seek to match the high frequency asymptote of body wave spectra by assuming an ω^{-2} to ω^{-3} decay of the source spectrum.

Improved understanding of earthquake and explosion source processes and broad band digital instrumentation now makes feasible a new method of measuring the frequency dependence of Q. This method consists in matching fine details in the pulse shapes of the body waves. If the trade-off between the source time function and Q operator can be minimized, the dispersive properties of intrinsic attenuation can be measured in the pulse shapes. This is the procedure we have used in modeling the P and S waves radiated by two deep focus earthquakes beneath the Sea of Okhotsk recorded by broadband digital instruments.

Experimental Procedure

The P waves radiated by two deep focus earthquakes, which occured on April 20 and April 23, 1984 beneath the Sea of Okhotsk, were modeled using the source parameterization and instrument deconvolution procedures described in Boatwright (1981) and Choy and Boatwright (1981). The multi-channel deconvolution procedure used on GDSN and RSTN data has been validated by comparison of the deconvolved vertical component of P waves recorded by the

SP and LP channels of the SRO station at Graefenburg with waveforms directly recorded as broadband velocity (Choy, 1981). An initial attenuation model was assumed in the P wave modeling and a trial and error search was made for a rupture model that produced P pulses, which when convolved with the attenuation operator, matched the observed P waveforms. The rupture model was a quasi-dyanamic shear crack that grows self-similarly and causally heals (Boatwright, 1981). The P waveforms of both events modeled suggested some complexity in the rupture process, consisting of two resolvable stopping events. This complexity can be easily identified in the broadband displacement and velocity P waveforms (Fig. 1).

The S waveforms were modeled by first taking the rupture parameters determined from the P waveforms to predict theoretical time functions for the S waves. Next a search was made for the minimum phase operator, which when convolved with the theoretical source-time functions of the S waves, matched the observed S waves. The form of this operator in the frequency domain was assumed to be given by

$$\hat{A}(\omega) = e^{i(\omega T_0 + \hat{\varphi}(\omega))}$$

with the imaginary part of the complex phase function $\hat{\varphi}(\omega)$ being defined in terms of a frequency dependent t^*

$$\text{Im}(\hat{\varphi}(\omega)) = \pi f t^*(f)$$

For linear anelasticity and causal propagation, the waveform of the attenuation operator will be a minimum-delay pulse that arrives after the reference arrival time T_0. Thus the real part of $\hat{\varphi}$ can be found from the Hilbert transform of the imaginary part of $\hat{\varphi}$. A minimum phase subroutine written to determine the phase response of a seismograph from its amplitude response can conveniently be used for this calculation simply by substituting for the amplitude response the function $|\hat{A}(\omega)| = e^{-\pi f t^*(f)}$.

In taking the attenuation operator to be minimum phase, a decision was made to neglect the effects of processes that cannot be described as minimum phase operators, such as scattering and multipathing. The appropriateness of this decision can be measured in several ways. The co-herence of pulse shapes across broadband arrays such as the one at Graefenburg can be checked to see whether fine scale features of the waveforms have been overinterpreted with a deterministic model of propagation. Also the relative success in explaining the waveforms of both P and S waves with a single rupture model and an attenuation operator in pure shear can be used as a measure of the importance of scattering attenuation. If scattering dominated throughout the band of interest, it would be difficult to construct a distribution of heterogenities that would reproduce the diferences observed between P and S waveforms in apparent dispersion and pulse broadening. These differences are consistent with intrinsic attenuation in pure shear.

Some restrictions on the allowable frequency dependence of $t^*(f)$ are imposed by linear anelasticity. In particular, since $t^* = \int \frac{Q^{-1}}{v} ds$, the frequency dependence of t^* must be consistent with $Q = Cf^n$, where $|n| \leq 1$. Also the width and intensity of an absorption band at any given depth must give a positive, non-zero relaxed modulus at the zeroth frequency limit.

In all cases attenuation in pure shear was assumed and the best fitting t^*_β models for S, ScS, and sS phases at varying distance ranges were used to determine a frequency and depth dependent model of Q_β. No attempt was made to invert for regional differences in Q. All of the paths were nearly pure continental, sampling a nearly identical mixed shield and tectonic region of the upper mantle.

Although trade-offs exist in the attenuation model and rupture model, it is important to note that the pulse width of the P waves for the events studied was

much less than that of the S waves (Fig. 1 vs. Fig. 2 and 3). When this is taken into account together with the evidence of rupture complexity and a source model that incorporates effects of both directivity and relative corner frequency shifts between P and S waves, the trade-off between the rupture parameters and Q operator is quite small. This trade-off does not strongly affect the shape and trend of the derived $t^*(f)$ curves. Similarly, the starting Q model used in the P wave modeling does not strongly affect the final Q_β model determined from the S waves. Lower error bounds have been set in Fig. 4 by explaining the P waveforms of the individual sub-events solely by the effects of attenuation, within a range of physically reasonable source-time functions. Similarly, upper error bounds have been set by explaining the P waveforms solely to the effects of the source-time functions.

Results for $t_\beta^*(f)$

A preliminary model of t_β^* for a deep focus event is shown in Fig. 4. This is appropriate for the continental shield paths studied. The corresponding model of t_α^* for attenuation in pure shear can be approximated by divividing the values by 4.5. In Figs. 4 and 5 we have shown a $t^*(f)$'s consistent with our data inversion and with a model of $Q_\beta(r,f)$ in which the mantle is divided into one region from the moho to 400 km. depth and a second region from 400 km. depth to 1600 km. depth. We have assumed a parameterization of Q_β similar to that taken by Anderson and Given (1982) with Q_β proportional to a power of frequency that may vary with depth and frequency band (Minster and Anderson, 1981). Note that the curves consist of concave upward segments. This will be a general feature of all t^* curve ploted against the log of frequency in regions where Q increases as a power of frequency.

The equivalent surface focus t^* for 66° can be estimated from operators determined for transverse sS and ScS as well as S for a range of distances

between 50° and 82°. It was found that crustal reverberations at the surface bounce point of sS can strongly affect the long period tail of sS. Reverberations in the receiver crust, however, have relatively minor effects on the waveforms of transverse S and ScS. A conspicuous difference was found in the decay of the long period tail of the displacement pulses between the S and ScS phases (Fig. 6). The direct S seems to have a much longer tail relative to the ScS phases. This difference seems to disappear as range increases toward 82°. The relative behavior of S versus ScS waveforms was also observed at all elements of the Graefenburg array. Since the angle of incidence on the receiver crust is nearly identical for S and ScS in the distance range investigated, this difference in the long period tail cannot be simply explained by the effects of the crustal response. Reverberations in layered structure that have been proposed near the core mantle boundary are likewise insufficient to produce destructive interference of the long period tail of ScS. The best explanation we found for this difference in the waveforms of S versus ScS is due to the frequency and depth dependence of intrinsic Q. By revising the values of parameters in the frequency and depth dependent Q_β models of either the Lundquist and Cormier (1980) or Anderson and Given (1982), $t^*(f)$ functions can be found that predict the observed differences between S and ScS waveforms. For example, the prediction of one such model is shown in Fig. 5. Note that t^* of S differs from the t^* of ScS in the low frequency band but is nearly identical in the band above 0.3 Hz. The high frequency band controls the rise times, but the frequencies below 0.3 Hz. control the decay of the tail of the displacement pulses.

Conclusions and Future Work

Two significant results on the frequency dependence of Q have been obtained in the work thus far. (1) Revisions in the high frequency cutoff parameter in the

models of $Q_\beta(r,f)$ proposed by Lundquist and Cormier (1980) and Anderson and Given (1980) are all that are required to satisfactorily explain the pulse shapes of S, sS, and ScS phases. This suggests that the basic form of $Q_\beta(r,f)$ is consistent with the hypothesis of these papers, i.e., that Q_β is due to thermally activated mechanisms of intrinsic anelasticity, with depth dependence controlled by the temperature and pressure profiles of the mantle. (2) The gradual decrease in intrinsic anelasticity throughout the body wave band very closely follows the shape of $t^*(f)$ curves given in Der et al. (1984), which they obtained from a summary of many spectral and time domain measurements of apparent attenuation. In detail, the gradual decrease in t^* as a function of frequency cannot be matched by any simple parameterization of the frequency dependence of Q, such as a single cutoff frequency in a relaxation spectrum which is constant with depth.

Broadband pulse modeling combined with the best possible source constraints offer a new means of determining the frequency dependence of attenuation in the Earth. Broadband pulses contain information on the dispersive property of intrinsic attenuation that can be used to retrieve the frequency dependence of t^*. The results reported here depended on a source analysis of earthquake P and S waves and on the existence of broadband digital, horizontal instruments. This configuration of instruments has, until quite recently, been rare. The GDSN day-tape has not contained short period horizontal instruments until RSTN stations have been added. In the future, broadband records from Graefenburg type stations or multi-band records from RSTN type stations can be used to investigate the frequency dependence of attenuation observed over body wave paths sampling different tectonic regions.

References

Anderson, D.L., and Given, J.W., Absorption band Q model for the Earth, *J.*

Geophys. Res., *87*, 3893-3904, 1982.

Boatwright, J., Quasi-dynamic models of simple earthquakes: application to an aftershock sequence of the 1975 Oroville, California, Earthquake, *Bull. Seism. Soc. Am.*, *71*, 69-94, 1981.

Choy, G. L., and Boatwright, J., The rupture characteristics of two deep earthquakes inferred from broadband GDSN data, *Bull. Seism. Soc. Am.*, *71*, 691-711, 1981.

Choy, G.L., Experiments with SRO and GRF-array data, USGS Open- File Report 82-216, 1982.

Der, Z.A., Lees, A.C., and Cormier, V.F., Frequency dependence of Q in the mantle underlying the shield areas of Eurasia, Part III: The Q model, Final Technical Report, ARPA Order No. 4493, Teledyne Geotech, Alexandria, VA, 1985.

Lundquist, G.M., and Cormier, V.F., Constraints on the absorption band model of Q, *J. Geophys. Res.*, *85*, 5244-5256, 1980.

Minster, J.B., and Anderson, D.L., A model of dislocation controlled rheology for the mantle, *Philos. Trans. R. Soc. London*, *299*, 313-356, 1981.
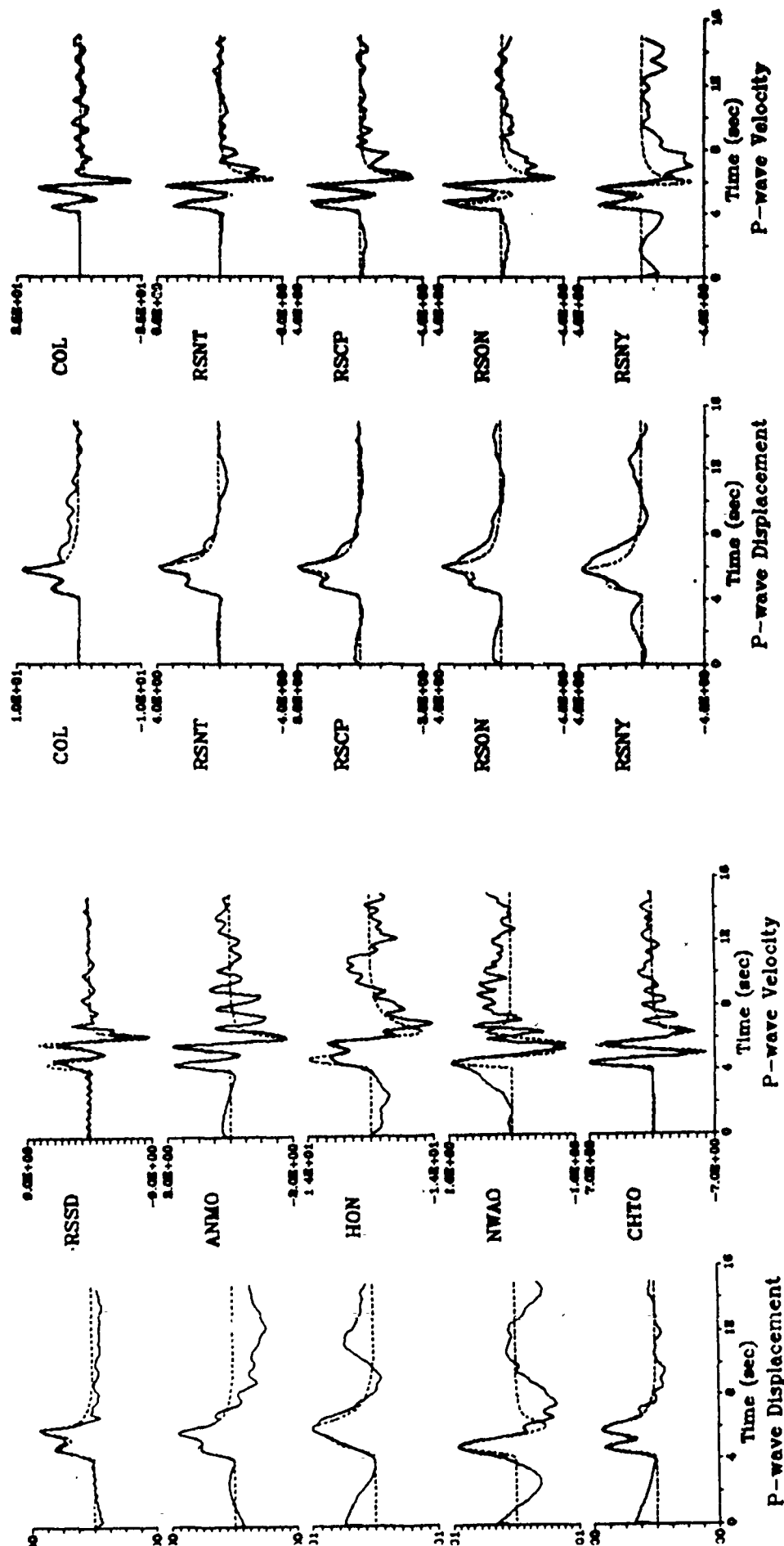
Figure 1. Broadband displacement (left columns) and velocity (right columns) of the P waveforms recorded from the April 20, 1984 deep focus earthquake beneath the Sea of Okhotsk. Theoretical waveforms for a rupture model and attenuation model are dotted. In addition to these stations, four additional DWWSSN stations were used in the modeling of P waveforms.

69
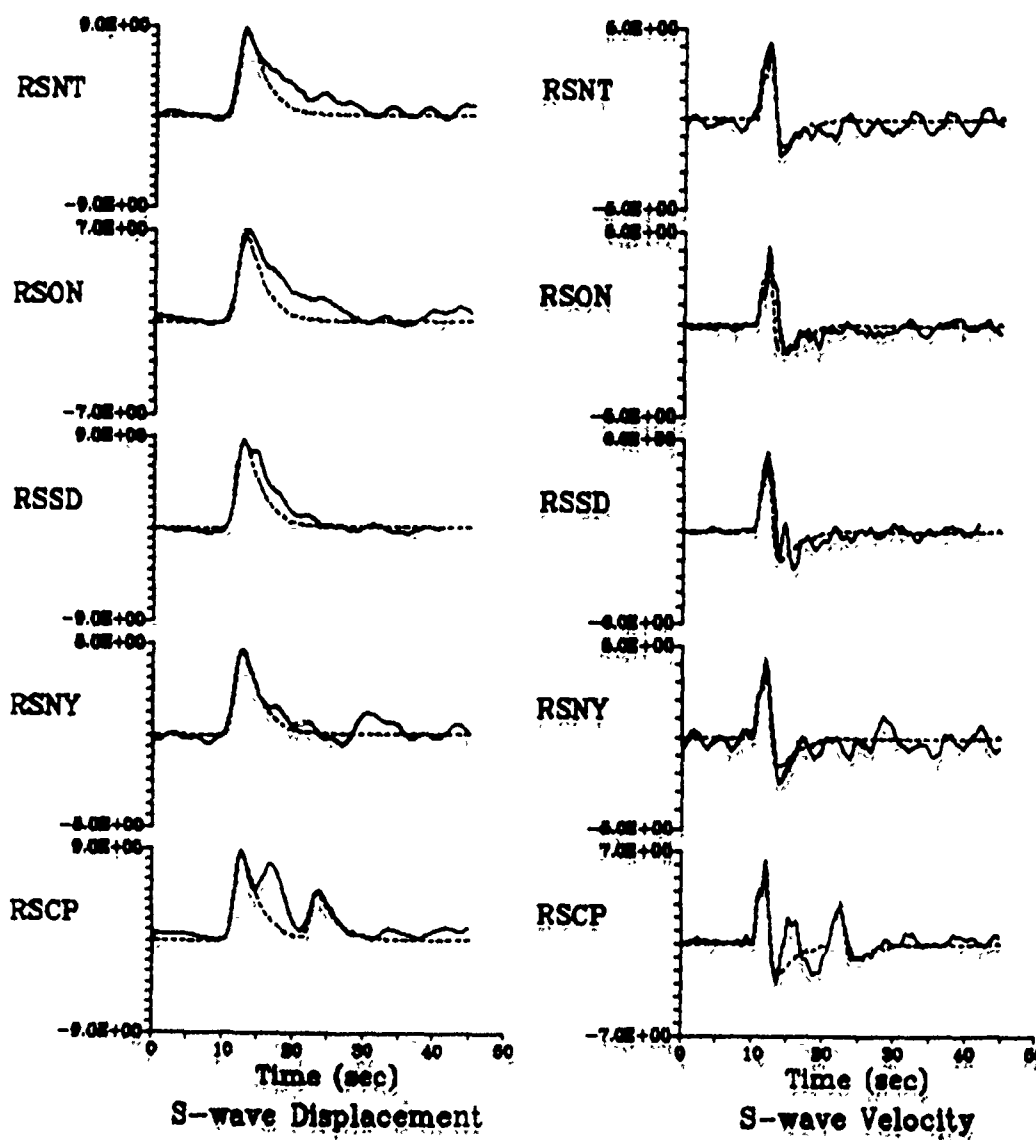
Figure 2. Broadband displacment and velocity of S waveforms for the Sea of Okhotsk event as described in Fig. 1.

RSNT

RSON

RSSD

Time (sec)

ScS Displacement

RSNT

RSON

RSSD

Time (sec)
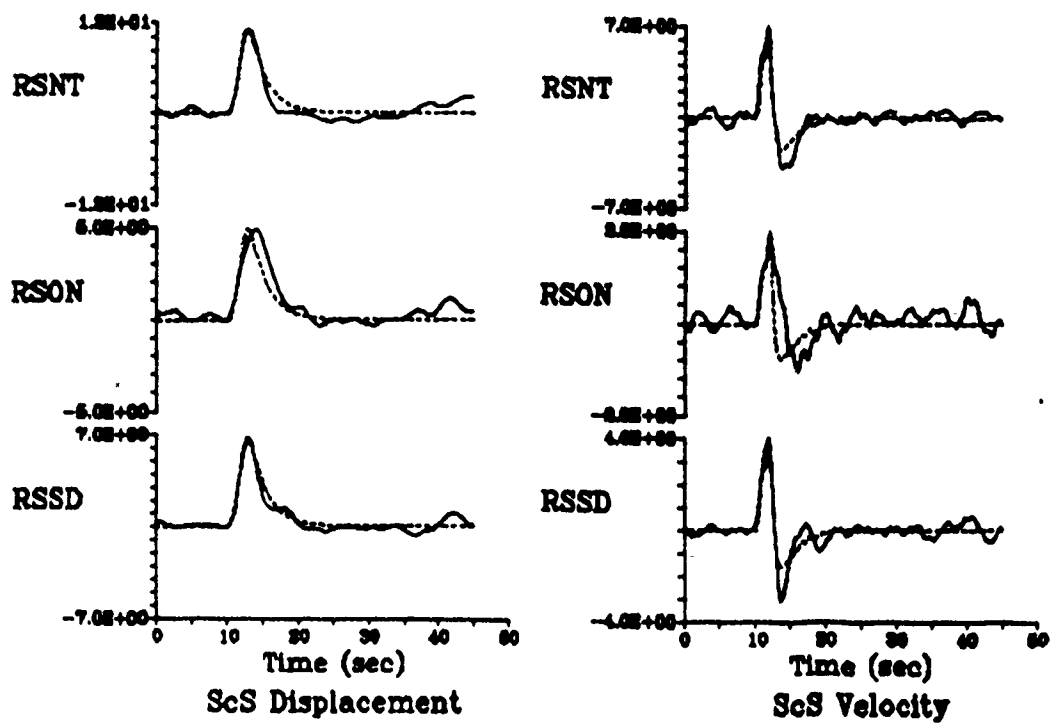
ScS Velocity

Figure 3. Broadband displacement and velocity of ScS waveforms for the Sea of Okhotsk event.as described in Fig. 1.
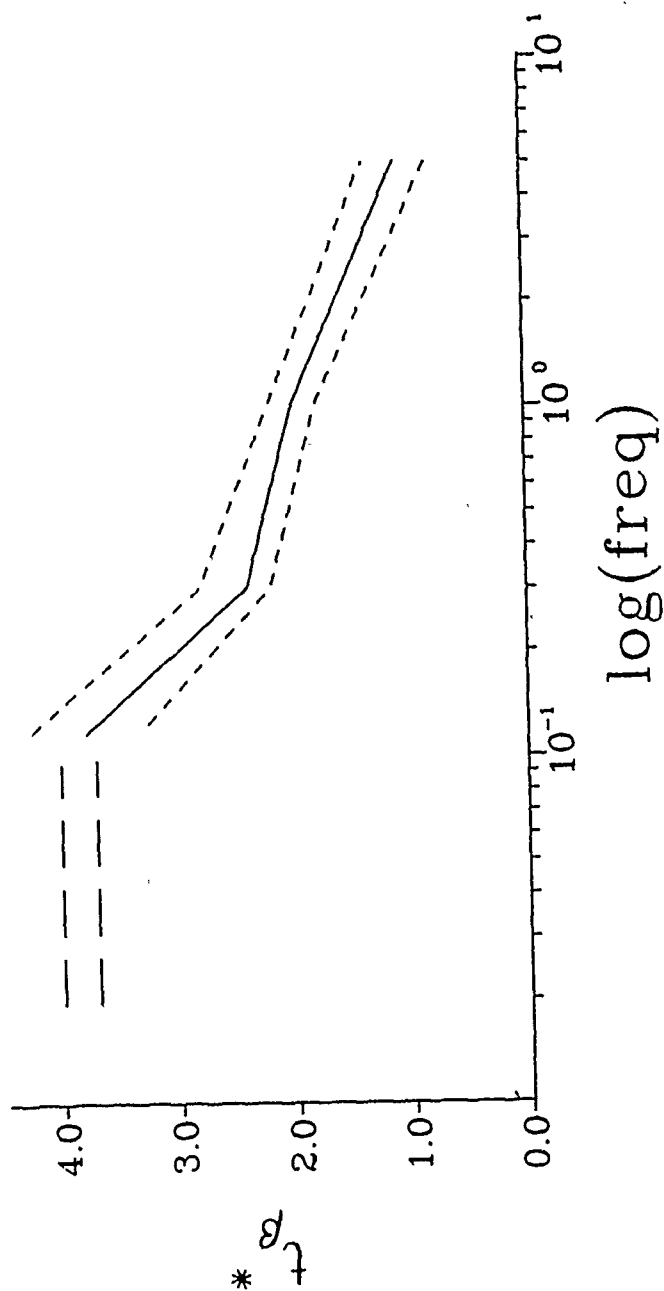
Figure 4. $t_\beta^*(f)$ at 66° based on the modeling of S waveforms from the deep focus Sea of Okhotsk event. An equivalent surface focus event is estimated to have a t_β^* 1's higher at the lowest frequencies. Tradeoff of the effects of Q versus crustal structure on sS preclude a better estimate of the surface focus t_β^*.
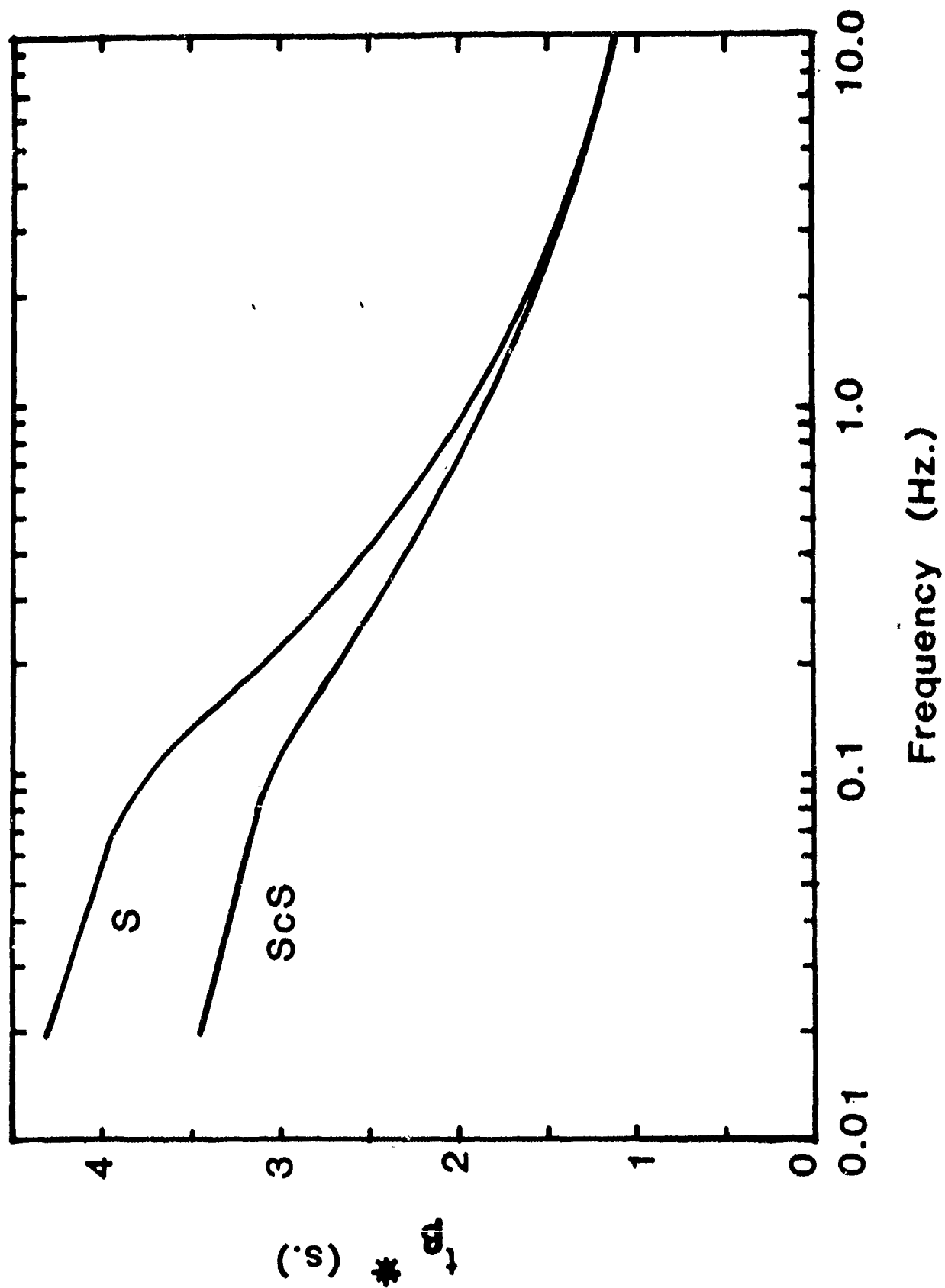
Figure 5. A comparison of $t_\beta^*(f)$ for deep focus S and ScS phases at 66°. Note the differences in the low frequency band, but the similarities in the high frequency band above 0.3 Hz. This is may be due to the distribution with depth and frequency dependence of Q_β.
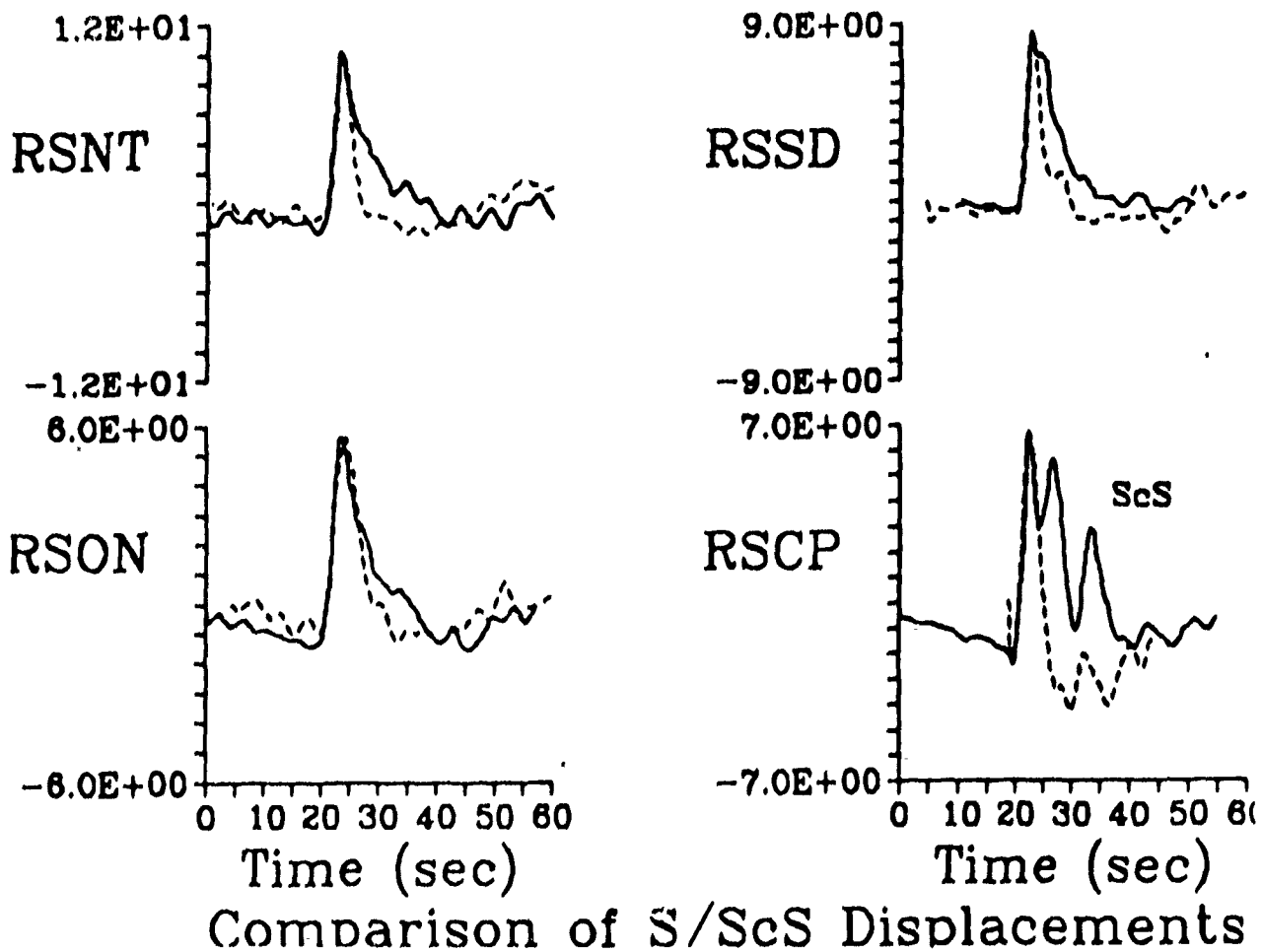
Figure 8. A comparison of S (solid traces) with ScS (dotted traces) of broadband displacements recorded from the Sea of Okhotsk earthquake. Note that rise times are nearly identical, but that differences in the long period tail become most pronounced at RSNT (50°) and progressively less pronounced at longer distances such as RSSD (66°) and RSCP (82°). We have not attempted to model the phase between S and ScS at RSCP with any structure near the core-mantle boundary.

74

PAPER TITLE:

Gaussian Beam Synthesis in 2-D and 3-D

PAPER AUTHORS:

Robert Nowack and V.F. Cormier M.I.T. Department of
Earth and Planetary Sciences

CONTRACT NUMBER:

"Teleseismic waveform modeling incorporating the
effects of known three-dimensional structure beneath
the Nevada test site"

SUMMARY:

The Gaussian beam method for the calculation of synthetic seismograms in
a smoothly varying heterogeneous medium is described. The choice of the com-
plex beam parameter is also discussed. An example of a 3-D structure is gotten
by using a derived model from an Aki-inversion of teleseismic travel times for
centre' California. 3-D ray diagrams and a synthetic seismogram profile are
computed for this model assuming an incident plane wave from below. The
amplitude variations for the given profile are smaller than the order of magni-
tude variations typically observed. Since amplitudes are sensitive to smaller
scale velocity features than travel times, this may indicate that a single scale
block model may have difficulty in satisfying both travel time and amplitude.

CONCLUSIONS AND RECOMMENDATIONS:

A test structure, determined from block 3-D inversion of teleseismic travel
ti~~, gave amplitude variations of about a factor of 2 along a 100 km. long
profile. The block sizes of the test structure varied from 10 - 20 km. in linear
dimension with velocity variations on the order of 2 to 8 per cent.

Future work will be directed toward comparing the amplitude fluctuations
predicted by 3-D models having varying degrees of resolution in order to deter-
mine the resolution required to obtain significant amplitude corrections. A
parallel series of experiments will be conducted on synthetic velocity models
constructed to have varying distributions of characteristic scale lengths and
velocity fluctuations within the domain of validity of the Gaussian beam method.

Gaussian Beam Synthesis in 2-D and 3-D

AUTHORS:
Robert Nowack and V.F. Cormier, Earth Resources Laboratory,
          Dept. of Earth, Atmos., and Planet. Sci., Massachusetts Institute
          of Technology, 42 Carleton St., Cambridge, MA 02142)

Abstract

The Gaussian beam method for the calculation of synthetic seismograms in a smoothly varying heterogeneous medium is described. The choice of the complex beam parameter is also discussed. An example of a 3-D structure is gotten by using a derived model from an Aki-inversion of teleseismic travel times for central California. 3-D ray diagrams and a synthetic seismogram profile are computed for this model assuming an incident plane wave from below. The amplitude variations for the given profile are smaller than the order of magnitude variations typically observed. Since amplitudes are sensitive to smaller scale velocity features than travel times, this may indicate that a single scale block model may have difficulty in satisfying both travel time and amplitude.

Introduction

Observations of teleseismic P waves at large aperture arrays have found amplitude fluctuations across the array as large as those observed over the world wide networks. The amplitude fluctuations and their correlation with travel time variations are consistent with the focussing/defocussing effects of three-dimensional velocity structure beneath the array rather than the effects of intrinsic attenuation. In this paper, the Gaussian beam method is used to predict the possible amplitude variations at a large aperature array due to a known 3-D structure. The known 3-D structure is taken to be one determined from a block-inversion of travel times of the type described by Aki et al. (1976). For body waves on the order of 1 Hz. dominant frequency, the scale length and intensity variations of the models commonly derived from such inversions are well within the bounds in which asymptotically approximate methods, such as the Gaussian beam method, are alid.

A goal of these experiments is to determine whether knowledge of the 3-D structure surrounding a given nuclear test site can be used to reduce the uncertainty in a yield estimate by providing an amplitude correction that is a function of source location within the test site. Although the spatial resolution of 3-D block inversions is much less than that obtainable from on-site reflection experiments and well-logs, it is a less intrusive experiment. Such inversions are always possible if the events within a test site are well timed and located. Thus it is important (1) to determine whether the spatial resolution of 3-D block inversions is sufficient to explain any significant amplitude variations in teleseismic P waves due to variations of event locations within a test site and (2) to determine the relation between characteristic scale lengths and intensities of velocity fluctuations of these models with predicted amplitude fluctuations.

The Gaussian Beam Method of Seismogram Synthesis

The Gaussian beam method is an extension of the ray method for the computation of seismograms in a smoothly varying heterogeneous medium (see Cerveny et.al., 1982). In comparison to other methods, the Gaussian beam method is fast, gives finite amplitudes at caustics, and requires no explicit two-point ray tracing. The method uses rays as a framework upon which the wavefield is built. The Gaussian beams are propagated along each ray and then superposed at the receiver. The beams are weighted in the superposition in order to satisfy a given source condition.

The individual beams in the superposition can be manipulated by a complex beam parameter which changes the beam curvature and beam width at the source. This is done in order to satisfy different objectives, such as small beam width at the source, receiver, or at a localized heterogeneity, or to satisfy a given curvature condition. It has been found that large initial beam widths

are more suitable for the decomposition of a point source into Gaussian beams and small initial beam widths are more suitable for the decomposition of a plane wave into Gaussian beams (see Nowack and Aki, 1984). The Gaussian beam method reduces to a plane wave expansion for large planar beams at a point source in a homogeneous source region. Finite beam widths have the effect of localizing the beams to a vicinity of each central ray, and reducing numerical end effects in the superposition (see Madariaga and Papadimitriou, 1985). Finite beam widths also reduce diffraction effects in certain cases, such as the generation of a head wave at a plane interface. The critical initial beam width gives the beam solution most concentrated about each central ray and is a compromise that has been found to give stable results. Tests at a simple caustic have nonetheless given the correct behavior over a range of initial beam widths. More work must be done, particularly in 1-D and 2-D, in choosing the appropriate beam parameter which gives the best results for a given heterogeneous medium.

The numerical advantages of using high frequency asymptotic methods are most pronounced in three dimensional cases. The finite difference method in contrast is slow for 2-D wave propagation problems, and impractical for most 3-D seismic wave problems. Still, many problems require approximate 3-D solutions. It is thus of interest to develop asymptotic methods such as the Gaussian beam method for the 3-D case.

Results

An example 3-D structure can be gotten by using a model derived for a particular region from a travel time inversion parameterized by blocks or by any other method. Here, the results from a teleseismic travel time inversion study for central California by Zandt [1981] are used. The model has four layers from 0.0 to 90.0 km in depth. The horizontal block size is 10.0 km in the

top layer and 20.0 to 25.0 km in the lower layers. Average velocity variations in the derived model are between 4.0 to 8.0 percent in the top layer and 2.0 to 4.0 percent in the lower layers. Comer and Aki [1982] investigated this structure using 3-D ray tracing in order to study the effect of ray bending on estimated take-off angles for shallow events. Figure 1a shows an example of down going rays from a shallow event in the central California structure. The 3-D ray tracer used is a modification of a code by R. Comer. The velocity model is interpolated using a 3-D splines under tension package by A. Cline. Figure 1b shows a top view of the ray paths in which ray bending can clearly be seen. The rays associated with a teleseismic plane wave incident from below is shown in Figure 2a. A more dense set of rays is shown in Figure 2b. Again, ray bending can be seen in the ray diagrams.

In order to compute synthetic seismograms, the paraxial ray equations must be solved along each ray. These equations are a linearized set of equations which can be used to obtain information in the vicinity of a ray that has already been traced using the kinematic ray equations. The paraxial ray equations are useful in a variety of ways including, the computation of geometric spreading and amplitude in the standard ray method, the calculation of local wave front curvature for phase interpolation, and the computation of polarization vectors, etc. (see Cerveny, 1985). Complex solutions of these equations are used in the Gaussian beam method. Thus, once the kinematic and paraxial ray equations are solved in the vicinity of the receiver, this information can be input directly into a Gaussian beam synthesis program.

As an example, Gaussian beam synthetics are computed for the teleseismic plane wave incident from below in the central California model. The endpoints of the rays are shown in Figure 3a. Seismograms are computed along profile A-A' and shown in Figure 3b. A 2.0 Hz Gabor wavelet is used as the source time function, and a critical initial beam width used. A correlation between lower

amplitudes and earlier arrivals can be seen on the synthetics. The lower amplitude can be identified on Figure 3a near the point A, where the rays are being pulled apart. In Figure 3b, the amplitude varies by a factor of about 2 along the profile. Observations of amplitude at the Montana LASA by Aki [1973] showed variations in the amplitude by a factor of 10. This difference in the amplitude variation may be related to the block sizes used to satisfy the travel time data for the inverted block model. Since travel time is related to the velocity field and amplitude is related to the second derivative of the velocity field, different heterogeneity scales may be required to satisfy both travel time and amplitude variations. In any event, high freqency asymptotic methods such as the Gaussian beam method will play an important role in seismic modelling using amplitude and travel time in both 2-D and 3-D cases.

Future Work

Future work will be directed toward comparing the amplitude fluctuations predicted by 3-D models having varying degrees of resolution in order to determine the resolution required to obtain significant amplitude corrections. A parallel series of experiments will be conducted on synthetic velocity models constructed to have varying distributions of characteristic scale lengths and velocity fluctuations within the domain of validity of the Gaussian beam method.

References

Aki, K., Scattering of P waves under the Montana LASA, J. Geophys. Res., 78, 1334-1346, 1973.

Aki, K., A. Christoffersson, and E.S. Husebye, Determination of three-dimensional seismic structures of the lithosphere, J. Geophys. Res., 82, 277-296, 1976.

Cerveny, V., The application of ray tracing to the propagation of shear waves in

complex media, in Seismic Exploration, eds. Treitel, S. and Helbig, K., Vol. Seismic Shear Waves, ed. Dohr., G., Geophysical Press, in press, 1985.

Cerveny, V., M.M. Popov, and I. Psencik, Computation of wavefields in inho inhomogeneous media - Gaussian beam approach, Geophys. J.R. atron. Soc., 70, 102-128, 1982.

Comer, R. and K. Aki, Effects of lateral heterongeneity near an earthquake source on teleseismic raypaths, Earthquake Notes, vol. 52, no. 1, 1982.

Madariaga, R. and P. Papadimitriou, Gaussian beam modelling of upper mantle phases, preprint, 1985.

Nowack, R. and K. Aki, The 2-D Gaussian beam method: testing and application, J. Geophys. Res., 89, 7797-7819, 1984.

Zandt, G., Seismic images of the deep structure of the San Andreas Fault system, Central coast ranges, California, J. Geophys. Res., 86, 5039-5052, 1981.
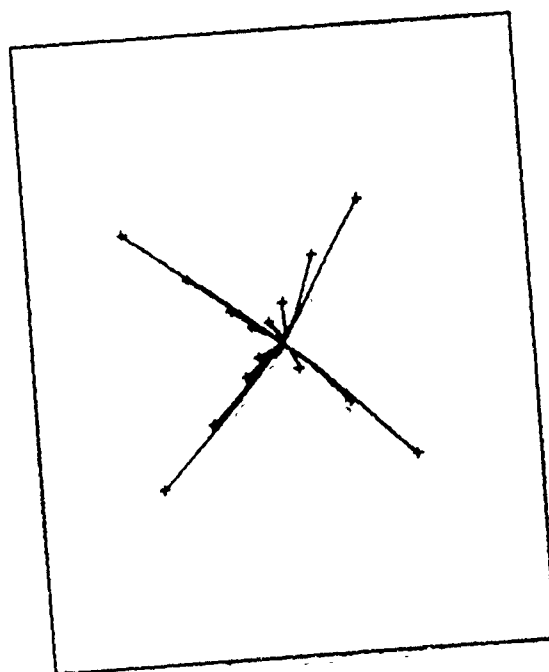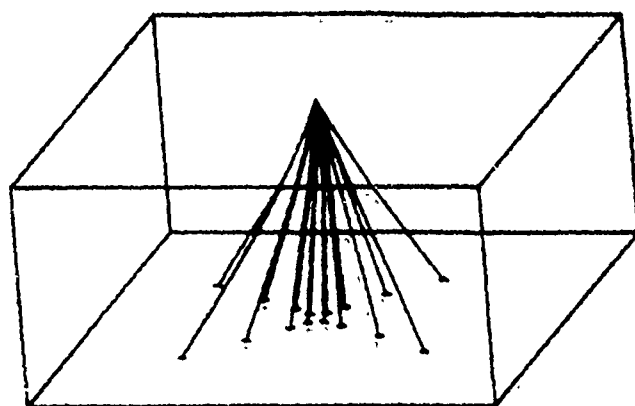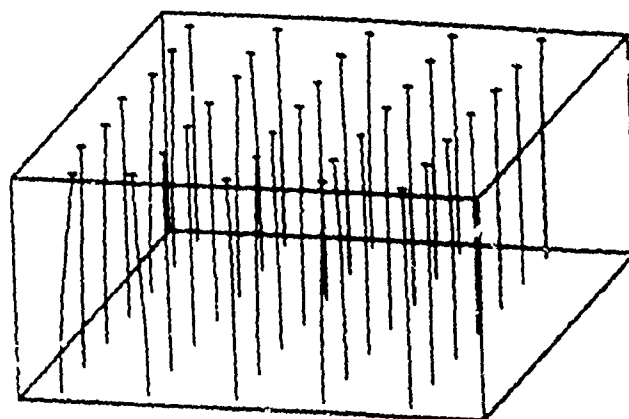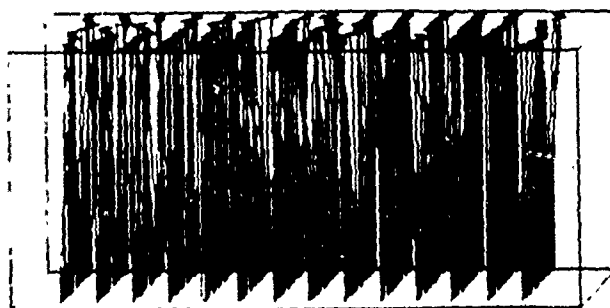
Figure 1
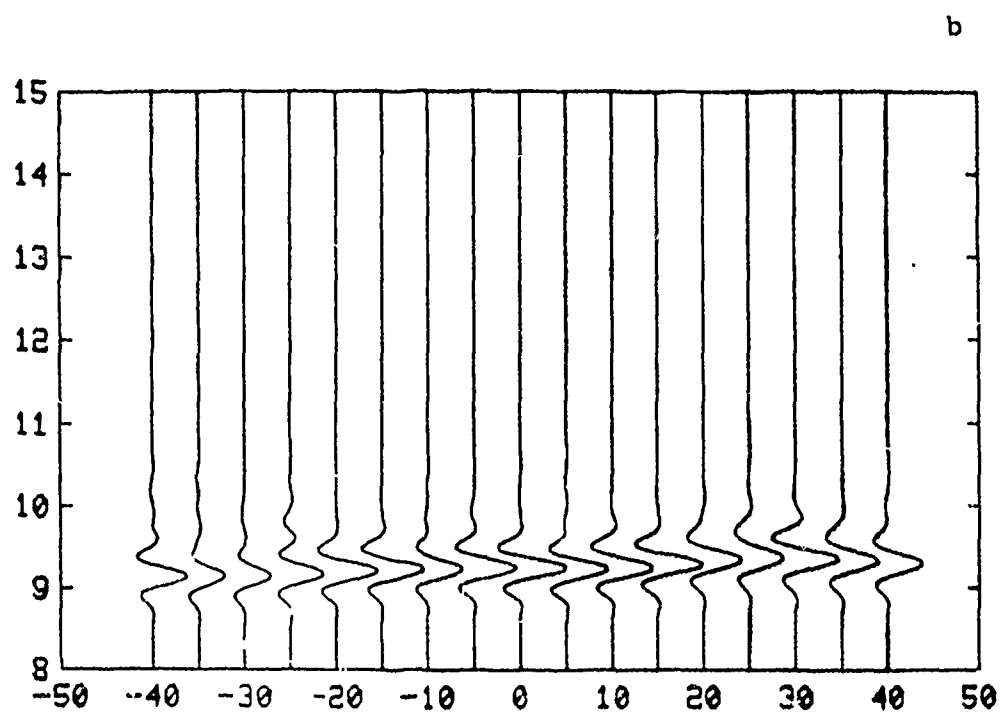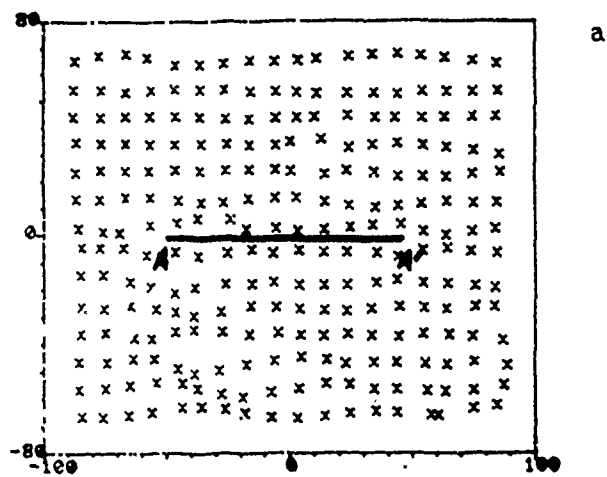
a

b

82

Figure 2

a

b

83

Figure 3

a

b

84

PAPER TITLE: Regional Studies with Broadband Data

PAPER AUTHORS: T. V. McEvilly and L. R. Johnson

CONTRACT NO: F19628-85-K-0025

SUMMARY:

During the past year the problems which have received the most attention
are the structure of the shallow crust at Pahute Mesa, the locations of
afterevents of NTS explosions, moment tensor inversions of broadband data
recorded near NTS explosions, and improvements in source locations which
can be obtained with regionalized travel time data.

Composite record sections from several explosions have been used to
estimate the shallow crustal structure for Pahute Mesa. First arrival
times for direct P and S waves have allowed a standard refraction interpretation.
Reflection processing techniques have also been applied to the data in order
to identify possible refections.

Hypocenters from several hundred afterevents of the explosion Chancellor
occurring within one day define two concentrations of activity. One is a
narrow chimney of activity extending from the explosion to the surface and
the other ⹁ a lobe extending about 3 km to the southwest at the source depth.

CONCLUSIONS AND RECOMMENDATIONS:

A new average velocity model has been obtained for the shallow structure
at Pahute Mesa. This model should be used to calculate new Green functions
which can be used to estimate moment tensors for some of the Pahute Mesa
events. Afterevents of the explosion Chancellor indicate a concentration
of activity extending 3 km from the explosion source. The physical cause
of this activity deserves further investigation.

STATEMENT OF THE PROBLEM

The research supported by this grant is directed toward the general problems of detection and identification of underground explosions through the study of radiated seismic waves. Particular emphasis is on the collection and analysis of broadband seismic data at near and regional distances.

During the past year specific aspects of these general problems which have received the most attention are the structure of the shallow crust at Pahute Mesa, the locations of afterevents of NTS explosions, moment tensor inversions of broadband data recorded near NTS explosions, and improvements in source locations which can be obtained with regionalized travel time data.

Improved velocity models for the crust at NTS could be very helpful in modelling the radiation of elastic waves from explosions. For instance, in using the moment tensor inversion method any uncertainty in the velocity structure gets translated into inaccurate Green functions and possibly into incorrect estimates of the moment tensor. Better knowledge of the shallow velocity structure also results in more accurate locations for explosion afterevents. Unfortunately, the type of standard refraction or reflection profiles which are generally used to infer models of crustal structure have not been generated for the Pahute Mesa part of NTS.

Studies of the locations of explosion afterevents in time and space have been initiated in order to obtain information on possible tectonic release events that may accompany the explosions. The difficulty is that these afterevents are typically very small and very numerous, and several hundred have to be analyzed in order to obtain a relatively complete picture of any patterns which may be present. This argues for some type of automatic processing, at least during the initial stages of the analysis.

VELOCITY STRUCTURE AT PAHUTE MESA

Broadband accelerometer data have been collected at close distances to 9 different explosions at Pahute Mesa. These events and the locations of the recording stations are shown in Figure 1. While the coverage is not uniform, much of the mesa has been sampled at shallow depths by the seismic waves travelling between these various source-receiver pairs.

In order to estimate an average velocity structure for the mesa, all of the data for the different events have been combined and treated as a one-dimensional single coverage reflection/refraction survey. With the exceptions of Jorum and Handley, all of these explosions have depths that are not much different from 0.6 km, which facilitates such an approach. The combined data set consists of 45 recordings for each of three components spread out over a distance range of 0.5 to 15 km. With this amount of data, one can use the standard techniques of interpreting reflection and refraction seismic surveys to obtain an estimate of the average velocity structure as a function of depth in the upper few kilometers of the mesa.

Figure 2 is a composite record section for the vertical component of acceleration. The travel time curve for first arrivals is well defined, and some of the later arrivals show coherence over several km. Similar sections for the radial and transverse components of motion allow the direct S waves to be identified and their arrival times measured.

Figures 3 and 4 show the measured first-arrival times for direct P and S waves, respectively. It is obvious that there is a considerable amount of scatter in these times and a number of factors contribute to this. First, there are timing inaccuracies in the recording instruments which can be as large as a few tenths of a second in the worst cases. Second, there are the unknown static corrections due to variations in the material in the first few meters beneath the recording sites. Third, there are the true lateral variations in the velocity structure of the mesa.

In spite of this scatter, it was possible to fit smooth curves through the first-arrival times for both P and S waves and interpret these curves in terms of velocity sturctures. Such curves are shown in Figures 3 and 4 and the results of a standard refraction interpretation are shown in Figure 5.
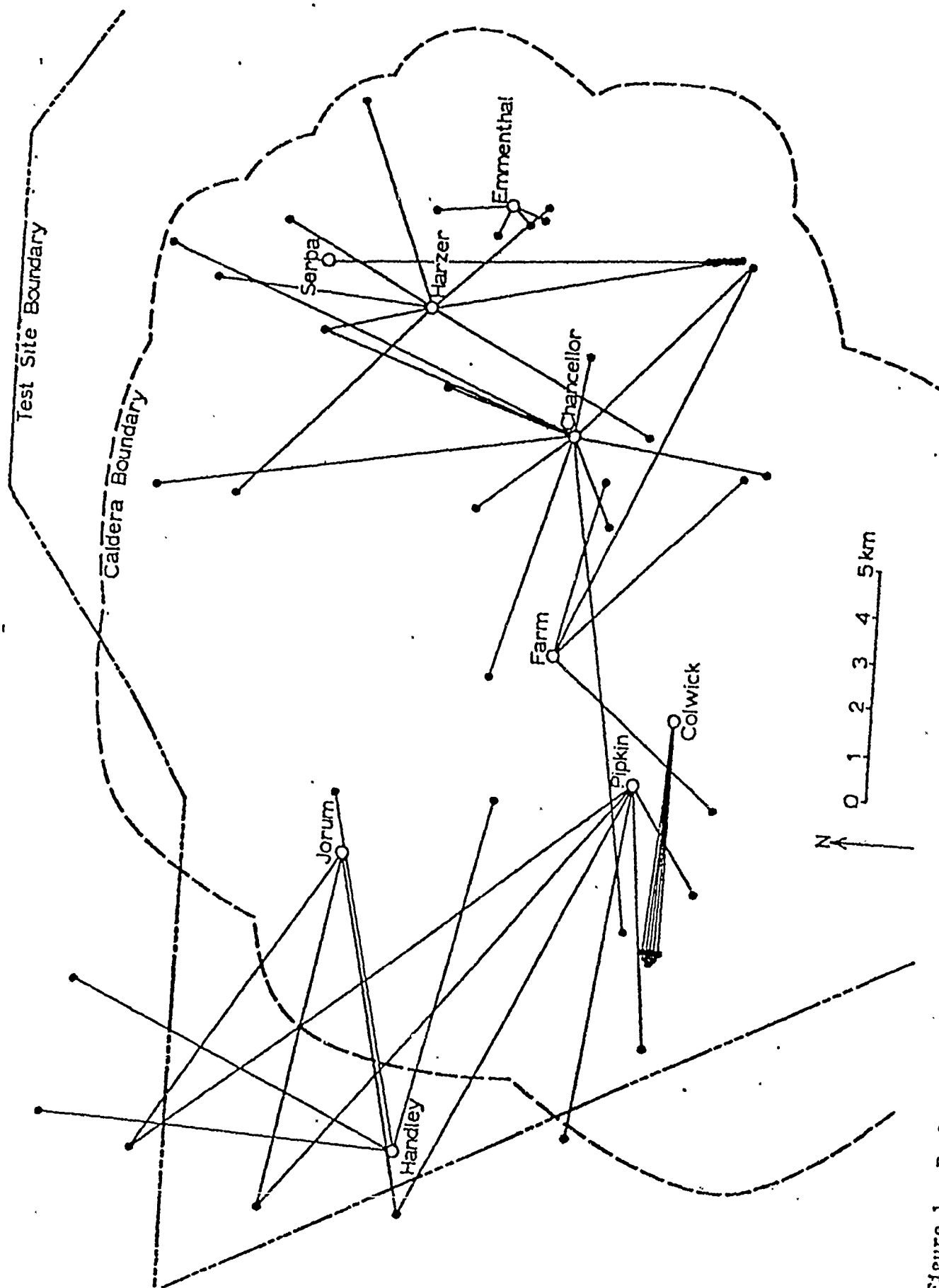
Figure 1. Explosion sites (open circles with names) and respective recording sites (filled circles) for near field data acquisition at Pahute Mesa.
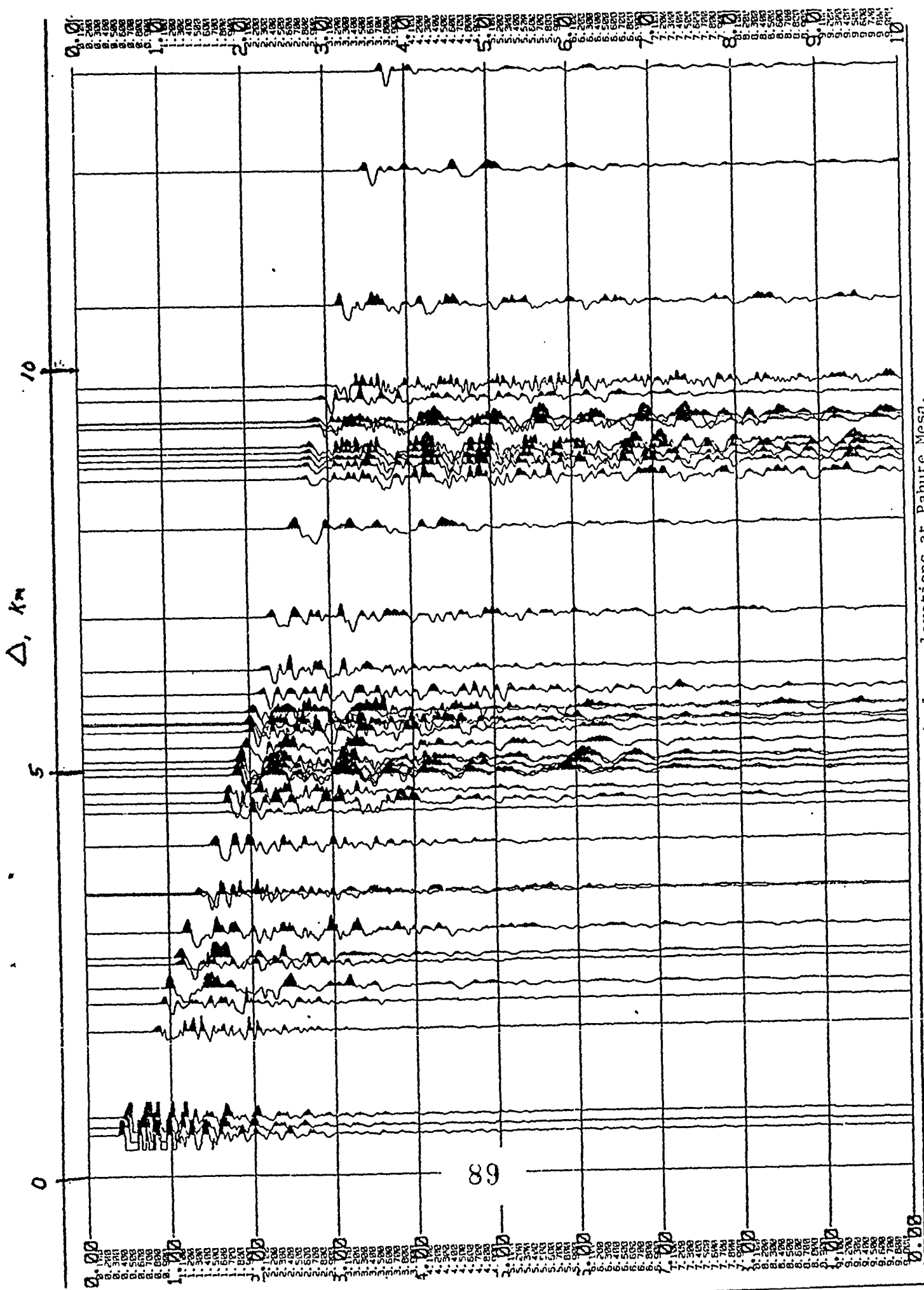
Figure 2. Composite record section for vertical accelerations at Pahute Mesa.
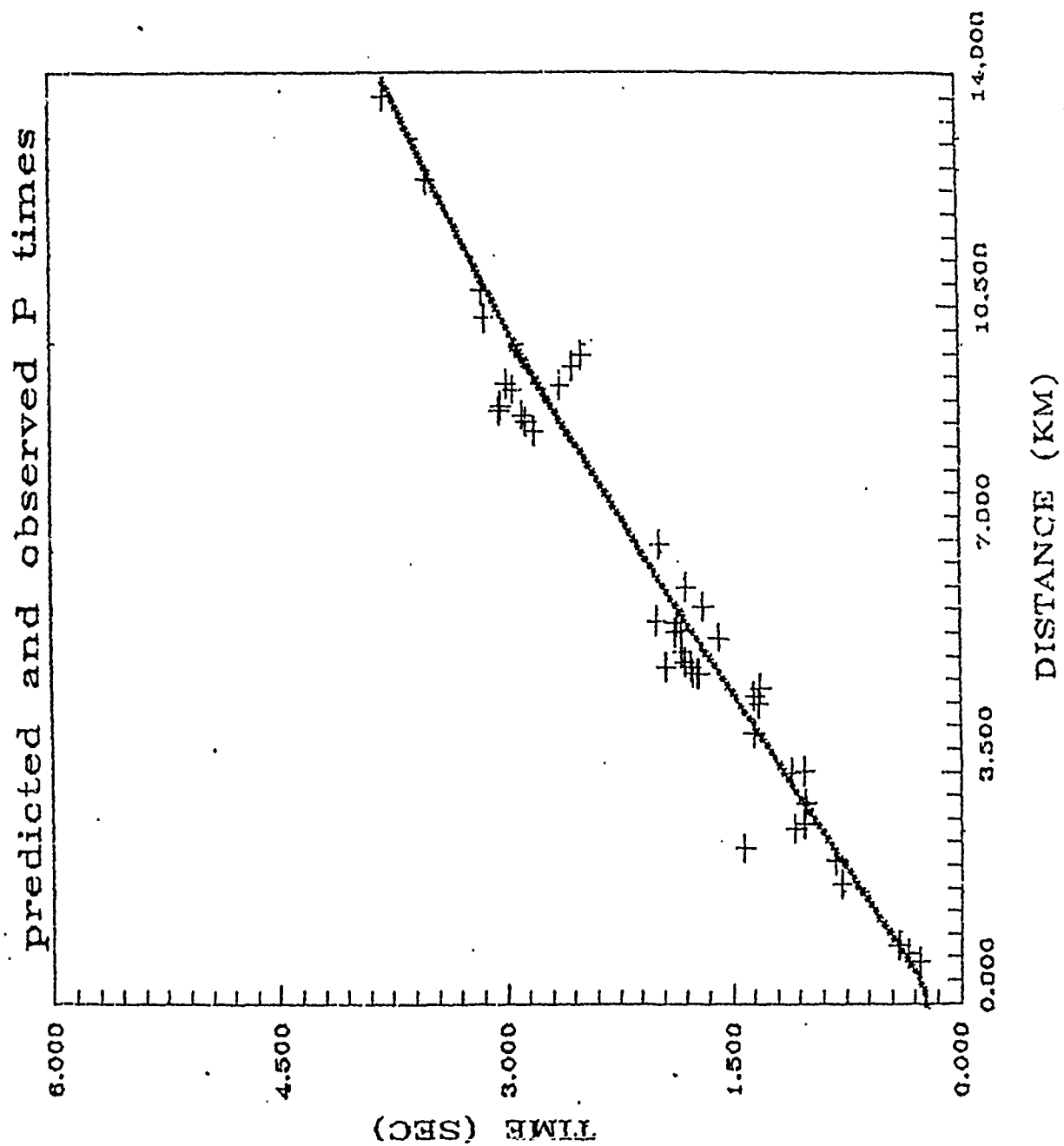
89

predicted and observed P times

Figure 3.

90

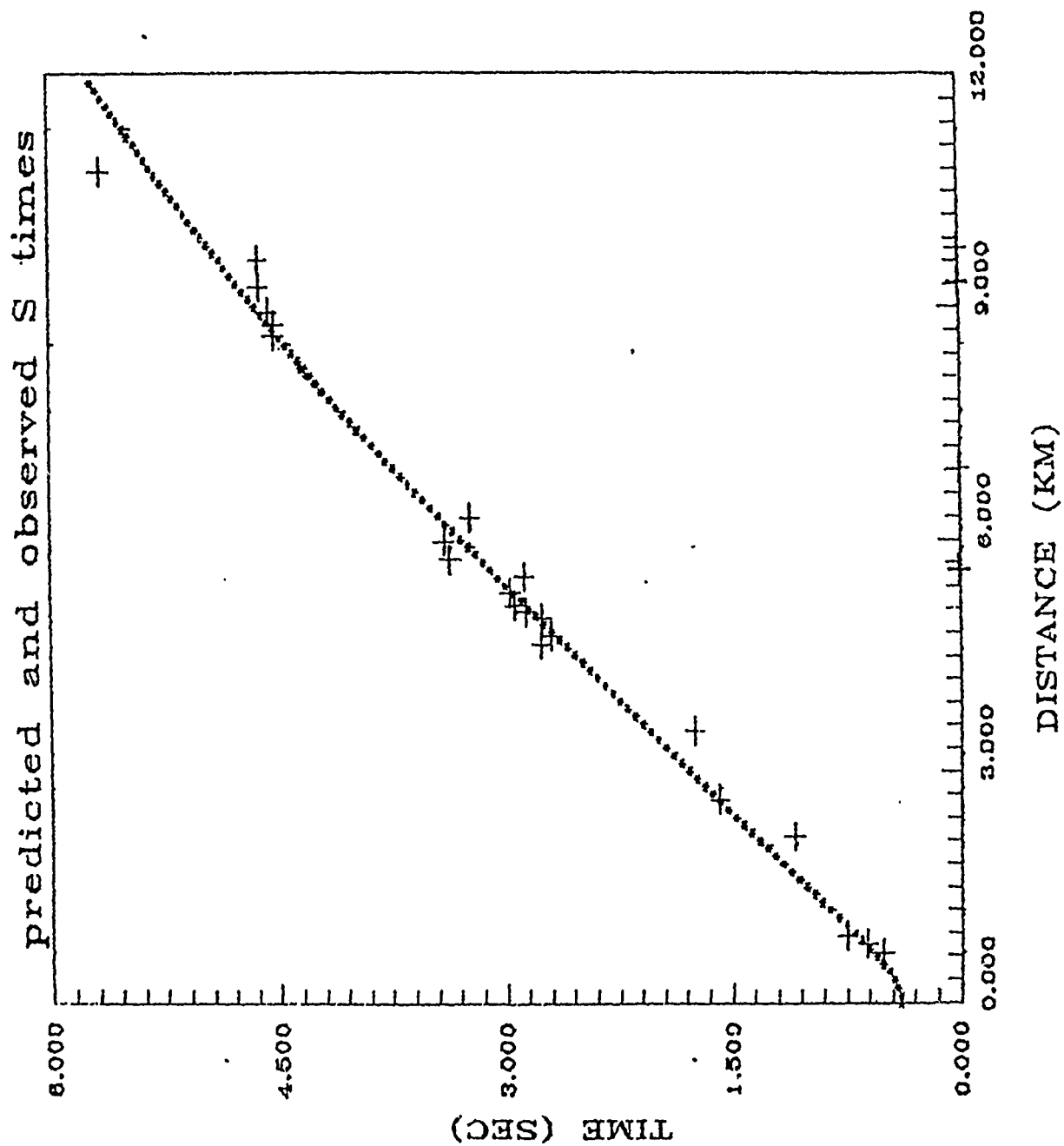predicted and observed S times

TIME (SEC)

DISTANCE (KM)

Figure 4.

91

A considerable amount of well-log data is available for the mesa and this was used to help constrain the upper 0.6 km of the P-velocity model.

One reason for combining the data into the form shown in Figure 2 is that it allows the application of many standard processing techniques that have been developed in the seismic exploration industry for treating reflection data. If reflections could be identified in these data, they would provide useful constraints on the velocity structure. A number of such processing techniques have been applied, but so far the results have been rather indefinite.

Velocity spectra calculations were performed on the data in Figure 2 in an attempt to identify coherent reflections and estimate their rms velocity and depth. In spite of various types of filtering and gain control, a consistent and reliable interpetation has not emerged from this approach. There are of course several reasons why one might expect standard refelction processing techniques to have trouble with these data. The station spacing is uneven and sometimes sparse. Strong surface waves are present. The different explosions may have different source time functions.
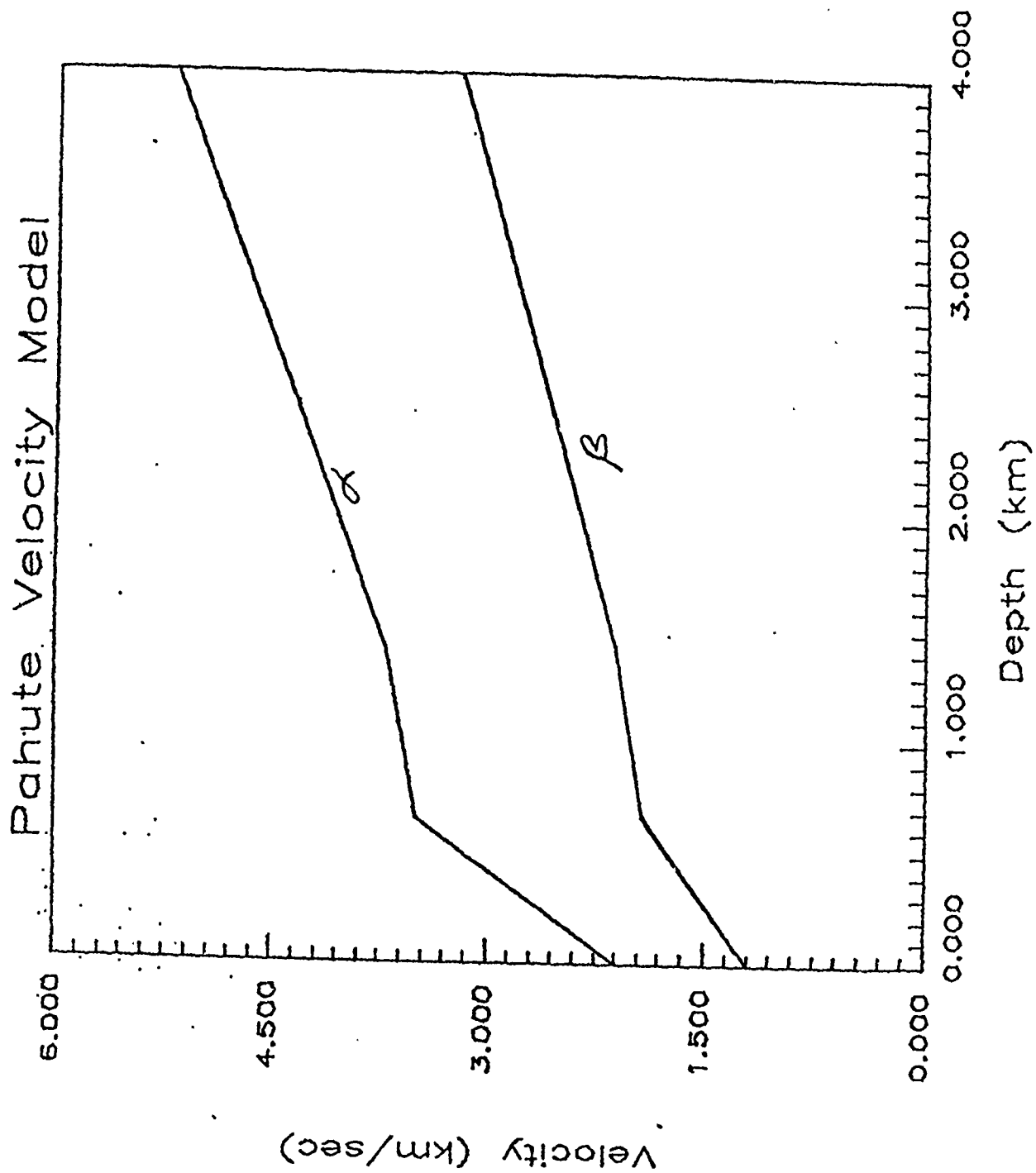
Figure 5.

93

AFTEREVENTS OF NTS EXPLOSIONS

A standard method of identifying the dimensions and orientations of fracture surfaces which are active during earthquakes is to study the locations of small aftershocks. With the considerable evidence for tectonic energy release accompanying nuclear explosions, it seems logical to determine if possible fracture surfaces can also be identified by the explosion afterevents.

For NTS explosions under the control of the Los Alamos Scientific Laboratory (LASL) it is a common practice to record seismic data from a number of instruments located at and around ground zero. Such data are recorded on magnetic tape during the explosion and often the recording continues for as much as a day afterwards. Our approach has been to obtain data of this type from LASL and run it through an Automatic Seismic Processor (ASP) which detects events, measures arrival times and amplitudes, and estimates locations and source parameters.

Figure 6 shows some of the preliminary results for the Chancellor event, a Pahute Mesa explosion in 1983. Data were available for 11 different surface sites within the circle shown on the figure. The dots are epicenters of 257 events which occurred in the time interval of 4-22 hours after the explosion and which had the best time residuals for the estimated hypocenters and origin times. Figures 7 and 8 show the same results plotted on North-South and East-West sections, respectively.

While these preliminary results for the Chancellor event exhibit a considerable amount of scatter and will require more analysis, they suggest some interesting features in the afterevent pattern. There are two main contentrations of activity, one a narrow chimney of activity extending from the shot to the surface, and the other a lobe of activity extending about 3 km to the southwest at the approximate depth of the explosion. This second concentration of activity is unexpected and could have important implications for the source mechanism of this event. Further studies are now underway to check and refine the accuracy of the locations of the afterevents and to determine how this pattern develops in time.
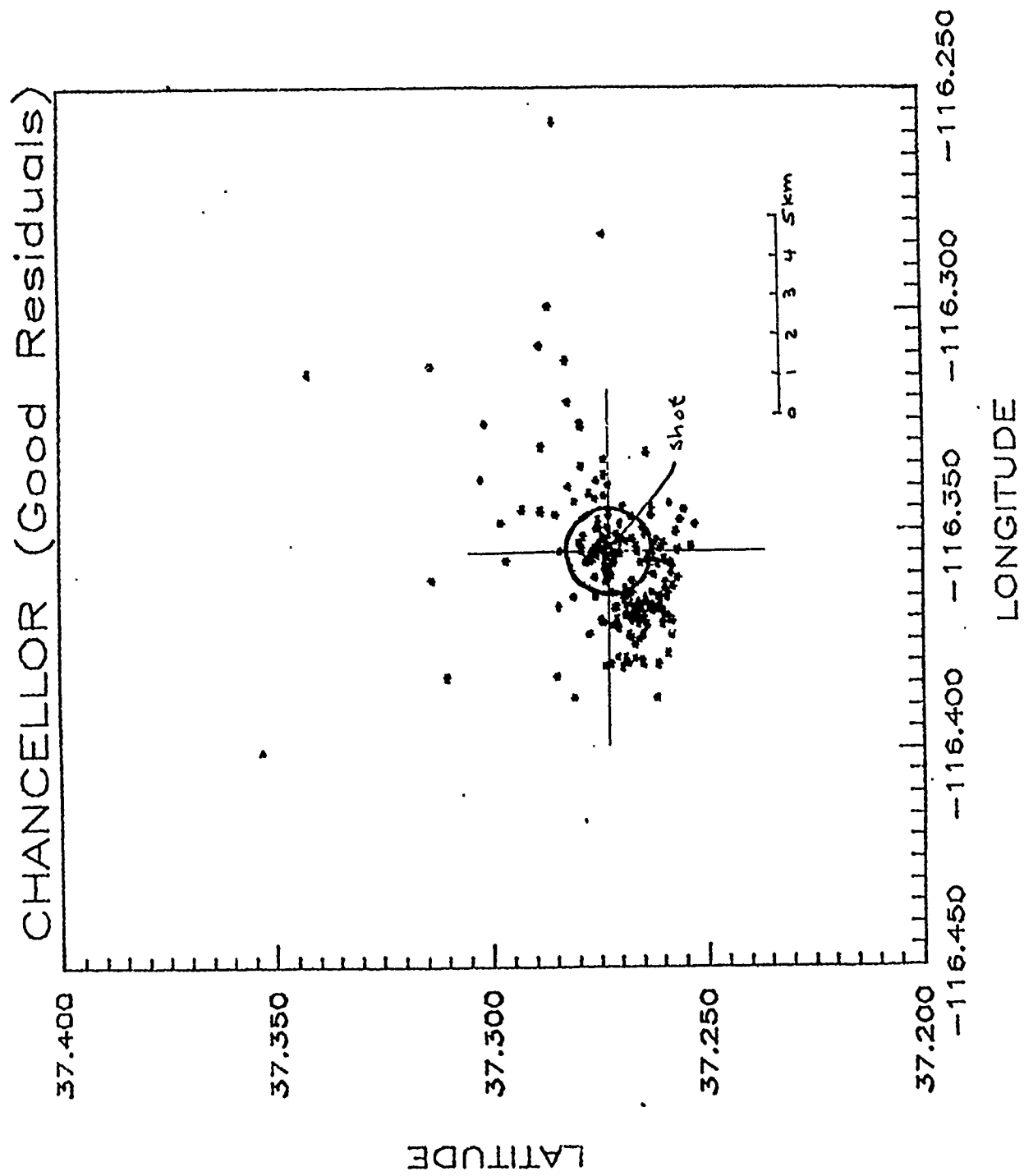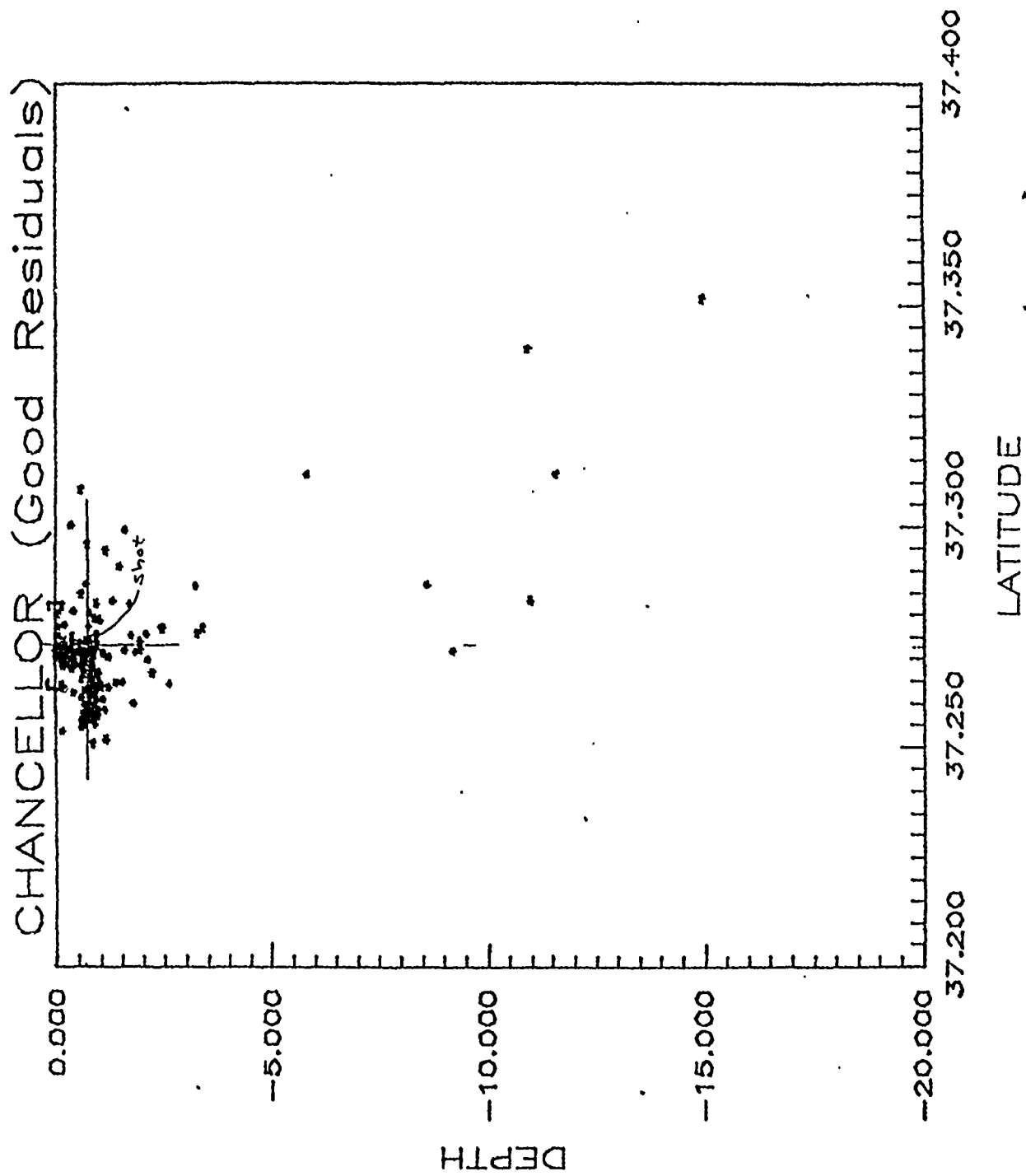
94

Figure 6.

Figure 7.

96

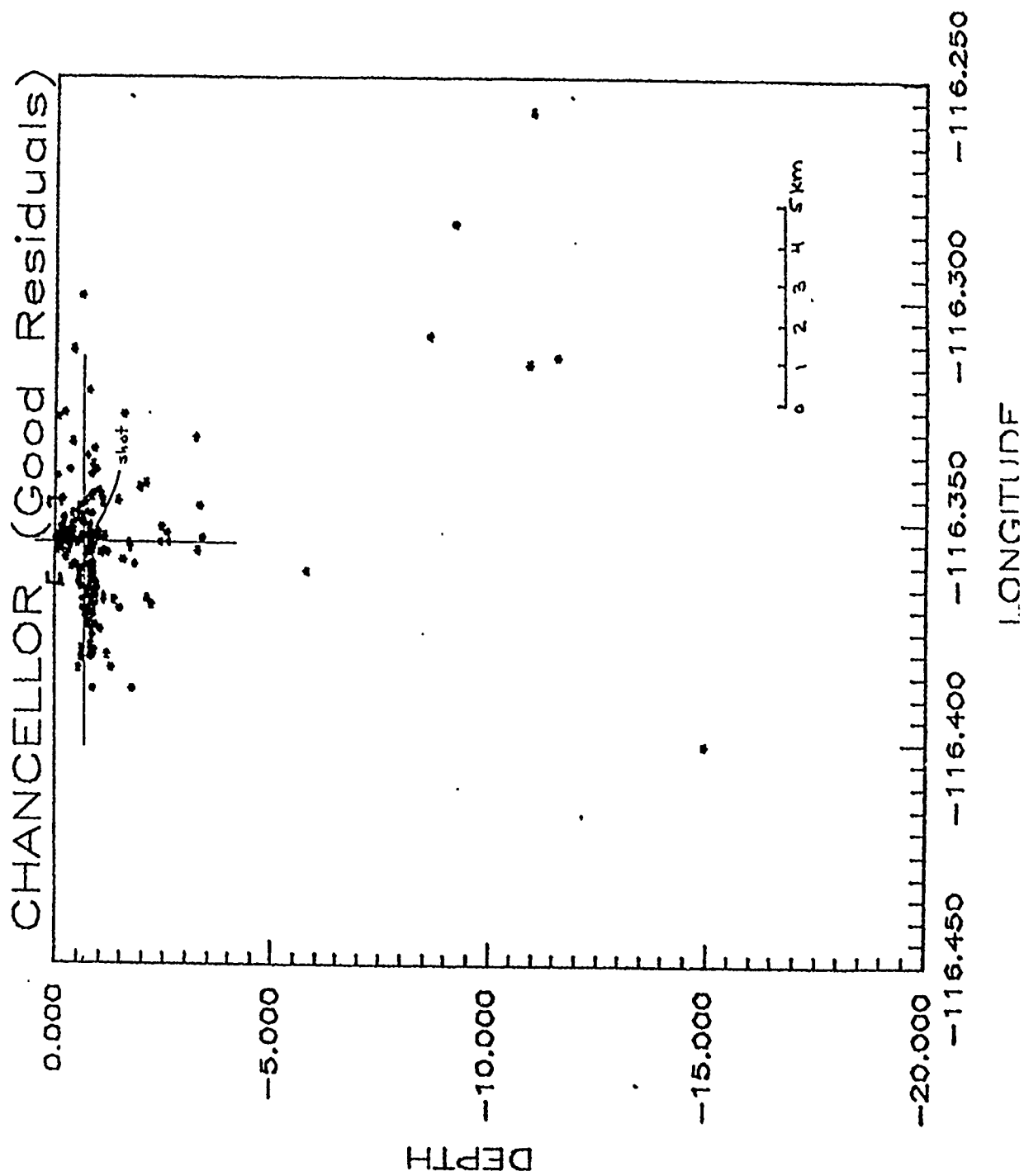CHANCELLOR (Good Residuals)

Figure 8.

97

PAPER TITLE: The Analysis of Seismic Data from the 1983 NGENDEI Expedition

PAPER AUTHOR: John A. Orcutt

CONTRACT NO: AFOSR-84-0043

SUMMARY: The 1983 NGENDEI Experiment conducted in the southwest Pacific to test
the DARPA Marine Seismic System (MSS) successfully collected seafloor and sub-seafloor
estimates of seismic noise levels, extensive refraction profiles and teleseismic and
regional earthquake records. The seismic noise levels within the basement were signi-
ficantly lower than those encountered at the seafloor while the signal levels from both
local explosions and distant earthquakes were essentially identical. This led to a
favorable signal-to-noise ratio for the MSS. The refraction profiles revealed com-
pressional wave anisotropy within the upper crust as well as the upper mantle. S_n
velocity was independent of azimuth. Modeling of the high frequency regional phases
P_n and S_n has been quite successful and we have found the mode of propagation does
not require a high degree of scattering or special waveguides within the lithosphere.

CONCLUSIONS AND RECOMMENDATIONS: Sensors such as the MSS buried within the seafloor
enjoy an enhanced signal-to-noise ratio vis-a-vis seafloor seismometers such as ocean
bottom seismographs (OBS's). The increase in sensitivity, on the order of 18 dB in
this case, may be attractive for applications in nuclear discrimination even though
the operational costs are quite high. The P_n model developed to study the propagation
of these high frequency regional phases is a significant departure from the scattering
theories advanced to explain the extended wavetrain. The extension of these studies
to continental regional phases such as P_g and L_g is recommended particularly if small
arrays are available for measuring the wavenumber content of the seismic waves. An
array study of regional phases on the seafloor is also an attractive experiment and
would, in addition, permit detailed testing of microseismic noise models. Finally,
the apparently high discretization noise levels encountered with the 24-bit EDME
encoder and the acausal signal associated with the FIR filter should be examined in
detail prior to any large-scale implementation.

My current research is centered on the interpretation of the several data sets
collected during the DARPA-sponsored NGENDEI seismic experiment in the southwest
Pacific during 1983. This experiment, which was conducted during Leg 91 of the
Deep Sea Drilling Project, was designed to test the DARPA Marine Seismic System (MSS)
in a realistic environment near an active trench environment. An earlier test of the
system in the northwest Pacific had been unsuccessful because of difficulties in drilling
an acceptable borehole on the seafloor. The Scripps' ship, The R/V Melville, was used
in addition to the D/V Glomar Challenger for tasks related to site surveying, ocean
bottom seismograph (OBS) deployment and refraction shooting. The experiment was
quite successful and accomplished all major goals. The MSS was recorded aboard the
D/V Glomar Challenger for several days of earthquake, refraction and environmental
noise experiments. The subsequent deployment of an autonomous recording package on
the seafloor was successful, but a leak in one of the spheres housing the batteries
resulted in a power loss after approximately two days. The OBS's, launched several
times during the course of the experiment, operated correctly in all instances including
the 45 day teleseismic recording phase at the end. The MSS recording package as well
as the six OBS's were recovered at the end of the experiment by the R/V Melville.

The MSS was left in the borehole and the coaxial cable was terminated in a dummy load. The mooring system used for recovery was redeployed in the event a future experiment became necessary or desireable.

A summary of major results includes:

- Approximately 5 days of MSS recordings were obtained. The data are catalogued and archived at Scripps. The data have been distributed to several investigators and and are available upon request.

- Noise levels on the seafloor, as measured by the OBS's, and within the oceanic basement by the MSS are approximately equal at the microseismic peak, but the OBS levels exceed the MSS levels by 20 dB at higher frequencies.

- Borehole or MSS noise levels are comparable to average continental sites and approach exceptionally quiet land levels at frequencies near 10 Hz.

- The signal levels for local explosions and regional earthquakes are nearly identical within the borehole and at the seafloor. This equality of signal levels leads to an 18 dB signal-to-noise advantage for the MSS recording explosions and a 13 dB advantage for regional and teleseismic events.

- Many observations of high frequency lithosphere phases P_n and S_n were made during the NGENDEI Experiment. Subsequent synthetic seismogram calculations successfully modeled these long wavetrains as a set of refractions from the lower lithosphere with subsequent water and sediment reverberations.

- The low spatial attenuation observed for P_n propagation is associated with the presence of the high Q water column and does not require an intrinsically high Q lithosphere.

- The MSS detection threshold for earthquakes less than 30° distant is ≈ 3.7 because of the ubiquitous, high energy regional phases P_n and S_n.

- The measured ratio of OBS power to MSS power is ≈ 1.2 for explosions and 2.3 for regional earthquakes. These levels are comparable to those predicted by theoretical calculations.

- An anisotropy in the velocity of compressional wave propagation in the upper crust was observed for the first time and was perpendicular to the direction of upper mantle anisotropy. These observations are consistent with a popular model of lithosphere genesis.

- Synthetic P_n wavetrains with durations on the order of 100 s and which are directly comparable to the NGENDEI observations were generated in the complete absence of scattering.

- P_n propagation does not require low velocity channels or waveguides, anomolously high Q values or thin, high velocity lenses within the lithosphere.

- P_n wavetrains are coherent over baselines of 1 km and are "similar" over distances as great as 30 km.

- The observations of P_n and S_n during the NGENDEI Experiment are not depleted in low frequencies as has been reported for observations elsewhere in the Pacific. We attribute this observation to the high bandwidth of the experimental data from NGENDEI.

- The rate of decay of the noise spectra toward higher frequencies is consistent with a model of gravity wave forcing of the microseisms. The flattening of the spectra at frequencies in excess of 2 Hz is due to local and distant shipping noise.

99

- Microseismic noise is coherent over distances of at least 700 m.

- The substantially higher noise levels observed on the OBS horizontal instruments, compared to the vertical levels, and the equality of displacements on the MSS sensors is consistent with the propagation of noise as a fundamental mode interface wave.

- The digital implementation of the low-pass finite impulse response (FIR) filter on the MSS 24-bit A/D system introduced acausal precursors which are most apparent in recordings of impulsive, high amplitude signals.

- A previously hypothesized "reverberant layer" underlying the transparent pelagic sediments was not observed in the survey data and was not found during the drilling program. We attribute previous reports of this "layer" to inadequacies in survey tools.

Simultaneous measurements of ambient microseismic noise at and below the seafloor have been compared over the band 0.2-7.0 Hz using MSS and OBS data collected during NGENDEI. The MSS formed the center of a seafloor array composed of six OBS's deployed at distances ranging from 0.5 to 30 km from the borehole. Noise spectra of displacement power density at both borehole and ocean bottom sites typically displayed the microseism peak between 0.1 and 0.3 Hz (Figure 1). Vertical ocean-bottom and borehole noise levels are nearly identical at the microseism peak, on the order of 10^8 nm/^{2}/Hz, but OBS values exceed MSS values by 20 dB or more at frequencies between 0.5 and 7 Hz. If microseism peak noise is a trapped wave phenomenon as we propose, then the observation that the noise levels were comparable in the OBS and MSS at the microseism peak suggests that the borehole sensor was not sufficiently deep in the basaltic basement to diminish noise levels over the entire band of frequencies. At the microseism peak vertical component noise levels at the quietest land sites are between 10 and 30 dB lower than those measured in the borehole during NGENDEI. At higher frequencies the noise levels measured in the borehole approached those of the quietest land sites.

Figure 2 compares P-wave spectra between the MSS and OBS for nine shots at ranges from 40 to 60 km. The spectral estimates were stabilized by stacking over these nine realizations and the resultant spectra are plotted against the MSS and OBS noise levels. The signal levels on the two types of instruments are essentially identical. This signal level, coupled with the much lower MSS noise level, indicates a signal-to-noise improvement of about 18 dB for the MSS over the OBS.

Both the OBS's and the MSS recorded significant numbers of regional events ($<30°$) several of which were coincidental. Figure 3 is a plot of a seismogram recorded by the MSS at an epicentral range of $12.9°$ and a focal depth of 293 km. The first wave group is comprised of the P waves triplicated by interaction with the 400-km discontinuity. Because the sub-lithosphere mantle beneath this part of the Pacific Basin is highly attenuative, these arrivals are relatively depleted in high frequencies. After $\approx$ 10 s, however, the amount of high-frequency energy increases, corresponding to the arrival of the P_n wave refracted up and around the corner of the descending slab. Both the P_n and S_n phases are apparent in the seismograms and appear as the extended, complex wavetrains beginning at 110 and 240 s.

A complete synthetic seismogram generated for a sub-Moho thrust fault at an epicentral range of 1000 km is plotted in Figure 4. The vertical component is illustrated in (a) and the horizontal component is in (b). The division of these seismograms into two groups facilitates the schematic identification with the oceanic P_n and S_n phases. The group with an onset velocity near 4.7 km s^{-1} is grossly identified as the S_n phase. The first arriving energy within this group is entirely comprised of horizontally polarized shear waves and is absent from the vertical component. The first arriving group has an onset velocity of 8.1 km s^{-1}, a duration on the order of 100 s and extends into the onset of S_n. This group is characteristic of the oceanic P_n phase.

Figure 1. Comparison of vertical-component noise observations from the NGENDEI
Experiment with extremely low-level observations at land sites. The
composite of the Queen Creek and Lajitas spectra may be taken as the
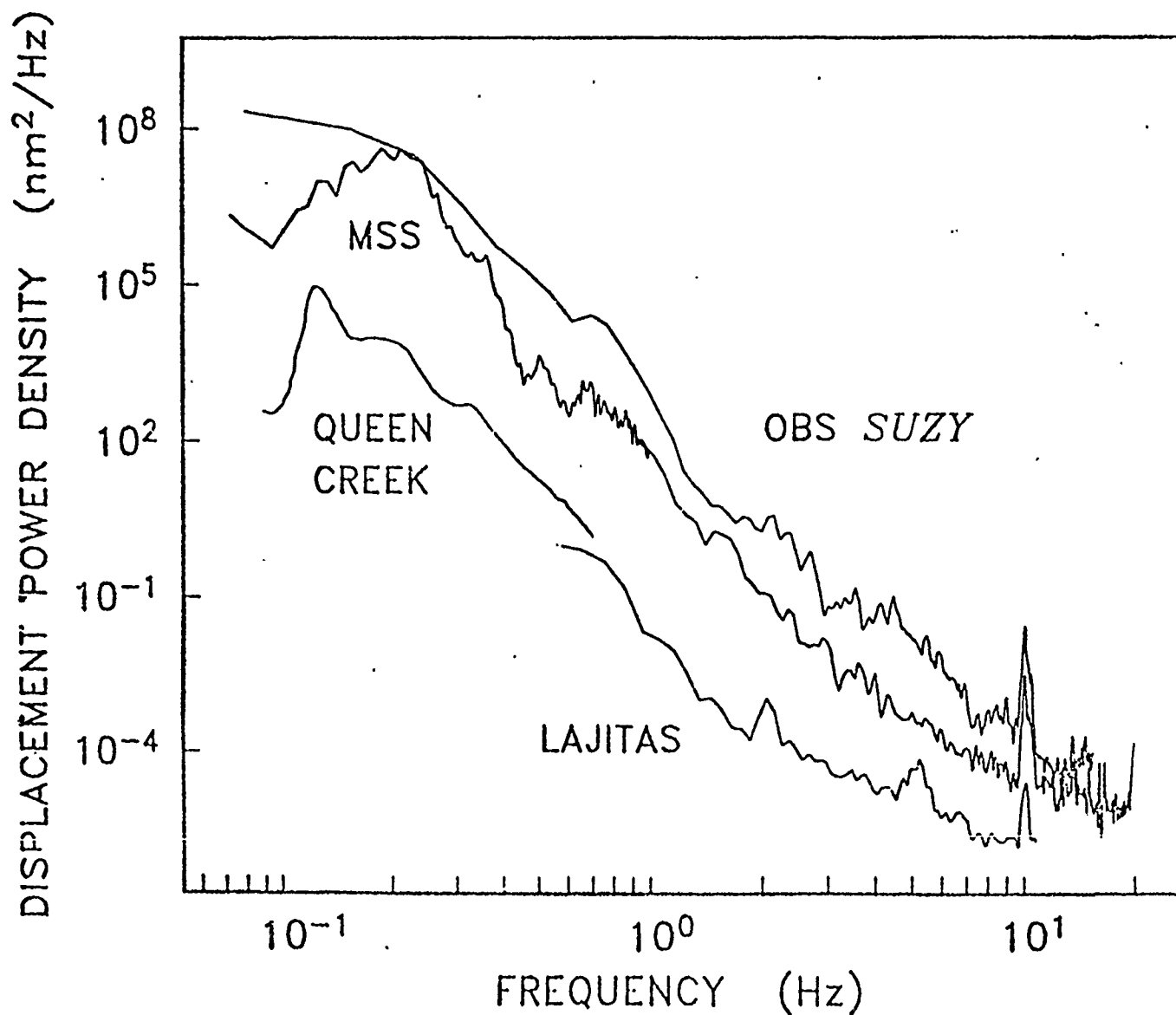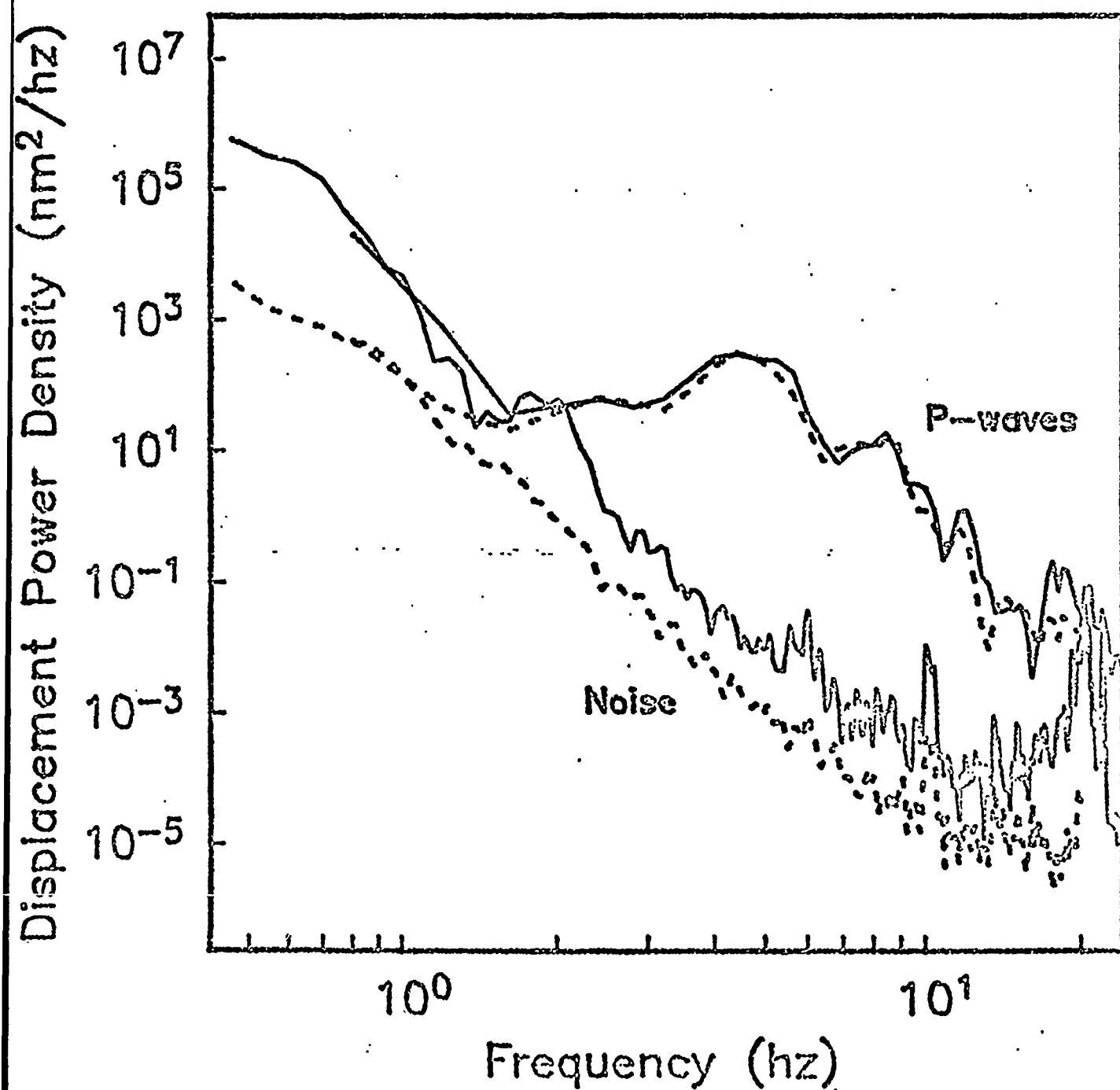lowest-known microseism levels at these frequencies.

Figure 2. Comparison of MSS and OBS spectra of 2.5 seconds of P-wave for 9 shots from line 4b at ranges of 40 to 60 km. Average noise spectra are shown below for comparison. The MSS enjoys a signal-to-noise advantage for recording these shots of about 18 dB.
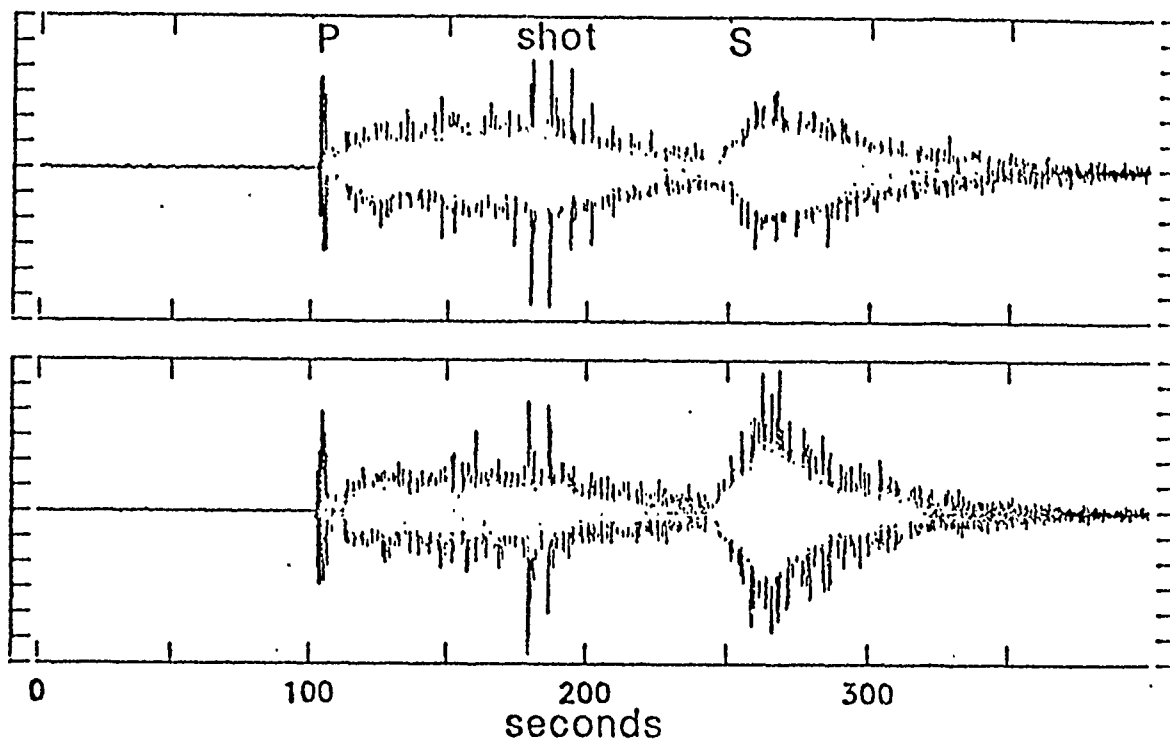
OBS Karen (solid) vs. MSS (dashed)

102

Figure 3a. Short-period vertical (top panel) and horizontal (bottom panel) seismograms recorded on the MSS from the intermediate-focus (h = 293 km) Kermadec earthquake of 7 Feb 83 (m_b = 5.0, Δ = 12.91°). Time is in seconds after 17:57:04.49 Z; tic-mark interval on vertical axis is 5 x 10^3 counts. Spikes between 175 s and 205 s are arrivals from a refraction shot.
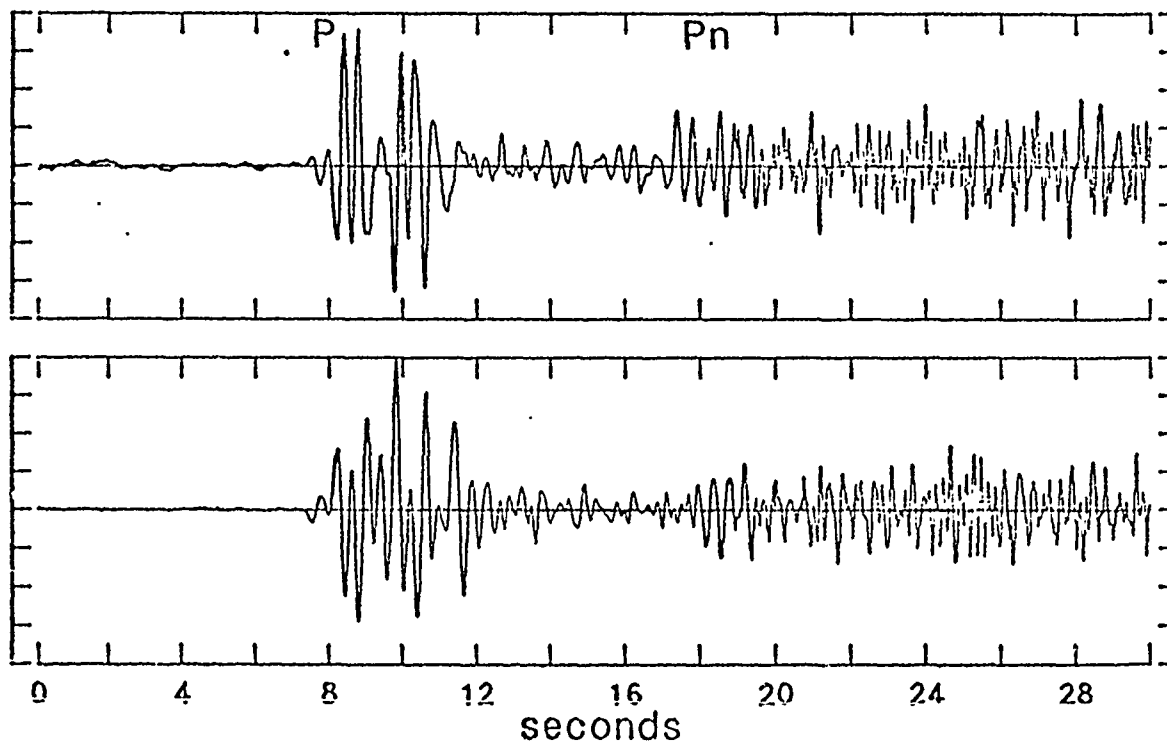
Figure 3b. Short-period vertical (top panel) and horizontal (lower panel) seismograms from the intermediate-focus earthquake of Figure 10, showing P-wave arrivals on expanded time scale. Time is seconds after 17:58:39.49 Z; tic-mark interval on vertical axis is 5 x 10^3 counts. Complex P waveform between 7 s and 12 s is a triplication from the 400-km discontinuity. Arrivals following 18 s are Pn waves refracted up and around the corner of the lithospheric waveguide; their enrichment in high frequencies relative to P is indicative of the low Q of the sub-lithospheric mantle beneath the Southwest Pacific Basin.

103
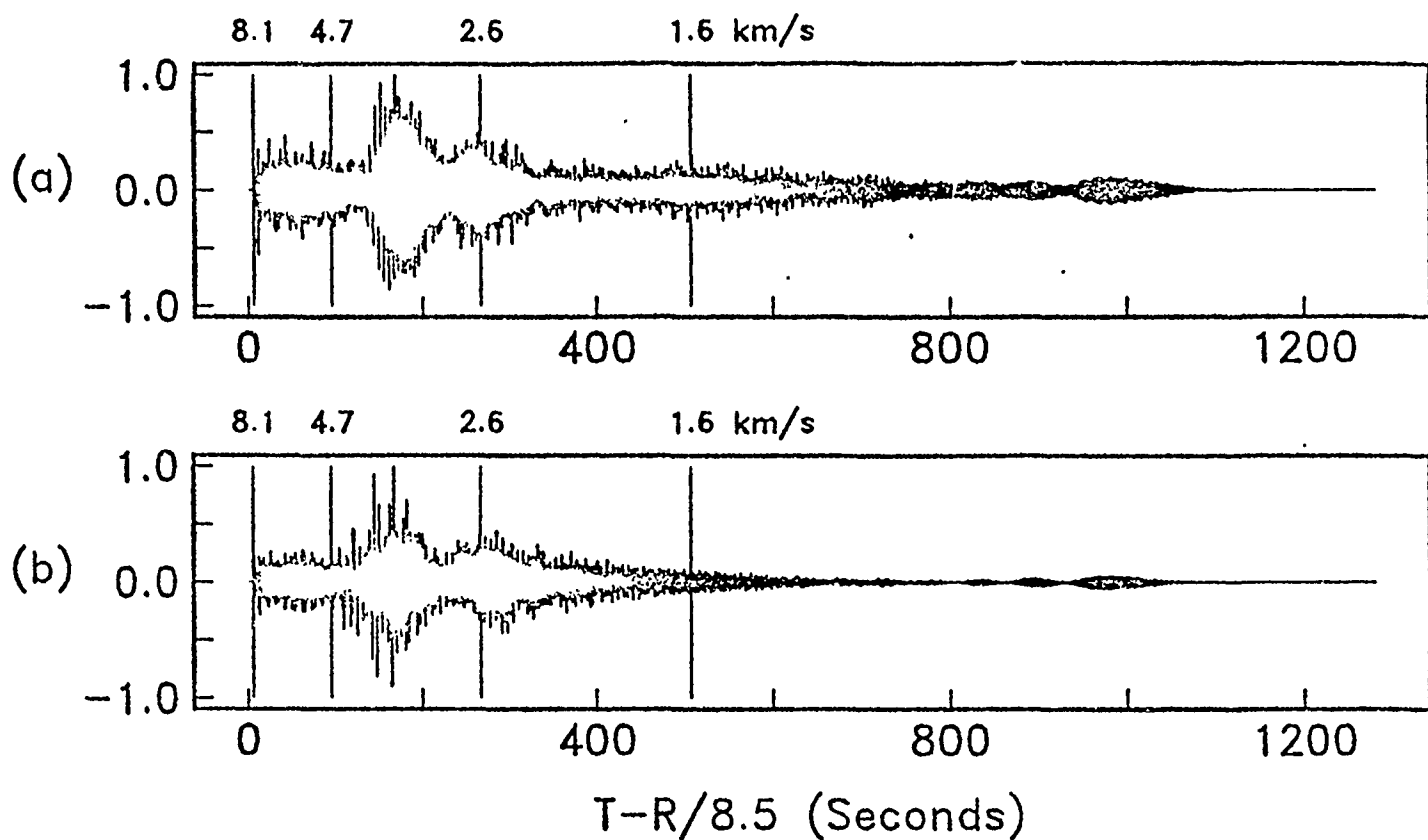
Figure 4. Complete synthetic seismograms at an epicentral range of 1000 km for a thrust fault source at 14.0 km depth. The fault had a dip of 45°, a rake of 270° and an azimuthal relative to the receiver of 60°. (a) Vertical component and (b) horizontal component rotated 25° clockwise from the radial direction. Group velocities of 8.1, 4.7, 2.6 and 1.6 km s^{-1} are indicated. Phase velocities between 3.85 and 25.0 km s^{-1} were included in the calculation.

TITLE: ESTIMATES OF SOURCE AND PATH CHARACTERISTICS IN THE USSR AND NORTH
AMERICA USING SHORT PERIOD (Lg) AND LONG-PERIOD SURFACE WAVE SPECTRA

AUTHOR: Shelton S. Alexander, Department of Geosciences,
The Pennsylvania State University, University Park, PA 16802

SUMMARY: For each of a number of Soviet explosions two different spectral
approaches were used to determine the average Q for Lg signals arriving in a
velocity window ranging approximately from 3.5 to 3.0 km/sec. The mean spectral
slope based on all the events analyzed is then used to calculate the average
attenuation coefficient $(QU)^{-1}$. Results from individual stations of the
Grafenberg array (6 to 13 stations) were averaged for each event and compared
to the single station (A1) results. Additionally, transverse component data
were available for three of the GRF stations. At MAIO only vertical component
Lg data were available. For the propagation path from Semipalatinsk to GRF,
the narrow-band filtering method and the noise-corrected power spectra of both
vertical and transverse components give an average Q for Lg of approximately
1000. For the path from Azgir to GRF the average Q is around 1100. For the
path from Semipalatinsk to MAIO the average Q is approximately 625. There appear
to be no significant differences in the results among individual events for each
path, indicating that the strong tectonic release effects in evidence at long
periods for some of the Semipalatinsk events do not influence the Lg spectra of
those events appreciably in the frequency band .3 to 1.2 Hz, and the best band to
use to establish an m_{bLg} vs m_b relationship is centered at .6 to .7 Hz.
    To overcome long-period non-isotropic source effects for Shagan River events
several very low tectonic release events are used to obtain an empirical "pure
explosion" Rayleigh signature (shape) which then is incrementally scaled and
subtracted from the total Rayleigh wave signature of high tectonic release
events until the best double-couple solution that also fits the Love wave
signals is found (i.e. when the trace of the moment tensor is closest to zero);
the scaled signal is then the appropriate explosion contribution. The
remaining "pure earthquake" Rayleigh and Love wave signals for each event are
interpreted in terms of a best-fitting equivalent earthquake model.
    To determine the approximate threshold for obtaining source parameters from
long-period surface waves in an intraplate setting, the phase matched filtering
method is used to analyze the 1982 New Brunswick aftershock sequence with the
well-recorded mainshock seismograms as the reference signals. The source
excitation function of each aftershock is extracted from the observed signal
spectrum by correcting for the path transfer function and the main shock source
excitation. Preliminary results using this approach on recordings at GDSN
stations in North America indicate that source parameters (including depth) can
be extracted for events as small as about m_b 4 to 4.5.

CONCLUSIONS AND RECOMMENDATIONS: The conclusions are included above.
The principal recommendations are: 1) carry out further evaluations of Lg as
an independent measure of yield, including especially transverse component Lg
observed at local (e.g. NORESS) and more distributed arrays (e.g. GRF, NORSAR);
2) further investigate source parameter estimation methods using 3-component
broad-band recordings at regional distances; and 3) assess relative effects of
scattering vs. absorption for Eurasian and North American Lg propagation paths.

ESTIMATES OF SOURCE AND PATH CHARACTERISTICS
IN THE USSR AND NORTH AMERICA
USING SHORT PERIOD (Lg) AND LONG-PERIOD SURFACE WAVE SPECTRA

S.S. Alexander
Geosciences Department
The Pennsylvania State University
University Park, PA 16802

Several approaches can be used to obtain improved absolute estimates of yield from Lg. One is the approach of von Seggern and Alexander (1983) where path effects are estimated and automatically taken into account to obtain the source moment (yield) for each event. Another is to use a local array such as Grafenberg or NORSAR (NORESS) to obtain the mean, noise-corrected Lg spectrum (with station structure effects averaged out) from which the path Q can be estimated, provided the source spectral shape for Lg excitation can be inferred. Estimates of average Q of Lg signals in the frequency range .3 to 1.2 Hz have been obtained for propagation paths from the Semipalatinsk and Azgir areas of the USSR to the Grafenberg, West Germany (GRF) array and from Semipalatinsk to Mashed, Iran (MAIO). For each of a number of presumed explosions two different spectral approaches were used to determine the average Q for Lg signals arriving in a velocity window ranging approximately from 3.5 to 3.0 km/sec. One involves using a sequence of narrow-band filters at different center frequencies and determining the spectral slope based on both the maximum amplitude and the rms amplitude of the filtered signal in the velocity window. The other involves computing the spectral slope from noise-corrected power spectra of the same velocity window. The mean slope based on all the events analyzed is then used to calculate the average attenuation coefficient $(QU)^{-1}$. In the case of GRF results from individual stations of the Grafenberg array (6 to 13 stations) were averaged for each event and compared to the single station (A1) results. Additionally, transverse component data were available for three of the GRF stations. At the MAIO station only vertical component Lg data were available. For the propagation path from Semipalatinsk at GRF, the narrow-band filtering method gives an average QU of 2980 and 2940 for vertical and transverse components, respectively. The noise-corrected power spectra also give a comparable average QU of 3190. These results indicate an average Q for Lg propagation to GRF of approximately 1000. For the path from Semipalatinsk to MAIO the average QU value is approximately 1480 corresponding to an average Q of around 450. For the path from Azgir to GRF the average QU is approximately 2360 corresponding to an average Q of around 680. Examples of these spectral results for different events are shown in Figure 1.

There appear to be no significant differences in the results among individual events for each path, indicating that the strong tectonic release effects in evidence at long periods for some of the Semipalatinsk events do not influence the Lg spectra of those events appreciably in the frequency band .3 to 1.2 Hz. In addition, plots of Lg spectral amplitude at selected frequencies vs m_b for GRF and MAIO paths indicate that the best frequency band to use to establish an m_{bLg} vs m_b relationship is centered at .6 to .7 Hz. Results for this frequency range are shown in Figure 2. The Lg signal level in this frequency range, corrected back to the source using the estimated $(QU)^{-1}$ value appropriate for each path, as discussed above, gives an estimate

of source strength (yield). Similar analysis of NTS and Hoggar events of known yield is in progress to develop the appropriate conversion of source terms from this method to yield.

To overcome the biasing perturbations on long-period surface waves caused by non-isotropic source effects, a formal moment tensor decomposition (properly constrained) can be used to estimate the isotropic (explosion) contribution if there is sufficient azimuthal coverage. However, in many instances surface wave data from relatively few stations are available, so other techniques are needed, especially for thrust-type tectonic release associated with Shagan River events. Our alternative approach for the Shagan River area is to use several very low tectonic release events to obtain an empirical "pure explosion" Rayleigh signature (shape) which then is incrementally scaled and subtracted from the total Rayleigh wave signature of high tectonic release events until the best double-couple solution that also fits the Love wave signals is found (i.e. when the trace of the moment tensor is closest to zero). This scale factor times the "pure explosion" signature then gives approximately the equivalent Rayleigh wave for the explosion without tectonic release. For each event, these derived "pure explosion" Rayleigh waves for the network stations are then used to estimate M_s (yield). The assumptions in this approach are (a) that "pure explosion" Rayleigh waveform shapes are the same for events of comparable yield in the same source region and (b) the long-period Rayleigh and Love wave signatures generated by non-isotropic source effects can be represented by a double-couple earthquake source. The remaining "pure earthquake" Rayleigh and Love wave signals for each event, interpreted in terms of a best-fitting equivalent earthquake model (strike, dip, rake, depth, moment), characterize the corresponding tectonic stress field at the source. To the extent that similar mechanisms are found for events located in sub-areas of the test site, a further iteration can be made to correct for the tectonic release contribution to the Rayleigh waves observed for the low-tectonic release calibration events.

In order to determine the approximate threshold for determining source parameters from long-period surface waves in an intraplate setting, the phase matched filtering method is used to analyze the 1982 New Brunswick aftershock sequence by using the well-recorded mainshock seismograms as the reference signals. This method not only significantly increases S/N for the aftershock records, but also separates primary Rayleigh or Love wave trains from multipaths and other contaminations. The well-documented mainshock source parameters have been used to synthesize the source excitation function of the reference filter. Hence, we obtain the path transfer function by division of the observed mainshock signal spectrum at each station by the complex-valued, mainshock source excitation function for that source-station azimuth. The source excitation function of each aftershock can then be extracted from the observed signal spectrum through division by the path transfer function. Finally, the resulting Love and Rayleigh source spectral excitation vs frequency and azimuth is used in an inverse calculation to derive the strike, dip, slip, depth, and moment of each aftershock. Preliminary results using this approach on recordings at GDSN stations in North America indicates that source parameters (including depth) can be extracted for New Brunswick aftershocks as small as about m_b 4 to 4.5. Figure 3 and Table 1 give examples of results for four of the New Brunswick events.

Figure 1a

108

Figure 1b

109
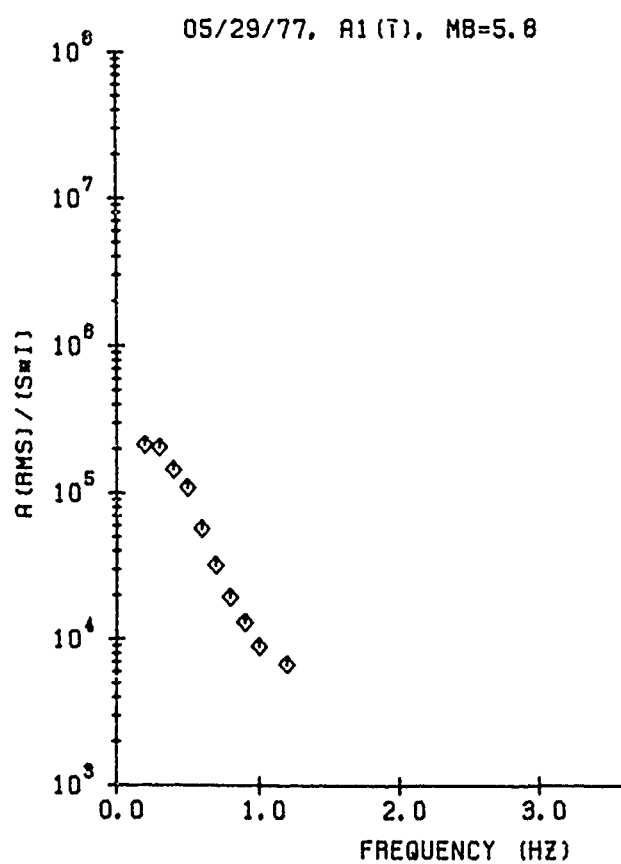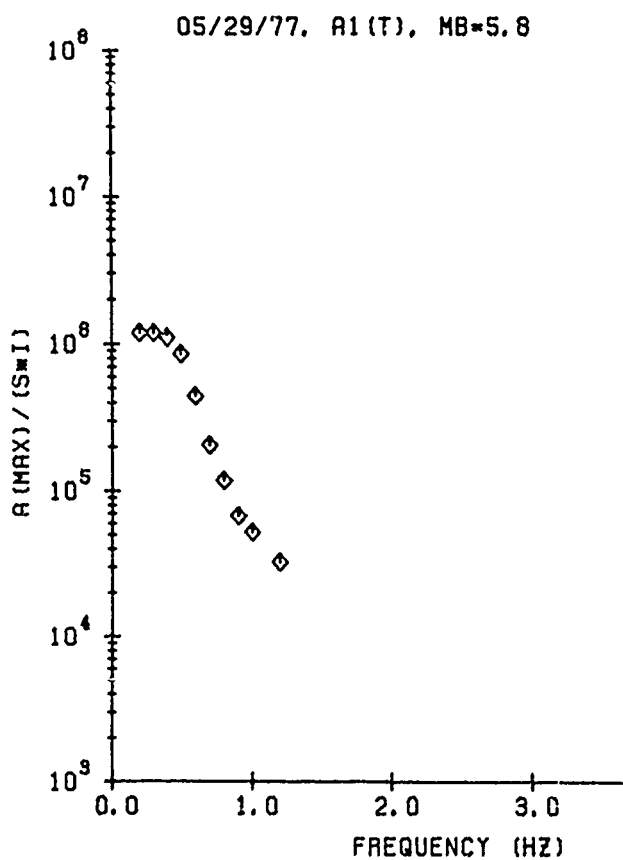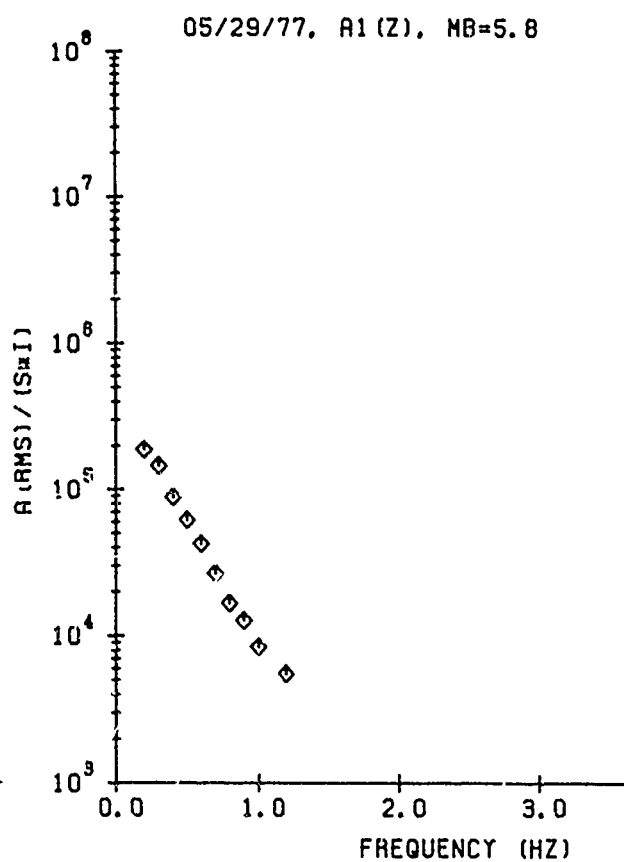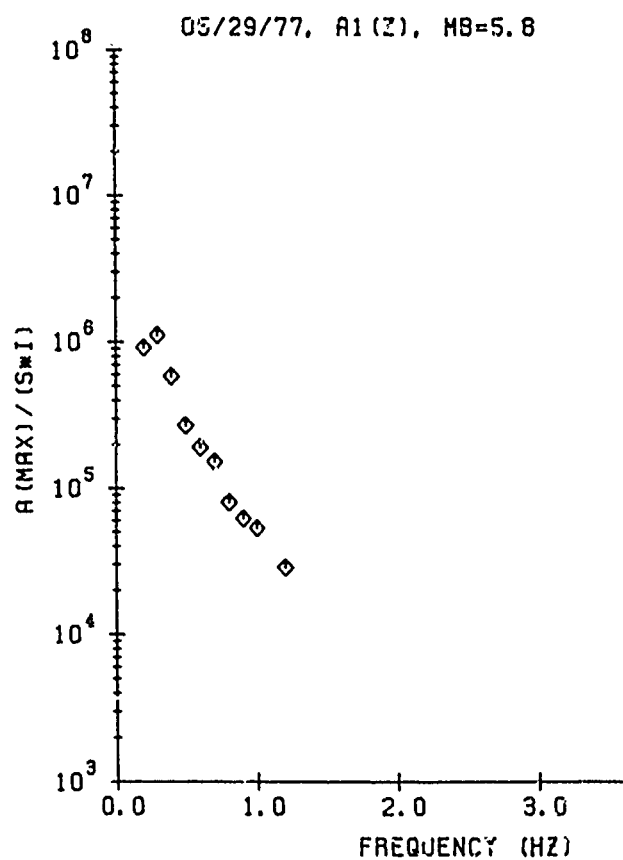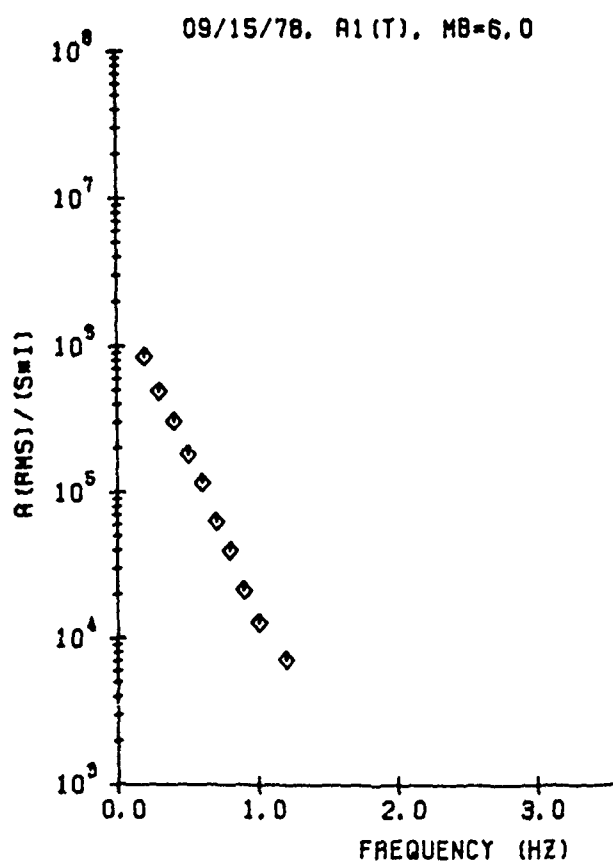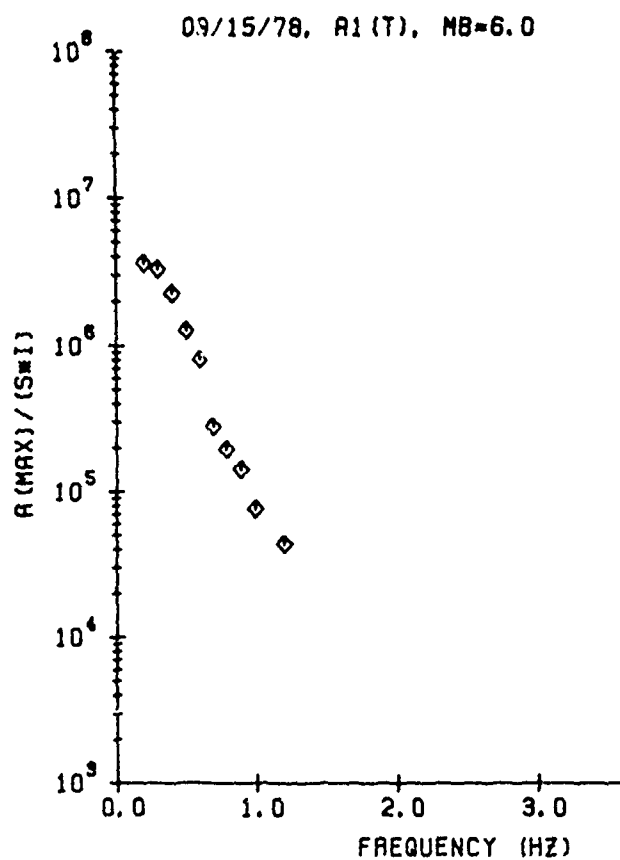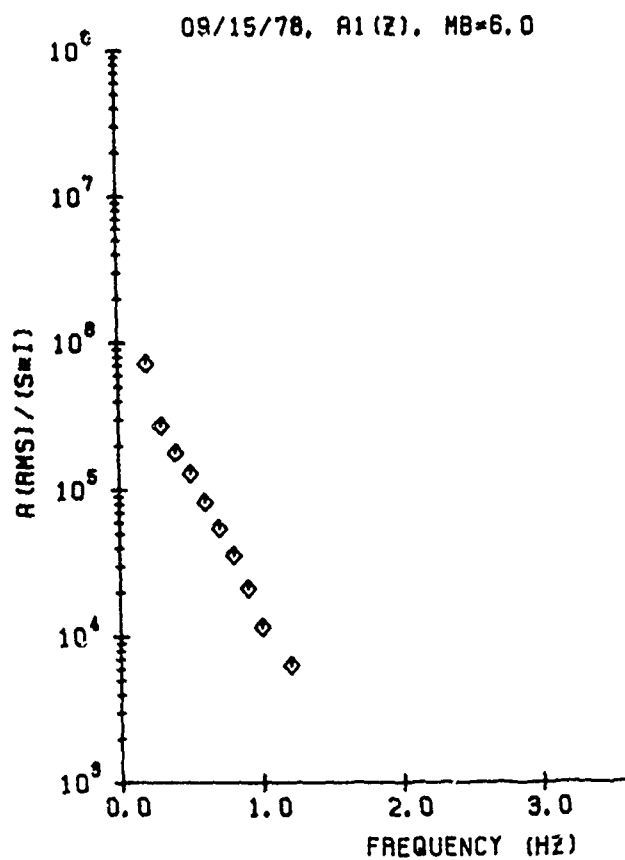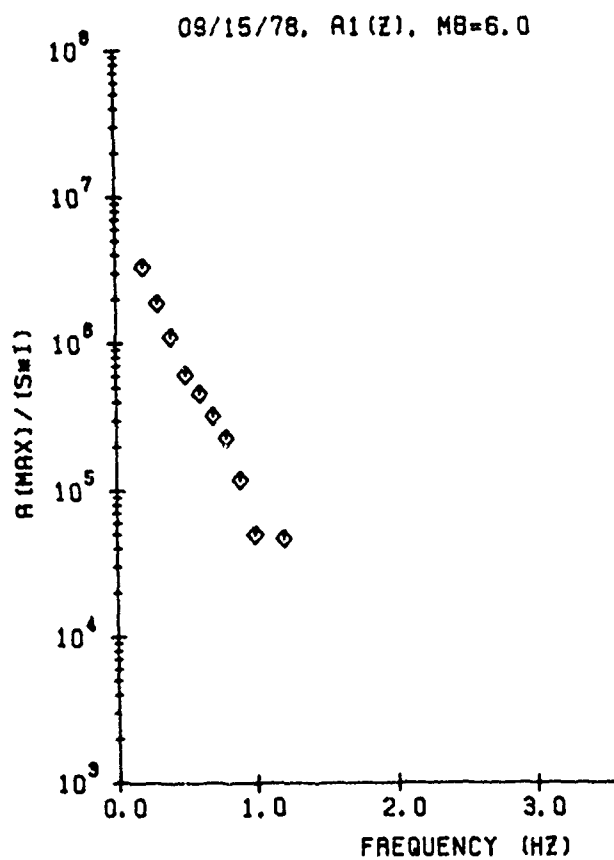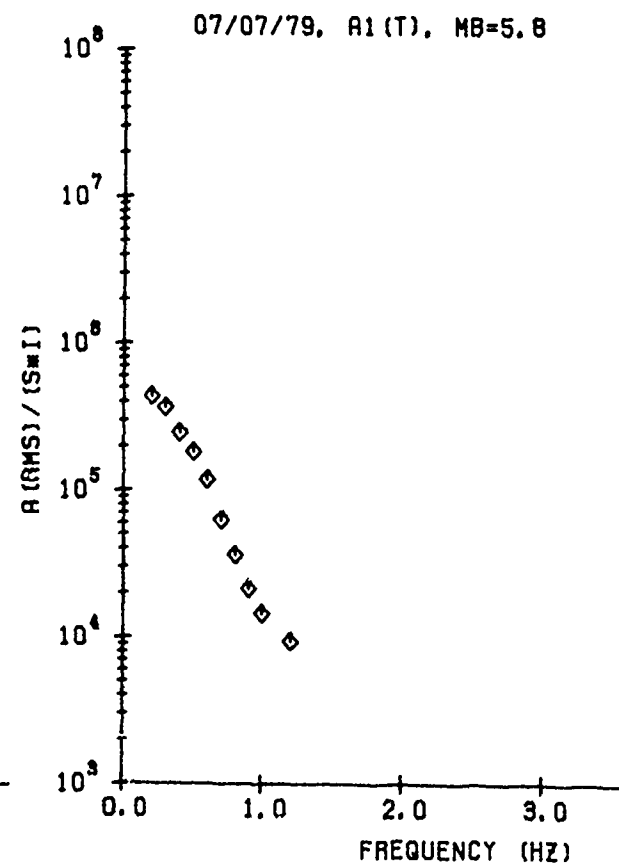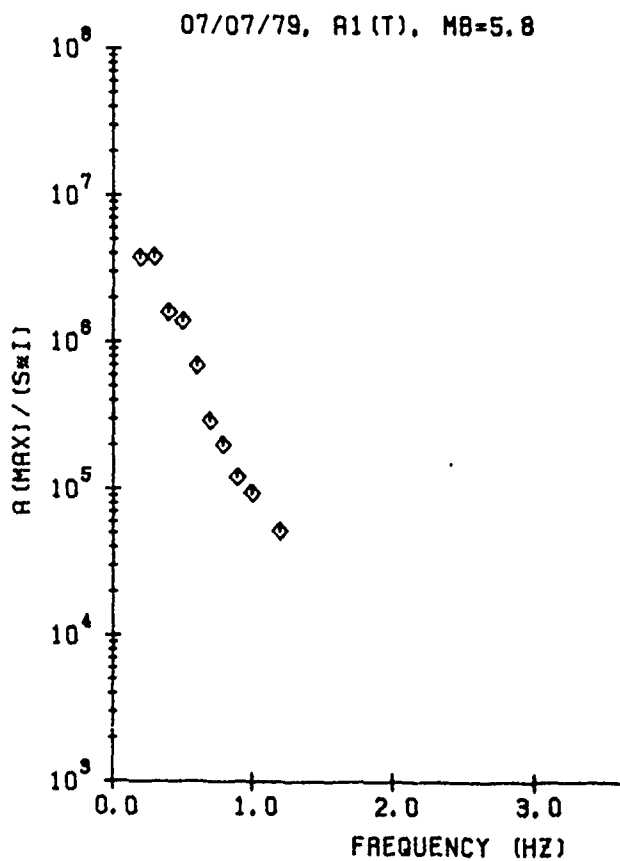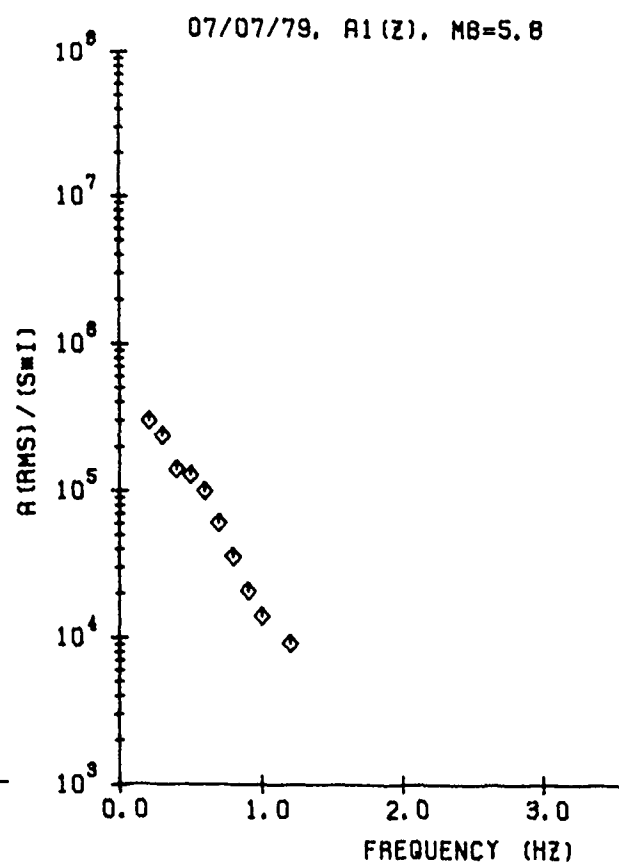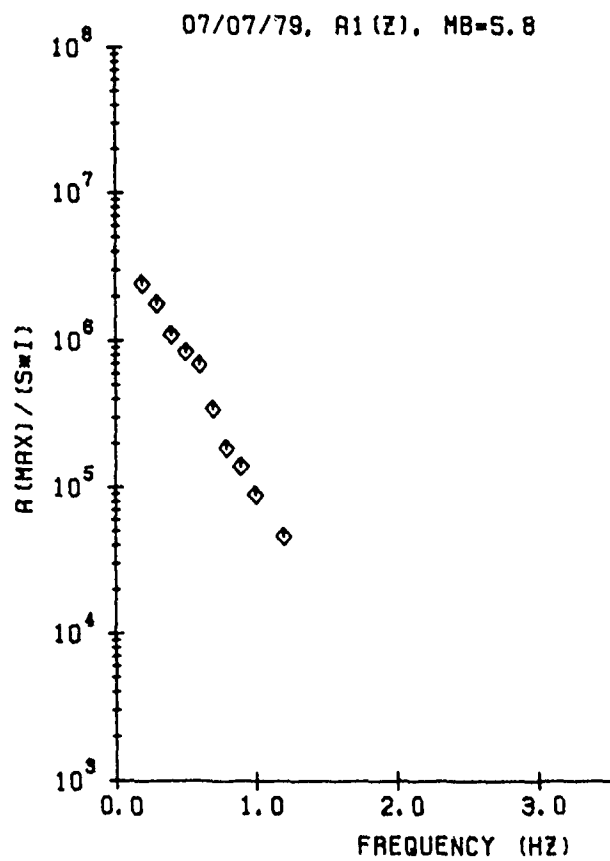
Figure 1c

Figure 1d

111

Figure 1e

112

Figure 1f

113
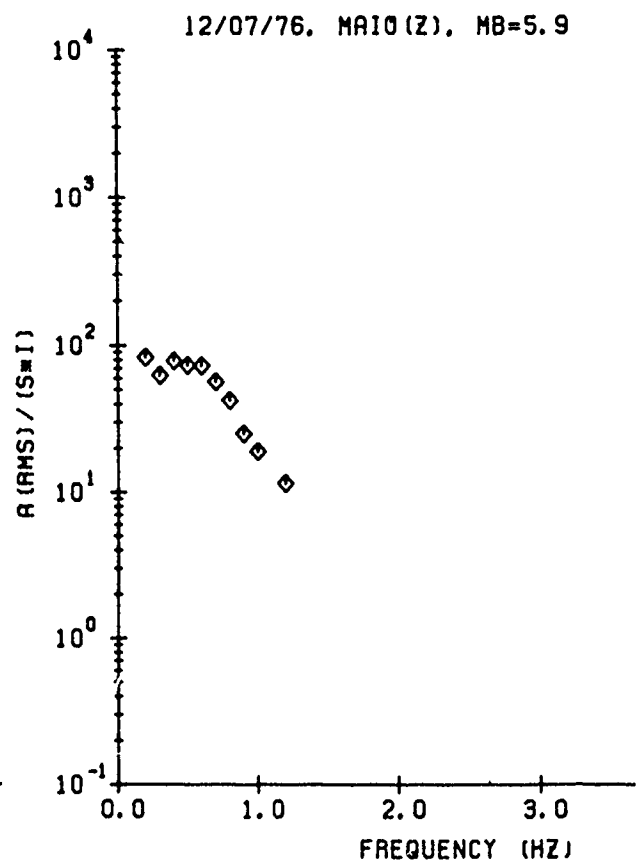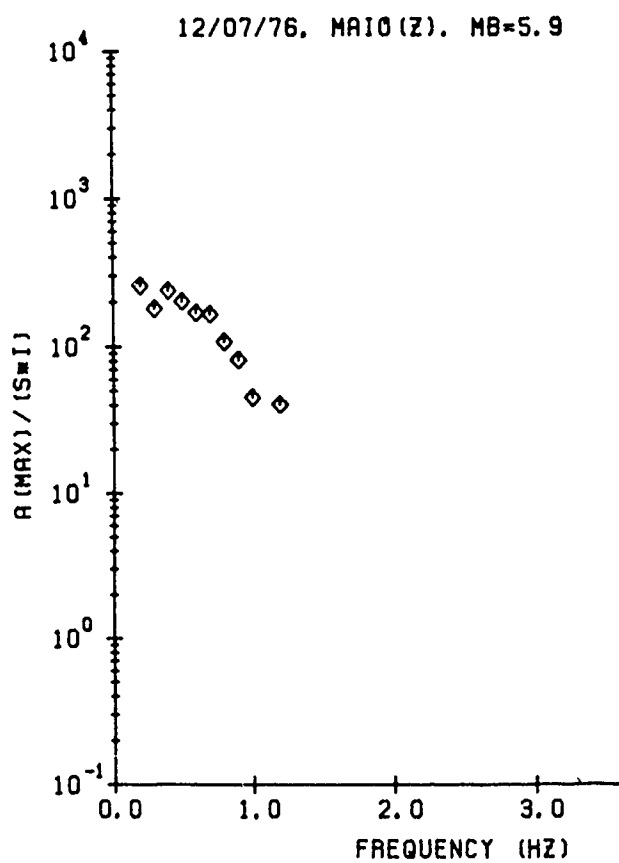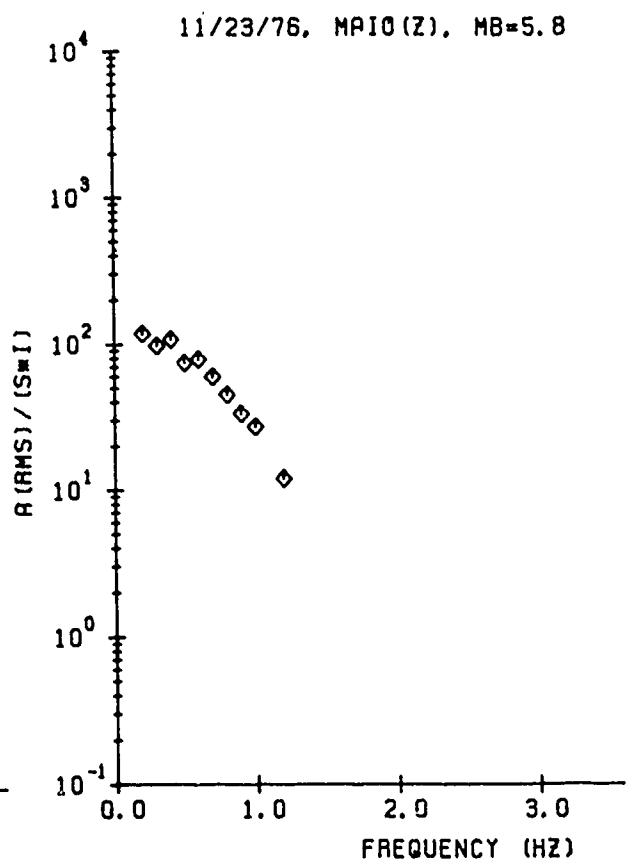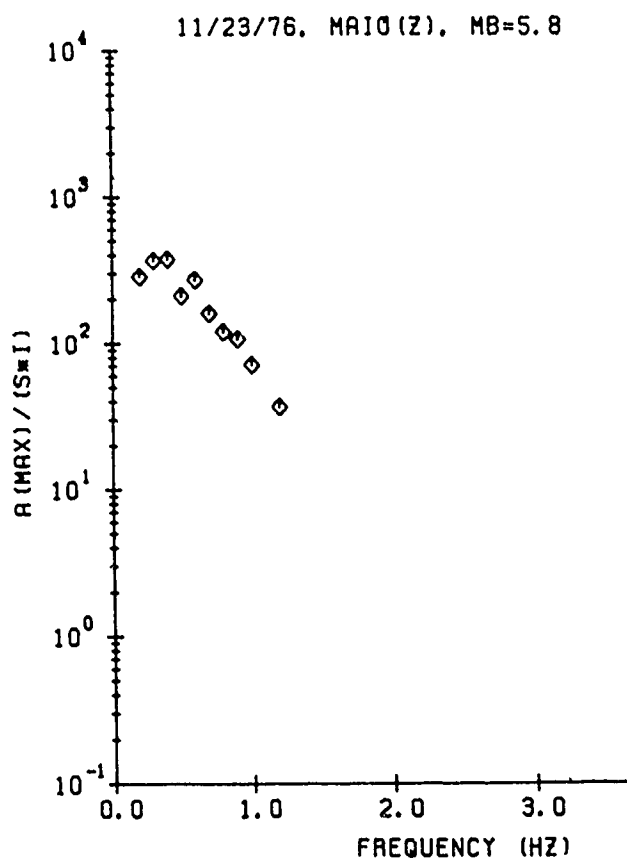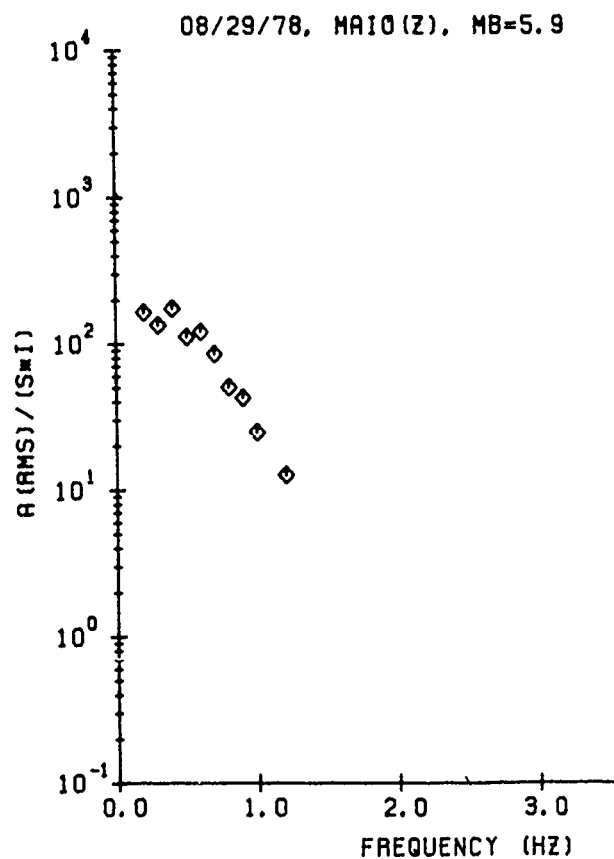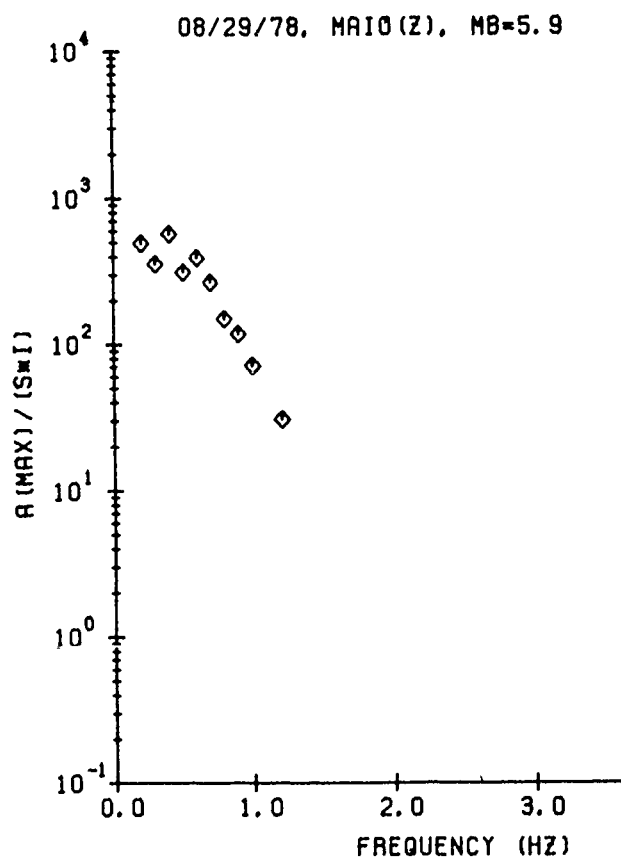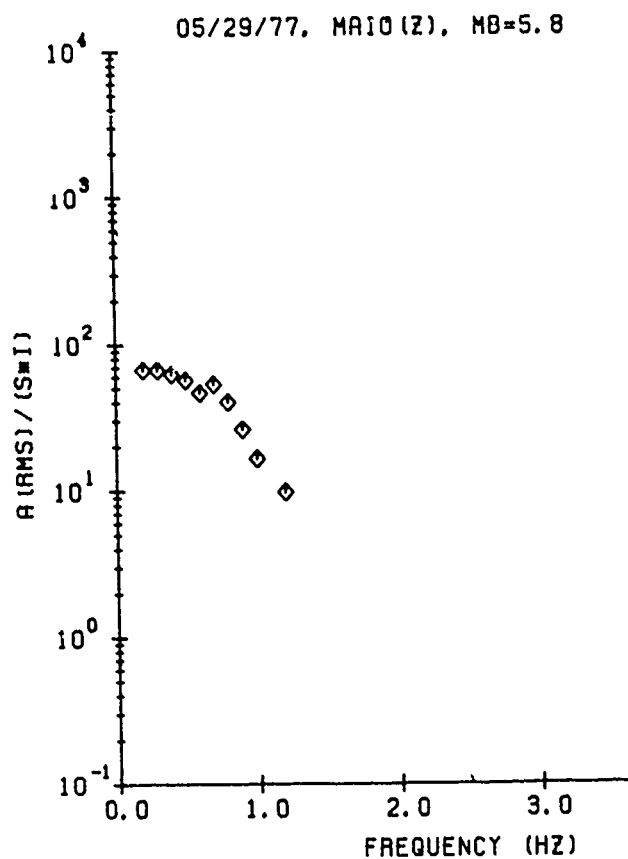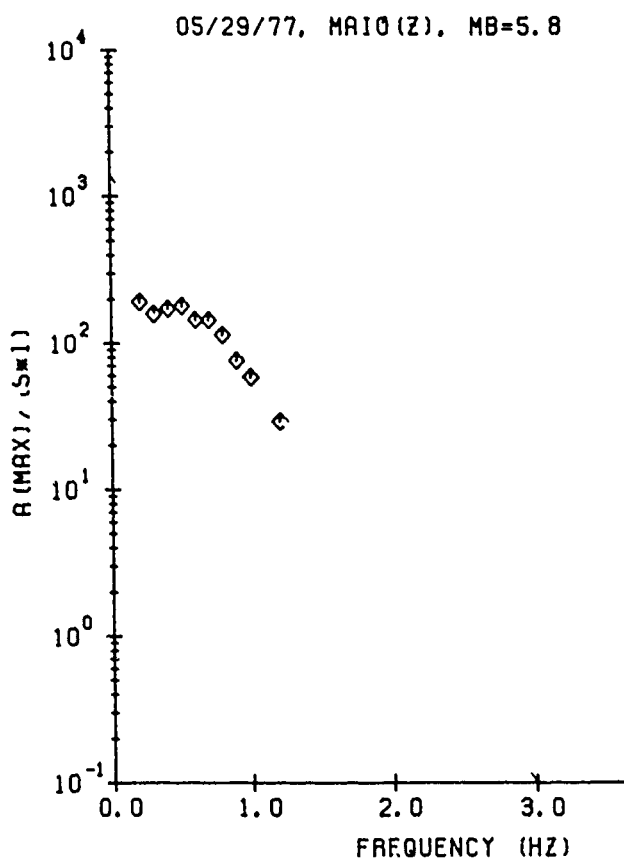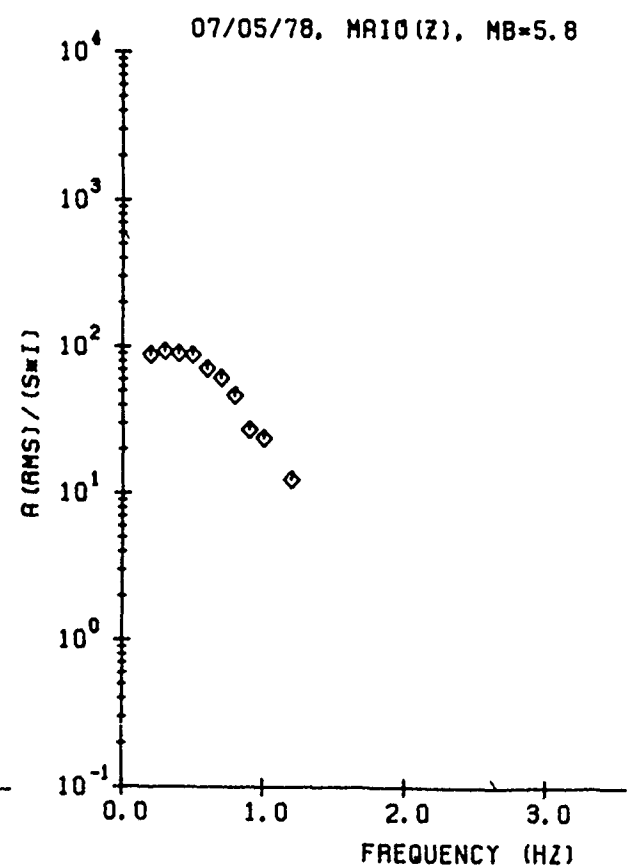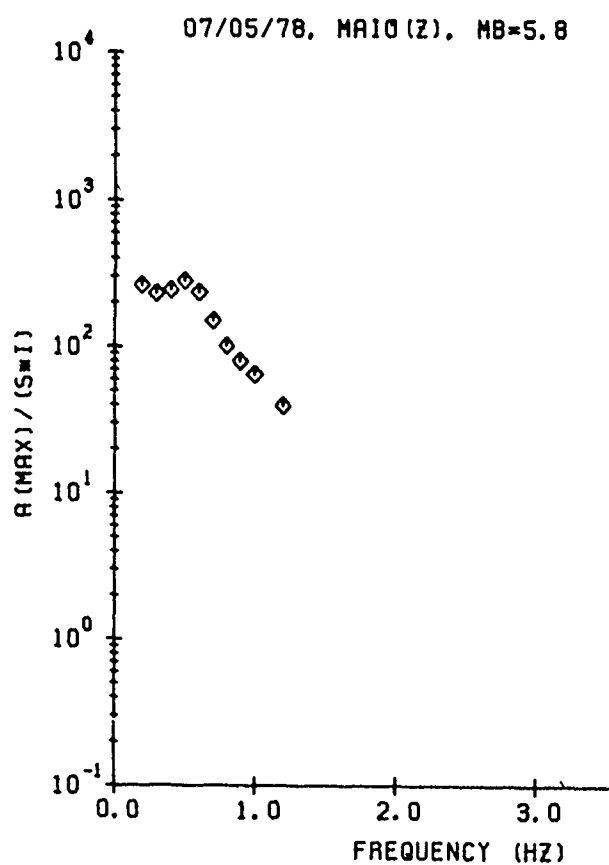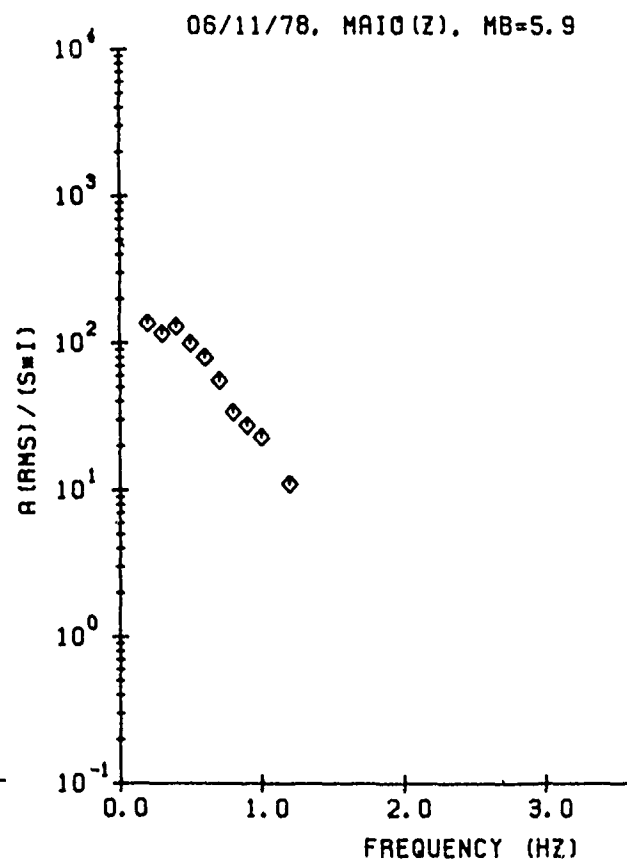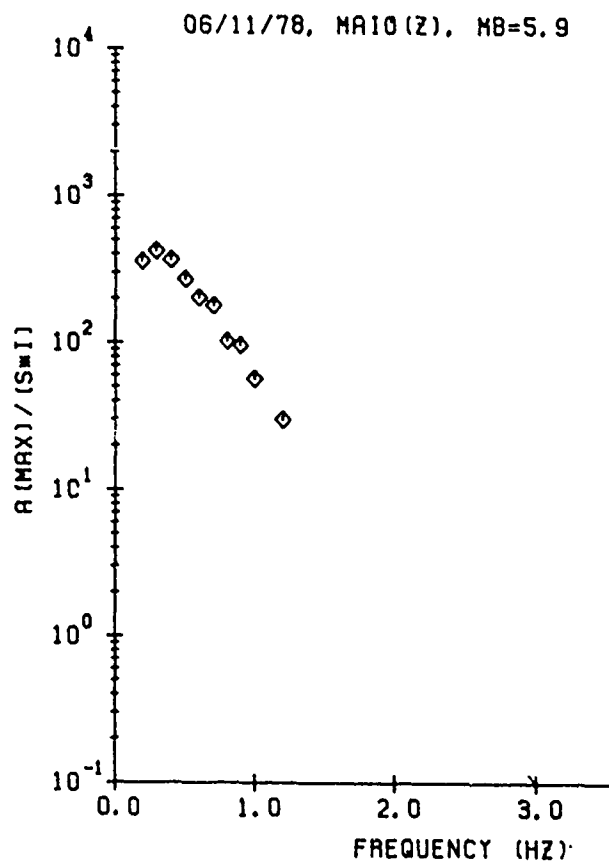
GRAFENBERG A1

CENTER FREQUENCY = 0.7 HZ
⊖– LGZ(RMS)

CENTER FREQUENCY = 0.7 HZ
⊖– LGZ

AMPLITUDE (NM/SEC)

MAGNITUDE (ISC-Mb)

AMPLITUDE (NM/SEC)

MAGNITUDE (ISC-Mb)
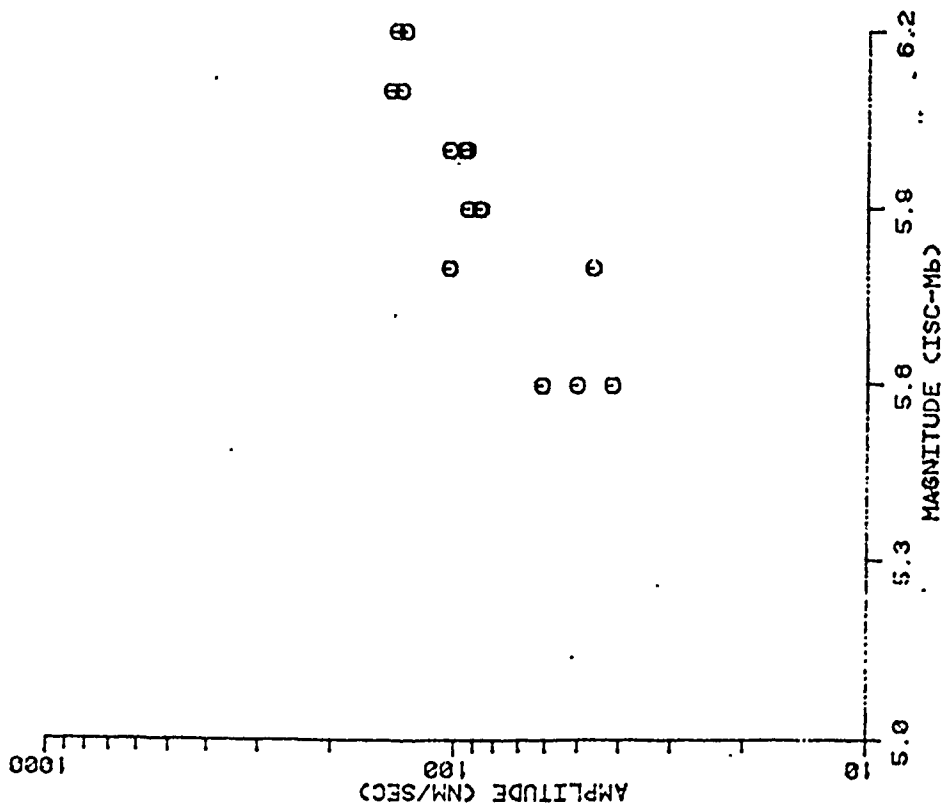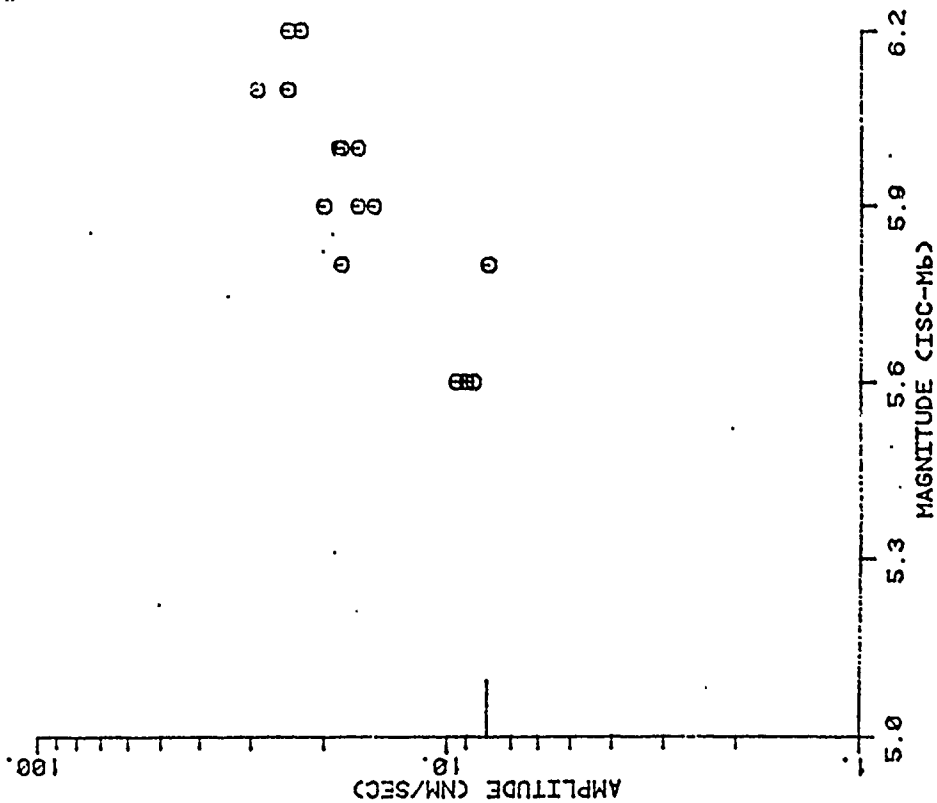
Figure 2a   Observed Lg amplitude vs m_b for the center frequency indicated for Semipalatinsk explosions. Left-hand figure is the maximum amplitude and the right-hand figure is the RMS in the lg velocity window.

114
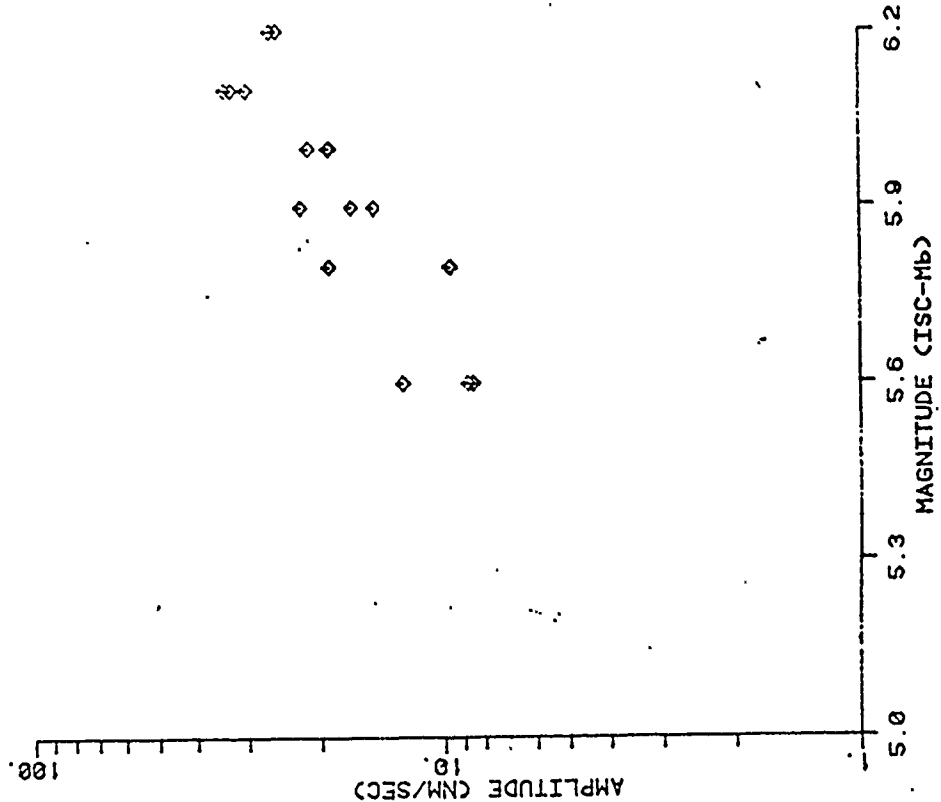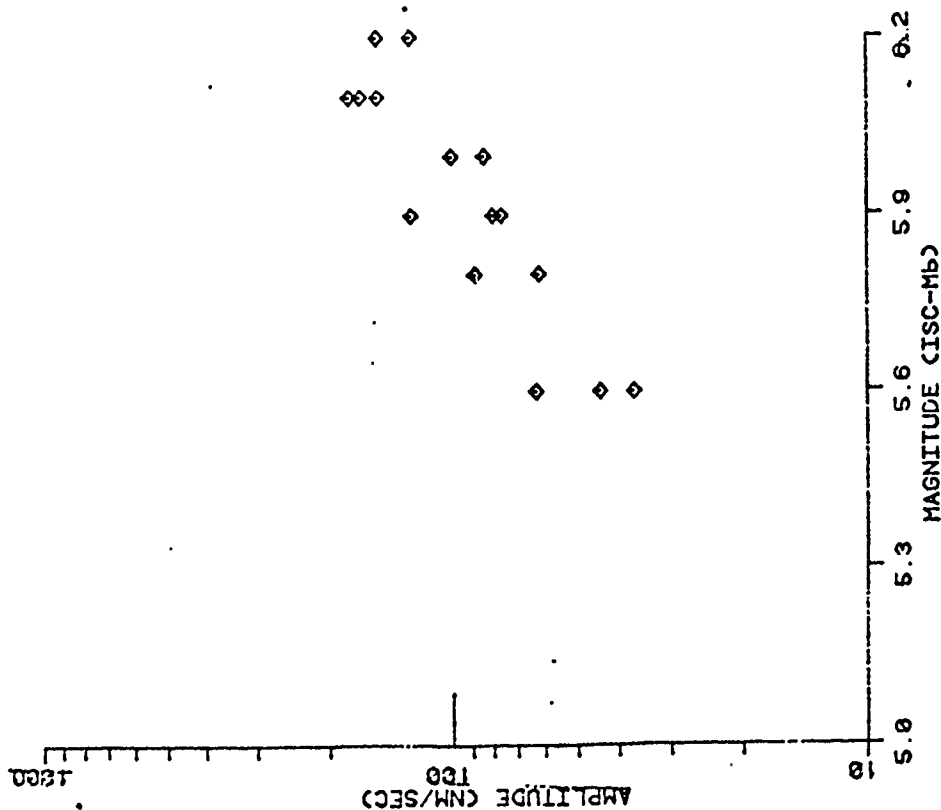
Figure 2b   Observed Lg amplitude vs m_b for the center frequency indicated for Semipalatinsk explosions. Left-hand figure is the maximum amplitude and the right-hand figure is the RMS in the Lg velocity window.

Figure 2c   Observed Lg amplitude vs m_b for the center frequency indicated for Semipalatinsk explosions. Left-hand figure is the maximum amplitude and the right-hand figure is the RMS in the Lg velocity window.
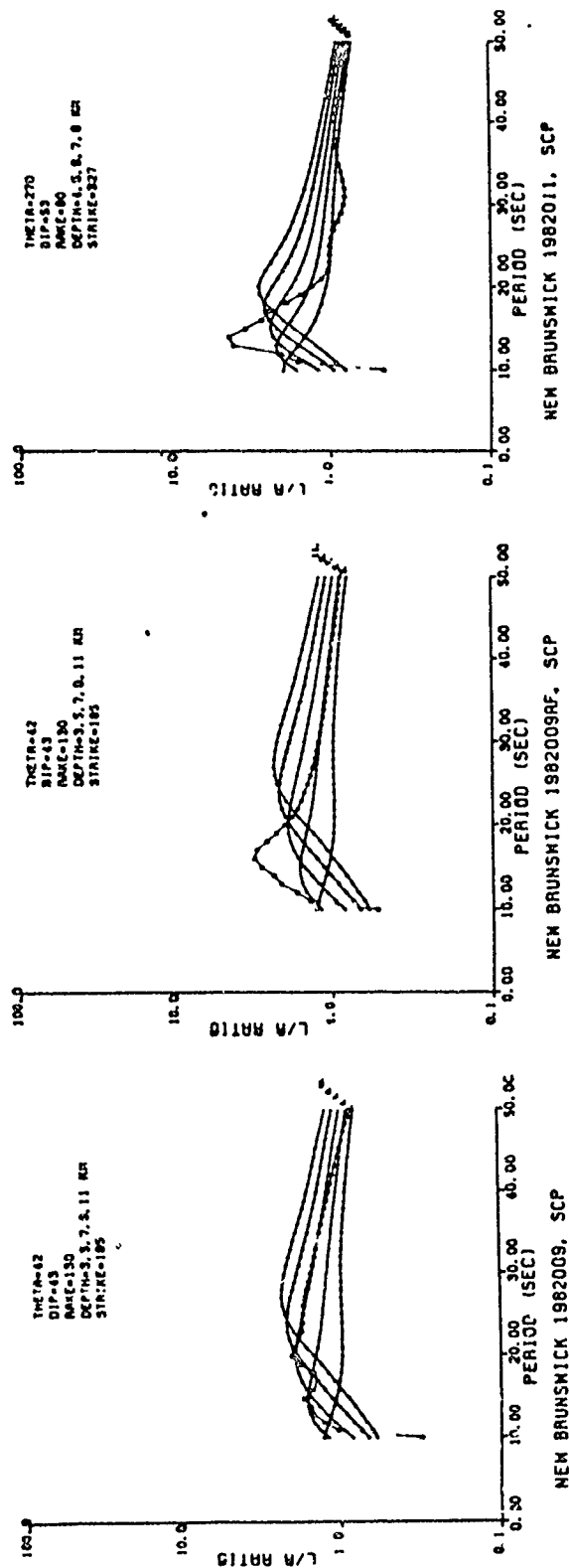
Figure 3. Focal depth and other source parameters for New Brunswick events.

NEW BRUNSWICK 1982009, SCP

NEW BRUNSWICK 1982009AF, SCP

NEW BRUNSWICK 1982011, SCP

Table 1

Summary of Depths Determined by Various Methods

Event	m_{bLg}	Body Wave Evidence	Aftershock Evidence	Surface Wave Evidence of Present Study
1/9/82 mainshock	5.8	9 km	7 km	7 ± 1.5 km
1/9/82 aftershock	5.3	7.5 km	7 km	3 - 5 ± 2 km
1/11/82 aftershock	5.5	6 km	6 - 7 km	6 ± 1 km
6/16/82	4.6	-	7 km	8 ± 2 km

AFGL/DARPA REVIEW OF NUCLEAR TEST MONITORING BASIC RESEARCH
US AIR FORCE ACADEMY, 6-8 MAY 1985

PAPER TITLE: Recent Developments in SV Wave Propagation

PAPER AUTHOR: Charles A. Langston and Chang-Eob Baag

CONTRACT NO: F49620-83-K-0019

SUMMARY: Teleseismic SV waves have been generally ignored in
wave propagation and source studies because of known
complications in wave propagation for structure near the source
and near the receiver. We have studied two aspects of the use of
SV waveforms in seismological studies. In the first, we examined
the validity of ray approximations in the computation of the SV
waveform at typical teleseismic distances. This is important in
the source inversion problem since fast methods of computing the
neccessary Green's functions are needed for efficient inversion
algorithms. Synthetic seismograms computed using ray theory,
Chapman's WKBJ method, and a spectral WKBJ method were compared
to examine ranges where the ray theory approximation was valid.
The second aspect of the study of SV waves consisted of the
inversion for P wave upper mantle structure using observations of
the Sp diffraction seen in teleseismic data recorded at the WWSSN
station at Mundaring, Australia. In this study, we examined the
utility of using this unusual data set for determining regional
variations in P velocity structure.

CONCLUSIONS AND RECOMMENDATIONS: Ray theory gives a poor
approximation to the wave propagation of teleseismic SV waves at
teleseismic distances less than 60 degrees. Diffracted Sp and
the SPL waves interfere with near-source SV phases for a shallow
event giving rise to complex waveforms. It appears that a robust
method, like the spectral WKBJ method, must be used to construct
the Green's functions for SV data recorded at these ranges. This
also implies that earth structure near the source and the
receiver must be reasonably known to get accurate synthetics for
particular data sets.
   A study of SV waves radiated from deep earthquakes near Japan
and Tonga and recorded at the Mundaring station revealed regional
variations in upper mantle P velocity for western Australia. The
data showed large Sp diffractions arriving after the direct SV
wave. The timing of the Sp diffraction, relative to direct S,
is a direct indicator of average upper mantle P velocity. We
find that the southwestern margin of Australia has a high mantle
P velocity of 8.4 km/sec. The velocity along a northern azimuth
from the station appears to be slightly lower at 8.1-8.2km/sec.
The Sp diffraction samples the upper mantle in much the same way
that does the regional phase Pn. The use of this phase in the
teleseismic waveform appears to be a useful and new way of
determining upper mantle structure. The method has the advantage
of using data recorded passively at isolated receivers.

Synthetic seismograms were calculated for the three fundemental sources needed to construct an arbitrarily oriented dislocation or deviatoric moment tensor source (Langston, 1981). These are the vertical strike-slip, vertical dip-slip and 45 degree dip-slip terms of the dislocation and moment tensor formulations. Source depth was taken to be 15km in an earth model, SNA, developed from SH wave travel-time and waveform data by Grand and Helmberger(1984). The WWSSN long-period instrument response(T_o=100 sec, T_s=15 sec) and a trapezoidal far-field time function were convolved with all earth responses. In addition, the ray method results included a convolution with a Futterman(1962) attenuation operator. To be consistent with the attenuation structure assumed in the wavenumber integration, a T/Q ratio of 4.5 was assumed. The trapezoidal time function had rise, constant level, and fall-off time durations of 1., 3., and 1. seconds, respectively.

Figure 1 shows detail of the complexity of the SV waveform for the 45 degree dip-slip source at 60 degrees distance. These waveforms were constructed using the wavenumber integration(WI) method (Baag and Langston, 1985b) and contain all propagation effects. A time increment of 2 seconds was used in all WI synthetics which accounts for the sharpness of some peaks and troughs in the figures.

Both components of ground motion show complicated wave motion. The first arrival is the S-to-P conversion and P-to-S conversion at the Moho of the receiver and source crust, respectively, although the receiver conversion predominates. The arrival labeled "S" is actually composed of near source phases S, sS, and pS interfering with each other. Immediately after S is the Sp diffraction which produces the relatively high frequency sinusoidal motion on the vertical component. This phase was studied by Frazer(1977) and Baag and Langston(1985a). It is set up in the uppermost mantle by an incident SV wave inside the range of 45 to 50 degrees(Figure 2). The SV wave converts to a P wave which travels horizontally below the Moho not unlike the P_n head wave. Depending on the velocity gradient in the upper mantle, this wave may take on the attributes of a "whispering gallery" phase in that multiple reflections and turning points may occur. The Sp diffraction grades into the SPL phase which is the large long-period sinusoid in the remainder of the waveforms. Particle motion of SPL is prograde elliptical.

From a ray theory point of view, these phases are set up when the incident SV wave has a ray parameter greater than 1/8 sec/km, i.e., for receiver distances less than 45 degrees. Converted P waves get trapped in the crust and upper-most mantle and then propagate with a phase velocity roughly that of upper mantle P velocity. If crustal structure is relatively homogeneous and continuous over distances of approximately 30 degrees, the SPL and the Sp diffraction may be prominent out to distances of 70 degrees or more (Baag and Langston, 1985a).

Figure 3 shows the comparison of synthetic seismograms computed using wavenumber integration(WI), Chapman's(1978) WKBJ seismogram method(WKBJ), and ray theory or the first motion approximation method(FMA). Vertical and radial displacements for the three fundemental source terms are shown since each source

119

excites the SV wave in different ways. The FMA seismograms are all relatively simple since they only contain the direct wave and surface reflections near the source. It is assumed that the receiver structure is a homogeneous half-space. The WKBJ synthetics include the effect of receiver structure. At ranges of 70 degrees or more, the effect of receiver structure is primarily shown by the Sp precursor phase. In all WKBJ cases it shows up as a small phase of the same polarity as S on the vertical component and of opposite polarity on the radial just before the S arrival. Compare Figure 1 with Figure 3 for example. Other than this Sp phase, the WKBJ synthetics closely match the amplitude and shape of FMA synthetics at the three farther ranges. This is particularly true of the radial components since Sp is small compared to S.

At ranges of 80 and 90 degrees, SPL and the Sp diffraction phases occur late in time, relative to direct S, so the WI synthetics generally match the WKBJ synthetics. At closer ranges SPL and diffracted Sp significantly interfere with the SV body wave to produce varying levels of distortion of the waveform among the three fundamental sources. Note, for example, the 30 to 50 degree cases where these phases produce very complex vertical and radial waveforms. The Sp diffraction is most pronounced for the 45 degree dip-slip source for the vertical component at close ranges.

The WKBJ seismograms are principally affected by the phase shifts due to complex transmission and conversion coefficients at close ranges. However, the synthetics for 30 degrees range show a shortcoming of the WKBJ method. The diffraction from the cusp of the triplication from the 670 km discontinuity dominates the waveform as a second arrival. This is the cause, for example, of apparently large amplitudes seen in 45 degree dip-slip case(Figure 3c). Inclusion of the WKBJ approximation in the wavenumber integration method does not give rise to this effect as shown in Baag and Langston(1985b).

The comparison of synthetics in Figure 3 shows that there are ranges and time intervals in which ray methods are sufficient for the task of computing accurate Green's functions describing the wave propagation. The first 30 seconds of the waveform at ranges of 70 to 90 degrees appear to be usefully modelled using geometrical or WKBJ ray theory. At some closer ranges, the WKBJ technique appears to be adequate provided the appropriate rays for source and receiver structure are included and only the first half cycle of the SV waveform is considered. Even at 60 degrees distance, however, the radial displacement for the vertical strike-slip term is contaminated with the SPL phase early in the waveform (Figure 3a). At 30 and 40 degrees distance it appears that the wavenumber integration method must be used to produce the Green's function since both amplitude and waveshape appear to be severely affected by non-geometrical wave effects.

At ranges less than 50 degrees the WKBJ seismogram method as used here clearly only gives the initial portion of the waveform since the number of rays is practically limited by computational considerations. Converted S-to-P waves will increasingly become important for these distances since they become trapped in the source and receiver crusts by the critical angle at the Moho. At

ranges greater than or equal to 50 degrees these rays do not become trapped in the crust from conversion from the direct SV wave. However, the SPL wave can be thought of as result of these converted waves interfering with each other at closer distances and propagating to greater distances in the crustal waveguide. These effects are similar to the excitation of higher mode surface waves which is impossible or exceptionally difficult to compute with ray or generalized ray theory.

The severity of these effects will change with frequency or the pass-band of the recording instrument. The SPL phase response can be expected to decrease significantly at high frequencies so that the contamination for short-period or intermendiate-period records will be much less than seen here. However, the Sp diffraction may still be a significant arrival even at high frequencies. This depends on the crustal and upper mantle velocity structure over which it propagates. It may be expected that positive velocity gradients in the structure below the Moho will produce turning points for P waves composing the diffracted Sp phase which will cause these P waves to be strong at high frequency (Frazer, 1977; Baag and Langston, 1985b). In any event, these effects must be considered for any SV data set before relying on a ray theory approximation in the computation of the Green's functions.

In this study we have explicitely considered a crustal source in which reverberations and wave effects are equally strong in the source and receiver structure. Baag and Langston(1985a) show that the SPL and diffracted Sp waves are less severe for mantle depth sources. Although the relative timing of these phases is the same for deep and shallow sources, excitation is confined to the structure in the vicinity of the receiver. Synthetic calculations show that SPL and diffracted Sp are smaller than their shallow source counterparts by factors of 2 to 10, with relative amplitude decreasing with range. Thus, the SV body wave dominates the waveform at most ranges for a deep source. The use of ray theory for the study of SV waves from deep sources may be more justified for ranges starting at 50 degrees but data will still be significantly contaminated by non-ray effects.

We collected body wave data recorded at the Mundaring seismic station(Figure 4) from deep-seated earthquakes ocurring at the Tonga, south Honshu, and Bonin seismic regions and with body wave magnitude greater than 5.8. The Mundaring station is located at the south-western tip of the Australian continent. The western and central parts of the continent have a shield type of structure in contrast to the aseismic platform (Knopoff,1972) of the eastern part which could also be classified as having a "tectonic" velocity structure. All the epicentral distances are greater than 55 degrees being in the range of possible detection of the Sp-diffraction. The expected horizontal paths of S and diffracted Sp waves from these events are shown in Figure 4. Possible diffracted Sp waves excited by the two Tonga events occur beneath the continental shelf and their path to the Mundaring station is confined to the south-western part of the continent. On the other hand, possible diffracted Sp waves set up by the Bonin and two Honshu events pass through the north-western Australian shield.

121

Shown in Figure 5 are the digitized and rotated S wave data recorded at Mundaring. Simple wave forms for SH waves imply that source mechanisms of the events are not complicated. Radial components of the SV waves also have simple waveforms. However, wave shapes of the vertical components appear distorted and are quite different from those of radial and tangential components.

Particle motion plots of the 66/3/17 event and 74/11/29 event SV waveforms show that there must be large later arriving P waves in them. Moreover, these P waves are not likely to be S-to-P conversions or reverberations in the local receiver crust. It is seen that the particle motion of teleseismic P waves from these same events show virtually no P-to-S conversions or reverberations caused by crustal discontinuities under the station.

Using techniques outlined by Burdick and Langston(1977) and Langston(1977;1979) an attempt was made to simultaneously model the P and SV waveforms with just the effects of plane wave conversions and reverberations in the local crust. This proved impossible since the radical layered or dipping crustal structure needed to produce large reverberations in the SV waveforms also produced comparable effects in the P waveforms.

Diffracted Sp satisfies the characteristic features of the disturbing wave. It is a P-type of wave, and its arrival time is close to, but after the direct S. We compute synthetic seismograms of SV waves including the diffracted Sp for these events in order to prove quantitatively that the disturbing waves in the data are from the Sp diffraction.

The initial earth model of the crust and mantle down to the 200 km depth was compiled from the P-wave velocity structure of Mathur(1974) which is based on seismic refraction studies of south-western Australia, and from the S-wave velocity structure of Goncz and Cleary (1976) based on a Rayleigh wave dispersion study of the Australian continent. The extended SNA model (Baag and Langston, 1985a) compiled from SNA (Grand and Helmberger, 1984) and the Jefferey-Bullen-A earth model are used for the velocity below 200 km depth. The Q structure used is a modified SL8 model (Baag and Langston, 1985a) from the original SL8 Q structure by Anderson and Hart (1978).

Before the flat-earth transformation (Muller, 1977) is applied to the original spherical earth model, the near-surface structure is divided into layers, and the other part of the vertical structure beolow the stack of layers is finely sampled simulating a vertically inhomogeneous profile for WKBJ rays. The base of the deepest layer is put at 200 km in oder to include the whispering gallery effect of the diffracted Sp phase below the Moho and allowing multiple reflections in each layer.

By trial-and-error, the upper 200 km of the velocity structure was perturbed and synthetic seismograms were computed for the SV waveform data of Figure 5. The primary features of the waveforms of interest were the relative arrival time and amplitude of the Sp diffraction with respect to the direct SV wave. A cursory examination of the data shows that the Sp diffraction is significantly delayed in time for the events in northern azimuths relative to the Sp diffraction set up by events to the east. This a accounts for the compact waveforms of the

Tonga events compared to the waveforms from the Honshu events. It was found that the average P velocity of the uppermost mantle primarily affected the Sp diffraction - S differential time. Thus, the final models shown in Figure 6 primarily reflect this fact. The deduced upper mantle structure from the data from eastern events (SWA) show slightly higher overall P velocities compared to structure deduced from the northern event data (NWA). It was also found that the amplitude of the Sp diffraction was not a sensitive function of details of the P velocity gradient in the upper mantle.

SV waves at several ranges for the south-western shield model, SWA, are computed for the Tonga 1966/3/17 event to demonstrate the wave shape changes and the arrival time variations relative to direct S waves(Figure 7). This plot scheme makes it easy to identify the Sp-diffraction phase among the other seismic phases. In both the radial and vertical components appear Sp, direct S, diffracted Sp, and SPL waves in the order of arrival time. The diffracted Sp is close to the direct S at the epicentral distance of 52 degrees, and gradually separates from it with increasing distance. However, it is not completely separated even at 70 degrees due to high P-velocity at the Moho in the SWA model. It is seen that wave forms of the vertical components are more disturbed by diffracted Sp waves than those of radial components, which is in accordance with observations. The synthetic wave form for the epicentral range of 58 degrees in Figure 7 corresponds to the observed source distance.

Figure 8 shows synthetics for the direct S and the Sp precursor computed using ray theory. Also shown are the data waveforms and synthetics computed using the WKBJ spectral method. The ray synthetic shows only the Sp and S phases; the majority of the waveforms showing direct S. The WKBJ synthetics demonstrates that the Sp diffraction arrives soon after S, at this range, and severely distorts the vertical waveform relative to the ray result and in accordance with the data.

In Figure 9 synthetics for the two Tonga events are computed using the SWA velocity model for the south-western Australian shield (Figure 5), and those for Bonin and two Honshu events are computed using the north-western shield model, NWA. Since the upper mantle P-velocity of the north-western shield is smaller than that of the south-western shield, central swings in the vertical components of the S waves of the Bonin and two Honshu events become broader than those of two Tonga events due to the arrival time delay of Sp-diffraction.

References

Anderson, D.L and R.S. Hart (1978). Q of the earth, <u>Jour. Geophys. Res.</u>, 83, 5869-5882.

Baag, Chang-Eob and C.A. Langston (1985a). Shear coupled PL, <u>Geophys. Jour. Roy. astr. Soc.</u>,80,363-386.

Baag, Chang-Eob and C.A. Langston (1985b). A WKBJ spectral mwthod for computation of SV synthetic seismograms in a sylindrically symetric medium, <u>Geophy. Jour. Roy. astr. Soc.</u>, 80,387-418.

Burdick, L.J. and C.A. Langston (1977). Modeling crustal structure through the use of converted phases in teleseismic body-wave forms, <u>Bull. Seism. Soc. Am.</u>, 67, 677-691.

Chapman, C.H.(1978). A new method for computing synthetic seismograms, <u>Geophysical J. R. astr. Soc.</u>, 54, 481-518.

Frazer, N.L. (1977). Synthesis of Shear coupled PL. Ph.D. Thesis, Princeton University.

Futterman, W.I. (1962). Dispersion of body waves, <u>Jour. Geophys. Res.</u>, 67, 5279-5291.

Goncz, J.H. and J.R. Cleary (1976). Velocities in the structure of the upper mantle beneath Australia, from Rayleigh wave observations, <u>Geophys. Jour. Roy. astr. Soc.</u>, 44, 507-516.

Grand, S.P. and D.V. Helmberger (1984). Upper mantle shear structure of North America, <u>Geophy. Jour. Roy. astr. Soc.</u> 76, 399-438.

Knopoff, L. (1972). Obsevation and inversion of surface-wave dispersion, <u>Tectonophysics</u>, 13, 497-519.

Langston, C.A. (1977). Corvallis, Oregon, crustal and upper mantle receiver structure from teleseismic P and S waves, <u>Bull. Seismol. Soc. Am.</u>, 67, 713-724.

Langston, C.A. (1979). A single-station fault-plane solution method, <u>Geophys. Res. Lett.</u>, 6, 41-44.

Langston, C.A.(1981). Source inversion of seismic waveforms: The Koyna, India, earthquakes of 13 September 1967, <u>Bull. Seismol. Soc. Am.</u>, 71, 1-24.

Mathur, S.P. (1974). Crustal structure in southwestern Australia from seismic and gravity data, <u>Tectonophysics</u>, 24, 151-182.

Muller, G. (1977). Earth-flattening approximation for body waves derived from geometric ray theory - improvement, corrections, and range of applicabilty, <u>Jour. Geophys.</u>, 42, 429-436.

124

45 DEGREE DIP-SLIP SOURCE
60 DEGREES DISTANCE

RADIAL

1.91 microns

S
Sp

Sp diff + SPL

VERTICAL

0.93

Sp S

180 sec

FIGURE 1

CRUST
MANTLE
DIFFRACTED Sp
s p
P
s
S
S
SRC
RCV

FIGURE 2

VERTICAL DISPLACEMENT
VERTICAL STRIKE-SLIP

Δ	WI	WKBJ	FMA
30°	3.0	4.0	1.5
40°	2.0	1.5	1.1
50°	1.1	1.2	0.8
60°	0.8	0.6	0.5
70°	0.5	0.4	0.4
80°	0.4	0.3	0.3
90°	0.2	0.2	0.2

60 sec

RADIAL DISPLACEMENT
VERTICAL STRIKE-SLIP

Δ	WI	WKBJ	FMA
30°	8.7	5.5	2.8
40°	4.9	2.7	1.9
50°	3.5	2.0	1.4
60°	1.9	1.9	1.1
70°	0.8	0.7	0.8
80°	0.8	0.7	0.7
90°	0.5	0.6	0.6

60 sec

FIGURE 3A

FIGURE 3B

FIGURE 3C

126

PATHS OF S & DIFF.-Sp

FIGURE 4

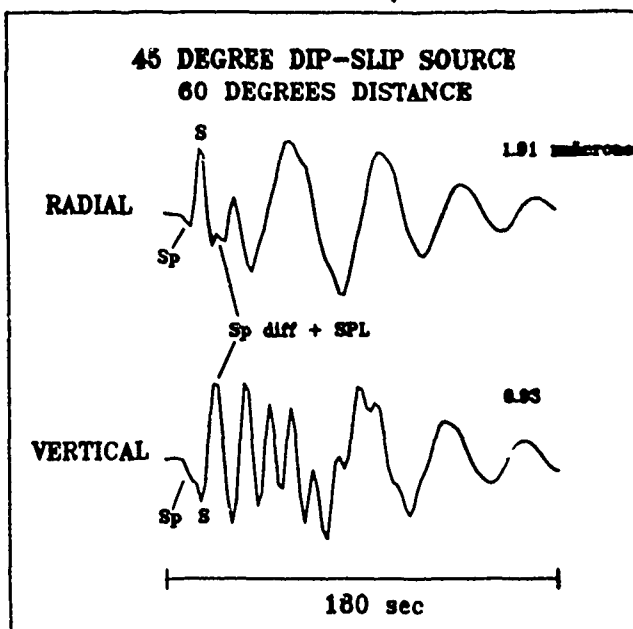| EVENT	LPZ	LPR	LPT	DEPTH (KM)	RANGE (DEG)
TONGA 66/3/17	173.	219.	123.	630	58
TONGA 67/10/9	22.	29.	93.	605	58
BONIN 68/10/7	141.	163.	62.	515	62
S. HONSHU 74/11/29	18.	16.	29.	420	66
S. HONSHU 74/2/22	10.	17.	30.	391	68

60 SEC   AMPLITUDE IN MICRONS   MUNDARING STATION

FIGURE 5

127
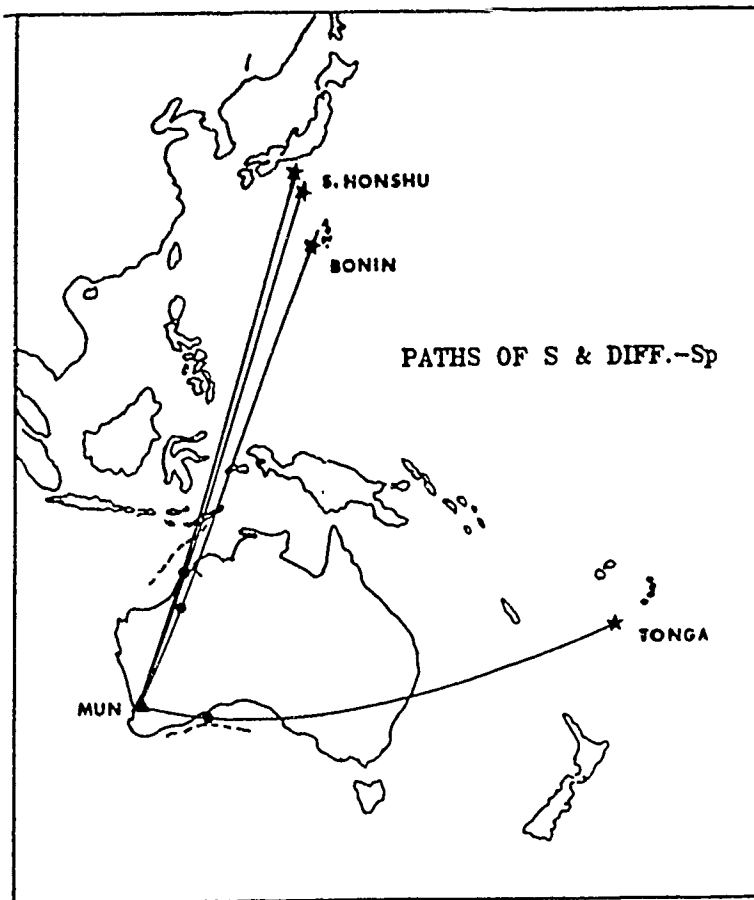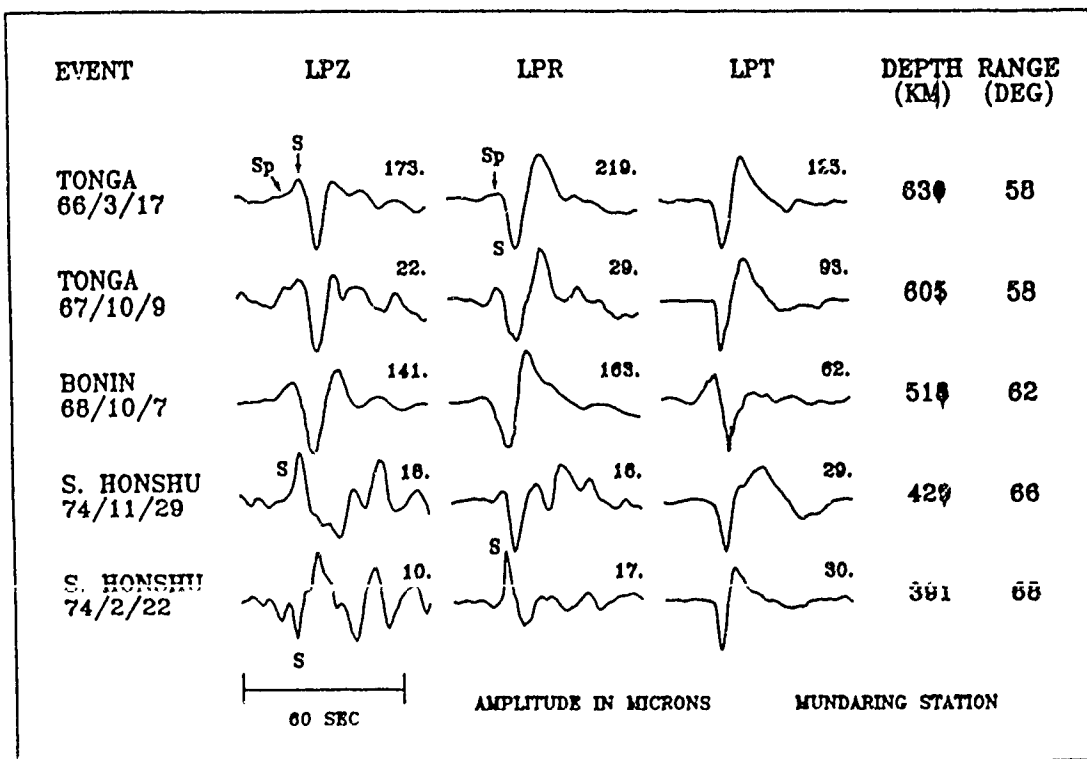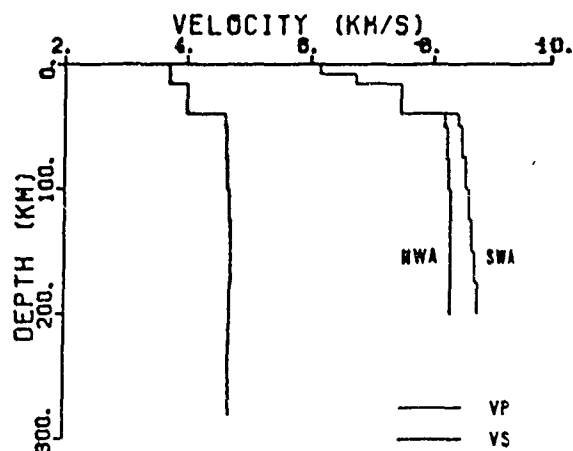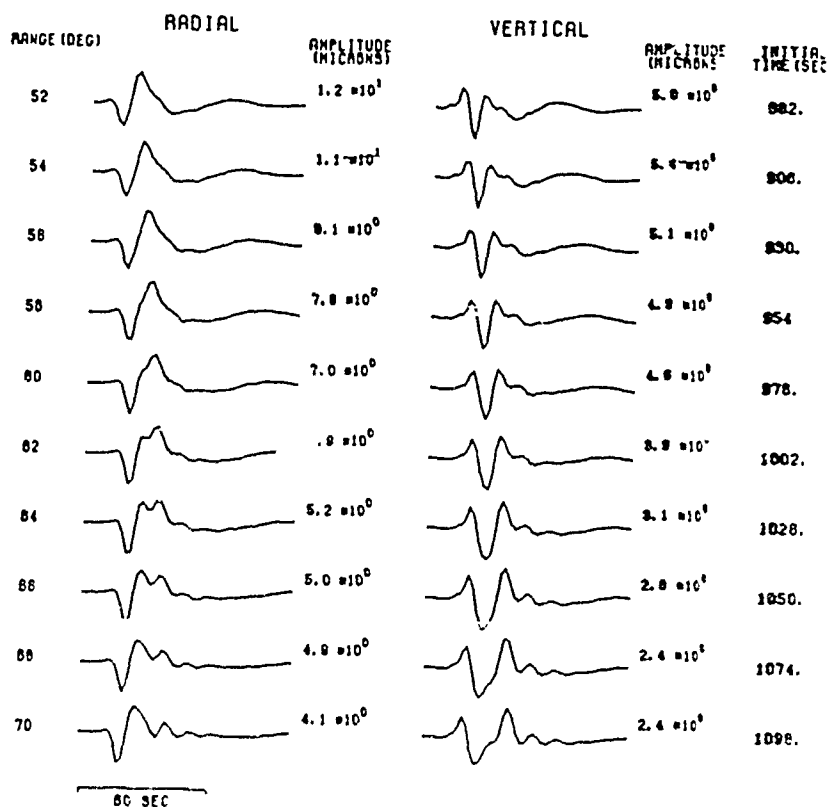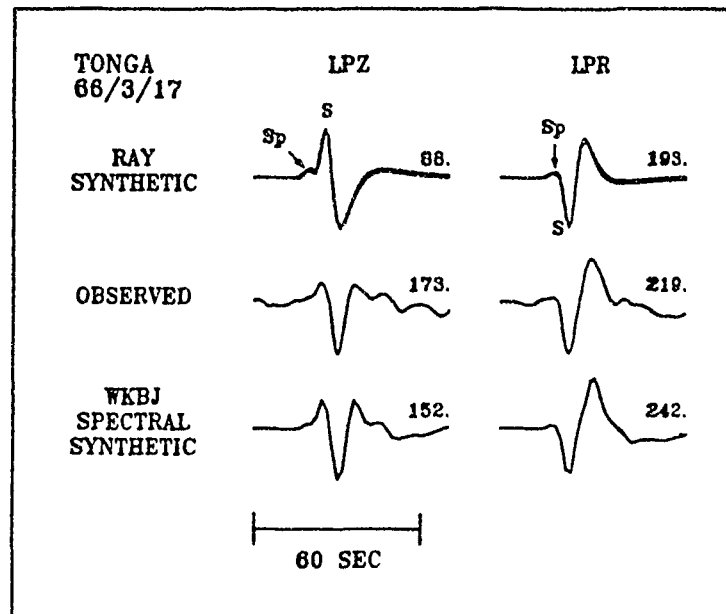
FIGURE 6
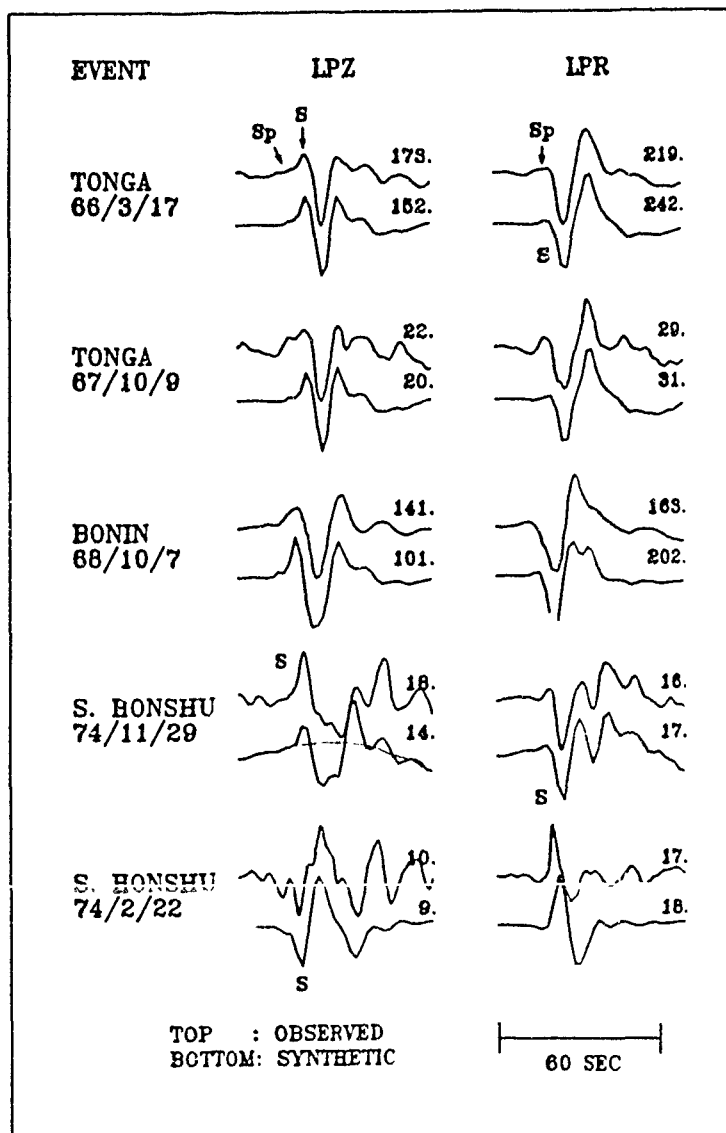
FIGURE 7

FIGURE 8

FIGURE 9

Abstract

ULTRASONIC MODELING OF RAYLEIGH WAVE SCATTERING

M. Nafi Toksöz

Earth Resources Laboratory
Department of Earth, Atmospheric, and Planetary Sciences
Massachusetts Institute of Technology
Cambridge, MA 02139

The effects of topographic features on Rayleigh wave propagation and scattering are investigated in the laboratory using two- and three-dimensional ultrasonic models. Starting from simple steps, different topographic features are modeled. The effects of these features on Rayleigh wave transmission and scattering are examined as a function of wavelength and as a function of shape. In general, backscattered or reflected Rayleigh waves are small, compared to transmitted waves. However, a significant fraction of the Rayleigh wave energy is scattered into body waves. The scattering pattern is complex and highly lobate. A greater fraction of Rayleigh wave energy is scattered into shear than into compressional waves.

Finite difference calculations are made for two-dimensional features studied in the laboratory. In order to separate the shear and compressional waves in the scattered field, the divergence and the curl of the displacement are calculated. These show clearly the scattering patterns for P and S waves and the complex phenomena of multiple scattering.

Scattering of Rayleigh waves from three-dimensional topographic features is studied using ultrasonic models. The effect of angle of incidence of the Rayleigh waves on a simple step as well as on round objects is investigated. At each angle, transmission coefficient (amplitude and phase) varies with frequency. Using model-derived transfer functions, the effects of such steps on dispersed wave trains are calculated. These show that some features of crustal Rayleigh waves commonly attributed to multipathing (e.g., "beat" phenomena) could be due to scattering.

Analysis of Coda at NORSAR and NORESS

Anton M. Dainty

Georgia Institute of Technology

David B. Harris

Lawrence Livermore National Laboratory

(both also at NTNF/NORSAR, P.O. Box 51, 2007 Kjeller, Norway)

Abstract

A suite of explosions from Semipalatinsk, deep focus events in the
Kurile and Japan regions and local events near the NORSAR and
NORESS arrays has been selected for analysis of the teleseismic
and local coda at frequencies of 1 Hz and greater. Fitting of the
coda decay with time from the deep focus events gives a local Q
of 850 ± 50 for NORSAR at 3.6 Hz; the equivalent coda Q for Semi-
palatinsk explosions is 1200 ± 150. This indicates that coda Q at
Semipalatinsk is higher than coda Q at NORSAR. The ratio of coda
amplitude to P amplitude for the deep focus events compared to
the Semipalatinsk explosions suggests that a substantial part,
perhaps half of the total coda power, is produced near the NORSAR
array. Use of the NORESS array to determine phase velocities and
azimuths in the coda of a Semipalatinsk event confirms that some
of the coda is generated at teleseismic distances, but some con-
sists of locally scattered surface or shear waves. NORESS data
also indicate that scattered surface or shear waves are important
in local coda.

Introduction

In recent years the influence of scattering on the propagation of seismic waves has attracted increasing attention. This study investigates the nature of the teleseismic P coda, the scattered train of waves following the first P arrival at distances between 30 and 80°. The study uses short period (1-10 Hz) data from presumed explosions and a possible earthquake at Semipalatinsk recorded at the NORSAR and NORESS arrays (Slide 2). Other data have also been examined but shall not be discussed in detail here. The P coda in this frequency range has been suggested as a measure of yield (Baumgardt, 1983; Ringdal, 1983; Bullitt and Cormier, 1984) and may be useful as a discriminant. To evaluate these possibilities, an understanding of the P coda is necessary.

Models and Theory

Two models are important in considering the coda: a model of those features of the earth that are supposed to produce the coda, and the resulting model of the coda in terms of seismic waves. The model of the earth adopted for coda purposes is shown in Slide 3. Inhomogeneities ("point scatterers") are randomly distributed throughout the lithosphere only. The distribution of scatterers is considered to be laterally quasi-stationary, i.e., in a given broad region (e.g. Norway, East Kazakh) the statistical properties of the scatterers does not vary laterally. The properties may be different between regions, however. The scatterers may be characterized either by a number density and a cross-section or by turbidity, which may be regarded as the cross-section per unit volume. Scattered intensity depends on the scattering angle and frequency, according to the size, shape and elastic characteristics of the scatterers (Dainty et al, 1984).

The theory used to translate the earth model into a model of seismic waves in the coda is the single scattering, independent scatterers model as used by Aki and Chouet (1975). From Slide 3, we see that all scattering will occur in the lithosphere "near" either the source or

132

the receiver. For the purpose of this paper, we shall consider only the coda at times greater than 20 sec after the arrival of first P, thus allowing us to ignore the question of forward scattering in the lithosphere near the source or receiver. Also, from other work (Baumgardt, 1983) and for signal-to-noise considerations only times less than 200 sec are considered. The geometry of the scattered rays at time t after P onset then looks like the lower half of Slide 2 near the source and the reciprocal picture near the receiver. Best results in comparison with data from this theory are obtained by assuming that Lg is scattered into P near the source and P to Lg near the receiver (cf. Greenfield, 1971). The formulas for the power spectrum P_c of the coda as a function of time t after P onset take the form

$$P_c(f,t) = A_p^2(f) \cdot g \cdot \exp[-2\pi ft/Q] \tag{1}$$

In (1), f is frequency, $A_p(f)$ is the Fourier amplitude of first P, g is a scattering parameter here called the apparent scattering turbidity, and Q is the Q factor. For deep-focus earthquakes, there is only scattering near the receiver and

$$g = g_{PL}(f) \tag{2}$$

where g_{PL} is the side-scattering turbidity for P → Lg (Slide 3). Q for this case will refer to the receiver site, i.e., NORSAR. For explosions and shallow-focus earthquakes

$$g = \frac{A_L^2}{A_{po}^2} \cdot g_{LP} + g_{PL} \tag{3}$$

where $A_L(f)$ and $A_{po}(f)$ are the amplitude of Lg and P, respectively, at unit distance from the source. Q will be a weighted average of Q in the source (Semipalatinsk) and receiver (NORSAR) region. It should be

133

noted that "near" the source (or receiver) means within about 500 km
in this theory.

Teleseismic Codas at NORSAR

To date, two data sets have been assembled and preliminary studies
have been made using data from NORSAR. The two data sets are a set of
deep focus events from the Kurile-Japan region, and a set of explo-
sions (and one other event) from the Semipalatinsk region (Slide 4,
Slide 5). The events have been selected for maximum signal to noise
without clipping. We shall only examine the Semipalatinsk events in
detail here. At present, these events have been analyzed by using the
equations of the last section on individual seismograms and averaging
the results. The methods used are similar to those used in Dainty
et al (1984) to analyze local codas. A sliding window (6.35 sec long)
was moved 3.2 sec successively along the seismogram. The Fourier
transform was taken at each position and the amplitude averaged over
octave bands around 0.9, 1.8 and 3.6 Hz. The time of the estimates was
taken to be the center of the window; a plot of Fourier amplitude
against time for the event shown in Slide 5 is shown for the fre-
quency band 3.6 Hz in Slide 6. So far, data from the 02B and 03C
subarrays (Slide 2) have been used. At present, the band around 3.6 Hz
has given the best results - the bands at 0.9 and 1.8 Hz have tended
to suffer from signal-to-noise problems and contamination from PP,
which arrives at about 80-90 seconds after P.

The explosion records from Semipalatinsk look reasonably similar to
the deep focus records, and to each other. Three sites are represented
(Slide 4) within about 50 km of each other. The value of Q obtained by
fitting (1) is 1200 ± 150 at 3.6 Hz, a value that is significantly
higher than the deep focus value of 850 ± 50. The value of $\log_{10}(g)$ is
-2.9 ± 0.3, a similar value to that found for deep focus events. This
similarity is surprising, since one would expect the coda power at
Semipalatinsk to be higher relative to P by the amount of coda pro-
duced near the source. However, if the coda power produced near the

explosion is just as great as that produced near the receiver, this will increase the coda power by a factor of 2, or $\log_{10}(g)$ by 0.3. This is within the limits of error. The value of Q should be an average of Q at NORSAR (850) and Q at Semipalatinsk, appropriately weighted. This indicates that Q at 3.6 Hz at Semipalatinsk is higher than 1200, perhaps as high as 2000 if equal weighting is used.

One other event occurring on March 20, 1976, near the Semipalatinsk site (the most NW event, Slide 4) has been examined. In appearance, it is dramatically different from the nearby explosions (Slide 7). The value of Q obtained from the coda is 1200 ± 250, in agreement with the explosion results, but $\log_{10}(g) = -1.3 \pm 0.3$, 40 times higher than the explosion value! This can be explained by the more efficient production of Lg by a dislocation event, if this is what the event is. It is classified in some catalogs (e.g., NORSAR) as an explosion, but see Alexander (1984), Pooley et al (1983). This event is strong evidence for the production of coda near the source by the scattering of Lg to teleseismic P. Bennett et al (1984) show some other examples from the Semipalatinsk region that appear to show a correlation between high teleseismic P coda and strong Lg. This may enable the use of P coda as a discriminant.

Wavenumber Analysis using NORESS

Since late 1984 the NORESS array has been in operation (Slide 2, Slide 10). The close spacing of seismometers in this array permits the calculation of high wavenumber spectra at high frequencies, allowing an investigation into the nature of the coda using phase velocity and azimuth. So far, a few trial investigations of a presumed explosion at Semipalatinsk on February 10, 1985, have been carried out. Only vertical seismometers have been used, and an analysis frequency of 3.6 Hz was chosen.

The Semipalatinsk event is shown in Slide 11, as received at the NORESS center seismometer, with a window for wavenumber analysis. A contour map of the power at linear wavenumbers north and east is shown in

Slide 12 for the window (circles at phase velocities of 8 km/sec and 3.6 km/sec have been drawn). The high phase velocity peak shows the arrival of P energy presumably from the source, through the mantle; the azimuth of this peak is appropriate for energy arriving from Semipalatinsk.

Several strong peaks are seen near a phase velocity of 3.6 km/s; none of them are at the Semipalatinsk azimuth. The beam pattern has small sidelobes ($\sim$ 6 dB below the main peak; two contour levels above 0 on Slide 12) at a wavenumber of 2 away from the main peak. This should not affect the contours shown in Slide 12 except possibly in the northwest (+ ve KY, - ve KX) quadrant. Since the interseismometer spacing is 0.15 km in the array center, the Nyquist wavenumber is over 3. The results shown suggest that the coda consists of two parts - a part produced near the source (Semipalatinsk) and a part scattered into Lg near the receiver (NORESS). The identification of the energy scattered near the receiver as "Lg" is made on the basis of the phase velocity ($\sim$ 3.6 km/s).

To investigate further, two other calculations have been made on Slide 12. One is an integration around a circle centered on the origin at a specified total horizontal wavenumber (= square root of the ~~area~~ sum of the squares of KX and KY) such as the two shown on Slide 12. This leads to a plot of power as a fraction of total horizontal wavenumber, which is inversely proportional to phase velocity. Also, an integration along a straight line starting at the origin and ending at a specified total wavenumber at a specified azimuth, such as that shown at azimuth 143° on Slide 12.

Slide 13 shows a plot of power as a function of total horizontal wavenumber for the window shown in Slide 11 at a frequency of 3.6 Hz. A scale of phase velocity has been added to this plot. Two peaks may be seen, one at a high phase velocity corresponding to coda generated near the source, another at lower (4.3 km/s) phase velocity corresponding to coda generated near the receiver. However, in addition there is a linear trend on Slide 13 leading to higher values of

power with increasing total horizontal wavenumber. Such a trend would be expected if there were a component of "white noise" in the wave-number spectrum - a possible trend line is indicated in Slide 13.

Slide 14 shows a plot of power as a function of azimuth at a frequency of 3.6 Hz for the window shown in Slide 11. Note that while there is a peak at the appropriate azimuth for energy coming from Semipalatinsk, indicated by the arrow, there is also energy at azimuths away from Semipalatinsk, indicating two components for the coda. The second, presumably local, component is not uniformly distributed; however, there is an East (0°-180°) - West (180°-360°) asymmetry, indicating that the coda is not entirely statistical.

Acknowledgements

References

Aki, K. and B. Chouet (1975). Origin of coda waves: source, attenuation and scattering effects. J. Geophys. Res. <u>80</u>, 3322.

Alexander, S.S. (1984). Relationship among near-field, regional, and teleseismic observations of seismic source parameters. "Basic Research in the VELA program 1959-1984", DARPA, Santa Fe, NM.

Baumgardt, D.A. (1983). Teleseismic P-coda stability and coda-magnitude yield estimation. Fifth Ann. DARPA Symp. on Seismic Detection, Analysis, Discrimination and Yield Determination, p. 77.

Bennett, T.J., J.R. Murphy, D.G. Lambert and J.M. Savino (1984). Discrimination with regional phases in the Western U.S. and Eurasia. "Basic Research in the VELA Program 1959-1984", DARPA, Santa Fe, NM.

Bullitt, J.T. and V.F. Cormier (1984). The relative performance of m_b and alternative measures of elastic energy in estimating source size and explosion yield. Bull. Seis. Soc. Am. <u>74</u>, 1863.

Dainty, A.M., R.M. Duckworth and A. Tie (1984). Influence of scattering on Q in the lithosphere. Final Technical Report, Contract AFOSR-83-0037.

Greenfield, R.J. (1971). Short-period P-wave generation by Rayleigh wave scattering at Novaya Zemlaya. J. Geophys. Res. <u>76</u>, 7988.

Pooley, C.I., A. Douglas and R.G. Pierce (1983). The seismic disturbance of 1976 March 20, East Kazakhstan: earthquake or explosion? Geophys. J. <u>74</u>, 621.

Ringdal, F. (1983). Magnitude from P-coda and Lg using NORSAR data. Fifth Ann. DARPA Symp. on Seismic Detection, Analysis, Discrimination and Yield Determination, p. 34.

Slide 1

ANALYSIS OF CODA AT NORSAR AND NORESS

BY

ANTON M. DAINTY

NORSAR AND GEORGIA INSTITUTE OF TECHNOLOGY

DAVID B. HARRIS

LAWRENCE LIVERMORE NATIONAL LABORATORY

NORSAR

NORSAR

140
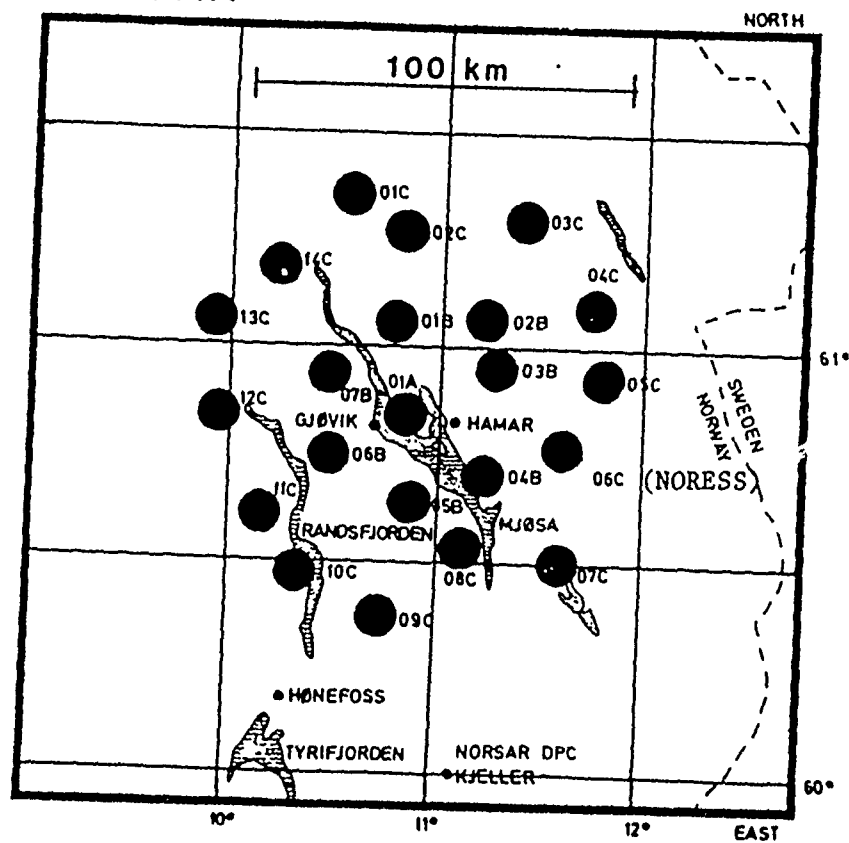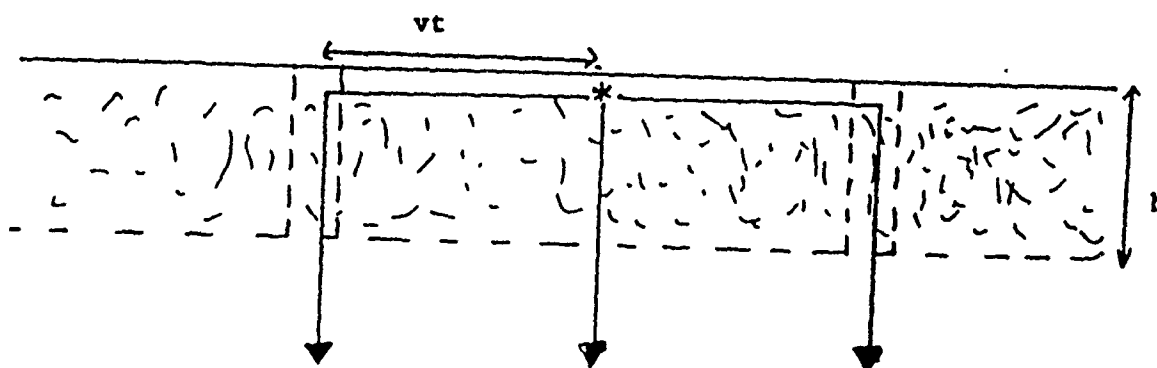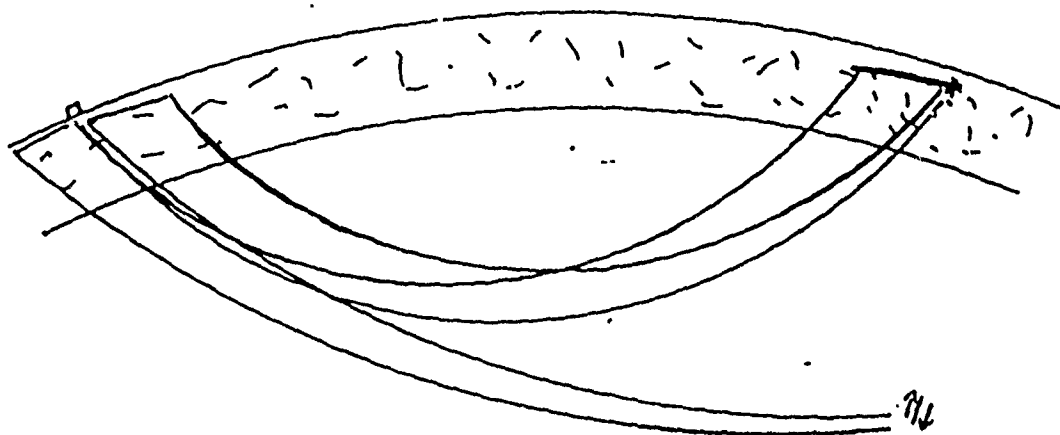
$$P_c(F,T) \doteq A_p^2 \cdot G \cdot \exp(-2\pi FT/Q)$$

$$G = G_{pL} \qquad\qquad \text{(DEEP FOCUS)}$$

$$G = (A_L^2/A_{po}^2) \cdot G_{Lp} + G_{pL} \qquad \text{(EXPLOSION)}$$

141

SEMIPALATINSK TEST SITE

1976 MAR 20

100 KM

50°N

78°E

79°E

Slide 4

142

SEMIPALATINSK 1978 APR 22

60 SEC

1:78 112/ 3.13.30.0 NSMP 5000 FHZ 20.0 TSC 500.0 NS1,NS2 1. 5000

06C6
5112.

04C6
5152.

03C6
5728.

02C6
2336.

02B6
3040.

01B6
2272.

01A6
24C0.

143

Slide 5

START: 1978:112: 3:13:30   INSTR. 61   CF   3.6 HZ

03C1 SEISMOMETER
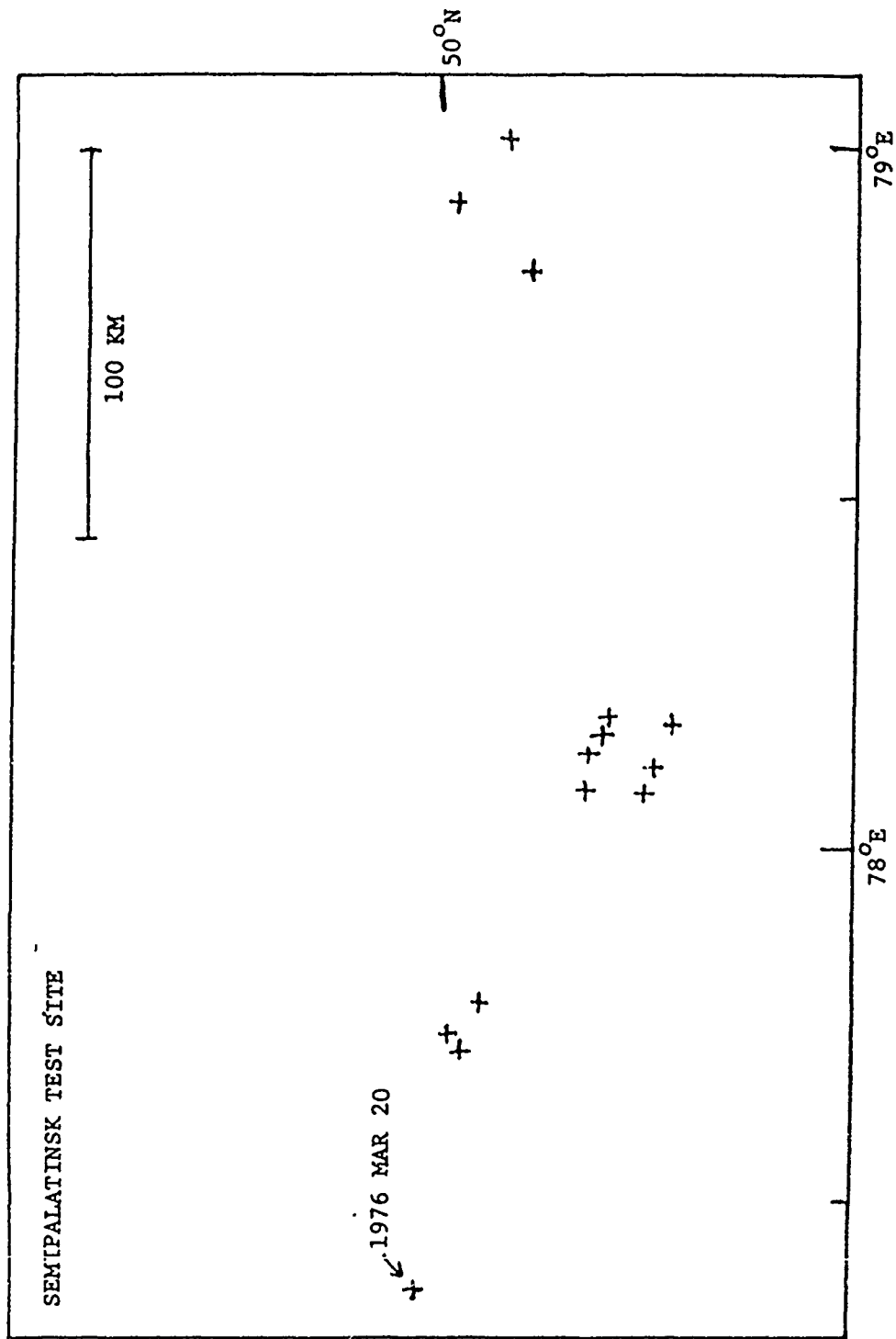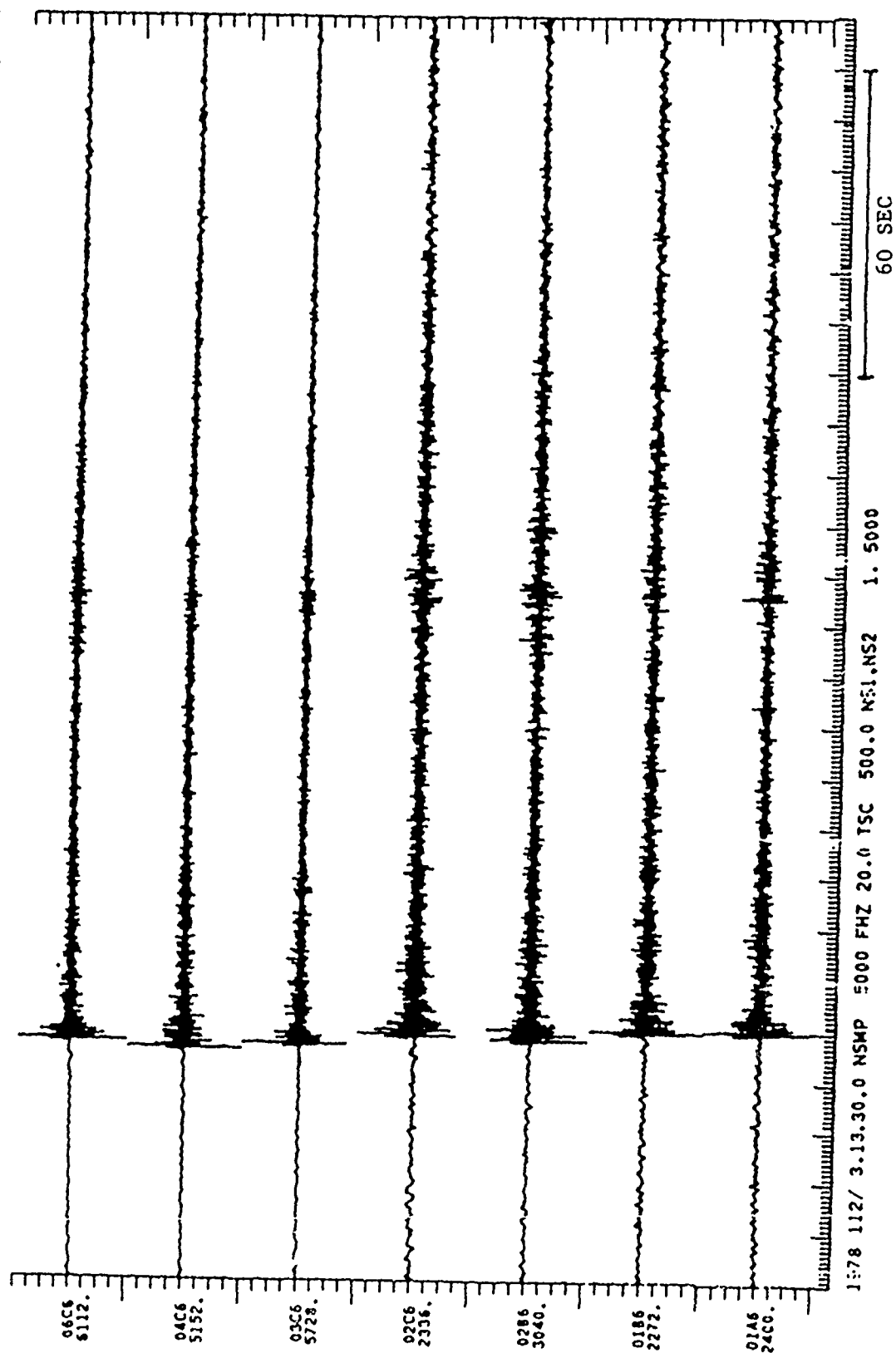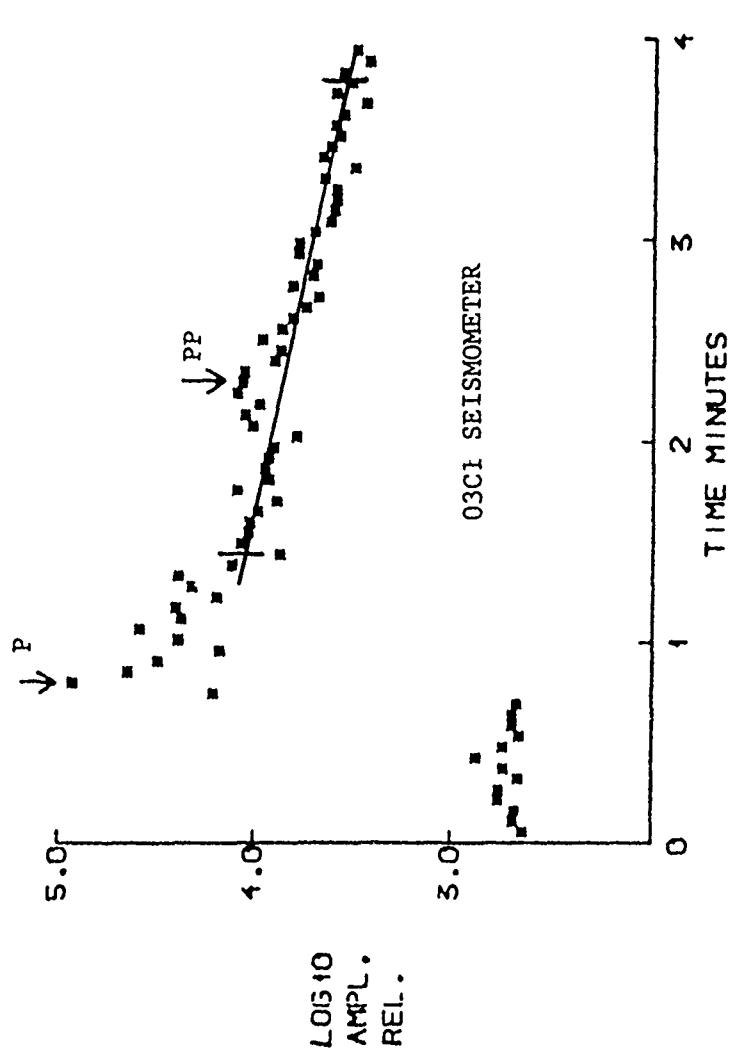
Slide 6

SEMIPALATINSK 1976 MAR 20

60 SEC

Slide 7

145
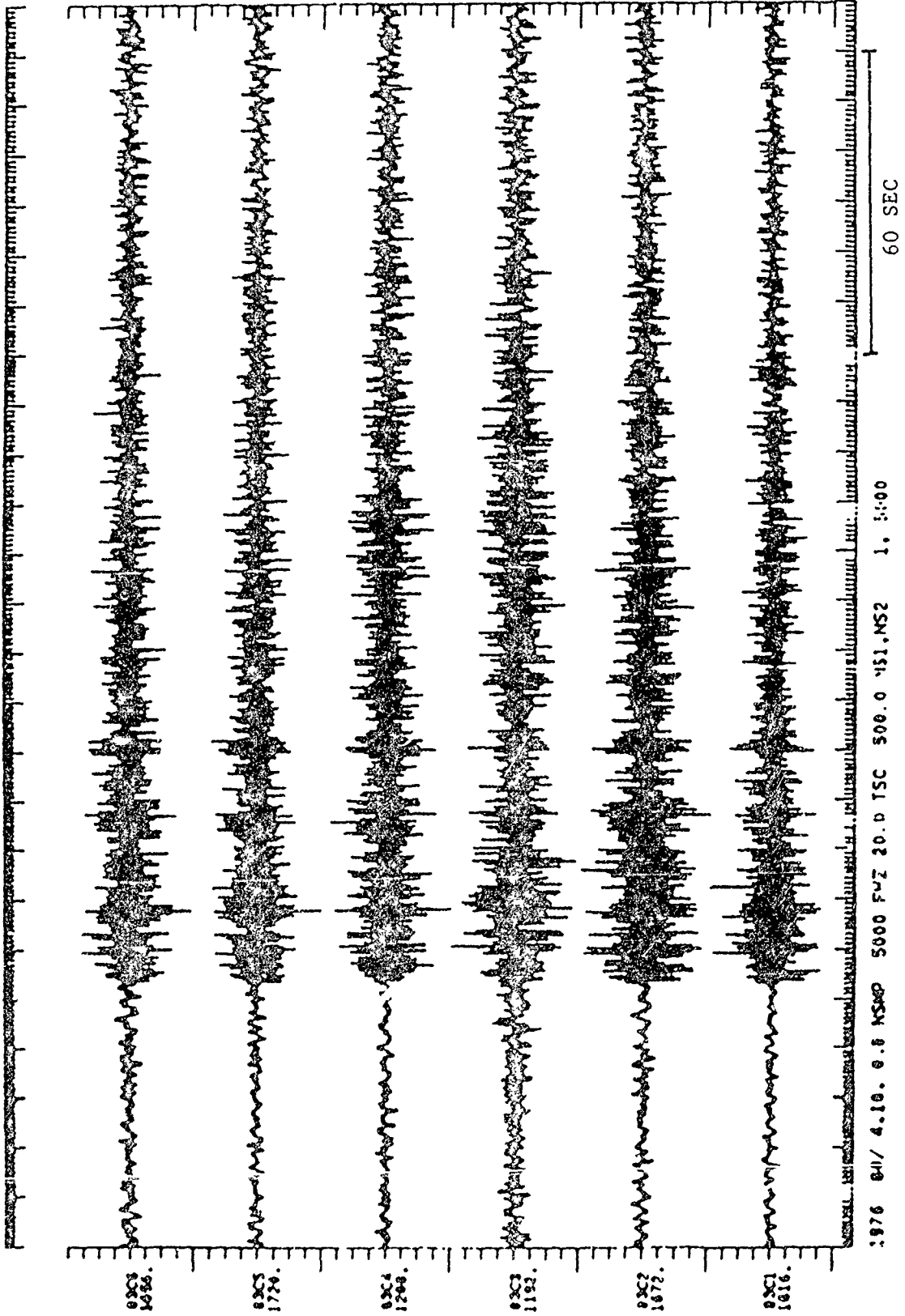
RESULTS FROM CODA SPECTRUM AS A FUNCTION OF TIME

BAND 2.4 - 4.8 HZ

	Q	G
SEMIPALATINSK EXPLOSIONS	1200±150	10^{-3} KM^{-1}
SEMIPALATINSK EARTHQUAKE (?)	1200±250	5×10^{-2}
DEEP FOCUS EVENTS	850±50	10^{-3}

CONCLUSIONS:

(1) MODEL FITS OBSERVED DECAY (EXPONENTIAL) IN 2.4 - 4.8 HZ BAND

(2) Q IS HIGH (1000) IN THIS BAND AT BOTH NORSAR AND SEMIPALATINSK

(3) EARTHQUAKE (?) AT SEMIPALATINSK HAS MUCH HIGHER G THAN

EXPLOSIONS - DISCRIMINANT ?

(4) ALL EXPLOSIONS EXAMINED AT SEMIPALATINSK HAVE SIMILAR CODA

CHARACTERISTICS

147

MAP OF ARRAY ELEMENT LOCATIONS

NORTH

EAST

1 KILOMETER

Slide 10

148

SEMIPALATINSK 1985 FEB 10

AOZ 5.74E+05

Time (seconds)

Slide 11

149
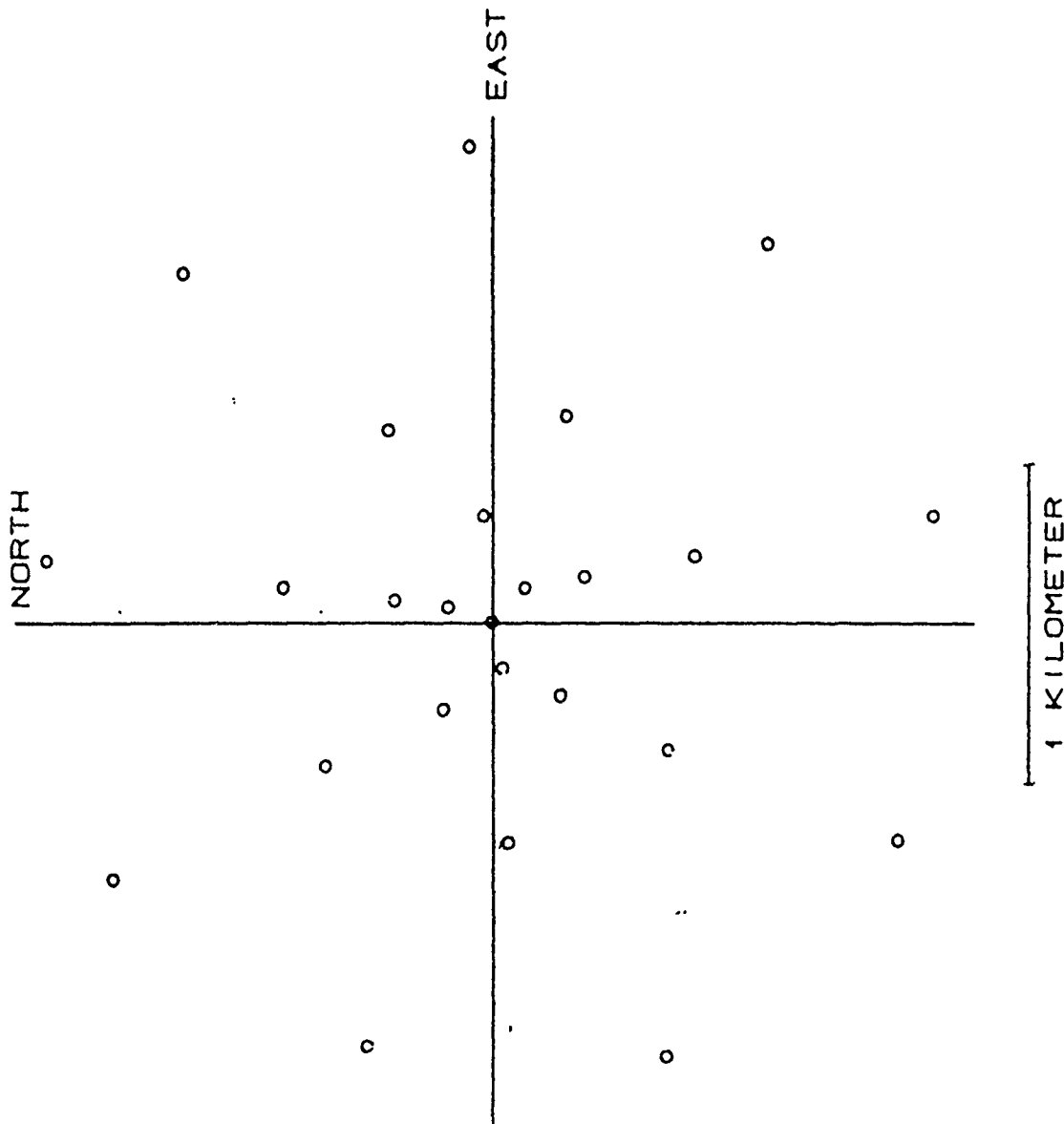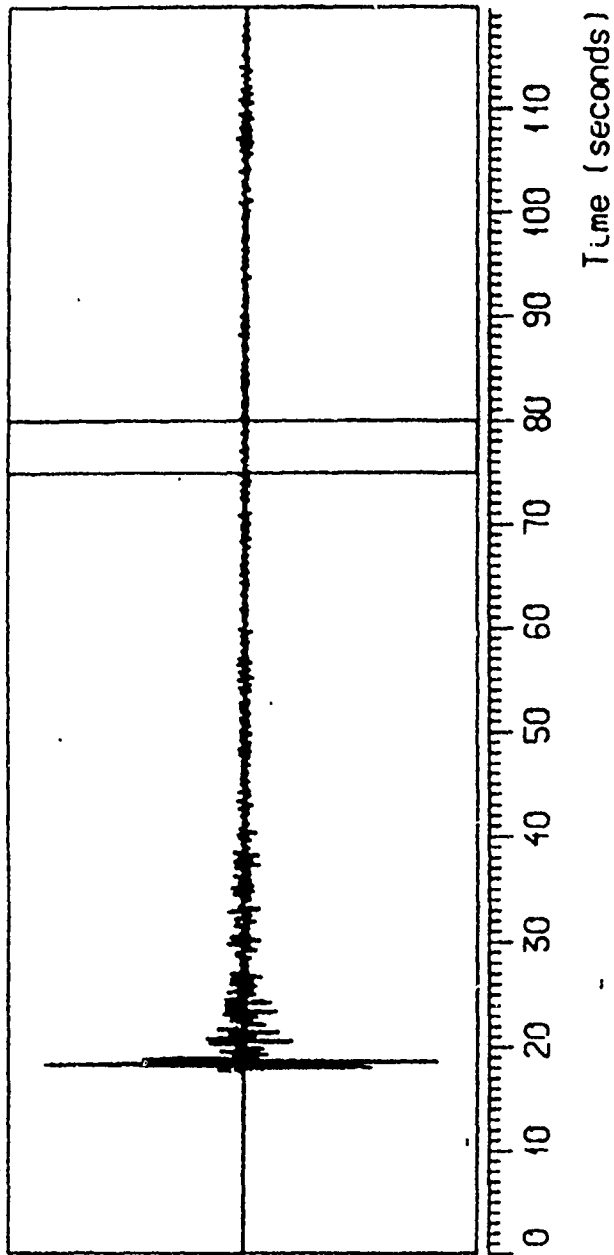
MONOCHROMATIC F-K ANALYSIS
CONVENTIONAL RESOLUTION
LINEAR DEPENDENCY BETWEEN CONTOURS
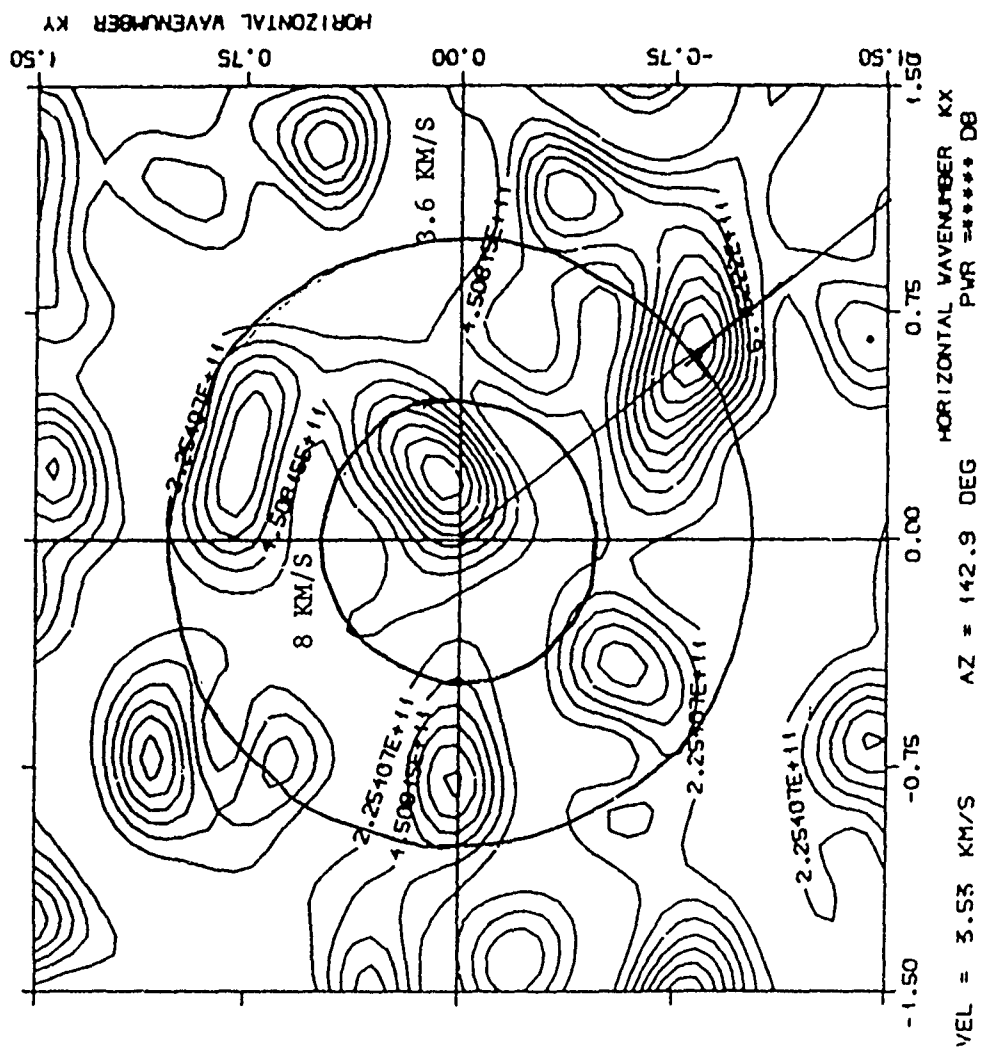
VEL = 3.53 KM/S   AZ = 142.9 DEG   HORIZONTAL WAVENUMBER KX
                                       PWR =#### DB
PREFILTER FREQUENCY INTERVAL: 0.0 - 0.0 HZ   ANALYSIS FREQUENCY: 3.6 HZ

CODA

Slide 12

SEMIPALATINSK 1985 FEB 10

VELOC. 3.60E+12

4.3 KM/S

18 KM/S

"WHITE NOISE"

WAVENO. (1/KM)

0.0 0.1 0.2 0.3 0.4 0.5 0.6 0.7 0.8 0.9 1.0 1.1 1.2 1.3 1.4 1.5

VELOCITY (KM/SEC)

12   6   4   3

Sed 13

151

SEMIPALATINSK 1985 FEB 10

Azimut 8.54E+12

AZIMUTH (DEG)

Slide 19

152
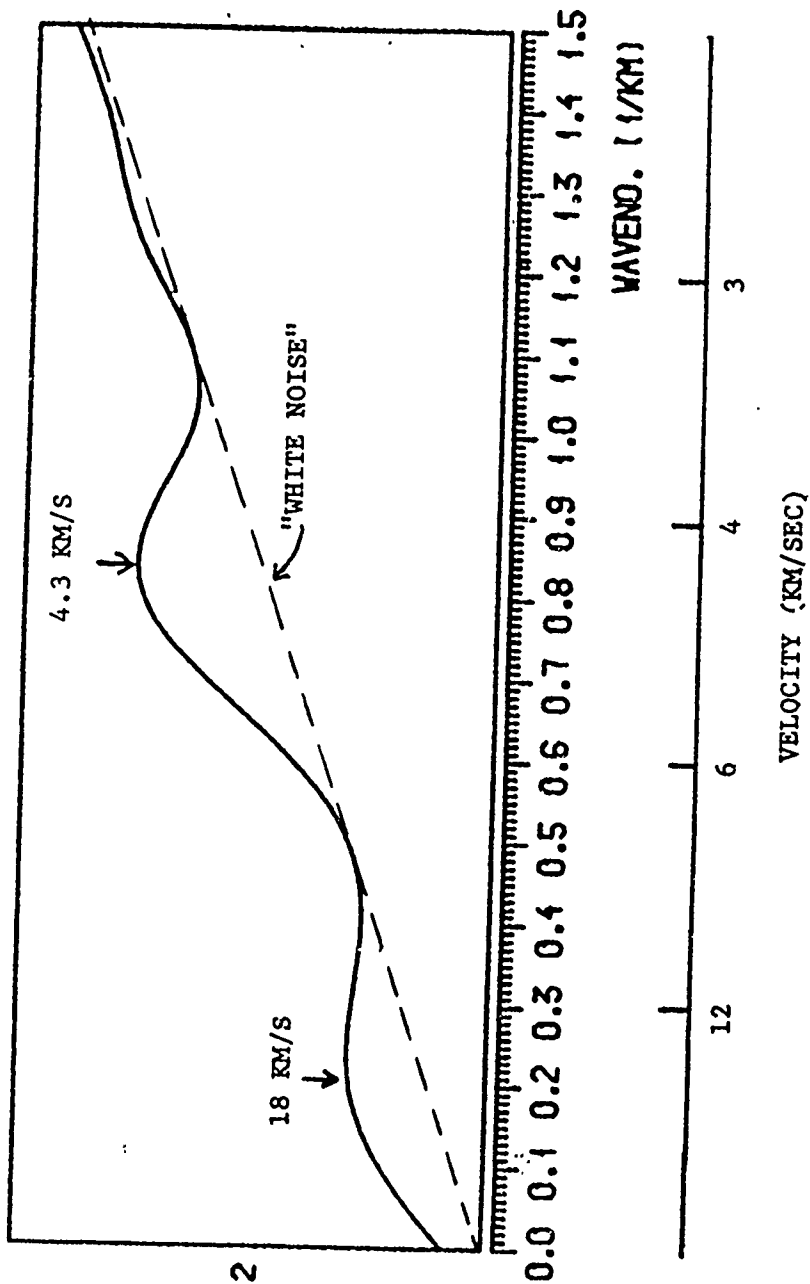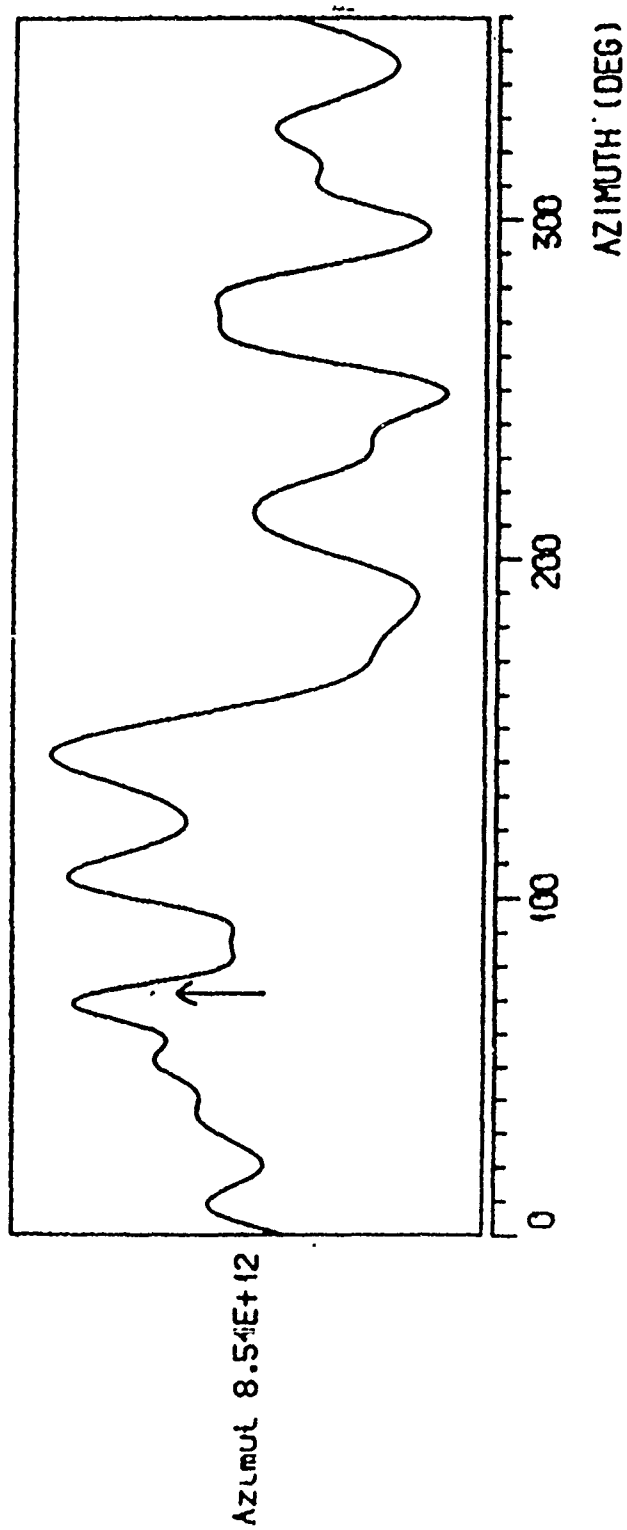
TITLE: Regional Variations in Surface Wave Attenuation, Q Structure, and Lg Amplitude

AUTHORS: J.J. Chen, H.J. Hwang, and B.J. Mitchell

CONTRACT NO: F19628-85-K-0021

SUMMARY:

Surface waves at intermediate periods (5-100s) have been used to obtain models of shear wave Q for various regions of the world. Particle motion diagrams, time-variable filtering, and phase-matched filtering have been employed in order to isolate modes and obtain stable amplitude determinations. In cases where two-station data were used, these processes were followed by Wiener filtering to obtain values for Q, phase velocity and group velocity of fundamental- and higher-mode surface waves.

In North America, an extensive new data set for paths entirely confined to that continent lead to new velocity and Q models which satisfy both fundamental- and higher-mode data. The inversion of Love and Rayleigh wave velocities for paths in the stable region of eastern North America produces a model which is isotropic in its elastic properties and which does not include a significant low-velocity zone in the upper mantle. Inversion of surface wave attenuation coefficients for that region produces models with a relatively low-Q upper crust (250) and monotonically increasing values with increasing depth. Velocity models

obtained for the tectonically active region of western North America are also isotropic, but in contrast to eastern North American models, they include an extensive low-velocity, low-Q zone in the upper mantle.

Low-Q sediments have a strong effect on the regional variations of 1-Hz Lg wave attenuation in regions such as eastern North America where the crust is characterized by high-Q values, but have only a small effect in regions such as the western United States where the crust has low-Q values.

CONCLUSIONS AND RECOMMENDATIONS

1. Introduction

Surface waves at periods between 5 and 100 s are sensitive to the properties of both the crust and upper mantle, regions which strongly influence the propagation and attenuation of Lg waves and teleseismic body waves, respectively. An understanding of the elastic and anelastic properties of these regions should therefore contribute to our understanding of the factors which affect magnitude determination and yield. We are particularly studying the regional variation of the anelastic properties of the crust and upper mantle to see if there are systematic relations between such properties and surface tectonics. In this paper we present new results for North America where we have obtained new shear velocity and shear wave internal friction models for the stable region of eastern North America and the more tectonically active region of western North America. In addition we have studied the effects which accumulations of low-velocity, low-Q sediments will have on the attenuation of the Lg phase.

2. North American Crust and Upper Mantle

Fundamental-mode and higher-mode Rayleigh and Love wave dispersion and attenuation data were obtained for the paths shown in Figure 1. The map indicates that the data paths for this study are restricted to the North American continent, thus avoiding paths which traverse major lateral structural changes at continental margins. Rayleigh wave group velocities and attenuation coefficients were obtained using standard methods (Figures 2 and 3) and were inverted to obtain shear wave velocity and internal friction (Q^{-1}) models (Figures 4 and 5). Note that the velocity models obtained from separate inversions of Rayleigh and Love waves are very similar in their major features for both eastern and western North America. Any differences can be explained by differences in resolving power between the two types of waves.

For eastern North America, our data do not require a low-velocity in the upper mantle, although a minor low-velocity zone, not resolvable with our data, could occur there. By contrast, a well-developed low-velocity zone occurs in the upper mantle beneath western North America. That zone is clearly resolvable with our data set.

Inversions for Q structure in the two regions yield models which are analgous to those derived from the velocity inversions. There is no evidence for a low-Q zone in the upper mantle beneath eastern North America whereas an extensive region of low-Q values occurs beneath western North America. The low-Q zone beneath western North America roughly coincides with the low-velocity zone there.

3. Effect of Surficial Sediments on Lg Attenuation

155

In previous work (Mitchell, 1984), we reported a correlation between thick accumulations of sediment and high attenuation rates for Lg in the eastern United States. Moreover, it was possible to model several regions of sediment accumulation and to roughly predict the observed Q values of Lg for those regions. Q values in the crust for those regions were taken from the frequency-dependent model of Mitchell (1980) in which shear-wave Q varies as $\omega^{0.5}$.

Tests were conducted to see whether or not regional variations in Q values observed for Lg waves in the western United States could also be related to varying thicknesses of sediment there. It is assumed that the upper crust is comprised of relatively low-Q material (150) and that the Q values for the sediments can be predicted from the laboratory measurements of Q as a function of pressure by Winkler and Nur (1979) for partially saturated sandstone.

Shear wave Q values for three hypothetical models are shown in Table 1. Compressional wave Q values are assumed to be the same as the shear wave Q values in each layer. Predicted attenuation coefficients and Q values for Lg are obtained by computing Lg synthetic seismograms for several distances, measuring the amplitudes, and calculating attenuation from those values. The Q values for Lg waves for three models in Table 1 indicate that in regions where crustal Q values are relatively low, varying thicknesses of low-Q surficial sediments produce only small changes in Q values of Lg waves. Such variations are much too small to explain the observed regional variation of Lg Q values in the western United States.

References

Brune, J. and J. Dorman, Seismic waves and Earth structure in the Canadian shield, Bull. Seism. Soc. Am., 53, 167-209, 1963.

Cara, M., Lateral variations of S velocity in the upper mantle from higher Rayleigh modes, Geophys. J. Roy. Ast. Soc., 57, 649-670, 1979.

Cheng, C.C. and B.J. Mitchell, Crustal Q structure in the United States from multi-mode surface waves, Bull. Seism.Soc. Am., 71, 161-181, 1981.

Grand, S.P. and D.V. Helmberger, Upper mantle shear structure of North America, Geophys. J. Roy.Ast. Soc., 76, 399-438, 1984.

Hashizune, M., Two earthquakes on Baffin Island and their tectonic implications, J. Geophys. Res., 78, 6060-6081, 1973.

Hasegawa, H.S., Surface- and body-wave spectra of Cannikin and shallow Aleutian earthquakes, Bull. Seism. Soc. Am., 63, 1201-1225, 1973.

Herrmann, R.B. and B.J. Mitchell, Statistical analysis and interpretation of surface-wave anelastic attenuation data for the stable interior of North America, Bull. Seism. Soc. Am., 65, 1115-1128, 1975.

Lee, W.B. and S.C. Solomon, Inversion schemes for surface wave attenuation and Q in the crust and upper mantle, Geophys. J. Roy. Ast. Soc., 43, 47-71, 1975.

Mitcnell, B.J., Frequency dependence of shear wave internal friction in the continental crust of eastern North America, J. Geophys. Res., 85, 5212-5218, 1980.

Mitchell, B.c., N.K. Yacoub, and A.M. Correig, A summary of seismic surface wave attenuation and its regional variation across continents and oceans, Geophysical Mono. 20, The Earth's Crust, Am. Geophys. Union, 405-425, 1977.

Patton, H.J. and S.R. Taylor, Q structure of the Basin and Range from Surface Waves, J. Geophys. Res., 89, 6929-6940, 1984.

Priestly, K. and J. Brune, Surface waves and the structure of the Great Basin of Nevada and western Utah, J. Geophys. Res., 83, 2265-2272, 1978.

Mitchell, B.J., Effect of crustal velocities and Q on the amplitudes of Lg at short and intermediate periods, in Semi-Annual Technical Report No. 1 of Saint Louis University to DARPA/AFOSR, 1 October 1982 - 31 March 1983, 32-54, 1983.

Winkler, K., and A. Nur, Pore fluids and seismic attenuation in rocks,

Table 1

Lg Q Values Predicted

by Three Sedimentary Models

Thickness	Q_β (= Q_α)	Thickness	Q_β (= Q_α)	Thickness	Q_β (= Q_α)
0.1 km	30	0.1 km	30	0.1 km	30
0.2	50	0.2	50	0.2	50
0.3	75	0.3	75	0.3	75
0.4	100	1.4	100	3.4	100
21.0	150	21.0	150	21.0	150
---	500	---	500	---	500

$$\gamma = 0.0035 \pm 0.0008 \qquad \gamma = 0.0040 \pm 0.0010 \qquad \gamma = 0.0042 \pm 0.0008$$
$$Q = 267 \qquad\qquad Q = 229 \qquad\qquad Q = 219$$
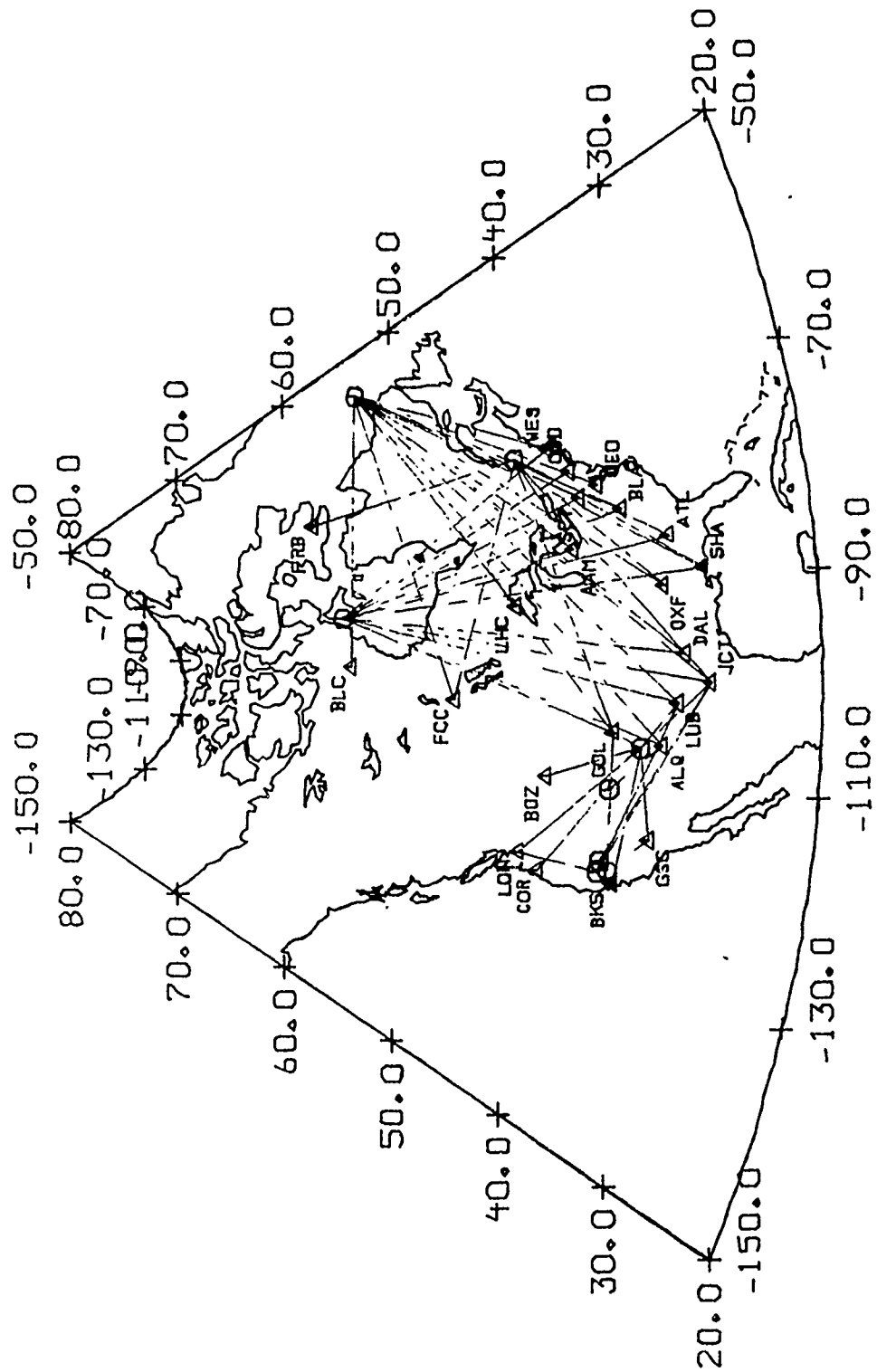
Figure 1. Map showing paths over which group velocities and attenuation coefficients were determined.
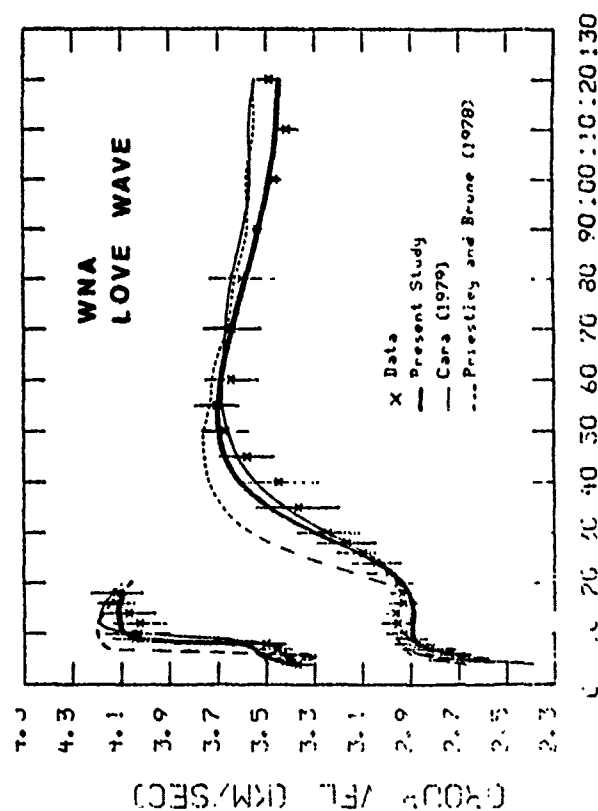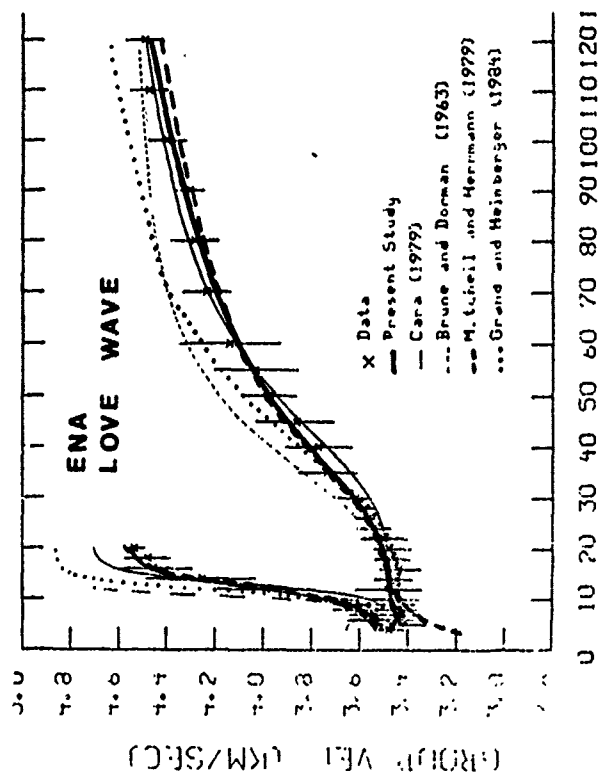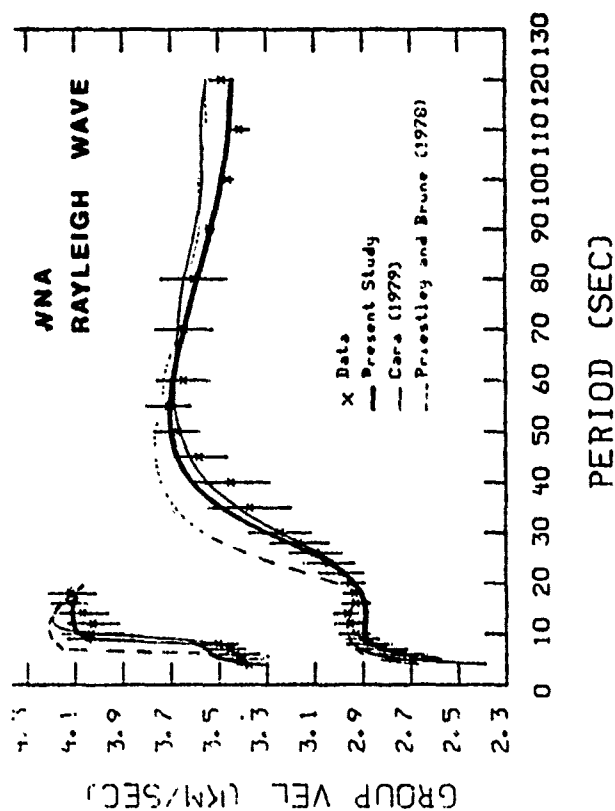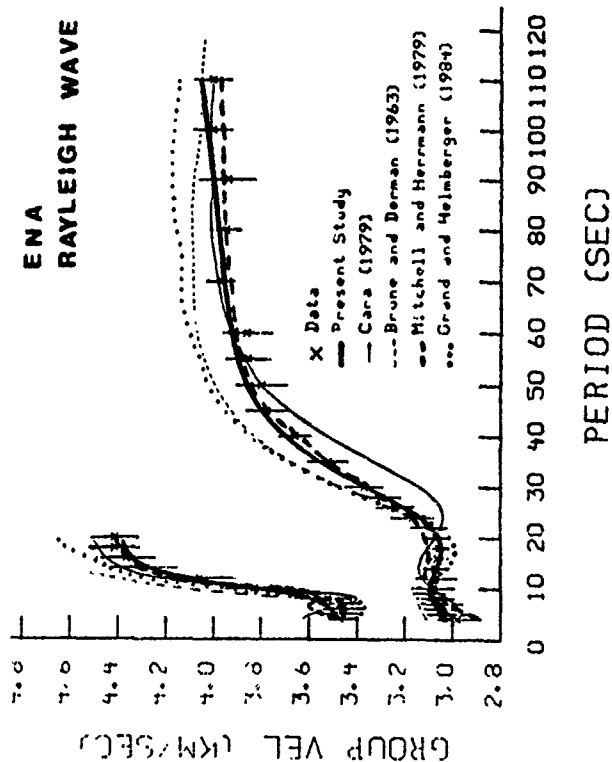
Figure 2. Rayleigh and Love wave group velocities determined for eastern (left) and western (right) North America compared with velocities predicted by various models.
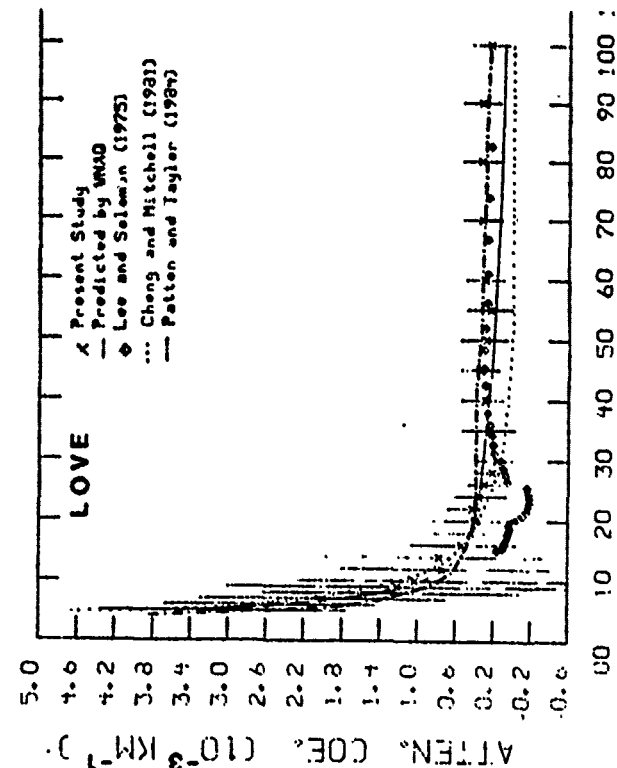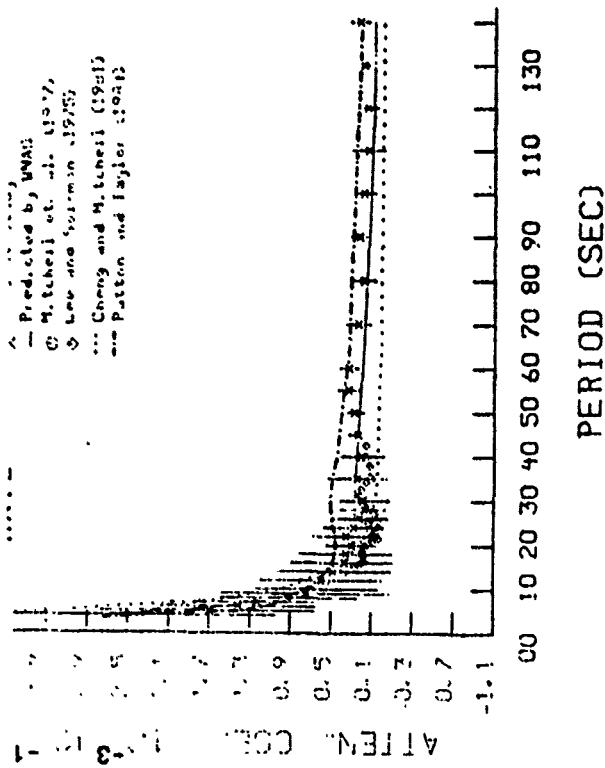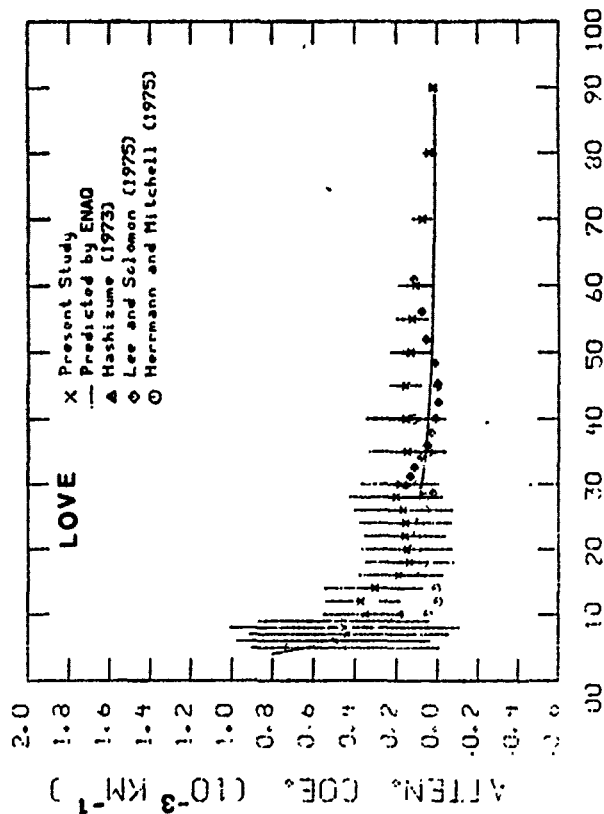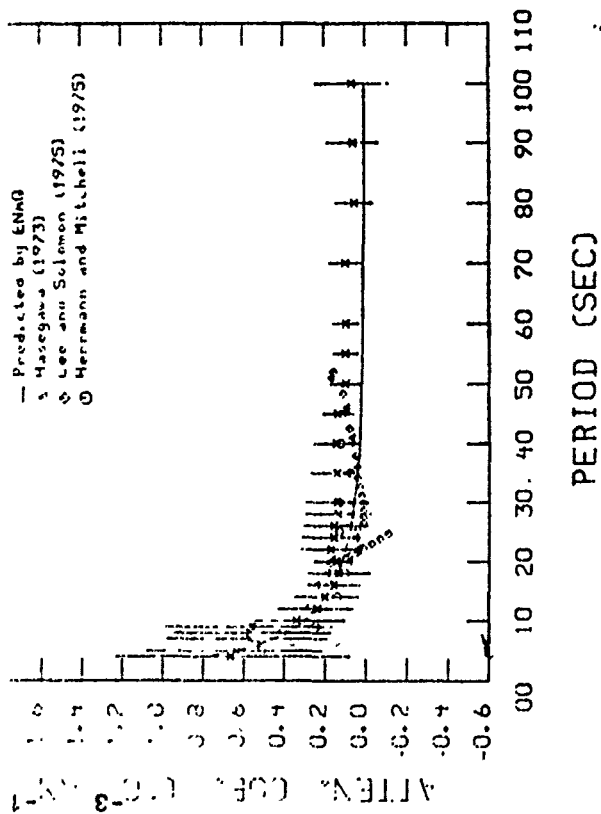
Figure 3. Rayleigh and Love wave attenuation observed for eastern North America (left) and western North America (right) compared with predicted values for various models.
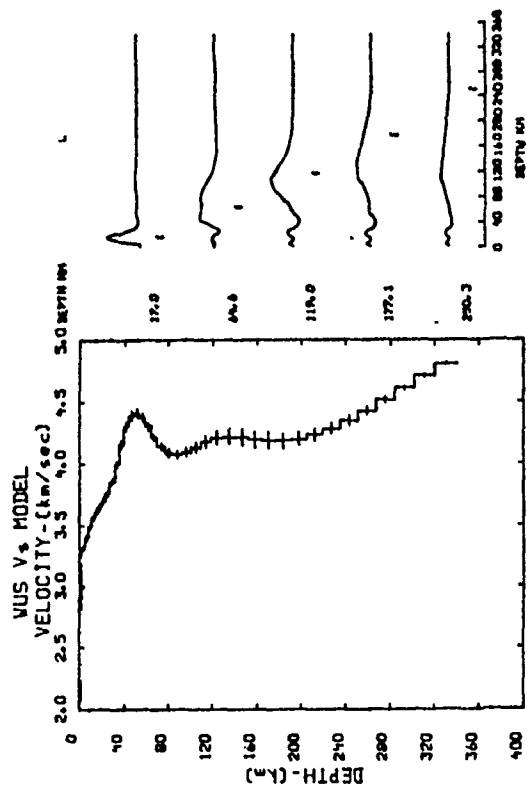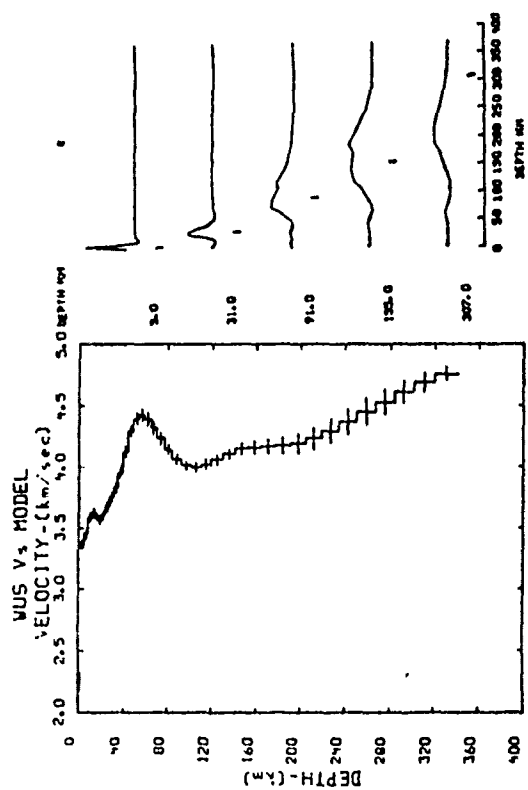
Figure 4. Shear velocity models obtained from inversion of Rayleigh waves (top) and Love waves (bottom) for eastern (left) and western (right) North America.

163
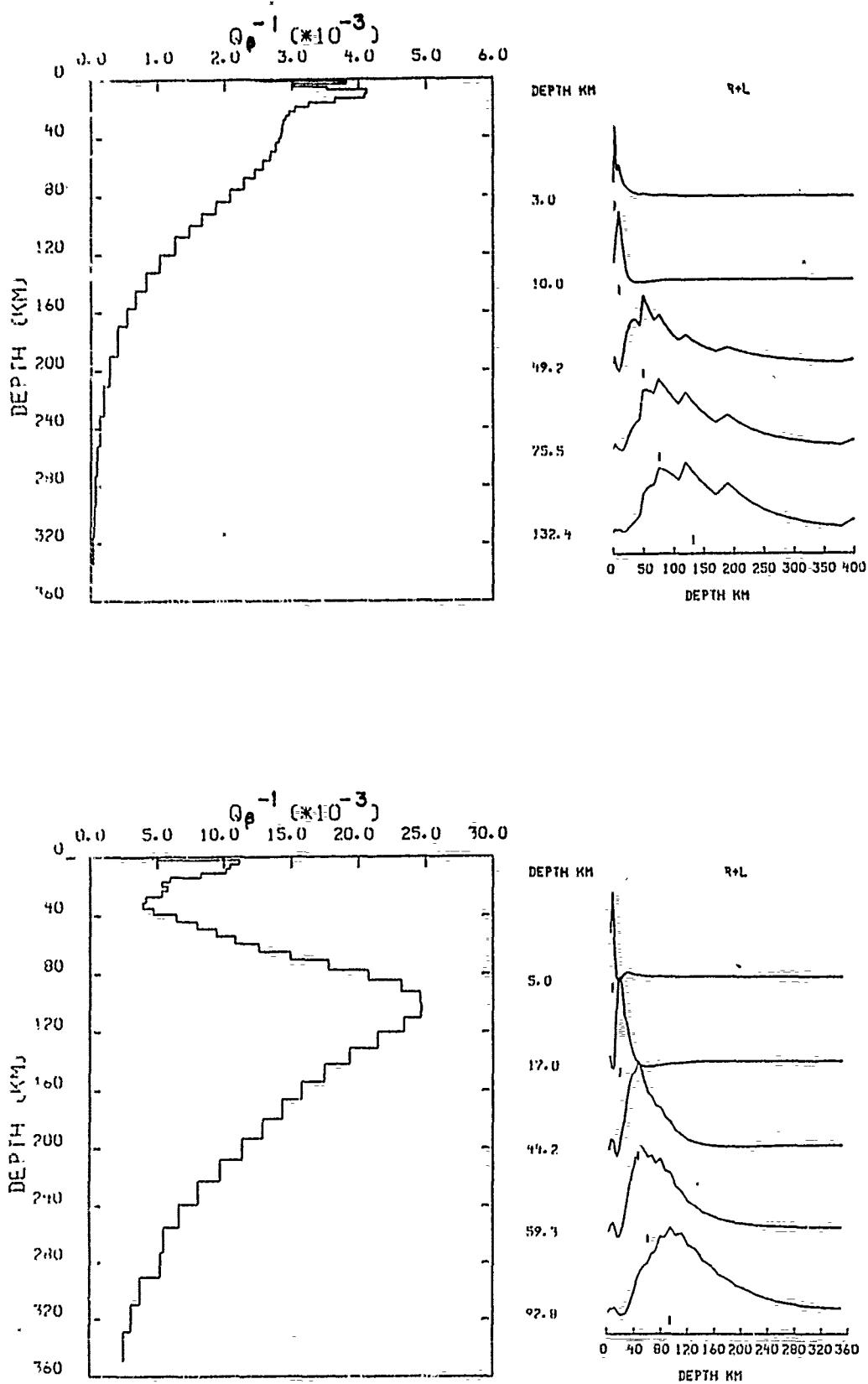
Figure 5. Shear wave Q models obtained from inversion of observed attenuation coefficients in eastern (top) and western (bottom) North America.
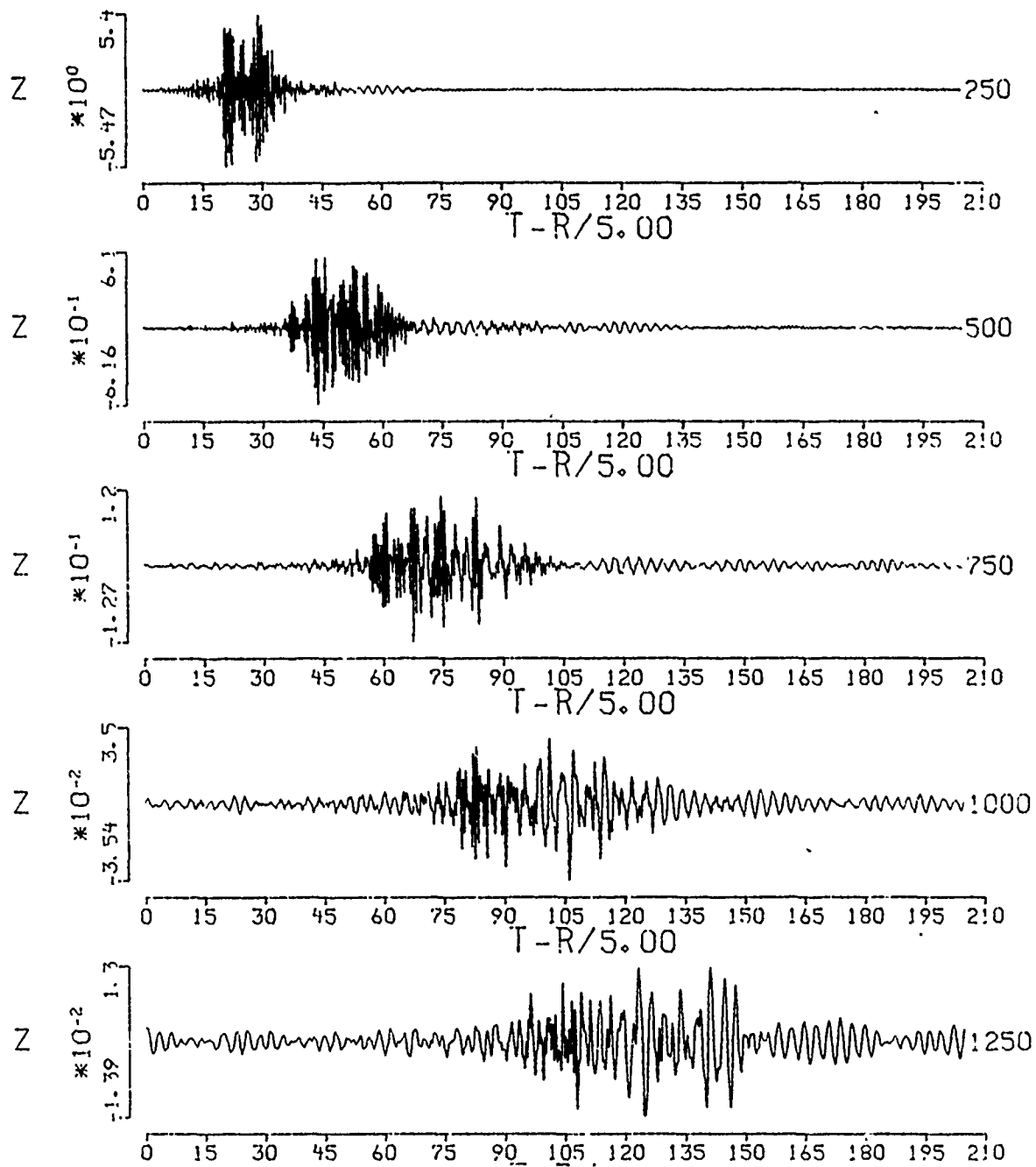
Figure 6. Synthetic seismograms predicted by Model 2 of Table 1.

165

PAPER TITLE: Yield Estimates of Nevada Test Site Explosions Obtained
from Seismic Lg Waves

PAPER AUTHOR: Otto W. Nuttli

CONTRACT NO.: F19628-85-K-0021

SUMMARY: A methodology is presented for determining the yield of
underground nuclear explosions from Lg-wave amplitudes.
The methodology is applied to Nevada Test Site explosions,
for which the data from short-period, vertical-component
analog seismographs at three stations are used to develop
calibration curves for dry alluvium and hard-rock source
conditions. The hard-rock curve is found to provide
reasonably accurate estimates of the yields of explosions
in other areas of the United States and in the French
Sahara, suggesting that it may be applicable to all conti-
nental areas. If so, it also can provide an estimate of
the bias of $m_b(P)$ magnitudes between different continental
sites. For example, the Lg data from NTS explosions indi-
cate a 0.31 ± 0.02 magnitude unit bias between NTS and
eastern North America, similar to the approximately 0.33
unit bias found between western and eastern North America
previously by use of earthquake data.

CONCLUSIONS AND RECOMMENDATIONS: Lg-wave amplitudes recorded at near-
regional distances from NTS appear to give stable estimates
of yield of underground explosions. For hard-rock explosions
of announced yield the standard deviation is 0.08 magnitude
units, or about 25% at 100 kt. The calibration equation
developed from the $m_b(Lg)$ versus log yield data for explosions
of announced yield at NTS gives yield estimates of about the
same accuracy for the non-NTS shots GASBUGGY, RIO BLANCA,
RULISON and SALMON in the United States and the French Sahara
shots RUBIS and SAPHIR. This suggests, but does not prove,
that the same calibration curve can be used for hard-rock
sites in all continental areas. It further suggests that the
difference in m_b(teleseismic P) minus $m_b(Lg)$ values at any
two sites can be used to estimate the $m_b(P)$ bias between the
sites. For example, between eastern North America and NTS it
is found to be 0.31 ± 0.02 magnitude units.

Assuming that the $m_b(Lg)$ versus explosion yield relation is
universally applicable to all hard-rock continental test
sites, it is recommended that the best possible relation be
developed. This can be done by adding to the data of this
study that of all the NTS hard-rock explosions whose yields
are classified. An independent determination of Q_0 and its
frequency dependence at NTS can be obtained by using Lg
amplitude data from LRSM and LLNL stations to supplement
those from the WWSSN.

Lg-wave amplitudes of 1-sec period appear to be robust and stable estimators of body-wave magnitude, m_b. Because the Lg-wave paths are confined to the crust and propagate horizontally, they are not affected by anomalous attenuation in the asthenosphere or by focusing and defocusing due to lateral velocity variations, such as P waves are. They also appear to show less azimuthal amplitude variation than P waves. Furthermore, at regional distances Lg has larger wave amplitudes than P, allowing the threshold of yield determination to be lowered.

The disadvantages of Lg waves for yield determination are that they only can be used for continental paths, the observations must be made at regional distances (out to about 1000 km for tectonic areas and to about 4000 km for shield areas) and that they require an accurate average value of the coefficient of anelastic attenuation, $\gamma(f)$, for each source-to-station path, where f is wave frequency.

The coda-Q method is used to obtain a first approximation to the γ values, although they could be obtained by observing amplitude attenuation with epicentral distance in either the time or frequency domain if profiles of seismographs were available for a few explosions. The second and final approximation to γ is obtained by making station corrections.

Fig. 1 shows a portion of the Lg coda for the BKS short-period, vertical-component seismogram for the NTS explosion ALMENDRO. The frequencies and travel times of the wavelets, marked by lower-case letters, are used to determine $Q(f)$ and $\gamma(f)$ by the coda-Q method. Wavelets that must be avoided are those due to fundamental-mode Rayleigh waves of group velocity about between 2.6 and 1.4 km/sec, indicated by upper-case letters, and wavelets with nearly constant frequency that arrive at the end of the coda, indicated by numbers in Fig. 1.

Fig. 2 shows coda-Q data for three selected NTS events, STANLEY, NASH and ALMENDRO, as recorded at BKS. The x's are the wavelets used to determine Q_0 and γ. The +'s are the fundamental-mode wavelets and the o's the constant frequency wavelets. Also shown are the Q_0 and frequency exponent, ζ, which were obtained by a fit of master curves to the x's (solid-line curve) and those obtained by Rondout Associates (dashed-line curve) who fitted coda-Q data by least squares. Fig. 3 shows the coda-Q data for DUG, BKS and TUC from a larger number of NTS explosions, and the corresponding Q_0 and ζ values obtained in this study.

ALMENDRO, JUNE 6, 1973, $13^h\,00^m\,00^s$

BKS SPZ, M = 25K AT I SEC, Δ = 524 KM
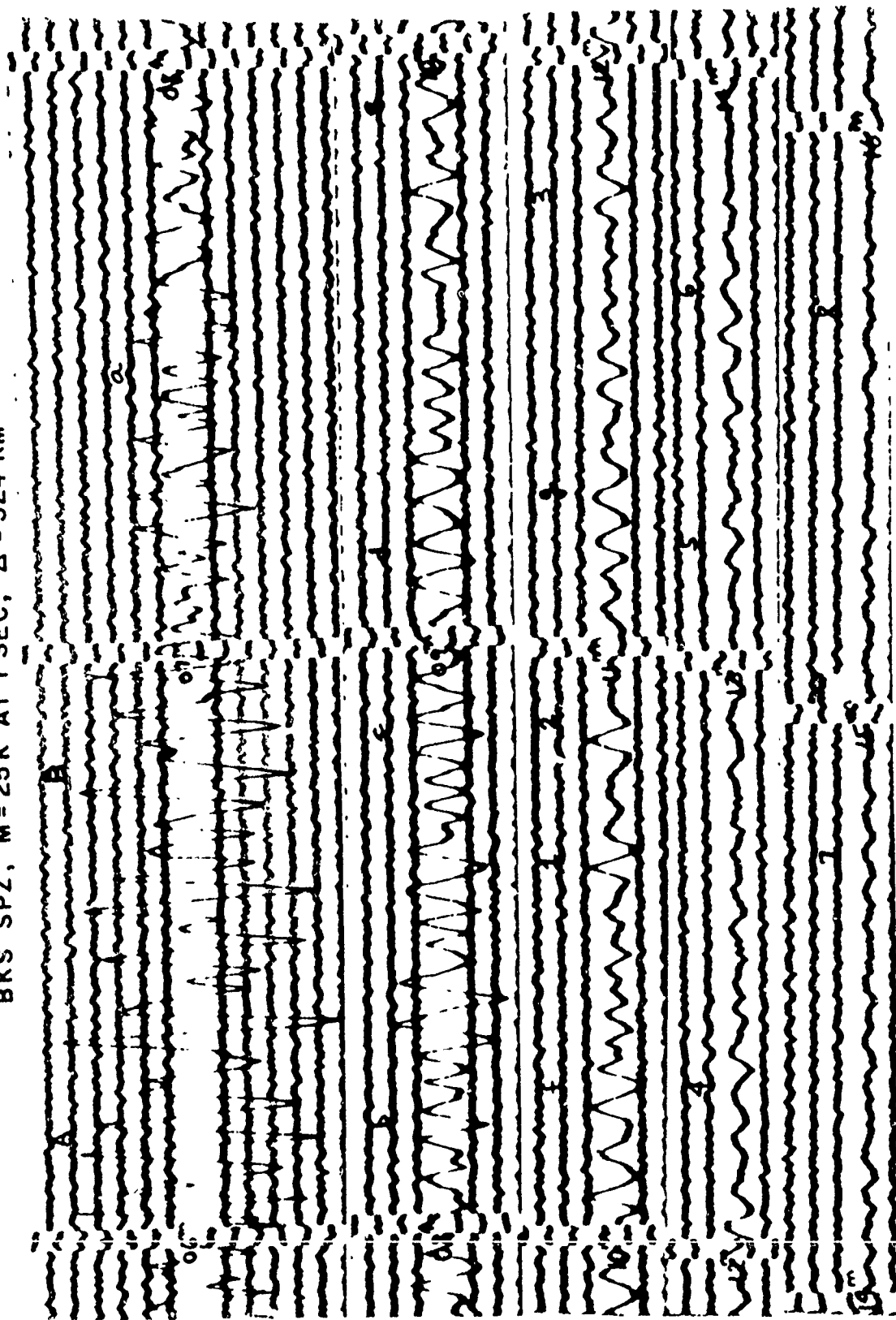
Fig. 1. Copy of a portion of the BKS short-period, vertical-component seismogram for NTS explosion ALMENDRO. The figure includes the time interval of 6 to 16 min after the explosion. The wave amplitudes are too large in the preceding minutes to be reproduced conveniently. Wavelets used to obtain Q_0 and ζ values by the coda-Q method are indicated by lower-case letters.
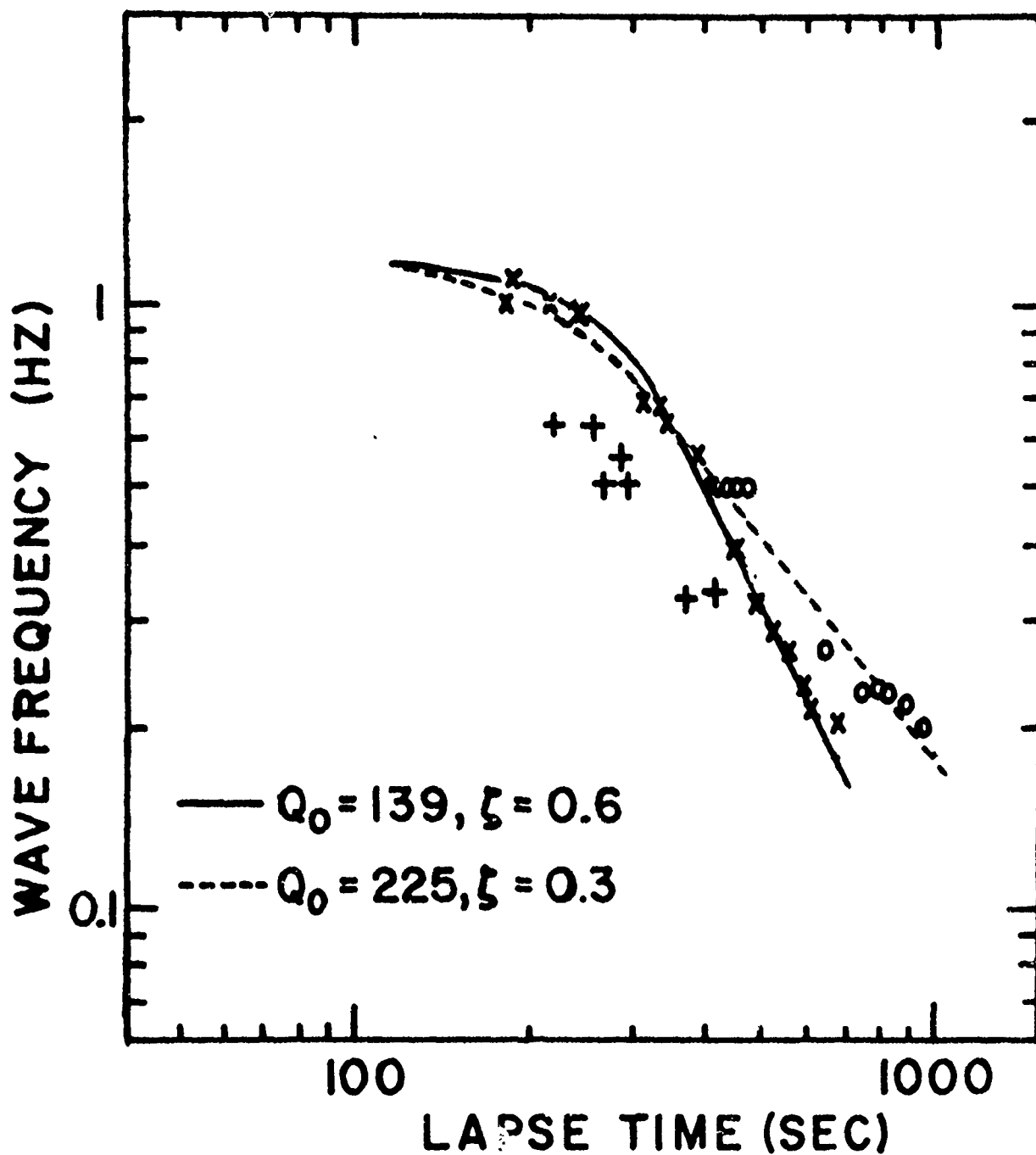
Fig. 2. Plot of the wavefrequency versus lapse time data for the Lg coda of the BKS seismograms for STANLEY, NASH and ALMENDRO. The x's correspond to the lower-case letters of Fig. 1, the +'s to fundamental-mode Rayleigh waves (upper-case letters) and the o's to constant frequency coda wavelets (numbers in Fig. 1). The solid-line curve is taken to be the approximate fit to the data (the x's). The dashed-line curve is that obtained by Rondout Associates for NTS events recorded at BKS.
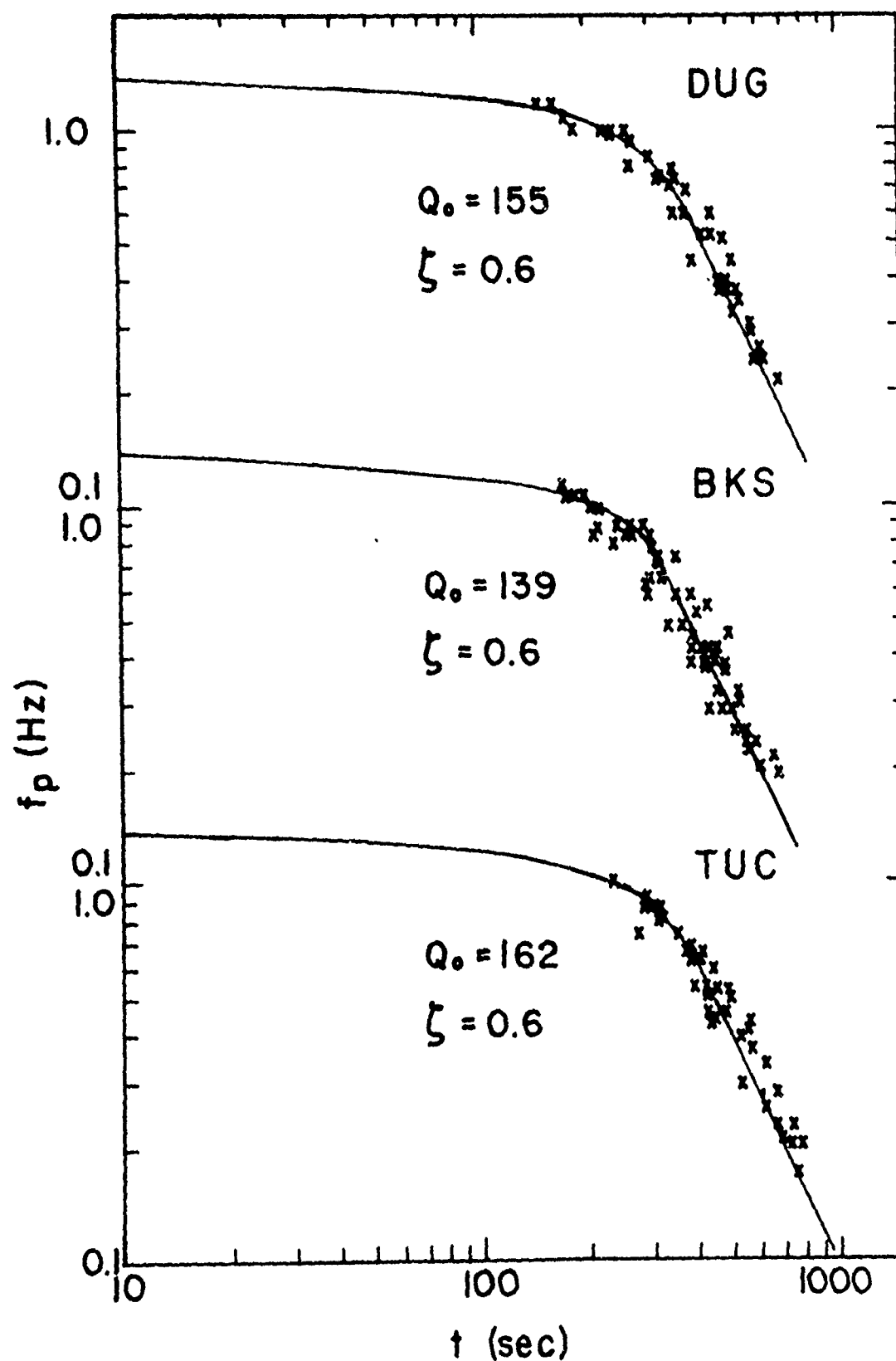
Fig. 3. Wave frequency versus lapse time data for selected NTS events recorded at DUG, BKS and TUC. The data originally were fitted by curves of = 0.6 and Q_o = 150, 143 and 160, respectively. The curves plotted in the figure correspond to Q_o values after station corrections were made.

Figs. 4 and 5 show $m_b(Lg)$ versus explosion yield data and least-square quadratic fits to the data points for hard-rock and dry alluvium NTS shots, respectively, for explosions of announced yield. The equation of the hard-rock curve is

$$m_b(Lg) = 3.868 + 1.181 \log Y (kt) - 0.093\ (\log Y)^2$$

and of the dry alluvium curve is

$$m_b(Lg) = 3.796 + 1.008 \log Y (kt) - 0.0629 (\log Y)^2$$

The standard deviation of the former is 0.08 magnitude units, and of the latter 0.07 units.

Application of the same methodology and of the hard-rock calibration equation to non-NTS United States explosions and French Sahara explosions gives yield estimates as shown in Fig. 6. The Nevada explosions PILE DRIVER and SHOAL had positive $m_b(Lg)$ residuals of 0.21 and 0.16, respectively. If the Sahara shots RUBIS and SAPHIR, which were in granite, are assumed to show a similar source effect, taken to be 0.18 magnitude units, their estimated yields are lowered to 45 and 72 kt, respectively.

$m_b(Lg)$ values were determined for 63 NTS explosions whose yields remain classified. These data, taken together with $m_b(P)$ estimates given by the International Seismological Centre, indicate a 0.31 ± 0.02 $m_b(P)$ bias between NTS and eastern North America, where 0.02 is the standard error of the mean. This is in good agreement with other estimates obtained by independent methods, such as 0.33 by Chung and Bernreuter.
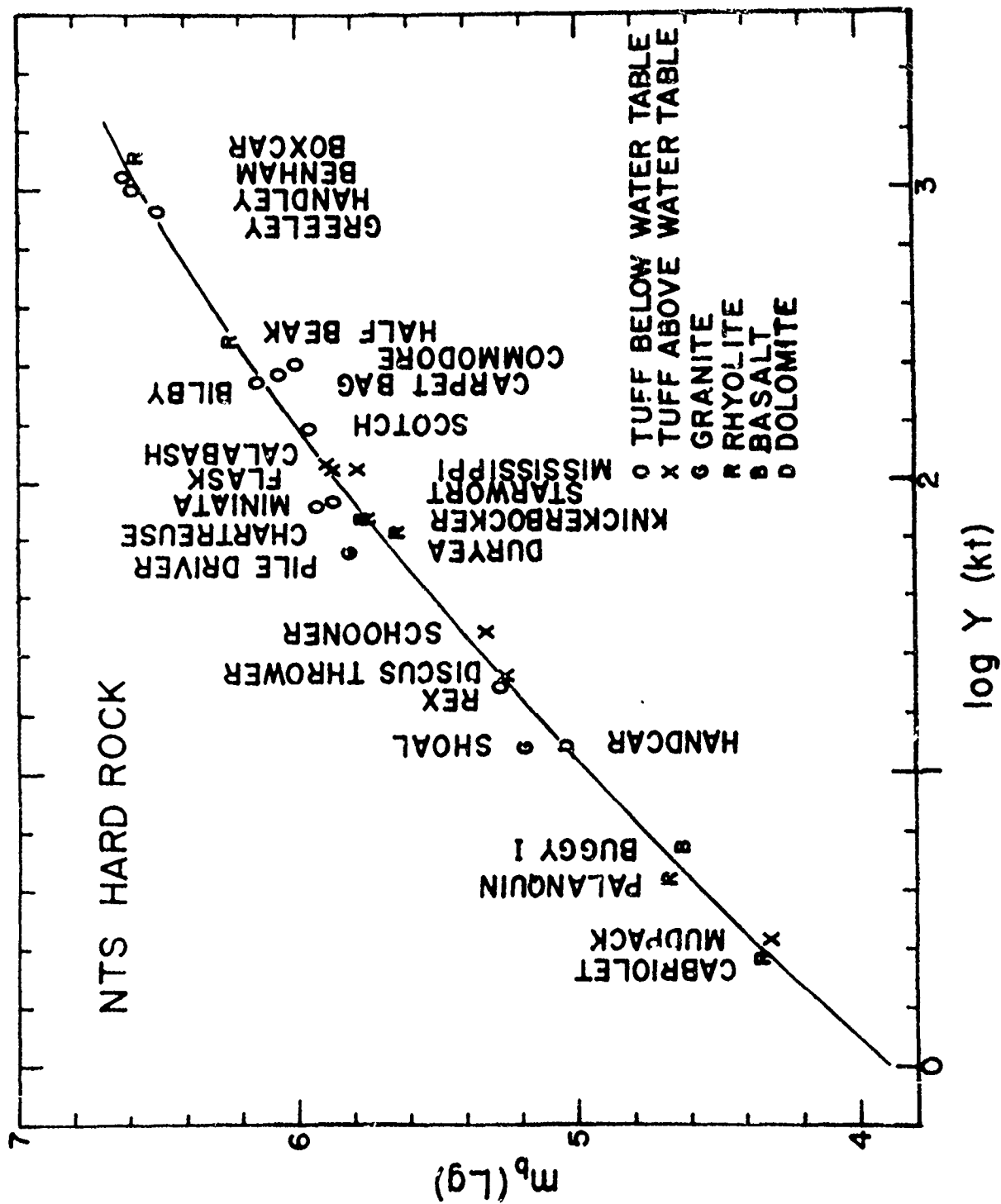
Fig. 4. $m_b(lg)$ versus logarithm of explosion yield for hard-rock NTS explosions of announced yield. The curve is a second-degree polynomial obtained by least-squares fit to the data.

Fig. 5. $m_b(lg)$ versus logarith of explosion yield for dry alluvium NTS explosions of announced yield. The curve is a second-degree polynomial obtained by weighted least-squares fit to the data.

173

Figure 6

Yield estimates of non-NTS explosions in the continental United States

Date	Name	Rock Type	Station	Q_0	γ	Δ(km)	m_b(Lg)	m_b(P-ISC)	Announced yield (kt)	Yield from m_b(Lg) (kt)*
10/22/64	SALMON	salt	BLA	600	0.4	1075	4.77			
			DAL	280	0.4	850	4.63			
			FLO	420	0.4	890	4.51			
			OXF	400	0.4	370	4.67			
			RCD	720	0.3	1995	4.71			
			Average				4.66	4.6	5.3	5.1
12/10/67	GASBUGGY	shale	DUG	150	0.6	625	5.38	4.8	29	28
09/10/69	RULISON	sandstone	TUC	185	0.6	828	5.56	5.0	~40	45
05/17/73	RIO BLANCA	sandstone	TUC	185	0.6	858	5.71	5.1	~90**	66

* Uses NTS hard-rock relation, equation (5)

** Three 30-kt explosions fired simultaneously [Springer and Kinnaman, 1975]

Yield estimates of French Sahara explosions in granite

Date	Name	Station	Q_0	γ	Δ(km)	m_b(Lg)	m_b(P-USCGS)	Announced yield (kt)	Yield from m_b(Lg) (kt)*
10/20/63	RUBIS	AAE	750	0.3	3947	5.72	5.6	52	68
02/27/65	SAPHIR	AAE	750	0.3	3947	5.96			
		HLW	700	0.3	3146	5.92			
		SDB	720	0.4	4414	5.79			
		Average				5.89	5.8**	120	111

* Uses NTS hard-rock relation, equation (5)

** ISC gave m_b(P) = 5.6

174

PAPER TITLE: Fundamental Studies on Lg-Coda and Coda Excitation

PAPER AUTHOR: R. B. Herrmann and C. Y. Wang
       Department of Earth and Atmospheric Sciences
       Saint Louis University
       P.O. Box 8099
       St. Louis, MO 63156

CONTRACT NO: F19628-85-K-0029

SUMMARY:

A computer model for synthesizing Lg coda generated by three-dimensional heterogeneity has been constructed using a Born approximation. Using locked modes of higher mode surface waves, the effect of point scatterers at different spatial locations in the media can be modeled at any distance. Extensive modifications have been made to surface wave dispersion programs in order to avoid dropping modes at higher frequencies.

Observations of Lg-coda in southeast Canada have been performed using the digital ECTN data of Miramichi aftershocks. Attempts have been made to reconcile Lg-Q estimates to coda-Q estimates using the Aki-Chouet approach. The dependence of coda-Q upon analysis window has been modeled. The Miramichi data are very interesting because of the presence of very high frequency signals at large distances. As a matter of fact, at a 1000 km distance, Lg is only well seen at 1-3 Hz. At higher frequencies, it disappears into a mantle S-wave coda which in turn sits upon a mantle P-wave coda.

CONCLUSIONS AND RECOMMENDATIONS:

1. A sensitivity study of of the effects of near source, near receiver, deep point scatterers on the nature of the Lg-coda is feasible.

2. The proper use of an Aki-Chouet coda-Q method requires long window lengths and a $t^{-1/2}$ geometrical spreading term primarily because the Lg-coda is composed of scattered, dispersed waves.

3. Use of the excellent ECTN data set points out some very interesting features at high frequencies, that points out the care required for proper interpretation and, perhaps more importantly the effect of scattering mechanisms in the crust and the upper mantle. Ten Hertz and higher mantle P and S coda are observed, indicating something about an effect upper mantle Q. It would be very interesting to look at some western U. S. data at these high frequencies to obtain some independent evidence of crust and mantle Q distribution.

OBJECTIVE

The object of these studies is to obtain a fundamental understanding of the nature of the coda of the Lg wave, so that the use of the Lg-wave coda as an estimator of source excitation and as an inticator of whole path attenuation can be properly judged.

BASIC STUDIES

1. Modeling the effect of three-dimensional heterogeneities on the the excitation and attenuation of the Lg-wave coda

We have extended the work of Malin (1980) in order to deterministically model the effect of point scatterers. A typical modification of the seismic wave equation is performed in order to express the scattered wavefield, except that the case of incident surface waves is included. This formulation thus permits both wavetype conversion, e.g., between SH-Love and P-SV-Rayleigh, and also mode conversion. Since surface-wave theory is being used, body-wave scattering within the waveguide can also be considered just by including the higher modes required to synthesize the body waves. Figure 1 shows how the method can be used to synthesize the effect of complex scatterers. In this figure, the source and receiver are separated by a distance of 100 km. Discrete scatterers are placed at various points on an ellipse defined by a given source-scatterer-receiver distance of 110, 300 or 500 km. The resultant waveforms from each discrete scatterer and ellipse sum are displayed. Differences are seen in forward, side and backscattered wavefields.

Figure 2 shows the waveforms due to a distribution of scatterers on various ellipses with the source-scatterer-receiver distance varyuing from 110 to 450 km. The source of seismic energy is an arbitrary earthquake dislocation. Only the scattered wavefield is displayed. One interesting feature to note is the increase in signal duration, which is to be expected since the Lg-wave itself disperses.

Obviously, we have only just begone a complex validation, testing and analysis phase.

2. Analysis of ECTN Data

Shin (personal communication) studied the vertical component Lg-waves generated by Miramichi aftershocks and recorded by the ECTN. The fascinating feature of these data is the ability to observe the wavefield at distances between 135 and 1000 km at frequencies between 1 and 15 Hz. Figure 3 shows the observed waveforms and filtered traces at distances of 561 km (MNT1) and 994 km (JAQ1). Note the presence of the Lg wave, indicated by the arrow, in the broadband and low-pass filtered data. At higher frequencies the Lg and its coda disappear into the mantle S and its coda, which in turn is superimposed on the mantle P and its coda. This observation means that any attempt to infer high frequency Q values, either of the direct Lg wave of the coda, must take into account the superposition of wavefields and mis-attributing of inferred Q to a particular wavetype. For example, blind use of amplitude spectra in the Lg-wave time window would yield a higher 10 Hz Q than there actually is, since the Lg has essentially disappeared. On the other hand, high frequency signals, emanating at the source are propagating to large distances.

Shin also noticed that direct application of an Aki-Chouet coda Q technique led to differences in the estimated coda Q as a function of distance, even when a Sato correction is made for observations near the direct Lg-wave arrival. Using the results of the synthetic modeling, we realized that the Aki-Chouet model had to properly account for the dispersion in the coda. Using the observation that the Lg-wave amplitude decreases as R^{-1} with distance and that the Lg signal duration increases with distance, R, we were forced to conclude that the coda amplitude geometric attenuation factor should be $t^{-1/2}$. Even after using this modification and extending the Sato correction to surface waves, there was still a discrepancy between the coda Q estimates made at times near the Lg and those made at times much later than the Lg arrival.

This difference is illustrated in a simple experiment shown in Figure 4 We synthesize the

Scatterer Position Test

110

300

500

composite
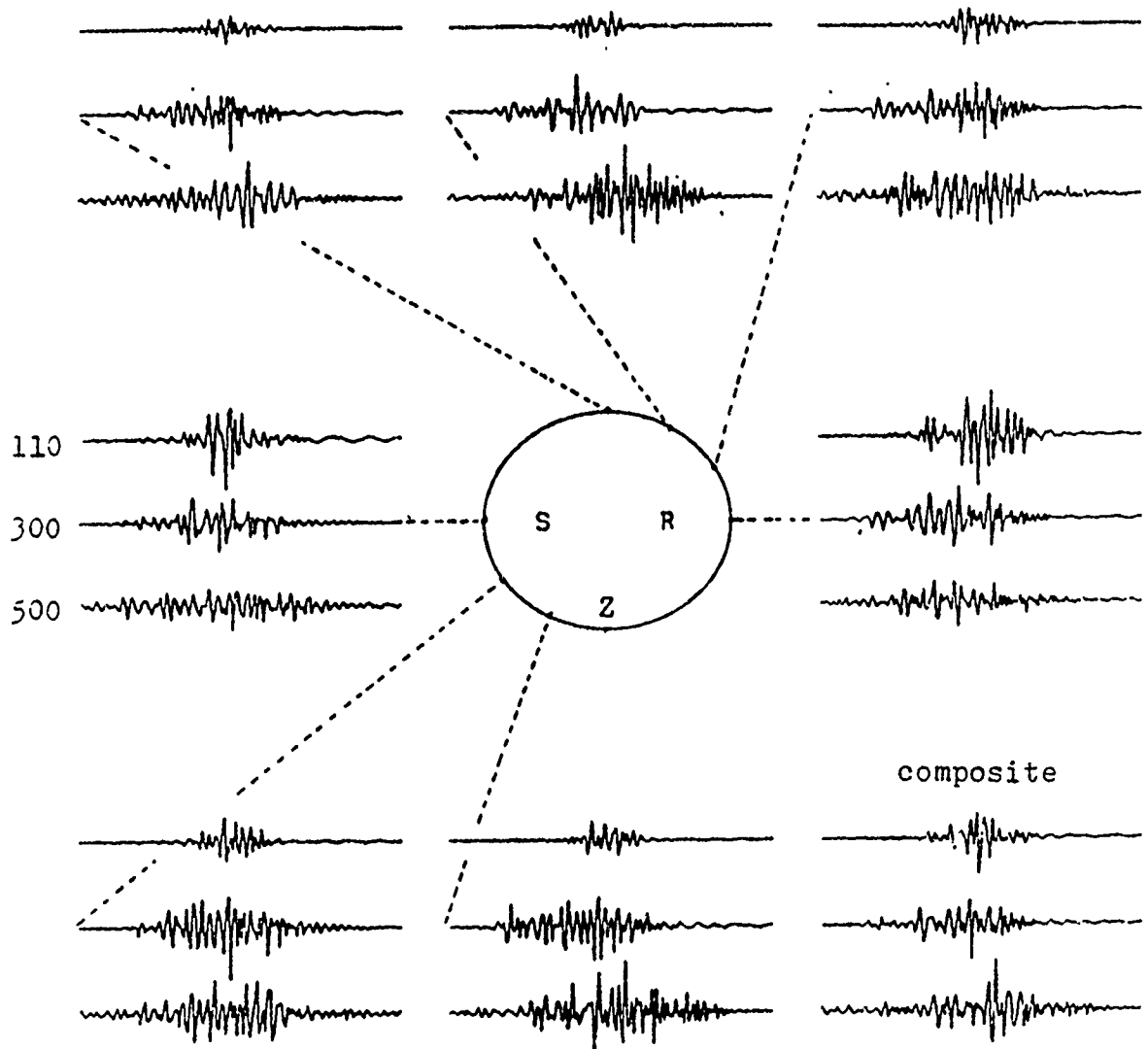
Figure 1

Lg Scattered Waves
(5 layer CUS model, 5 Hz, Q:400)

Figure 2

Figure 3

179

Q low

Q high

narrow
sparse

wide
dense
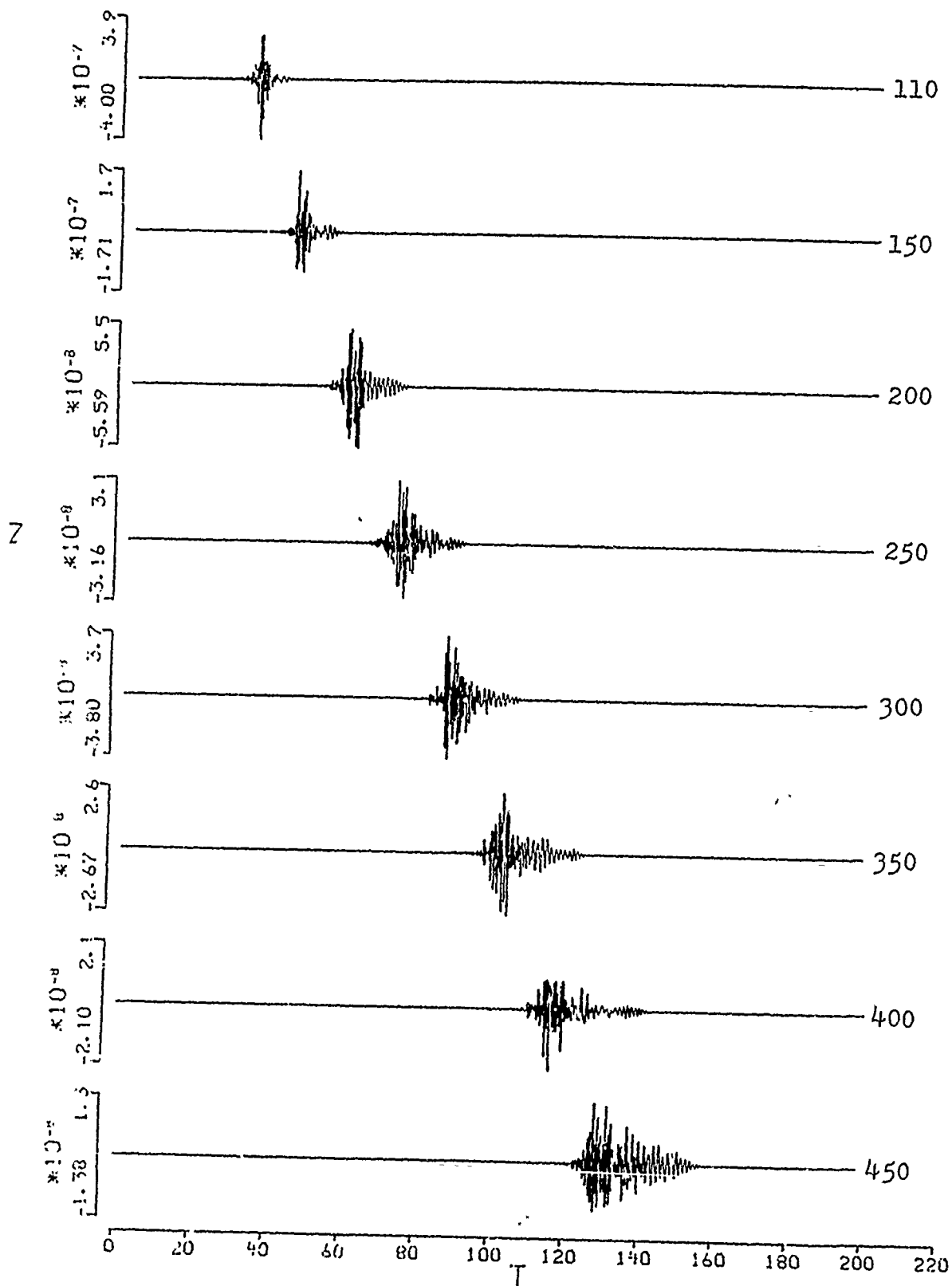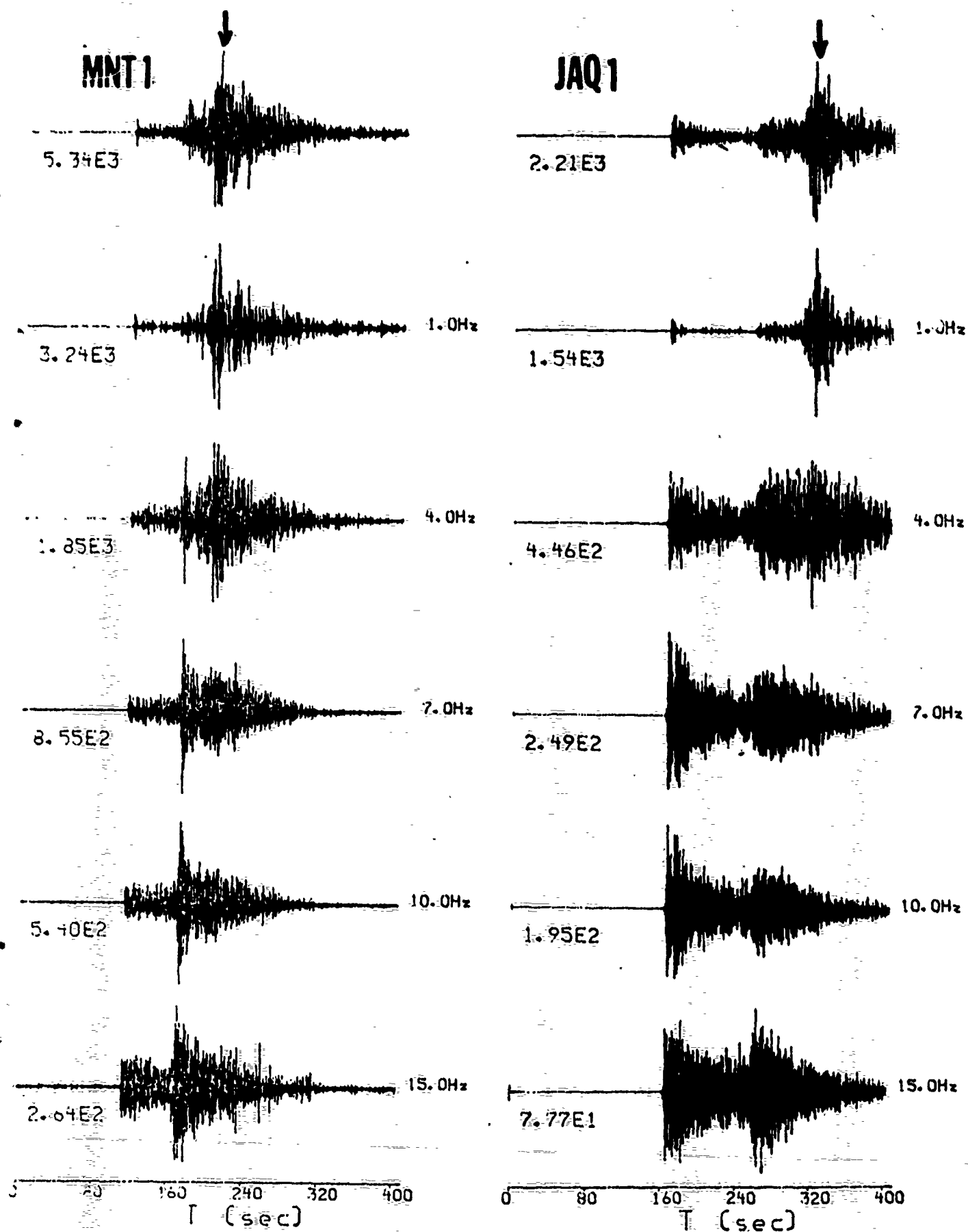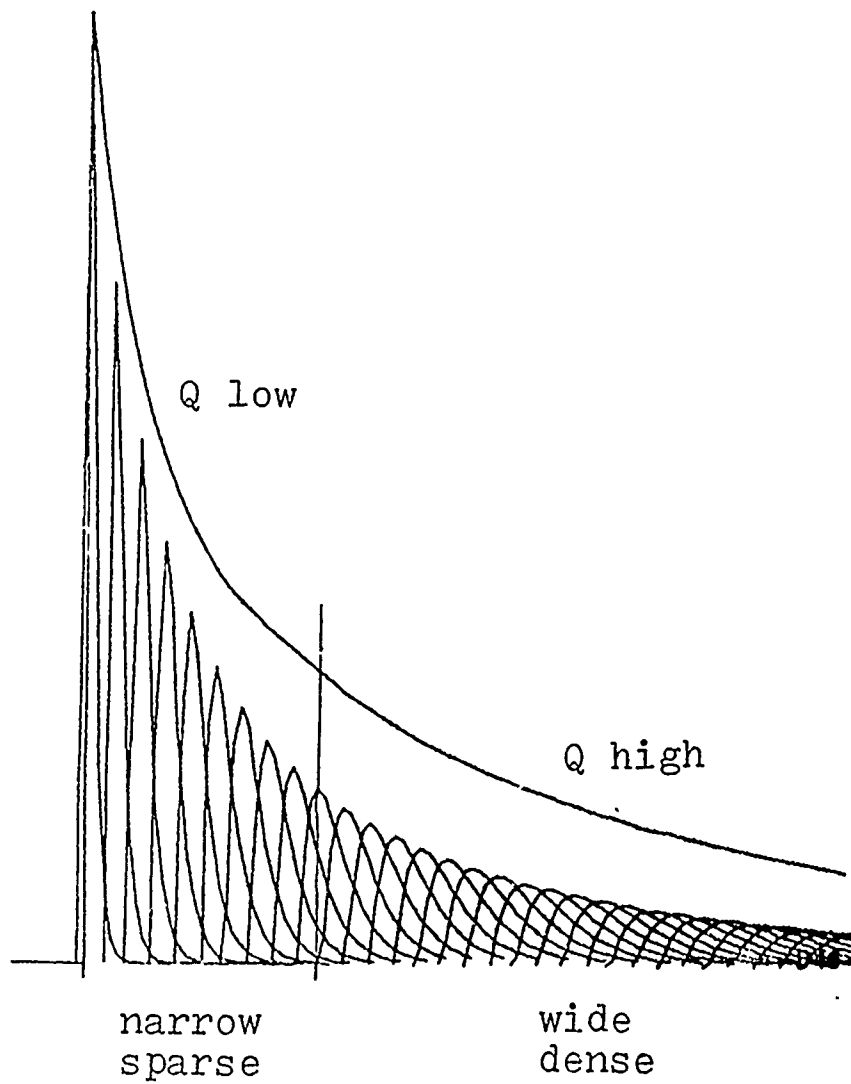
Figure 4

coda envelope by performing an RMS superposition of envelopes of scattered coda from different distances. Since the later arrivals have traveled greater distances, they are more dispersed, but since they are still Lg-wave, their peak amplitudes vary as t^{-1}. When a sufficient number of these envelopes superimpose, the resultant envelope does in fact vary as $t^{-1/2}$, however near the first scattered arrival, this continuum has not yet build up and the envelope varies at t^{-1}. Thus the application of a single coda geometrical spreading term to the entire envelope is not appropriate. Underestimates of coda Q occur if only data from very short times after the Lg-wave are used.

TITLE: "APPARENT ATTENUATION DIFFERENCES BETWEEN FRENCH, SOVIET AND U.S. TEST SITES"

AUTHORS: Thomas C. Bache and Steven R. Bratt
Science Applications International Corporation

CONTRACT NO.: F19628-85-C-0021

SUMMARY:

The four United Kingdom arrays provide high quality digital data and have been operating continuously since the mid-1960's. We have been analyzing spectra from these arrays and NORSAR to determine source differences among events and attenuation differences among travel paths. A remarkable feature of the spectra from NTS, French Sahara, Mururoa and E. Kazakhstan explosions is that there is little or no difference in the spectral slope above 2 or 3Hz, (the one exception is the E. Kazakh-NORSAR path where the source-corrected spectrum is essentially constant above 3Hz). If we overlay the high frequencies, large differences can be seen below 2Hz. Some correlate with m_b and are clearly due to source differences, and some are clearly due to attenuation differences. The two must be separated when comparing different test sites. We are estimating the source and effective Q and verifying the results with synthetic seismograms that match the data in both time and frequency domains. This requires explicit statement of all assumptions and provides a framework for quantifying the uncertainty.

CONCLUSIONS AND RECOMMENDATIONS

Only a few paths have been analyzed in detail, but these are for the important NTS and E. Kazakh sites. The attenuation is strongly dependent on frequency, and we also observe both absorption and scattering attenuation. This complicates the modeling, but we are able to fit the data by varying only one parameter. Attenuation is greater for the NTS paths, however there is a strong tradeoff with the source assumptions. In the example given here, a 50% shift in the corner frequency changes the attenuation bias estimate by $0.34m_b$. More detailed analysis should substantially narrow the range of admissible corner frequency assumptions, and it is crucial to do so. The uncorrected data indicate that attenuation for French Mururoa is as large or larger than for NTS, while the evidence is somewhat ambiguous for the French Sahara site where the source correction is more important. When we complete our analysis, the key issue will be to determine how well the paths analyzed represent the larger set of paths that influence m_b. Results from studies of larger data bases, should resolve this issue. Many seismologists have been modeling explosion P waves, but use different data and emphasize different features. We recommend that this expertise be combined to determine how well we really understand test site differences.

INTRODUCTION

A difference in the m_b-log yield relationship for different test sites is called m_b bias. It can be due to different source coupling, effects of pP, or attenuation. There are other factors as well (e.g., network bias), but we are not concerned with them here. The bias due to pP is apparently small (it seems unlikely to be as large as $0.1m_b$ for the events of interest). Most of the emphasis has been on bias due to attenuation, but large source coupling variations are also possible. They can influence both the amplitude and shape (overshoot and corner frequency) of the seismic source, and there is a strong tradeoff between source and attenuation effects.

There are many methods for estimating the short period P wave attenuation difference between test sites, but the most direct is to analyze the P waves themselves. Explosion data, especially from the Nevada and E. Kazakhstan sites, have been intensively studied for this purpose. Our contribution has been to analyze data from the four UKAEA arrays (GBA, EKA, WRA and YKA) and NORSAR. We have obtained very smooth and consistent spectra that are shaped almost entirely by the source spectrum and attenuation (stacking over the array suppresses many of the variations seen in single station spectra). One drawback is that these stations may not adequately represent the "average path attenuation" for the larger set of stations used to compute m_b, and this must be checked.

Our approach is to determine Q and source models that fit the data in both the time and frequency domains. Synthetic seismograms are used and require explicit statement of all assumptions being made. After all the work of the past decade, the bias assumed to occur between test sites should be demonstrable with synthetic seismograms that match the robust characteristics of the data in both domains. Otherwise, there are some major gaps in our understanding that should be highlighted.

E. Kazakhastan Data

Bache et al. (1985) developed a Q model for the paths from the E. Kazakhstan site to the UKAEA arrays. Since corner frequency effects were apparent, the Q model was fit to a subset of events (southwest Shagan River explosions with $m_b > 6$) with corner frequency effects below 2Hz. Some key results are shown in Figure 1. A frequency-dependent Q is required below 3Hz, and this is represented with an absorption band. The three paths were not the same, and the differences can be represented by varying t_m between 0.05 and 0.1 seconds. The low frequency limit (t_0*) controls the synthetic m_b, but is not very well constrained by these data without an accurate source correction.

A dramatic feature of these spectra is that they all follow the same nearly constant slope above 3Hz. To represent this, a constant t* was added to the absorption band. Comparison of long and short time window spectra and examination of the apparent dispersion at high frequency suggest that this represents attenuation by scattering. We also studied NORSAR data (Bache and Bungum, 1985) and found the effect of attenuation to be much the same below 3Hz, but quite different at high

frequency. In fact, between 3 and 7Hz the source-corrected NORSAR spectrum is nearly flat, suggesting Q f. This can be represented by deleting the constant t* from the models in Figure 1. Scattering attenuation could still be important, but represented by Q f, as is anticipated under some circumstances. We have no explanation for why the path to NORSAR should be so different from the others for frequencies above 3Hz.

Spectra for Other Test Sites

Some typical array spectra for other test sites are shown in Figure 2. A major feature is that we see little or no difference above 2 or 3Hz, (the E. Kazakhstan to NORSAR path is the one exception we have seen to this general behavior). The significant differences occur below 2Hz, which is where there are large source differences (e.g., compare Piledriver or Colwick with the Pahute Mesa data). There are also low frequency variations due to Q (e.g., compare the Shagan River spectra at the three array stations). Thus, both Q and source differences can be large enough to explain the spectral differences between test sites. To separate the two is not easy, but the data impose many constraints. For example, the corner frequency should depend on yield or m_b, and this is seen in the data. The Q effect is constant for each test site-station pair, while the source effect is constant for each event over the network. Perhaps most important, we must be consistent with the well-supported results from many studies of explosion source spectra, source spectral scaling and attenuation.

Some conclusions about the apparent attenuation differences between test sites can be drawn from Figure 2, assuming they adequately represent the much larger set of paths that contribute to m_b. The apparent attenuation for Mururoa appears to be even larger than for NTS, assuming no large source coupling differences. For the French Sahara data the question is more subtle and depends more strongly on the source assumptions. There is little apparent difference between the Piledriver spectrum and those for the Sahara events of equal (Rubis) and twice the Piledriver yield. On the other hand, the Saphir (120Kt) spectrum represents the Sahara data and falls quite close to the GBA Shagan River spectrum. Reasonable source corrections will probably show that the attenuation is somewhat larger for the French Sahara data, but this must be carefully worked out.

Correction for the Source Spectrum

We have recently begun to explore the effect of the source assumptions on estimates for attenuation and bias, and will describe here some preliminary results. In Figure 3 we show several source corrections applied to EKA Shagan River data. Current ideas about the explosion source spectrum and its dependence on yield and depth are best represented by the Mueller and Murphy (1971) source, though the relative scaling is much better supported than the absolute level. Based on the results shown in Figure 3, it is difficult to choose which source representation is best. Formal inversion using data from several stations will better constrain the optimum source spectral scaling.

184
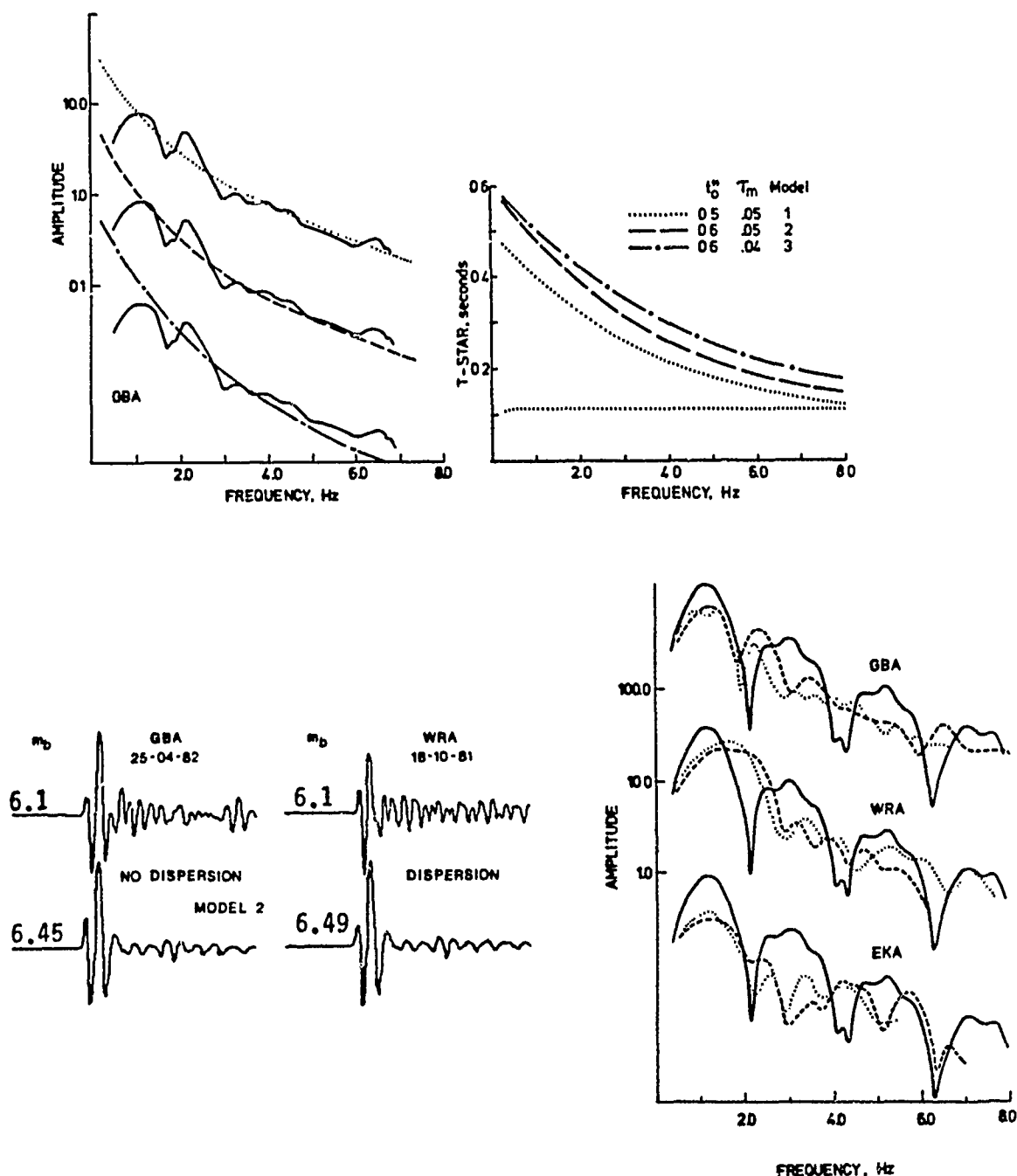
Figure 1.   At the top the GBA spectrum obtained from five m_b>6 events is plotted with the three effective attenuation models shown at the right in terms of t* versus frequency.   The total t* includes two parts: an absorption band specified by the indicated parameters, and an essentially constant t* (which is the same for all three).   At the bottom some typical observed seismograms and spectra are compared to synthetics computed with the "Model 2" t*, a 150Kt Mueller-Murphy granite source, and a P-pP lag time of 0.46 seconds.   The observations are single element recordings and the ISC m_b is indicated.   The two synthetic waveforms differ only in the dispersion associated with the constant t*.   In one case the phase velocity is constant, while in the other there is dispersion with phase velocity decreasing by 0.1% between 0 and 9Hz.   The usual absorption band dispersion is used for the frequency-dependent portion of the t* model.

185
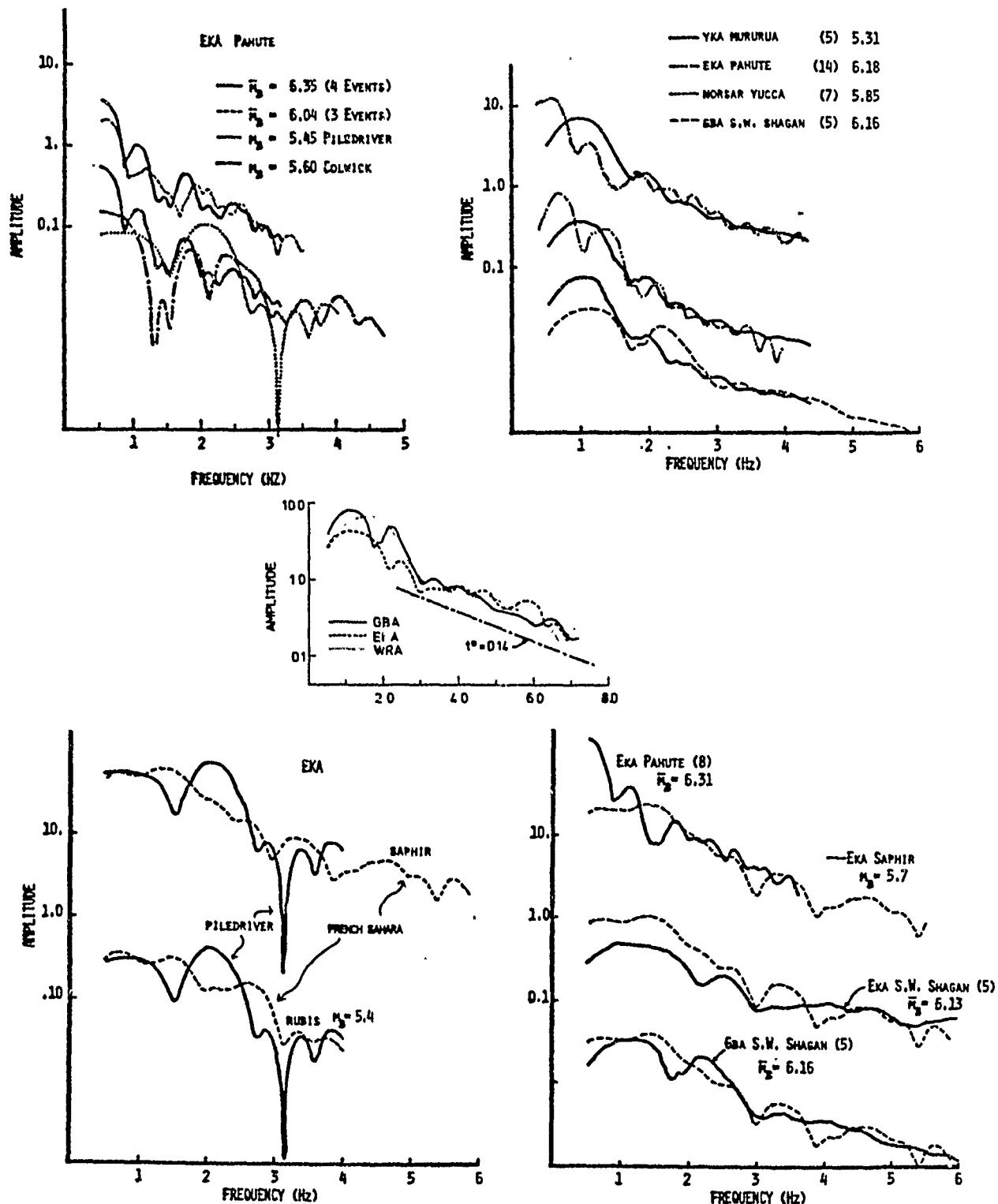
Figure 2. Spectra are compared for NTS, Mururoa, Sahara and Shagan River events. Some represent individual events while others are stacks of several event spectra, with m_b the mean for the set. For Mururoa, WRA spectra are similar to those shown for YKA. At EKA, Pahute Mesa and Yucca Flat spectra are nearly the same.

186
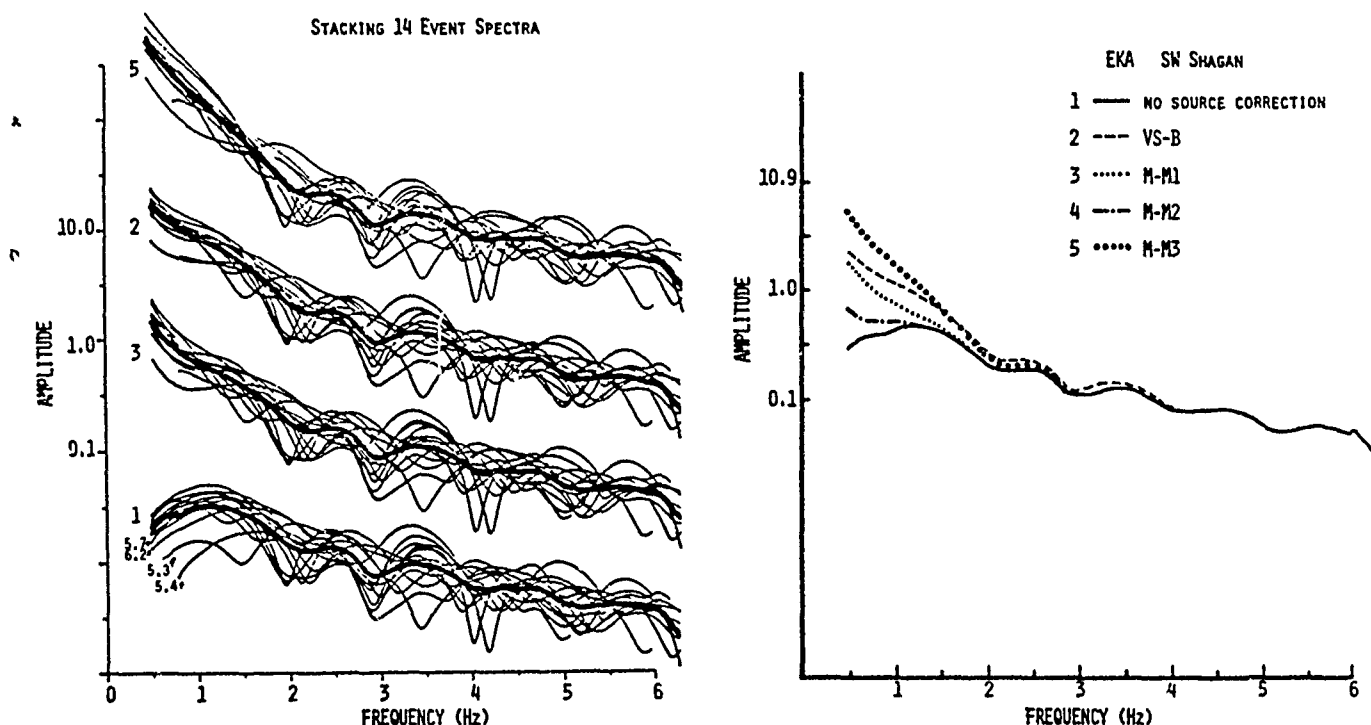
Figure 3. Several source corrections are applied to the EKA spectra from 14 southwest Shagan River events (6.22 > m_b >5.28) and the results stacked to obtain an average spectrum for the path. For four cases the stacking is shown at the left and the average spectra (heavy lines) for these and one other are compared at the right. The m_b of several events is indicated. Only two have m_b<5.7, and these plot well below the others at low frequency. Identifying the sources, VS-B and M-M1 are the von Seggern and Blandford (1972) and Mueller and Murphy (1971) granite source functions with m_b 6.0 corresponding to 150Kt. For VS-B the frequencies cube-root scale, assuming m_b $\propto$ 0.9 log yield (W). For the Mueller-Murphy source this scaling is reduced by the factor $h^{0.42}$, assuming $h=122W^{1/3}$. The M-M2 and M-M3 sources differ from M-M1 in having the corner frequency shifted down (M-M2) or up by 60%.

The event spectra in Figure 3 show little evidence for strong spectral scalloping due to pP interference. This is not surprising since many other studies have concluded that pP is not as calculated elastically, but is usually later and smaller. The pP spectrum is enough unlike P to obscure the nulls, as can even be seen in detailed non-linear source calculations (Bache, 1982). We do expect nearly elastic pP at long periods, so it should shape the spectrum at very low frequencies. There are some cases where the first pP null may be present, but this is inconsistent and the expected periodicity is clearly not seen in the broad band cases.

Estimating a Q Model and m_b Bias

The Mueller/Murphy wet tuff/rhyolite source should represent the Pahute Mesa explosions very well, since the model is based on such events. Indeed, we find that this source does correct Pahute Mesa spectra events to be nearly the same for a broad range of m_b. Stacking these corrected spectra gives an average spectrum that displays the effect of Q, plus some minor perturbations due to interference with pP or other later phases like spall slapdown.

For Shagan River events it is not so clear how to represent the source. A plausible first estimate is M-M1 of Figure 3. The curling up at low frequencies seen in several of the corrected spectra suggests that the corner frequency or overshoot is incorrectly modeled. Increasing the corner frequency removes this effect, as is demonstrated by M-M3 in which the source corner frequencies of all events have been increased by 60%.

We fit Q models to the corrected EKA Pahute Mesa spectrum and two versions of the corrected GBA Shagan River spectrum, and the results are plotted in Figure 4. The Q model differences are simple; only the t_0^* difference is significant. The synthetic spectra fit the data rather well, and would fit even better if the theory were adjusted to smooth out the pP peaks and nulls. If there were no pP modulation, the synthetic spectrum would be very close to the smooth curve showing the spectral effect of the Q model.

In Figure 5 we show the waveforms corresponding to these spectra. The synthetics represent fairly well the robust features of the waveforms, particularly those controlling m_b. At Pahute Mesa we know we can improve the fit by introducing a later phase representing (probably) spall slapdown (e.g., Bache, 1982), but this has almost no effect on m_b. Note that the two Pahute Mesa synthetics define the line $m_b = 1.03$ log W + 3.26, which is not a good fit to the m_b-yield data for Pahute Mesa events. However, this is typical for synthetics with elastic pP.

The bias estimate consistent with these assumptions can be read directly from Figure 5. That is, the m_b for a 150Kt Shagan event is 0.73 m_b or 0.40 m_b larger (depending on the source assumptions) than for the same yield explosion in tuff at Pahute Mesa. However, there is clearly some inconsistency in the assumptions about the source amplitude. Note that the synthetic Shagan River m_b for 150Kt is several tenths larger than for the largest events that have occured at that
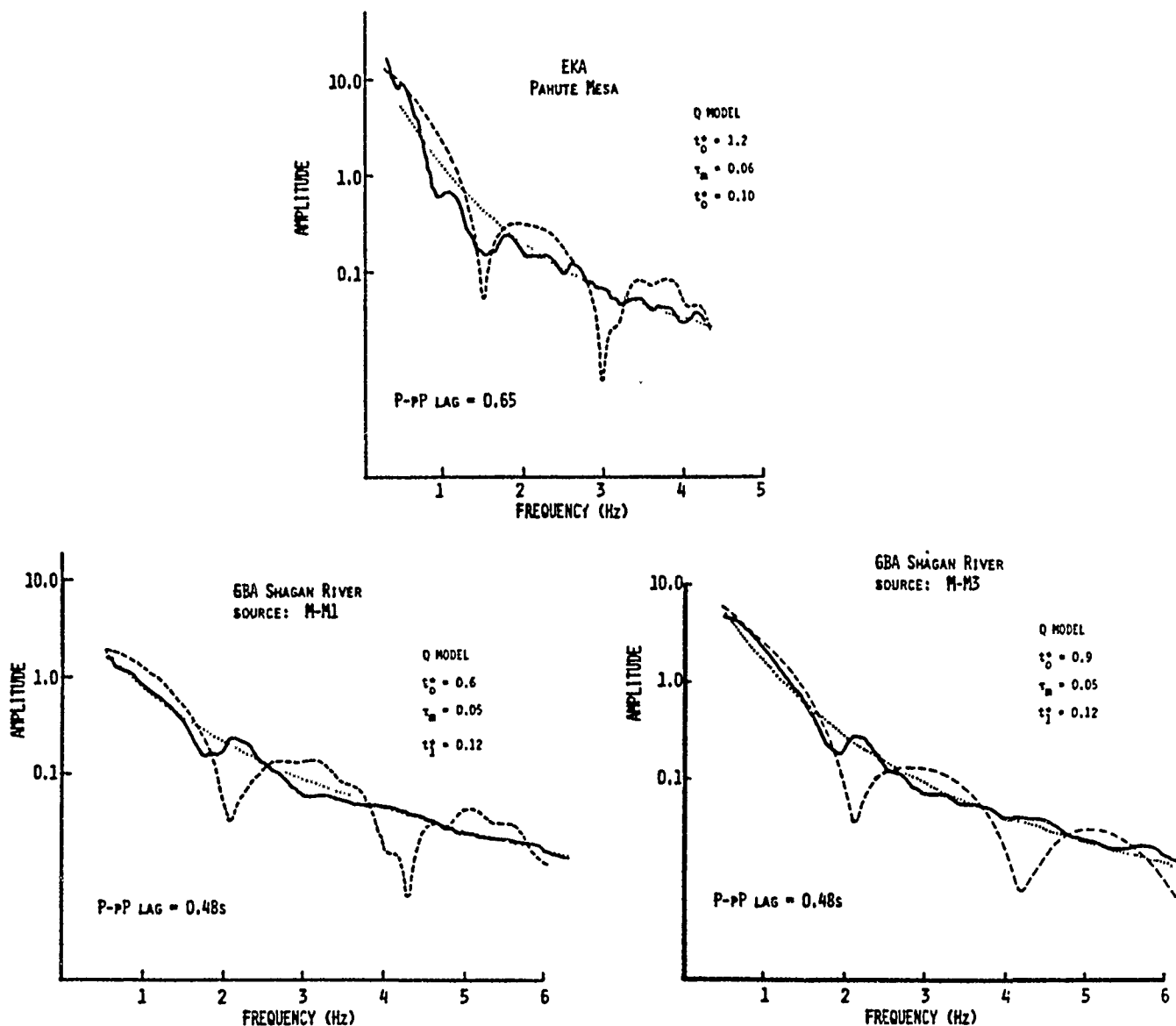
Figure 4. Source-corrected spectra from EKA Pahute Mesa and GBA Shagan River are plotted with the spectral effect of the Q model specified. The GBA spectrum is an average of 13 events ($6.31 > m_b > 5.4$). The Q model is the sum of two parts, as in Figure 1 (the M-M1 case is fit with Model 2 of Figure 1). Also shown is the spectrum of a synthetic seismogram (processed the same way as the data) with the indicated P-pP lag time. The latter was chosen to give waveforms like the observations of m_b 6.1 events at Shagan River and m_b 6.2 events at Pahute Mesa.
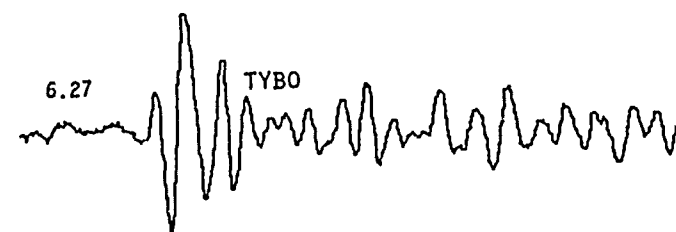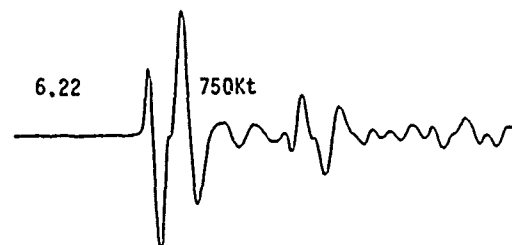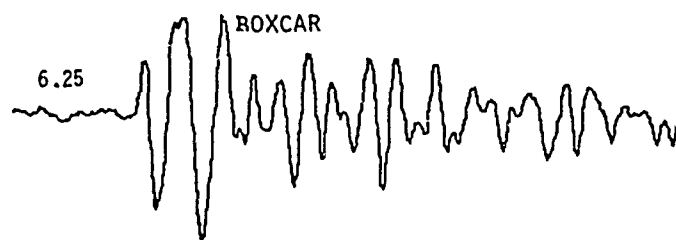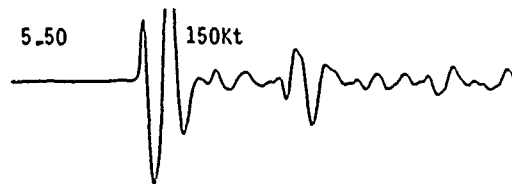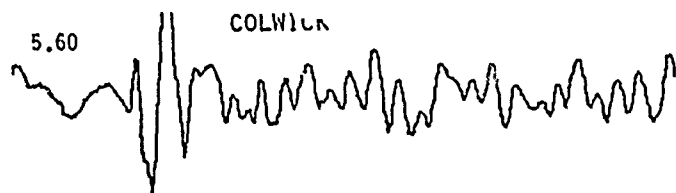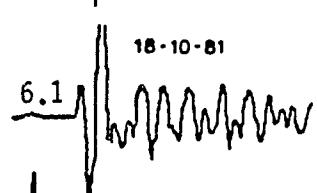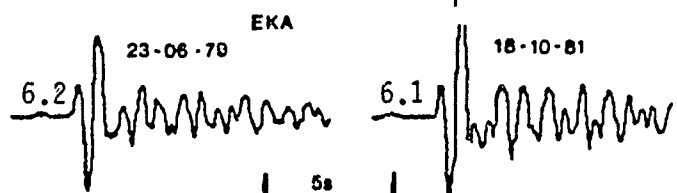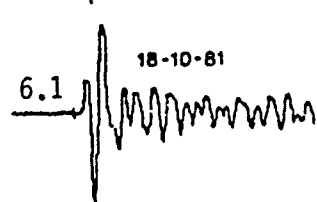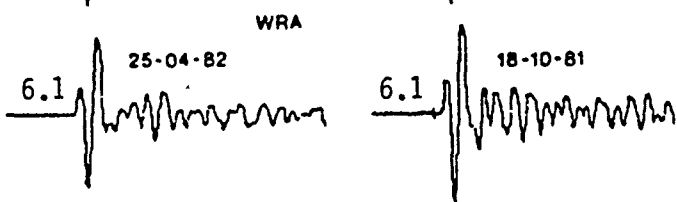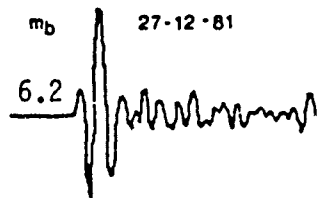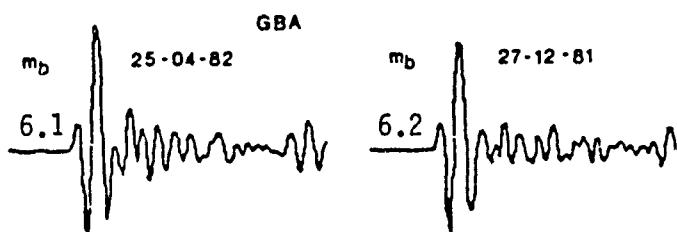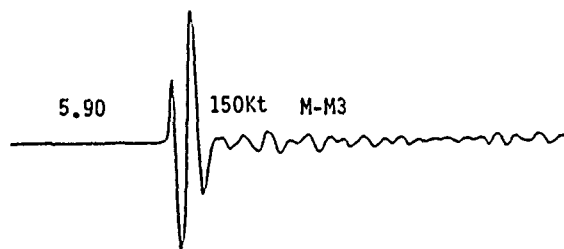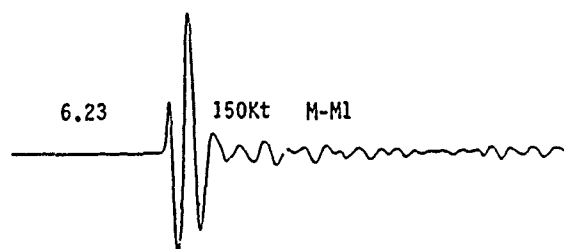
Figure 5. Synthetic seismograms corresponding to the spectra in Figure 4 are shown together with typical observations. The Pahute Mesa synthetics were done with the Mueller/Murphy source at depths of 0.65 and 1.1 km and P-pP lag times of 0.65 and 0.9 seconds. The Shagan synthetics were done with the Mueller-Murphy granite source at a depth of 0.65 km and P-pP lag time of 0.48 seconds. Shagan River data are from single elements of the indicated arrays. The Pahute Mesa data are EKA beam sum recordings (the signal/noise is too low at high frequency on the individual elements).

site, while the synthetic Pahute Mesa m_b are smaller than for events of comparable yield. The difference in pP effects is insignificant; only about 0.02 m_b (increasing the apparent bias). The combined effect of differences between the Mueller-Murphy tuff and granite source potentials and differences due to the source region velocities cause about 0.1m_b of the difference in synthetic m_b. This may represent an inaccurate calibration of the source models.

The bias due to Q model differences alone is 0.60 m_b for M-M1 and 0.27 m_b for M-M3. This is a very large spread, and illustrates the sensitivity due to the assumptions about the source. It also illustrates how forward modeling requires explicit statement of all assumptions, allows them to be checked with the data, and provides a framework for quantifying the uncertainty.

Improving the Estimates

There is much more information that can be used to improve the Q models and the estimates for m_b bias and its uncertainty. The examples shown are for only one path for two sites. It is straightforward to extend the analysis to include the other array data (e.g., Figures 1 and 2), as well as more events (e.g., Northeast Shagan, Degelen, Yucca Flat), and this is being done. The number of paths will still be rather small compared to those included in m_b calculations (though in some respects the array data set is large since each event spectrum includes up to 20 individual seismometer recordings). To be sure the array data are representative, we need to compare, where possible, with results from other studies of data from the lower quality, but more widely distributed SRO and WWSSN stations.

REFERENCES

Bache, T.C., Estimation of the yield of underground nuclear explosions, Bull. Seism. Soc. Am., 72B, 5131-5168, 1982.

Bache, T.C., P.D. Marshall, and L.B. Bache. "Q for teleseismic P waves from central Asia," J. Geophys. Res. 90, 3575-3587, 1985.

Bache, T.C. and H. Bungum. "High frequency P wave attenuation from central Asia to Norway," submitted to Geophys. J.R. astr. Soc., 1985.

Mueller, R.A. and J.R. Murphy, "Seismic characteristics of underground nuclear detonations," Bull. Seism. Soc. Am., 61, 1675-1692, 1971.

von Seggern, D.H. and R.R. Blandford, "Source time functions and spectra for underground nuclear explosions," Geophys. J.R. astr. Soc., 31, 83-97, 1972.

Recovery of Eurasian Crustal and Upper-Mantle Structure by Higher-Mode Waveform Analysis

Thomas H. Jordan, Arthur L. Lerner-Lam*, and Lind S. Gee

Department of Earth, Atmospheric and Planetary Sciences
Massachusetts Institute of Technology, Cambridge, MA 02139

Summary. This paper reviews the waveform inversion technique of Lerner-Lam and Jordan [1983] and reports on its application to the study of Eurasian crustal and upper-mantle structure. We have successfully fit complex P-SV wavegroups on vertical-component seismograms for paths crossing northern Eurasia with a model having a 39-km crust and no asthenospheric low-velocity zone. Between the Moho and the 400-km discontinuity, the shear velocities found from the P-SV waveform analysis are consistently lower than those inferred from the SH waveform modeling of Grand and Helmberger. We suggest that this discrepancy is diagnostic of a polarization anisotropy associated with the olivine-rich mineralogy of the thick, basalt-depleted chemical boundary layer that characterizes the upper mantle beneath stable continents. The algorithms employed in this study will be generalized to incorporate such anisotropic structures and can be applied to the construction of fully three-dimensional models of Eurasia, as well as to the study of upper-mantle attenuation structure.

Introduction. Seismological methods to determine the yields of underground nuclear explosions rely on models of the crustal and upper-mantle structure, particularly attenuation structure in the vicinity of the testing areas. Estimates of the body-wave magnitude bias between the Eastern Kazakh Test Site, where the recent large Soviet shots have been fired, and the Nevada Test Site, which provides the bulk of the magnitude-yield calibration data, range from 0.2 to 0.4 magnitude units, corresponding to factors of about 1.6 to 2.8 in yield. The uncertainty in this bias dominates the errors in the yields estimated from teleseismic P waves and has proven to be a source of controversy in verifying compliance with the Threshold Test Ban Treaty.

For fixed receiver networks, the body-wave attenuation bias is primarily controlled by local and regional variations in upper-mantle structure beneath the sources. These variations appear to be largest in the asthenosphere below 100 km. Recent models of the subcontinental mantle suggest that substantial variations in temperature and composition extend to depths exceeding 200 km and that these variations correlate with the long-term tectonic history of the overlying crust [Jordan, 1981]. Therefore, the problems of yield estimation are coupled

---

* Now at Lamont-Doherty Geological Observatory, Palisades, NY 10964

to fundamental questions regarding continental evolution.

Previous work on mapping the three-dimensional structure of Eurasia has employed fundamental-mode surface waves [e.g., Feng and Teng, 1983], which lack sufficient resolution below 100-km depth, or a limited number of multiply reflected body waves with restricted geographical coverage [e.g., Sipkin and Jordan, 1976; Burdick et al., 1982]. Grand et al. [1985] have recently extended the SS-S technique of Burdick et al. [1982] to include SSS phases and thereby increase the geographical range of the body-wave observations, but their work has thus far been confined to the forward modeling of SH-polarized signals.

In a DARPA/AFGL-sponsored project initiated this year, we are attempting to develop techniques for the systematic inversion of both P-SV and SH waveforms from higher-mode dispersed wave groups (which include multiply reflected body waves) for lateral heterogeneity. These methods are capable of giving much better vertical resolution of path-averaged properties than the dispersion of the fundamental-mode surface waves alone. They will be applied to large data sets collected from GDSN, NARS, WWSSN and other seismic networks to obtain three-dimensional models of Eurasian crustal and upper-mantle structure. Here we describe the formulation of the waveform inversion procedure and give the results of some preliminary modeling of the structure along paths traversing the northern part of Eurasia.

Formulation of the waveform-inversion technique. Our formulation is based on the waveform-inversion procedures described by Lerner-Lam and Jordan [1983]. The observed seismogram is represented as the sum of fundamental (n = 0) and higher-mode (n ≥ 1) surface waves:

$$s(t) = \sum_{n=0}^{N} u_n(t)$$

$u_n(t)$ is the seismogram for the nth mode branch. A synthetic seismogram $\overline{s}(t)$ is calculated for a chosen, spherically symmetric earth model $\overline{m}(r)$, and the difference between the observed and the synthetic is formed:

$$\Delta s(t) \equiv s(t) - \overline{s}(t) = \sum_{n=0}^{N} \Delta u_n(t)$$

$\Delta u_n(t)$ is the differential seismogram for the nth mode branch.

To increase the signal-to-noise ratio (SNR) for a specified mode and reduce the interference from spurious signals and other modes, we construct matched filters from the synthetic branch seismograms. At the lag time τ we define the observed branch cross-correlation function (BCCF)

$$S_m(\tau) = \overline{u}_m(t) * s(t) = \int_{-\infty}^{\infty} \overline{u}_m(t) s(t+\tau) dt$$

and the synthetic BCCF

$$\overline{S}_m(\tau) = \overline{u}_m(t) * \overline{s}(t)$$

$\overline{S}_m(\tau)$ provides an approximate description of the mode-mode interference, so an appropriate data functional for the structural inverse problem is the differential BCCF,

$$\Delta S_m(\tau) = S_m(\tau) - \overline{S}_m(\tau) = \overline{u}_m(t) * \sum_{n=0}^{N} \Delta u_n(t)$$

In our procedure, we seek a model perturbation which to first order minimizes a quadratic form in ΔS_m. The quadratic form includes a symmetric taper about zero lag, so the points near $\tau = 0$, where the SNR is greatest, receive the most weight.

For the first-orbit, vertical-component surface waves received at stations far away from the source and its antipode, branch seismograms can be approximated by an integral over continuous wavenumber λ, whose asymptotic form is

194

$$u_n(\Delta,t) = \int_0^\infty G_n(\lambda,\Delta,t)\cos\xi_n(\lambda,\Delta,t)\,d\lambda$$

Δ is epicentral distance, and G_n and ξ_n are the amplitude and phase kernels

$$G_n(\lambda,\Delta,t) = \frac{|U_n|\,E_n}{2\pi\sqrt{\sin\Delta}}\exp[-\alpha_n(\lambda)t]$$

$$\xi_n(\lambda,\Delta,t) = \lambda\Delta - \pi/4 - \omega_n(\lambda)t + \Phi_n$$

U_n and E_n are displacement and excitation scalars, Φ_n is the source phase, ω_n is the dispersion function, and $\alpha_n = \omega_n/2Q_n$ is the decay function. E_n and Φ_n depend on the source mechanism, whereas ω_n and α_n depend on the path-averaged elastic and anelastic parameters, respectively. The horizontal-component seismograms have similar forms.

We have developed an efficient algorithm for computing branch synthetics which is based on Filon quadrature. The algorithm is adaptive and reduces computation time by an order of magnitude over conventional mode-summation techniques [Lerner-Lam and Jordan, 1983].

Departures of the real earth from the spherically symmetric reference model $\bar{m}$ are represented as perturbations to the amplitude and phase kernels:

$$G_n(\lambda,\Delta,t) = \bar{G}_n(\lambda,\Delta,t)\,[1 + \gamma_n(\lambda)]$$

$$\xi_n(\lambda,\Delta,t) = \bar{\xi}_n(\lambda,\Delta,t) - \Delta\omega_n(\lambda)t$$

Here $\gamma_n(\lambda)$ is the perturbation to the relative amplitude of the nth mode, and $\Delta\omega_n = \omega_n - \bar{\omega}_n$ is the perturbation to its dispersion fuction. If the perturbations to the displacement scalar U_n and the excitation scalar E_n can be ignored, a good approximation when the lateral variations along

the path are small, then the relative amplitude perturbation can be written

$$\gamma_n(\lambda) = -\Delta\alpha_n(\lambda)\,t$$

where $\Delta\alpha_n = \alpha_n - \overline{\alpha}_n$, which in turn can be related to the perturbation in the specific attenuation $Q_n^{-1}(\lambda)$. In terms of the differential BCCF, the linearized forward problem becomes

$$\Delta S_m(\tau) = \sum_{n=0}^{N} \int_0^{\infty} [B_{mn}(\lambda,\tau)\Delta\omega_n(\lambda) + D_{mn}(\lambda,\tau)\Delta\alpha_n(\lambda)]\,d\lambda$$

The partial derivatives B_{mn} and D_{mn} can be evaluated by the same adaptive Filon algorithm used to compute the synthetic seismograms. The integrals over wave-number are thereby discretized on the Filon grids $\{\lambda_\ell : \ell = 1, 2, \ldots, L_n\}$. To set up a matrix system describing the differential BCCFs for $M+1$ mode branches ($m = 0, 1, \ldots, M \le N$) at each of P stations ($p = 1, 2, \ldots, P$), we discretize the cross-correlations at the set of lag times $\{\tau_k = k\Delta\tau : k = -K, -K+1, \ldots, 0, \ldots, K-1, K\}$ and define the vectors

$$[\Delta S]_{mpk} = \Delta S_{mp}(\tau_k)$$

$$[\Delta\omega]_{n\ell} = \Delta\omega_n(\lambda_\ell)$$

$$[\Delta\alpha]_{n\ell} = \Delta\alpha_n(\lambda_\ell)$$

and the matrices

$$[B]_{mpk,n\ell} = B_{mnp}(\lambda_\ell,\tau_k)$$

$$[D]_{mpk,n\ell} = D_{mnp}(\lambda_\ell,\tau_k)$$

This yields the linearized, discretized forward problem

$$\Delta S = B\,\Delta\omega + D\,\Delta\alpha \tag{1}$$

The matrices appearing in this linear system have $I = (M+1) \times P \times (2K+1)$ rows and

$$J = \sum_{n=0}^{N} L_n$$

columns. For typical ranges of indices used in our work to date, these dimensions are on the order of 10^4 and 10^2, respectively.

The vector ΔS can be computed from a set of observed seismograms, and equation (1) inverted for the perturbations to the dispersion and the attenuation functions. In practice, it is convenient to parameterize the vectors $\Delta \omega$ and $\Delta \alpha$ by perturbations Δm to the radial starting model. This reduces the dimension of the system and constrains the perturbed seismograms to correspond to a realistic earth structure. We interpret the resulting one-dimensional model as the average of the three-dimensional structure along the path between the source and receiver. Inversion procedures based on this representation have been discussed by Lerner-Lam and Jordan [1983].

Application to Eurasian data. The waveform-inversion technique has been applied to seismograms recorded at five WWSSN stations in western Europe from four earthquakes in the Kuril-Kamchatka Seismic Zone (Figure 1). The focal depths for the events range from 134 km to 544 km, and the epicentral distances from 55° to 78°. The data set comprises a total of fourteen paths traversing a variety of tectonic structures in northern Eurasia, from the tectonically active region east of the Verkhoyansk Suture Zone to the Baltic Shield. The long-period, vertical-component seismograms were digitized, response-normalized, and low-pass filtered with a corner at 35 mHz.

In our original analysis of this data set [Lerner-Lam and Jordan, 1983], we chose the very smooth structure of Cara et al. [1980] as a starting model and solved for shear-velocity perturbations that were a smooth function of depth. The modeling presented in this report is based on a layered structure with four upper-mantle discontinuites below the crust-mantle boundary and polynomial variations in the seismic velocities and density of each layer; the polynomials were taken to be linear throughout the upper mantle. Perturbations were allowed in the
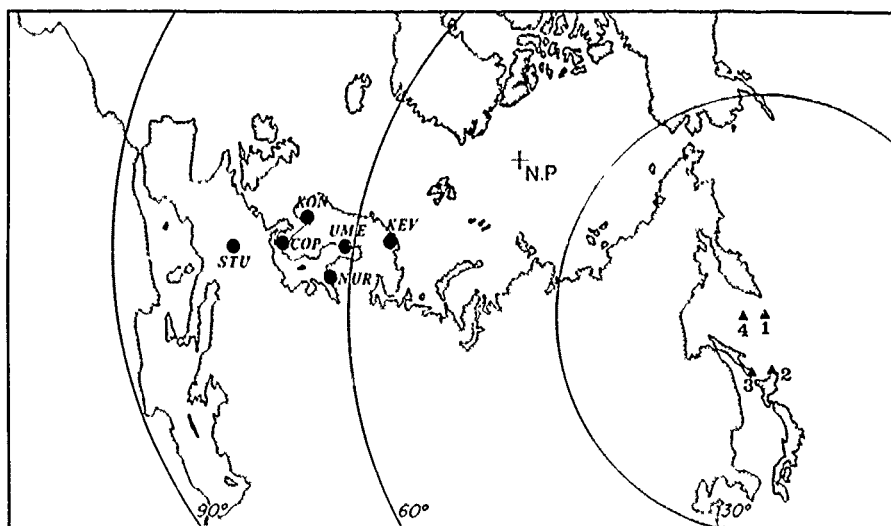
Figure 1. Azimuthal equidistant projection of the event-station distribution for the northern Eurasian path, with the pole centered on the epicenter of Event 1. The events, shown as triangles, range in focal depth from 134 to 544 km. The stations are shown as circles.

depths of all discontinuites, as well as in the parameters of the polynomials. The starting model was set equal to PREM [Dziewonski and Anderson, 1983] in the lower mantle and conformed to regionalized body-wave and surface-wave models of continental structure above this depth; it contained no low velocity zone.

The attenuation model used in our calculations was that of Masters and Gilbert [1983]. In these preliminary experiments, we did not attempt to invert for attenuation structure. We did, however, desensitize the inversion to possible amplitude fluctuations associated with Q variations and source effects using the normalization scheme described by Lerner-Lam and Jordan [1983, sect. 5.2], which employs a projection operator to annihilate the second term on the right-hand side of equation (1) for a restricted class of amplitude perturbations.

The model obtained from waveform inversion, EU2, is plotted in Figure 2. Comparisons of observed and synthetic waveforms and BCCFs are displayed in Figures 3-6. The structure is a simple one, but it provides a remarkably good fit to the phase of the waveforms over the entire range of focal depths, including both the fundamental Rayleigh mode and the complex wave groups respresenting the interference of the
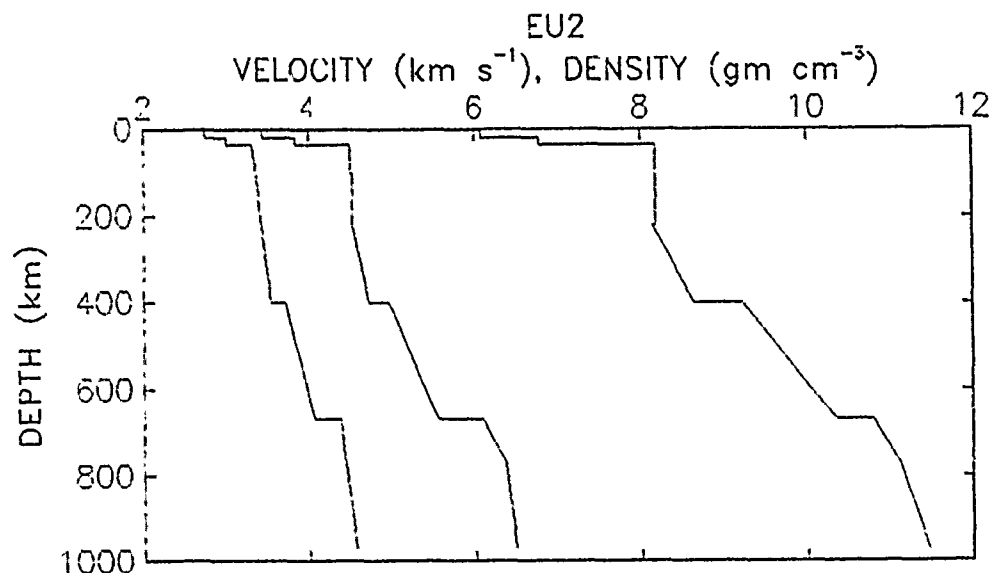
Figure 2. EU2, a path-averaged model of northern Eurasia obtained by waveform inversion of fundamental and higher-mode surface waves.

higher modes. The pulses seen on the seismograms in Figure 6, for example, where the match is nearly wiggle-for-wiggle, are dominated by contributions from the third and fourth overtones. These waveforms can also be represented as the sum of multiply reflected P-SV body phases, predominantly SS and SSS; the agreement shows that the model satisfies their travel times. Our waveform analysis is thus the P-SV equivalent of the SH analysis performed by Grand and Helmberger [1984a,b], and our resolution of sub-lithospheric structure should be comparable to theirs. (Because our technique is formulated as a linearized inverse problem, its resolving power can be analyzed using formal linear methods, which is one of its major advantages over forward modeling. Preliminary calculations have been made by Lerner-Lam [1982], and a more detailed resolving-power study is underway [Gee et al., 1985].)

EU2 shear velocities are compared with the SNA model of Grand and Helmberger [1984a] in Figure 7. The latter structure was derived from S and SS waves traversing the Canadian Shield, but Grand et al. [1985] have shown that it also provides a good description of SH propagation across the stable platforms of Eurasia. The two models have comparable

EVENT 1 NUR

EVENT 2 KON

DATA

SYNTHETIC

DATA

SYNTHETIC

| 20 | 24 | 28 | 32 | 36 |

TIME (min)

| 20 | 25 | 30 | 35 | 40 |

TIME (min)

EVENT 1 NUR

0

2

3

4

| -100 | -50 | 0 | 50 | 100 |

LAG (s)

EVENT 2 KON

0

2

3

4

| -100 | -50 | 0 | 50 | 100 |

LAG (s)
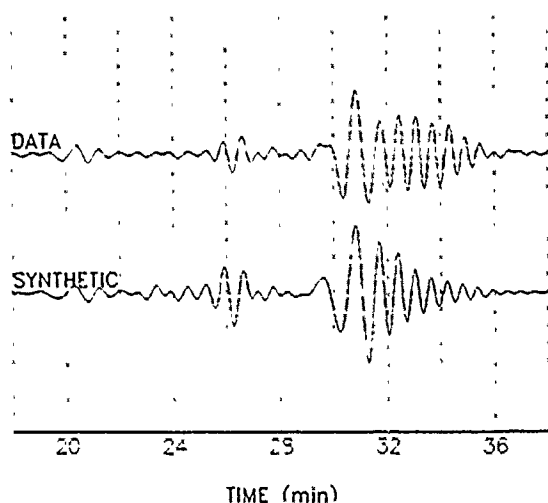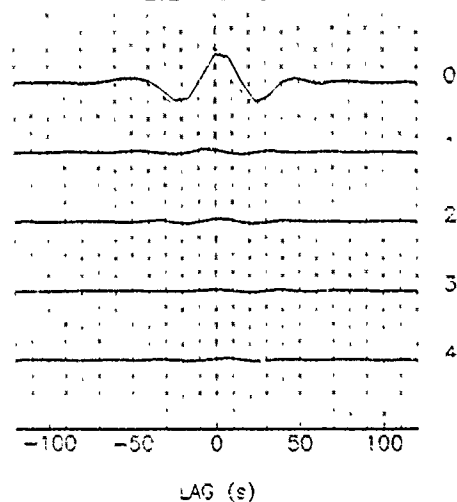
Figure 3. Comparisons of observed and synthetic waveforms (top panel) and BCCFs (bottom panel) recorded at NUR for Event 1 (h = 134 km). BCCFs plotted as solid lines are observed, those plotted as dotted traces are synthetic. The BCCF mode number is to the right of each pair of traces in the lower panel. The energy in the waveforms is concentrated in the fundamental mode, which appears as the well-dispersed wavetrain beginning at about 29 min, although the S and SS arrivals are also visible at 20 min and 25 min.
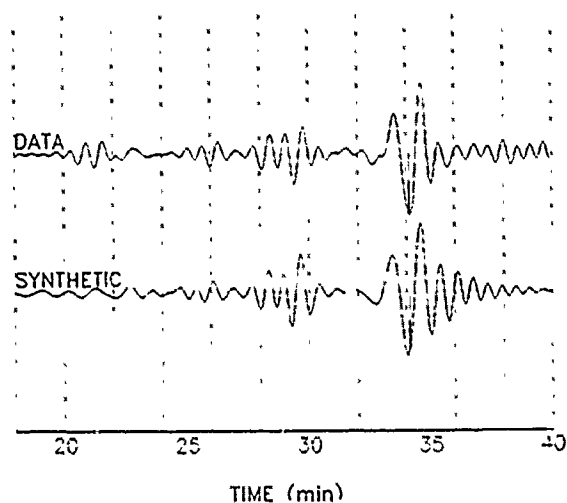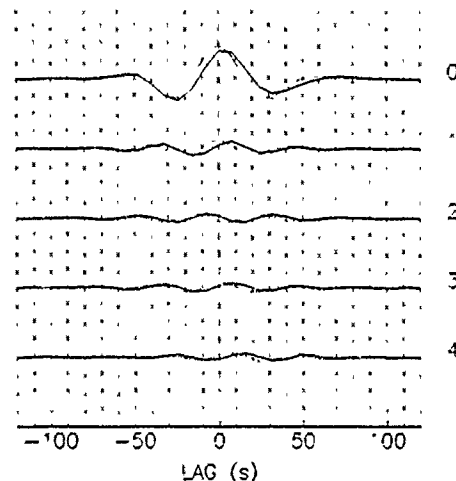
Figure 4. Comparisons of observed and synthetic waveforms and BCCFs for Event 2 (h = 181 km) recorded at KON. Increased relative amplitude levels of the higher-modes are due to the increase in source depth.

200

EVENT 3 UME

DATA

SYNTHETIC

'6 '8 20 22 24 26 28 30 32 34

TIME (min)

EVENT 4 NUR

DATA

SYNTHETIC

'6 '8 20 22 24 26 28 30 32 34

TIME (min)

EVENT 3 UME

0
1
2
3
4

-100 -50 0 50 '00

LAG (s)

EVENT 4 NUR

0
1
2
3
4

-100 -50 0 50 100

LAG (s)
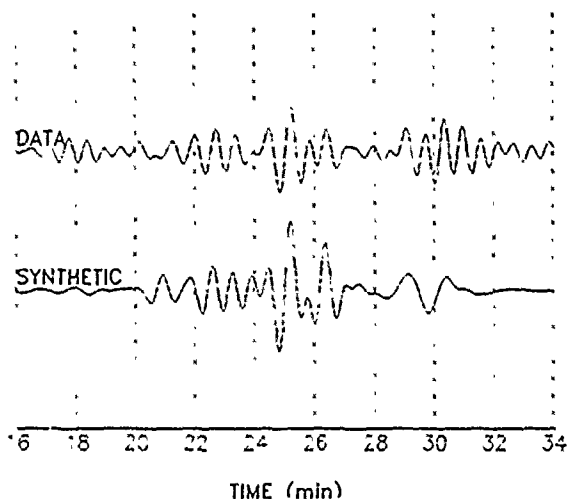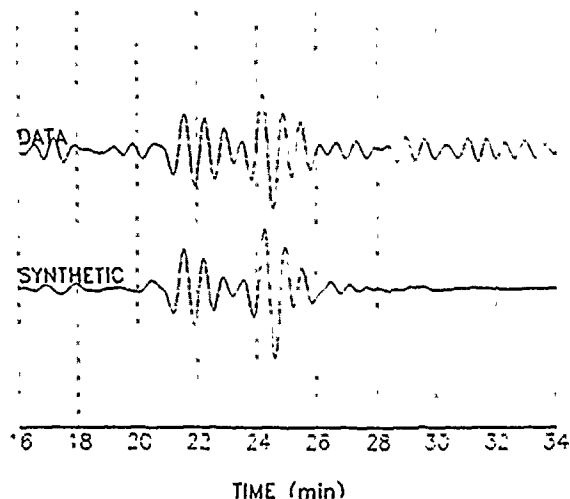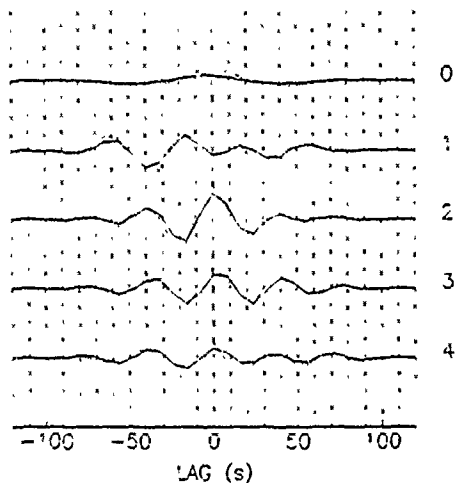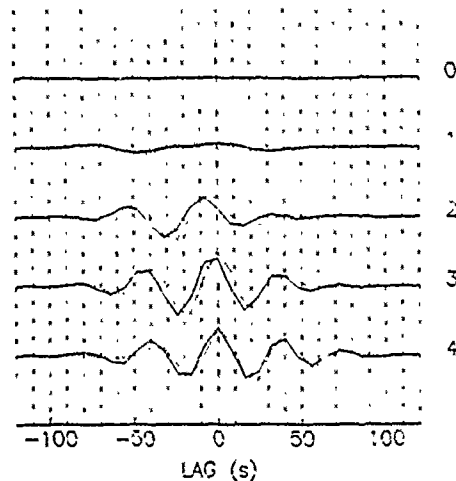
Figure 5. Comparisons of observed and synthetic waveforms and BCCFs for Event 3 (h = 344 km) recorded at UME. Fundamental mode energy is still visible at 29 minutes, but the record is dominated by higher-mode arrivals.

Figure 6. Comparisons of observed and synthetic waveforms and BCCFs for Event 4 (h = 544 km) recorded at NUR. Fundamental mode energy is almost totally absent from the waveforms; complex higher-mode arrivals dominate the signal. Near wiggle-for-wiggle fits are seen for the second, third, and fourth higher modes.

velocity jumps at 400 km and are in good agreement below this depth. However, above 400 km, there are significant differences between the two structures. SNA has a low-velocity zone centered at about 200-km depth, whereas the shear velocities in EU2 increase monotonically throughout the upper mantle. Experiments with this and other parameterizations, including structures parameterized by continuous
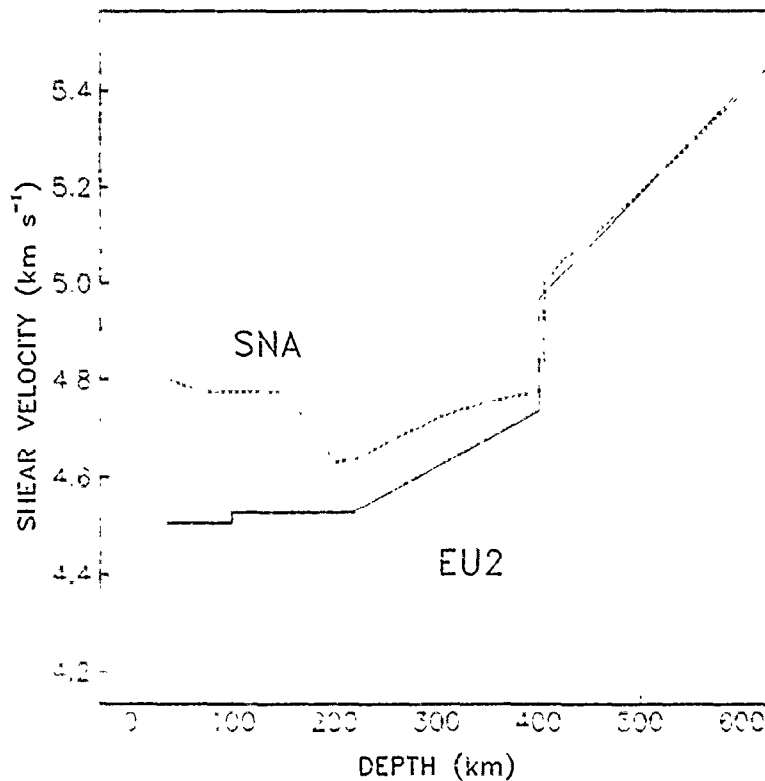
Figure 7. Comparison of EU2 shear velocities (solid line) with model SNA (dotted line) of Grand and Helmberger (1984 a). SNA was derived from SH-polarized S and SS waves traversing the Canadian Shield, but is representative of SH propagation across stable Eurasian platforms (Grand et al. 1985). EU2, derived from vertical-component higher-mode surface waves, is representative of P-SV propagation. The structures are virtually identical below the 400 km discontinuity, but exhibit distinct velocity differences in the upper mantle above 400 km.

variations with depth, indicate that our data set cannot be satisfied by a model with an LVZ as pronounced as SNA; the velocity variation between 100 km and 200 km is tightly constrained by the difference in the arrival times of the fundamental and first higher-mode wave groups, which are well observed on many of the seismograms used in this study.

The most obvious discrepancy between the two models is the negative offset in the shear velocity of EU2 relative to SNA throughout the mantle above 400 km, which averages 0.16 km/s. The differences are largest in the uppermost mantle (the lid of SNA), where they locally reach 0.27 km/s, but remain substantial even below 200 km. Given the high resolution of both methods in the interval 200-400 km, the differences appear to be real. For example, inversions of our data set with the velocities in this layer constrained at SNA values yield very poor fits to the observed seismograms.

Some of the discrepancy may result from the lower velocities encountered along the portions of the surface-wave paths traversing the tectonically active areas of northeastern Asia, but we are skeptical that an explanation based on path differences can account for it entirely. Grand et al. [1985] have modeled the transition from the active foldbelts of central Asia to the Russian platform using their multiple-S technique, and the lowest average velocities they find are still higher than those of EU2, even though the latter is derived from a data set primarily sampling the high-velocity shields and platforms of northern Eurasia.

Although a definitive statement must await the treatment of both P-SV and SH data sets from common paths by the same inversion technique (which is one of our goals for the next year), we suspect that the discrepancy in the average shear velocity between EU2 and SNA is diagnostic of deep-seated polarization anisotropy in the Eurasian upper mantle. Moreover, we speculate that this anisotropy is associated with the existence of a thick, basalt-depleted (and therefore olivine-rich) chemical boundary layer beneath Eurasia [Jordan, 1981].

Future work. The waveform-inversion technique described in this report will be extended to include polarization anisotropy and variations in attenuation structure. We will apply the method to three-component data collected from GDSN, NARS, WWSSN and other seismic networks to obtain models of the crust and upper mantle over various Eurasian paths. These models will be employed to constrain the three-dimensional structure of the Eurasian continent.

References

Burdick, L.J., S. Grand, D.V. Helmberger, T. Lay, and J. Rial, Remote Sensing of Attenuation Bias using SS, Report WCCP-R-83-01, Woodward-Clyde Consultants, Pasadena, 158 pp., 1982.

Cara, M., A. Nercessian, and G. Nolet, New inferences from higher mode data in western Europe and northern Eurasia, Geophys. J. R. Astr. Soc., 61, 459-478, 1980.

Dziewonski, A.M., and D.L. Anderson, Preliminary reference earth model, Phys. Earth Planet. Inter., 25, 297-356, 1981.

Feng, C.-C., and T.-L. Teng, Three-dimensional crust and upper mantle structure of the Eurasian continent, J. Geophys. Res., 88, 2261-2272, 1983.

Gee, L.S., A.L. Lerner-Lam, and T.H. Jordan, Design of PASSCAL experiments for the recovery of upper mantle structure by higher-mode waveform analysis, Eos, in press, 1985.

Grand, S.P., and D.V. Helmberger, Upper mantle shear structure of North America, Geophys. J. R. Astr. Soc., 76, 399-438, 1984a.

Grand, S.P., and D.V. Helmberger, Upper mantle shear structure beneath the northwest Atlantic Ocean, J. Geophys. Res., 89, 11465-11475, 1984b.

Grand, S.P., D.V. Helmberger, and L.J. Burdick, Attenuation Bias Measurements of the Semipalatinsk and North African Test Sites from Multiple S Phases, Report WCCP-R-85-01, Woodward-Clyde Consultants, Pasadena, 27 pp., 1985.

Jordan, T.H., Continents as a chemical boundary layer, Phil. Trans. R. Soc. London, Ser. A, 301, 359-373, 1981.

Lerner-Lam, A.L., Linearized estimation of higher-mode surface wave dispersion, PhD thesis, University of California, San Diego, 1982.

Lerner-Lam, A.L., and T.H. Jordan, Earth structure from fundamental and higher-mode waveform analysis, Geophys. J. R. Astr. Soc., 75, 759-797, 1983.

Masters, G., and F. Gilbert, Attenuation in the earth at low frequencies, Phil. Trans. R. Soc. London, Ser. A, 308, 479-522, 1983.

Sipkin, S.A., and T.H. Jordan, Lateral heterogeneity in the upper mantle determined from the travel times of multiple ScS, J. Geophys. Res., 81, 6307-6320, 1976.

204

PAPER TITLE: Surface-wave Ray Tracing and Ms:Yield Determination

PAPER AUTHOR: Ta-liang Teng, Keiiti Aki, and John Faulkner

CONTRACT NO: AFOSR-F19628-85-K-0018

SUMMARY: A detailed surface-wave tomographic mapping of the crustal and upper
mantle structure for the Eurasian continent and the Pacific ocean basin has
been completed. Significant lateral heterogeneities are found in many regions
that are sometimes strong enough to cause perturbations on the propagating
surface-wave wavefront and therefore modify the surface wave amplitude. This
amplitude modificaiton will have a direct bearing on the Ms:yield
determination. We are developing necessary softwares based on techniques of
dynamic ray-tracing and Gaussian beam formulation to study the lateral
heterogeneous effect on the surface-wave amplitude.

CONCLUSIONS AND RECOMMENDATIONS: This is a new project started just three
months ago. We have already comr'eted extensive computation for over 180
crustal and upper mantle structures, each represents a specific 10°x10° grid
element of the earth surface. For each grid region, contour maps of
surface-wave phase velocity, displacement eigenfunctions, and energy integrals
are generated for both Rayleigh and Love waves. These results are needed for
the dynamic ray-tracing and Gaussian beam formulation. Necessary computer
programs are being written in order to generate a series of surface-wave ray
maps and synthetic seismograms for surface waves originating from a number of
notable nuclear test sites such as the Eastern Kazakh, Novaya Zemlya, NTS, and
Lop Nor, etc. These ray maps and amplitude information should provide the
Ms:yield determination with a fine calibration necessary to improve its
absolute accuracy. This research will proceed one step further by combining
information on global tectonics and surface-wave attenuation with the
surface-wave ray maps to delineate possible efficient "transmission corridors"
or non-caustic "converging regions" for surface waves. With respect to a
given nuclear test site, these "transmission corridors" or "converging
regions", if existing, would provide the most sensitive and strategic
observation sites to monitor nuclear tests.

Surface-Wave Ray Tracing and Ms:Yield Determination

Ta-liang Teng, Keiiti Aki and John Faulkner
Department of Geological Sciences
University of Southern California
Los Angeles, CA 90089-0741

I. ABSTRACT

We have completed a detailed surface-wave tomographic mapping of the crustal and upper mantle structure for the Eurasian continent and the Pacific ocean basin. Significant lateral heterogeneities are found in many regions that are sometimes strong enough to cause perturbations on the propagating surface-wave wavefront and therefore modify the surface-wave amplitude. This amplitude modification will have a direct bearing on the Ms:yield determination. A surface-wave ray tracing theory is formulated to evaluate the focusing and defocusing of surface-wave rays and their effects on amplitude variations. Based on this theory, together with the Gaussian beam formulation, necessary computer programs are being written in order to generate a series of surface-wave ray maps and synthetic seismograms for surface waves originating from a number of notable nuclear test sites such as the Eastern Kazakh, Novaya Zemlya, NTS, and Lop Nor, etc. These ray maps and amplitude information should provide the Ms:yield determination with a fine calibration necessary to improve its absolute accuracy. This research will proceed one step further by combining information on global tectonics and surface-wave attenuation with the surface-wave ray maps to delineate possible efficient "transmission corridors" or non-caustic "converging regions" for surface waves. With respect to a given nuclear test site, these "transmission corridors" or "converging regions", if existing, would provide the most sensitive and strategic observation sites to monitor nuclear tests.

II. INTRODUCTION

This is the first report of the two-year contract that started in January, 1985. The subject matter deals with the improvement of absolute accuracy on the problem of Ms:yield determination. We wish to evlauate the focusing and defocusing of surface-wave amplitudes due to lateral heterogeneities and their effects on the yield determination.

Recently research in the area of surface-wave tomography (Feng and Teng, 1983a; 1983b; Teng, 1983), inversion of global phase velocity (Tanimoto and Anderson, 1983, Nakanish and Anderson, 1982), and whole earth imaging using free oscillation data (Dziewonski and Woodhouse, 1983) has led to a good first order picture of the earth's lateral heterogeneities. Particularly relevant to our present research are findings of curstal and upper mantle heterogeneities of Eurasia and the Pacific ocean basin based on a three-dimensional surface-wave mapping procedure (Feng and Teng, 1983a; 1983b). These findings are most timely for our work to study the surface-wave amplitude variation due to lateral heterogeneities. Moreover, recent developments on the surface-wave ray tracing technique and Gaussian beam formulation (Cerveny et al., 1982; Cerveny, 1983, Wong and Woodhouse, 1983; Novik and Aki, 1983; Yomogida and Aki, 1985; and Yomogida, 1985) represent a very dynamic progress from which calculationls of surface-wave ray distribution, geometrical spreading, and synthetic waveforms are possible for an arbitrary laterally heterogeneous medium. Based on these findings and developments, this project formulates the following objectives:

(1) Based on the developed procedure of three-dimensional surface-wave mapping, we will make extensive use of data from the Center of Seismic Studies to refine the picture of lateral heterogeneities of Eurasia and

the Pacific basin, and further extend the three-dimensional mapping to the remaining part of the world, particularly the North American and the Atlantic areas.

(2) We will apply the developed theory of surface-wave ray tracing to the crustal/upper mantle heterogeneity data, so as to generate a series of surface-wave ray maps and amplitude tables of the world that will give the lateral focusing/defocusing effects for waves originating from a number of notable nuclear test sites such as Eastern Kazakh, Novaya Zemlya, NTS, Lop Nor, etc. These maps and the amplitude tables should provide the M_S:yield determination with a fine calibration necessary to improve its absolute accuracy.

(3) We will combine information on global tectonics and surface-wave attenuation with the above surface-wave ray maps to delineate over the earth surface possible efficient "transmission corridors" or non-caustic "converging reions" of surface-wave rays. With respect to a given nuclear test site these "transmission corridors" or "converging regions", if existing, would provide the most sensitive and strategic observation sites to monitor nuclear tests.

III. PROGRESS REPORT

During the first three months, the following research progress has been made:

1. Extensive Computation for Phase Velocity, Eigenfunctions, and Energy Integrals.

This is the first step to approach the dynamic surface-wave ray tracing and Gaussian bean formulation. Based on our earlier studies using a 3-dimensional surface-wave tomographic mapping technique, we have obtained

208

the crustal and upper mantle structures for a total of 183 regions of the earth each of 10°x10° in dimensions. These regions (called grid elements) essentially cover the Eurasia and the Pacific ocean basin. For each grid element, the earth's structure is obtained to a depth of 300 km from Rayleigh and Love wave group velocity measurements from a large number of paths over a period band from 15 to 250 sec. An example of our data base is shown in Figures 1 and 2.

Based on the velocity structure of each grid element, we have completed computations of phase velocity, displacement eigenfunctions, and energy integrals for both Rayleigh and Love waves. These computations are made for a period band from 15 to 250 sec. With 183 structures, this represents an enormous amount of computations. The output data are organized into disk files suitable for the downstream computations of dynamic ray tracing and Gaussian bean formulation. Figure 3 shows sample outputs of the phase velocity distribution for two periods for the Eurasia and the Pacific ocean basin contour maps of the phase velocity that show the degree of lateral heterogeneities. The heterogeneities are strong enough to cause perturbation of surface-wave ray path and therefore amplitude variations due to focusing and defocusing of the rays. However, these heterogeneities are not too strong ! violate the basic assumptions associated with the ray approximation. The phase velocity is needed in the eikonal equation for the dynamic ray tracing of surface waves, and both the displacement eigenfunctions and the energy integrals are needed in the formation of Gaussian beams and synthetic seismograms. Figure 4 gives a sample result of the ellipticity of surface displacements as a function of period, and Figure 5 the energy integral as a function of period. Since both quantitites will enter into Gaussian bean formation (see below), these two figures show how velocity structure will

affect the waveforms of the final synthetic seismograms.

2. Development of Software Package for Both Dynamic Ray Tracing and Gaussian Beam Formulation:

This part of the software development has been benefited by an existing package of a

2-D ray tracing program written originally by Cerveny. Since this program was for wave propagation on a flat surface, we need to map the spherical surface (radius R) of the earth onto a 2-dimensional Cartesian system before the program can properly be used. A Mercator projection proposed by Jobert and Jobert (1983) is used that maps the co-latitude θ into Θ by the transformation:

$$\Theta = \ln [\tan (\theta/2)], \quad 0 < \theta < \pi \text{ and } \infty < \Theta < \infty .$$

This transforms the phase velocity $C(\theta, \phi)$ into $V(\Theta,\phi)$ by

$$V(\Theta,\phi) = C(\theta,\phi)/(R\sin\theta)$$

and the eikonal equation from

$$(\nabla\tau)^2 = 1/R^2 \, (\partial\tau/\partial\theta)^2 + 1/R^2\sin^2\theta \, (\partial\tau/\partial\phi)^2 = 1/C(\theta,\phi)$$

for the spherical earth into

$$\partial^2 C/\partial\Theta^2 + \partial^2 C/\partial\phi^2 = 1/V^2(\Theta,\phi)$$

for a two-dimensional Cartesian system. To include the ellipticity e of the real earth, one needs to modify the coordinate transformation (Yomogida and Aki, 1984) by

$$\Theta = \ln \{\tan (\theta/2)[(1+e\cos \theta)/(1-e\cos\theta)]^{e/2}\}$$

with the attendant phase velocity mapping:

$$V(\Theta,\phi) = [1-e^2\cos^2\theta]^{1/2} C(\theta,\phi)/(R\sin\theta)$$

After all the related variables are written in the new Cartesian coordinates, the displacement components of surface waves can be written as:

$$\underline{u}(s,n,z,t) = \phi_L \sqrt{[q(s_0)U_g(s_0)I_1(s_0)]/[q(s)U_g(s)I_1(s)](\sin\theta/\sin\theta_0)^2}$$

$$\cdot [\underline{n} - \{np(s)C(s)/q(s)\}\underline{t}]\ell_1(s,z) \cdot \exp i[\theta(s,t) + (\omega/2[p(s)/q(s)]n^2]$$

for Love waves, and

$$u(s,n,z,t) = \phi_R \sqrt{[q(s_0)U_g(s_0)I_1(s_0)]/[q(s)U_g(s)I_1(s)] \cdot (\sin\theta/\sin\theta_0)^2}$$

$$\cdot [r_1(s,z)(\underline{t} + \{np(s)C(s)/q(s)\}\underline{n}) + ir_2(s,z)\underline{z}]$$

$$\cdot \exp i[\theta(s,t) + (\omega/2)\{p(s)/q(s)\}n^2]$$

for Rayleigh waves. Here,

ϕ_L and ϕ_R are functions depending on the source excitation,

θ_0 and θ are co-latitudes of the points s_0 and s, respectively,

q is the geometrical spreading factor,

U_g is the group velocity,

I_1 is the energy integral defined by

$$I_1 = 1/2 \int_{\zeta}^{\infty} \rho\, l_1^2\, dz$$

for Love waves, and

$$I_1 = 1/2 \int_{\zeta}^{\infty} \rho(r_1^2 + r_2^2)\, dz$$

for Rayleigh waves,

$\underline{t}$ and $\underline{n}$ are unit vectors tangential and normal to the ray, respectively,

$I_1(s,z)$ is the displacement eigenfunction for Love waves, and

$r_1(s,z)$ and $r_2(s,z)$ are vertical and horizontal displacment eigenfunctions, respectively, for Rayleigh waves.

We are presently working on the software to calculate the above expressions. This probably will take a good part of this summer. In this Fall, we will proceed with the Gaussian bean superpositon with assumed source excitations. This will eventually lead us to the construction of synthetic seismograms.

REFERENCES

Cerveny, V., Synthetic body wave seismograms for laterally varying layered structures by the Gaussian beam method, Geophys. J. R. Astron. Soc., 73, 389-426, 1983.

Cerveny, V., M. M. Popov, and I. Psencik, Computation of wave fields in inhomogeneous media-gaussian beam appraoch, Geophys. J. R. Astron. Soc., 70, 109-128, 1982.

Dziewonski, A. M., and J. H. Woodhouse, Centroid-moment tensor inversion in a laterally heterogeneous earth model, EOS, vol. 64, No. 5, p. 775, 1983.

Feng, C. C., and T. L. Teng, Three-dimensional crust and upper mantle structure of the Eurasian continent, J. Geophys. Res., vol. 88, 2261-2272, 1983b.

Feng, C. C., and T. L. Teng, An error analysis of FTAN, Bull. Seismol. Soc. Am., vol. 73, 143-155, 1983a.

Nakanishi, I. and D. L. Anderson, Spherical heterogeneity of the mantle from phase velocities of mantle waves, Nature, in press, 1983.

Nowack, R. L., and K. Aki, the 2-D Gaussian beam synthetic method: testing and application, J. Geophys. Res., submitted, 1983.

Tanimoto, T., and D. L. Anderson, Mapping convection in the mantle (Preprint), 1984.

Teng, T. L., Seismic surface-wave tomography, EOS, vol. 64, p. 775, 1983.

Wong, Y. K., and J. H. Woodhouse, Ray theory for surface waves on a sphere (abstract), EOS Trans. AGU, 64, 260, 1983.

Yomogida, K., The detection of surface waves velocity anomalies: Ray-theoretical approach, EOS, vol. 64, p. 755, 1983.

Yamogida, K., Gaussian beam for surface waves in slowly-varying media, Geophys. J. R. Astron. Soc. (in press), 1985.

Yomogida, K., and K. Aki, Total waveform synthesis of surface waves in laterally heterogeneous earth by Gaussian beam method, J. Geophys. Res., (in press), 1985.

Fig. 1
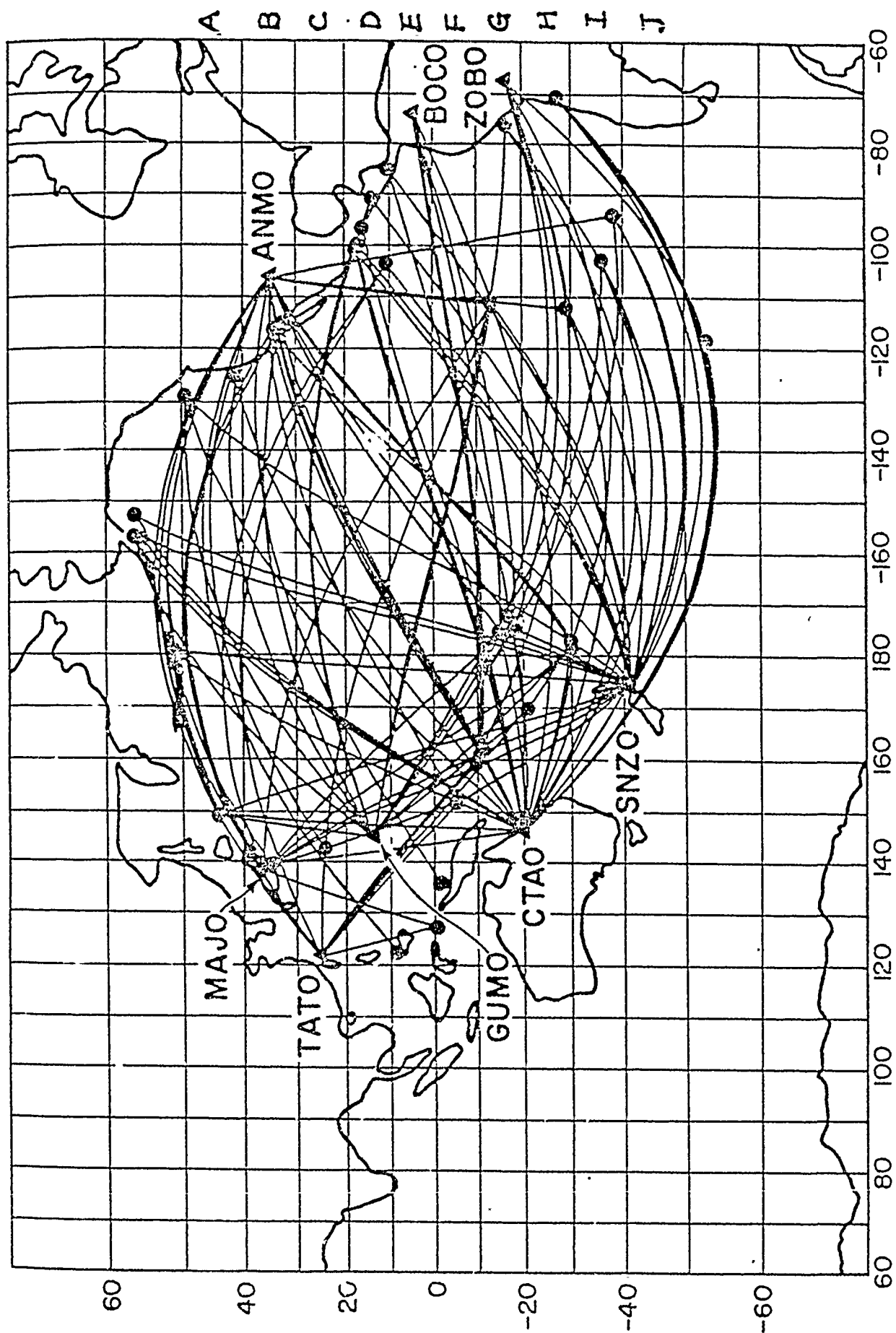
E-W CROSS-SECTIONS

Fig. 2a

214

Fig. 2b

215

$C_R \sim 3.70\, Km/sec.$ $T = 18\, Sec.$

$C_R \sim 3.70\, Km/sec.$ $T = 42\, sec.$

216

Fig. 3a
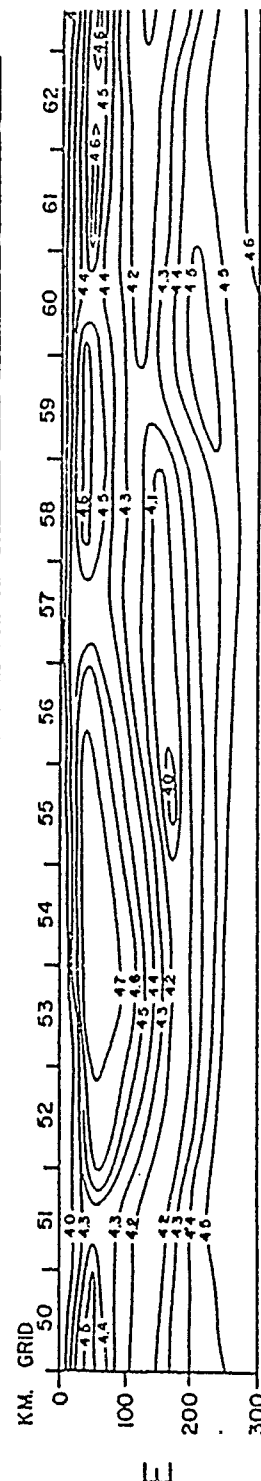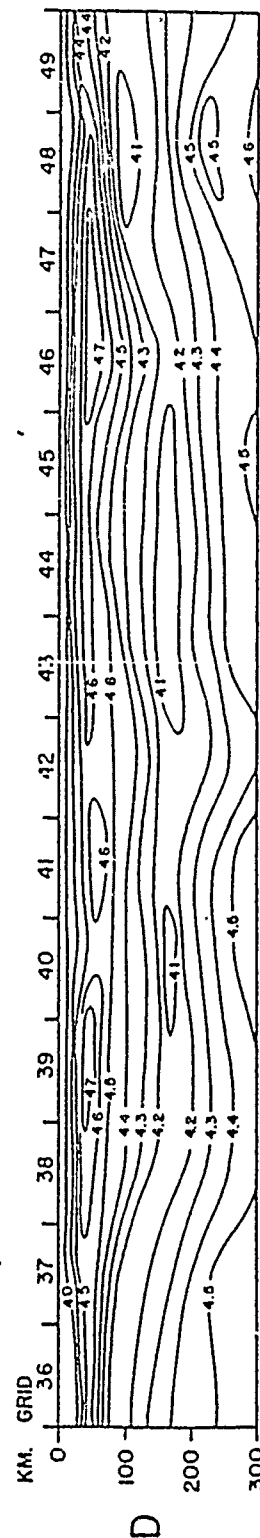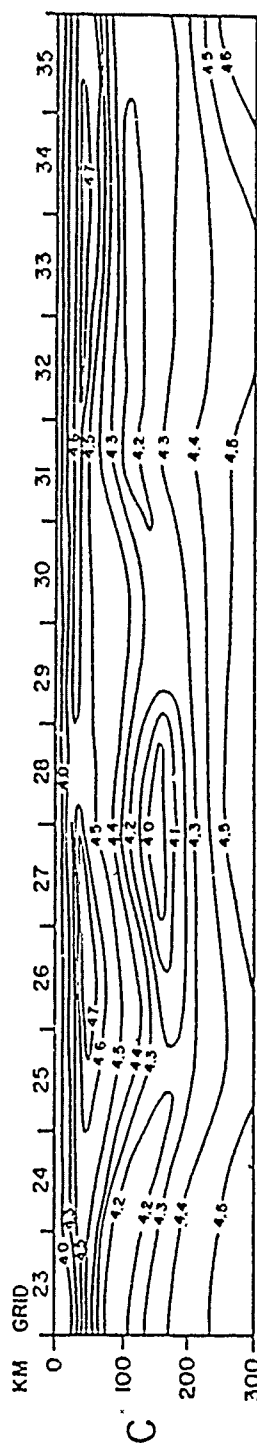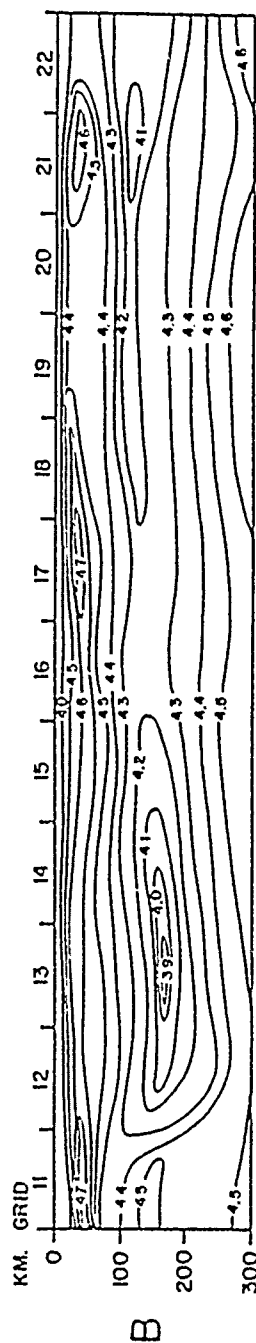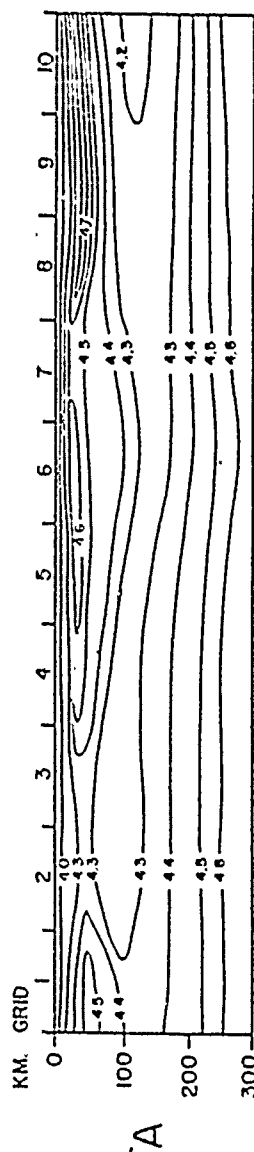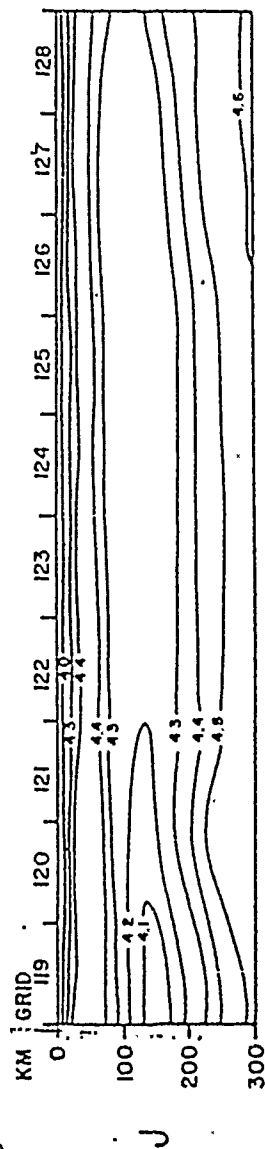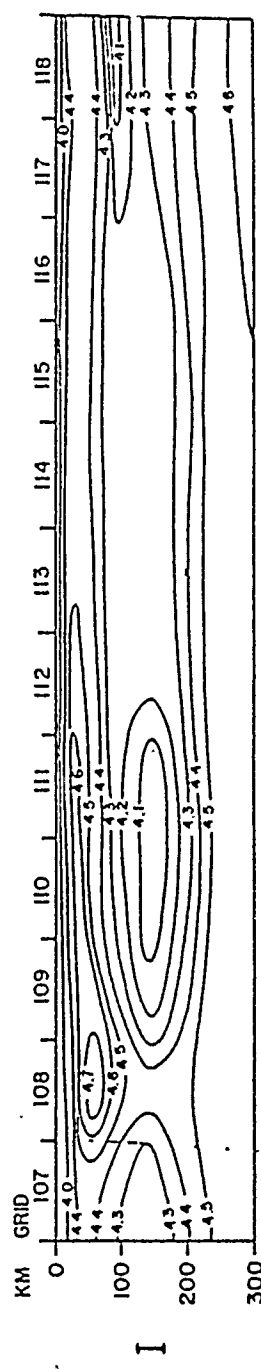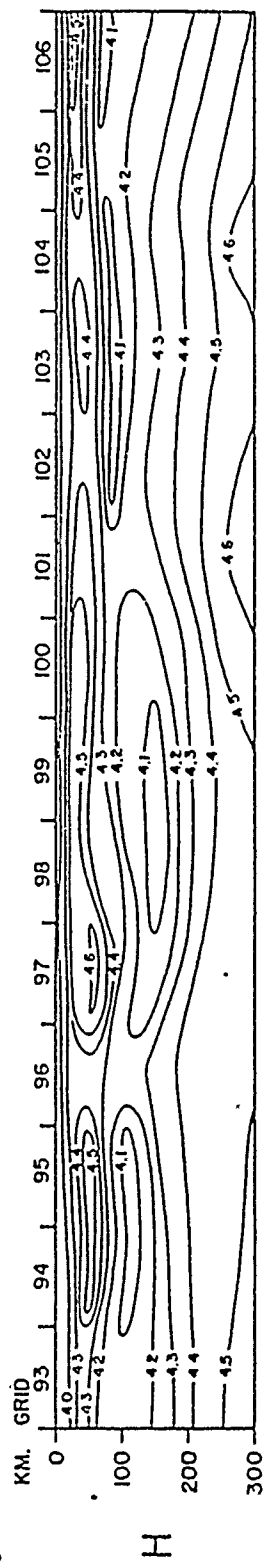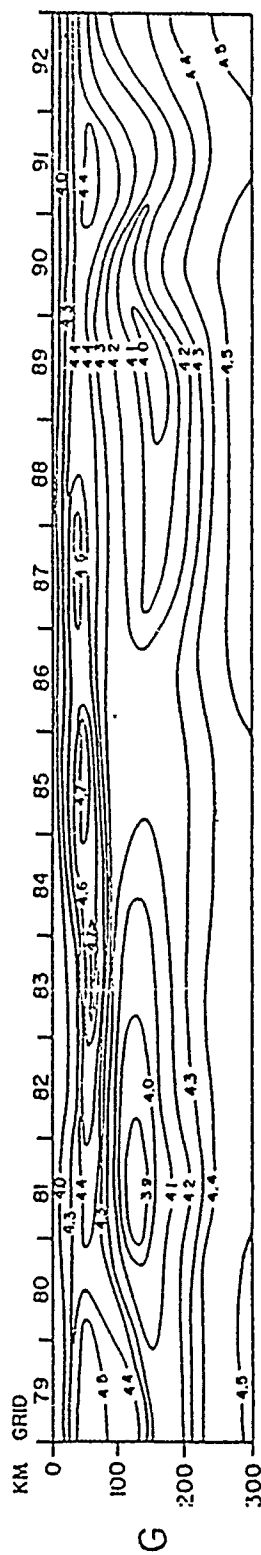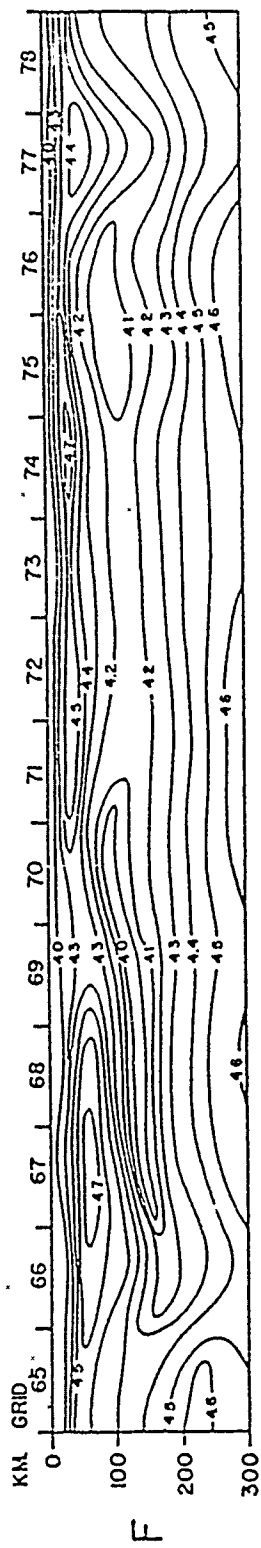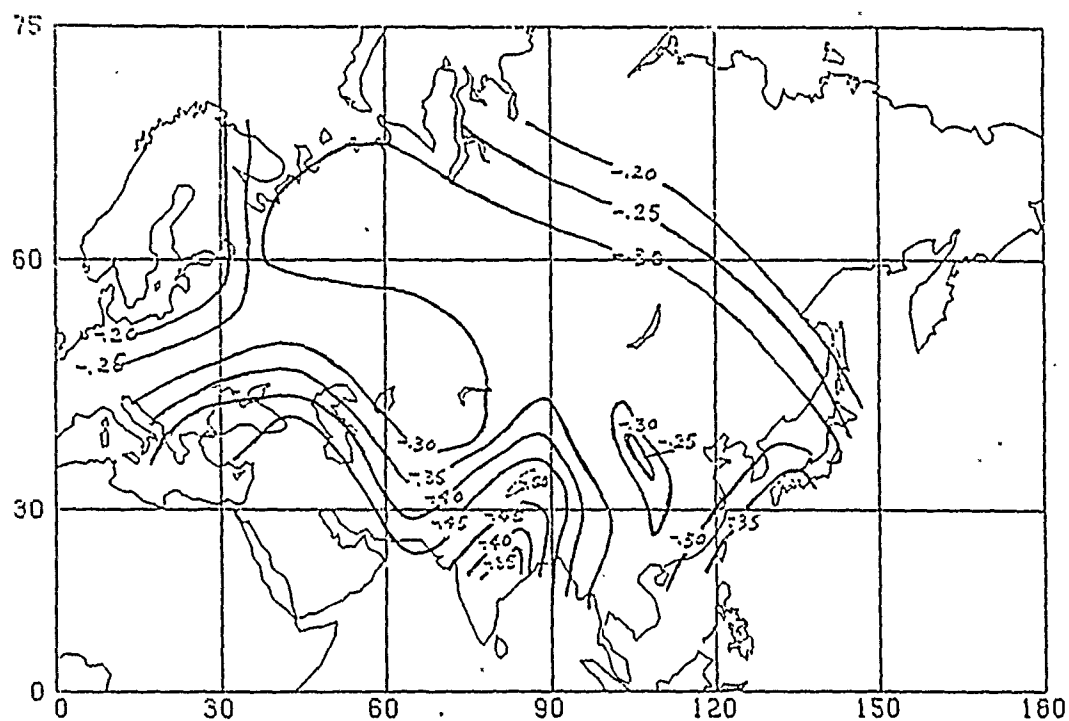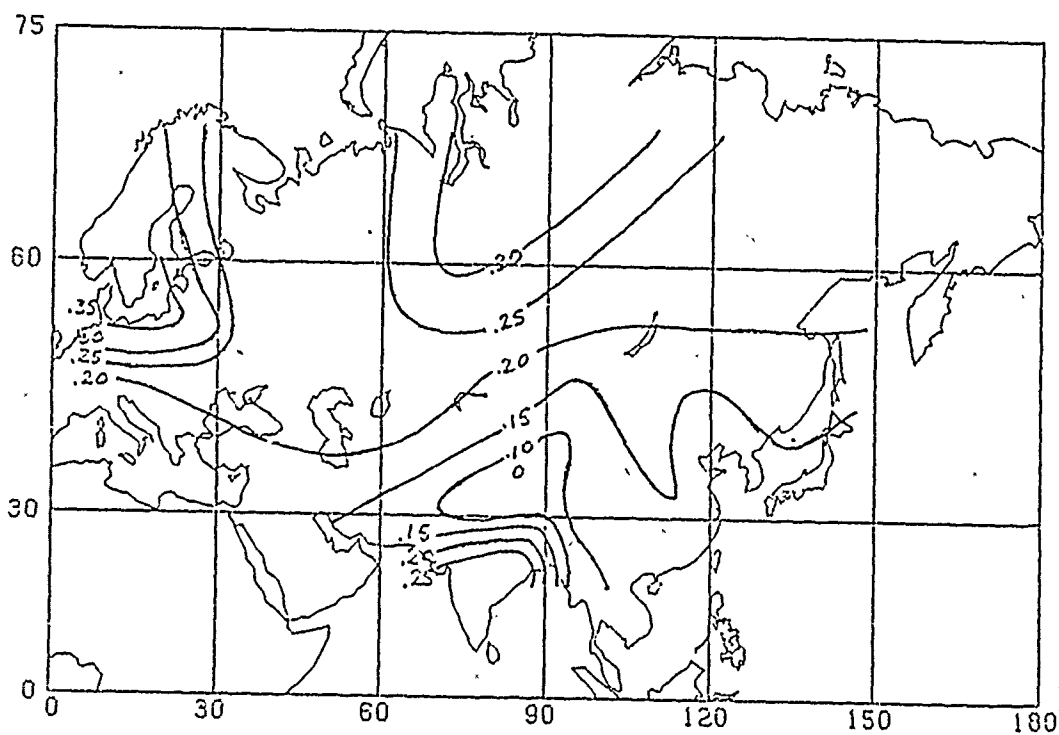
$C_R - 3.70 \, km/sec.$ $T = 18 \, sec.$

$C_R - 3.70 \, km/sec.$ $T = 42 \, sec.$

Fig. 3b

217
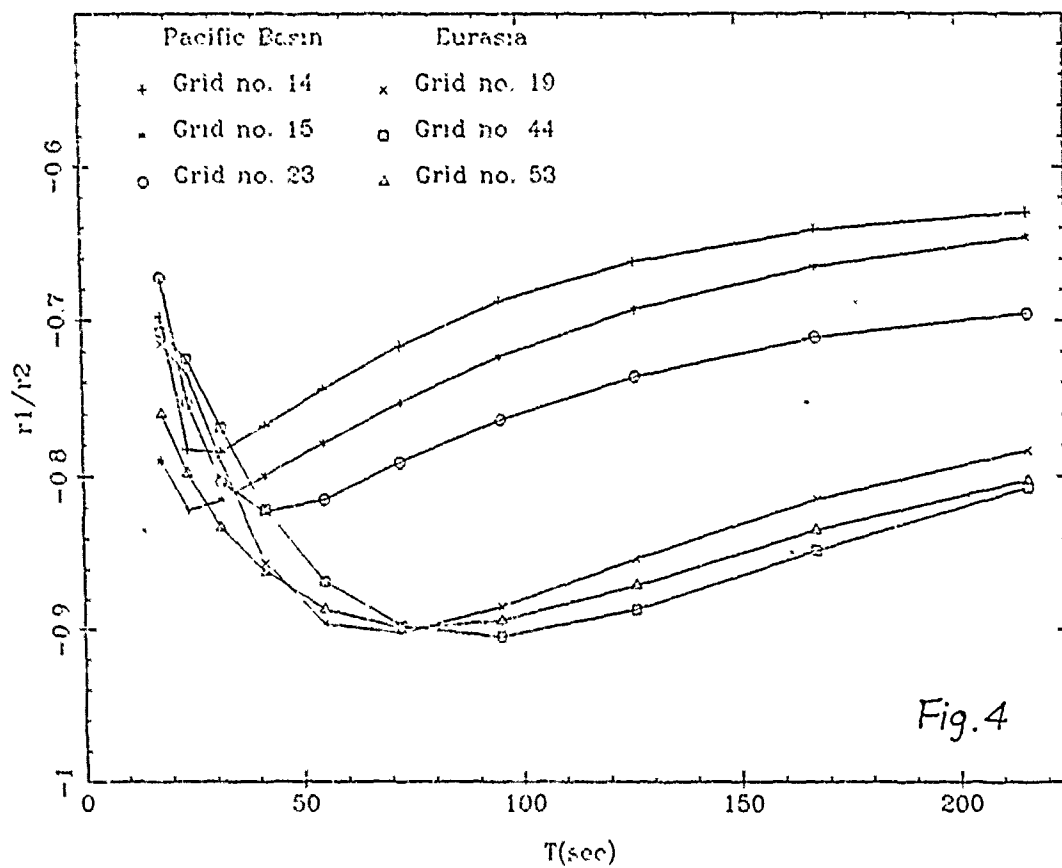
Fig.4

Kinetic Energy vs Period
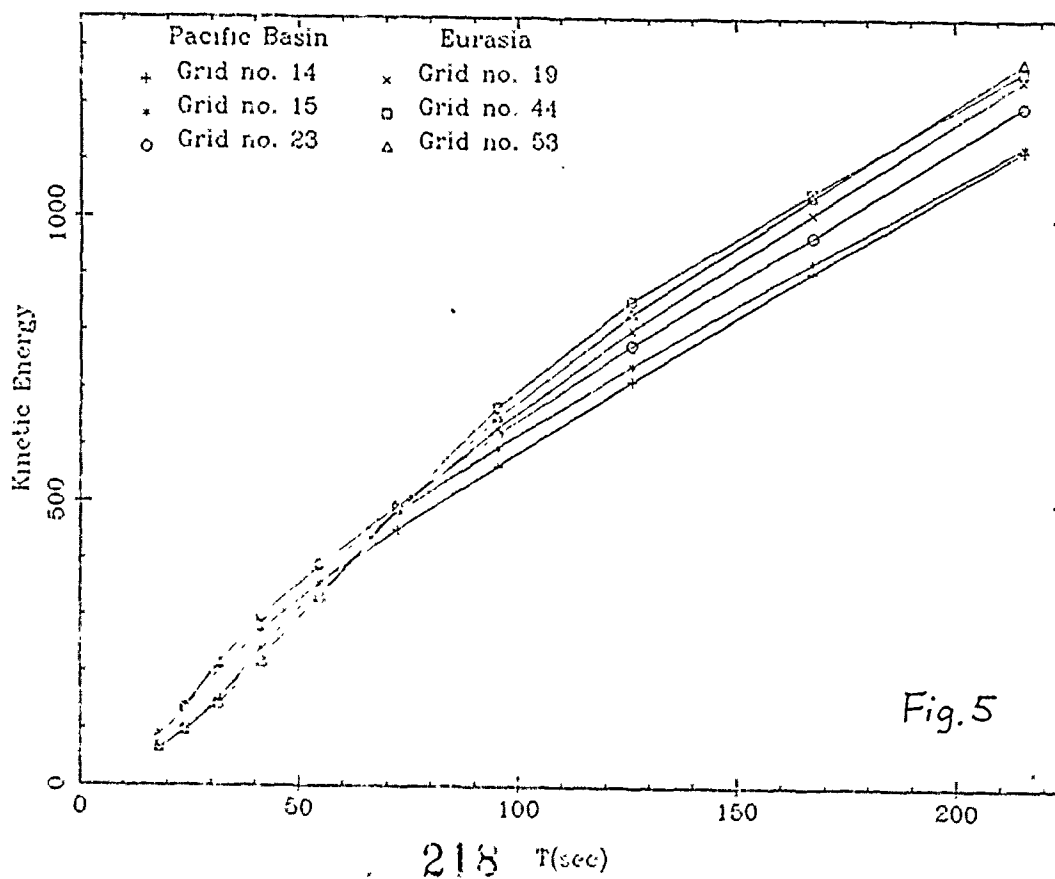
Fig.5

T(sec)

PAPER TITLE: Nonlinear Wave Propagation in Rock

PAPER AUTHORS: J.R. Bulau, B.R. Tittmann, and M. Abdel-Gawad (Rockwell International Science Center, Thousand Oaks, CA 91360)

CONTRACT NO: F49620-83-C-0065

SUMMARY: In this paper, we report the results of combined high amplitude tensile and compressive loading experiments on four different rock types: Westerly granite, Boise sandstone, Berea sandstone, and Indiana limestone. The details of the stress-strain hysteresis loops are examined, with emphasis on investigating the elastic and inelastic properties of rocks at nonlinear amplitudes in both tension and compression.

CONCLUSIONS AND RECOMMENDATIONS: In most rock specimens, the stiffness is greater in compression than in tension. Preliminary results also indicate that most of the energy loss during a full cycle of loading occurs as a result of strain in extension: if the strain on the rock is restricted to compression, the response is nearly nonlinear elastic, but with little energy loss. However, when the rock is exposed to tensile stresses, a hysteresis loop develops, indicating significant energy dissipation. The details of the hysteresis loops also appear to be independent of frequency. These observations are consistent with a loss mechanism associated with intergranular friction. Intergranular sliding appears to be restricted by the closing of cracks in compression, since the rock is stiffer in compression than in tension and a large hysteresis loop develops only when the rock is subjected to tensile stresses. However, relatively large strains and large frictional losses are possible in tension because intergranular bonding is relatively weak.

The results of this study indicate that the mechanical behavior of rocks can be significantly different in compression than in tension. As a result, the onset of nonlinear effects with increasing strain may not be the same for extensional loads as for compressive loads. More experimental work will shed light on this issue and will provide realistic detailed information about rock rheology for the purpose of numerical modeling of near-field seismic pulse propagation.

INTRODUCTION

The mechanics of wave propagation through the near field of an explosive seismic source are not completely understood. A number of rather complete data sets acquired over the years describe near-field particle motion in polycrystalline salt as a function of scaled distance (distance/yield$^{1/3}$). The data set now includes measurements from (a) the 5.3 kT nuclear event, SALMON (Perret, 1967; Trulio, 1978); (b) the medium to large scale chemical explosions of the COWBOY experiments, which took place in a natural salt dome (Trulio, 1978, 1981); and (c) a series of small scale chemical explosions in pressed polycrystalline salt in the laboratory (Larson, 1982). When all available data are combined, it appears that wave propagation satisfies cube root of yield scaling. That is, the decay of peak particle velocity and displacement can be defined as a function of distance/yield$^{1/3}$ (Trulio, 1978, 1981; Larson, 1982). This appears to be the case, even though available data cover approximately 10 decades in yield, 4 decades in peak particle velocity, and 4 decades in frequency. However, the data fit a line that decays much faster than r^{-1}, which would be the case if the material behaves in a perfectly elastic manner. Thus, the behavior of salt in the range of available free field measurements cannot be regarded as perfectly elastic (Trulio, 1978, 1981). Because of the uncertainties regarding the amount of energy that can be dissipated as a seismic pulse propagates through the near field of an explosion, Bache, et al (1981) have questioned the usefulness of reduced displacement potential (RDP) calculations based on close range data for the purpose of defining a seismic source function.

The exact nature of attenuation in the near field of an explosive seismic source remains a controversial subject. In fact, the evidence regarding the issue of linearity appears to be a bit ambiguous. Using small scale chemical explosions in pressed salt in the laboratory, Larson (1982) measured a Q of 12.5 near 10^{-3} strain, and a Q of 24.9 near 6 x 10^{-4} strain. The fact that Q is amplitude dependent is evidence for nonlinear response. However, Larson also demonstrated an approximately linear superposition of waveforms at strains higher than 10^{-4}, which suggests near-linearity. The experimental results reported in Tittmann (1983) using resonating bars of natural halite indicate that the linear anelastic Q of halite is quite high, near 500, with a transition to an amplitude dependent nonlinear Q at strain amplitudes greater than approximately 2 x 10^{-6}. Burdick, et al (1984a) have argued that it is possible to model a seismic source function for the Amchitka tests assuming linear behavior in the near field just outside the spall zone (approx. 700-1200 m/kT$^{1/3}$). Furthermore, Burdick, et al (1984b) contend that the same model can be used to predict the first vertical pulse arrival and rise times even within the spall zone. They used the concept of a compressional elastic radius that in fact may be considerably smaller than a tensional elastic radius and that must extend at least as far as the outer limits of the spall zone. Minster and Day (1985) recently re-examined the COWBOY data set, and concluded that it is possible to explain simultaneously the radial decay of peak displacement and peak velocity by either (a) a linear anelastic model with low Q (approx. 20) or (b) a nonlinear model with amplitude dependent Q. MacCarter and Wortman (1985) conclude that the free field motion measurements from the SALMON event are consistent with an amplitude independent Q of about 10.

While generally it is acknowledged that Q is defined rigorously only when the material through which a wave propagates behaves linearly, it is common (McCarter and Wortman, 1985; Minster and Day, 1985) to assume for theoretical purposes that "nonlinear Q" can be defined using the equation derived by Mavko (1979) and Stewart, et al (1983):

$$Q^{-1}(\omega,\epsilon) = Q_0^{-1}(\omega) + \alpha\epsilon \qquad (1)$$

where Q^{-1} is nonlinear Q, Q_0^{-1} is linear anelastic Q, α is a constant, and ϵ is strain. This equation considers the combined effects of Coulomb-type friction from many intergranular contacts on the energy dissipated during one full elastic wave cycle. In their derivations, Q^{-1} was defined as

$$Q^{-1} = (1/2\pi)(\Delta W/W) \qquad (2)$$

where ΔW is the energy dissipated in one full cycle, and W is the peak strain energy stored per cycle.

One technique used in the laboratory to estimate nonlinear Q involves the forced resonance of bars. As pointed out in previous reports (Tittmann, 1983a, 1983b, 1984) the various resonating bar techniques offer a particularly sensitive tool for detecting the onset of nonlinearity, even at very low strains. The data reported by Tittmann (1983a) indicate that the intrinsic linear attenuation of dome salt is quite low ($Q \approx 500$), and that the onset for nonlinear behavior is near 2×10^{-6} strain, corresponding to approximately 1 bar of stress. Similar behavior has been reported for other rock types, including granite, limestones, sandstones, and miscellaneous igneous rocks (cf Mavko, 1979; Stewart et al, 1983). These measurements suggest that nonlinear response should persist to large scaled distances from explosions, on the order of 10^4 m/kt$^{1/3}$. Furthermore, the low Q values calculated by Larson (1982) [laboratory measurements], Trulio (1979, 1981) [COWBOY], Minster and Day [COWBOY] and McCarter and Wortman [COWBOY, SALMON] from free field measurements in salt are much lower. This constitutes additional evidence of nonlinearity in available free-field measurements.

It is also quite tempting to use the nonlinear Q measurements reported from forced resonance-type experiments to estimate the coefficient α in Eq. (1). There are certain dangers in doing this, however. First, it must be recognized that resonating bar specimens are not subjected to homogeneous strain. This is not a problem as long as material response is linear. However, it tends to lead to an underestimation of the value of α. Minster and Day (1985) indicate that α from flexural resonance measurements is probably underestimated by about a factor of 2, and α from torsional measurements is underestimated by about a factor of 3. A second hazard with using nonlinear Q values from resonance measurements is related to the fact that Q is calculated from the bandwidth of the resonance peak, assuming linear anelastic behavior. The distortion of the resonance peak shape associated with nonlinear resonances has been described by Tittmann (1983b) and casts an element of suspicion on the significance of the nonlinear Q values reported. Finally, during both extensional and flexural resonances each increment of volume within the specimen is subjected to tensile stresses half of the time and to compressive stresses the other half. A tacit assumption is that the material behaves the same in compression as it does in tension. The apparent drop in bar modulus with increasing vibration amplitude has been noted (Tittmann, 1983a, 1983b, 1984), and is probably also related to the distortion of the resonance peak shape with increasing strain. It has not been proven, however, whether either the frictional losses or the effective modulus of a rock are the same in tension as they are in compression. Resonating bar-type measurements are not capable of resolving the details of the rheological response of materials to nonlinear loading. Some studies of the

details of stress-strain hysteresis loops under nonlinear conditions have been reported (Gordon and Davis, 1968; McKavanagh and Stacey, 1974), but in these cases only compressional measurements were performed.

In this paper, we report the results of combined high amplitude tensile and compressive loading experiments on four different rock types: Westerly granite, Boise sandstone, Berea sandstone, and Indiana limestone. We examine the details of the stress-strain hysteresis loops, and demonstrate that both the elastic and the inelastic properties of rocks at nonlinear amplitudes are quite different in compression than in tension. Results to date indicate that the behavior in compression is nonlinear, but nearly elastic. The behavior in tension is also nonlinear, but with relatively strong frictional losses.

EXPERIMENTAL PROCEDURES

Cylindrical rock specimens 2.54 cm in diameter and 6.35 cm long were cut from blocks of Boise sandstone, Berea sandstone, Westerly granite, and Indiana limestone. A resistance-type strain guage was bonded to the surface of each specimen to respond to strains in the longitudinal direction. The rock was then bonded adhesively to stainless steel mounting fixtures using a semiplastic polymer resin (Crystal Bond #509, Aremco Products) that is quite brittle and stiff at room temperature, but that softens readily at approximately 70 C. By keeping the specimen warm while mounting it in the apparatus, residual stresses could be removed. After cooling to room temperature, a series of eight cycle bursts of load-controlled constant rate triangle wave loading were applied to each spedcimen. Experiments were run using an MTS electro-hydraulic, closed-loop load frame equipped with the hydraulic hardware and controls necessary to apply alternating tensile and compressive loads. The frequency of loading was generally 1 Hz, except for one series of measurements at 0.1 Hz on Westerly granite. Measurements of load and strain were collected simultaneously for eight cycles, digitized, and stored in the computer. Measurements then were obtained on each sample using bursts of increasing maximum stress. As many as 5 bursts of 8 waves each were applied at low amplitudes in order to enable satisfactory signal averaging when the signal to noise ratio was low. At higher amplitudes the signal-to-noise ratio was good, and only one eight-cycle burst was run in order to avoid excessive damage to the specimen.

EXPERIMENTAL RESULTS

To test (a) the linearity of the experimental apparatus and (b) the stiffness of the adhesive bonds, the first phase of the experimental study involved measurements of stress and strain on an aluminum bar that has a relatively ideal linear elastic response. A typical curve of stress vs. strain for an aluminum bar is shown in Fig. 1. Extensional stresses and strains carry a positive sign. Only a small amount of hysteresis is observed in this set of measurements, and it is apparent that the relationship between stress and strain is very close to being linear. The small amount of hysteresis may be attributed to plastic flow in the resin used to bond the aluminum bar to the loading fixtures. This is a relatively insignificant effect compared with the large amounts of hysteresis and nonlinearity observed in rocks under corresponding stresses.

Experimental results show that each rock also displays nearly linear behavior when the loading is very small, around 4.5×10^4 Pa, resulting in sample strains between 2×10^{-6} and 6×10^{-6}, depending on rock type (Fig. 2). At higher load levels (Fig. 3) there is evidence of strong nonlinearity and inelasticity in the weakest frame rock, Berea sandstone, while the nonlinear and inelastic effects are more subtle in the stronger frame rocks.

In some cases evidence of nonreversible changes observed in the rock during the first excursion to a "new" maximum load perhaps was associated with intergranular cracking. This is apparent when the hysteresis loop is not clearly established until at least the second cycle of loading. In the case of Berea sandstone subjected to 1.25×10^5 Pa axial stress (Fig. 4a), the result of the first full loading cycle was a net shortening of the specimen. In other cases (Fig. 4b), especially in the stronger frame rocks, there appears to be little or no evidence for nonreversible changes after the first loading cycle at a given stress.

Effects of tensional loading and compressive loading can be isolated by reversing the direction of initial loading. In Fig. 5a and 5b we show the effects of reversing the direction of loading from tension first to compression first, and from compression first to tension first, respectively. It is apparent that the opening of the loop is primarily a tensile effect, and that the compressive behavior is nearly nonlinear elastic. In this particular rock specimen the frictional losses are associated primarily with tensile stresses.

Finally, the effect of frequency on the shape of the hysteresis loop has also been examined. The results of measurements on Boise sandstone at 1 Hz and at 0.1 Hz are shown in Fig. 6. The curves superimpose very well, so evidently the inertial and viscous effects on the relaxation mechanics are not particularly significant, at least for dry rocks in this range of frequency.

DISCUSSION AND CONCLUSIONS

In this study we have examined the details of stress-strain hysteresis loops when rock specimens are subjected to alternating compressive and tensile stresses. In most rock specimens the stiffness of the rock is greater in compression than in tension. Furthermore, preliminary results indicate that most of the energy loss during a full cycle of loading occurs as a result of strain in extension: if the strain on the rock is restricted to compression the response is nearly nonlinear elastic, but with little energy loss. However, when the rock is exposed to tensile stresses a large hysteresis loop develops, indicating significant energy loss. The details of the hysteresis loops also appear to be independent of frequency. These observations are consistent with a loss mechanism associated with intergranular friction. Intergranular sliding appears to be restricted by the closing of cracks in compression, since the rock is stiffer in compression than in tension and a large hysteresis loop develops only when the rock is subjected to tensile stresses. However, relatively large strains and large frictional losses are possible in tension because intergranular bonding is relatively weak and cracks can open.

The results of this study indicate that the mechanical behavior of rocks can be significantly different in compression than in tension. As a result, the onset of nonlinear effects with increasing strain may not be the same for tensile loads as for compressive loads. More experimental work in this area will shed light on this issue and will provide realistic detailed information about rock rheology for the numerical modeling of near-field seismic pulse propagation.

REFERENCES

Bache, T.C., W.J. Best, R.R. Blanford, G.V. Bolin, D.G. Harkrider, E.J. Herrin, A. Ryall and M.J. Shore (1981) A Technical Assessment of Seismic Yield Estimation, DARPA Report, January 1981.

Burdick, L.J., T. Wallace and T. Lay (1984a) Modeling Near-field and Teleseismic Observations from the Amchitka Test Site, Jour. Geophys. Res., 89, 4373-4388.

Burdick, L.J., T. Lay, D.V. Helmberger and D.G. Harkrider (1984b) Implication of Records from the Spall Zone of the Amchitka Tests to Nonlinear Losses in the Source Region and to Elastic Radiation by Spall. Annual technical report for the period November 15, 1982 to November 15, 1983. Prepared for the Advanced Research Projects Agency.

Gordon, R.B. and L.A. Davis (1968) Velocity and Attenuation of Seismic Waves in Imperfectly Elastic Rock, Jour. Geophys. Res., 73, 3917-3935.

Mavko, G.M. (1979) Frictional Attenuation: An Inherent Amplitude Dependence, Jour. Geophys. Res., 84, 4769-4775.

McCarter, G.D. and W.R. Wortman (1985) Experimental and Analytic Characterization of Nonlinear Seismic Attenuation, Final Report for the Period March 21, 1984 through March 20, 1985. Prepared for the Advanced Research Projects Agency.

McKavanagh, B. and F.D. Stacey (1974) Mechanical Hysteresis in Rocks at Low Strain Amplitudes and Seismic Frequencies, Phys. Earth Planet. Interiors, 8, 246-250.

Minster, J.B. and S.M. Day (1985) Decay of Wavefields Near an Explosive Source Due to High-Strain, Nonlinear Attenuation, Unpublished Manuscript.

Perret, W.R.(1967) Free-Field Particle Motion from a Nuclear Explosion in Salt, Part I, Project Dribble, Salmon Event, VUF-3012, Sandia Laboratory.

Stewart, R.R., M.N. Toksoz, and A. Timur (1983) Strain Dependent Attenuation: Observations and a Proposed Mechanism, Jour. Geophys. Res., 88, 546-554.

Tittmann, B.R. (1983) Studies of Absorption in Salt, Final Report for the period December 1, 1981 through November 30, 1982, Prepared for Air Force Office of Scientific Research.

Tittmann, B.R. (1984a) Non-linear Wave Propagation Study, Semi-annual technical report no. 1 for the period June 1, 1983 through November 30, 1983, Prepared for Air Force Office of Scientific Research.

Tittmann, B.R. (1984b) Non-linear Wave Propagation Study, Semi-annual technical report no. 2 for the period December 1, 1983 through May 31, 1984, Prepared for Air Force Office of Scientific Research.

Trulio, J.G. (1978) Simple Sr ... g and Nuclear Monitoring, Final Report of DARPA supported research program, April 1978.

Trulio, J.G. (1981) State-of-the-Art Assessment: Seismic Yield Determination, in A Technical Assessment of Seismic Yield Estimation, DARPA Report Appendix, January 1981.

ALUMINUM TEST BAR

+2.0E+6

ALUM31
CYCLES 1-8 (AVE)

AXIAL STRESS

(Pa) 0

-2.0E+6

-2.5E-5   0   +2.5E-5

SAMPLE SURFACE STRAIN
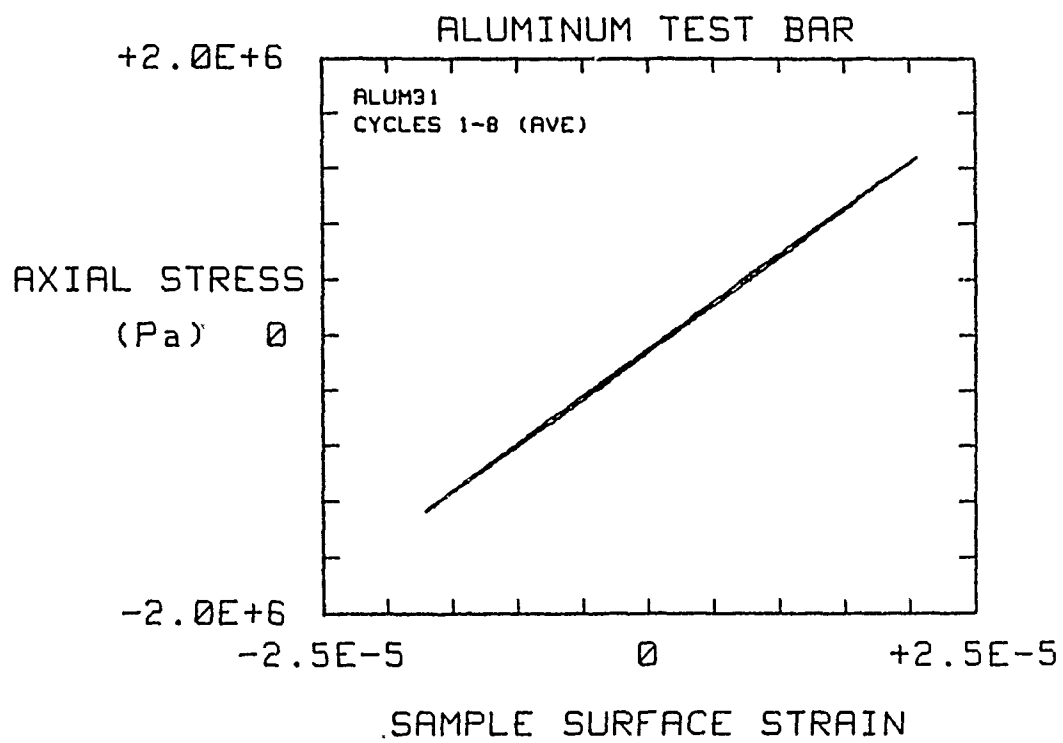
Fig. 1 Cyclic loading response curve
for standard aluminum bar.
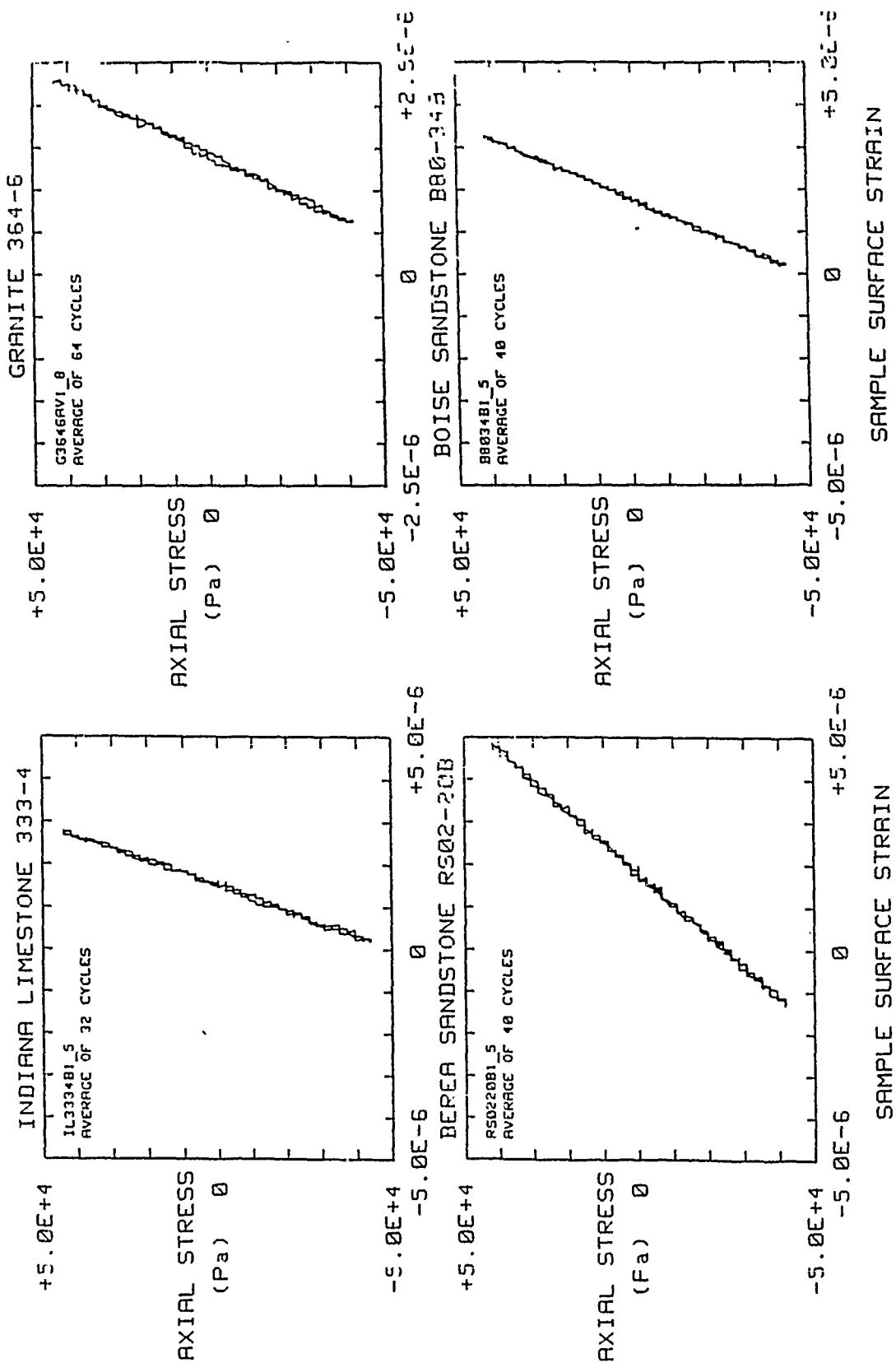
Fig. 2 Cyclic loading response curve
for four rock types at low strain.
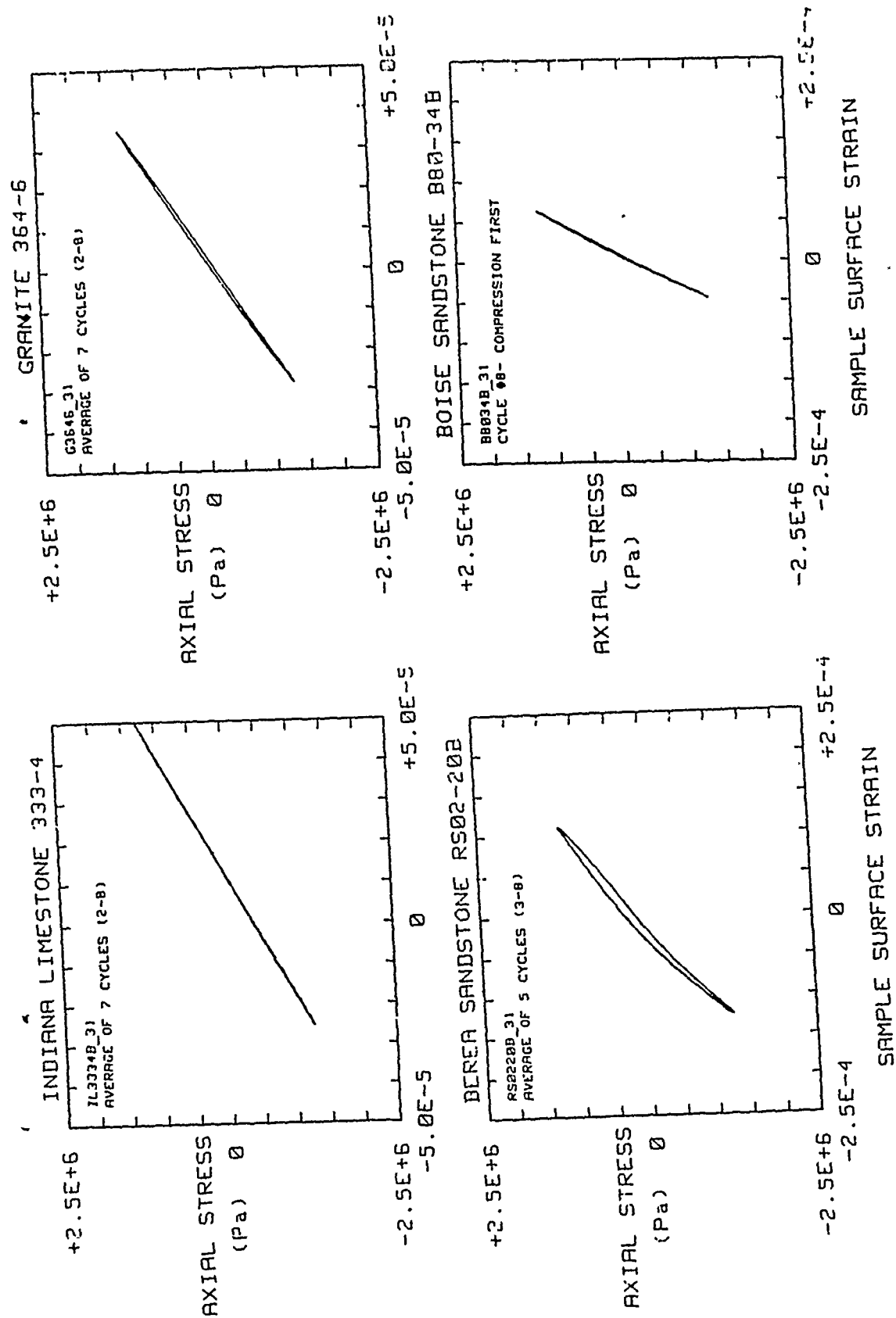
Fig. 3 Cyclic loading response curve
for four rock types at moderate
strain.

227

GRANITE 364-5

G3615_41
CYCLE #1

AXIAL STRESS (Pa)

+5.0E+6

0

-5.0E+6

+1.0E-4

0

-1.0E-4

GRANITE 364-5

G3615_41
AVERAGE OF 7 CYCLES (2-8)

AXIAL STRESS (Pa)

+5.0E+6

0

-5.0E+6

SAMPLE SURFACE STRAIN

+1.0E-4

0

-1.0E-4

BEREA SANDSTONE RS02-20B

RS0220B_31
CYCLE #1

AXIAL STRESS (Pa)

+2.5E+6

0

-2.5E+6

+2.5E-4

0

-2.5E-4

BEREA SANDSTONE RS02-20B

RS0220B_31
CYCLES 2-8

AXIAL STRESS (Pa)

+2.5E+6

0

-2.5E+6

SAMPLE SURFACE STRAIN

+2.5E-4

0

-2.5E-4

Fig. 4b Comparison of first cycle hysteresis loop with average of cycles 2–8 for Westerly granite.

Fig. 4a Comparison of first cycle hysteresis loop at 1.25×10^5 Pa stress with cycles 2–8 for Berea sandstone.

228

BOISE SANDSTONE B80-34B

BOISE SANDSTONE B80-34B

BOISE SANDSTONE B80-34B

BOISE SANDSTONE B80-34B

B8034B_181
CYCLE #16- TENSION FIRST

B8034B_111
CYCLE #1- COMPRESSION FIRST

B8034B_81
CYCLE #8- COMPRESSION FIRST

B8034B_91
CYCLE #1- TENSION FIRST

AXIAL STRESS (Pa)

SAMPLE SURFACE STRAIN

SAMPLE SURFACE STRAIN

+5.0E+6   0   -5.0E+6

+2.5E-4   0   -2.5E-4

BEREA RS02-20A

RS0220A_61
AVERAGE OF 8 CYCLES (9-16) @ 0.1 Hz

AXIAL STRESS (Pa)

SAMPLE SURFACE STRAIN

BEREA RS02-20A

RS0220A_51
AVERAGE OF 7 CYCLES (2-8) @ 1 Hz

AXIAL STRESS (Pa)

SAMPLE SURFACE STRAIN

Fig. 6 Loading response curves for
Berea sandstone at 1 Hz and at 0.1 Hz.

PAPER TITLE: Physical Model Investigations of Elastic Wave Propagation
and Scattering

PAPER AUTHOR: M. Abdel-Gawad, F. Cohen-Tenoudji, J. R. Bulau and B. R. Tittmann

CONTRACT NO: F19628-85-C-0034.

SUMMARY:

The paper describes the objective of the scaled ultrasonic physical modeling
research program, instrumentation and research plans to study the effects of
modeled geological structures on the propagation of sound waves. Preliminary
results on scattering from spherical inclusions and the conversion of P- to S-
waves are presented.

CONCLUSIONS AND RECOMMENDATIONS:

In the short time since the start of this program in mid-February 1985, considerable
progress has been made in the following areas:

a) Setting up the electronic data processing system

b) Characterization of the elastic properties of candidate model materials

c) Definition of model scaling and experimental approach.

d) Theoretical and experimental studies of the effect of scattering angle
on the generation of mode-converted S-waves from P-waves incident on a spherical
body.

e) Design and fabrication of three-component capacitance transducers.

Emphasis during the next period will be placed on detailed definition of a
candidate geological model for study.

Physical Model Investigations of Elastic Wave Propagation and Scattering

M. Abdel-Gawad, F. Cohen-Tenoudji, J.R. Bulau and B.R. Tittmann

Rockwell International Science Center
Thousand Oaks, CA 91360

INTRODUCTION

Several recent studies appear to indicate that scattering plays a major role in affecting the amplitude of seismic body and surface wave phases. For example, large variations are often observed in short period P-wave amplitudes measured at different stations which results in large uncertainties in yield estimates based on P-wave magnitudes (mb). Some effects have been attributed to wave focusing/defocusing by complex structures deep in the crust (Bache, 1982). Others are attributed to variations in attenuation in the crust (Cormier, 1982; Blandford, 1982). In a review of regional phase studies, Herrmann (1981) also observed that scattering would have to be taken into account in order to obtain realistic synthetic seismograms. Most scattering problems simulating the real earth have, however, been difficult to solve even with modern high speed computers. It seems, therefore, that laboratory scale three-dimensional models of specific crustal structures studied by ultrasonic waves can provide valuable insight into the effects of scattering caused by inhomogeneities along the propagation paths. Furthermore, the mechanisms for the generation of shear component motion from explosions are still not clearly understood in spite of a large number of studies on the subject. It has also become increasingly clear that local geological structures and the nature of the host rock at the source have significant effects on the generation of seismic waves. Some of these factors have been studied by Der, et al (1981).

Ultrasonic model investigations of scattering of body and surface waves due to departures from plane parallel homogeneous, isotropic layers have been very few in number. There is, however, renewed interest in this field, especially at the Masssachusetts Institute of Technology. Toksoz, et al (1980) studied Rayleigh wave propagation across surface irregularities with average size comparable to wavelength. Dainty and Toksoz, (1977) investigated elastic wave propagation in highly scattering medium simulated by randomly distributed circular holes. Non-random distribution of scatterers has many analogs in the lithosphere which lend themselves to detailed studies on laboratory scale models.

The purpose of this paper is to describe the objective of the scaled ultrasonic physical modeling research program and the approach we will use to address some of these problems.

PROGRAM OBJECTIVES

The overall objective of this program is to improve understanding of the effects of local geological structures at the source and along the seismic raypath on the generation, propagation and scattering of seismic energy from explosions. The program involves both theory and experiments using three-dimensional scale models as analogs of crustal and upper mantle structures. The propagation of ultrasonic waves will be monitored by specially designed three-component capacitance transducers. Experimental results will be compared with computer-based methods such as finite-difference simulation when such data are available.

THE PHYSICAL MODELING APPROACH

One of the advantages of the scaled physical modeling approach lies in its ability to generate waveforms of particle motion at any number of carefully selected locations. This is due to the fact that a reproducible source can usually be used. In many cases, by using multiple models with carefully controlled differences it is possible to obtain records of particle motion with and without the scattering. Thus the effects of scattering alone can be isolated. Furthermore, data on particle motion can be obtained in three orthogonal directions at critical locations so that P, S and surface waves can be properly identified and examined separately. Ultrasonic modeling provides flexibility in the selection of source, transmitting medium, receiver location and receiver orientation. Both compressional and shear wave sources, with controlled source orientation can be modeled. The transmitting medium can consist of random heterogeneities using methods such as those used by Dainty and Toksoz, (1977). Alternatively, one may use an anisotropic medium such as a sheet of formica or several other commercially available products. The use of fillers in cast resins and plastics allows some variations in velocity and attenuation. Both vertical and lateral gradients of velocity can be modeled.

EXPERIMENTAL APPROACH

Figure 1 shows the logic flow chart for our physical modeling program. Candidate geological models are conceived based on (a) specific field seismological observations, (b) scattering theory, (c) data from finite-difference simulation, or (d) directly observed or inferred geological structure. Once a candidate geological model is defined, a three-dimensional scale model will be constructed from carefully selected materials with appropriate elastic properties as analogs of crustal and

upper mantle structures. Ultrasonic sources will simulate an explosive source. Small, specially designed three-component capacitance detectors are bonded to the model face at carefully selected locations to capture full waveforms. Data will be digitized for detailed analysis as outlined in Figure 1. Waveforms will be stored in formats compatible for transfer to the seismic data base at DARPA Center for Seismic Studies.

INSTRUMENTATION AND HARDWARE

Source

The major components and electronics used to capture ultrasonic waveforms are shown in Figure 2. Several types of source can be employed: (a) mechanical, (b) electromagnetic acoustic transducer (EMAT), (c) piezoelectric , (d) explosive and (e) laser. An effective mechanical source can be as simple as a pencil leadpoint snapped at the desired site. Using a simple lead-holding fixture it has been possible to obtain very repeatable pulses for use as an acoustic emission standard (L. Graham, personal communication). EMAT sources have been used successfully to locate and characterize cracks and inhomogeneities in metals, (Graham and Martin, 1983). Piezoelectric transducers are commonly used to generate and detect both compressional and shear waves. They are generally optimized for response in a specific window of frequency. Various sparkers, small explosive charges and exploding foils or wires have been used to simulate an explosive source. These devices are generally not very reproducible.

Laser-produced ultrasonic waves offer several advantages in physical model studies. Several reviews on laser-generated elastic waves exist in the literature (Scruby et al, 1981; Birnbaum and White, 1984). A laser beam can be focused to form a small diameter source which is important for realistic scaling of models in addition to its high repeatability. Several mechanisms of elastic wave generation are involved. The first is thermoelastic wave generation (Scruby et al, 1981), where the optical power density at the irradiated surface is sufficient to produce thermal strains without melting, and radiation of elastic waves. In this case, the forces tend to act parallel to the surface and are dipolar, causing primarily the generation of shear waves. A second type of laser-generated acoustic source is obtained by coating the surface of the model with a liquid that absorbs strongly at the laser frequency (e.g. oil, water), Dewhurst et al, (1982); Von Gutfeld and Melcher, (1977). In this case, the laser energy is absorbed within the liquid causing very rapid evaporation. The resultant forces tend to be concentrated normal to the surface, causing the generation of primarily P-waves.

We plan to explore the potential of laser-generated elastic waves as a means of varying the source parameters. A high power Q-switched Nd: YAG (neodymium yttrium aluminum garnet) laser will be used. An energy pulse of 800 mj can be delivered in 10 n sec., which is equivalent to 80 Mw of peak power. An aperture beam diameter of 8 mm will be focused to produce a sub millimeter source either on the model surface or at any desired depth by drilling a fine borehole.

Detectors

Three-component detection will be achieved using small capacitance transducers, which are mounted on three mutually perpendicular faces of a metallic cube (Figure 3). A number of detectors are bonded to the surface of the model at critical sites for optimum wave front interception. A detector can in fact be embedded inside the model, if such configuration is needed. Compressional and shear waves as well as surface waves can be monitored.

Data Processing Electronics

Signals from the capacitance transducers are amplified and input into a 16 channel digitizer and array processor. A Data General Nova II computer is used as controller and data buffer. Waveform analysis and detailed data processing will be performed on a VAX 11/780 using waveform processing software language (ISP) developed at Rockwell International Science Center.

SCALING AND MATERIALS

In order to simulate seismic wave propagation in the earth's crust, which consists of rocks with different elastic properties, one has to scale the dimensions of the model to the frequency range used in the laboratory. The models will nominally represent structures in the crust and upper mantle where P-wave velocities range from <4 Km/s to about 8 Km/s, and S-wave velocities from 2 to 4 Km/s. Frequencies are nominally in the range .05 to 20 Hz. The quality factor Q varies from 100 to 1000. Given these values, several considerations govern the choice of model size. First, the overall size should be practical in the laboratory environment and should allow the replacement of certain layers with materials of different elastic or structural properties. This consideration alone constrains the maximum size to approximately one meter in the horizontal directions. In scaling, the product of the wave-number by the characteristic length ka should remain constant. Considering a thickness a = 100 km and an average P-wave velocity of 6 km/s, for example, the product ka would vary from 6

to 2000. In a model, where the crustal thickness a = 13 cm, and longitudinal velocity of 6.4 km/s, the interval 6 < ka < 2000 would imply a laboratory frequency interval 0.05 MHz < f < 20 MHz. The higher part of this frequency range seems impractical. At frequencies higher than several MHz, the shear elastic waves become highly attenuated by grain scattering if the model material contains granular or crystalline components. Furthermore, the wavelength becomes so small that the detection of the different components of the displacement field is not feasible. For these reasons, our experiments will be limited to 2 MHz as an upper limit of frequency. The range of quality factor 100 < Q < 1000, known to occur in the lithosphere, will be simulated in the laboratory by using a combination of fine-grained metals and various plastics filled with controlled quantities of metal and silicate powders.

CANDIDATE MODELS

There are at present three candidate problems under consideration for modeling : (a) generation of mode-converted shear waves by scattering of P- waves from inhomogeneities, (b) the effect of a low Q layer in the lower crust on the attenuation of P- and S-waves, and (c) effect of topographic relief in the near-field of an explosion.

To shed light on the problem of mode conversion from P- to S-waves at scatterers we have examined the scattered radiation pattern from a WC inclusion in a tin alloy matrix. Fig. 4 shows the relative scattered power, normalized to an arbitrary reference, as a function of the scattering angle measured from the forward scattering direction. The ultrasonic pulses were at a frequency of 2.25 MHz and the spherical WC inclusion had a radius of 400 μm, so that the ratio of wavelength to radius was about 10. It is evident from the figure that over a large range of angles the mode-converted shear waves (T) dominate over the directly scattered P-waves (L). The relevant parameters for the matrix and inclusion are, respectively, V_P = 6.34, 6.65 km/sec.; V_S = 3.13, 3.98 km/sec.; ρ = 4.5, 13.8 gm/cc. It is seen, therefore, that in terms of V_P, the contrast is only 5% whereas for V_S and ρ the contrasts are 27% and 200%, respectively. The solid line in the figure is the result of calculations based on classical scattering theory for single spherical inclusions. The theory and data points are adjusted vertically to give the best fit.

Recently, Dr. John M. Richardson at the Science Center has developed a long wavelength theory for weakly scattering voids or inclusions. He has demonstrated its use in describing the scattering from ellipsoidal

inclusions in good agreement with experiments. This approach opens the door for examining the mode conversion of P to S waves for more realistic geological scatterers likely to be encountered in the igneous and metamorphic complex of the earth's crust. A fundamentally relevant question is the case of distributed scatterers and how the mode-converted S waves might add up to form a sufficiently well-developed wave to be detected by seismic stations as a separate arrival.

ACKNOWLEDGMENT

REFERENCES

Bache, T. C. (1982). Estimating the yield of nuclear explosions, Bull. Seism. Soc. Am. 72, 131- 168.

Birnbaum, G. and G. S. White (1984). In "Research Techniques in Nondestructive Testing," Vol. 7 (R.S. Sharpe, ed., Academic Press, London, 1984), pp. 259-365.

Blandford, R. R. (1982). Seismic event discrimination, Bull. Seism. Soc. Am. 72, 69-87.

Cormier, V. F. (1982). The effect of attenuation on seismic body waves, Bull. Seism. Soc. Am. 72, 169-200.

Dainty, A. M. and M. N. Toksoz (1977). Elastic wave propagation in highly scattering medium-a diffusion approach, J. Geophys. 43, 375-388.

Der, Z. A., A. O'Donnell, and P. J. Klouda (1981). An investigation of attenuation, scattering and site effects on regional phases, VSC-TR-81-11, Teledyne Geotech, Alexandria, VA.

Dewhurst, R. J., D. A. Hutchins, S. B. Palmer and C. B. Scruby (1982). J. Appl. Phys. 53, 4064.

Graham, L. J. and J. F. Martin (1983). Ultrasonic inspection of rails by electromagnetic acoustic transducers; Proc. Qualtest-II; Railroad Inspection Session, Dallas Texas, 11 p.

Herrmann, R. B. (1981). Review of regional phase studies, DARPA-NMR-81-04, Defense Advanced Research Projects Agency, Arlington, VA.

Scruby, C. B., R. J. Dewhurst, D. A, Hutchins and S. B. Palmer, (1981).
In "Research Techniques in Nondestructive Testing", Vol. 5 (R. S. Sharpe,
ed., Academic Press, London, 1981).

Toksoz, M. N., D.R. Nathman and J. R. Chameul (1980). A model study of
Rayleigh wave propagation across surface irregularities, Earthquake Notes
51 (3), 37 (abstract).

Von Gutfeld, R. J. and R. L. Melcher (1977). Appl. Phys. Lett.
30, 257.

FIGURE CAPTIONS

Figure 1. Flow Chart of Physical Modeling Program
Figure 2. Hardware for Data Collection and Analysis
Figure 3. Three-Component Capacitance Transducer
Figure 4. Scattered Radiation Pattern of Directly Scattered P-waves (L) and
Mode-Converted S-waves (T). The solid lines are theoretically
calculated for 2.25 MHz.

Figure 1

2.13

SC85-30876

Figure 2

(ANALOGIC)

240
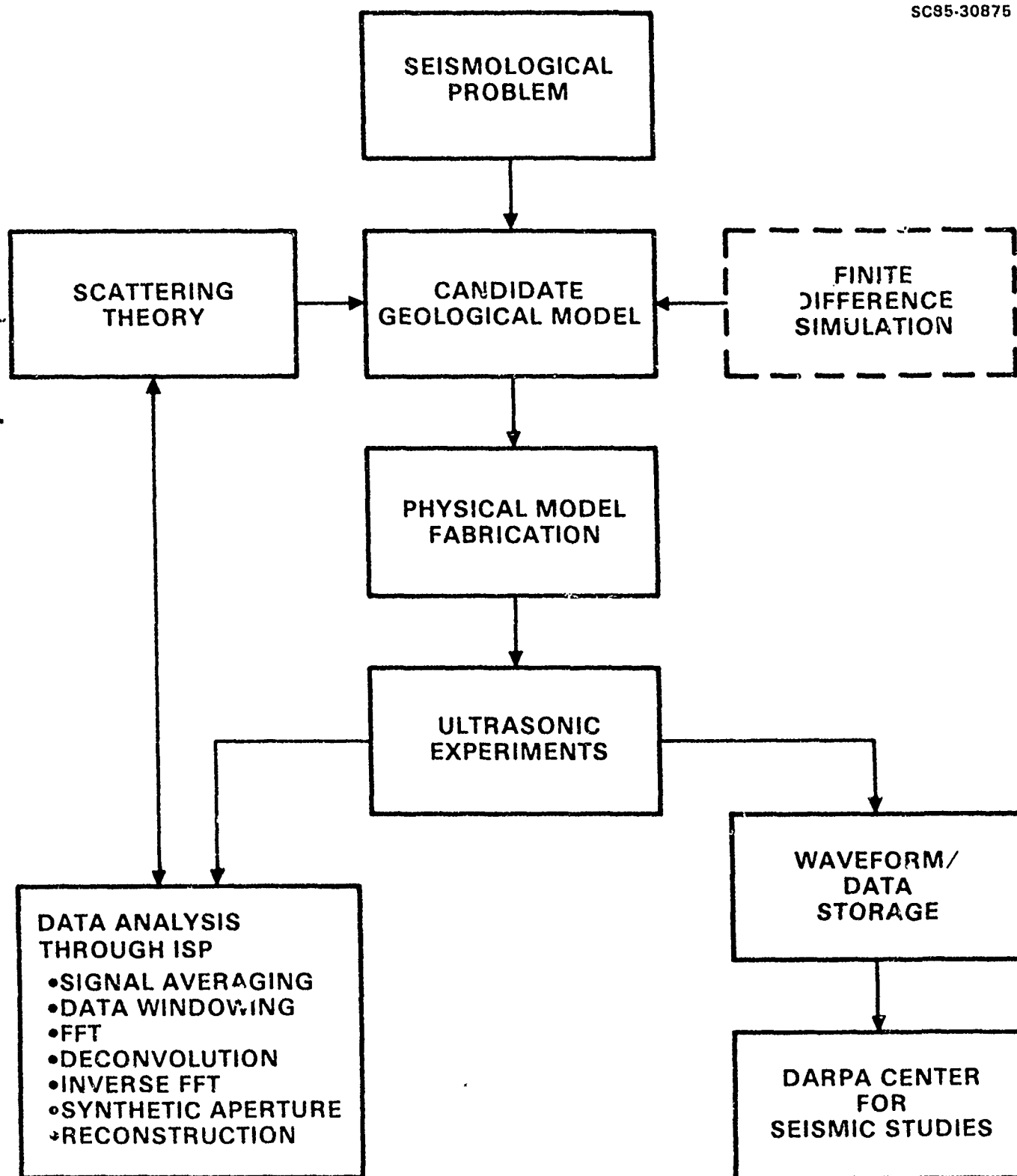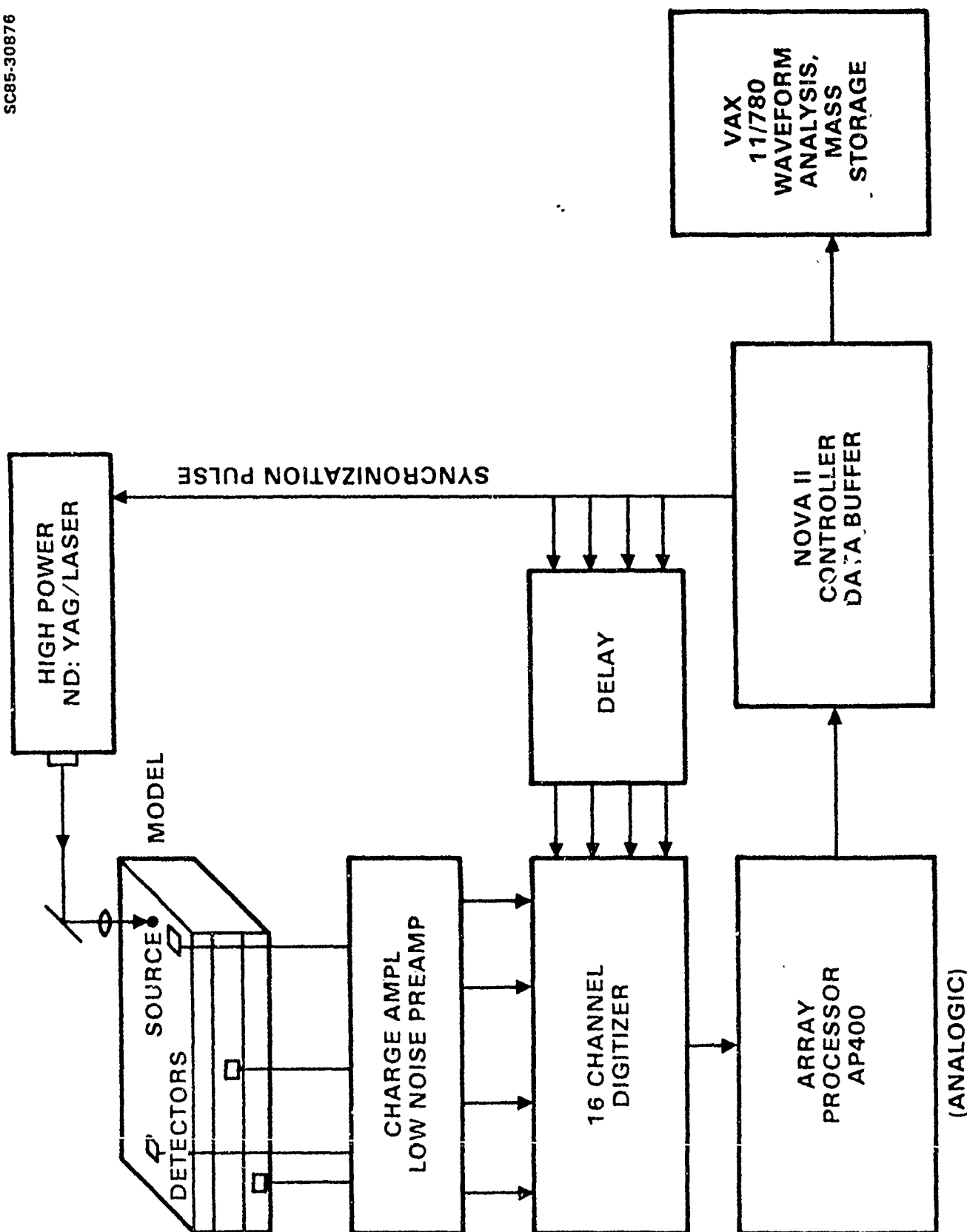
3-COMPONENT CAPACITANCE TRANSDUCER

Figure 3

241
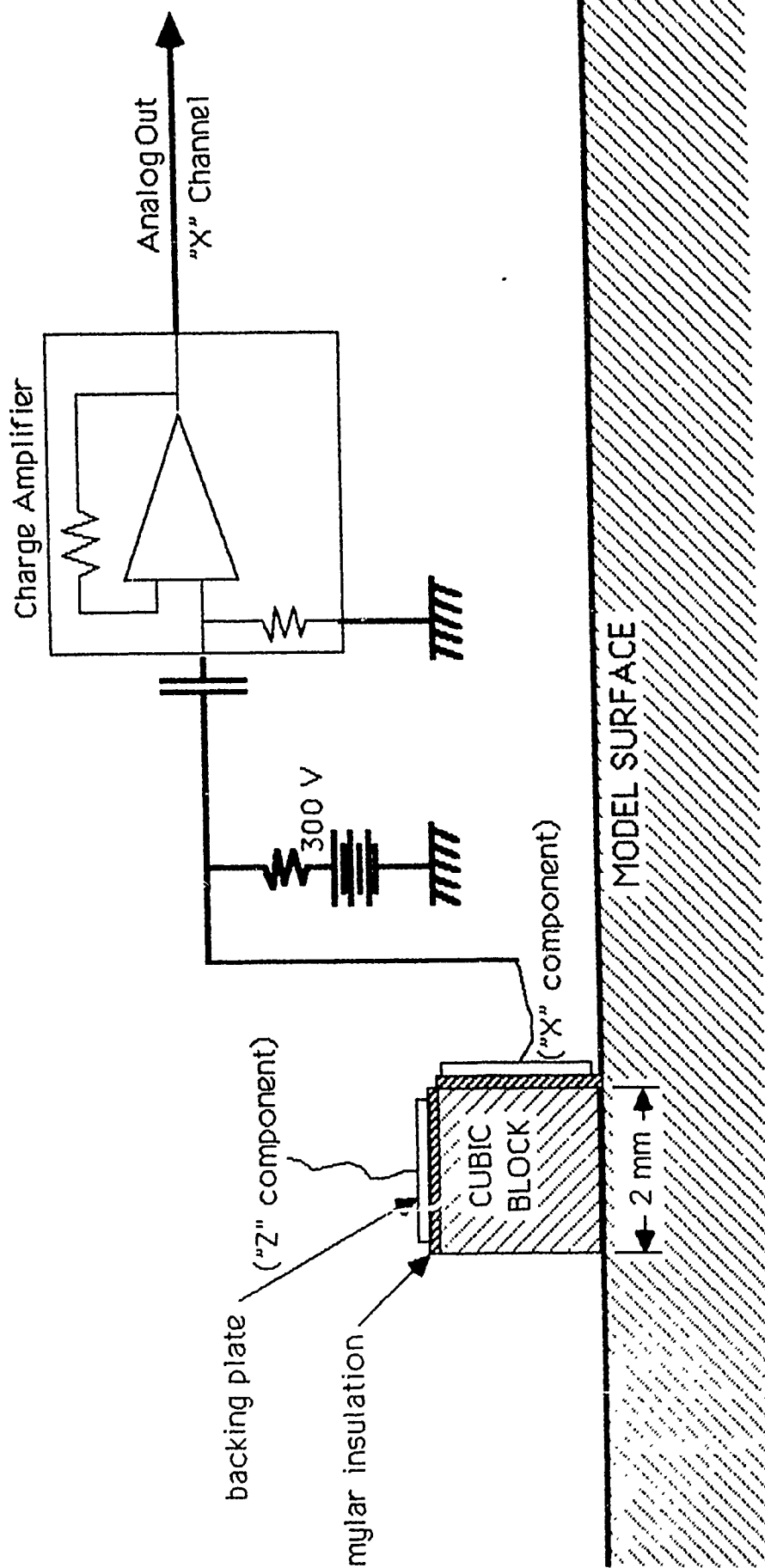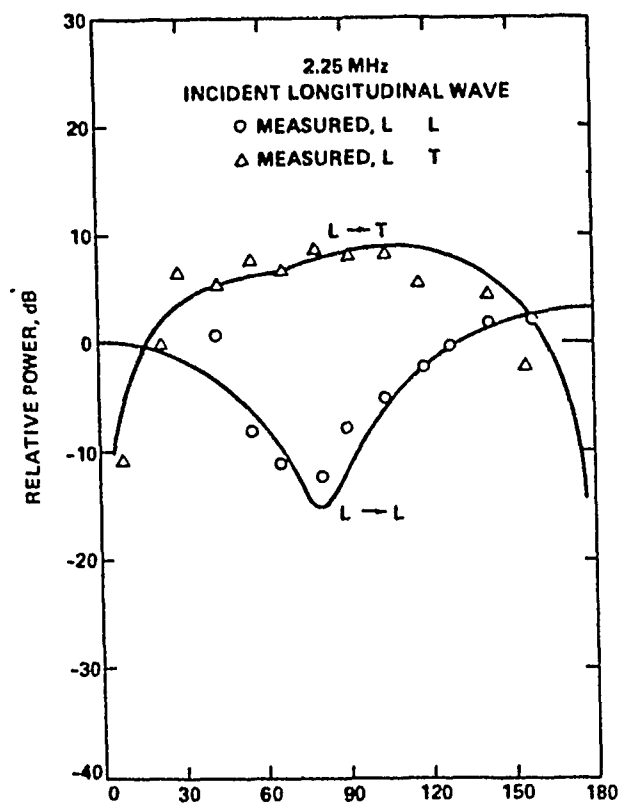
Figure 4

FINITE DIFFERENCE MODELING OF

BODY WAVES AND SURFACE WAVES

Work continues on several problems of interest using the
general method of linear elastic finite difference modeling.
Several advances have been made toward modeling lateral
heterogeneity of geologic structure and topography. Calculations
are performed on both the Center for Seismic Studies VAX-780's as
well as on commercial Cray computers. In the two short abstracts
below, we report on two aspects of the work in progress.

2-D LINEAR FINITE DIFFERENCE CALCULATIONS FOR EFFECTS OF LOCAL STRUCTURE ON TELESEISMIC EXPLOSION WAVEFORMS FORM YUCCA VALLEY, NTS.

K.L. McLaughlin, Z.A. Der, and L.M. Anderson
Teledyne Geotech, 314 Montgomery St., Alexandria, Va. 22314.

2-D linear-elastic finite difference calculations have been
made for a 2-D geologic model of Yucca Valley, NTS.
Calculations were used to produce synthetic teleseismic P-wave
seismograms for explosion line sources in the 2-D structure. P-
wave coda in the first 5 seconds is observed to be dependent on
the takeoff angle for teleseismic distances as well as the
location of the sources in the geologic structure. The P-coda
appears to originate from scattering of waves initially trapped
in the low-velocity near-surface alluvial and volcanic deposits.
The trapped energy is then scattered by lateral heterogeneities
at the faulted unconformity between the Tertiary volcanics and
the Paleozoic carbonates. The P coda in the first 5 seconds
following the P wave produce fluctuations in the maximum
amplitude of 0.3 magnitude units for source locations only 5 km
apart for the same teleseismic receiver. The "a" and "b" phase
amplitudes are not as significantly perturbed by the 2-D
structure with fluctuations less than 0.15 magnitude units. The
combination of teleseismic attenuation, source time function, the
instrument response, windowing, and scattered waves in the P coda
act to obfuscate the spectral modulation expected from the linear
P+pP interference.
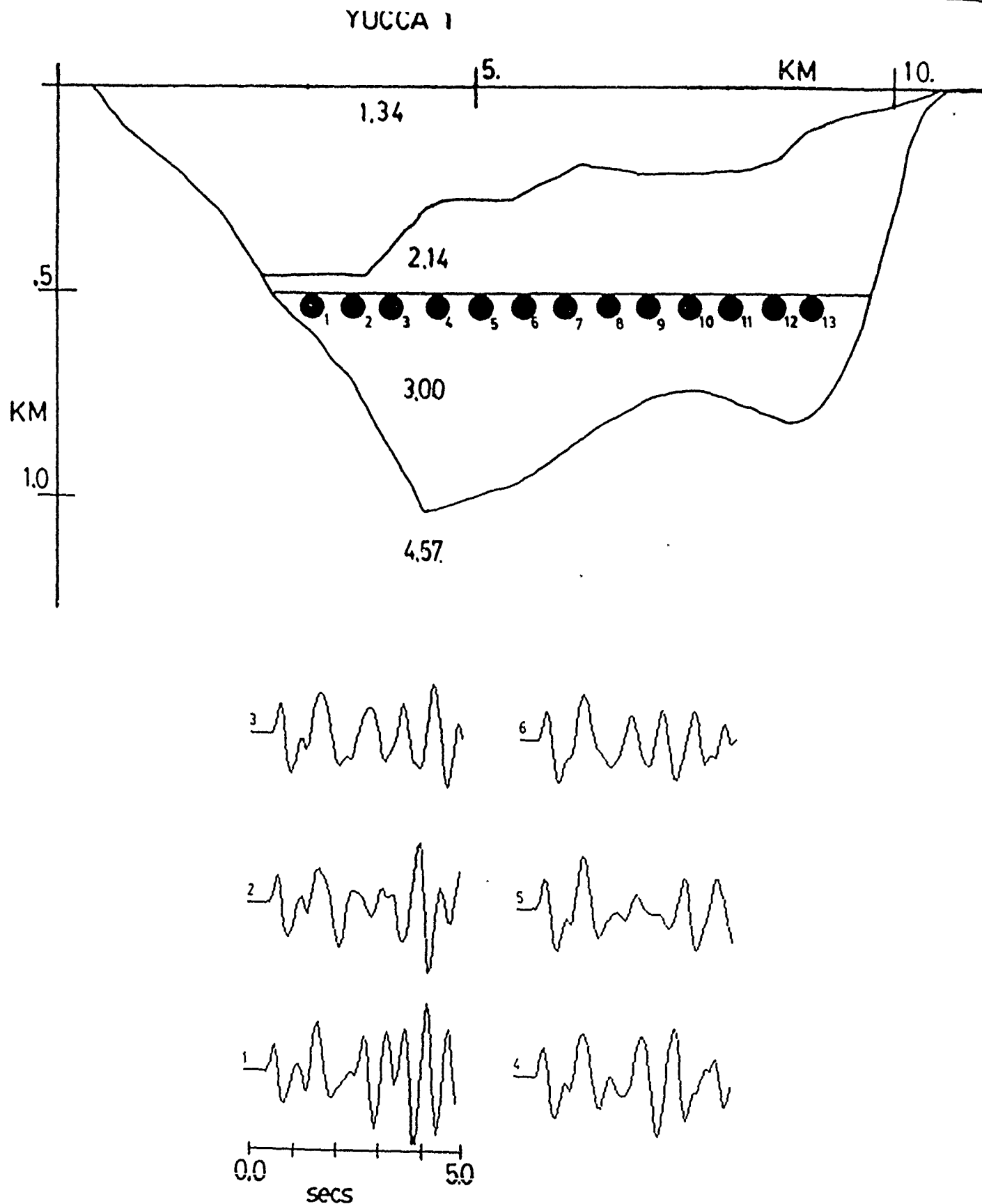
Figure 1. Top: 2-D model of Yucca Valley shallow structure. Below: synthetic teleseismic seismograms for the model shown above. Sources are located at the numbered locations in the model just below the water table. Takeoff angle in the lower half space is 15 degrees to the east. RDP is appropriate for a 100 KT explosion in hard rock.
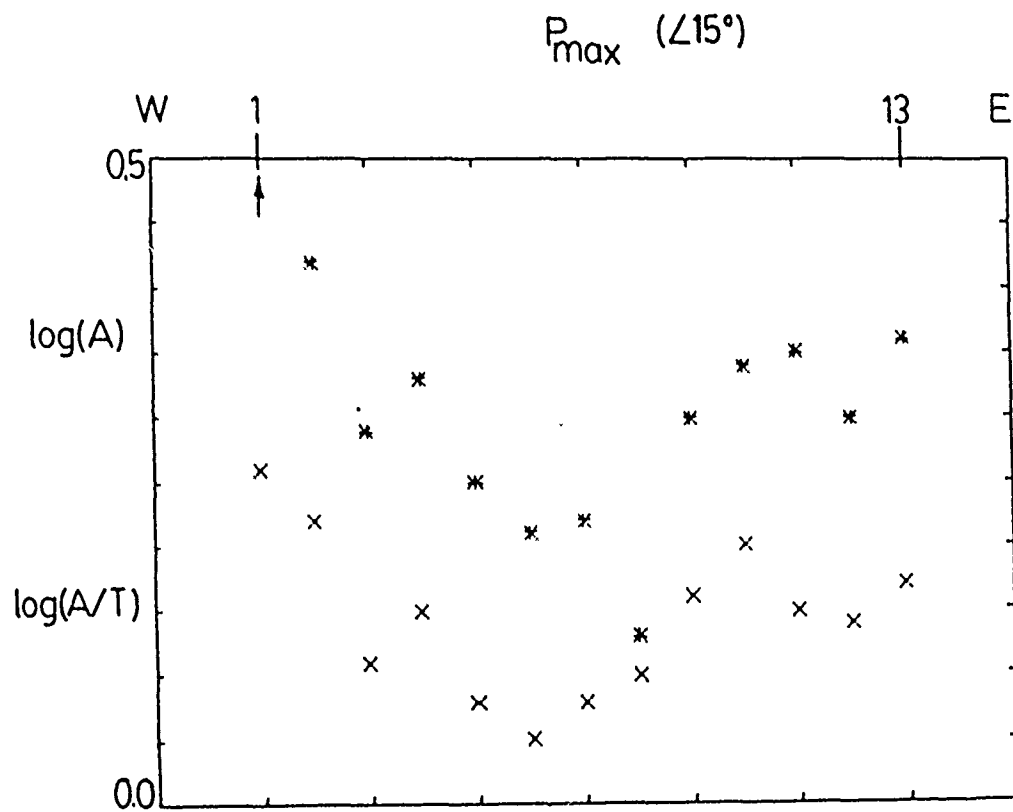
Figure 2. Predicted m_b variation for source locations shown in Figure 1. Note the east to west variation of the magnitude based on the maximum P phase in the first 5 seconds of P waveform.
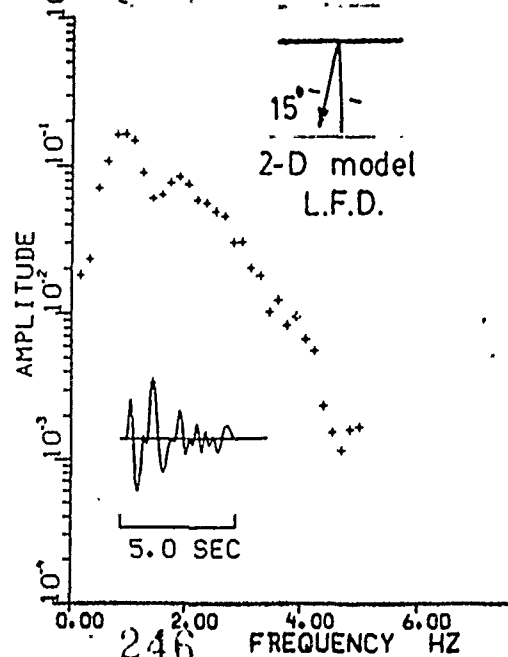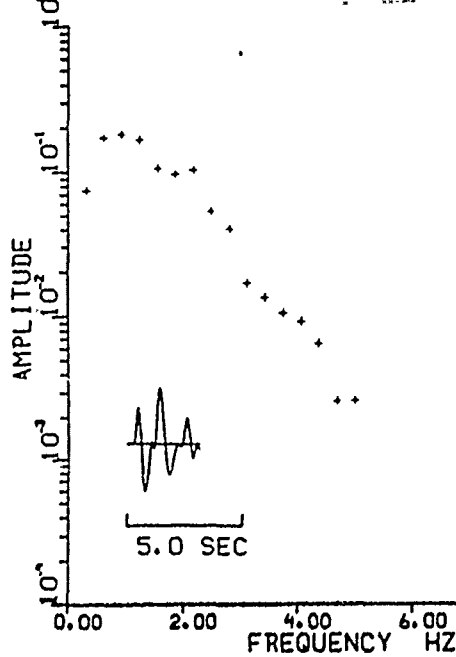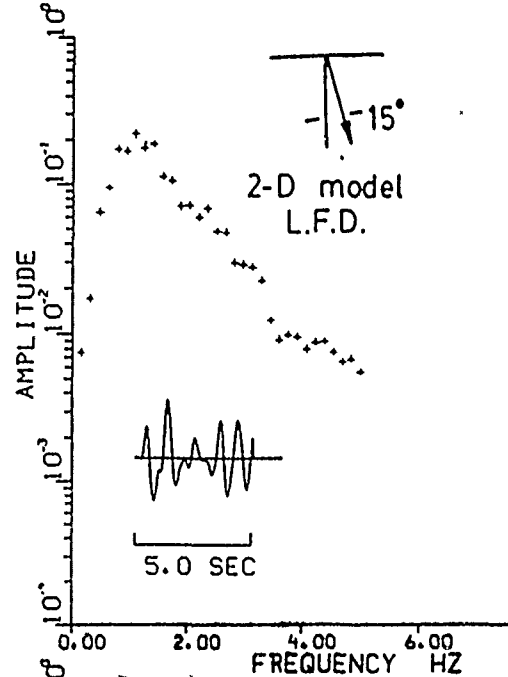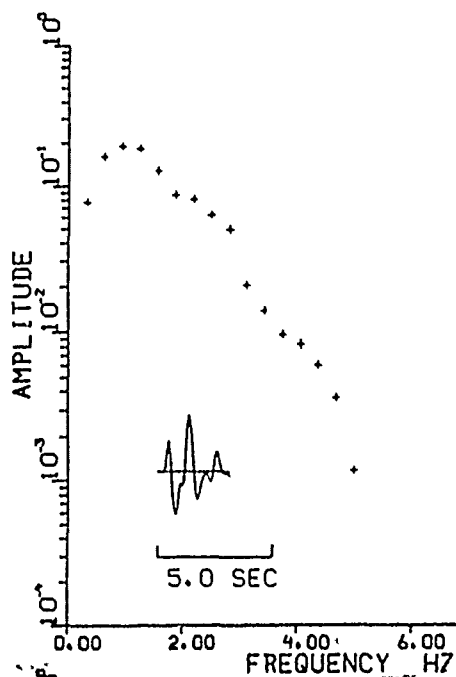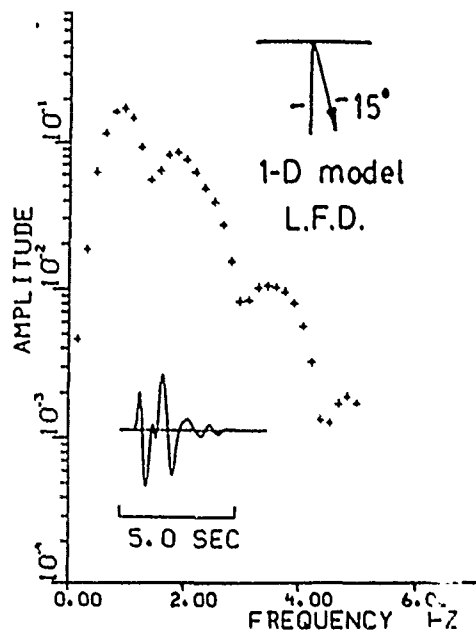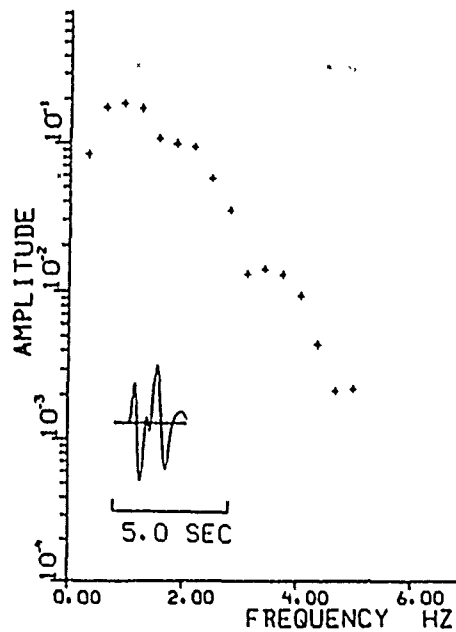
FIGURE 3. Spectra of synthetic teleseismic waveforms for 1-D (TOP) and 2-D models (MIDDLE and BOTTOM). The same location of the model shows two different responses for receivers to the EAST (MIDDLE) and to the WEST (BOTTOM). The short window is shown to the left. The long window is shown to the right. The effects of convolution with an attenuation operator, instrument response, and 100 KT hard rock RDP are included. The P+pP nulls are apparent in the spectra of the finite difference response for short windows, and for long windows with 1-D models but not when all effects are included (attenuation,instrument,and RDP).

INVESTIGATIONS OF SCATTERING AND ATTENUATION OF SEISMIC WAVES USING 2-DIMENSIONAL FINITE DIFFERENCE CALCULATIONS

K. L. McLaughlin, Z. A. Der, and L. M. Anderson

Teledyne Geotech Alexandria Labs
314 Montgomery St. Alexandria, Va. 22314.

2-D finite difference calculations for planar elastic P waves in Gaussian random media have been used as Monte Carlo experiments to simulate scattering in the range of $0.5 < ka < 10.$, where k is the wavenumber and a is the characteristic length of the heterogeneity. Calculations include P-to-S conversion, multiple scattering, and diffraction effects. Random velocity half spaces with variations of 10% and 5% rms and Gaussian spatial autocorrelations have been used. Normalized propagation distances range from $z/a = 15$ to $z/a = 3$. The numerical experiments have been used to estimate peak amplitude attenuation, $1/Q$, of individual seismogram realizations as well as spatial ensembles approximated by beams. Spatial coherency for a simulated seismic array on the surface of the Earth is explored.

Coda generation for 2-D media is much stronger compared to 1-D randomly layered media with the same statistics. Time domain peak amplitudes are attenuated more rapidly than frequency domain spectral amplitudes. Random modulation of the P-wave spectra may be strong while attenuation of the spectral level measured over two or more octaves may be slight. Consequently, thin zones of moderate heterogeneity may introduce significant peak amplitude attenuation and modulation of the P-wave spectra in narrow bandwidths. In accord with scalar theory, both 5% and 10% rms random velocity media appear to exhibit the same functional dependence of $1/Q(ka)$ with scaling proportional to the variance of the random velocity component. However, attenuation, $1/Q(ka)$, does not decline with increasing frequency as rapidly as predicted by scalar theory for Gaussian random media. $Q(ka)$ is roughly proportional to ka for $2 < ka\ 10$.

Comparison has been made of numerical 2-D results with small seismometer arrays, in the 1 to 10 Hz band for incoming teleseismic P waves. The spatial coherence declines rapidly for frequencies above 3 Hz. Also, high frequencies (5 Hz) are randomly but systematically delayed with respect to low frequencies (1 Hz). The transverse component of P wave motion is enriched in high frequencies and grows in the first 5 seconds after the P wave. All indications are that the scatterers responsible for the incoherency and high frequency delay are shallow and are on the order of 1 km. Current modeling efforts proceed to test the effects of deterministic layering of the crust, alternative spatial heterogeneity spectra, and trade-offs inherent in modeling. Future modeling may include the extension to 3-D random structure.

RMS=10%.   RMS=5%.
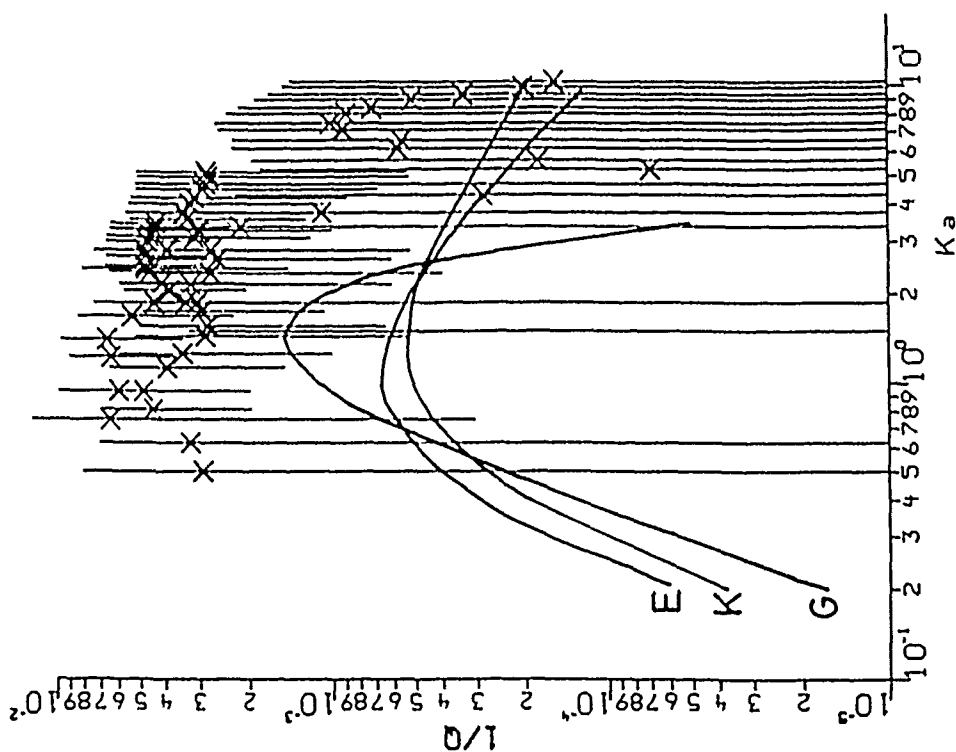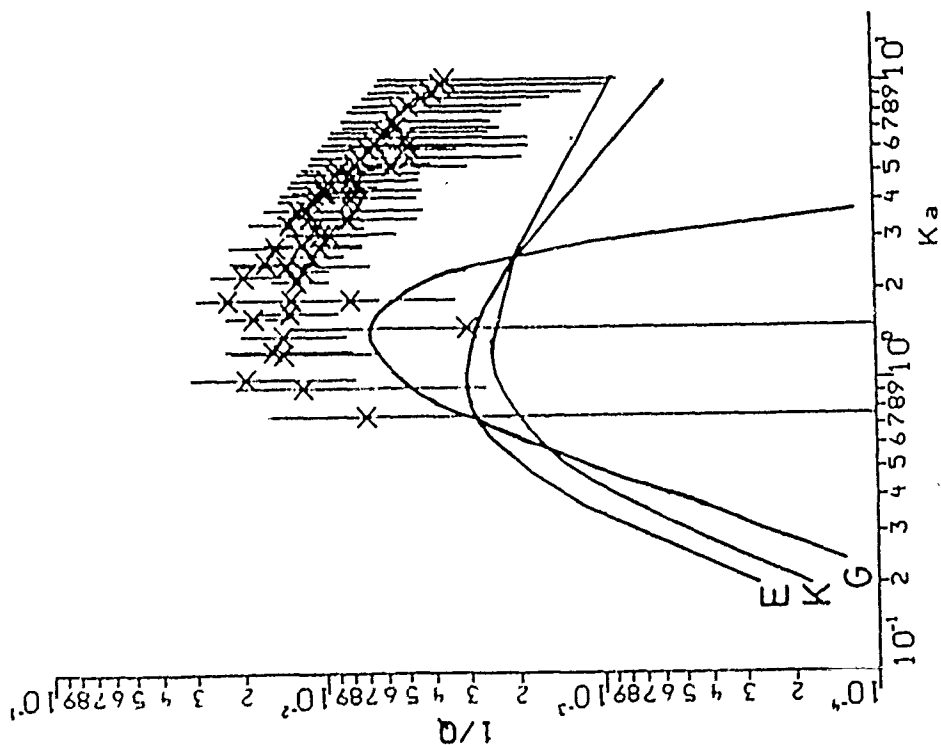
FIGURE 1. Attenuation, 1/Q, estimates for peak amplitude attenuation due to random media for rms velocity variations of 10% (LEFT) and 5% (RIGHT). Calculations are for Gaussian random half spaces with incident plane P waves. Peak amplitude attenuation is measured relative to the response of a uniform half-space. Errors are estimated from the variation of the peak amplitude attenuation of individual band-pass filtered seismograms on the free-surface of the half-space. The three curves labeled "E", exponential, "K", Kolmogorov, and "G", Gaussian, are predictions of 1/Q from 3-D scalar theory.

248
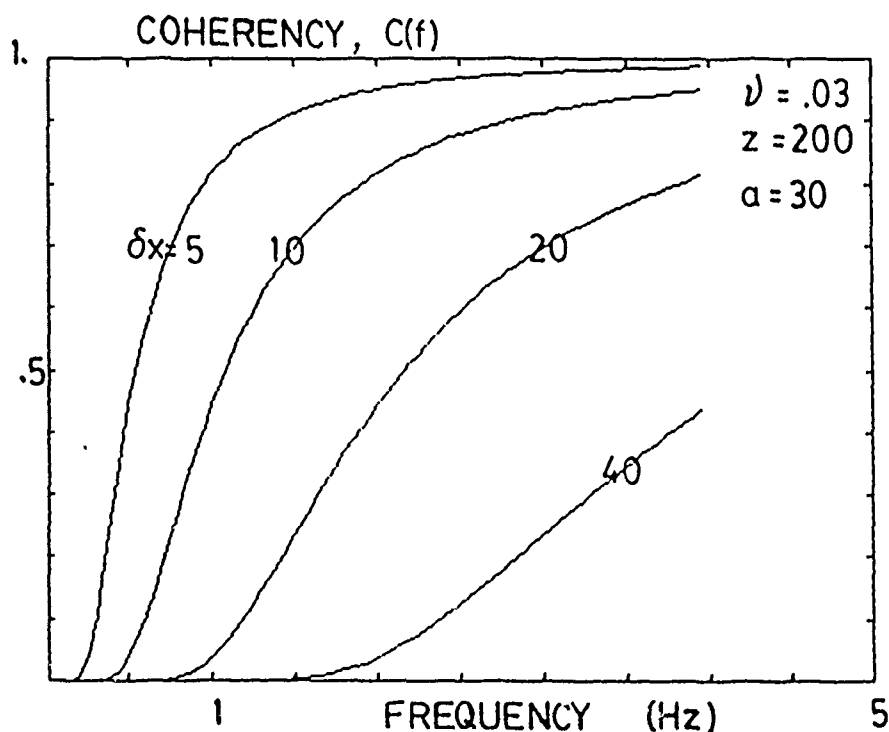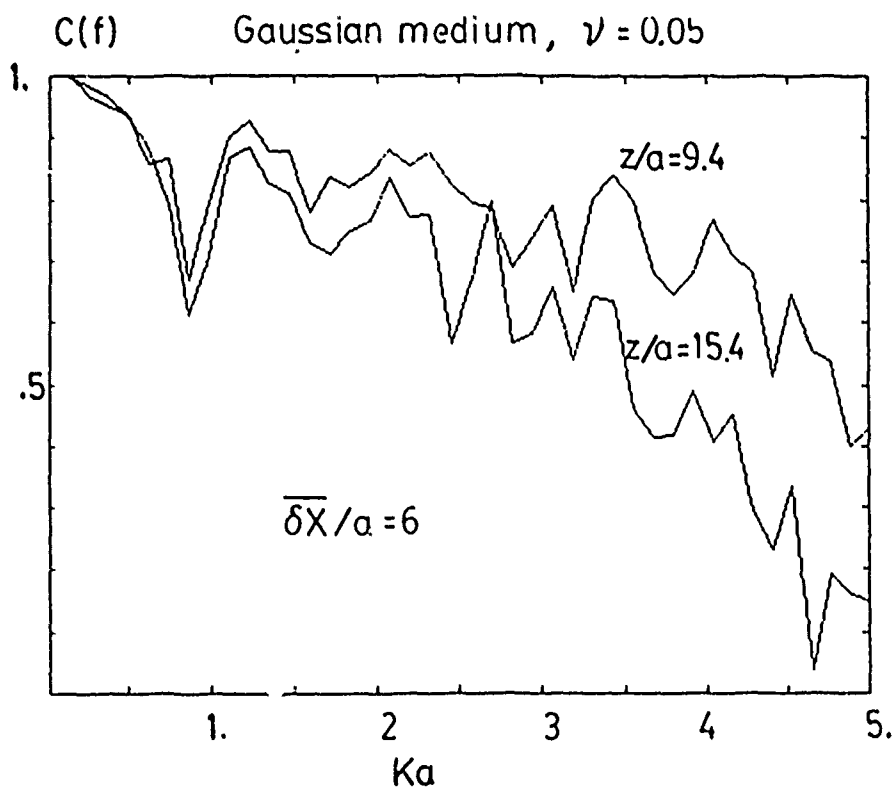
Figure 3. Top: Synthetic coherency estimates for an array of seismometers on the free surface of a 2-D random half space with 5% rms velocity variation. The frequency is normalized as ka, where k is the wavenumber and a is the scale length of the medium. The plane incident P waves traveled z/a = 9.4 and z/a = 15.4 normalized distance. Bottom: In contrast the functional form for coherency for forward scattering scalar theory for a random medium with scale length a = 30 km, z = 200 km, 3% rms velocity variation, sensor separations of δx = 6, 10, 20, and 40 km. Average velocity of 8 km/sec

EKA - E. Kazakh   C(f)

$\overline{\delta r}$ = 4km

FREQUENCY (Hz)

EKA - E. Kazakh

SEC.

FREQUENCY (Hz)
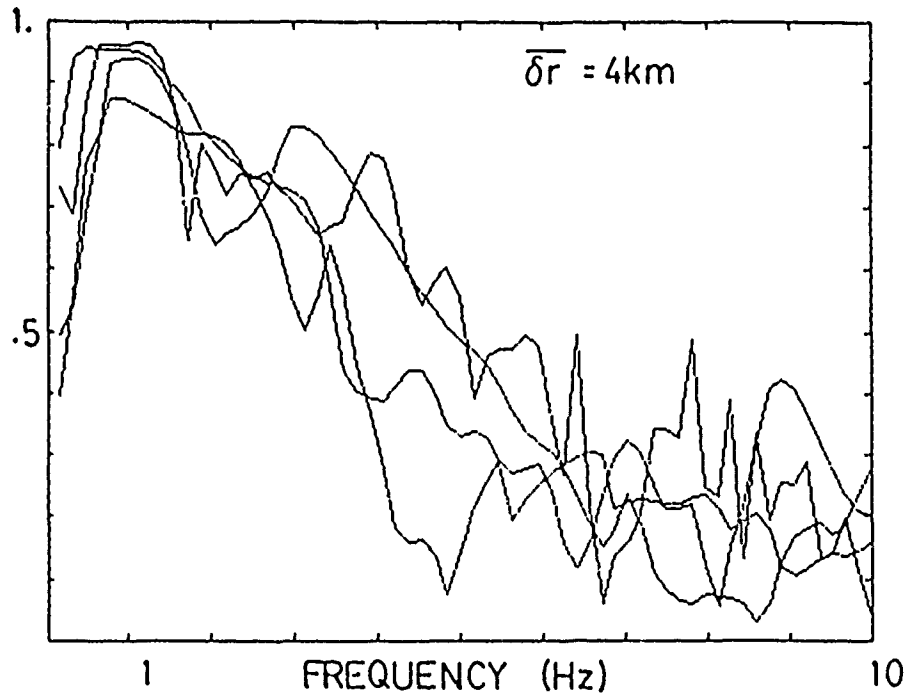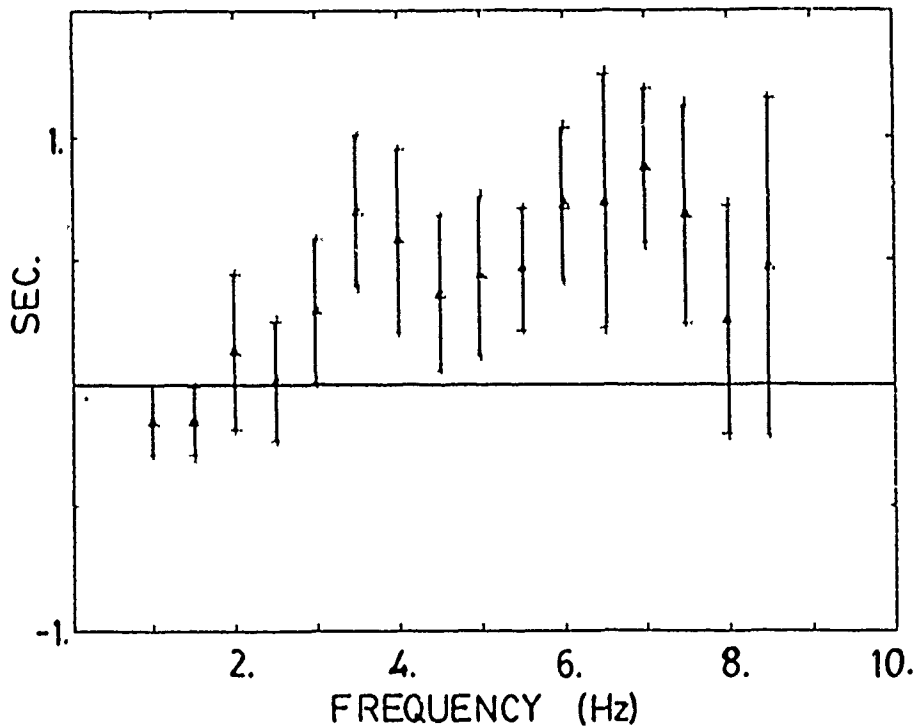
Figure 2. Top: Coherency measured at the EKA array with sources at E. Kazakh. Average inter-station spacing is 4 km. Coherency declines almost linearly above 2.0 Hz. Coherency is measured for a 6 second P wave window. Bottom: Temporal energy centroid delay as a function of frequency for the E. Kazakh to EKA data. Error bars represent the standard deviation of a single observation. Energy at frequencies above 3 Hz is systematically delayed by as much as 0.5 seconds with respect to 1 Hz energy. Onset of dispersion is coincident with the loss of coherence.

Experiment at the Lajitas Seismic Station
Eugene Herrin
Department of Geological Sciences
Southern Methodist University

Support for the operation of the Lajitas station and the analysis of data from the instruments there has been continued under an AFGL-DARPA contract starting 1 Feb 1985. Support has also been provided by Sandia National Laboratories. Sandia has installed nine additional seismometers at the Lajitas station, moved in a trailer with computer equipment for the acquisition and analysis of digital data and furnished a number of personnel under the direction of H. B. Durham to carry out the Sandia-SMU cooperative experiments this spring. Data have been collected with the folowing objectives in mind:

(1)   Determine the relationship between seismic noise to 100 Hz and wind noise at the Lajitas site.

(2)   Determine the attenuation of noise to 100 Hz with depth under various wind conditions.

(3)   Determine relative coupling of seismometers to the earth in boreholes, on a subsurface pier and grouted into a cavity to frequencies of 100 Hz.

(4)   Using Vibroseis sources determine propagation characteristics at Lajitas for distances from 1 km to 90 km.

In this brief paper we are reporting work done since February 1, 1985.

Figure 1 shows the approximate location of short-period seismic instruments at the central pad of the Lajitas station. Three component Teledyne-Geotech GS-13 and S-750 sensors are located in the walk-in vault and tank vault. An S-750 was grouted into a hand-dug hole about 5 feet deep adjacent to the walk-in vault. The grout material was selected to match the density of the limestone in which the hole was dug. This sensor is used as a standard in the study of coupling between the earth and the other sensors. Teledyne-Geotech GS-21 sensors were installed at the bottom of the two bore-holes. Data were digitized at 250 samples per second both during the noise measurements and the Vibroseis experiments. Figure 2 shows the

minimum noise levels observed at Lajitas during experiments in
February and March, 1985. These noise levels occurred during
periods when there was no observable wind, a minimum noise condi-
tion which occurs at Lajitas only a few percent of the time. Also
shown in Figure 2 are the observed low-noise levels at NORSAR
(Bungum, H., S. Mykkeltveit and T. Kvaerna, 1985, NORSAR Contribution
No. 352). As can be seen in this figure, the minimum noise levels
at Lajitas are about 20 dB lower than those NORSAR for frequencies
around 10 Hz and about 10 dB lower at 40 Hz. Thus the NORSAR noise
levels fall-off faster with increasing frequency above 5 Hz than do
those at Lajitas as has been previously stated in NORSAR reports.
Above 40 Hz these two minimum noise-level curves may continue to
converge.

The noise levels at Lajitas rise with increasing wind velocity
as is shown in Figure 3. The top curve in this figure is for a
frequency of 11 Hz, the middle curve for 20 Hz and the lowest curve
for 50 Hz. The two vertical bars represent noise levels at 10 Hz,
wind speed 8-10 m/sec, and at 20 to 30 Hz, wind speed 10 m/sec,
given by H. Bungum et al. in the previously referenced report. Bungum
observed that the relative increase in noise level with wind speed
does not appear to be as great at NORSAR as has been reported for
Lajitas. Figure 3 shows that the absolute value of seismic noise
(displacement power) is about the same for wind speeds of 8 to 10
m/sec. The relative effects observed by Bungum may result from the
higher noise levels at NORSAR when the wind speed is near zero.
Unlike the situation at Lajitas, we would expect to observe wind
induced noise at NORSAR only when the wind speed was fairly high,
say above about 5 m/sec. Studies are now underway to determine the
wind-induced noise levels at Lajitas as a function of time over a
two month period, and to predict the fall-off of wind-induced
seismic noise in bore-holes to depths of 2000 feet.

The studies of relative coupling of seismometers to the earth
in boreholes and vaults are still underway. Preliminary results
indicate that to frequencies of about 30 Hz, all systems seem to

couple about as well as the S-750 grouted into the limestone.
Above 40 Hz, however, significant difference in coupling have been
observed.

In February, a series of Vibroseis experiments were carried
out at the Lajitas station. Vibrator sites were located to the
northeast of the station at distances from about 1 to 90 km. (see
Table 1). Sweeps were from 50 Hz down to 5 Hz and from 20 Hz
down to 2 Hz at sites Alpha through Echo. For Foxtrot through
Lima, only the lower frequency sweep was used. The number of sweeps
was 16 at Alpha and Bravo, but was systematically increased with
distance to 128 at Lima. Data were recorded from the systems at
Lajitas station, from two outliner vaults 150 m. north and 150 m.
east of the main pad, and at our remote site located in an abandoned
mine about 5 km. west of the Lajitas station. We are currently
processing the record sections and will use the data to study
relative coupling at the Lajitas site and propagation characteristics
in the general vicinity of the Lajitas station.

LAJITAS SEISMIC STATION

Figure 1

254

Figure 2

255
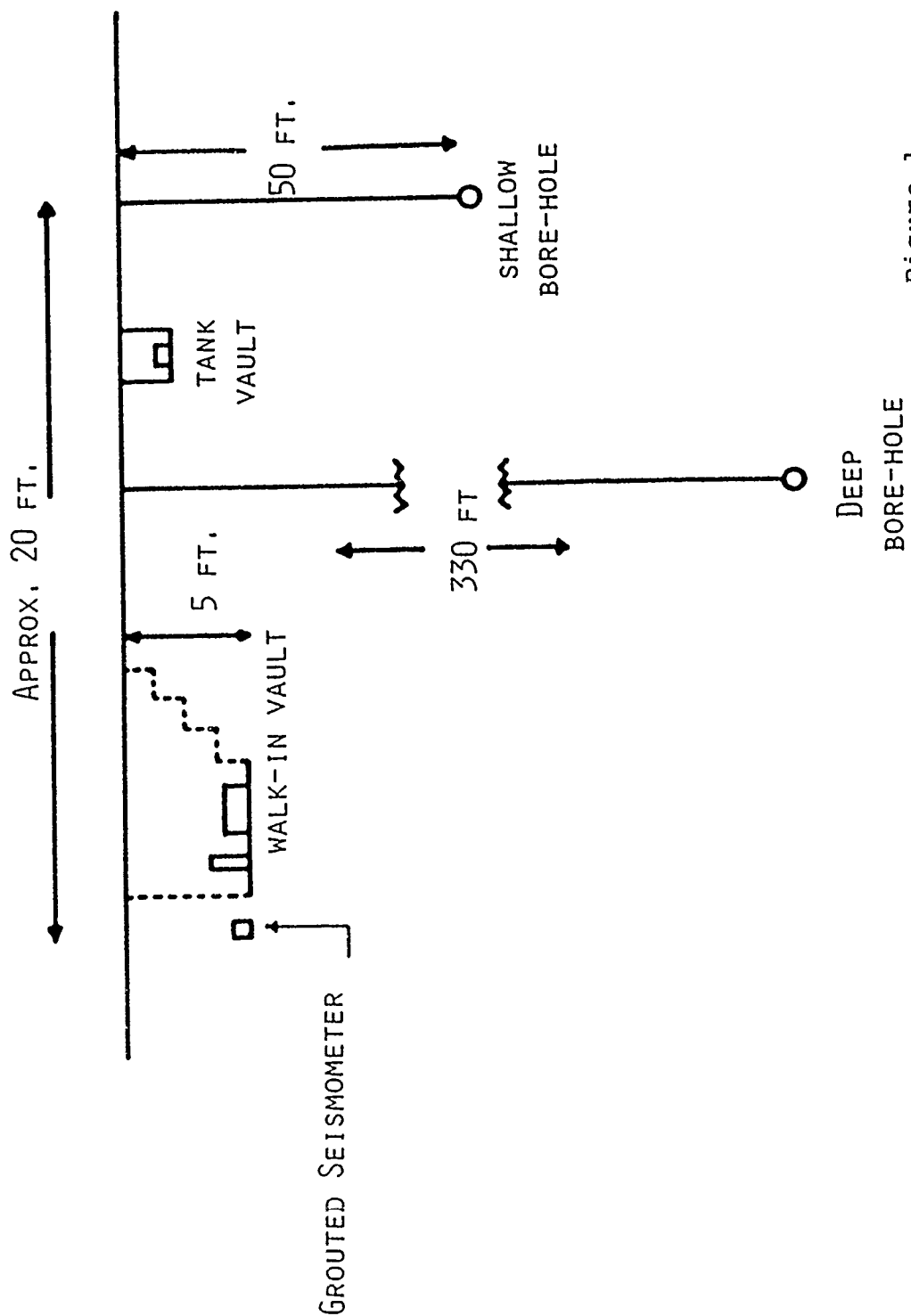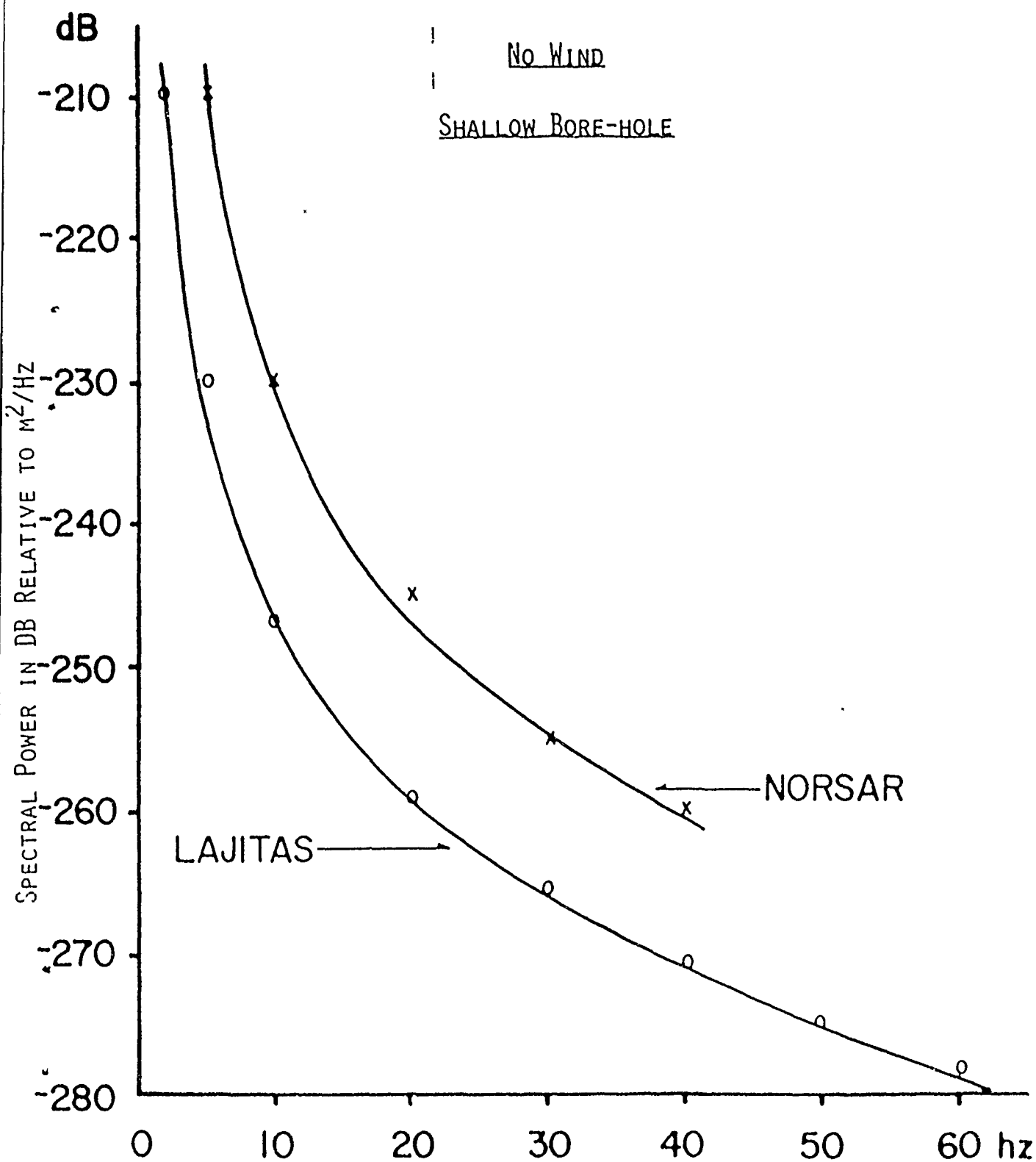
LAJITAS

Ambient Noise Power vs Wind Speed
Shallow Bore-Hole (50ft)

Figure 3

256
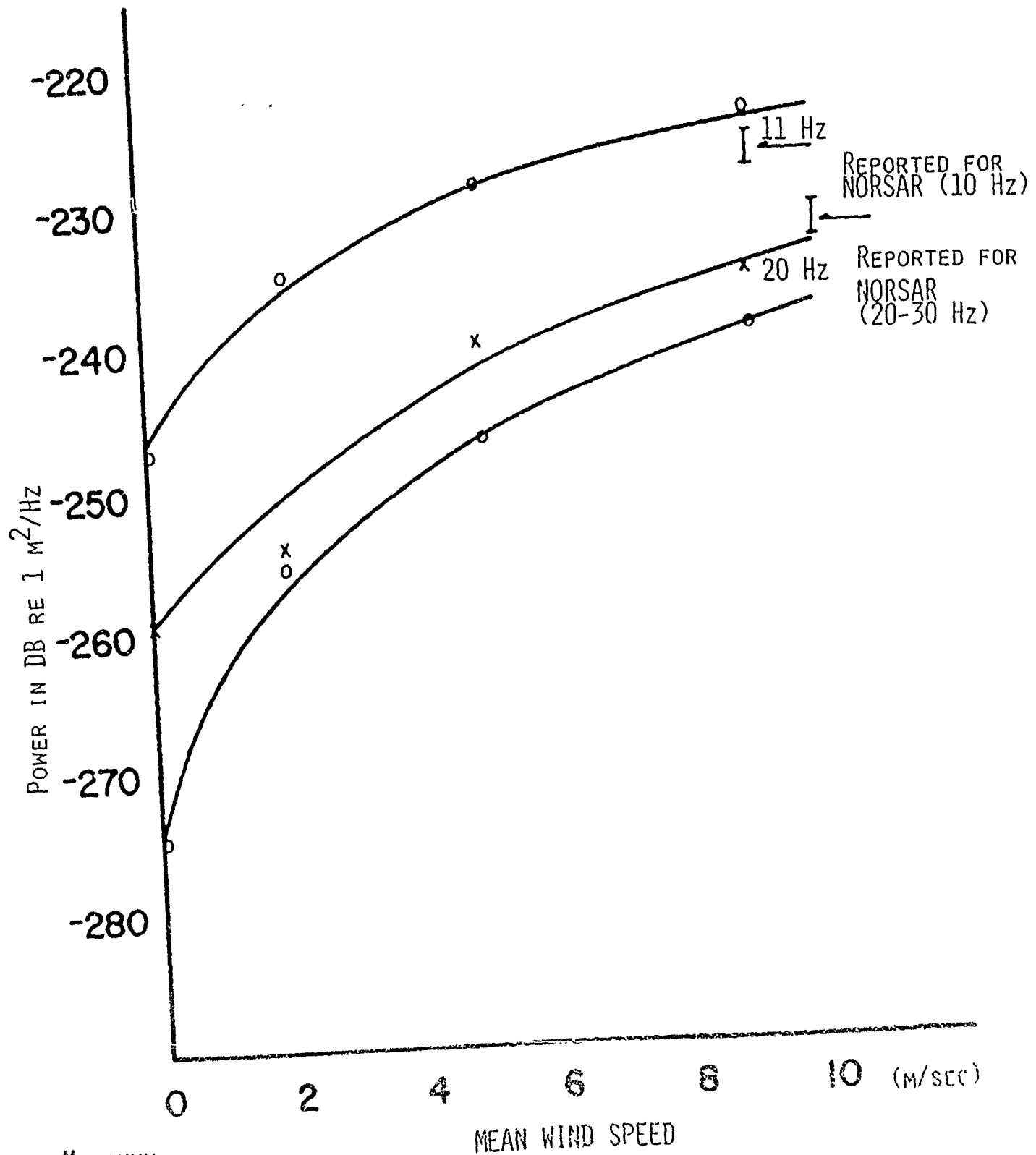
Table 1

Field Notes for Vibrator Sites

Name	Location	Distance from Lajitas (km)	Description
Lajitas Station	29° 20' 02" N 103° 40' 01" W		
Alpha Site	29° 19' 31" N 103° 39' 30" W	1.260 km	On Pepper's road, 0.75 mi. SSE of Lajitas seismic station, just north of intersection of road with draw. Amarilla Mtn. Quad.
Bravo Site	29° 19' 03" N 103° 38' 11" W	3.468 km	On Hwy. 170 at intersection with The Long Draw. Amarilla Mtn. Quad.
Charlie Site	29° 23' 30" N 103° 36' 01" W	9.116 km	On old Terlingua county road, approx. 6 mi. north of Hwy. 170, just south of 3-Bar Ranch fence line and just north of road intersection. Approx. 100 ft. sw of BM G-709 (2717'). Hen Egg Mtn. Quad.
Echo Site	29° 28' 32" N 103° 31' 44" W	20.663 km	On Hwy. 118 near Adobe Walls, 0.67 mi. n. of Adobe Walls at intersection of county road and Hwy. 118. Hen Egg Mtn. Quad
Foxtrot Site	29° 33' 39" N 103° 32' 57" W	27.695 km	On Hwy. 118 near Camel Hump, 0.7 mi. n. of Terlingua Ranch road, just south of Big Bend Baptist Church. Packsaddle Mtn. Quad.
Hotel Site	29° 42' 29" N 103° 34' 25" W	42.523 km	On Hwy. 118 south of Buck Hill, at pullout on top of ridge, 1.95 mi. n. of BM J-708 (3634') Dog Canyon Quad.
Juliet Site	29° 55' 32" N 103° 34' 25" W	66.374 km	On Hwy. 118 at north end of O-2 Flats near Whirlwind Spring, 0.2 mi. n. of BM S-707 (4026'). Whirlwind Spring Quad.
Lima Site	30° 09' 24" N 103° 35' 00' W	91.847 km	On Hwy. 118 at north most roadside park entrance 0.51 mi. north of BM 4736. Mount Ord Quad.

PROPAGATION AND EXCITATION OF REGIONAL PHASES IN WESTERN EUROPE

M. Bouchon*, M. Campillo*, B. Massinon and J. L. Plantet

Propagation of regional phases is strongly dependant on attenuation versus distance, that is to say elastic attenuation due to geometrical spreading and anelastic attenuation.

In a first approach, we have model regional phases by using the Bouchon's method in order to understand the influence of the propagation model on the seismograms built at various distances. This method has the advantage of a full waves method which computes exact seismograms. This theoretical study brings an estimation of the geometrical attenuation with epicentral distance for a Western Europe propagation model : Lg waves attenuate as $D^{-0,83}$, Pg attenuate as $D^{-1,5}$ (D being the distance).

Besides that result we found the excitation of Pg wave insensitive to the depth of the source within the crust while the Lg wave amplitude is 50 per cent higher for a source in the upper and middle crust than in the lower crust. Amplitudes of these two phases drastically decrease when the source is below the Moho which underlines the important role of wave guide played by the crust for the propagation of Pg and Lg.

Taking into account the last results obtained on the attenuation of Lg waves due to geometrical spreading, we made an attempt to compute the anelastic attenuation and consequently the Q factor. The method we have used also leads to the evaluation of the source spectrum of the quake and of the station response.

*Laboratoire de Géophysique Interne et Tectonophysique, Université de Grenoble, B. P. 68, 38402 St Martin d'Hères, France.

SEISMIC WAVE PROPAGATION IN A LATERALLY HETEROGENEOUS CRUST

by   Michel Bouchon   and   Michel Campillo

Radiomana,   27 rue Claude Bernard,   75005 PARIS,   FRANCE

Abstract

We extend the discrete wavenumber method to study the propagation of seismic waves in a layered medium having irregular interfaces. The method is valid at any frequency and gives the complete solution for the diffracted wave field. We describe the method and show its great accuracy by comparing the results of calculation with some existing solutions. We then apply the technique to the calculation of synthetic seismograms in an irregularly layered crustal structure. In order to access the effect of a laterally varying crust on regional wave propagation, we study the effect of an irregular Moho on Lg waves. The method is also applicable to study the radiation from a seismic source located in a complex geological structure.

Introduction

We propose in this paper a new method to calculate the diffraction of elastic waves at an irregular boundary (free surface, interface or closed outer surface of an inclusion for instance). The method is based on the discretization of the diffracted wave field in the horizontal wavenumber - frequency domain. It allows the generalization of the discrete wavenumber method (Bouchon and Aki, 1977) to irregularly layered media.

Description of the method

We shall describe the method in the simple case of a plane harmonic SH wave incident on an irregular free surface. We define a two-dimensional cartesian coordinate system (x,z) and denote by $z = \xi(x)$ the equation of the surface s and by $\vec{n}$ the normal to the surface. Assuming unit amplitude,

259

the displacement field can be written in the form

$$V_O(x,z) = e^{i\gamma_O z} e^{-ik_O x} \tag{1}$$

with $\quad k_O{}^2 + \gamma{}^2_O = \omega^2/\beta^2$ and $Im(\gamma_O)<0$

where β is the shear wave velocity, ω denotes the angular frequency of the excitation and where the $e^{i\omega t}$ time dependence is understood.

The resulting incident stress along the surface is:

$$\sigma_O(s) = \mu[n_x \frac{\partial V_O}{\partial x} + n_z \frac{\partial V_O}{\partial z}] = i\mu[-n_x k_O + n_z \gamma_O] e^{i\gamma_O \xi(x) - ik_O x} \tag{2}$$

where μ denotes the medium rigidity.

The proposed method consists in finding the force distribution along the surface which cancels the incident stress. Let us denote by Q(s) this distribution. Following Lamb's derivation , the displacement field produced at (x,z) by the line force $Q(s_O)$ acting in the direction normal to the (x,z) plane and applied at $s_O = (x_O, \xi(x_O))$ can be written

$$v(x,z;s_O) = \frac{Q(s_O)}{4\pi i\mu} \int_{-\infty}^{\infty} \frac{e^{-i\gamma|z-\xi(x_O)|} e^{-ik(x-x_O)} dk}{\gamma} \tag{3}$$

with $\quad k^2 + \gamma^2 = \omega^2/\beta^2 \quad$ and $\quad Im(\gamma) < 0$

A simple way to evaluate the integral is to introduce a periodicity in the surface shape, that is

$$\xi(x+nL) = \xi(x)$$

where L denotes the periodicity interval and n is any integer. The force distribution thus also obeys this periodicity and the intergration over the horizontal wavenumber in equation (3) is replaced by the discrete summation

$$V(x,z;s_O) = \frac{Q(s_O)}{2i\mu L} \sum_{n=-\infty}^{\infty} \frac{e^{-i\gamma_n|z-\xi(x_O)|}e^{-ik_n(x-x_O)}}{\gamma_n} \qquad (4)$$

with $\quad k_n = \frac{2\pi n}{L}, \quad k^2_n + \gamma^2_n = \omega^2/\beta^2 \quad$ and $\quad \mathrm{Im}(\gamma_n) < 0$

The displacement field produced by the total force distribution is therefore

$$V(x,z) = \int_{-L/2}^{L/2} v(x,z;s_O)dx_O \qquad (5)$$

that is

$$V(x,z) = \frac{1}{2i\mu L} \sum_{n=-\infty}^{\infty} \int_{-L/2}^{L/2} Q(s_O) \frac{e^{-i\gamma_n|z-\xi(x_O)|}e^{-ik_n(x-x_O)}}{\gamma_n} dx_O \qquad (6)$$

In order to evaluate this expression, we discretize the surface into 2M+1 points located at equal Δx interval. It comes

$$V(x,z) = \frac{1}{2i\mu N} \sum_{n=-\infty}^{\infty} \sum_{m=-M}^{M} Q_m \frac{e^{-i\gamma_n|z-\zeta(x_m)|}e^{-ik_n(x-x_m)}}{\gamma_n} \qquad (7)$$

with $\quad N = 2M+1 \quad$ and $\quad x_m = m\Delta x$

The discrete Fourier transform of equation (7) over the x-coordinate can be written

$$\hat{V}(k_p,z) = \frac{1}{N} \sum_{j=-M}^{M} V(x_j,z) e^{ik_p x_j}$$

$$= \frac{1}{2i\mu N^2} \sum_{n=-\infty}^{\infty} \sum_{m=-M}^{M} Q_m \frac{e^{-i\gamma_n|z-\zeta(m\Delta x)|}}{\gamma_n} e^{i\frac{2\pi}{N}nm} \sum_{j=-M}^{M} e^{i\frac{2\pi}{N}(p-n)j} \qquad (8)$$

where

$$\sum_{j=-M}^{M} e^{i\frac{2\pi}{N}(p-n)j} = \begin{cases} N & \text{for} \quad n=p \\ 0 & \text{for} \quad n\neq p \end{cases}$$

and therefore

$$\hat{V}(k_p,z) = \frac{1}{2i\mu N} \sum_{m=-M}^{M} Q_m \frac{e^{-i\gamma_p|z-\zeta(m\Delta x)|}}{\gamma_p} e^{i\frac{2\pi}{N}pm} \tag{9}$$

Taking the inverse discrete Fourier transform of equation (9), we finally get

$$V(x_j,z) = \sum_{p=-M}^{M} \hat{V}(k_p,z) e^{-i\frac{2\pi}{N}pj}$$

$$= \frac{1}{2i\mu N} \sum_{m=-M}^{M} Q_m \sum_{p=-M}^{M} \frac{e^{-i\gamma_p|z-\zeta(m\Delta x)|}}{\gamma_p} e^{-i\frac{2\pi}{N}pj} e^{i\frac{2\pi}{N}pm} \tag{10}$$

from which the resulting surface stress at the sampling points is readily obtained. This equation thus provides a simple relation between the surface force distribution Q_m and the resulting surface stress.

The force distribution which cancels the stress produced by the incident wave field along the surface can therefore be obtained by inverting the linear system of equations deduced from equation (10).

We can restrict the source distribution to the region of the irregularity by using half-space Green's functions instead of the full space solution of equation (3).

The method can be applied as well to P-SV problems and to irregular layering.

Test of accuracy of the method

In order to show the accuracy of the method we compare the results obtained with a finite difference solution. The problem considered is the diffraction of a P wave obliquely incident on a two-dimensional crack. Fehler and Aki (1978) have used a finite difference scheme to solve this problem and compute the resulting scattered wave field. Their solution shown in Figure 1B gives the particle motion at various locations for a P wave incident at 45° from the crack surface and having a wavelength equal to 3.46 times the crack length. The Poisson ratio is 0.25. Using these parameters we obtain a good agreement with Fehler and Aki's results (Figure 1A). The receiver locations used in the two solutions may differ slightly from one another so a better match should not be expected.

The method is also applicable to the case where the source of the elastic disturbance is located near the diffracting irregularity. To solve this problem we take advantage of the source - medium periodicity that we have introduced earlier. This allows the decomposition of the source wave field into a discrete set of homogeneous and inhomogeneous plane waves (Bouchon and Aki, 1977). Such an example of calculation is shown in Figure 2. The source is an explosion located near a crack and the results show the complete resulting seismic motion at various locations.

Application to Lg wave propagation in a laterally heterogeneous crust

We now apply the method to the simulation of regional wave propagation in an irregularly layered crust. The crustal model, chosen to investigate the effect of a bump in the Moho, and the receiver locations

are depicted in Figure 3. The source is located at a depth of 10 km

on the side of the Moho anomaly opposite the receiver array. Five source

locations ranging from 200 km to 0 km with respect to the top of the bump

are considered. Only SH waves are taken into account in the calculation.

The results are presented in Figure 4 (top) where they are compared with

the flat layers solution (bottom). Beyond the shortest distances, the

Lg wave train dominates the seismograms. In presence of the Moho anomaly

the Lg wave amplitude decay is less smooth than in the flat layers case

and sudden changes in amplitude can occur over short distances.

The difference of the two solutions is displayed in Figure 5 (bottom).

It shows that at the early times the two sets of results are identical.

At the short source - receiver distances, the arrivals on the difference

seismograms can be identified as the Moho reflections.

Conclusion

We have developped a new method of calculation to study the propa-

gation of seismic waves in irregularly layered media. The method is

applicable to near-field and regional wave propagation. It yields a com-

plete solution and is valid at any frequency. Its application to the

simulation of Lg wave propagation that we have begun in this paper is

promising.

References

Bouchon, M., and K. Aki, Discrete wave number representation of seismic
source wave fields, Bull. Seism. Soc. Am., 67, 259-277, 1977.

Fehler, M., and K. Aki, Numerical study of diffraction of plane elastic
waves by a finite crack with application to the location of a magma
lens, Bull. Seism. Soc. Am., 68, 573-598, 1978.

Figure 1. Comparison between the discrete wavenumber solution (A) and Fehler and Aki (1978)'s finite difference result (B) for the diffraction of a plane harmonic P wave by a crack.

INCIDENT
WAVE
WAVELENGTH = 3.46
TIMES CRACKLENGTH

TRANSVERSE

RADIAL

Crack

✳ Explosion
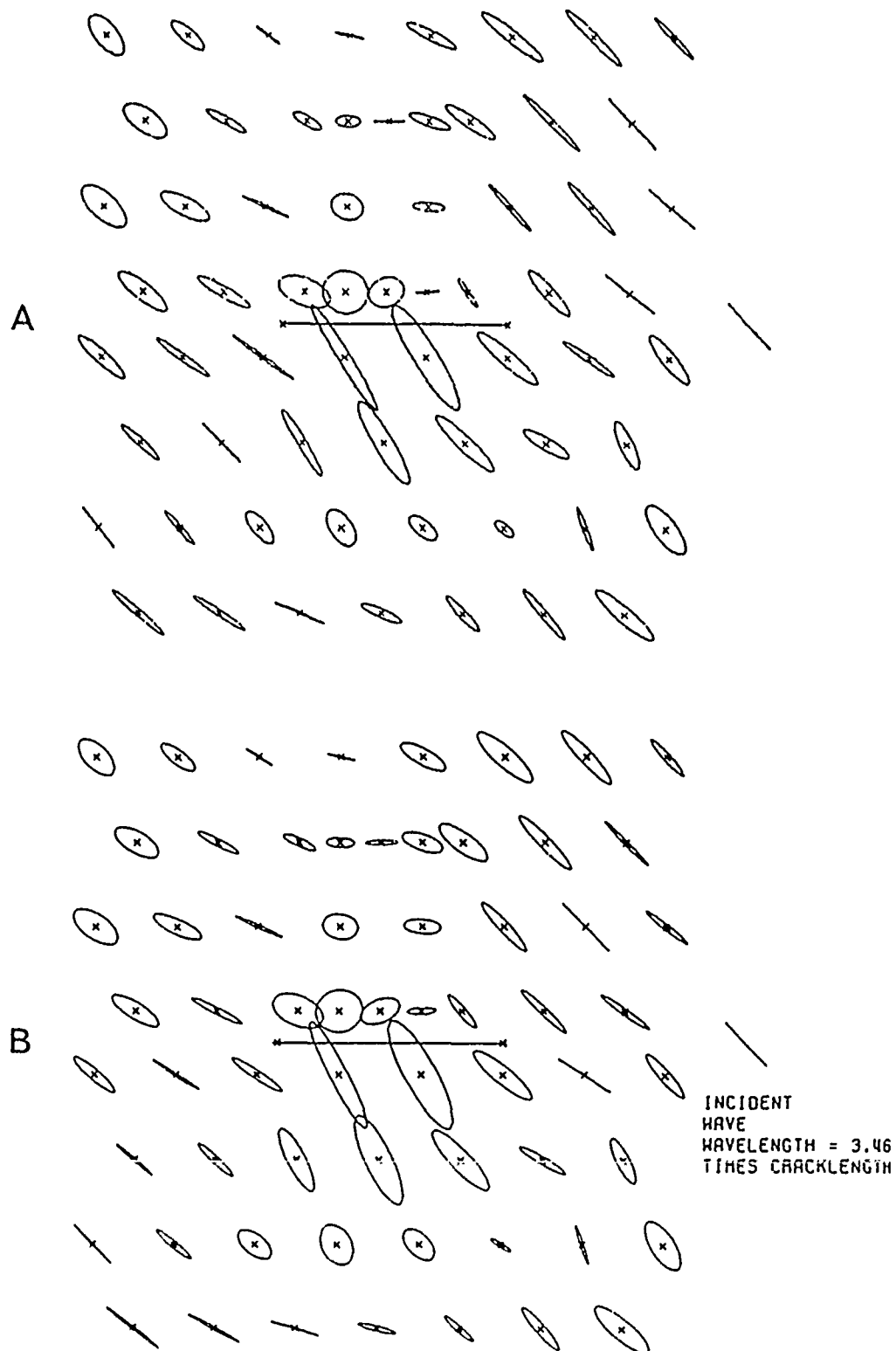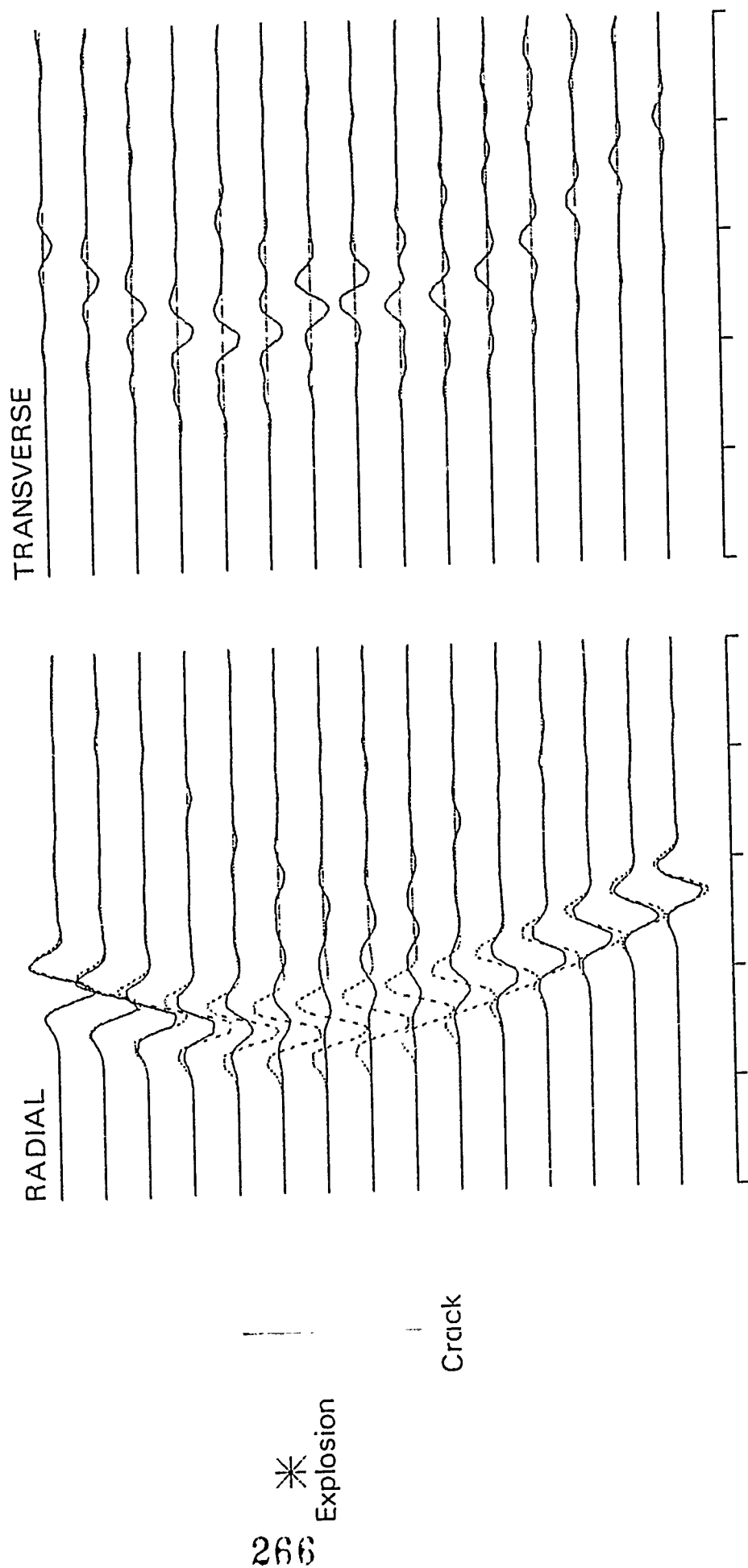
Figure 2. Radial and transverse displacement for the configuration depicted at the left of the figure. The receivers are located at the start of the radial traces. The displacements in the absence of the crack are shown by dotted lines.
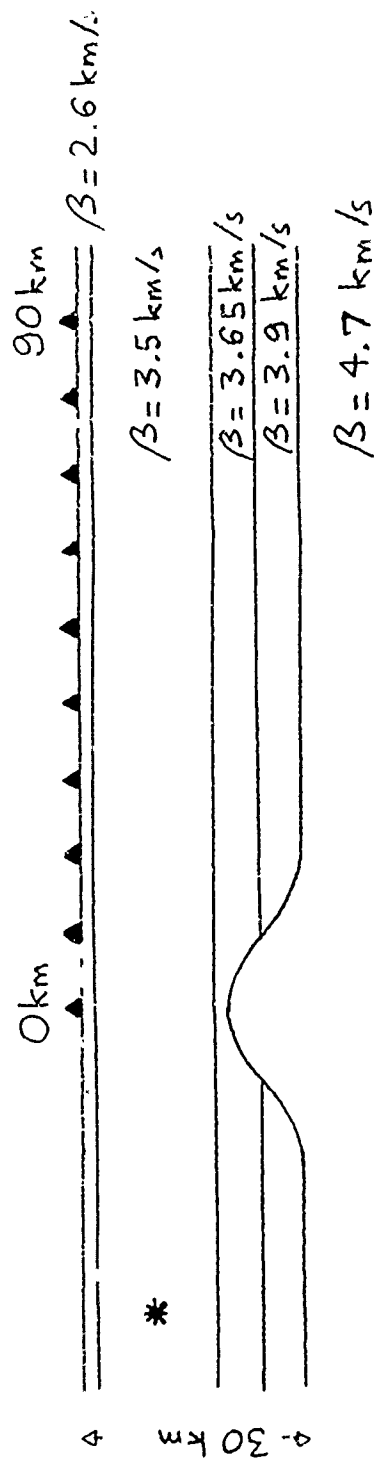
Figure 3. Crustal model and configuration used.
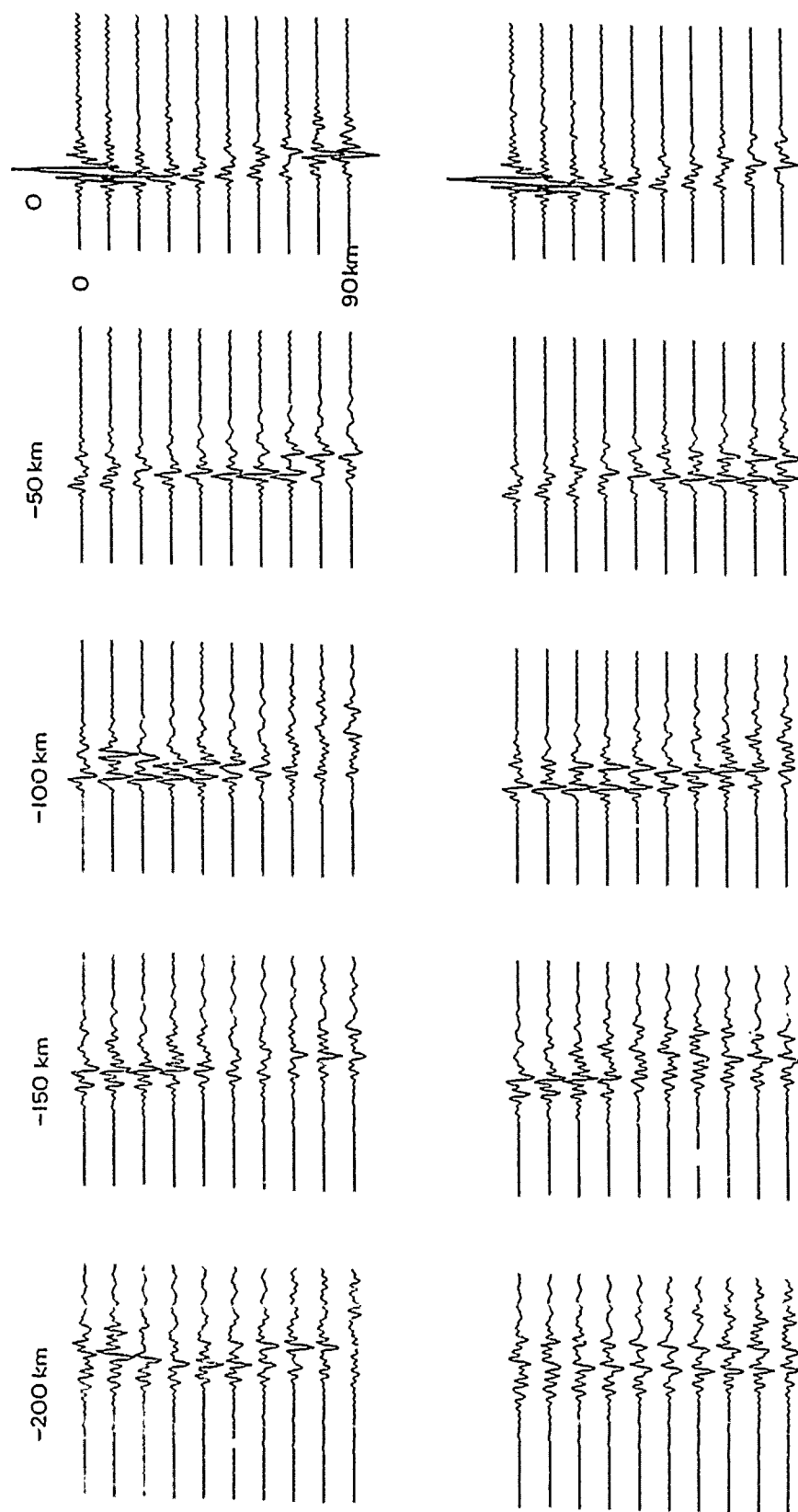
Figure 4. Top : Surface displacements obtained for the configuration of Figure 3

Bottom: Surface displacements in the case of a flat Moho.
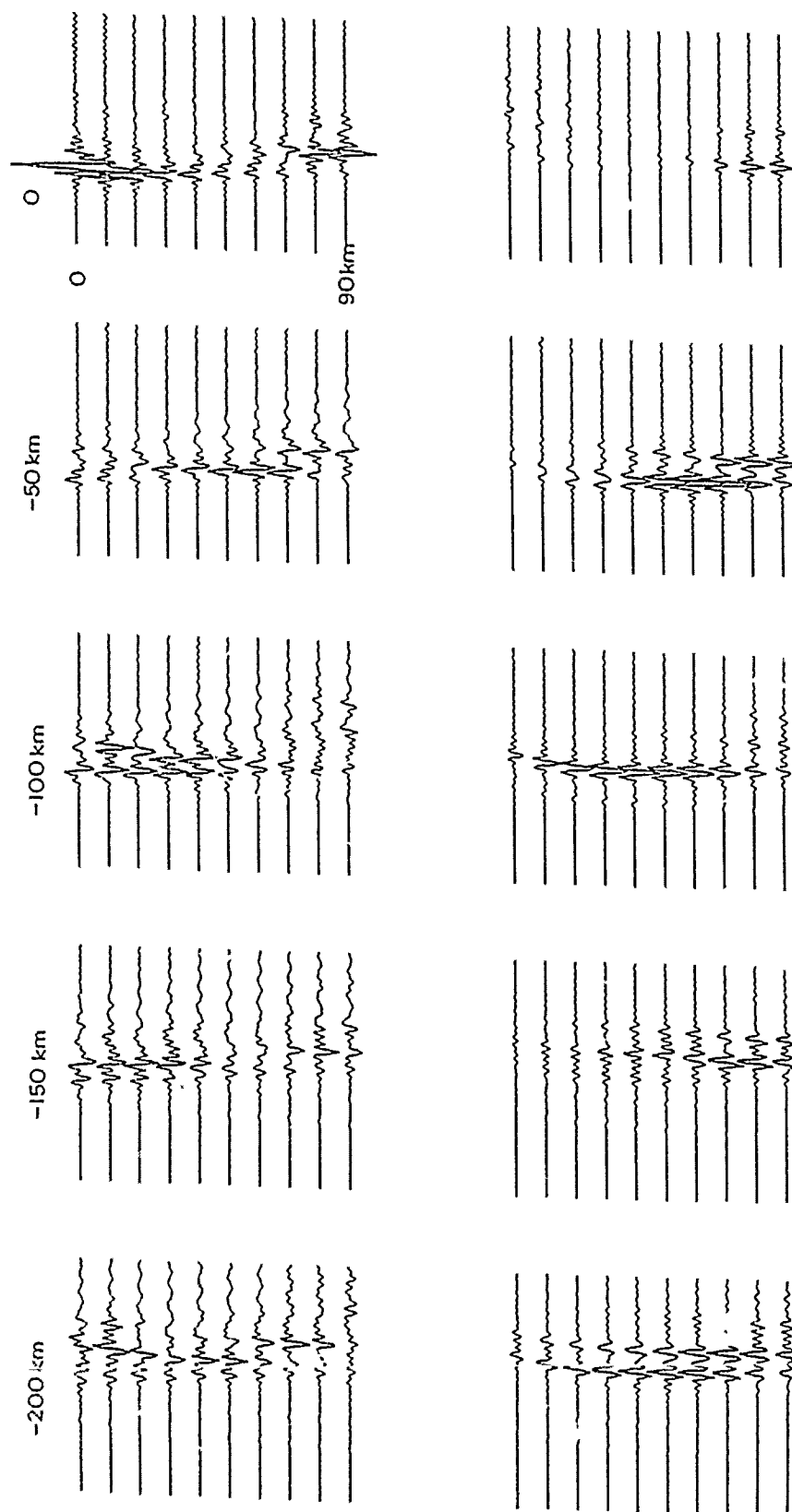
Figure 5. Top : Surface displacements obtained for the configuration of Figure 3.

Bottom: Difference displacements.

269

PAPER TITLE:

Inversion of Explosion-Generated Rayleigh Waves for Shear Velocity, Q and Moment

PAPER AUTHOR:

Jeffry L. Stevens

CONTRACT NO:

F19628-85-C-0045

SUMMARY:

Rayleigh waves from underground nuclear explosions are used to estimate scalar moments for Nevada Test Site (NTS) explosions and explosions at the Soviet East Kazakh test site. The Rayleigh wave spectrum is written as a product of functions that depend on the elastic structure of the travel path, the elastic structure of the source region and the Q structure of the path. We use our results to examine the worldwide variability of each factor and the resulting variability of surface wave amplitudes. The path elastic structure and Q structure are found by inversion of Rayleigh wave phase and group velocities and spectral amplitudes. The Green's function derived from this structure is used to estimate the moments of explosions observed along the same path.

CONCLUSIONS AND RECOMMENDATIONS:

This procedure produces more consistent amplitude estimates than conventional magnitude measurements. Network scatter in log moment is typically 0.1. In contrast with time domain amplitudes the elastic structure of the travel path causes little variability in spectral amplitudes. When the mantle Q is constrained to a value of approximately 100 at depths greater than 120 km the inversion for Q and moment produces moments that remain constant with distance. Based on the best models available, surface waves from NTS explosions should be larger than surface waves from East Kazakh explosions with the same moment. Estimated scalar moments for the largest East Kazakh explosions since 1976 are smaller than the estimated moments for the largest NTS explosions for the same time period. This contrasts dramatically with m_b values for the same events which show the opposite behavior.

I. OBJECTIVES AND THEORY

Accurate and unbiased surface wave measurements are required if surface waves are to be used for treaty monitoring purposes. Conventional time domain M_s measurements provide a rough estimate of the size of the seismic source. Differences in travel path, however, cause variations in M_s that are unacceptable in cases where 0.1 magnitude unit may be important. We describe a method for obtaining more stable and reliable surface wave measurements by using all of the information contained in the surface wave to estimate the Green's function for the path.

Figure 1 illustrates the difficulty in measuring surface wave amplitudes using standard methods. The top figure is a Rayleigh wave from an NTS explosion recorded at Station GOL, at a distance of 977 km. At this close distance many frequencies arrive at the same time, so that the seismogram is dominated by the Airy phase. Measuring the spectral amplitude instead of the seismogram removes this problem, however, the amplitude depends strongly on the frequency measured, changing by a factor of 2 between 0.035 Hz and 0.05 Hz, and by a factor of 5 between 0.02 Hz and 0.05 Hz. Figure 2 shows the amplitude and phase of the spectrum after the path correction has been applied. Notice that in addition to correcting for path effects, the path correction is also a frequency correction, flattening the spectrum over the frequency band of interest.

Our objective is to find the Green's function for a given source to receiver path which can be used to determine the explosion moment. Our approach to the problem has been to assume that the average path structure can be adequately modeled by a plane-layered, attenuating elastic medium. Since the explosions are located in a common source region, but the Rayleigh waves travel along different paths, we also use an approximation which allows us to separate the spectrum into source region and path dependent functions. This
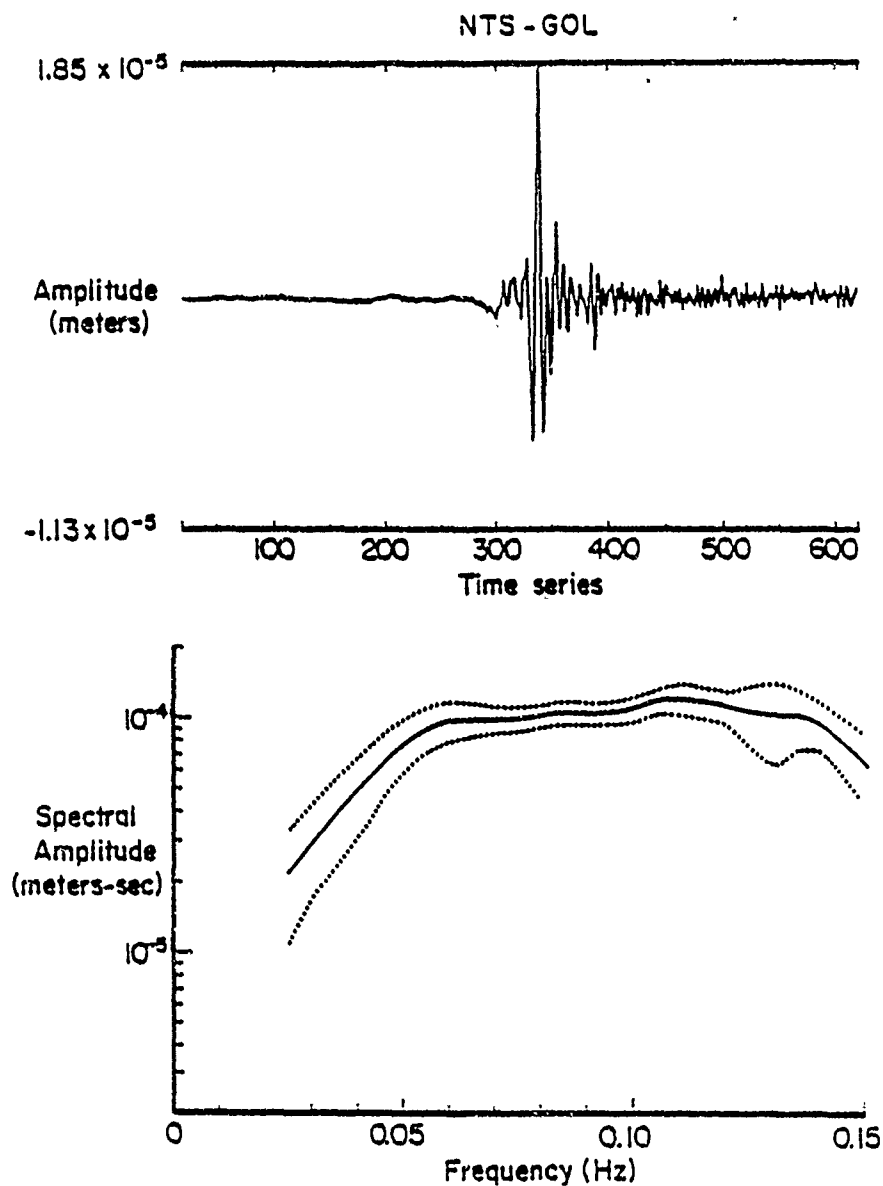
Seismogram and spectrum, NTS-GOL

Figure 1. This figure illustrates the difficulty in measuring surface wave amplitudes using standard methods. The top figure is a Rayleigh wave from the NTS explosion SANDREEF recorded at Station GOL. The seismogram is dominated by the Airy phase, so a reliable 20 second amplitude cannot be measured. The lower figure shows the average spectrum (solid line) and ± 1 standard deviation (dotted line) for 24 spectra at Station GOL. The amplitude depends strongly on the frequency measured.
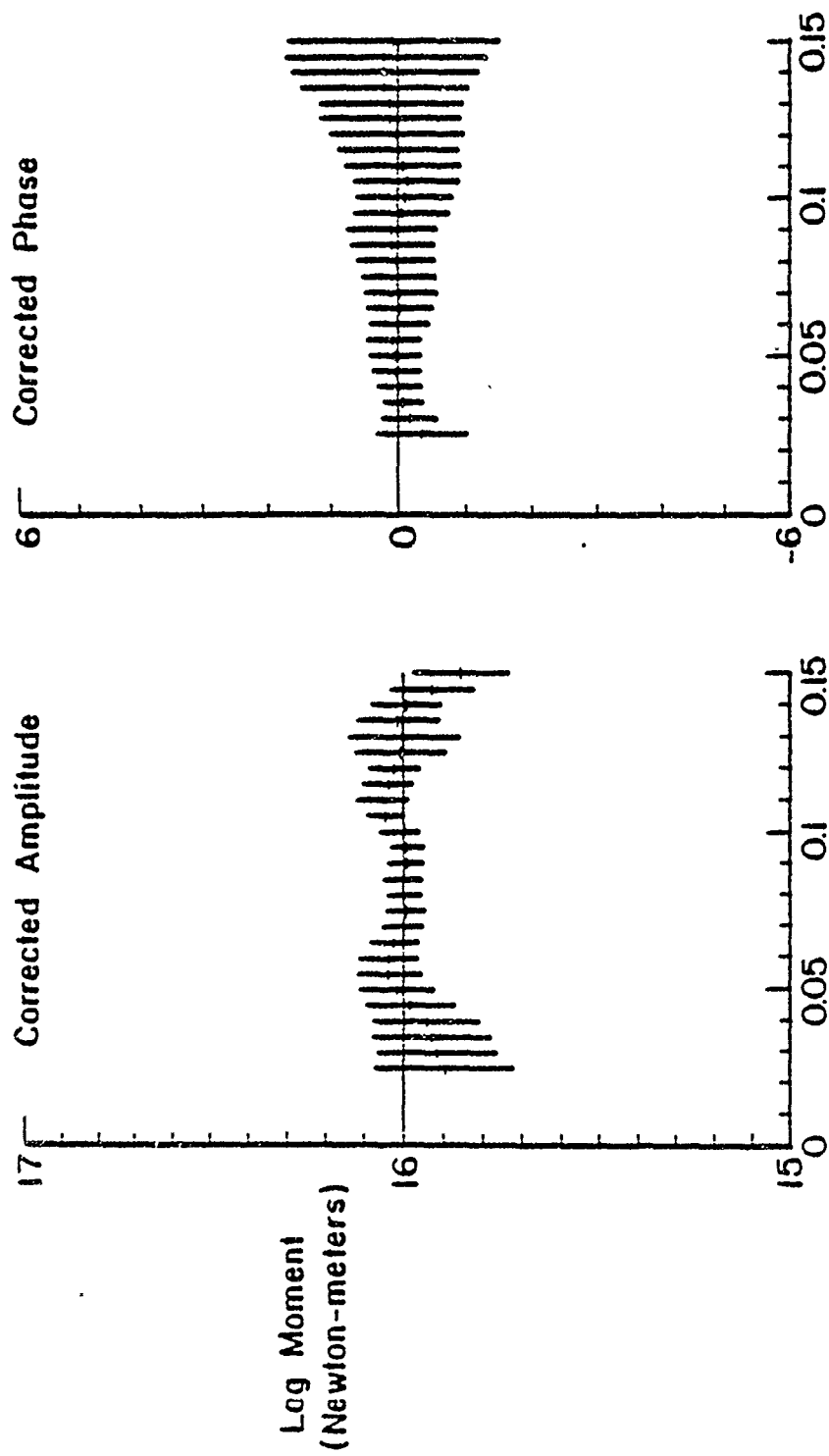
Figure 2. Path corrected amplitude and phase for the path NTS-GOL. The variation in amplitude with frequency is greatly reduced. The phase correction can be used to determine phase shifts (such as Rayleigh wave reversals) between events.

approximation assumes energy conservation and no mode conversion when a Rayleigh wave crosses a boundary between adjacent plane-layered structures.

The vertical component of the Rayleigh wave can be written:

$$u(\omega,r) = M_0 \, S_1(\omega) S_2(\omega) \exp(-\gamma_2 r) / \sqrt{a_e \sin(r/a_e)} \, \exp\left[i\left(\phi_0 - \omega r / c_2\right)\right] \quad (1)$$

where M_0 is the explosion moment, r is the source to receiver distance, a_e is the radius of the earth, c_2 is the frequency dependent phase velocity for the path structure, γ_2 is the frequency dependent attenuation coefficient due to the anelastic structure of the path, and ϕ_0 is the initial phase. $S_1(\omega)$ and $S_2(\omega)$ are real, positive functions that depend on the earth structure of the source region and path respectively.

II. DATA ANALYSIS AND INVERSION PROCEDURE

A block diagram of the method used for the data processing is shown in Figure 3. We start by finding a set of Rayleigh wave seismograms from a given source region and recorded at the same station which show consistent signals and have good signal-to-noise ratios. We then find the phase velocities, group velocities and amplitude spectra for each of these seismograms using narrow band filtering and phase matched filtering. We average the phase and group velocities and spectral amplitudes for the selected seismograms. This averaging serves three functions — it smooths the data, reduces the chance of error from inaccurate times or locations, and provides standard deviations on the data which are used as weights by the inversion code.

The shear velocity structure is found by simultaneously inverting the phase and group velocities. The inversion program
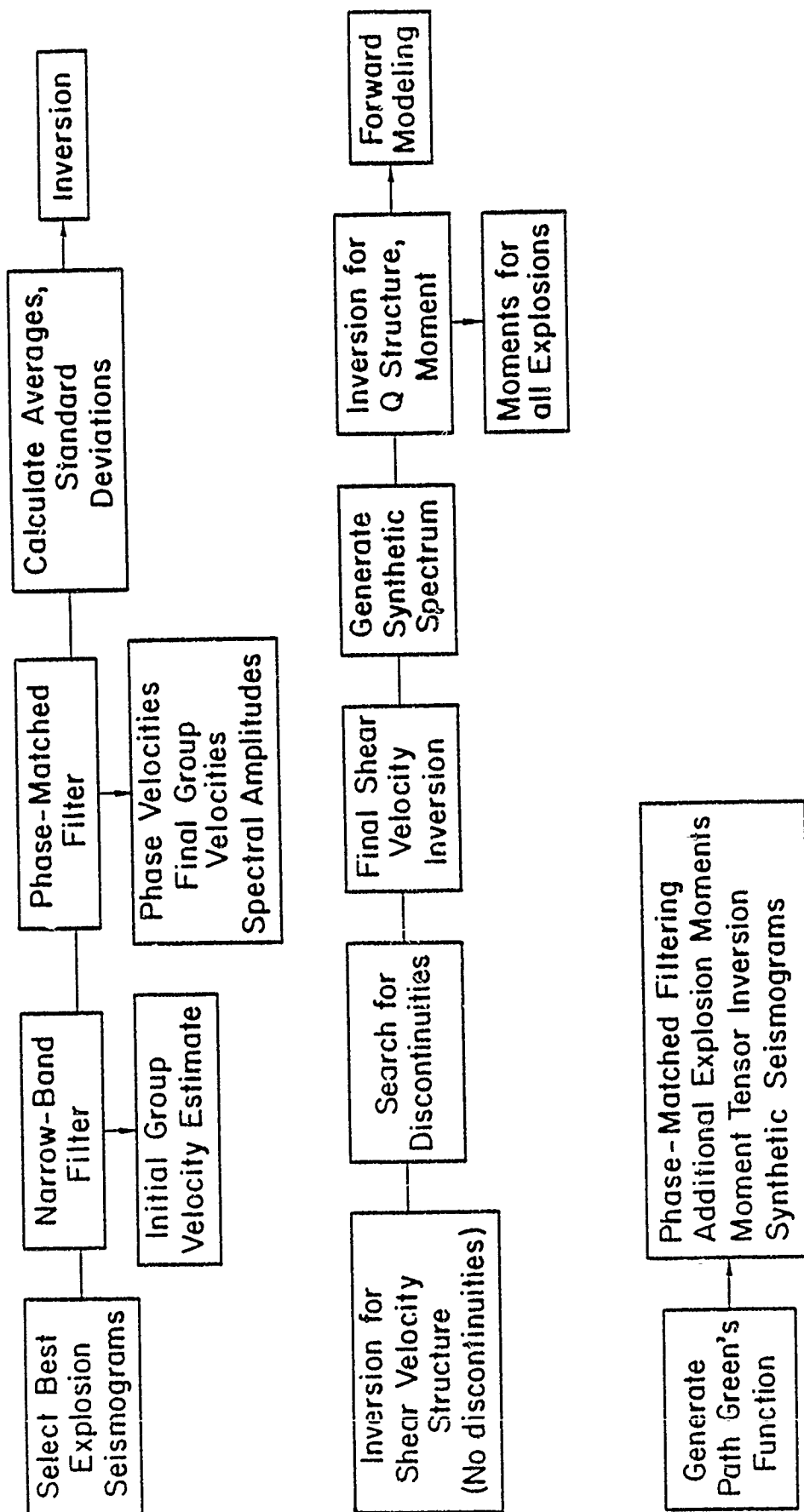
Figure 3. Block diagram of surface wave analysis procedure.

attempts to fit the data with a smooth model by minimizing the integral of $|d\beta/dz|$ over the structure, except across discontinuities at depths specified by the user. Discontinuities in the structure are explicitly allowed at the crust-mantle boundary and in some cases at shallower depths to allow for near surface sedimentary layers.

The final step in the inversion procedure is the inversion of the average spectral amplitude for Q and moment. The average spectral amplitude is the linear average of the spectra of the best events recorded for a given path. Once the absolute moment corresponding to the average spectrum is determined, the moments of all the events are determined.

Rewriting Equation (1), we define the data used for the inversion to be the ratio between the synthetic spectral amplitude $S(\omega)$ (for unit moment, without including attenuation) and the observed amplitude spectrum $u(\omega)$:

$$\frac{1}{r} \ln \frac{S_1(\omega) S_2(\omega) / \sqrt{a_e \sin (r/a_e)}}{u(\omega)} = \gamma(\omega) - \frac{1}{r} \ln M_0 . \qquad (2)$$

The attenuation coefficients $\gamma(\omega)$ are then expanded in terms of the Q structure of the path.

In the Q/moment inversion, the amplitude of the spectral ratio in Equation (2) determines the moment, while the shape determines the Q structure. We use a smoothness criterion, as in the inversion for shear velocity structure to damp oscillations in the solution. Since there is some correlation between low velocity zones and low Q zones in the earth, we invert for β/Q, and find the smoothest β/Q structure consistent with the data.

We impose one additional constraint on the Q inversion. Tests on synthetic seismograms show that while the Q inversion procedure accurately reproduces the Q structure of the crust, lower Q zones

beneath the crust are not well resolved. We reduce this problem by including an estimated value for the average mantle Q at depth as a data point. Based on a literature search for mantle Q estimates determined by interstation studies, we used the value $\beta/Q = 40$ ($Q \approx 100$) at depths between 120 and 150 kilometers as a constraint.

III. INVERSION RESULTS

Our main interest here is in the effect of the elastic and Q structures on surface wave amplitudes. In Figure 4, we show the path amplitude functions S_2 calculated using all of the path structures. The elastic structure of the source-to-receiver path has surprisingly little effect on the spectral amplitudes. The maximum variation in $\log (S_2)$ is only 0.15 at 20 seconds. The paths with the largest values of S_2 are the thick crust, low velocity paths, while the smallest values occur along oceanic paths.

These results mean that the surface wave amplitudes are not changed very much by the elastic properties of the travel path. This is, of course, only true for spectral amplitudes. Differences in dispersion can cause large differences in time domain surface wave amplitudes, especially at distances less than 30 degrees. On long or complex paths, when a plane-layered model is not a good approximation, interference will cause more spectral amplitude variation than is predicted by the smooth functions in Figure 4.

To invert for the path Q structures and the explosion moments, we need the excitation function S_1 for the source region structures. Our model for the East Kazakh source region was based on the structure inferred for the path from East Kazakh to station MAIO, modified to be consistent with reflection surveys in the area. The NTS model was derived from the NTS to Tucson crustal structure, with a well constrained structure for Pahute Mesa in the top four kilometers. The main differences between the two models are a thicker crust and higher surface velocity at the East Kazakh test site.
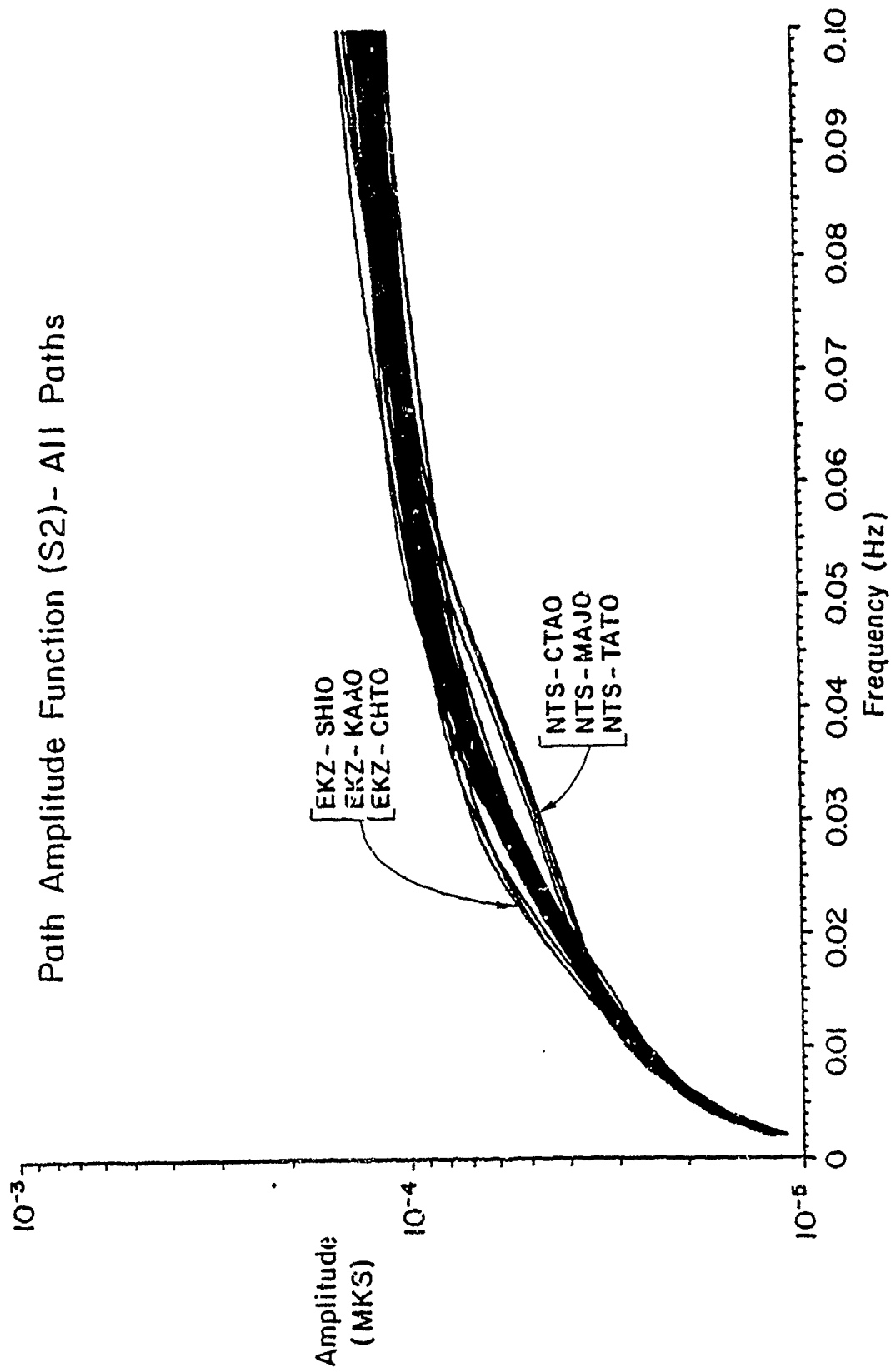
Figure 4. Path amplitude function S_2 for all paths from NTS and East Kazakh.

278

The excitation functions for the two source regions are shown in Figure 5. The excitation function for NTS is greater than the excitation function for East Kazakh at all frequencies of interest, and particularly at higher frequencies. We therefore expect an explosion at NTS to generate larger surface waves than an explosion at East Kazakh with the same moment.

In Figure 6, we show the inferred attenuation coefficients for all paths. Differences in attenuation may be responsible for large amplitude variations. Rayleigh waves observed along paths with attenuation coefficients of 1.0×1.0^{-7}/meters and 3.0×10^{-7}/meters (the $\pm$ one standard deviation values for all paths) will differ by 0.09 magnitude units at 1000 km, 0.43 magnitude units at 5000 km, and 0.87 magnitude units at 10,000 km.

V. ESTIMATED MOMENTS FOR NTS AND EAST KAZAKH EXPLOSIONS

We have estimated explosion moments for a number of NTS explosions and East Kazakh explosions. It is interesting to compare the results for recent events with theoretical explosion models. Since April 1976, underground explosions have been limited to a yield of 150 kilotons by the Threshold Test Ban Treaty. In Figure 7, we show the estimated moments for the largest explosions at NTS and East Kazakh since this date. Using a Mueller-Murphy explosion model, the log moment of a 150 kiloton explosion in a tuff/rhyolite medium should be 16.24. This agrees very well with the upper limit of the recent NTS explosion estimated moments.

A surprising result is the low values of moment estimated for the East Kazakh explosions. None of the explosions has an estimated log moment greater than 16.0. The upper limit of the log moments for East Kazakh is about 0.2 less than the upper limit of log moments for NTS. This contrasts dramatically with the NEIS m_b values for the explosions (also shown in Figure 7). Several of the East Kazakh

Source Region Excitation Functions (S1)
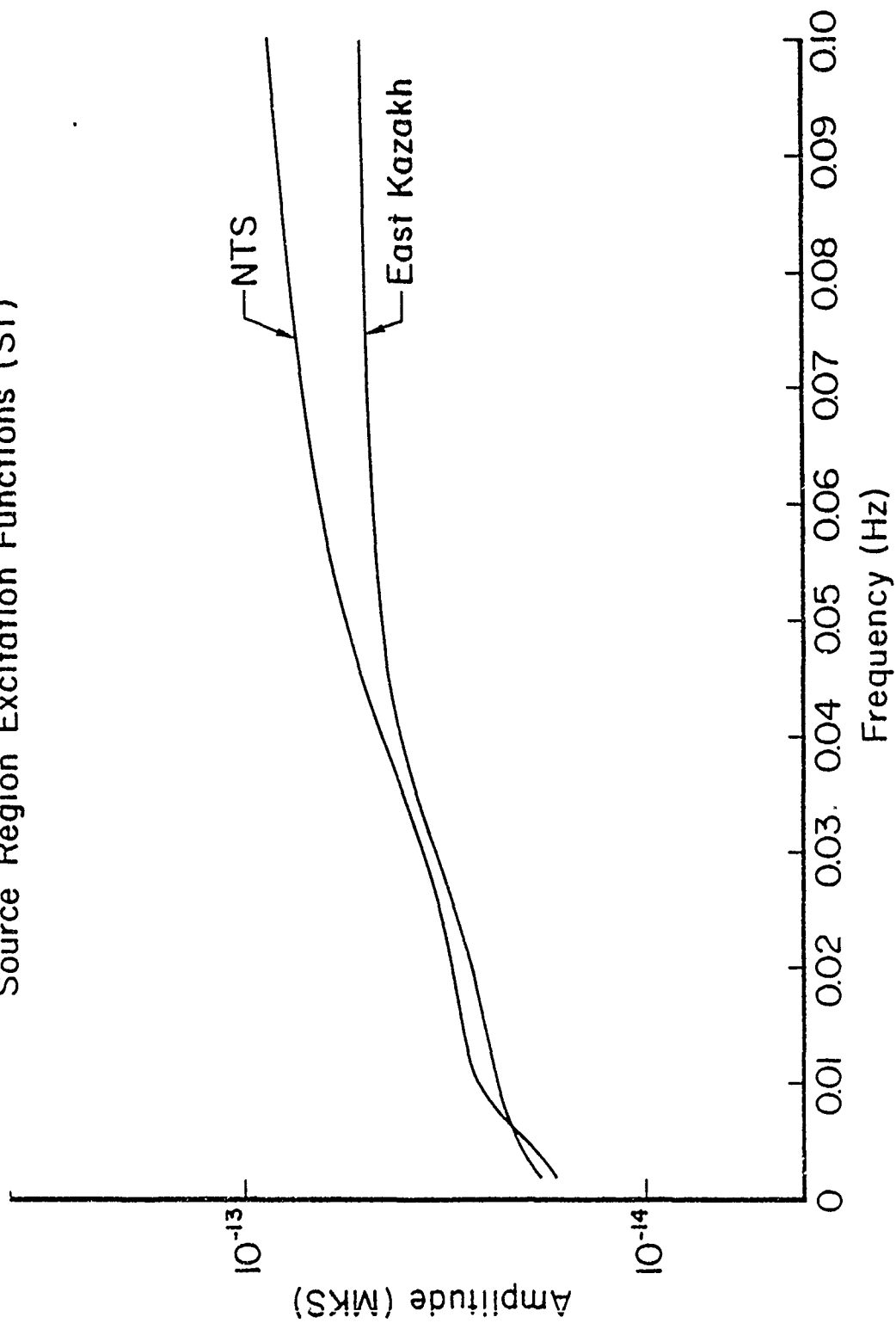
Figure 5. Excitation functions calculated at a depth of 1 km using the NTS structure and the East Kazakh structure.

288
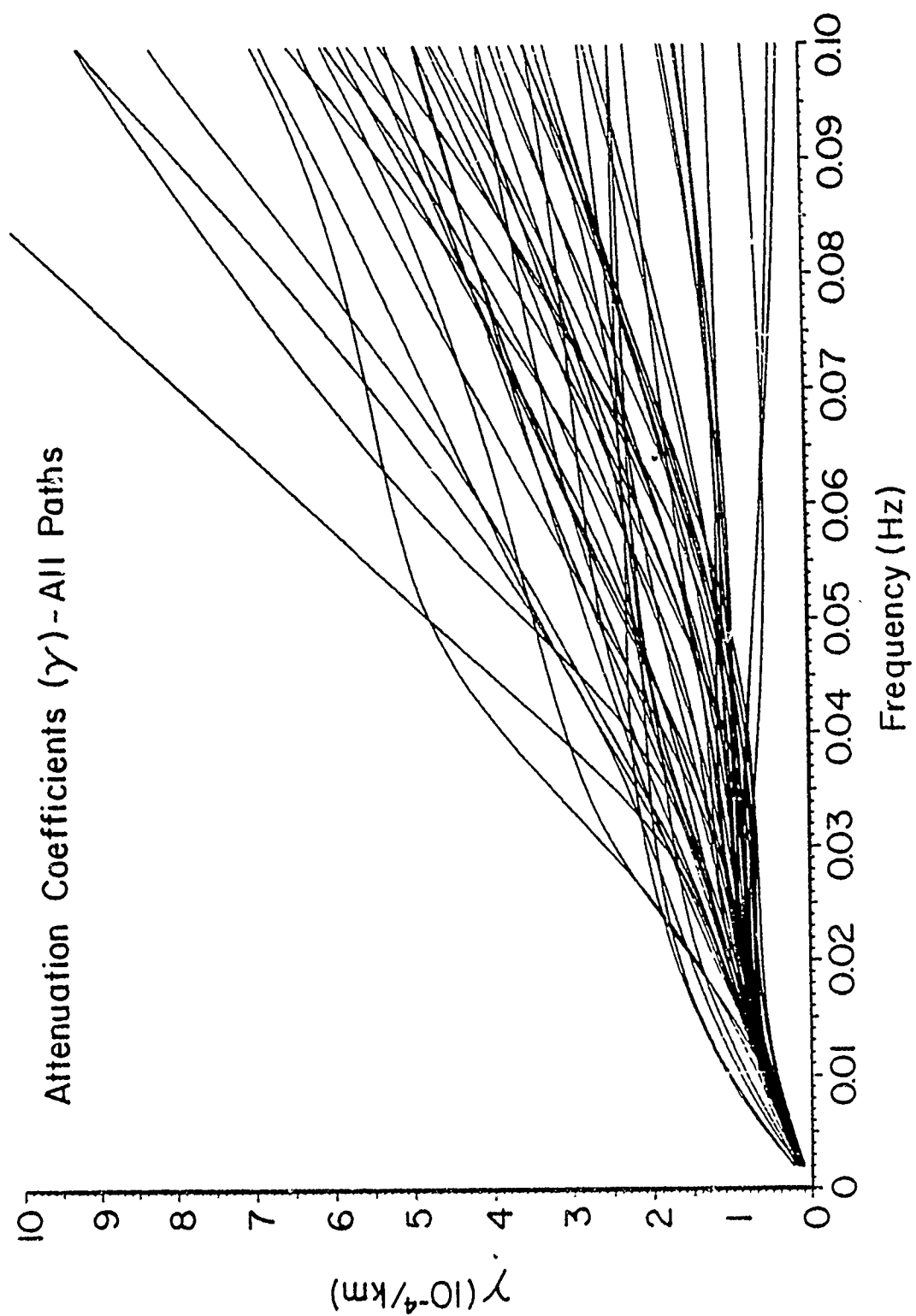
Figure 6.   Attenuation coefficients for all paths from NTS and East Kazakh.

Estimated Moments - Explosions Since 1976

East Kazakh

Event	MB
12/5/82	6.1
4/25/82	6.1
12/27/81	6.2
10/18/81	6.0
9/13/81	6.0
4/22/81	5.9
10/12/80	5.9
9/14/80	6.2
12/23/79	6.1
12/2/79	6.0
10/28/79	6.0
8/18/79	6.1
8/4/79	6.1
6/23/79	6.3
11/29/78	6.0
9/15/78	6.0
6/11/78	5.9
7/4/76	5.8

NTS

Event	MB
TAFI	5.5
KASH	5.6
COLWICK	5.4
PYRAMID	5.3
SHEEPSHEAD	5.6
HEARTS	5.8
PEPATO	5.5
FARM	5.5
RUMMY	5.7
PANIR	5.6
LOWBALL	5.5
ICEBERG	5.6
FARALLONES	5.7
SANDREEF	5.7
MARSILLY	5.6

Log Moment (Newton-Meters), NEIS MB: 16.30, 16.25, 16.20, 16.15, 16.10, 16.05, 16.00, 15.95, 15.90, 15.85, 15.80, 15.75, 15.70, 15.65, 15.60

Figure 7. Estimated moments for the largest NTS and East Kazakh explosions since April 1976.

explosions have m_b greater than 6.1, while none of the NTS explosions has an m_b greater than 5.8. Comparison with theoretical explosion models makes the contrast even larger. It is commonly believed that the source medium at the East Kazakh test site is a hard "granite-like" material, but the log moment for a 150 kiloton Mueller-Murphy explosion in granite is 16.52, more than 0.5 greater than the largest estimated moment at East Kazakh.

Several factors, including tectonic strain release, differences in body wave attenuation, or an unusual source medium could account for these differences. Correction for tectonic strain release could increase the moments of some events to the level of the largest NTS explosions, but could not increase them to the level expected for a 150 kiloton granite source. The East Kazakh explosions are therefore not consistent with a "granite-like" source medium. One possible explanation for the large body waves and small surface waves from East Kazakh explosions would be the presence of a source medium at the test site that resulted in a highly peaked source spectrum with a large amplitude near one Hz and an unusually small long period level.

A good check on the validity of the scalar moments is the variation of the moment estimates as a function of distance. In Figure 8, we show the station residuals for all NTS and East Kazakh paths plotted versus distance. The station residuals are small at close range, approximately 0.1 for most stations less than 5000 kilometers from a test site. The magnitude of the residuals increases with distance, as is to be expected with the increasing complexity of the path at large distances, but the residuals scatter evenly around zero. The lack of any trend in the data suggests that the attenuation correction has been properly estimated with the constraint of $\beta/Q = 40$ between 120 and 150 kilometers depth.
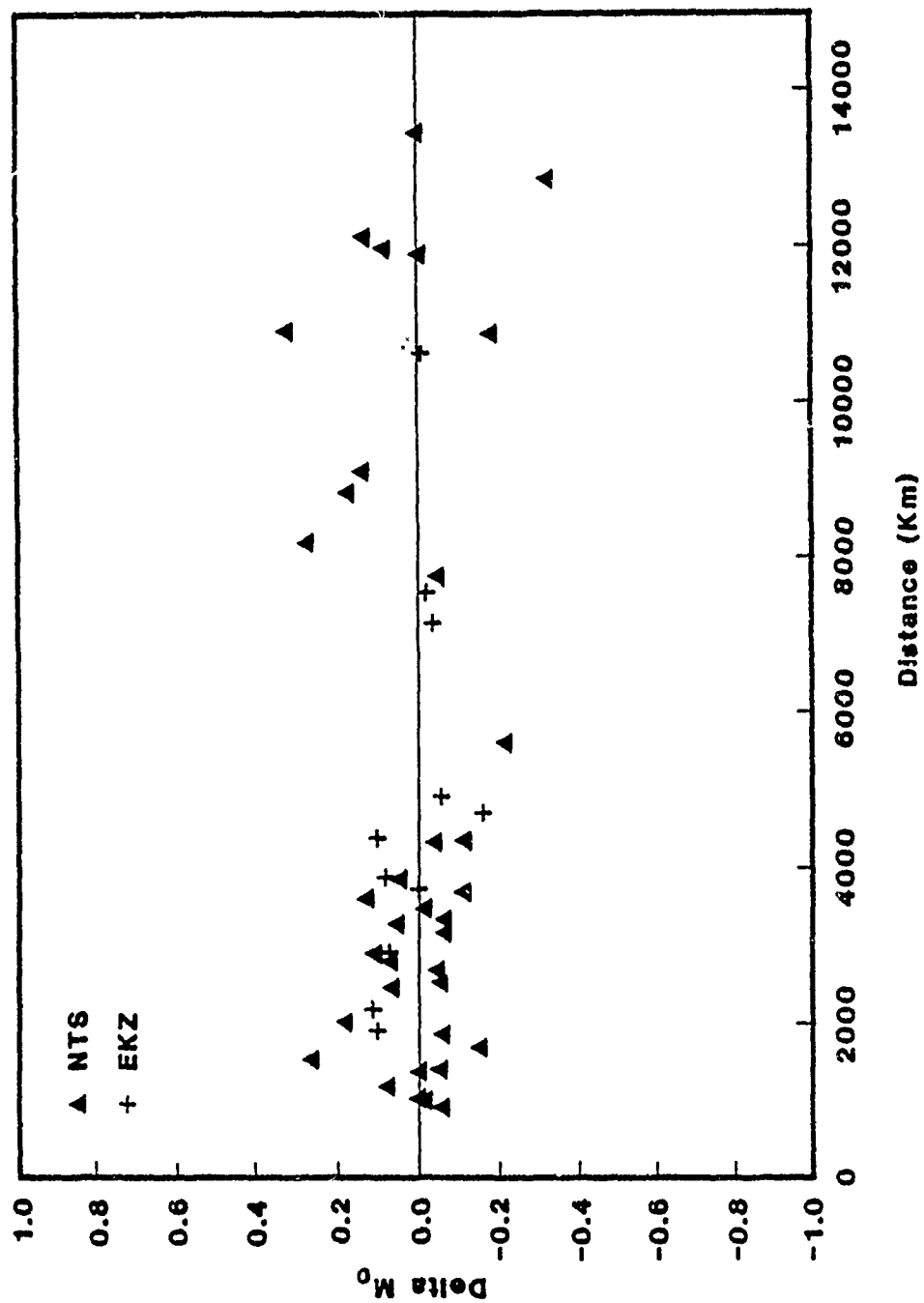
Figure 8. Station residuals with a mantle Q constraint of $\beta/Q = 40$.

TITLE: SOURCE PARAMETERS FOR NUCLEAR EXPLOSIONS
          AT NTS AND SHAGAN RIVER FROM OBSERVATIONS
          OF RAYLEIGH AND LOVE WAVES

AUTHOR: JEFFREY W. GIVEN AND GEORGE R. MELLMAN

CONTRACT NO: F19628-85-C-0028

I.   SUMMARY:

Yield estimates determined from the amplitudes of long period seismic waves are believed to be the most reliable for comparing test sites in different regions (Sykes and Cifuentes, 1984). However, these data are nearly always contaminated by energy radiated from extraneous, nonexplosive sources (e.g. possibly tectonic release). Calculation of the explosion size is dependent on the mechanism of the nonexplosive source, which is difficult to uniquely determine from long period observations. In the following, we describe a study of Love and Rayleigh waves from 16 events at Shagan River in the Soviet Union and 47 events from the Nevada Test Site.

The source parameters of the events were determined using a shallow (1 Km) source model. For a source with step function time history, at periods greater than 17s, the Rayleigh and Love wave radiation patterns, U_R and U_L are

$$U_R\ (\omega, \phi)\quad =\quad P_R^1\ (\omega)\ (S_0 + S_1 \cos 2\phi + S_2 \sin 2\phi) \qquad (1)$$

$$U_L\ (\omega, \phi)\quad =\quad P_L^1\ (\omega)\ (S_1 \sin 2\phi - S_2 \cos 2\phi) \qquad (2)$$

where ω is frequency, ϕ is azimuth, and P_R^1 and P_L^1 are excitation functions. S_0, S_1 and S_2 are related to the source moment tensor elements by

$$S_0 = 1/2 \, (M_{xx} + M_{yy}) - \lambda/(\lambda+2\mu) \, M_{zz}$$
$$S_1 = 1/2 \, (M_{xx} - M_{yy}) \tag{3}$$
$$S_2 = M_{xy}$$

Given estimates of U_R and U_L, Equations 1 and 2 are easily inverted for S_0, S_1 and S_2. The explosion (isotropic) moment is

$$M_I = 1/3 \, (M_{xx} + M_{yy} + M_{zz}) \tag{4}$$

Obviously M_I cannot be constrained from S_0, S_1 and S_2 but determining the necessary moment tensor elements is difficult without very accurate excitation functions and source-receiver path corrections.

U_R and U_L are measured by using phase velocity and attenuation corrections provided by S-Cubed (e.g. Stevens et al 1982). To account for some remaining inaccuracies in the estimates in U_R and U_L, and to correct for variability in the network coverage, additional frequency independent amplitude corrections were necessary. These were derived by simultaneously inverting several events from a single test site for source parameters and station corrections. If U_j^i is the observation at station (i) for the (j) event, then

$$U_j^i = \exp \, (a_i) \, G_{ik} \, S_{jk} \tag{5}$$

where G_{ik} is the excitation function, S_{jk} is S_0, S_1, and S_2 for the j-th event and $\exp \, (a_i)$ is the station correction. Of course, a different correction is used for Love and Rayleigh waves.

The inversion results from Shagan River are presented in Table 1. Figure 1 shows radiation patterns for two events with very different amounts of tectonic release. Explosion moments at Shagan River were estimated by assuming that the nonexplosive source was a thrust fault. Thrust faulting is the only double couple mechanism that can explain observations of reversed polarity Rayleigh waves at all azimuths, (Rygg, 1976; North and Fitch, 1981); we simply assumed that the tectonic release mechanism did not vary from event to event. Figure 2 shows the correlation of log M_l with m_b for Shagan River. With the exception of the event of 23 December 1979, events in the south west part of the test site are remarkably consistent (Figure 3). These events include that on 14 September 1980 (Figure 1) with substantial tectonic release. If we exclude the three anomolously low events then we obtain

$$\text{Log } M_l = m_b + 10.08 \pm 0.10 \text{ (n = 13)} \tag{6}$$

Table 2 gives the results for Pahute Mesa and Yucca Flats. Figure 4 shows two radiation patterns. Following evidence reviewed by Wallace et al (1983) the nonexplosive mechanism at NTS is taken to be strike-slip faulting. Figure 5 shows the correlations of log M_l with m_b provided by J. Murphy (personal communication). At NTS, many events were located in porous rock near the water table. The coupling of explosion energy to seismic wave energy varies substantially in gas-filled, porous rock and is difficult to predict. Therefore, we excluded those events near the water table. The m_b-Log M_l relation for Pahute Mesa is found to be

$$\text{Log } M_l = m_b + 10.65 \pm 0.14 \text{ (n=9)} \tag{7}$$

For Yucca Flats, the relationship is

$$\text{Log } M_l = m_b + 10.37 \pm 0.14 \text{ (n=18)} \tag{8}$$

For all NTS we have

$$\text{Log } M_l = m_b + 10.46 \pm 0.19 \text{ (n=27).} \tag{9}$$

II. CONCLUSIONS AND RECOMMENDATIONS

The Love and Rayleigh wave radiation patterns from nuclear explosions can be explained very well with a simple three parameter source when data are processed with accurate and precise path corrections. The isotropic moment is equivalent to a corrected M_S and can be used to calibrate m_b measurements from different test sites. An event at Shagan River has an m_b that is 0.36 higher than one at NTS with the same M_I.

Variations in m_b-M_I relations at each test site suggest that work be done on data from other test sites to gain further experience. More study is needed to determine the effects of nonexplosive radiation on the short period body waves.

III. REFERENCES

Marshall, P.D., T.C. Bache and R.C. Lilwall, 1984. Body wave magnitudes and locations of Soviet underground explosions at the Semipalatinsle test site, Atomic Weapons Res. Establishment Report 0 16/84.

North, Robert G. and Thomas J. Fitch, 1981, Surface wave generation by underground nuclear explosions, Seismic Discrimination, Semi-annual Technical Summary, March 31, No. ESD-TR-81-84 (Lincoln Laboratory, Mass. Inst. of Tech., Cambridge, Ma), 47-55.

Rygg, E., 1979, Anomalous surface waves from underground explosions, Bull. Seism. Soc. Am, 69, 1995-2000.

Stevens, J.L., W.L. Rodi, J. Wang, B. Shkoller, E.J. Halda, B.F. Mason, J.B. Minster, 1982(b), Surface wave analysis package and Shagan River to SRO station path corrections, S-Cubed Topical Report VSC-TR-82-21.

Sykes, L.R. and I.L. Cifuentes, 1984, Yields of Soviet underground nuclear explosions from seismic surface waves: compliance with the Threshold Test Ban Treaty, Proc. Natl. Acad. Sci. USA, 81, 1922-1925.

Wallace, T., D.V. Helmberger and G.R. Engen, 1983, Evidence of tectonic release from underground nuclear explosives in long-period body waves, Bull. Seis. Soc. Am., 73, 593-613.

TABLE 1
SHAGAN RIVER

	M_I	Log M_I	F	M_{DC}	STRIKE
08-29-78	6.2	0.79	0.68	4.2	318
09-15-78	9.7	0.99	0.29	2.8	326
11-04-78	6.1	0.78	0.63	3.8	319
11-29-78	10.3	1.01	0.33	3.4	331
06-23-79	16.4	1.22	0.39	6.1	325
07-07-79	8.4	0.92	1.37	11.5	323
08-04-79	16.4	1.22	0.34	5.6	318
08-18-79	8.0	0.91	0.84	6.7	320
10-28-79	17.6	1.25	0.37	6.5	341
12-02-79	12.2	1.08	0.16	1.9	324
12-23-79	7.6	0.88	0.32	2.4	323
09-14-80	17.3	1.24	0.66	11.4	318
10-12-80	13.1	1.12	0.29	3.9	330
12-14-80	11.0	1.04	0.38	4.2	320
12-27-80	3.04	0.48	1.31	4.0	322
04-22-81	11.5	1.06	0.27	3.1	376
09-13-81	14.8	1.17	0.34	5.0	317

Units of M_I are 10^{25} N-M

TABLE 2
YUCCA FLATS

		M_I	Log M_I	F	M_{DC}	Strike
CORDUROY	D	12.7	1.11	0.39	4.9	82
DUMONT	D	12.3	1.09	0.40	5.0	85
COMMODORE	D	22.3	1.35	0.28	6.0	94
ZAZA	D	19.5	1.29	0.25	4.4	99
LANPHER	D	7.2	0.85	0.15	1.0	104
NOGGIN	S	10.9	1.04	0.36	3.9	75
CALABASH	S	6.8	0.83	0.40	2.8	91
FLASK	S	3.6	0.55	0.07	0.23	93
TIJERAS	S	10.2	1.01	0.05	0.50	56
CARPETBAG	S	13.4	1.13	0.27	3.6	98
OSCURO	S	11.6	1.07	0.10	1.1	84
STARWORT	S	4.10	0.62	0.07	0.26	61
ESCABOSA	D	15.0	1.18	0.18	2.6	69
PORTMANTEAU	S	9.3	0.97	0.33	3.1	94
TOPGALLANT	D	6.6	0.82	0.25	1.7	86
MIZZEN	D	11.6	1.06	0.03	0.03	56
CHIBERTA	D	13.9	1.14	0.10	1.5	67
ESROM	D	11.1	1.05	0.45	0.49	79
KEELSON	D	9.0	0.96	0.26	2.3	78
STRAIT	D	16.1	1.21	0.20	3.3	87
MARSILLY	D	5.3	0.72	0.15	0.80	85
SCANTLING	D	11.1	1.05	0.07	0.82	88
LOWBALL	S	6.6	0.82	0.11	0.75	66
SANDREEF	D	17.7	1.25	0.64	5.5	83
FARALLONES	D	10.9	1.04	0.15	1.7	93
ICEBERG	D	10.6	1.02	0.08	0.77	70
QUINELLA	S	6.8	0.83	0.10	0.67	79
RUMMY	S	14.1	1.15	0.27	3.8	73
HEARTS	D	14.3	1.16	0.19	2.8	80

Units of M_I are 10^{25} N-m.

TABLE 2
PAHUTE MESA

		M_I	Log M_I	F	M_{DC}	Strike
SCOTCH	D	28.8	1.45	0.40	11.4	91
STILTON	D	18.2	1.26	0.26	4.8	95
STINGER	S	14.8	1.17	0.35	5.1	91
SLED	S	15.9	1.20	0.27	4.2	74
PURSE	S	23.2	1.37	0.28	6.5	68
ALMENDRO	D	55.8	1.75	0.38	20.9	79
TYBO	D	39.9	1.60	0.21	8.4	69
MAST	D	49.0	1.69	0.38	18.6	90
CHESHIRE	D	44.8	1.65	0.50	23.2	80
ESTUARY	D	58.5	1.77	0.35	20.2	79
POOL	D	31.7	1.50	0.45	14.2	82
BACKBEACH	S	9.4	0.98	0.23	2.2	92
PANIR	S	8.3	0.92	0.26	2.2	52
FARM	S	8.7	0.94	0.42	3.7	87
PEPATO	D	13.3	1.13	0.08	1.1	78
SHEEPSHEAD	S	9.6	0.98	0.13	1.3	84
KASH	S	13.4	1.13	0.17	2.3	78
TAFI	S	12.6	1.10	0.15	2.0	71

Units of M_I are 10^{25} N-m.

SHAGAN RIVER: 09/14/80
S0: -0.25 S1: 0.88 S2: -6.44 x 10¹⁵ N-M

SHAGAN RIVER: 12/02/79
S0: 5.27 S1: 0.34 S2: -1.34 x 10¹⁵ N-H
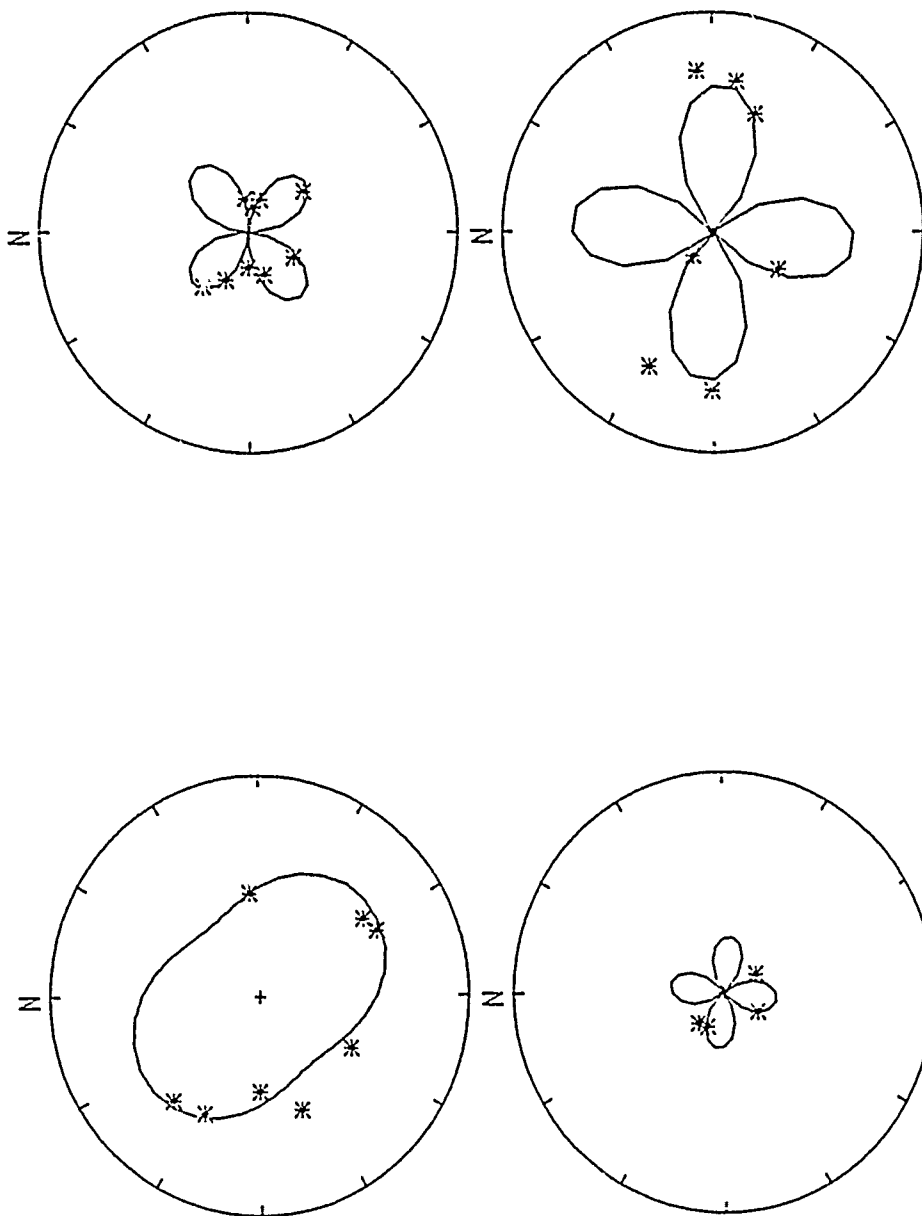
AZIMUTH VS. AVG. SPECTRAL AMPLITUDE   AZIMUTH VS. AVG. SPECTRAL AMPLITUDE
Maximum amplitude= 1.58 x 10⁻⁵ M-s   Maximum amplitude= 2.79 x 10⁻⁵ M-s

Figure 1. Observed and computed radiation patterns for Rayleigh waves (top) and Love waves (bottom) for two Shagan river events. The event of 14 September 1980 had significant tectonic release as indicated by the four-lobed Rayleigh wave radiation pattern.

291
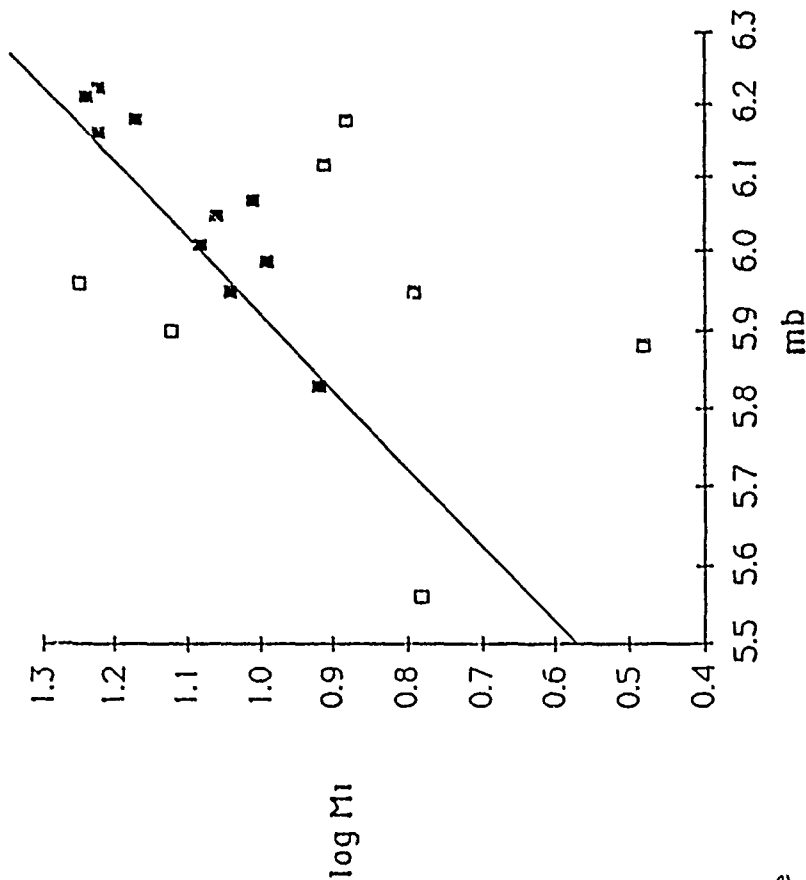
Figure 2. Log M_I vs m_b for Shagan River events. Log M_I has been reduced by 15. The open, solid and half squares indicate high, normal, and low M_I to be compared to Figure 3. Equation of line is given in text as Equation 6.
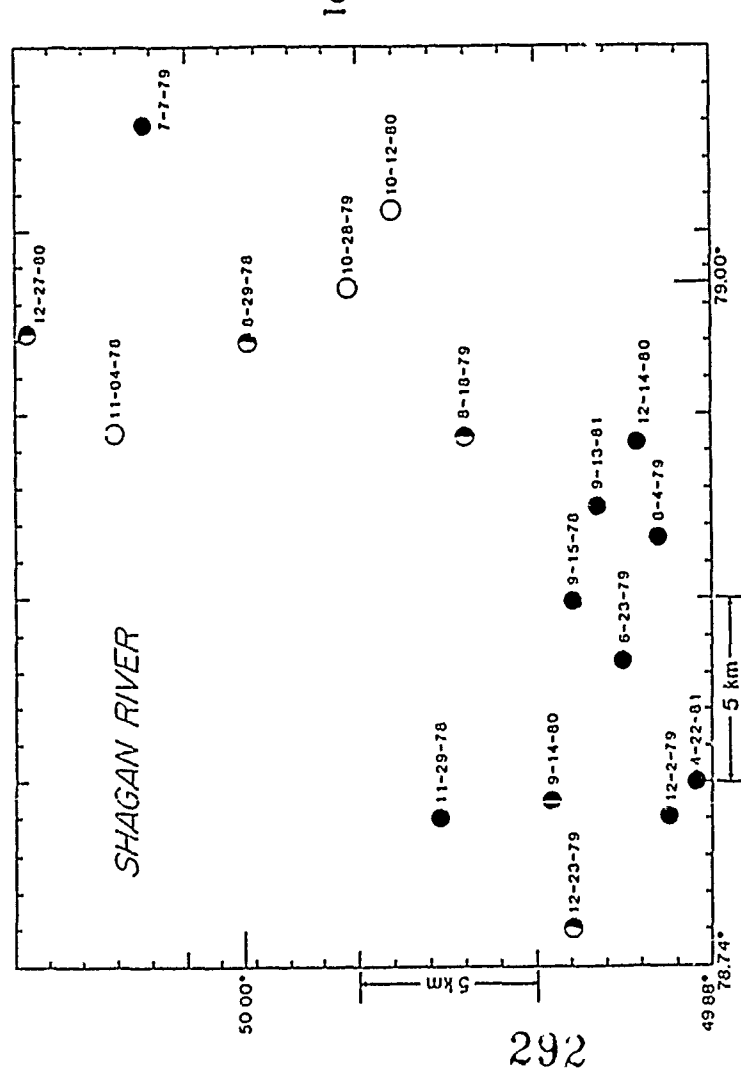
Figure 3. Location map for Shagan River events. The open, solid and half symbols correspond to high, normal, and low M_I as in Figure 2.
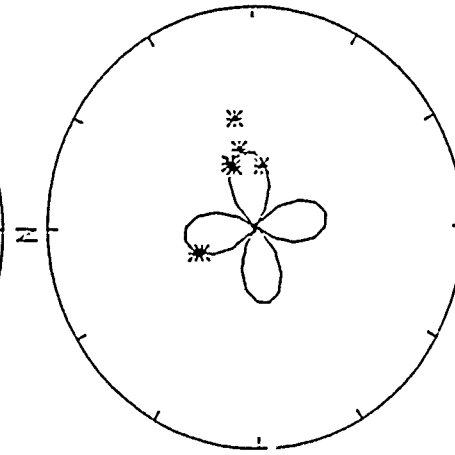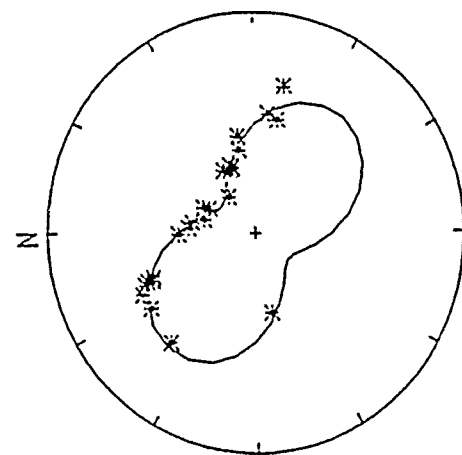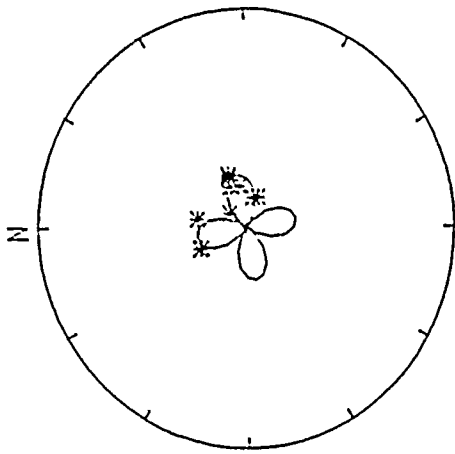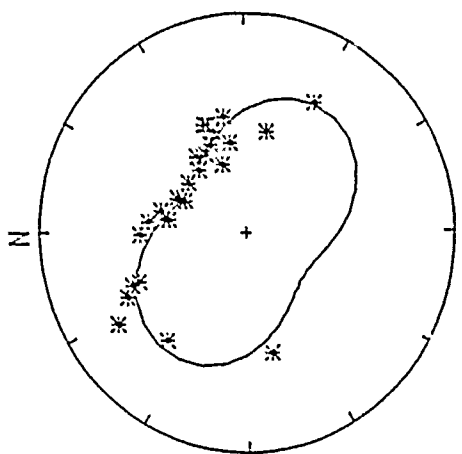
AZIMUTH VS. AVG. SPECTRAL AMPLITUDE AZIMUTH VS. AVG. SPECTRAL AMPLITUDE.
Maximum amplitude= 5.53× 10⁻⁵ M−s   Maximum amplitude= 3.82× 10⁻⁵ M−s

Figure 4.   Observed and computed Rayleigh wave (top) and Love wave (bottom)
radiation patterns for two Yucca flats events: SANDREEF (left) and HEARTS
(right).
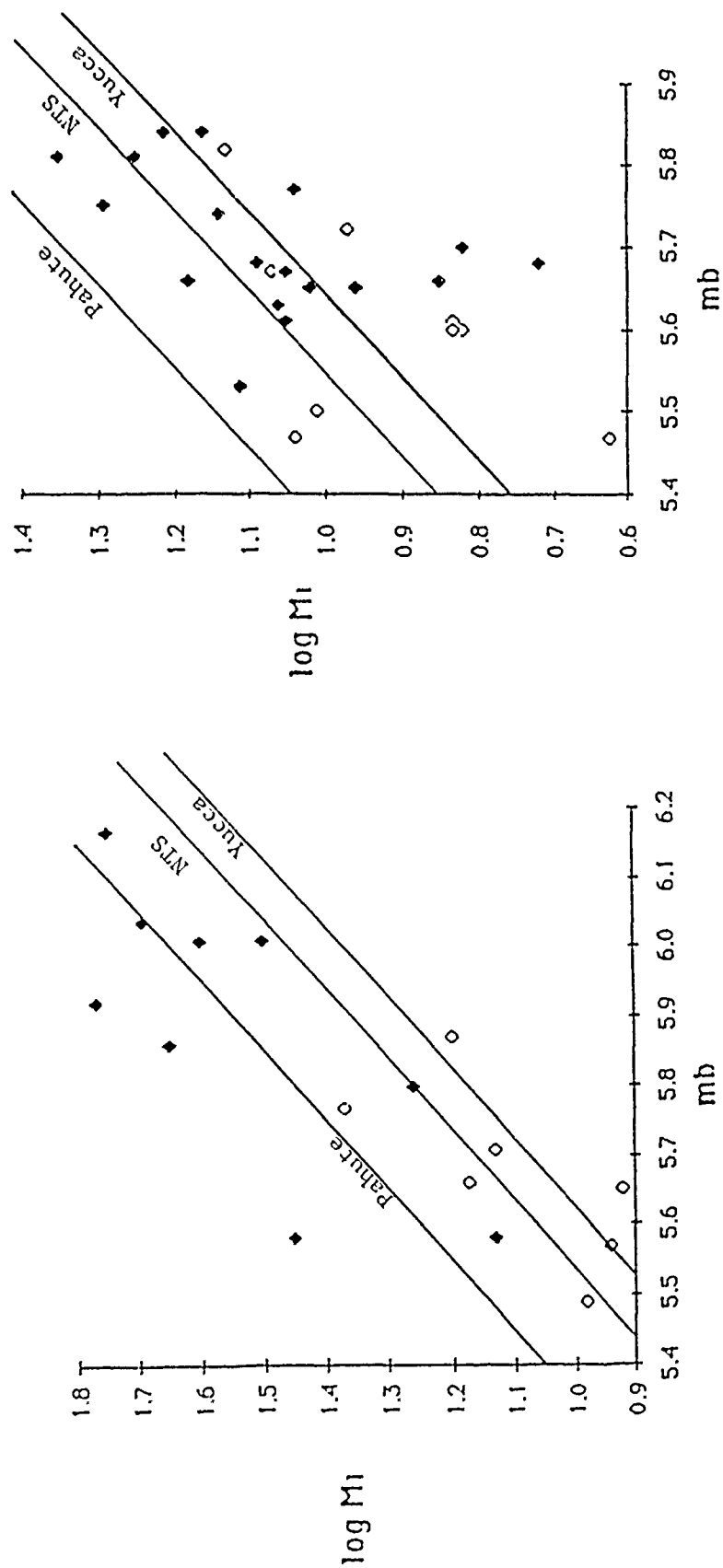
Figure 5. Log M_I vs m_b for Pahute Mesa (left) and Yucca Flats (right). Open symbols indicate those events near water table and not used to determine m_b-M_I relations. Log M_I was reduced by 15. Equations of lines are given in text as Equations 7, 8, and 9.

TITLE: The effects of Tectonic Release on Yield Estimation at Novaya Zemlya.

AUTHORS: R.W. Burger, L.J. Burdick, J.S. Barker, and P.G. Somerville

CONTRACT #:   F19628-85-C-0036

SUMMARY: Two studies have been carried out to investigate the possibility that tectonic release is strongly affecting short period P wave amplitudes at Novaya Zemlya. The first was a relative waveform analysis of 4 explosions at south and 11 explosions at north Novaya Zemlya. The purpose was to measure the size of the explosive events for use in computing F factors and to characterize the behavior of pP. It was found that 6 of the north Novaya Zemlya events were almost identical in size which was important in later parts of the investigation, since they have highly variable F factors. It was verified that the two subsites have substantially different azimuthal amplitude patterns. The second study was an attempt to characterize the tectonic release using long period S data. It was found that the southern site tectonic release has a vertical strike slip mechanism while the northern has an oblique normal mechanism. The size of the tectonic release events appears to be too small to be responsible for the differences in the azimuthal amplitude patterns.

CONCLUSIONS
   AND
RECOMMENDATIONS:

It currently appears that tectonic release is not strongly affecting short period amplitude pattern differences between north and south Novaya Zemlya. Further efforts should be made to characterize the tectonic release at north Novaya Zemlya to determine how large an absolute bias is caused by the oblique normal tectonic release. Correlations between travel time residuals and amplitude anomalies should be carried out at Novaya Zemlya to determine the importance of focusing of energy by lateral variations in velocity structure to azimuthal amplitude patterns.

INTRODUCTION

It is well known that there are amplitude patterns and magnitude biases associated with every test site which can not be explained in terms of Q variations along the raypath. The possible explanations for these phenomena include the effects of tectonic release, the effects of lateral variations in structure and variations in coupling efficiency. It is difficult to differentiate between these possible causes because their effects can be so similar in some cases. For instance, Lay et. al. (1984a) concluded that tectonic release was affecting the short period P wave amplitudes at NTS because they exhibited a $\sin(2\theta)$ azimuthal pattern. This is the azimuthal pattern which should be expected for vertical strike slip tectonic release which is the orientation of the tectonic release at NTS (Wallace et. al., 1983). Lay et. al. (1984a) point out that, moreover, the azimuthal positioning of the highs and lows in the amplitude pattern is exactly that which should be expected for NTS tectonic release. After this evidence was presented, Lynnes and Lay (1984) examined the travel time residual pattern from NTS and found that this too exhibited a $\sin(2\theta)$ azimuthal pattern. Tectonic release should not affect the travel time of the first arriving P energy. A correlation between time and amplitude is much more indicative of lateral variation in structure being the cause of the azimuthal pattern. There is no straightforward way to resolve the azimuthal amplitude effects of tectonic release and lateral variations in structure at NTS because, by coincidence, they are very similar. This will almost certainly not be true at other test sites, so it is important to examine azimuthal P wave amplitude patterns from them as well. For this purpose, we have measured the amplitudes of about 600 P waves from 15 events at the north and south Novaya Zemlya test sites. We have also studied the tectonic release orientations for both sites using long period S wave data. We present an assessment of the possible relationship between tectonic release and azimuthal P wave amplitude patterns at Novaya Zemlya in the following. We also present an initial investigation of the correlation between travel time and amplitude and its possible implications.

The study consisted of two parts with different goals. The first part of the investigation was directed towards characterizing and estimating the yields of 11 northern and 4 southern Novaya Zemlya events. This was necessary to determine whether pP was behaving normally, whether the network coverage of the sites was adequate and what the absolute size of the events was for the purpose of computing F factors. The method utilized in this part of the study was an advanced waveform analysis technique called intercorrelation. This is a waveform equalization procedure which takes advantage of all of the signal information in short period P waves and automatically measures pP amplitude and arrival time as well as producing an analytic measure of relative event size.

The second part of the study was directed at measuring the orientation and strength of tectonic release at the two Novaya Zemlya subsites. The data utilized for this work were long period SH and SV observations of the events from the WWSSN and CSN networks. Clear and consistent S wave polarity

reversals at several different azimuths provided good resolution of the tectonic release mechanisms. It appears that the orientation of the tectonic release is relatively constant at each site, though it has variable strength with respect to the explosive source. Interestingly, there was clear evidence that the tectonic release mechanism differs between the two subsites. If tectonic release is affecting short period P wave amplitudes, the azimuthal amplitude patterns of north and south Novaya Zemlya should be different. In fact, they are.

INTERCORRELAION ANALYSIS

Figure 1 shows a base map of the Novaya Zemlya test sites along with the stations in the WWSSN and CSN which can be used to study seismic signals from them. The data set used in the intercorrelation study consisted of all usable short period P waveforms from these networks at distance ranges between 25 and 95 degrees. Amplitudes were measured from all signals and any signals which could be seen clearly were digitized by hand. From this digitized data base, we determined pP amplitude and arrival time and relative source strength for all of the events studied.

The intercorrelation procedure has now been used to study a large number of US nuclear tests. These include the three Amchitka tests, (Lay et. al., 1984b) and 25 events from Pahute Mesa (Lay et. al., 1984c). The procedure is a waveform equalization technique used to compare all of the waveforms from previous events to the waveforms of a new event at common stations to establish analytically the relative size of the new event. Figure 2 illustrates the procedure for a single station. The records shown on the left are from WWSSN station ATL for the 10/27/66 and the 10/21/67 northern Novaya Zemlya events. It is assumed that when the signal from the later event was recorded, the signal from the earlier event would already have been processed and that we would have available for it an effective source or event equalizing function. This function is shown in the center column in the figure. It consists of an estimate of the teleseismic P pulse (upward) and a later, slightly smaller pP pulse (downward). The effective source of the earlier event is convolved with the signal of the later event as, shown in the bottom row. The resulting signal now contains the effects of both sources. The problem is to find an effective source for the new event which can produce the same resultant waveform when convolved with the signal from the earlier event (top row). This effective source is described by the absolute strength of the direct P arrival, the relative strength of pP and the relative arrival time of pP. The best fitting values are found by a grid searching procedure. The criterion for a best fit is the minimization of the standard least squares norm between the equalized signals shown on the right of figure 2. All stations which recorded both events are examined simultaneously. Figure 3 shows the complete data set of equalized waveforms for the 10/27/66 and 10/21/67 tests. The equalization procedure generally works very well, and the fact that there are usually so many observations ensures that the optimal estimates for event size and pP parameters for the new event will be well

defined.

The intercorrelation study and associated analyses provided several new and important results about Novaya Zemlya besides just new yield estimates for the 15 events. One of the events in the study, the 10/18/75 event, turned out to be a double bomb. (Two explosions were apparently detonated almost simultaneously at slightly different locations.) The pP arrival times of the events in the data set evolve in a smooth way with event size. The pP times are substantially smaller for events at south Novaya Zemlya indicating a harder rock type. The pP arrival times are all larger than one would expect for a hard rock site, but anomalously late pP times are observed for virtually every test site. One anomalous event which was apparently underburied was identified at the northern site and one which was overburied was identified at the southern site. The results of greatest importance to this discussion, however, are the relative size or yield estimates.

Figure 4 summarizes the event size estimates from the intercorrelation study. The 11 northern events ordered by size are shown on the left and the four southern events are shown on the right. The left hand axis indicates the log of the relative source strength, (ψ_∞/ψ_0), and the right is an uneven scale giving the yield. The relative source strengths are all normalized to the smallest northern event, 10/21/67. We estimate its yield at 61 kt. The largest northern event had a yield of 2831 kt. The smallest and largest southern events were 32 and 3700 kt., respectively. Of course, actual yield estimates such as these require estimates of the attenuation bias and coupling characteristics of the test site. We asssumed a t^* for P waves of 0.5 sec. and used the Amchitka relationship of Lay et. al. (1984b), which relates ψ_∞ to yield, to estimate coupling. The feature of most importance to this discussion is the plateau of equally sized events so obvious in figure 4. As we shall show in the following section, these events had highly variable F factors even though the explosions were all roughly the same size. Comparisons of the waveforms from these events allows us to search for arrivals associated with tectonic release without needing to be concerned about the effects of varying explosive event size.

As part of an intercorrelation analysis it is generally necessary to carefully measure classical event signal amplitudes in order to assess the relative performance of intercorrelation and m_b yield scaling. We did so in the Novaya Zemlya study, which permitted us to determine some information of importance to this study. The relative azimuthal amplitude pattern of north with respect to south Novaya Zemlya is displayed in figure 5. Taking the ratio of the amplitude patterns isolates the near source differences in short period amplitudes between the two test sites. As previously noted by Butler and Ruff (1980), there is a very large difference in the station anomalies for the two sites. The most remarkable feature in the relative patterns is the strong upward trend at the largest azimuths. It is our goal to determine whether this strong trend is due to source or propagational effects.

TECTONIC RELEASE AT NOVAYA ZEMLYA

It is very fortunate that the Novaya Zemlya test site is near the pole. This means that the SH energy will be natually isolated on the east-west component at most stations. This permitted us to make a few key observations about tectonic release at Novaya Zemlya which served to motivate our subsequent work. First was that the SH arrivals were large and impulsive at many stations in the networks and that they clearly exhibited several node crossings. The polarities of the SH arrivals were constant for either test site, but they definitely changed between test sites. The evidence that the level of tectonic release is substantial at both sites but that the orientations of the equivalent double couples are much different was clear from the outset of our investigation.

All usable WWSSN and CSN records were digitized and rotated into pure SH and SV motions. The SH motions were plotted on focal spheres and tectonic release orientations which fit them were determined by trial and error. The northern Novaya Zemlya mechanism is predominately dip slip with an oblique-normal sense of motion. The southern Novaya Zemlya mechanism is nearly pure vertical strike slip, although some additional information besides SH first motion data is required to show this completely. The SH waveforms were then modeled to enable us to compute the moments of the tectonic release events. Figure 6 summarizes these studies for the 9/12/73 northern Novaya Zemlya event. All of the first motion data is shown on the focal sphere along with selected observations and synthetics. Note the clear polarity reversals between azimuths of 165 and 183 degrees (QUE and SHI) and between 264 and 322 degrees (ESK and BLA). The synthetics shown are for a fault plane dipping 55°, with a rake of -41° and a strike of -20°. The tectonic release event is set at 3 km., t^{*}_{β} at 3.0 sec. and the time function at 0.6 sec. duration (triangular pulse). The moment determined for the tectonic release event was measured to be 9.1×10^{23} dyne cm. This results in an F factor estimate of 1.34. Table 1 summarizes the seismic moment and F factor measurements for the tectonic release events. The m_b measurements come from the short period P wave measurements and thus provide a first order estimate of explosion size.

The SH wave first motion data for the two Novaya Zemlya subsites is shown on an expanded scale in figure 7. The stations which clearly change polarity are to the northwest and southwest in the focal sphere. As noted previously, SH first motion data alone cannot be used to uniquely resolve that a mechanism is vertical strike slip. The 45° dip slip first motion plot is identical to the vertical strike slip for the SH component. It is necessary to rely on additional information to resolve this ambiguity. Fortunately, the SV data from southern Novaya Zemlya resolves that the vertical strike slip solution is the correct one. Figure 8 shows the observed and predicted SV and SH amplitudes for the correct fault plane solution. The observed SV amplitude has not been corrected for the presence of pS radiation from the explosion, but this should only cause a constant offset in the azimuthal pattern, which is in fact observed. Oscillating about this offset, we see the four lobed azimuthal pattern characteristic of SV radiation from a vertical strike slip event. The SH pattern is also matched by the theoretical predictions. Thus,

we have clearly resolved that the tectonic release orientations are substantially different for the north and south Novaya Zemlya subsites. The remaining question is whether or not these differences in tectonic release orientation are causing the differences in the short period P wave amplitude patterns evidenced in figure 5.

Before proceeding to address this question, it is worthwhile to note that there may be one additional clue to the effects of tectonic release on short period P waves. It is related to the fact that there is a large variation in F factor within both subsites as shown in table 1. It should be very instructive to compare short period P wave data from the two subsites for events with very high and very low F factors. This variability in F factor was determined by studying the amplitudes of the long period SH waves with respect to the short period P wave event size estimates. However, the variability can be clearly illustrated without relying on the short period P information. Figure 9 shows long period P, SH and SV motions for a suite of events from northern Novaya Zemlya as observed at the Canadian station MBC. The three traces for each event are normalized to the amplitude of the long period P arrival. The variability of the long period SH with respect to long period P is very clear. The SH amplitude for the 8/29/74 event, for instance is remarkably low. The strong changes in the waveshape of SV are caused by the strong interaction between pS from the explosion and the SV phases from the tectonic release. It is also important to note that F factor in table 1 is not systematically linked to event size as measured through m_b.

BIASING OF YIELD ESTIMATES BY TECTONIC RELEASE

The task remaining before us is to relate our study of tectonic release to our study of the azimuthal amplitude patterns. Is the difference in tectonic release orientation between the two subsites (figure 7) responsible for the trends illustrated in figure 5? To answer this question we can utilize our knowledge of the tectonic release focal mechanism and its moment or F factor to compute synthetic amplitude patterns. This will allow us to determine whether the tectonic release is strong enough to be affecting the short period amplitudes at the observed levels. The F factors at Novaya Zemlya observed here are much smaller in magnitude than those observed by Wallace et. al. (1983) at Pahute Mesa. This makes it less likely that tectonic release could be affecting the short period P amplitudes. On the other hand, the mechanism at north Novaya Zemlya has a significant dip slip component. Dip slip events are very much more effective than strike slip at changing teleseismic body wave amplitudes.

Many details of the tectonic release event must be assumed in order to carry out a forward calculation of its effects. The key ones are when to initiate the tectonic release, where to locate it and what time function to give it. Lay et. al. (1984c) located the event directly under the explosion, triggered it with the downgoing P arrival and assigned it an impulsive trapezoidal time function. We will make very similar assumptions because we wish to compare the observations at Novaya Zemlya with those from

NTS. We first computed synthetic explosion plus tectonic release synthetics for the vertical strike slip events at the southern site. We located the tectonic release event at a depth of 3 km., triggered it with the P wave and gave it a time function of 0.6 sec. duration. We assumed the largest observed F factor (table 1), but even so the predicted effect of tectonic release on short period P wave amplitude was minimal. The largest ratio of explosion plus tectonic release amplitude to explosion amplitude was only 1.04. We performed a similar calculation for the northern test site. We located the event 4 km. down dip on one of the fault planes rather than directly under the explosion to enhance the azimuthal variation. For the 9/12/73 event, the ratio of the composite event amplitude to explosion amplitude was 1.2. The maximum observed azimuthal amplitude variation is a factor of 1.34 from the maximum constructive to the maximum destructive interference. As shown in figure 5, it would be necessary to have at least a factor of 2.0 variation to match the observations.

Interestingly, the trends in the predicted amplitude pattern match the observations though its amplitude does not. This information is summarized in figure 10. We show m_b corrections on a focal sphere rather than just azimuthal patterns because this allows us to see the dependence on ray parameter as well as azimuth. The observed m_b variations are shown on the right and the synthetic variations on the left. The synthetic m_b corrections have been multiplied by a factor of 5 for ease of comparison to the observed. Synthetics were not computed for every station but for a dense enough sampling to clearly illustrate the major trends. The strong gradient in amplitude to the northwest is in both the observed and synthetic patterns, as well as the highs to the east. The large observed lows to the southwest are not predicted. If all of the assumptions involved in our calculations are correct, we must conclude that tectonic release radiation at Novaya Zemlya is too weak to be responsible for the observed azimuthal amplitude difference between the two subsites. It should be pointed out that the object of our modeling study was to match the azimuthal trend in figure 5. We briefly explored models that caused large m_b biases without inducing large azimuthal variations. We believe that such a model could be very appropriate for northern Novaya Zemlya.

DISCUSSION

Our fundamental result is clear enough. However, we do not regard it as absolute. We were required to make many assumptions in computing our synthetic amplitude patterns, and it is possible that if enough of them were substantially in error the effects of tectonic release on short period P wave amplitudes might be much larger than we predicted. It is worth noting that even though the ab amplitudes of the synthetic signals were not changed by tectonic release, in some instances the waveshapes were. It is not practical to attempt to match the waveshapes of short period P waves since the propagation effects are so strong. It may be interesting, however, to compare short period waveforms at common stations for events with variable F factors.

In fact, the data from northern Novaya Zemlya is uniquely interesting in this regard. We showed in figure 4 that there were six events of almost exactly the same size. Table 1 shows that they have a large range in F factor, and in fact they include the events with the largest and smallest factors. We selected from our data set all stations which recorded either at least 4 of the 6 events or 3 of the 6 events with both the largest and smallest F factor events included. We eliminated stations with very complex, ringing signals and arrived at the reduced data set in figures 11a and 11b. Many stations do show a systematic evolution with F factor as indicated by the arrows. This is about the level of change that we predicted in our forward calculations. The effect is nonuniform, however, and still difficult to treat in a purely forward modeling sense. The effect is most commonly seen in the second downswing of the P waves. For example, HKC in figure 11a and VAL in 11b show that the second downswing is enhanced for the lower F factors. This is consistent with the tectonic release strengthening the first cycle or diminishing the second cycle. Further relative waveform modeling of these data appears to be warranted.

If our basic result is correct and short period tectonic release radiation is very weak at Novaya Zemlya, then lateral variation in velocity structure is the probable cause of the change in amplitude patterns for the two sites. If this is the case, it will be important to examine the relationship between amplitude and travel time residuals at the site. Figure 12 shows some preliminary results. The top focal sphere shows the m_b anomalies for south Novaya Zemlya. The center sphere shows the travel time residuals measured from the WWSSN and CSN for the events we have studied. The bottom sphere shows the time residuals corrected by the azimuthally varying station corrections of Dziewonski and Anderson (1983). There are definite similarities in the amplitude and uncorrected travel time patterns. This indicates that focusing near the receiver might be playing an important role. In general, fast times seem to be related to low amplitude, which is indicative of defocusing.

As a final note, we point out that the basic problems with associating amplitude patterns with tectonic release are that it is difficult to keep the tectonic release energy concentrated in the first two swings of the signal, and even then there does not appear to be a large enough effect. Focusing and defocusing of seismic energy can have a very large effect at the beginning of the waveform. The three dimensional slownesss method of Frazer and Phinney (1980) makes it simple to compute the magnitude of these types of effects from just travel time information. If we assume that the travel time to a station at an epicentral range of 40 degrees is advanced by 1 sec. with the travel time perturbation falling off with distance from the receiver, r, as

$$T_p = 1.0 \text{ sec.}/(1 + (r/R_C)^2)$$

we compute the synthetic results shown in figure 13. On the left are shown step responses for variable correlation lengths, R_c, and on the right are short period synthetic P waves for an explosive source. An amplitude reduction of a factor of 5 is easy to achieve for very plausible correlation

lengths.

CONCLUSIONS

We have examined the possibility that tectonic release is responsible for the differences in azimuthal amplitude patterns at north and south Novaya Zemlya. To do so, we first had to characterize the tectonic release, since this apparently had not been done before. We found from long period SH first motion data that the tectonic release orientation is definitely different at the two subsites. The southern site is near vertical strike slip and the north is oblique-normal. The strength of the tectonic release appears to be too low to cause the differences in the amplitude patterns. Many assumptions were involved in arriving at this result, however, and further testing will be required. At the current time, focusing of energy by lateral variations in structure seems to be a more likely cause for the differences.

References

Butler, R. and L. Ruff; "Teleseismic short-period amplitudes: source and receiver variations," Bull. Seism. Soc. Am., 70, 831-850, 1980.

Dziewonski, A.M. and D.L. Anderson, "Travel times and station corrections for P Waves at teleseismic distances," J. Geophys. Res, 88, 3295-3314, 1983.

Frazer, L.N. and R.A. Phinney, "The theory of finite frequency body wave synthetic seismograms in inhomogeneous elastic media," Geophys J. R. astr. Soc., 63, 691-717, 1980.

Lay, T., T.C. Wallace and D.V. Helmberger, "The effects of tectonic release on short period P waves from NTS explosions," Bull. Seism. Soc. Am., 74, 819-842, 1984 a.

Lay, T., L.J. Burdick and D.V. Helmberger, "Estimating the yields of the Amchitka tests by waveform intercorrelation," Geophys. J. R. astr. Soc., 78, 181-208, 1984 b.

Lay, T., L.J. Burdick, D.V. Helmberger, C.G. Arveson, Estimating Seismic Yield and Defining Distinct Test Sites, WCCP-R-84-01, Woodward-Clyde Consultants, Pasadena, CA, 1984 c.

Lynnes C. and T. Lay, "Defocusing of short period P-waves by a high velocity anomaly beneath Pahute Mesa," (abstract), EOS, 994, 1984.

Wallace, T.C., D.V. Helmberger and G.R. Enren, "Evidence of tectonic release for underground nuclear explosions in long-period P waves, Bull. Seism. Soc. Am., 73, 593-613, 1983.

Table 1. Novaya Zemlya tectonic release

Northern Novaya Zemlya

Event	m_b	seismic moment	F-Factor
10/21/66	6.37	3.80×10^{23}	1.68
10/14/69	5.97	0.7	0.83
10/14/70	6.72	4.9	1.07
9/27/71	6.53	4.1	1.31
8/28/72	6.25	1.9	1.13
9/12/73	6.85	9.1	1.34
8/29/74	6.39	1.3	0.56
8/23/75	6.37	2.3	1.10
10/21/75	6.35	1.9	0.88

Southern Novaya Zemlya

Event	m_b	seismic moment	F-Factor
10/27/73	6.98	15.2×10^{23}	1.40
11/ 2/74	6.72	8.0	1.46
10/18/75	6.47	3.2	0.72
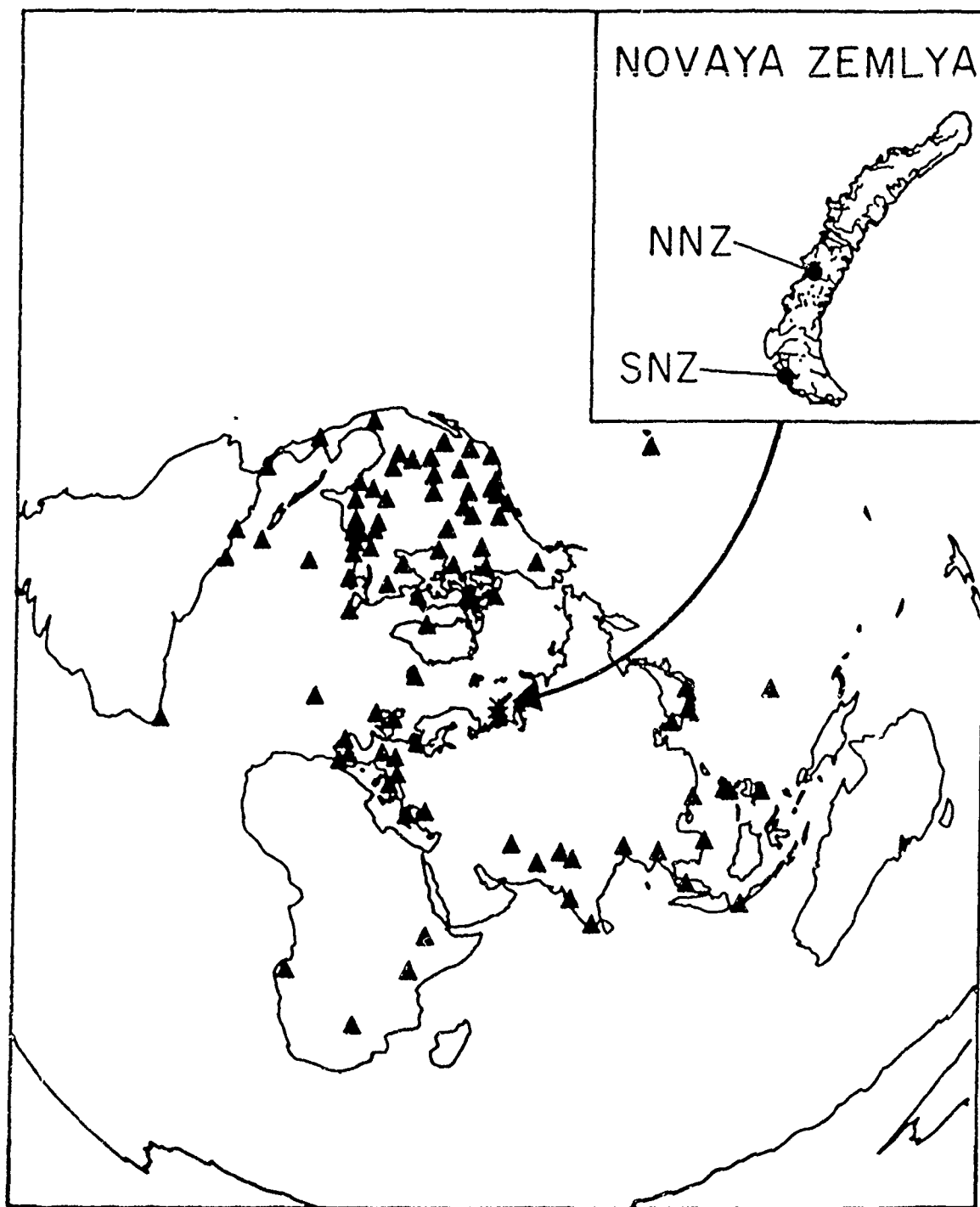
Figure 1: Base map of the Novaya Zemlya test sites. General
locations of the Northern and Southern testing areas are shown. An
azimuthal equidistance projection centered on Novaya Zemlya show the
distribution of stations used in the study.
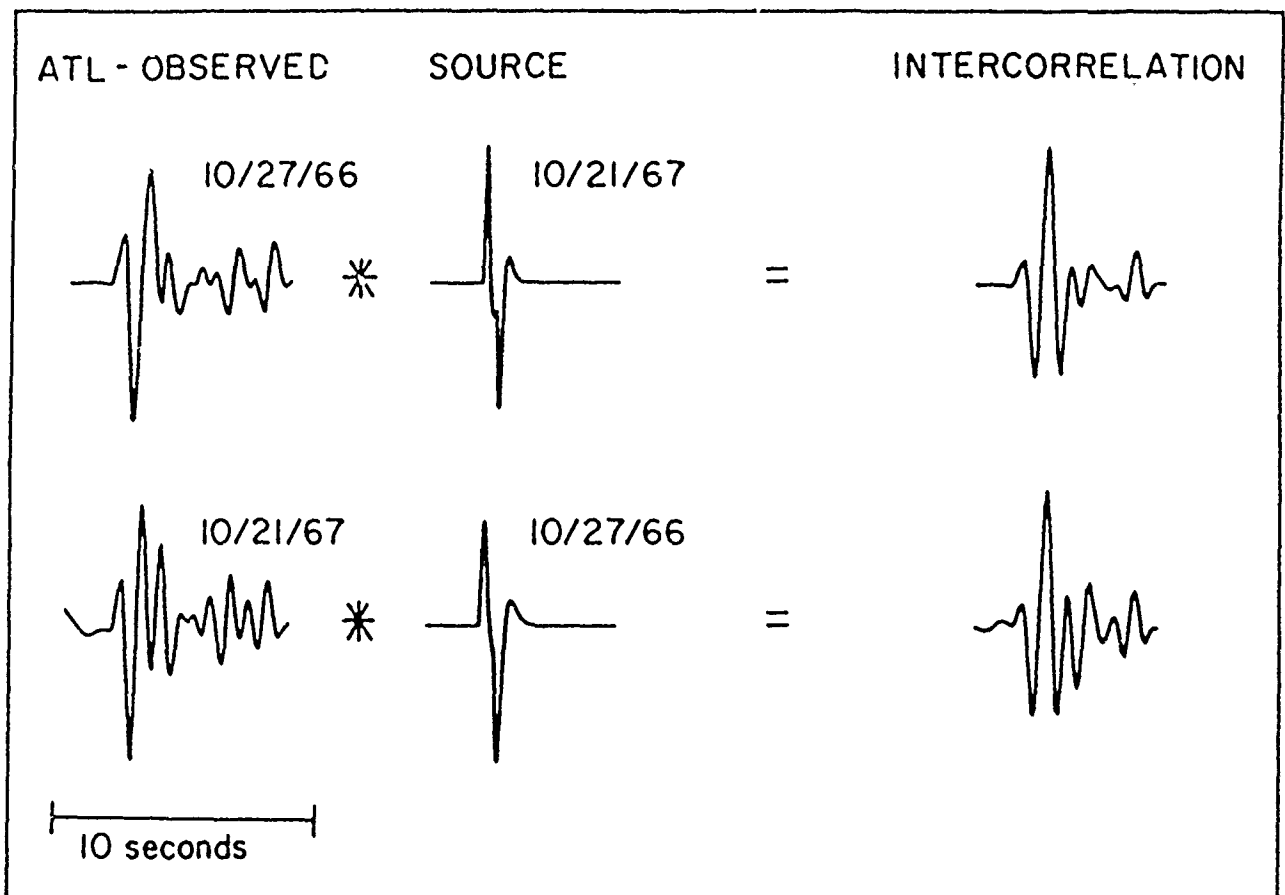
Figure 2: Illustration of how the intercorrelation procedure
accounts for waveform differences produced by the source. The observed
P-wave is convolved with the effective source function of the other
event. The effective source function includes the pP arrival and the
actual explosion time function.
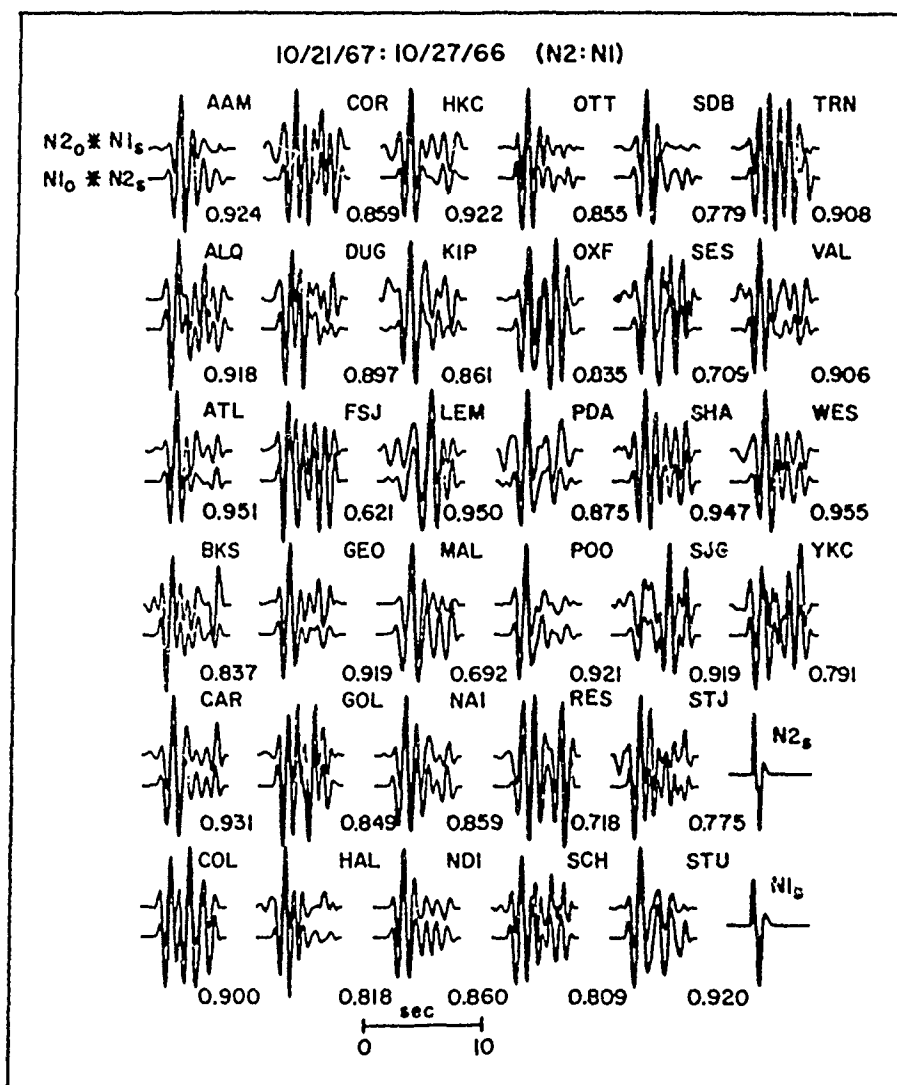
Figure 3: The intercorrelation waveforms of one of the two optimal intercorrelations of the 10/21/67 and 10/27/66 events. The top trace is the 10/21/67 observed signal convolved with the effective source function of 10/27/66. The bottom trace is the 10/27/66 observation convolved with the 10/21/67 effective source function. The numbers shown are normalized cross-correlation coefficients for each pair. The effective source functions for each event are given at the bottom.
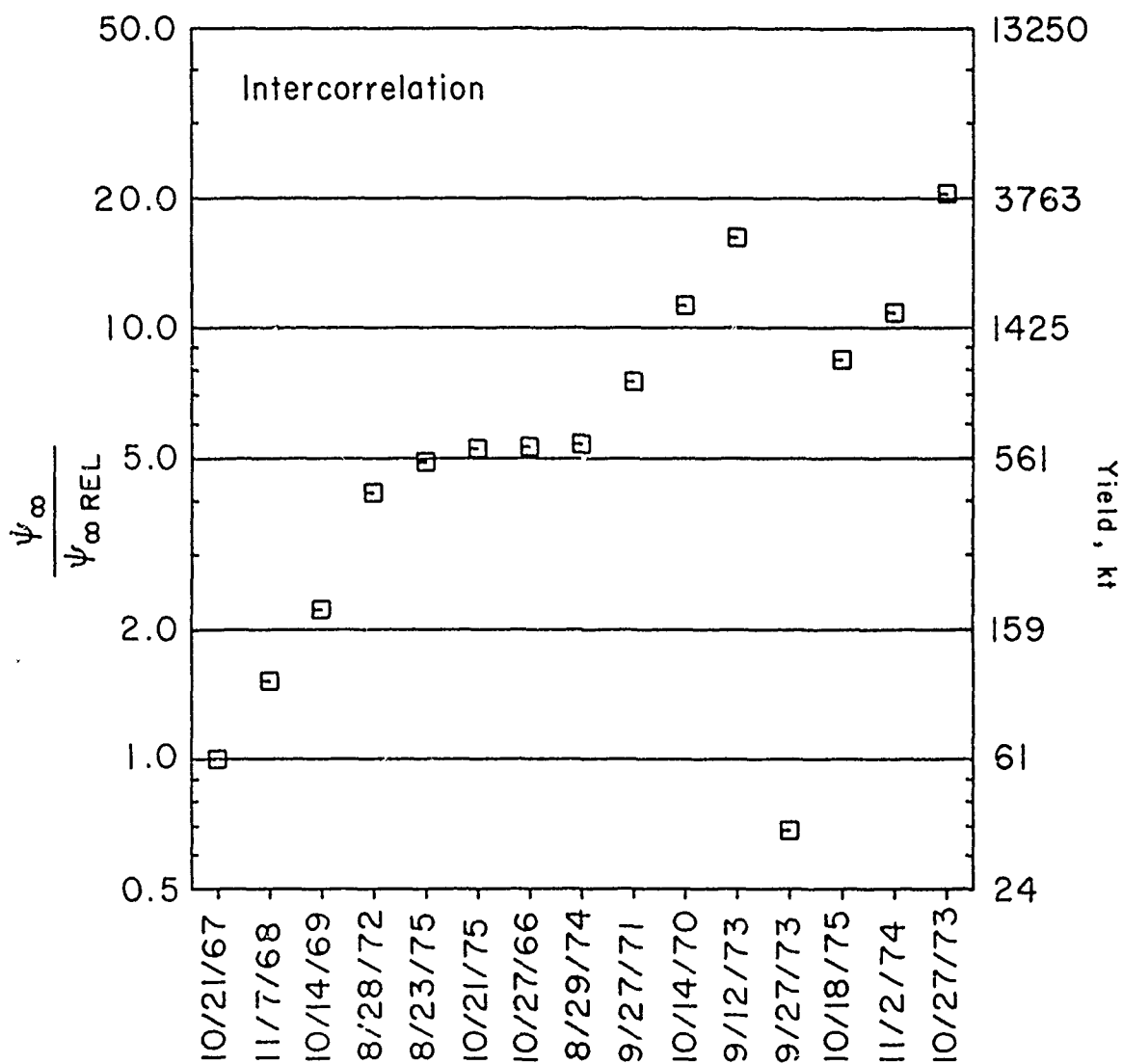
Figure 4: Intercorrelation source strength and yield estimates of the 11 Northern Novaya Zemlya (left) and 4 Southern Novaya Zemlya (right) explosions.
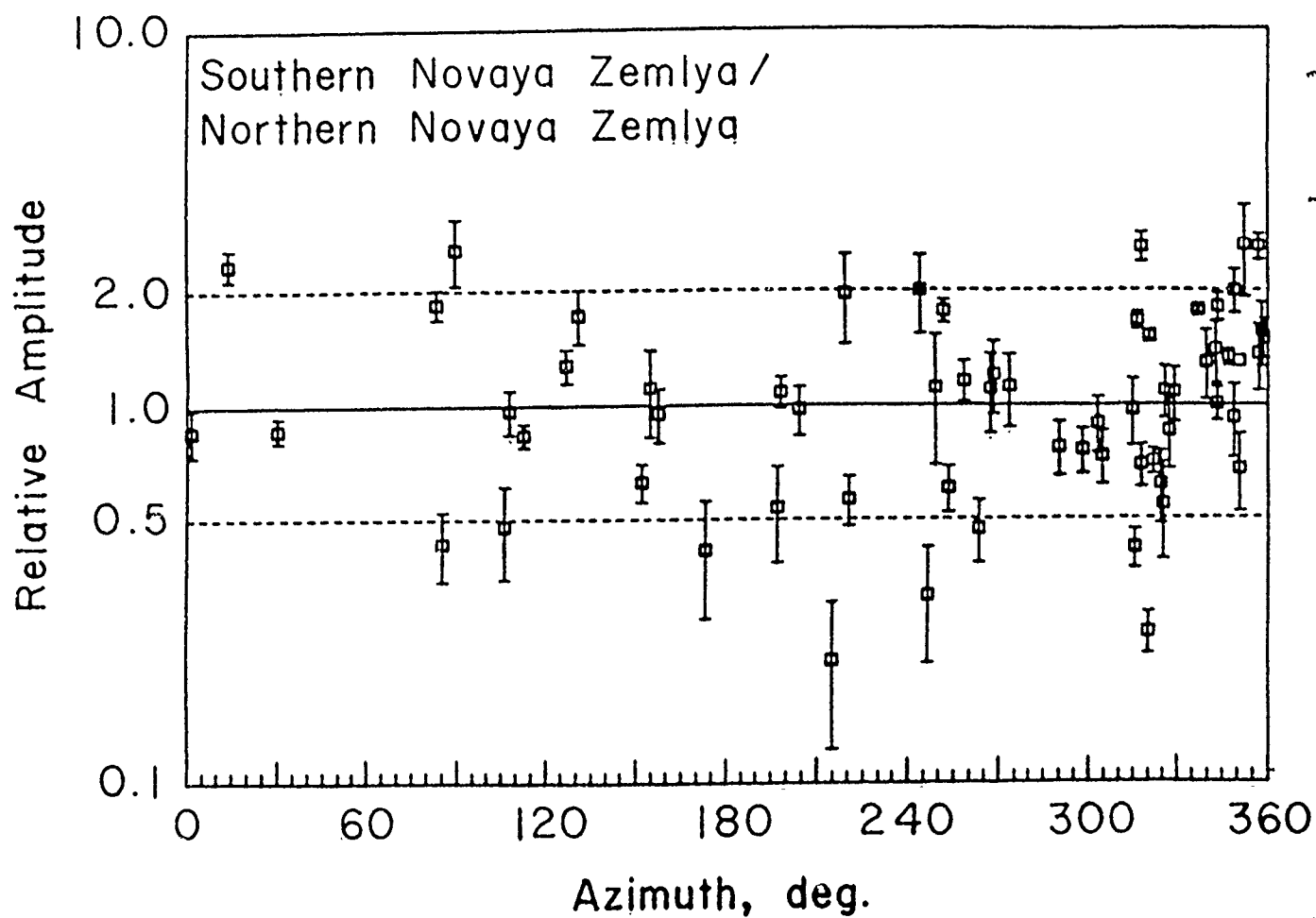
Figure 5: Azimuthal plot of the ratio of the mean station values for the Southern and Northern Novaya Zemlya test site.
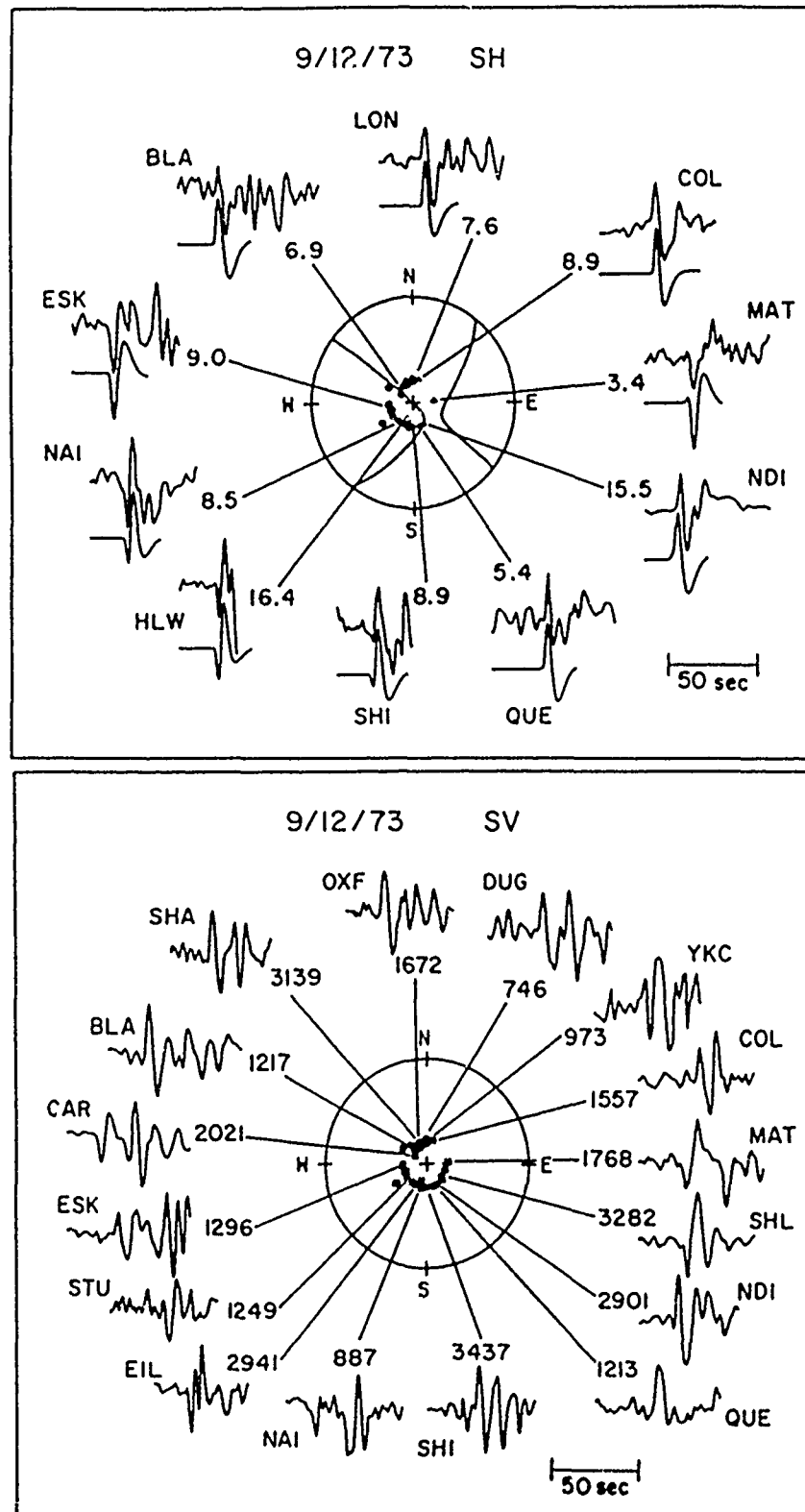
Figure 6: The upper panel displays SH waveforms and synthetics for the 9/12/73 NNZ event. Synthetics are for an oblique-normal dislocation dipping 55°. Numbers are moments required to match observations (in 10^{23} dyne-cm). The lower panel shows SV waveforms. Numbers are the observed amplitudes in millimicrons.

311
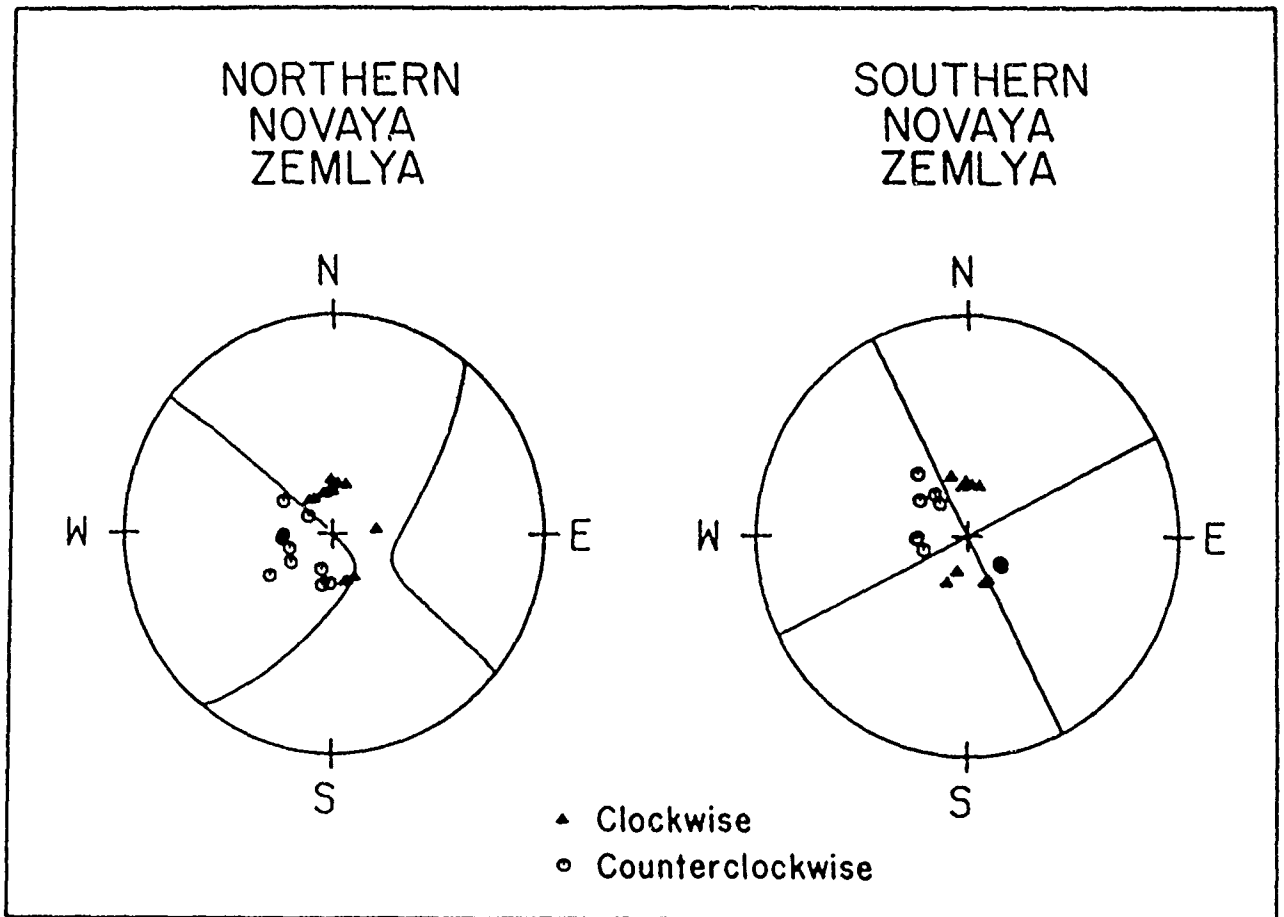
Figure 7: Comparison of SH first motions and focal mechanisms between the 9/12/73 NNZ event and the 11/2/74 SNZ event. Projections are lower hemisphere equal area projections.

11/2/74

SH Observed

SV Observed

SH Synthetic

SV Synthetic

Constructive Interference

Destructive Interference
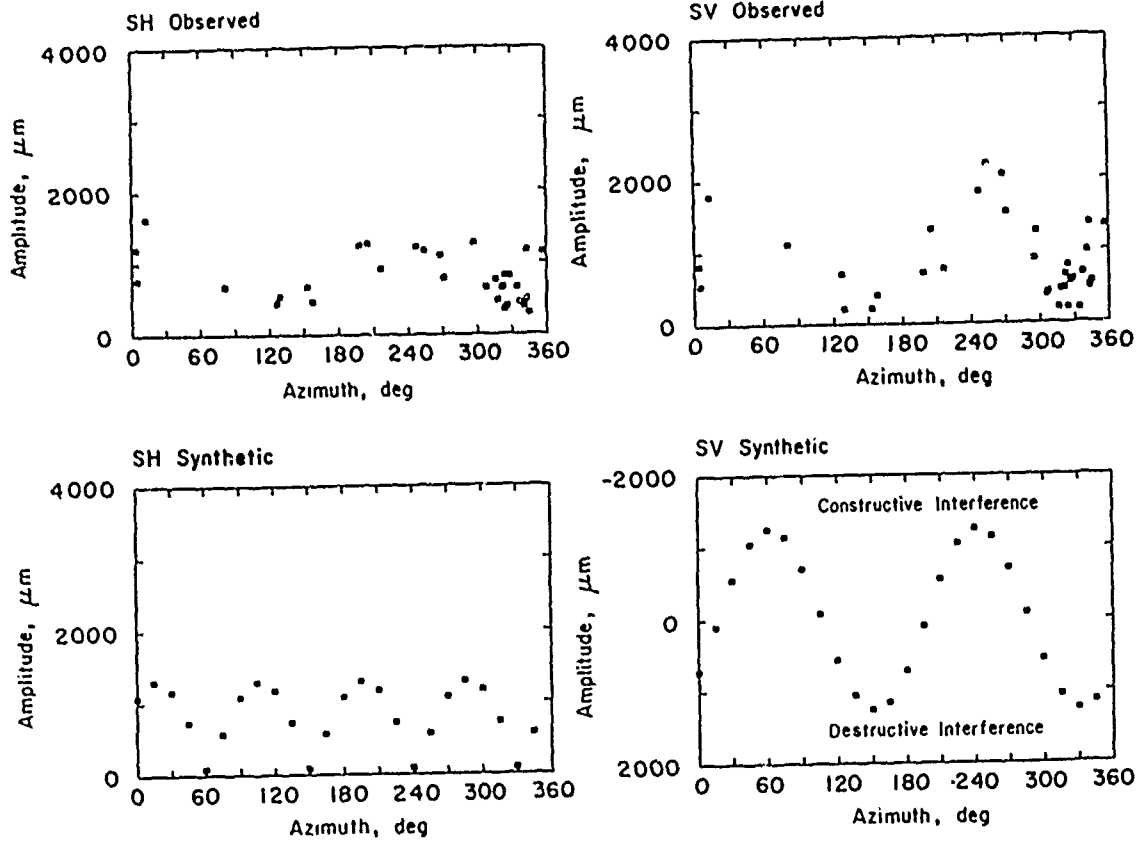
Figure 8: Observed and synthetic SH and SV amplitude patterns for the 11/2/74 SNZ event. The SV synthetic amplitudes are for a vertical strike slip dislocation only, but quadrants where these have destructive and constructive interference with the explosion pS are shown.
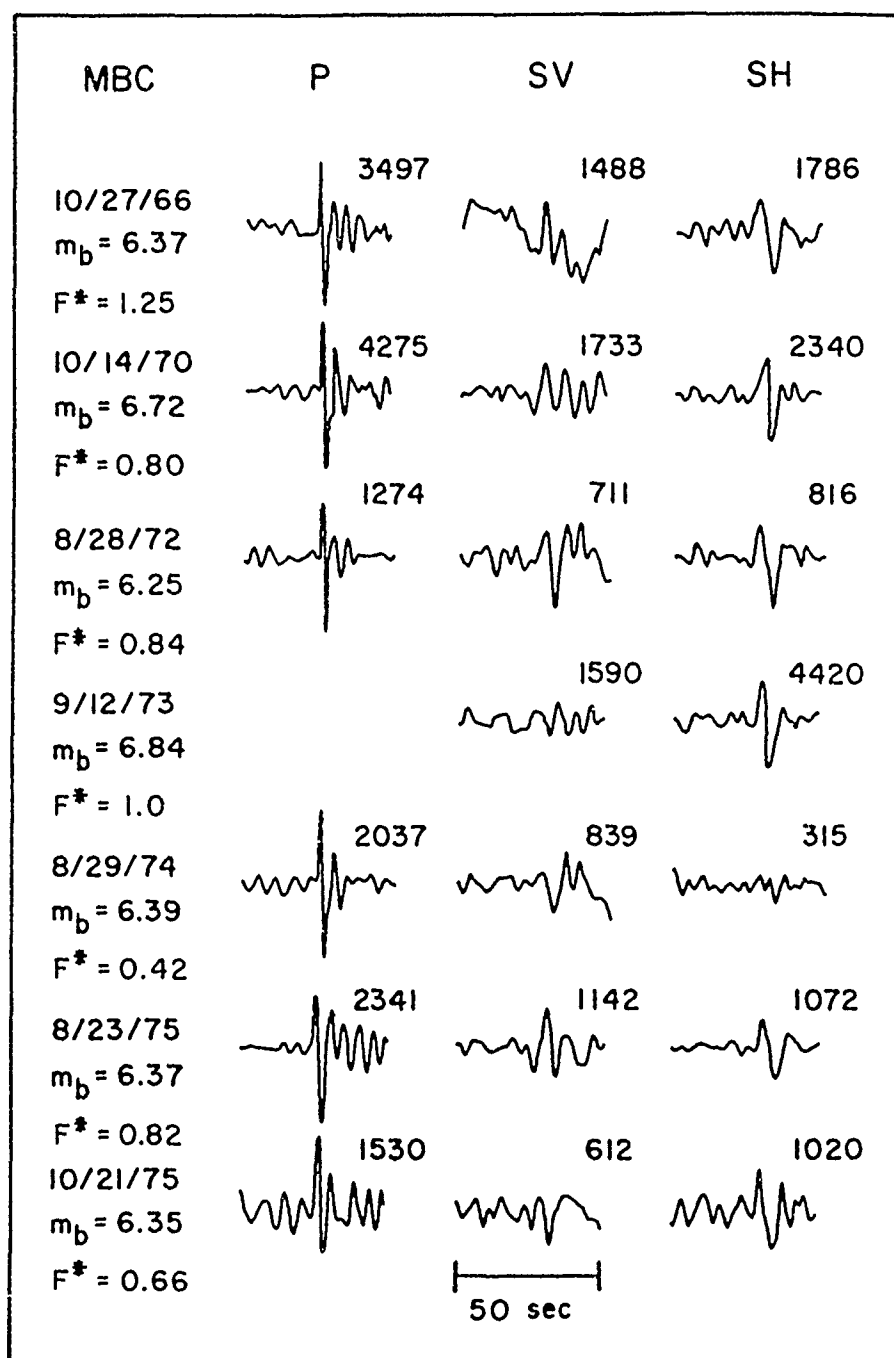
Figure 9: Comparison of three-component seismograms for several NNZ
events observed at MBC. Numbers are the observed peak-to-peak
amplitudes in millimicrons.
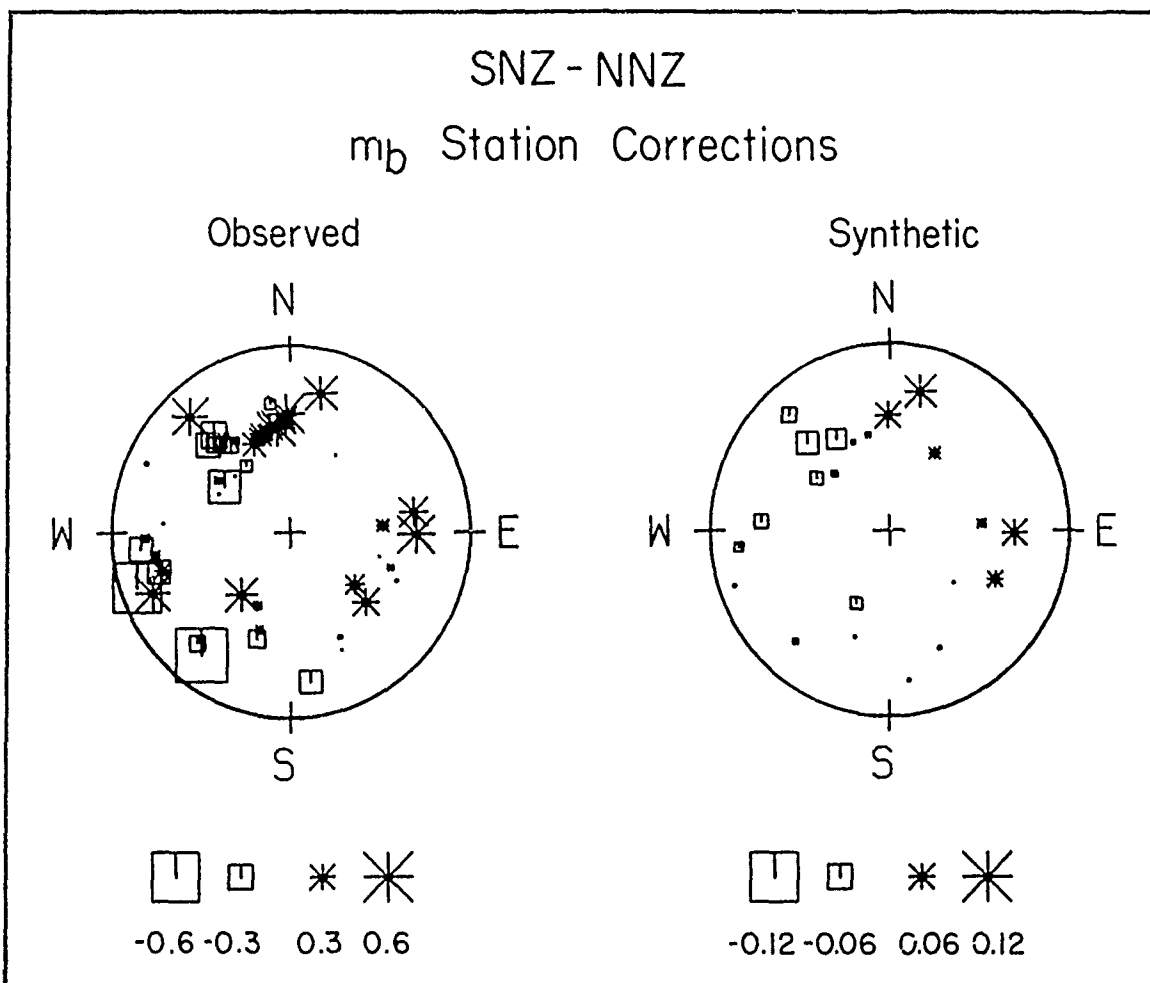
Figure 10: Comparison of observed (left) and synthetic (right) SNZ-NNZ magnitude station corrections. Note that the trends of the observed difference are well matched by the synthetic explosion plus tectonic release models, but the amplitude of the observed variation is much larger than the synthetic.
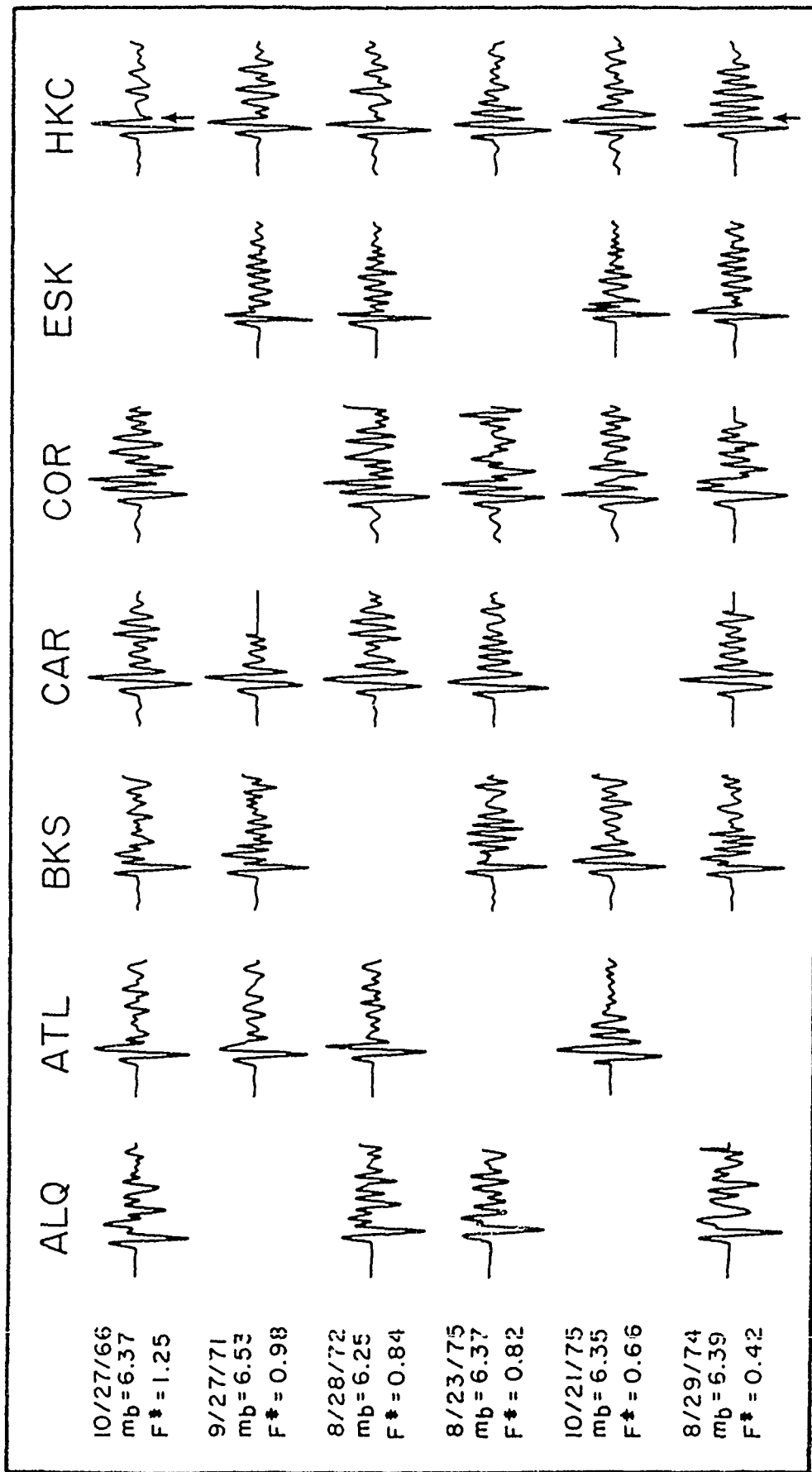
Figure 11a: Comparison of short-period P waves for NNZ events of nearly the same size but different F-factors. F-factor decreases downward. Notice the evolution of the waveform with F-factor, particularly in the second downswing.

316
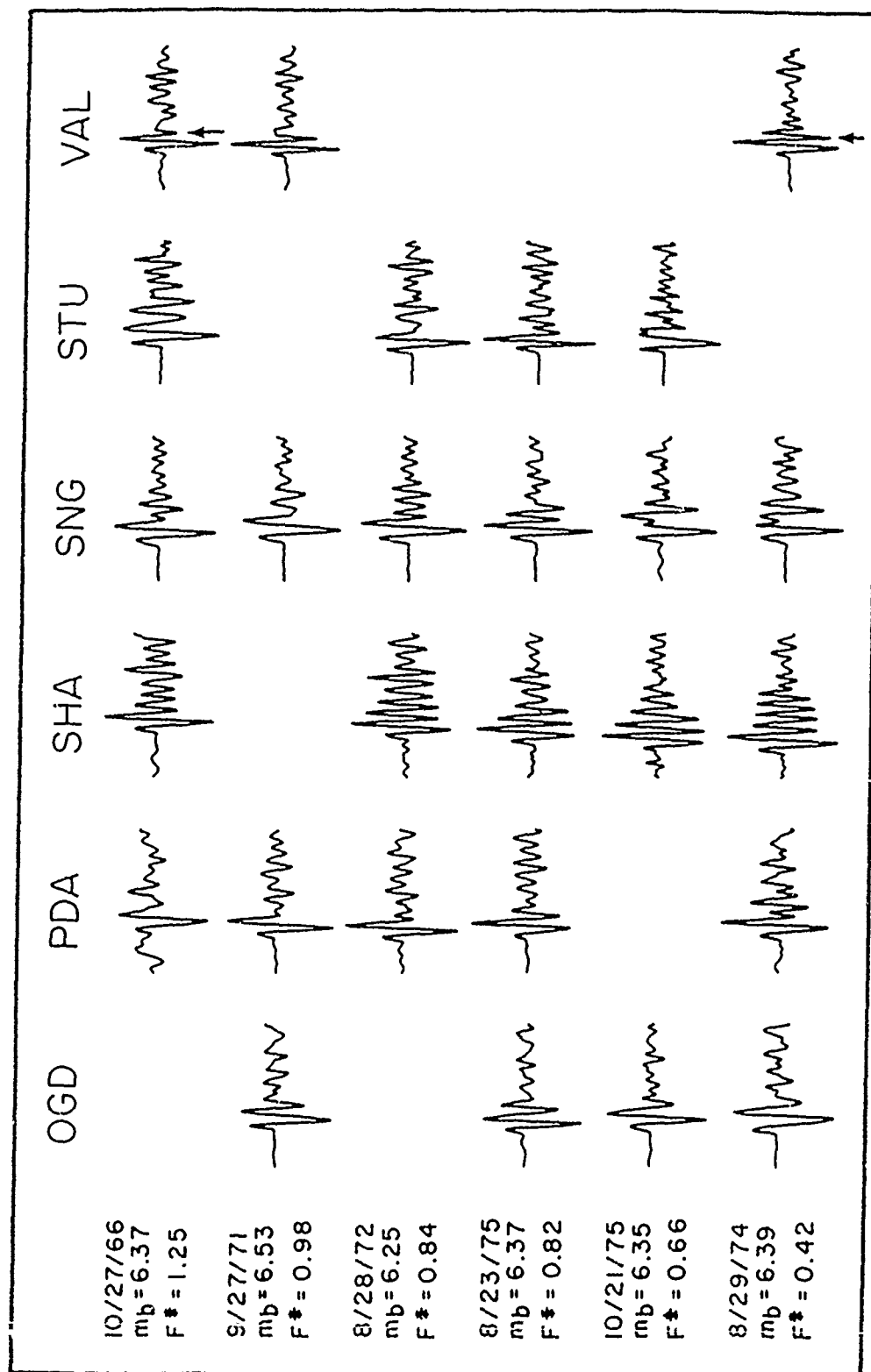
Figure 11b: Comparison of short-period P waves for NNZ events of nearly the same size but different F-factors. F-factor decreases downward. Notice the evolution of the waveform with F-factor, particularly in the second downswing.

OGD   PDA   SHA   SNG   STU   VAL

10/27/66
mb=6.37
F*=1.25

9/27/71
mb=6.53
F*=0.98

8/28/72
mb=6.25
F*=0.84

8/23/75
mb=6.37
F*=0.82

10/21/75
mb=6.35
F*=0.66

8/29/74
mb=6.39
F*=0.42

317
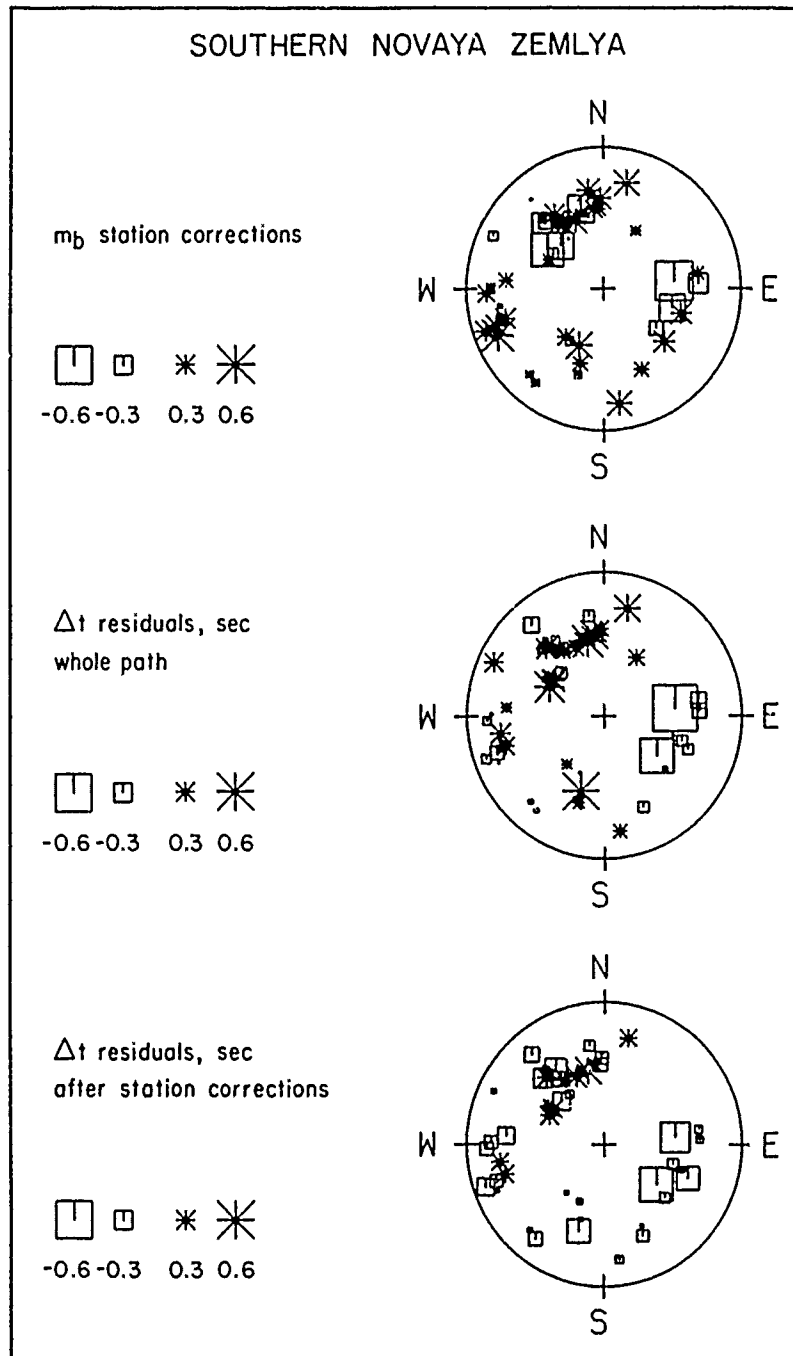
Figure 12: Comparison of the Southern Novaya Zemlya observed magnitude station corrections (top) with the travel time whole path corrections (middle) and travel time corrections after applying station corrections (bottom) from Dziewonski and Anderson (1983).
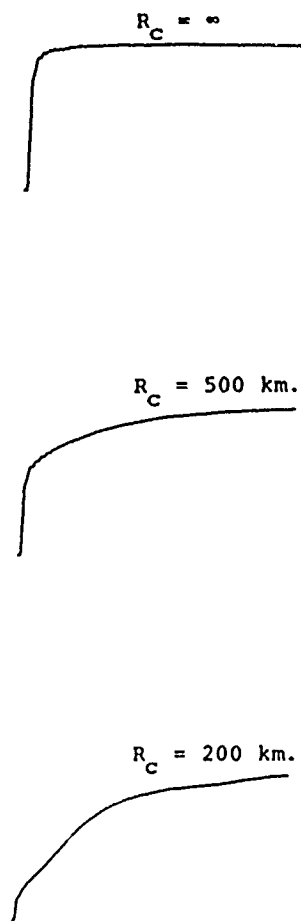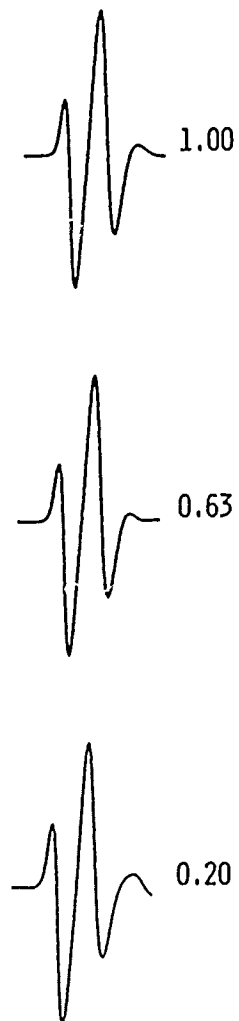
Figure 13: Output from a three dimensional slowness algorithm for
a simple assumed perturbation to the travel time field for a ray
turning in the smooth lower mantle. The amplitude of the perturbation
is 1.0 sec. R_c is a spatial correlation length. Step responses are
shown on the left and short period synthetic seismograms for an
explosive source are shown on the right. A large amplitude change
results from a relatively mild perturbation.

PAPER TITLE: Scattering Attenuation of P and Lg Waves and P-coda and Lg
                Yield Estimation

PAPER AUTHOR: Douglas R. Baumgardt   ENSCO, Inc.

CONTRACT NO.:   F19628-85-C-0057

SUMMARY:

The relative importance of focusing-defocusing and scattering attenuation
in causing P-wave amplitude variations around NORSAR was investigated by
comparing the variations in P and coda amplitudes around the array. Incoher-
ent array stacking of rms amplitudes of P coda and Lg waves recorded at NORSAR
from Soviet PNEs were used to study scattering attenuation and blockage of Lg
waves in Eurasia. The variances of Lg and P coda measurements at NORSAR and
Graefenberg for the largest Shagan River explosions were estimated to deter-
mine if these events had the same yield. Finally, we have initiated a magni-
tude yield study using P coda and Lg measurements on broadband digital data.

CONCLUSIONS AND RECOMMENDATIONS:

Scattering attenuation in the 0.6 to 3.0 Hz band may account for as much
as 0.05 of the 0.2 variation in m_b around NORSAR for P waves from Semipala-
tinsk. In the case of NTS events, however, scattering attenuation beneath
NORSAR does not appear to be as important. Although scattering attenuation
may not be large, it can cause significant m_b variations over small areas
(< 50 km) at regional distances. At frequencies greater than 3 Hz, scattering
attenuation may be more severe. However, by measuring the inverse relation
between P and coda magnitudes across a regional array, scattering attenuation
effects can be identified and corrected.

Lg waves propagating across the Urals to NORSAR are attenuated by about
0.4 to 0.5 log-rms units. A portion of the attenuated Lg energy appears to be
forward scattered into Lg precursor coda waves suggesting that coda measure-
ments may be useful for determining Lg-magnitude correlation for scattering
attenuation. However, we also observed complete blockage of Lg with no coda
generation in the Kola Peninsula. We recommend that modeling studies need to
be done to determine how Lg is scattered or blocked by lateral heterogenei-
ties.

The standard deviation of m_b measurements for all Shagan events with
$m_b > 6$ is about 0.9 to 1.0 m_b units. However, that for Lg and coda amplitudes
is about half that value indicating that the largest Shagan events may be
closer in yield than indicated by m_b. However, more measurements need to be
made to make this conclusion with any high degree of statistical confidence.

INTRODUCTION

The principal objective of this study is to investigate the utility and reliability of alternative magnitude measures, primarily Lg and P coda, made on broadband and high-frequency digital recordings, for estimating the yields of undergound nuclear explosions. The main task areas of this study are the following:

- Assemble a large database of broadband (where available) and/or high frequency digital recordings of P, P-coda, Lg, and Lg-coda waves from underground nuclear explosions of known and unknown yield to be used for yield estimation research.

- Investigate empirically the role of scattering in the attenuation of P- and Lg-wave amplitudes and how coda measurements can be used to correct for the effects.

- Develop and study a variety of analysis techniques for using digitally recorded P-coda and Lg waves for yield estimation. The issues of the precision of these measurements for relative yield estimation and reliability for absolute level measurements will be addressed.

This paper reviews our progress to date in accomplishing these tasks and our planned future research. The topics which will be discussed are the following:

- Relative importance of focusing-defocusing and scattering attenuation on P-wave amplitudes at NORSAR.

- Investigation of scattering and blockage of Lg waves from Soviet PNEs recorded at NORSAR.

- A relative magnitude - yield study of the largest Shagan River explosions using P-coda and Lg measurements at NORSAR and Graefenberg.

- A brief review of yield estimation studies with broadband data.

Comparison of P and P-coda Amplitudes at NORSAR:
Focusing-Defocusing and Scattering Effects

Scattering is generally believed to be the principal cause of P-coda waves from explosions. A variety of deterministic and stochastic scattering mechanisms in the source and receiver regions and along the path between source and receiver can generate P coda waves, including scattering of the P wave itself. If the P wave is significantly attenuated by scattering and if the scattering generates P coda waves, there should be some relationship between the amplitudes of P and coda waves.

Figure 1 shows the variation of P and coda amplitudes in the 0.6 to 3.0 Hz band measured at the NORSAR subarray centers for an explosion at Degelen Mountain in eastern Kazakh. The P wave amplitudes were measured on the ab swing and the coda amplitudes are rms amplitude averages in the coda between 5 and 50 seconds after P. This plot reveals that the P and coda amplitudes are positively correlated with high scatter. The scatter is caused by clusterings of points which are associated with spatial groupings of subarrays (Figure 2). Within the clusters, the P and coda residuals seem to be inversely correlated, i.e., higher P amplitudes correlate with lower coda amplitudes and vice-versa. Most striking are the sensors in the vicinity of the Oslo graben (Figure 3), which have much reduced P-wave amplitudes compared with the rest of the array, but more comparable coda amplitudes. The inverse correlation may reflect the effect of scattering attenuation in regions where focusing and defocusing is approximately constant.

In the case of NTS events, clustering and inverse correlation of P and coda amplitude residuals have not been observed. One possible explanation for this may be that the P and coda waves from NTS approach from the northern part of NORSAR which may be more homogeneous geologically than the southern part. Thus, more of the coda from NTS may have been generated far from NORSAR with little contribution from within the array itself. Another explanation is that NTS is farther from NORSAR (65°) than Degelen (38°), and thus, the P waves

from Degelen impinge on the structure beneath NORSAR at a shallower angle and are thus scattered more than those from NTS.

We conclude from the initial study that scattering beneath NORSAR does noticeably attenuate P waves from Soviet explosions, although the effect is small (no greater than ±0.05 units) and that this effect may be corrected with coda measurements.

Observations at NORSAR of Lg
Scattering and Blockage
in Eurasia

We studied P codas and Lg waves recorded at NORSAR for several Semipalatinsk explosions using incoherent stacking and rms power estimation techniques. Figure 4 shows rms coda envelopes for three events at Semipalatinsk recorded at NORSAR. One noticeable feature of these coda envelopes is that they do not decay exponentially, but rather exhibit a number of breaks in trend and flattenings. Three of these features are associated with the onset of the S, Sn, and Lg phases as indicated in Figure 4. However, the first flattening, between 200 and 340 seconds after P, is consistent on the basis of timing with forward scattering of Lg to P in the Urals (Figures 5 and 6).

Could Lg, which propagates from Semipalatinsk to NORSAR and the other Scandinavian stations, be attenuated by scattering in the Urals, and if so, by how much? To investigate this, we are currently analyzing P coda and Lg waves recorded at NORSAR from several PNEs located in various locations in Eurasia. Figure 7 shows two events which we have analyzed, one of which (7/10/71) was on the west side of the Urals and the other (10/04/79) was on the east side. Thus, the Lgs from the former event did not have to cross the Urals, whereas the Lgs from the latter event did have to cross the Urals.

Comparison of the coda envelopes for the two events reveals that the P-wave amplitudes for the two events are about the same, whereas the Lg amplitude of the larger event, 10/04/79, is about 0.5 log-rms units less than that of the smaller event, 7/10/71. Also, the Lg precursor coda for the 10/04/79 event is about 0.1 to 0.3 units larger on average, than that of the 7/10/71. Moreover, the Lg precursor coda of the 7/10/71 event decays more rapidly with time than that of the 10/04/79 event. These results are completely consistent with the Lg forward scattering theory. We estimate that Lg is attenuated by 0.4 to 0.5 log units by scattering in the Urals. Not all the Lg energy is forward scattered since the increase in Lg precursor coda does not exactly equal the decrease in Lg amplitudes. A portion of the Lg energy must also be back scattered.

Another example of Lg blockage is shown in Figure 8 where the envelopes of two events with the same NEIS magnitudes (m_b=5.2) are compared. The Lg from event 1 to NORSAR crosses the Southern Russian Platform (Δ=26°), whereas the Lg from event 2 crosses the Kola Peninsula on its way to NORSAR (Δ=23°). Clearly, the Lg wave is blocked along the Kola Peninsula path, but there appears little forward scattering of the kind observed for the Urals.

These results raise a number of questions about how Lg waves are scattered or blocked by laterally varying structures in the earth. In some cases, Lgs are only weakly attenuated and forward scattered to P waves, such as in the Urals, whereas in other cases, Lg is completely trapped, blocked or back-scattered with little or no forward scattering, as in the case of the Kola Peninsula. Modeling studies would shed some light on how laterally heterogeneous structures scatter Lg waves.

Relative Magnitude Yield Analysis
of the Largest Shagan River Explosions

In a recent study of the magnitudes of the largest Shagan River explosions, Sykes and Cifuentes (1984) argued that the explosions with $m_b > 6.0$ have nearly the same yield and that the m_b variations for these events are caused by coupling and focusng-defocusing differences. We tested this conjecture by comparing the amplitudes of P coda and Lg waves from Shagan events with $m_b > 6.0$. Average log-rms amplitudes of coda out to 50 seconds past P and in the Lg, beginning 40 seconds before the 3.5 km/sec group velocity time and averaged over a two minute window, were measured for broadband Graefenberg and high-frequency NORSAR data. The variance estimates for the coda and Lg measurements for the largest events were generally smaller by a factor of two than the corresponding m_b estimates of Sykes and Cifuentes (1984) (Table 1). We conclude that this result is consistent with the largest explosions having the same yield although more data must be examined to place any statistical confidence on this conclusion.

We are currently analyzing digital GDSN, RSTN, asnd additional Graefenberg data for a number of recent large Shagan explosions. Our goal in this study is to use Lg and P coda measurements to determine if the recent Shagan events have increased significantly in size, as suggested by m_b measurements, and if so, by how much.

Broadband Yield Estimation Studies

This work has just been initiated and is focusing on P coda and Lg measurements at the RSTN stations for NTS explosions. To date, we have collected and analyzed RSTN recordings of 16 NTS explosions with $m_b \geq 5.0$ which have occurred since early 1982. We are also supplementing this data with older LRSM data, including stations located near the present day RSTN sites. Time domain spectral magnitudes are being made on bandpass filtered traces in

the time domain on both the SP and MP bands using two methods: average envelope peak values and rms amplitudes. The measurements will be analyzed to assess the precision and reliability of using Lg and P coda measurements for relative and absolute yield estimation.

References

Ringdal, F. (1972). P-wave amplitudes and sources of scattering, in m_b observations, J. of Geophys., <u>43</u>, 611-622.

Sykes, L. R. and I. L. Cifuentes (1984). Yields of Soviet underground nuclear explosions from seismic surfaces waves: compliance with the Threshold Test Band Treaty, <u>Proc. Nat'l Acad. Sci. USA</u>, <u>81</u>, 1922-1925, 1984.

DEGELEN MOUNTAIN EVENT
22 NORSAR SUBARRAY CENTERS
FILTER 0.6 – 3.0 Hz
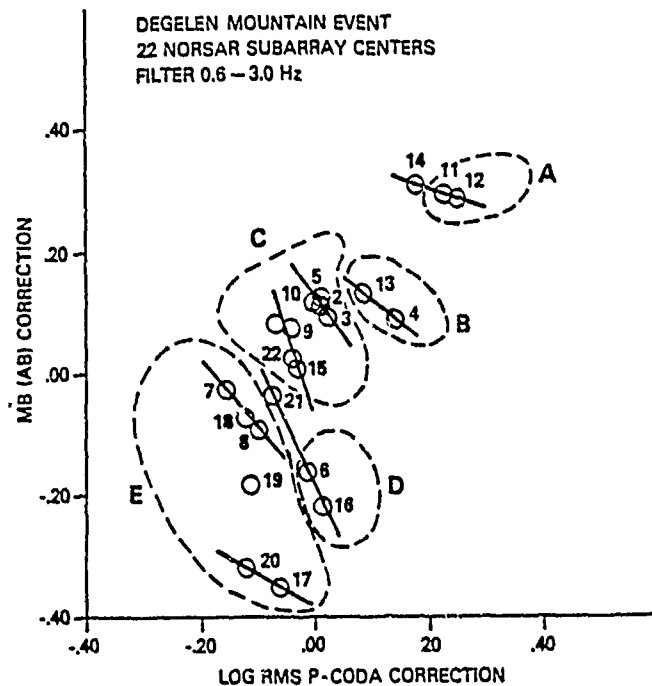
FIGURE 1 Plot of the residuals of P and coda amplitudes with
respect to the mean for 22 NORSAR subarray center
elements for the 22 April 1971 Degelen Mountain event.
The dashed lines encircle clusters labelled A, B, C, D,
and E, for subarrays which cluster spatially.
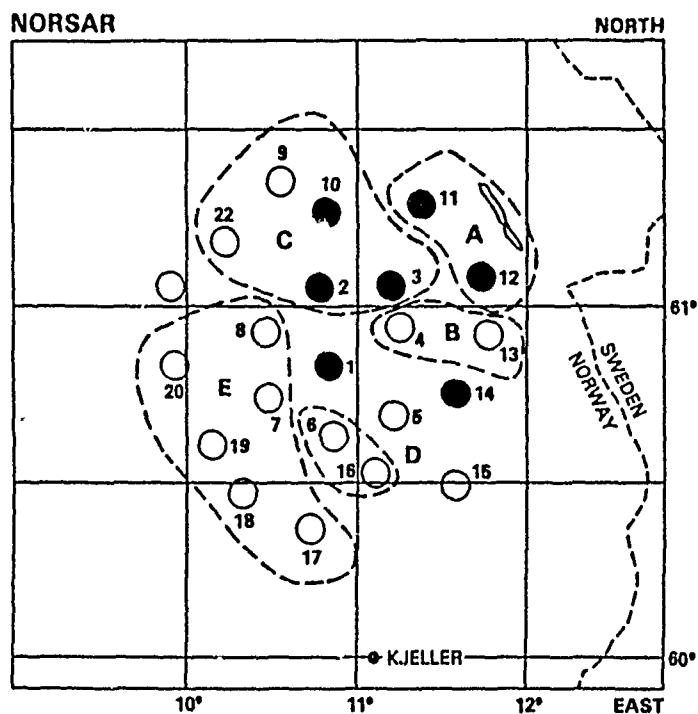
FIGURE 2 Map of NORSAR subarray centers showing spectral clusters corresponding
to the clustering of points on the scatter plot in Figure 1.
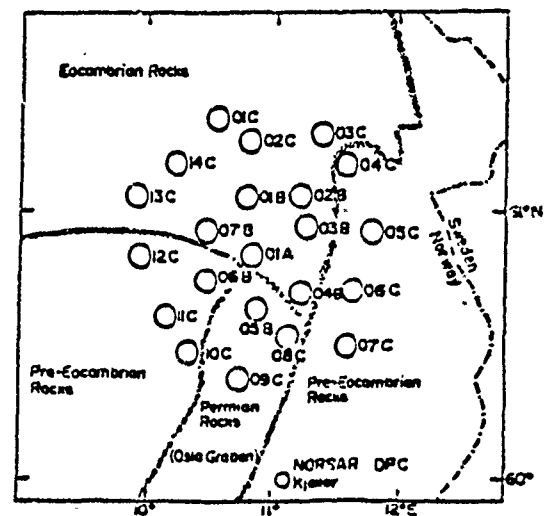
FIGURE 3 NORSAR Array Configuration. The geological structure
in the siting area are briefly outlined.

327
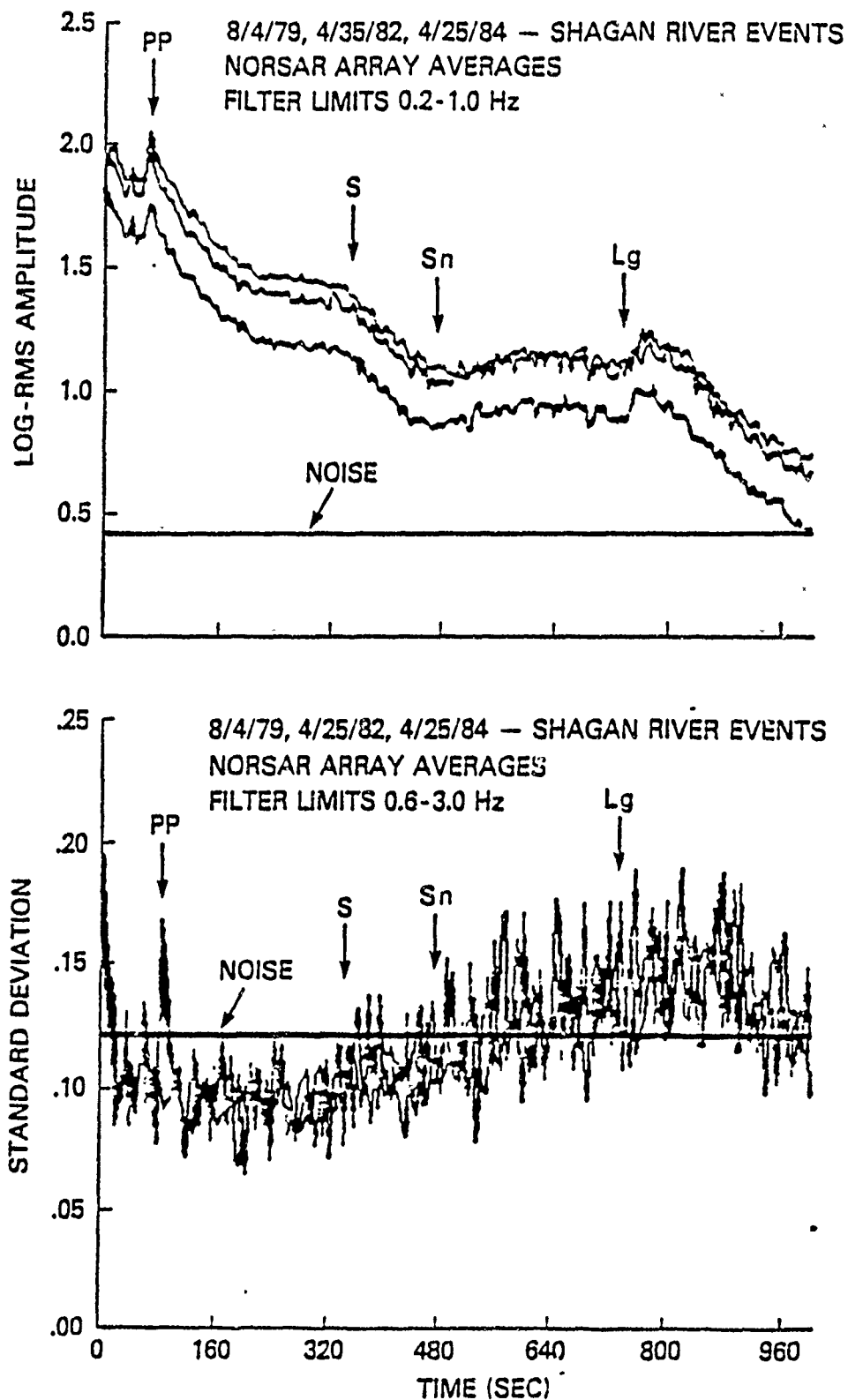
FIGURE 4   Log-rms Amplitude and Standard Deviations for P-coda
and Lg Waves Recorded at NORSAR from Three Shagan River
Explosions
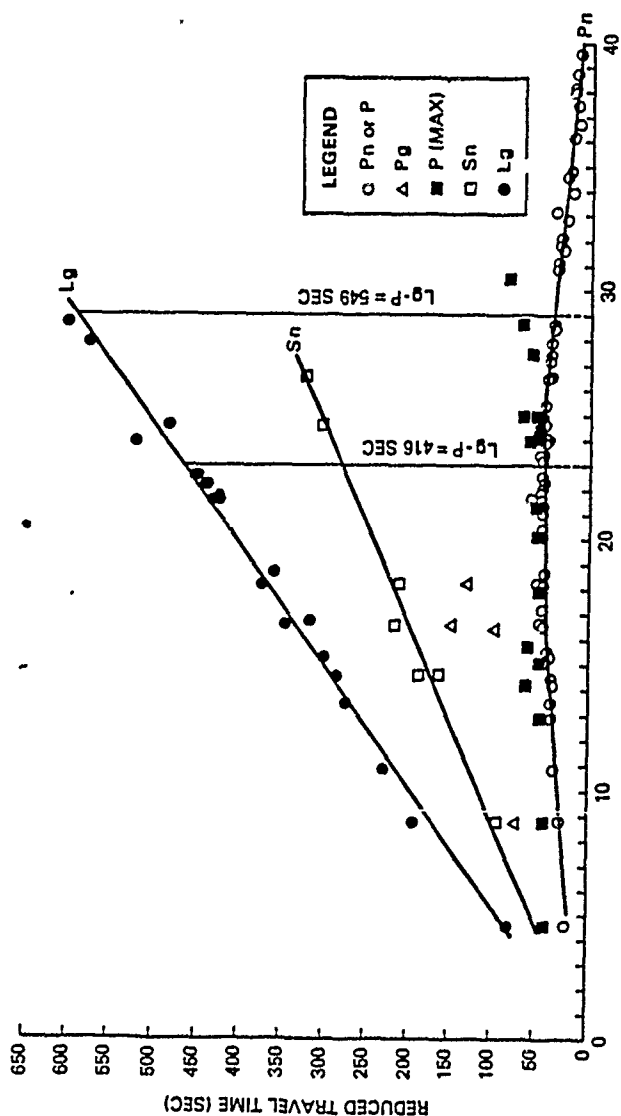
FIGURE 5   Regional Travel-time Curves, Reduced to a velocity of 10 km/sec, for western Russia (after Gupta et al, 1980). The vertical lines indicate the distance corresponding to the Lg-P times for the beginning and end of the flat portion of the NORSAR P-coda log-rms amplitude plots in Figure 4.
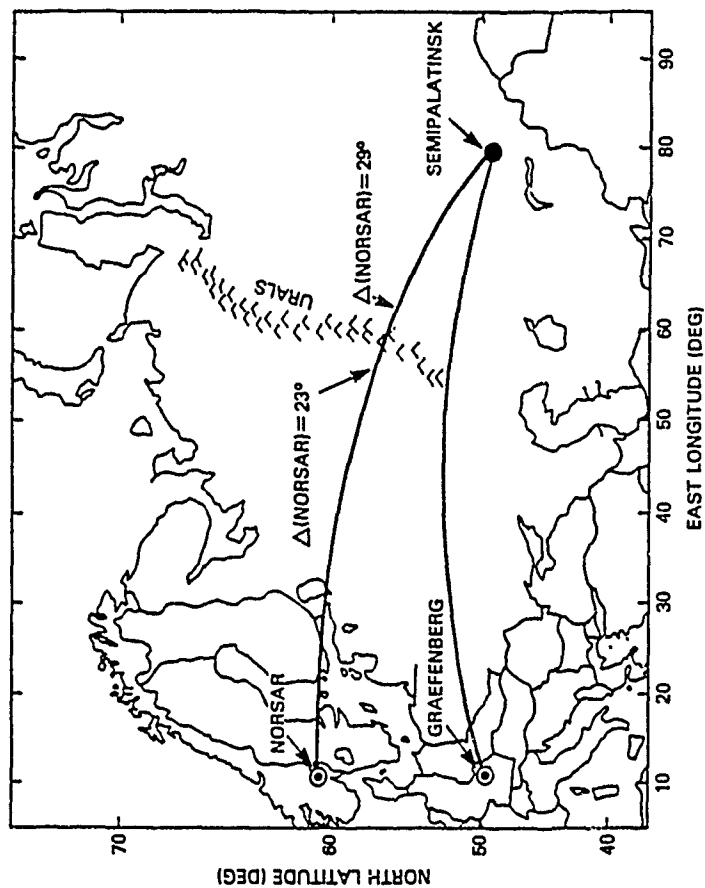
FIGURE 6   Map showing prppagation paths from Semipalatinsk to NORSAR and Graefenberg. Distances corresponding to the beginning and end of the flat part of the NORSAR codas are indicated on the NORSAR path.

329

NORSAR CHANNEL AVERAGES
FILTER 0.6 – 3.0 Hz

PNE – 10/4/79
$\Delta = 29°$
$m_b = 5.4$

PNE – 7/10/71
$\Delta = 20°$
$m_b = 5.2$
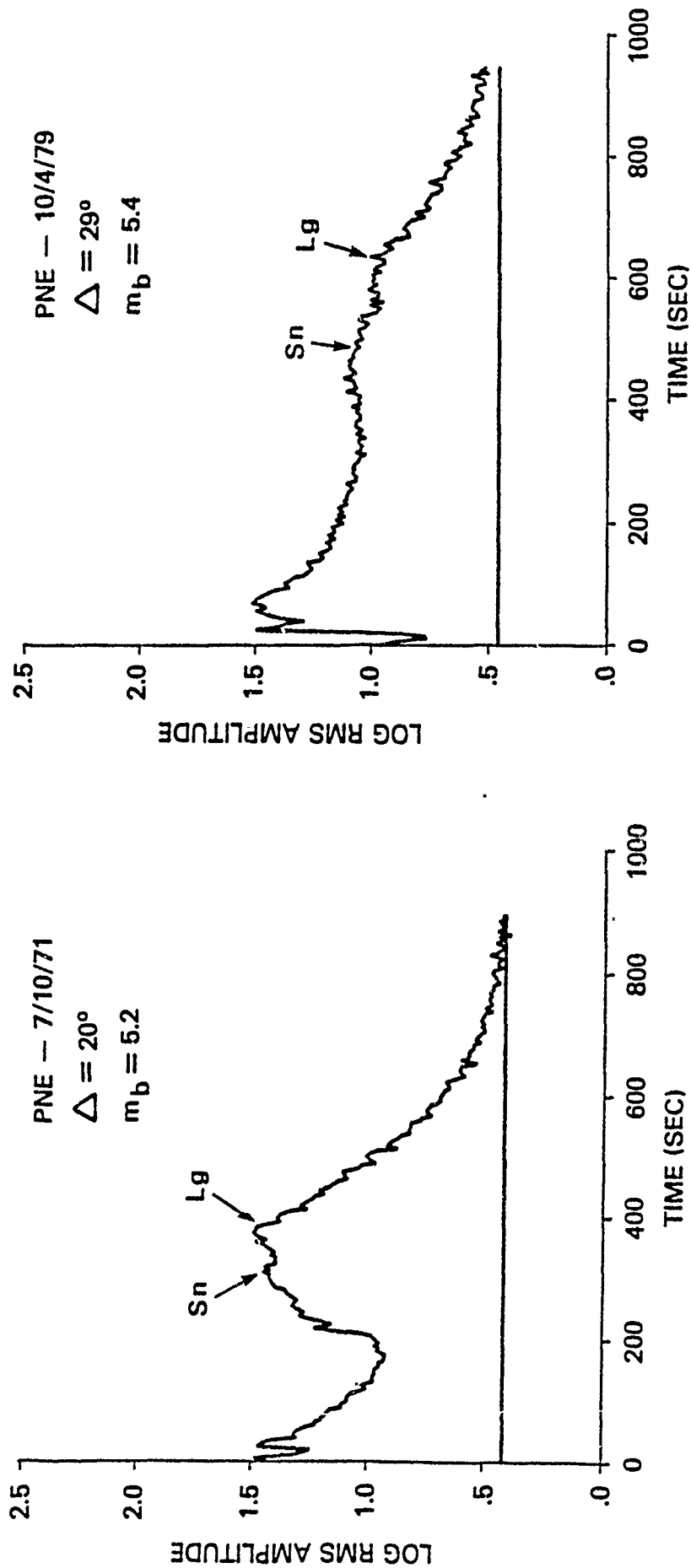
FIGURE 7   P-coda Envelopes for PNE Events Located West (left) and East (Right)
of the Ural Mountains Recorded at NORSAR

330
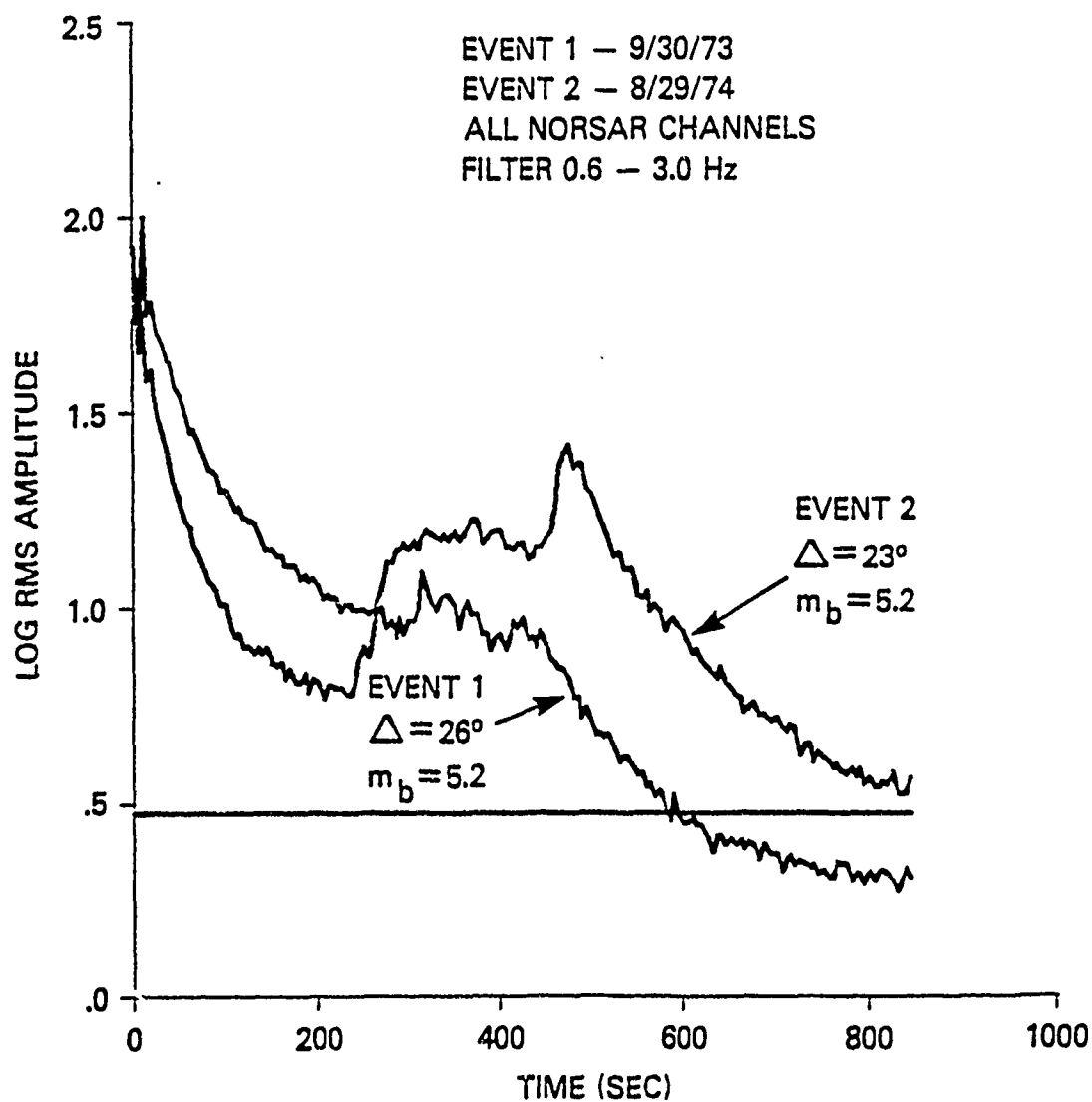
FIGURE 8   P-coda Envelopes for Two PNEs in Eurasia Recorded at
NORSAR. Event 1 Lg Crosses the Kola Peninsula and
Event 2 Lg crosses Southern Russian Platform

331

TABLE 1
MEANS AND STANDARD DEVIATIONS FOR MAGNITUDE
MEASUREMENTS OF LARGEST SOVIET EXPLOSIONS, 1976-1982

Method	Mean	Standard Deviation	No. of Events
1. Single-Channel Lg NORSAR⁻	3.11	0.04	5
Multi-Channel Lg NORSAR⁻⁻	3.01	0.05	5
NEIS m_b Corresponding Events	6.12	0.13	5
Corrected m_b Corresponding Events*	6.143	0.092	5
2. Multi-Station Lg WWSSN**	6.01	0.07	4
NEIS m_b Corresponding Events	6.18	0.10	4
Corrected m_b Corresponding Events*	6.167	0.036	4
3. Single-Channel P-coda NORSAR⁺	1.97	0.05	6
Multi-Channel P-coda NORSAR⁺⁺	1.96	0.06	6
NEIS m_b Corresponding Events	6.17	0.10	6
Corrected m_b Corresponding Events*	6.160	0.082	6
4. Vertical Lg Graefenberg Al 0.6-3.0 Hz	1.840	0.033	5
Vertical Lg Graefenberg Al 0.2-1.0 Hz	2.231	0.033	5
Transverse Lg Graefenberg Al 0.6-3.0 Hz	1.972	0.037	5
Transverse Lg Graefenberg Al 0.2-1.0 Hz	2.401	0.047	5
Vertical Coda Graefenberg Al 0.6-3.0 Hz	2.508	0.051	5
Vertical Coda Graefenberg Al 0.2-1.0 Hz	2.506	0.051	5
Transverse Coda Graefenberg Al 0.6-3.0 Hz	2.203	0.057	5
Transverse Coda Graefenberg Al 0.2-1.0 Hz	2.231	0.029	5
Corrected m_b Corresponding Events*	6.149	0.069	5

TITLE: Analysis of Teleseismic P Wave Amplitude and Coda
           Variations for Underground Explosions at U.S. and
           Soviet Test Sites

AUTHORS: Thorne Lay, Christopher Lynnes and Larry Ruff

CONTRACT NO.:   F19628-85-K-0030

SUMMARY: A detailed analysis of the amplitudes, travel times, and coda
           characteristics of teleseismic short period P waves from 25 Pahute
           Mesa tests has been conducted with the intent of establishing the
           near-source contribution to observed variations in the signals. A
           strong correlation is found between early arrival times and
           diminished initial amplitudes. This indicates that defocussing by
           a high velocity anomaly in the upper mantle beneath the test site
           produces the observed azimuthal amplitude pattern. However, the
           travel time anomaly pattern for Pahute Mesa tests strongly
           resembles, though is enhanced relative to, that for Yucca Flats
           events, requiring that much of the travel time pattern be produced
           deep in the mantle or near the receivers. Three dimensional ray
           tracing experiments are conducted to constrain possible velocity
           structures consistent with the travel time and amplitude data. The
           P wave coda in the first 15 sec of the waveforms is analyzed in an
           effort to further constrain tectonic release and near-source
           structure effects on the signals.

   CONCLUSIONS AND RECOMMENDATIONS: There is good reason to believe that
           most of the azimuthal amplitude pattern observed for Pahute Mesa
           explosions is produced by defocussing propagation effects rather
           than by tectonic release interference. However, reliable
           determination of the responsible velocity structure will require
           additional careful analysis of Yucca Flats events. There is cause
           for concern about the robustness of recent upper mantle velocity
           models for NTS given the fact that the differential travel time
           pattern between Pahute Mesa and Yucca Flats events has the same
           azimuthal variation as their individual patterns.

Introduction

The accuracy of seismologically determined yield estimates for underground nuclear explosions appears to be delimited by our poor understanding of short period wave propagation phenomena. We lack a detailed knowledge of regional variations and frequency dependence of attenuation, and of scattering effects arising from seismic wave interactions with complex velocity structure near the source, along the path through the mantle, and near the receiver. These effects are responsible for the order of magnitude variation of short period P wave amplitudes, and the large P wave spectral content variations, observed for every event. To improve our understanding of short period wave propagation, we are conducting detailed analysis of short period P waveforms from underground explosions in both U.S. and Soviet test sites. By systematic analysis of large data sets with good azimuthal coverage, we are striving to characterize path, receiver and source region propagation effects. This paper presents preliminary results of analysis of short period P waves from Pahute Mesa explosions.

Amplitude and Travel Time Anomalies for Pahute Mesa Explosions

Lay et al. (1984) showed that the first cycle (ab amplitude) of short period P waves from Pahute Mesa explosions have a systematic azimuthal amplitude pattern. This is shown in Figure 1, with stations on the northeast recording amplitudes averaging a factor of 2.5 lower than observed at other azimuths. This pattern is common to all Pahute Mesa explosions, though there are subtle variations from event to event. The azimuthal amplitude patterns for events in other subsites of NTS differ significantly from that for Pahute Mesa events, as shown in Figure 2. The existence of such an azimuthal variation can potentially bias yield estimates; thus, it is important to determine the cause of this variation. The plausible explanations fall into two categories: 1) tectonic release contamination of the radiated wavefield, and 2) earth structure effects.

Lay et al. (1984) explored the tectonic release explanation, finding two lines of supporting evidence for this hypothesis. The most important is the fact that the azimuthal amplitude pattern has a clear sin2θ component, with an orientation and amplitude consistent with the known tectonic release parameters determined from long period P and SH waves (Wallace et al., 1983, 1984). Figure 3 shows theoretical calculations of the predicted short period azimuthal amplitude pattern for explosion plus double couple models compared with the observed Pahute Mesa amplitude variations. The other line of evidence is a correlation found between F-factor and the sin2θ component for individual events, with larger tectonic release associated with less scatter in the sin2θ pattern. The latter observation is difficult to appraise because F-factor also has correlations with burial depth and with position in the Mesa. In order for the tectonic release model to explain the ab amplitude variations in the first 1/2 sec of the P arrivals, the explosion P waves must drive the rupture, and each event must have a similar proportion of high frequency tectonic release radiation.

The Pahute Mesa amplitude pattern could also be produced by propagation effects, rather than by a source process such as tectonic release. Either an attenuation anomaly or complex velocity structure resulting in focussing-defocussing or multipathing could be responsible. Travel time studies of the upper mantle velocity structure beneath NTS by Spence (1974), Taylor (1983) and Minster et al. (1981) all suggest the presence of a high velocity body localized beneath Pahute Mesa, extending from the crust down 100 km or more

into the upper mantle. This is based on early arrival times recorded at
stations northeast from Pahute Mesa. These results indicate a correlation
between early arrivals and low amplitudes, which is inconsistent with an
attenuation explanation. However, a high velocity body to the northeast of
Pahute Mesa at upper mantle depths could possibly defocus the P wave field,
producing low-amplitude, early arrivals. Figure 4 presents a northeast
trending cross section through the upper mantle velocity model obtained by
Minster et al. (1981), along a plane intersecting the Pahute Mesa events.
Note the high velocity tongue of material extending off to the northeast.
This body is actually cylindrical in shape, and the lateral velocity gradients
would deflect energy away from the high velocity material, causing
defocussing. It is important to note that all of the travel time studies that
obtain this type of structure do so by stripping out any anomaly pattern
common to the entire NTS source region. The data used to determine the common
pattern are dominated by events in Pahute Mesa and Yucca Flats.

In order to discriminate between the tectonic release and earth structure
explanations we have sought to establish the degree of correlation between
travel time and amplitude anomalies. The tectonic release hypothesis predicts
no specific correlation, while a strong correlation is suggestive of a
structural effect. To provide a one-to-one comparison of travel time and
amplitude anomalies, we measured travel times for 25 Pahute Mesa shots, as
well as for COMMODORE, PILE DRIVER and FAULTLESS, using the same WWSSN and
Canadian recordings for which ab amplitudes were previously measured. The
travel times were corrected for (1) clock corrections; (2) ellipticity
corrections following Dziewonski and Gilbert (1976); (3) shot elevation
corrections using the structures from Bache et al. (1979); and (4) station
corrections, using the azimuthally-dependent corrections from Dziewonski and
Anderson (1983). If either clock or station corrections could not be
obtained, the datum was discarded, leaving 1156 travel times for Pahute Mesa
events. Residuals were then calculated using the 1968 travel time tables.
The average station residuals for the Pahute Mesa events are compared with the
average station amplitude anomalies in Figure 5. The travel time anomalies
also show a strong azimuthal pattern, with stations to the northeast recording
travel time anomalies about 2 sec faster than at other azimuths. The patterns
are remarkably similar though slightly phase shifted, and the correlation
coefficient of the amplitude and travel time station anomalies is 0.39. This
clear association of early arrival times and diminished amplitudes, and the
long wavelength azimuthal patterns, strongly suggest an elastic defocussing
effect.

Comparison of the travel time pattern for Pahute Mesa events with those
for other events in NTS allows us to isolate the near-source contribution.
This leads to an interesting observation, illustrated in Figure 6, which is
that the other NTS events have a very similar azimuthal pattern in their
·travel time anomalies. When a sin2θ curve is regressed through the Pahute
Mesa station residuals, it has a peak-to-peak amplitude of 1.5 sec, compared
to 1.3 sec for a sin2θ curve fit to the average of the three non-Pahute Mesa
events. The sine curves have almost the same orientation. While the
azimuthal patterns are very similar, the Pahute Mesa pattern is slightly
stronger. Thus, it appears tht most of the 2 sec azimuthal variation in the
Pahute Mesa travel time anomalies is produced by deep path or receiver
variations. If the travel time pattern is a result of systematic receiver
effects, then it is clear that the station corrections of Dziewonski and
Anderson (1984) are inadequate, and the travel time pattern is unrelated to
the amplitude pattern, despite their similarity. The station corrections that

335

were applied do not show any systematic azimuthal pattern, so it seems
unlikely that near-receiver effects are responsible. The early arrival times
could be produced by a high velocity anomaly either deep in the mantle, or in
the upper mantle at depths greater than 150 km. It is then problematic
whether the Pahute Mesa events have a slightly stronger pattern because of an
additional shallow mantle anomaly beneath the Mesa, as in the model of Minster
et al. (1981), or whether the difference in source location relative to the
deeper mantle anomaly accentuates the pattern for Pahute Mesa.

If the average travel time pattern for NTS events outside of Pahute Mesa
is removed from that for the Pahute Mesa events, the residual pattern still
has early arrivals to the northeast, but the travel time anomalies involved
are on the order of 0.5 sec or less. Thus, the resolution of shallow velocity
heterogeneity beneath the Mesa relies on a small difference between relatively
large numbers. This removal of a common pattern was performed in all of the
previous travel time studies, and all of these have limited resolution of the
depth extent of the additional velocity heterogeneity affecting Pahute Mesa.
This is apparent in Figure 4, where the velocity heterogeneity is stretched
out along the ray paths. Our approach has been to use three dimensional ray
tracing to compute amplitude and travel time anomalies for different upper
mantle heterogeneity configurations in order to constrain the range of
possible structures.

Determining the depth of the velocity heterogeneity is particularly
difficult, though the data do provide control on the minimum depth extent.
Figure 7 shows a projection of the observed m_b anomalies from Pahute Mesa
explosions at the position each ray path would intersect surfaces at depths of
10, 35 and 140 km below the Mesa. The rays were traced down through a
laterally homogeneous structure. This type of projection is used in "thin
lens" modeling. The figures on the right show the average value of the
amplitude anomalies in each bin of the gridded surface. No coherent pattern
of high or low amplitudes can be seen in the 10 km deep projection, indicating
that the velocity heterogeneity must extend below this depth. An image is
apparent in the 35 km projection, but it is still a bit incoherent, while for
greater depths, such as 140 km, the image is quite sharp. At the greater
depths we are basically seeing the overall average azimuthal pattern. Thus,
the anomalous structure should probably extend deeper than 35 km and certainly
deeper than 10 km in order to produce the observed long wave length azimuthal
amplitude pattern.

A similar down-projection of the travel time anomalies is shown in Figure
8. Once again a coherent image begins to form near 35 km depth, and this
sharpens with increasing depth. Note the similarity between the amplitude and
travel time data in Figures 7 and 8. The travel times appear to have a ray
parameter dependence in the northeastern azimuth, with closer stations
recording later arrivals. A similar, but weaker trend is apparent in the
amplitudes. Stations due north of the site have small travel time anomalies,
but low amplitudes. The geometry of the defocussing body may be responsible
for this breakdown in the correlation between amplitude and travel time
anomalies.

In order to determine velocity heterogeneity configurations that could
produce the observed amplitude and travel time anomalies, we performed a
series of three dimensional ray tracing calculations through smoothly varying
structures. For each model we compute theoretical amplitude and travel time
anomalies, with the amplitude calculations based on geometric ray divergence.
This is probably quite accurate for our models, which have very smooth
velocity gradients, except in the vicinity of caustics. We specify a

structure, then trace the rays down to a depth below which the model is laterally homogeneous. Anomalies are defined relative to amplitude and travel times computed for a reference, laterally homogeneous, structure. In order to directly compare our synthetic anomalies with the data, we match the terminating ray parameter and azimuth of the calculated ray paths with the values for individual observations, approximately solving the two-point problem.

The initial calculations were made for the velocity structure of Minster et al. (1981). Figure 9 compares observed, synthetic, and residual log amplitude anomalies for the Pahute Mesa event GREELEY. The terminating depth is 140 km. Clearly, this model underpredicts the amplitude variation, though it should satisfy the travel time data because it was derived by block inversion of ISC travel times.

A simple velocity model, motivated by the Minster et al. (1981) and Taylor (1983) results, that does match the long wavelength azimuthal amplitudes is shown in Figure 10. Figure 10a shows a cross-section through a vertical tabular structure, such as a dike. The dike is infinite in length and has an average of 2% faster velocity over a width of about 10 km. Figure 10b shows a vertical velocity profile through the center of the dike, indicating that it has a depth range of from 10 to 100km. Figure 11 shows the results of raytracing at 2° azimuth intervals through this structure to a depth of 140 km, for a surface source centered above the dike. The dike is oriented N-S in this figure, but the pattern can simply be rotated 15° clockwise to match the Pahute Mesa trend. The amplitudes (Figure 11a) show a clear zone of defocussing parallel to the dike, with a maximum amplitude range of 3.7. The travel time anomalies (Figure 11b) track the amplitude pattern closely, with a range of 0.4 sec. While it appears that the azimuth range of the anomalous low amplitudes and fast travel times is very narrow, the terminating ray azimuths (Figure 11c) actually span a full quadrant in the far-field, because of the significant ray deflections. If the source is laterally offset by 5 or 10 km from the center of the dike (Figure 12) a distortion of the azimuthal amplitude pattern occurs, though there is still a broad range of low amplitudes along the strike of the dike. A caustic develops for the offset sources, but this would affect only a narrow azimuth range teleseismically. Thus, such a structure could affect all of the Pahute Mesa events, with small changes in the teleseismic amplitude pattern resulting from the variation in source position relative to the defocussing body.

Figure 13 compares the complete set of Pahute Mesa amplitude anomalies with corresponding synthetic amplitudes for the infinite length dike model. The difference in the observed and synthetic values is shown on the right. Below the projections, which are for 140 km depth, are shown bin-averaged grids of the log amplitude anomalies. The long wavelength patterns of the synthetic and observed amplitude are strikingly similar. Although the residuals do not vanish, there is a significant variance reduction obtained by removing the long wavelength pattern. Recall that no station amplitude corrections have been applied, and much of the residual variance may be due to receiver effects. The two-dimensional tabular geometry is actually more efficient at defocussing the wavefield than the cylindrical structure in the Minster et al. (1981) structure. A finite slab model, which extends from directly under the test site to about 65 km northeast of Pahute Mesa reduces the variance an equal amount. The preceding models were based on the assumption that the Pahute Mesa events are affected by a shallow mantle anomaly that causes both the amplitude pattern and the enhanced travel time variatons relative to the overall NTS pattern. It is possible that deeper

heterogeneity is responsible for all of the travel time pattern and possibly the amplitude pattern as well. To explore this possibility we will need to model the FAULTLESS, PILEDRIVER and COMMODORE observations as well. While any deeper heterogeneity must be spread over a wider region if it is to affect the broad azimuth range of the anomalies, the velocity heterogeneity must still have strong lateral gradients if a significant effect on the amplitudes is to be produced. We are currently investigating such structures.

P wave Coda Measurements for Pahute Mesa Events

While the evidence cited above indicates an earth structure origin for the azimuthal patterns in the short period P waves from Pahute Mesa, this does not rule out tectonic release contamination of the waveforms. Lay et al (1984) showed that the tectonic release parameters determined from long period signals predict observable teleseismic short period effects, whether or not the front part of the waveform is affected by propagation effects. Douglas (1984) reports evidence for aftershock arrivals in the P wave coda for GREELEY. We are systematically evaluating the first 15 sec of the short period P waveforms from the Pahute Mesa tests in order to determine whether near source effects such as tectonic release, burial depth, or position within the Mesa affect the teleseismic signals. We are using the same data set from 71 WWSSN and CSN stations that was used above in order to attain good azimuthal coverage. This azimuthal coverage is needed if the causes of the coda variations are to be determined.

Figure 14 compares the first 10 sec of short period P waveforms for a high tectonic release event (GREELEY) and a low F-factor event (COLBY). The data are distributed around the strike slip radiation pattern of the tectonic relase mechanism for GREELEY. It is difficult to identify systematic differences in the raw data that can be attributed to differential tectonic release. However, these differences may be quite subtle, as shown by Lay et al. (1984), so it is necessary to develop a quantitative measure of the signal variations. Because the coda is probably dominated by scattered energy, we feel that seeking deterministic models is unwarranted at this point and have decided to follow an empirical approach.

Clearly, there is a large receiver structure contribution to the teleseismic waveforms, but there is also a substantial source region signature. This is demonstrated in Figure 15, which compares waveforms from UME and OGD for the larger Pahute Mesa tests as well as FAULTLESS, COMMODORE and PILEDRIVER. It is readily apparent that some events, such as HALFBEAK, CAMEMBERT, MUENSTER and PILEDRIVER have anomalous waveforms. These differences are more apparent at UME, which lies in the loop of the tectonic release P radiation pattern than at OGD, which lies along the node. Stations at other azimuths also tend to show enhanced complexity in the P wave coda for these events, as shown in Figure 16.

In order to characterize these coda variations as a function of azimuth, we are using the seismic envelope of the short period traces (Farnbach, 1975). This provides a smoothed version of the short period waveform that can be easily compared between stations and between events. The envelopes for the teleseismic observations for GREELEY are shown in Figure 17. Note the diversity of envelope shapes between stations. A large component of this variation is due to receiver structure, which must be accounted for before azimuthal patterns in the coda can be detected. The coda envelopes for the first 15 sec of the P waves recorded for the 28 NTS tests at station OGD are shown in Figure 18a. The differences in the curves should be principally due

to source variations. Squaring the envelopes accentuates the larger coda arrivals, as seen in Figure 18b, and allows ready identification of events that have greater coda complexity, such as CAMEMBERT, CHESHIRE, ESTUARY, HALFBEAK, MUENSTER, POOL, SCOTCH, COMMODORE, and PILEDRIVER. A linear stack of these envelopes is also shown, giving an approximation of the intrinsic receiver effects. The envelopes in Figure 18 are simple enough to be visually compared or measured by simple parameters such as the time it takes for 1/2 of the total envelope area to be covered.

A similar comparison of coda envelopes and their squares for station UME is shown in Figure 19. The coda envelopes are easier to characterize and compare than the raw traces in Figure 15. Some events are complex at both UME and OGD, notably HALFBEAK, MUENSTER, and COMMODORE, while some events have different relative complexity, such as SCOTCH, STINGER and PILEDRIVER. We intend to map out the azimuthal variations in these signals by using summary envelope parameters as well as by characterizing relative source complexity. These measurements will then be correlated with F-factor, burial depth, and source location.

CONCLUSIONS

By a data-intensive analysis of travel times, amplitudes and coda variations of short period P waves from Pahute Mesa explosions the near-source contributions to the signals are being determined. A clear correlation of early arrival times with diminished initial amplitudes suggests that the azimuthal patterns for Pahute Mesa are produced by defocussing by a high velocity structure under the Mesa. There is substantial uncertainty in the depth of the velocity heterogeneity, and further analysis of Yucca Flats events is required. Analysis of coda envelopes appears to be a promising procedure for characterizing near-source effects. Correlation of coda characteristics with F-factor, burial depth, and position in Pahute Mesa will shed further light on the wave propagation effects near the sources.

REFERENCES

Bache, T.C., S.M. Day and J.M. Savino (1979). Automated magnitude measures, earthquake source monitoring, VFM discriminant testing and summary of current research, Quarterly Report, SSS-R-79-3933, S-Cubed, La Jolla, California.

Douglas, A. (1984). Teleseismic observation of aftershocks immediately following an underground explosion, Geophys. J. Roy. Astron. Soc., 77, 503-515.

Dziewonski, A.M. and F. Gilbert (1976). The effects of small, aspherical perturbations on travel times and a re-examination of the corrections for ellipticity, Geophys. J. Roy. Astron. Soc., 44, 7-17.

Dziewonski, A.M. and D.L. Anderson, (1983). Travel times and station corrections for P-waves at teleseismic distances. J. Geophysics. Res., 88, 3295-3314.

Farnbach, J.S. (1975). The complex envelope in seismic signal analysis. Bull. Seismol. Soc. Amer., 65, 951-962.

Lay, T., T. C. Wallace and D.V. Helmberger (1984). The effects of tectonic release on short-period P waves from NTS explosions, Bull. Seismol. Soc. Amer., 74, 819-842.

Minster, J.B., J.M. Savine, W.L. Rodi, T.H. Jordan, and J.F. Masso (1981). Three-dimensional velocity structure of the crust and upper mantle beneath the Nevada test site, Final Technical Report, SS-R-81-5138, S-Cubed, La Jolla, California.

Spence, W. (1974). P-wave residual differences and inferences on an upper mantle source for the Silent Canyon volcanic centre, Southern Great Basin, Geophys. J. R. Astron. Soc., 38, 505-523.

Taylor, S.R., (1983). Three dimensional crust and upper mantle structure at the Nevada Test Site, J. Geophys. Res., 88, 2220-2232.

Wallace, T.C., D.V. Helmberger and G.R. Engen (1983). Evidence of tectonic release from underground nuclear explosions in long period P waves, Bull. Seismol. Soc. Amer., 73, 593-613.

Wallace, T.C., D.V. Helmberger and G.R. Engen (1984). Evidence of tectonic release from underground nuclear explosions in long period S waves, Bull. Seismol. Soc. Amer., 75, 157-174.
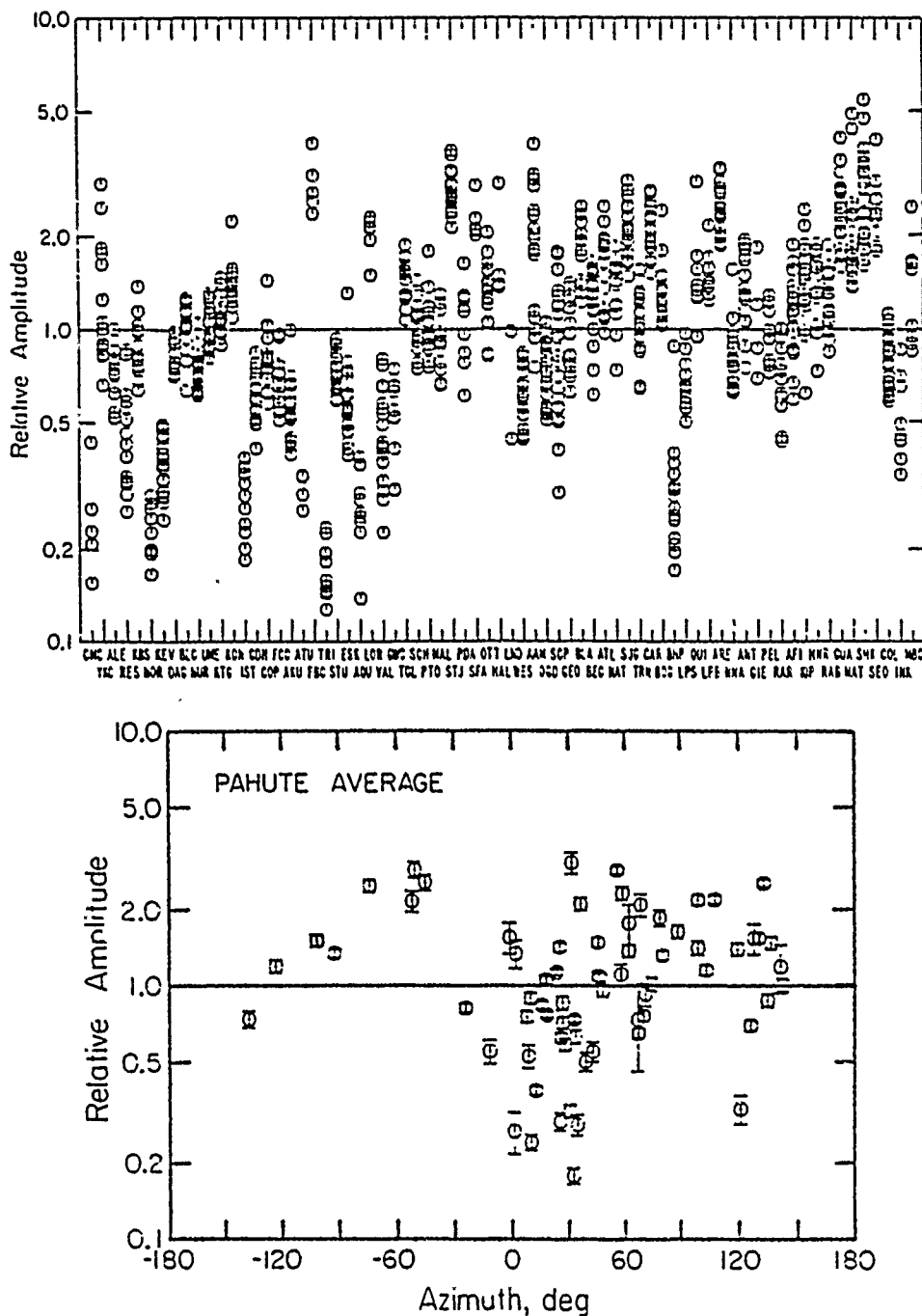
Figure 1. Top: Relative short period ab amplitudes for 25 Pahute Mesa events
with yields larger than 50 kt. WWSSN and CSN observations are included. The
absolute amplitudes have been adjusted to remove the effect of different
source size. Bottom: The average station amplitudes from the top figure
plotted as a function of azimuth from NTS. The mean and standard error of the
mean is shown for each station.
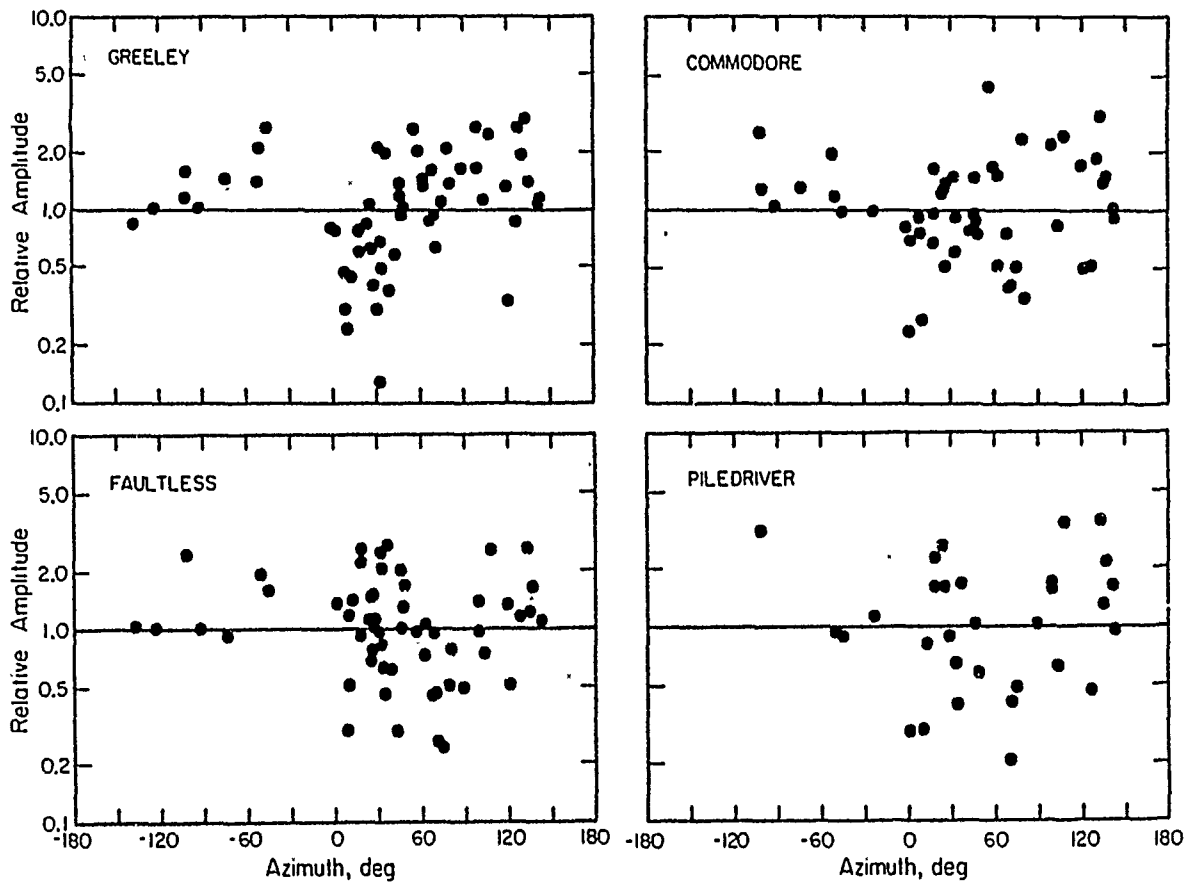
Figure 2. Azimuthal short period ab amplitude patterns for events at different subsites within NTS. GREELEY (Pahute Mesa) differs significantly from COMMODORE (Yucca Flats), FAULTLESS (150 km north of Pahute Mesa) and PILEDRIVER (Climax Stock).

TECTONIC RELEASE HYPOTHESIS
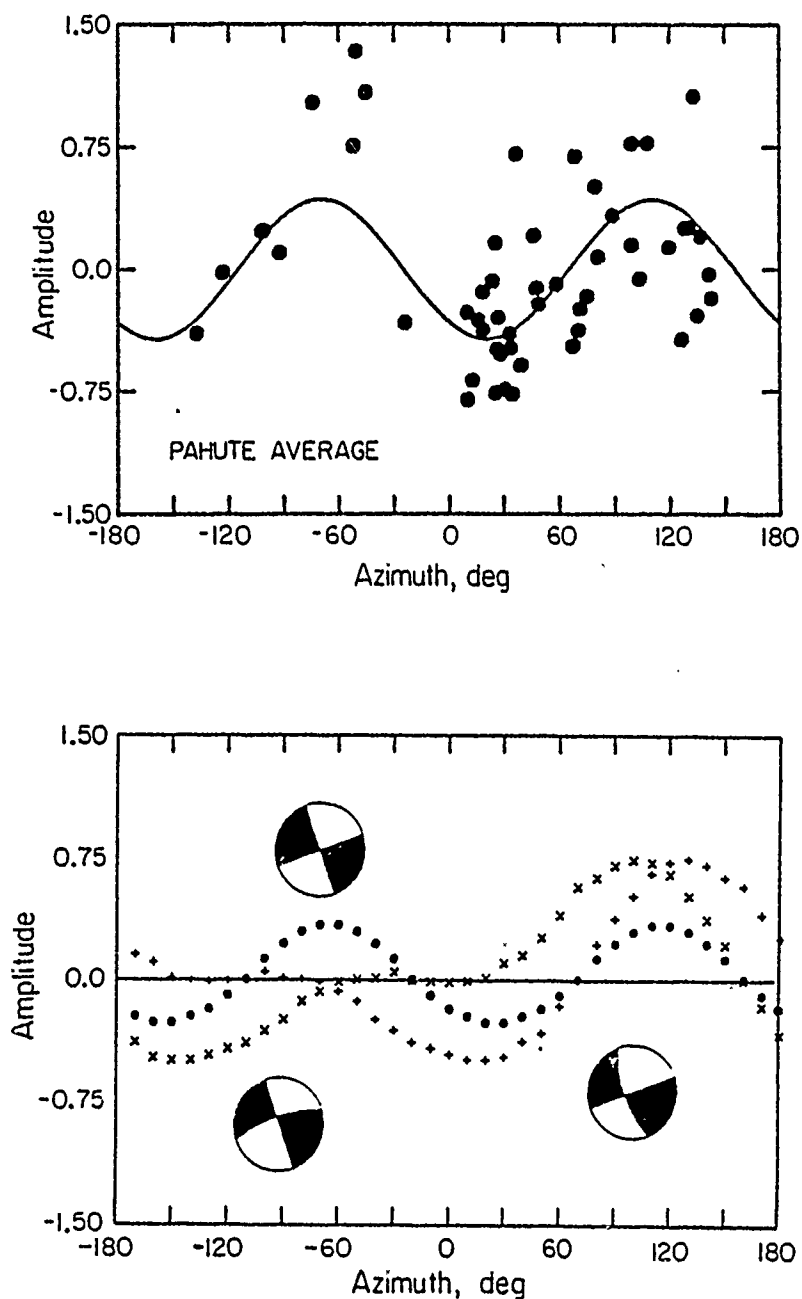
Figure 3. Top: Average ab station amplitudes anomalies for Pahute Mesa
events along with the best fit sin(2θ) curve. Bottom: Synthetic calculations
of short-period ab amplitudes for explosion plus double couple point sources.
The tectonic release moment and time function is derived from long period body
waves.

VELOCITY STRUCTURE HYPOTHESIS
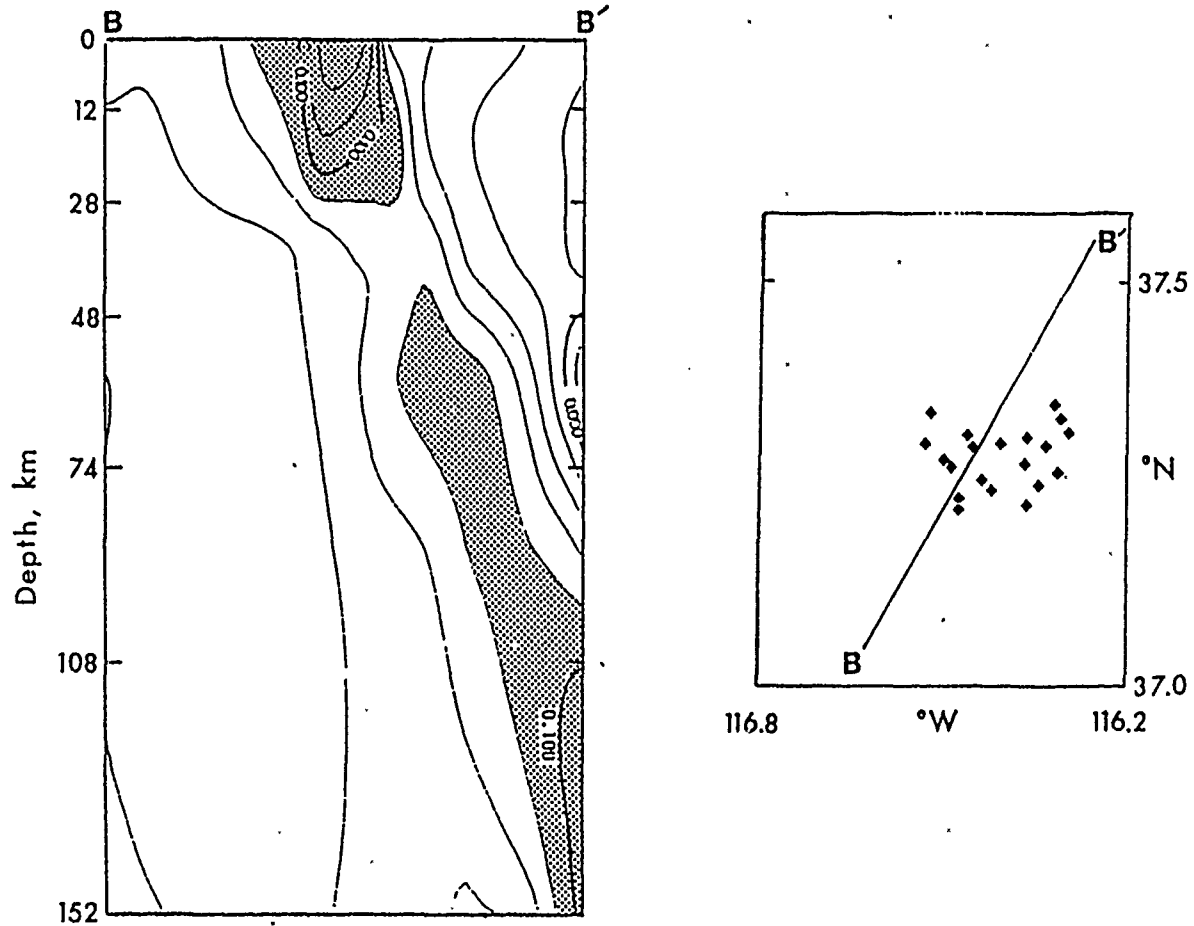
Figure 4. Cross section through the upper mantle velocity structure beneath Pahute Mesa from Minster et al. (1981). The hachured region is a high velocity cylindrical pipe trending off toward the northeast.
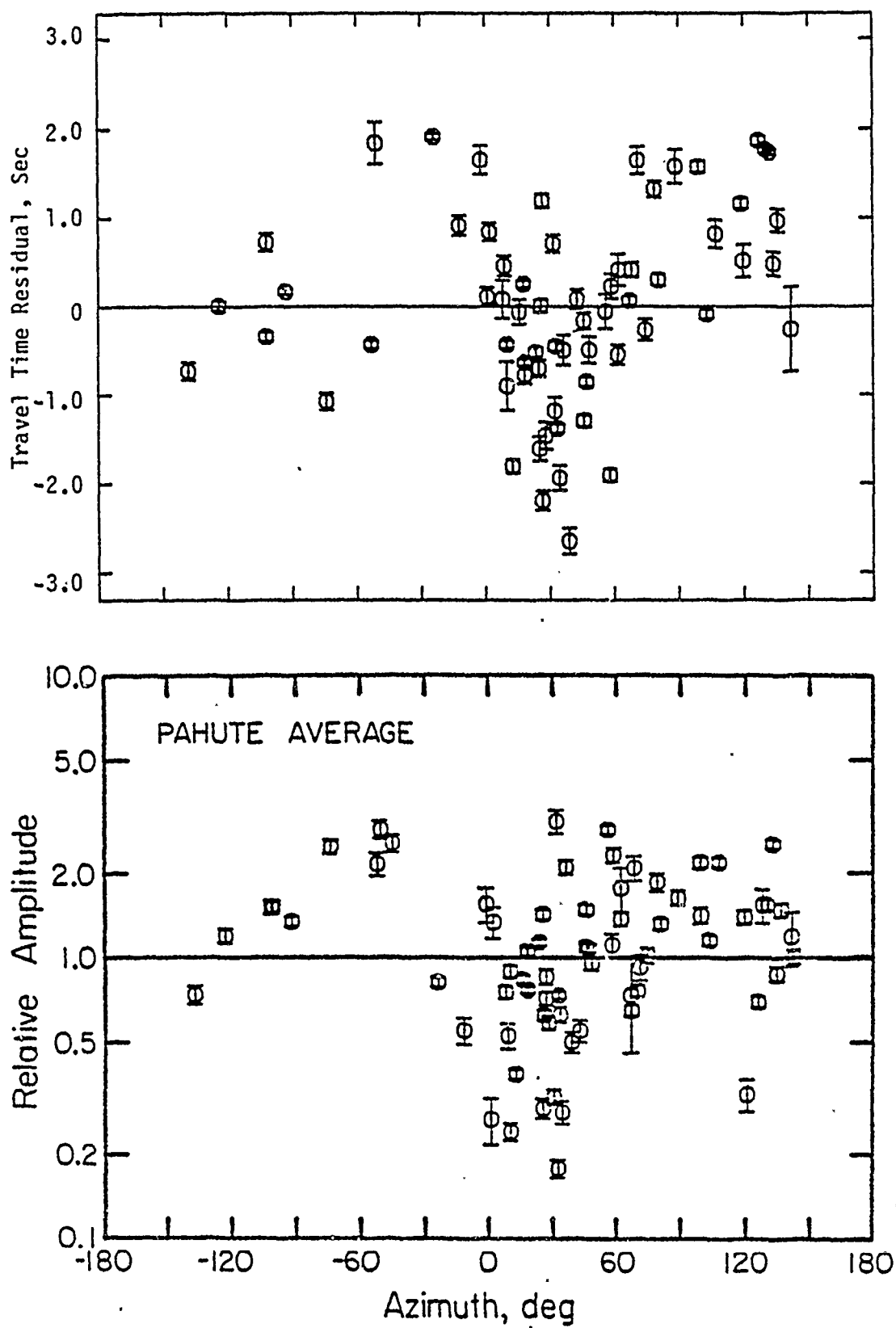
Figure 5. Comparison of average station travel time residuals (top) and ab
amplitude anomalies (bottom). Note the general correlation in the azimuthal
patterns.
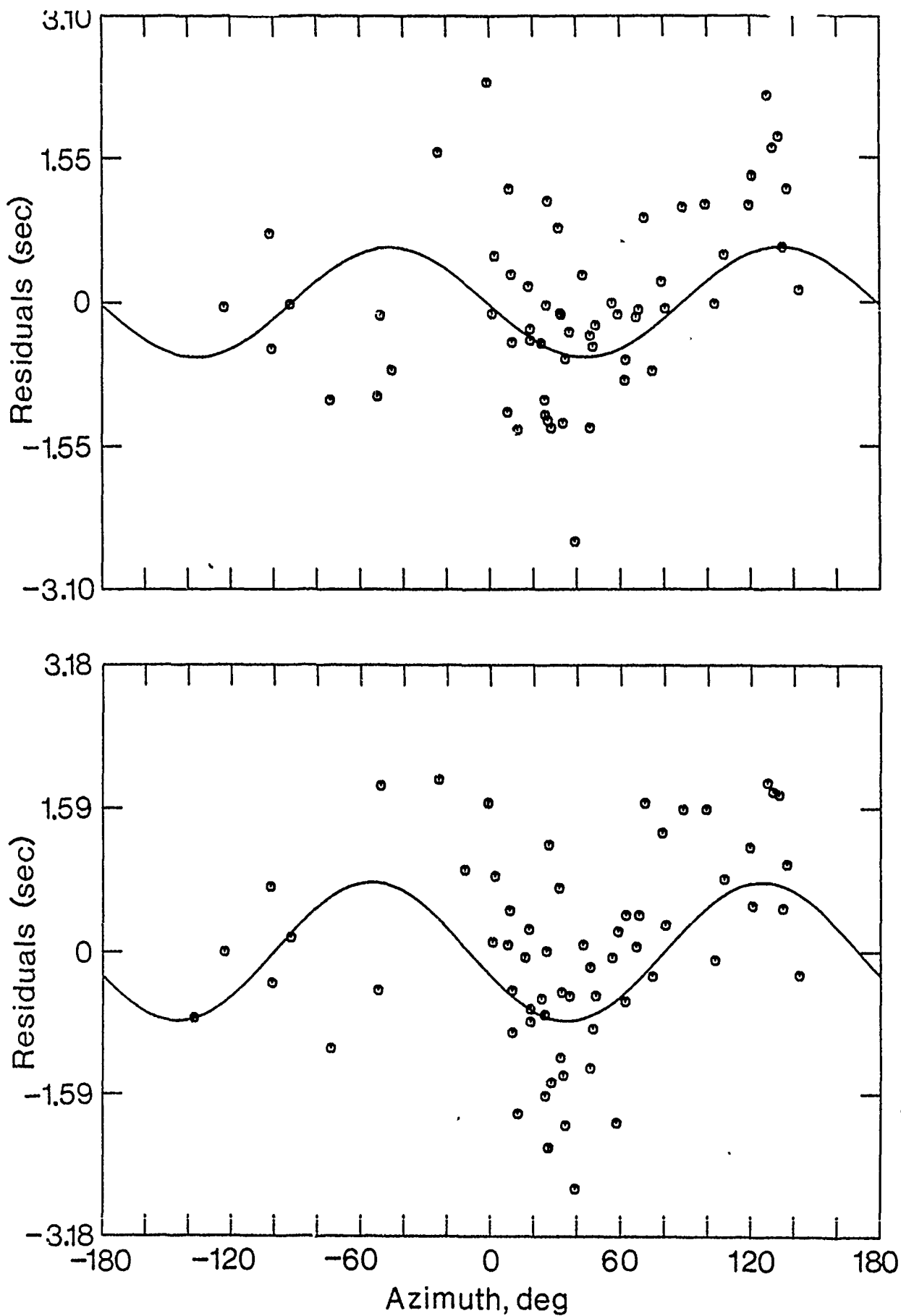
Figure 6. Comparison of the average station travel time anomalies for Pahute
Mesa events (bottom) and for other NTS events (top). Sin(2θ) curves are fit
to both data sets, with the range in travel time anomalies being slightly
greater for Pahute Mesa.

346
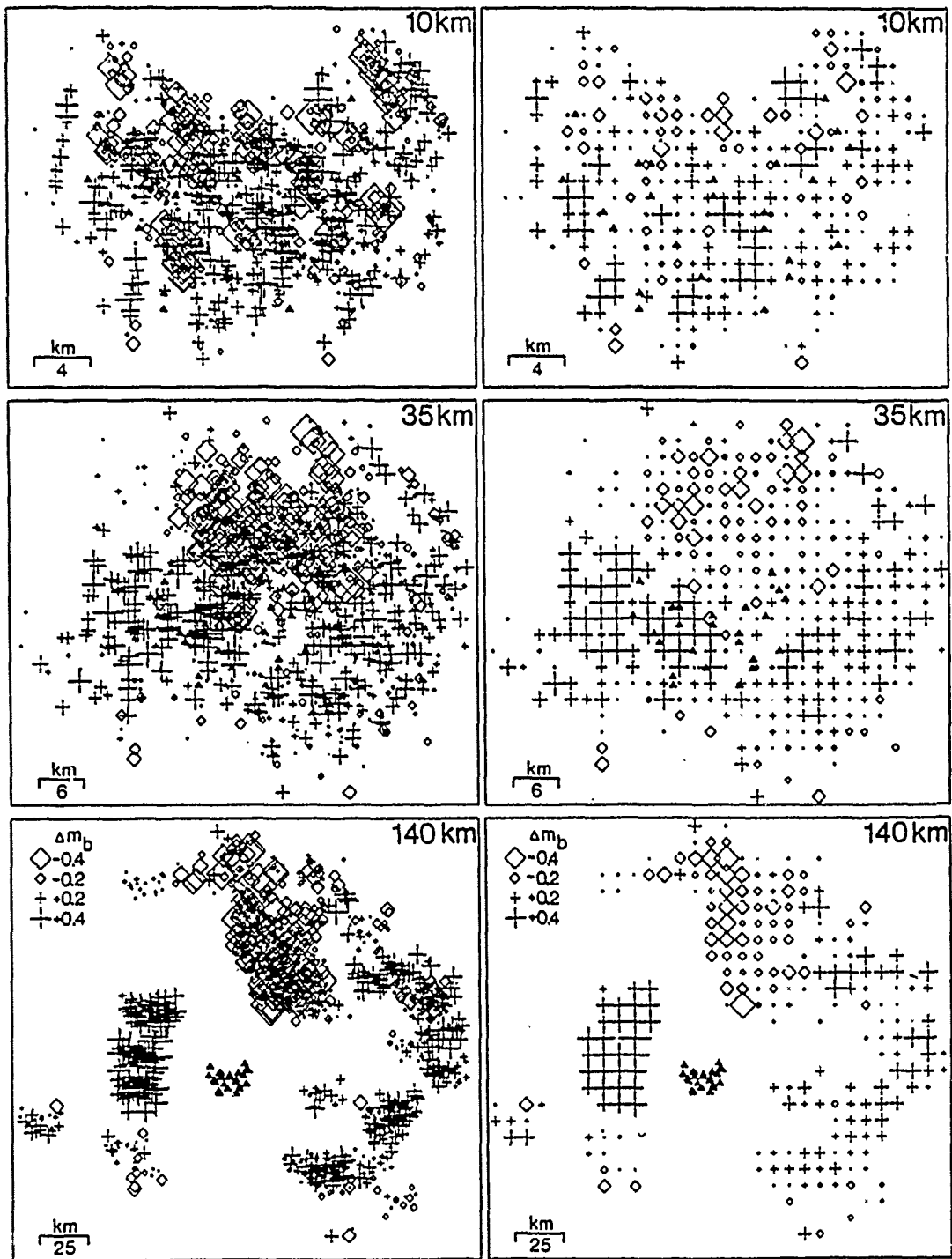
Figure 7. Projections of M_b anomalies for 25 Pahute Mesa events onto surfaces at different depths beneath the test site. The anomalies are plotted at the position where the ray paths to each station intersect the surface. The right column shows the average of the anomalies falling into each bin when the surface is gridded. The shot locations are indicated by the triangles.
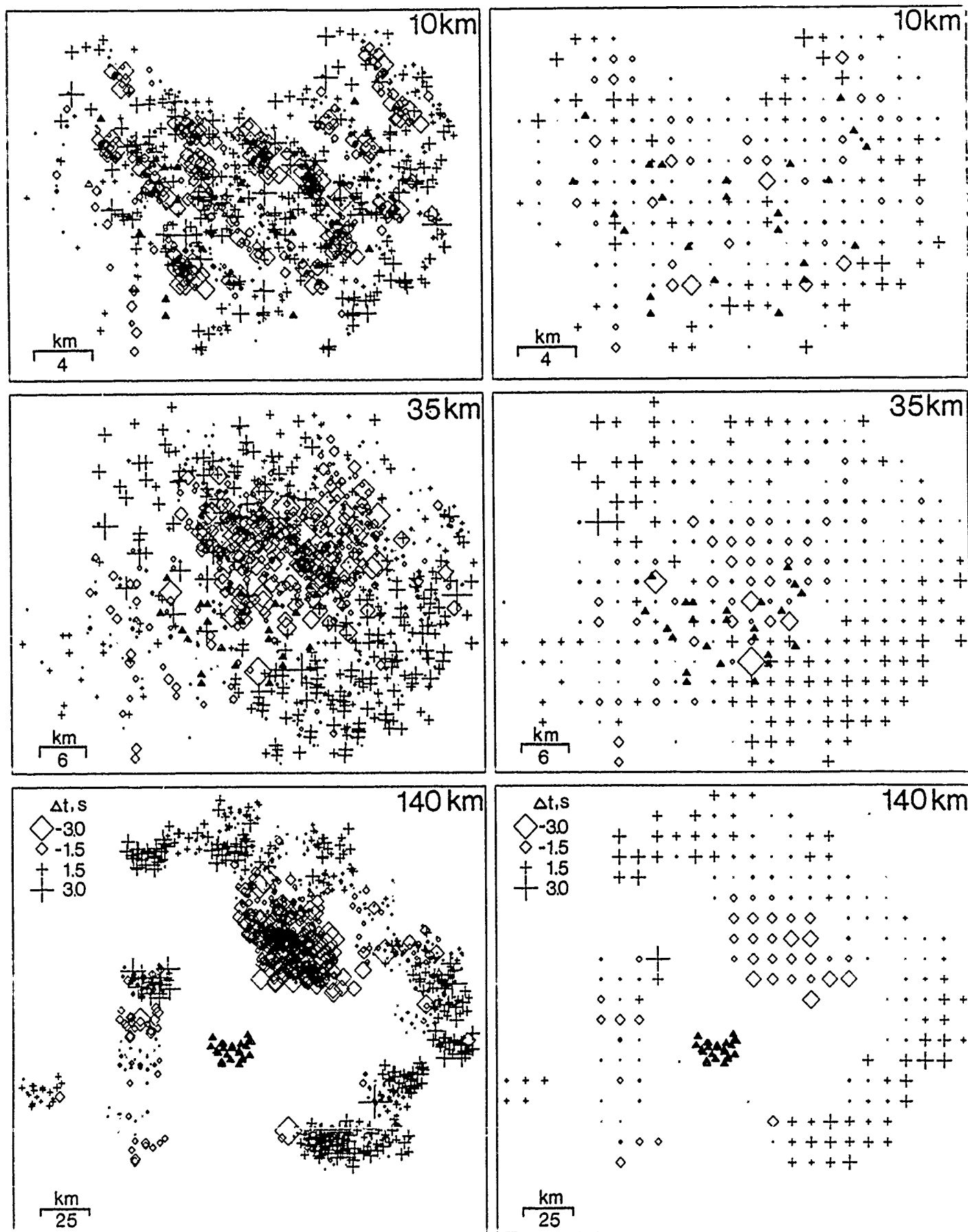
Figure 8.   A similar set of projections to Figure 7, but for the corresponding
travel time anomalies.   Note the similarity between Figures 7 and 8.
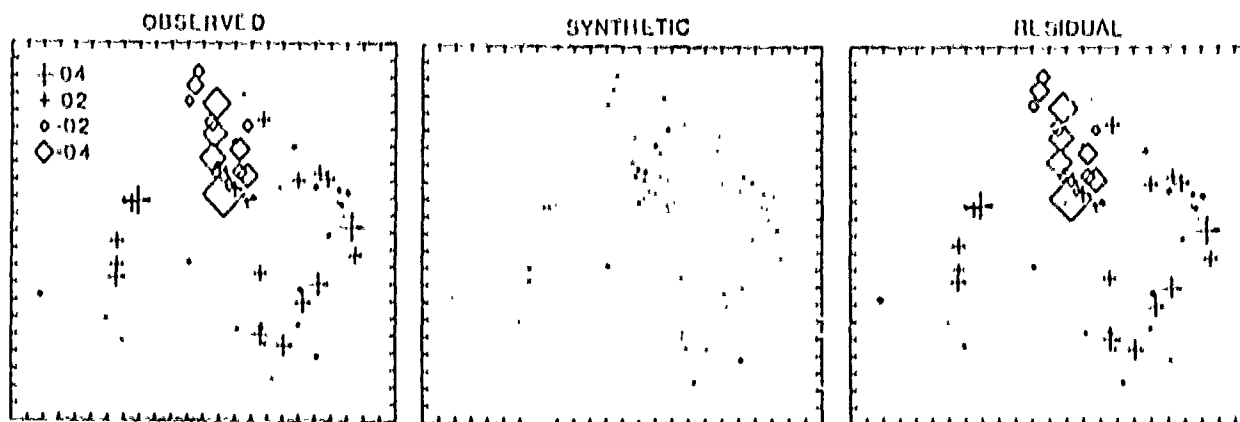
Figure 9. Projection of the observed amplitude anomalies for GREELEY onto a surface 140 km below the test site (left). The center figure shows predicted anomalies found by raytracing through the Minster et al. (1981) structure. The right figure shows the difference in the observed and predicted values.
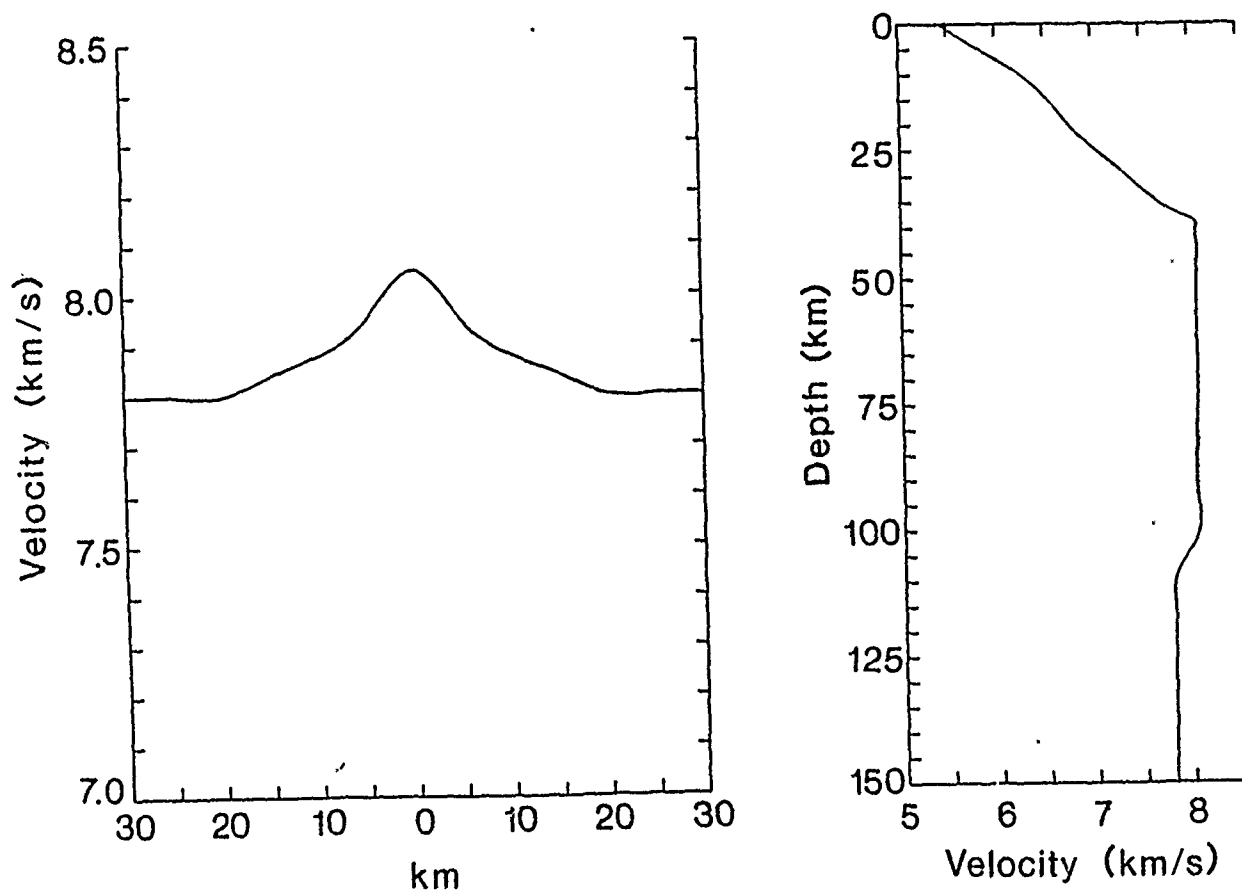
Figure 10. Cross sections through a vertical slab model that predicts the observed amplitude and travel time anomalies for the Pahute Mesa events. The left figure shows a horizontal velocity profile at 50 km depth showing the 2% high velocities in the center of the slab, which has infinite length. The depth range of the anomaly is shown on the right, with the high velocities extending from 10 to 100 km depth.
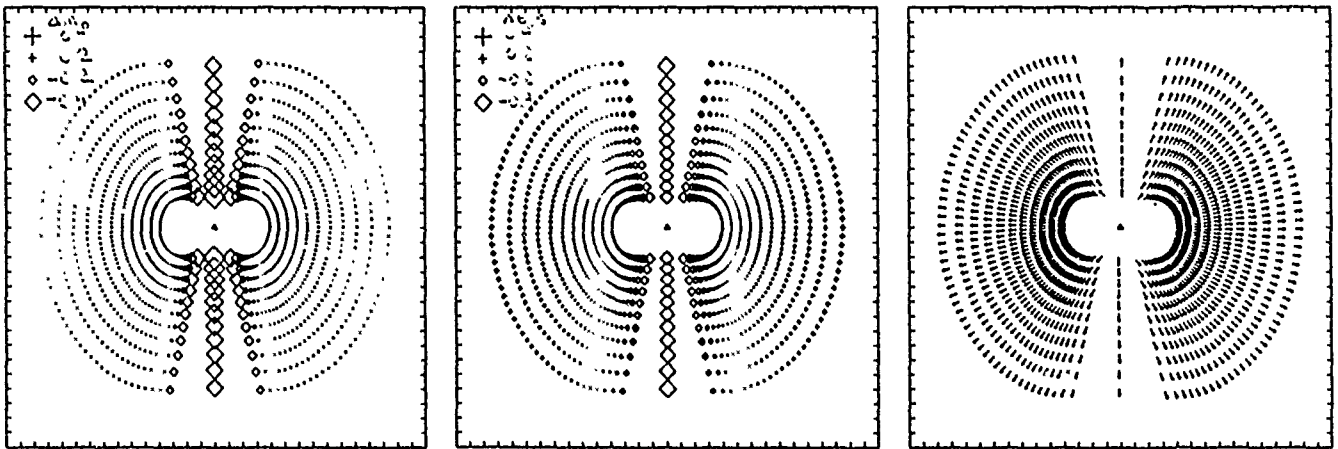
Figure 11. Raytracing calculations of amplitude (left) travel time (middle) and terminating azimuth (right) anomalies for a surface source centered on the vertical slab in Figure 12. The anomalies are shown at a depth of 140 km. The slab trends north-south in these figures.
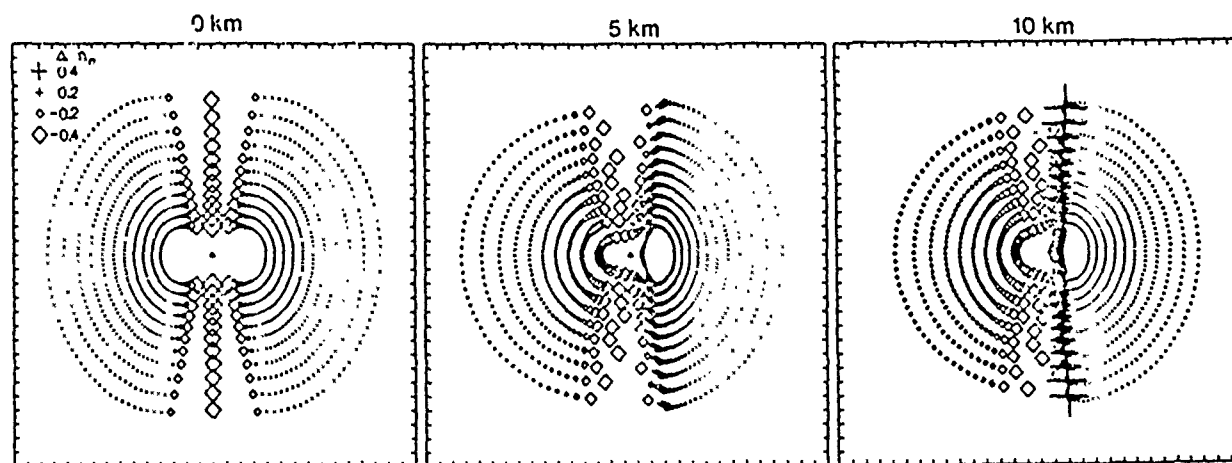
Figure 12. Synthetic amplitude anomalies for sources directly above (left), 5 km to the east (center) and 10 km to the east (right) of the vertical slab which trends north-south.
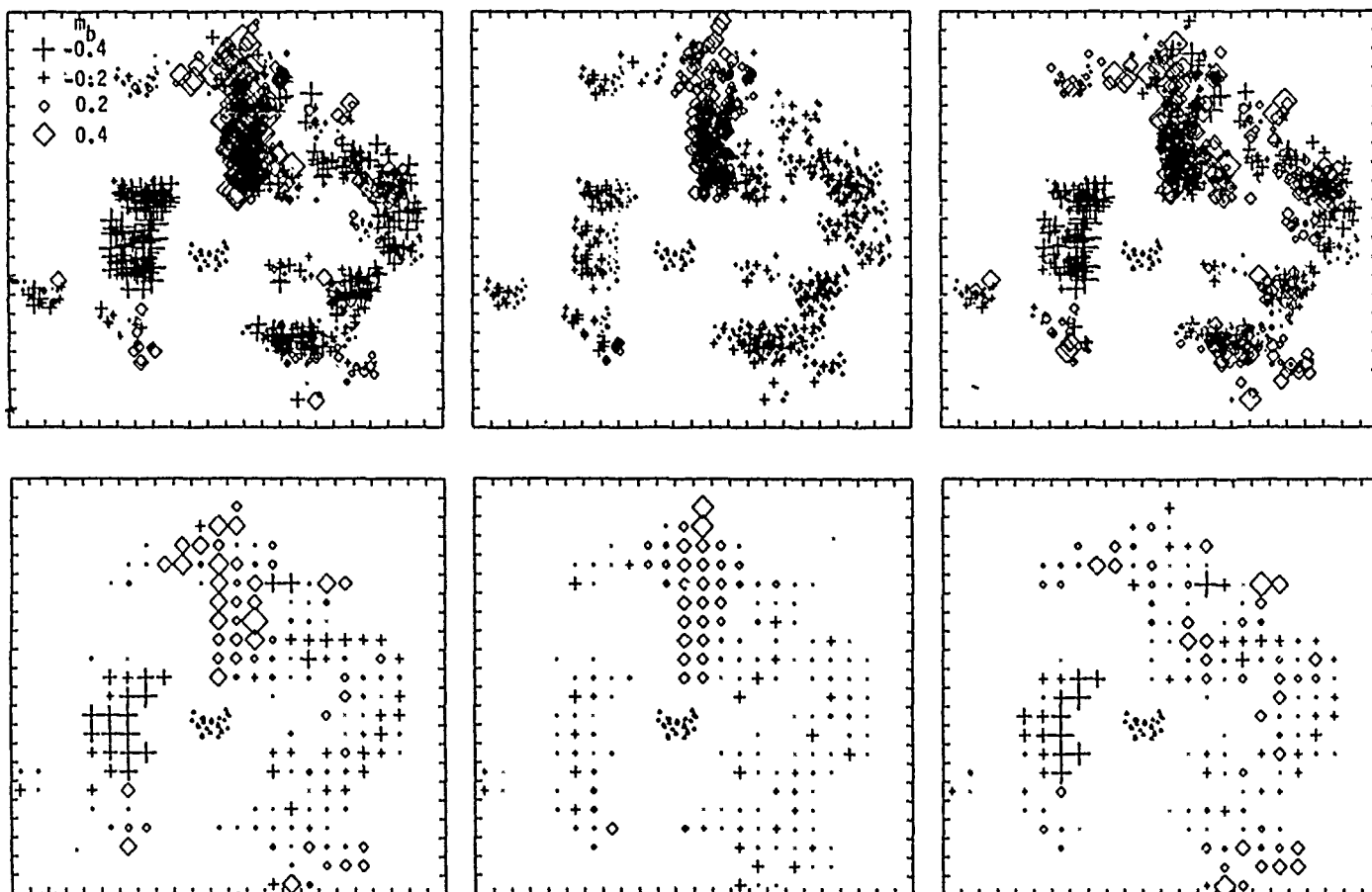
Figure 13. Comparison of the complete Pahute Mesa amplitude anomaly data set (left) with theoretical predictions for the infinite length slab model (center). The difference between the patterns is shown on the right. The data are plotted on a surface 140 km deep, at the position that the actual raypaths intersect the surface. The bottom row shows the average anomaly in each bin of the gridded surface for the Figures at the top.
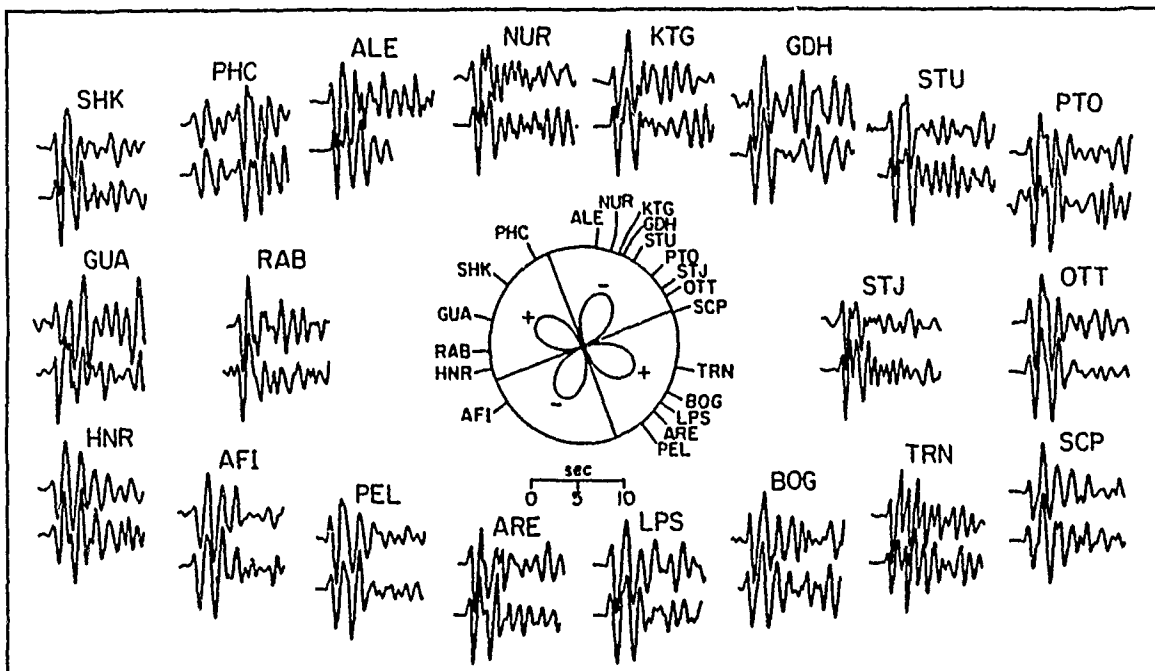
Figure 14. Comparison of the short period P waveforms for GREELEY (top trace) and COLBY at different azimuths from the source region. The azimuths are indicated on the circle. Within the circle the P-wave radiation pattern for the GREELEY tectonic release is shown. The negative lobes would be opposite in polarity to the explosion arrival.
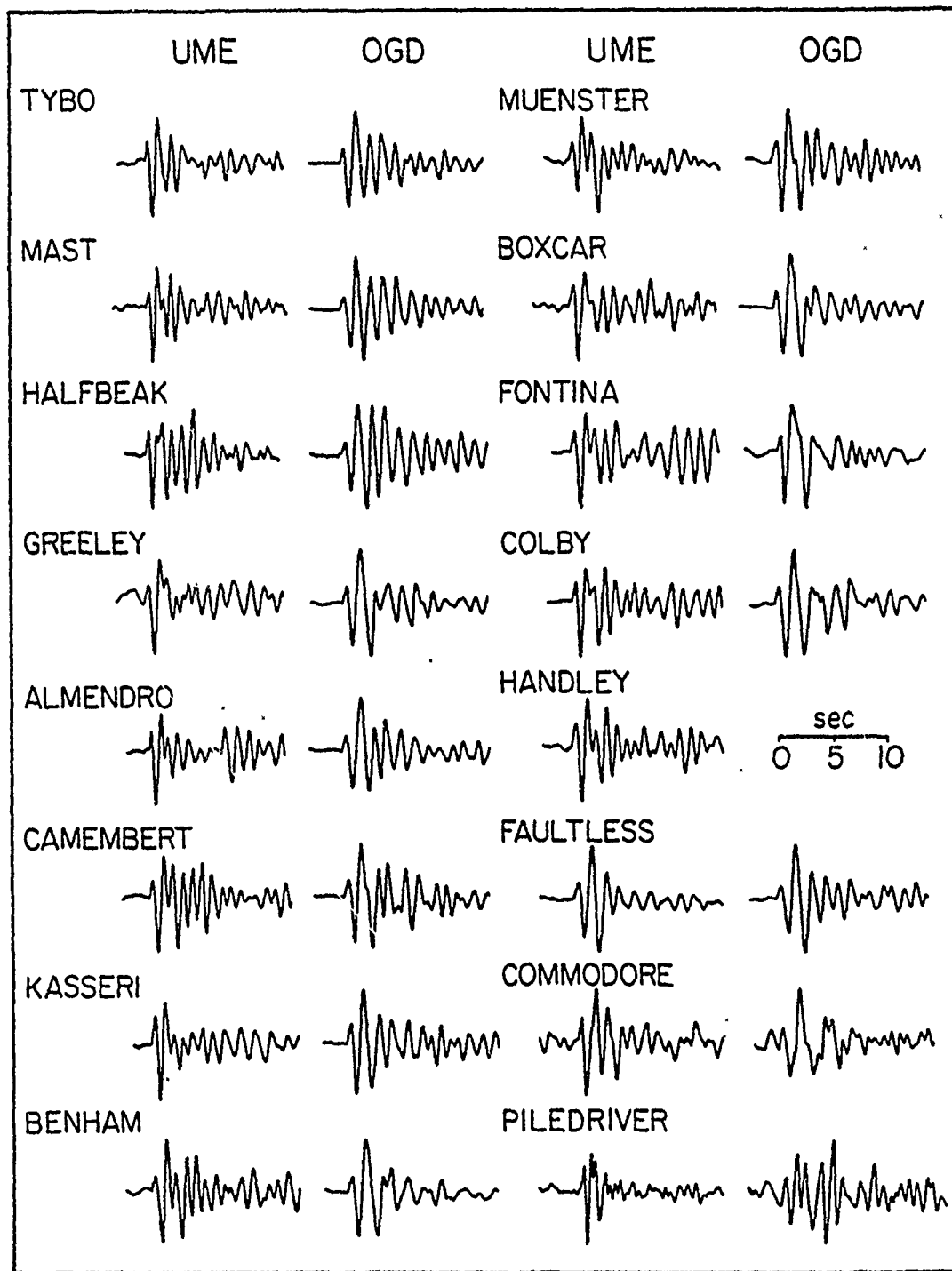
Figure 15. Short period P waves for various NTS events at WWSSN stations UME and OGD. The peak amplitudes are equalized. UME is at an azimuth of 19° and OGD is at 70°.
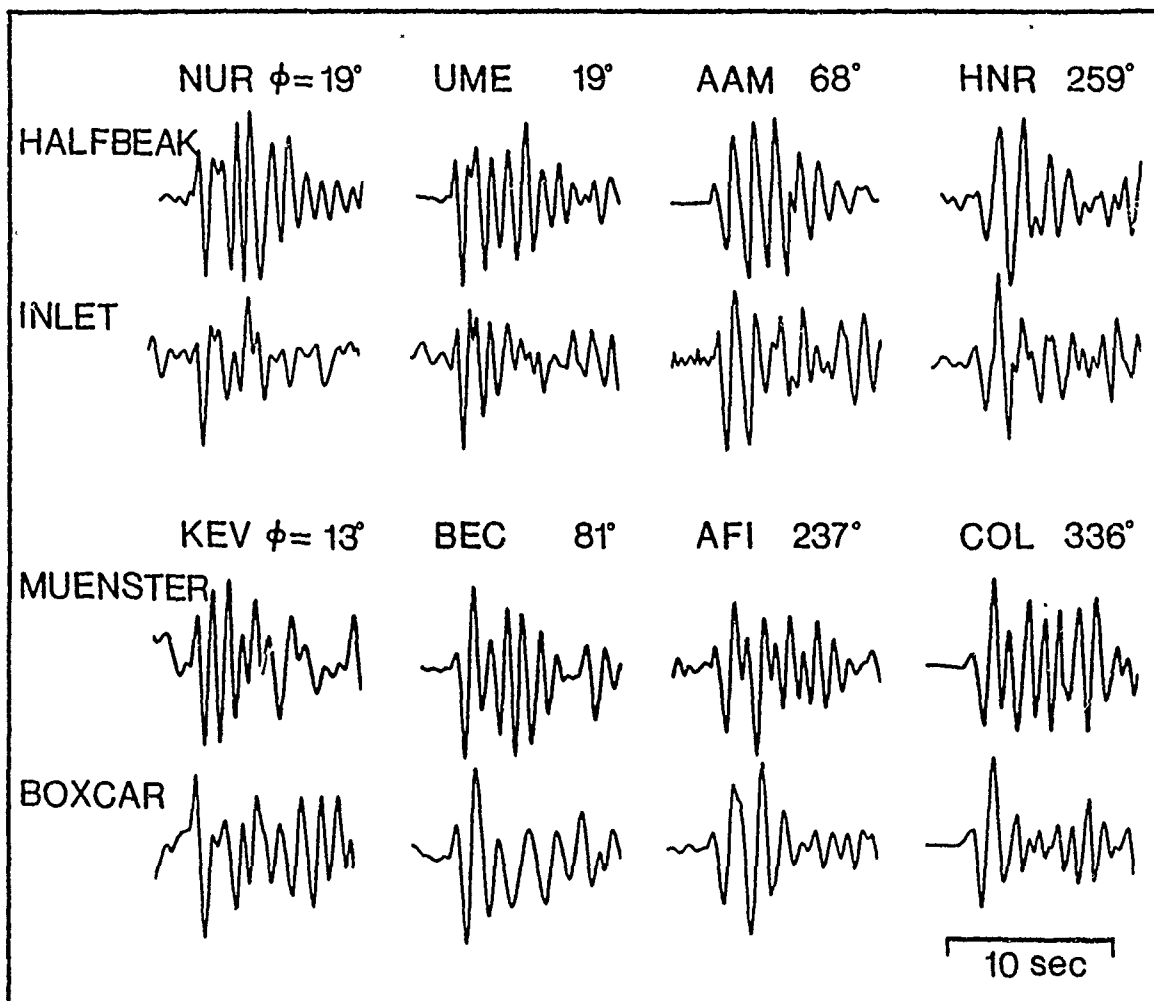
Figure 16. Comparison of short period P waves for HALFBEAK and INLET and
MUENSTER and BOXCAR. Note the additional arrivals several seconds into the
HALFBEAK and MUENSTER waveforms.
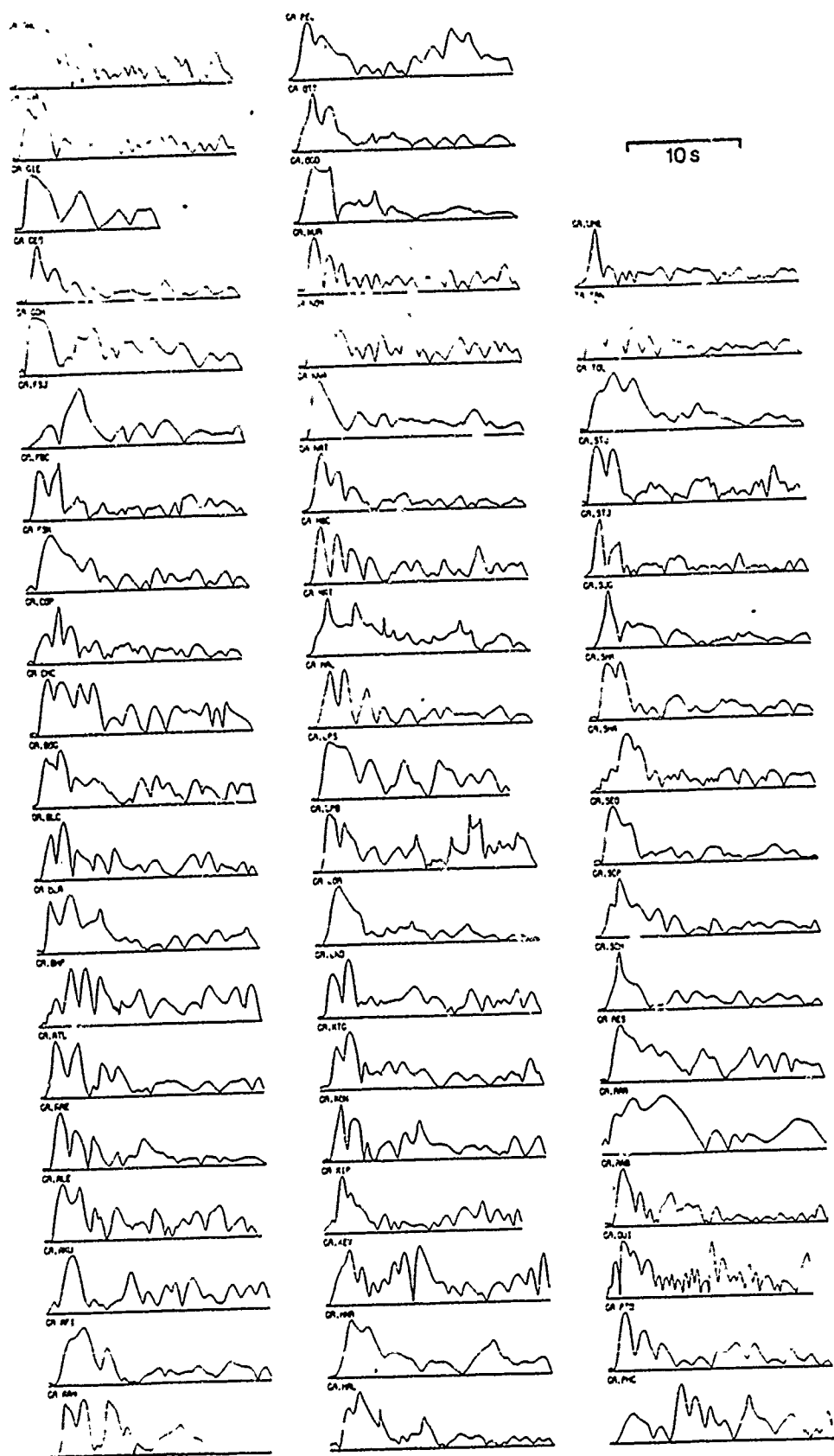
Figure 17. The envelope of the first 15 sec of the short period P waves for GREELEY. Note the variation in coda characteristics between stations.

357
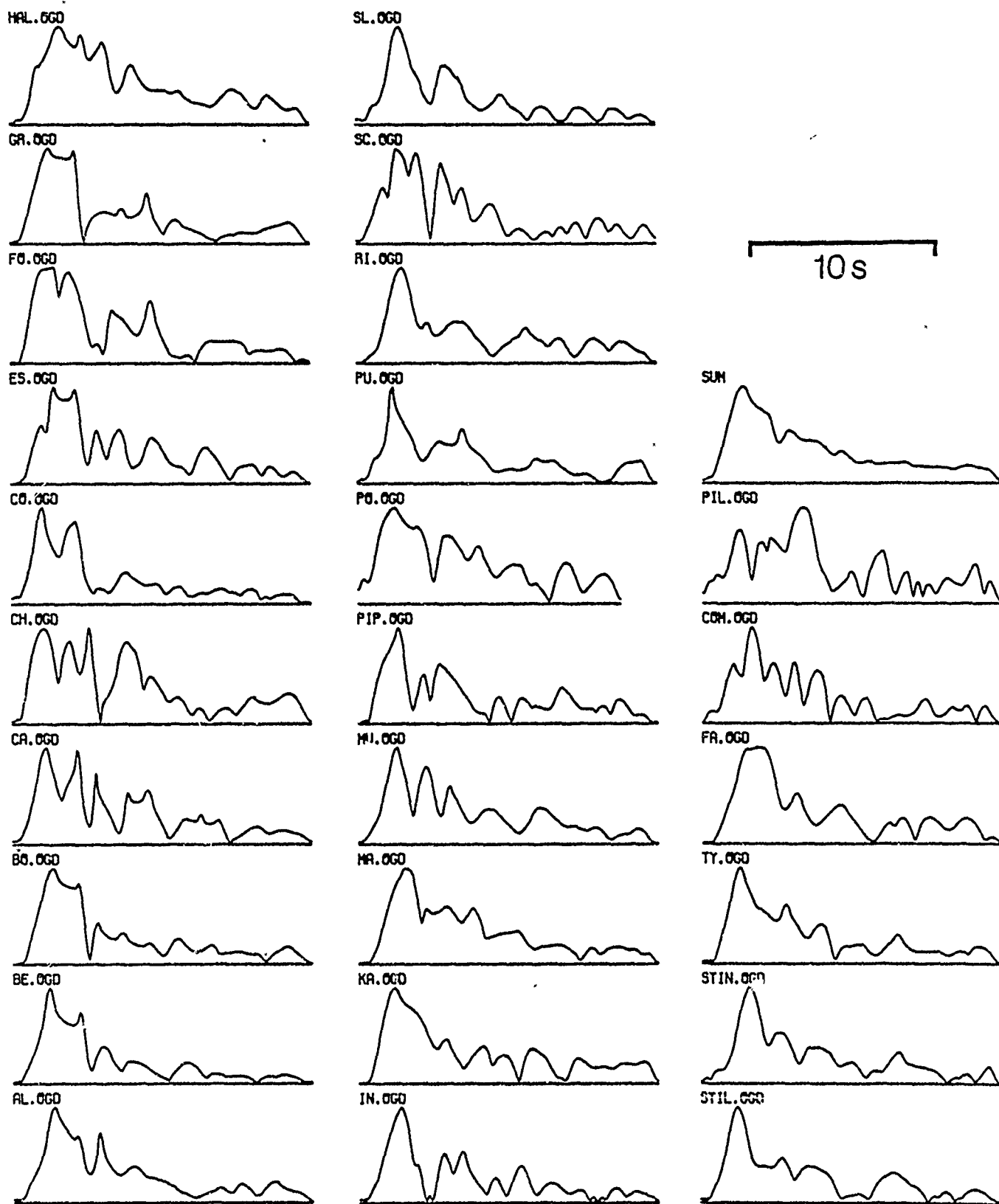
Figure 18. a. The envelope of the NTS events recorded at OGD. The traces are aligned on the P arrival. The variations between traces are presumably due to near-source effects. A stack of the envelopes is shown on the top right column, representing an "average" OGD envelope. b. The square of the envelopes in part a are shown.

358
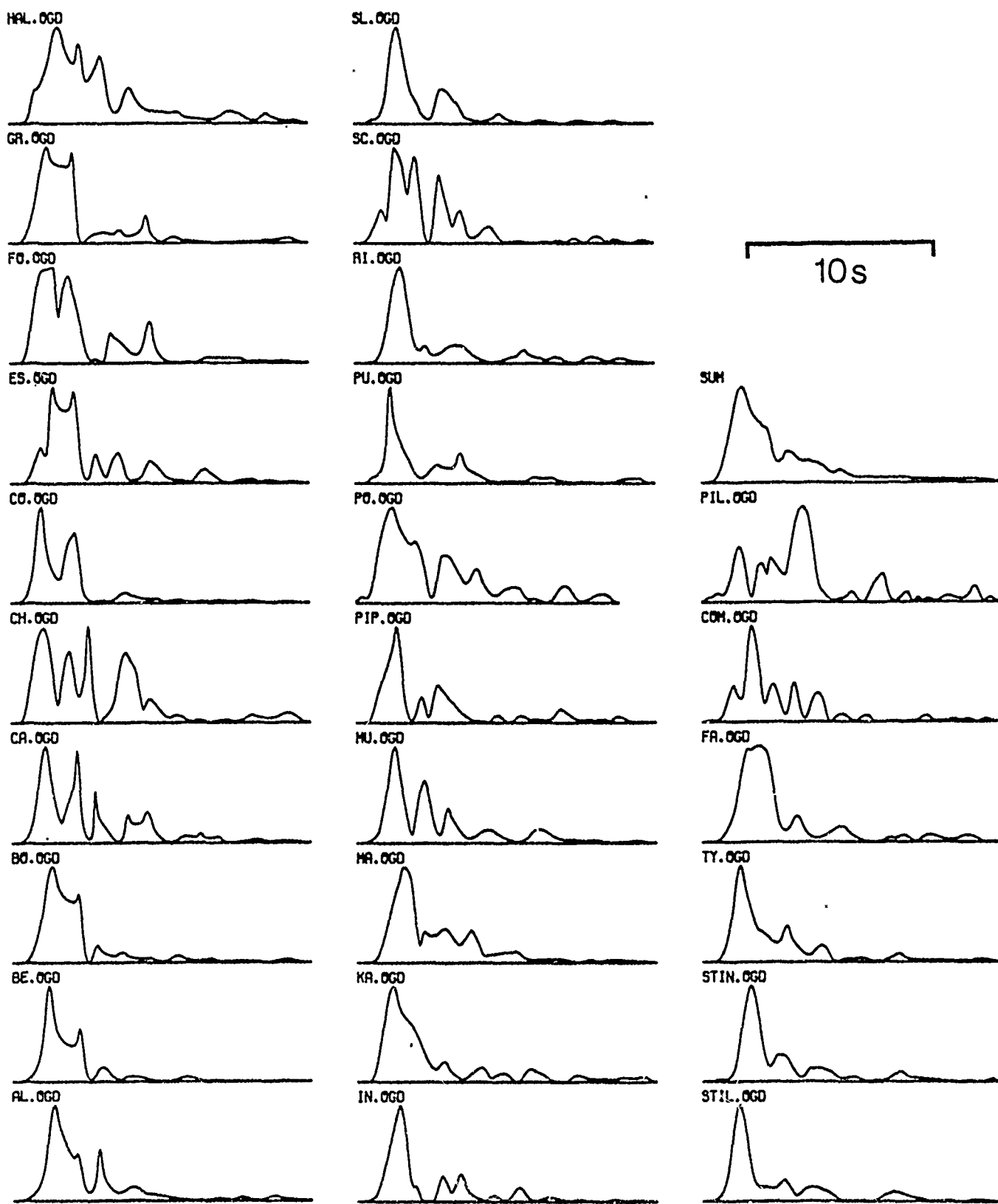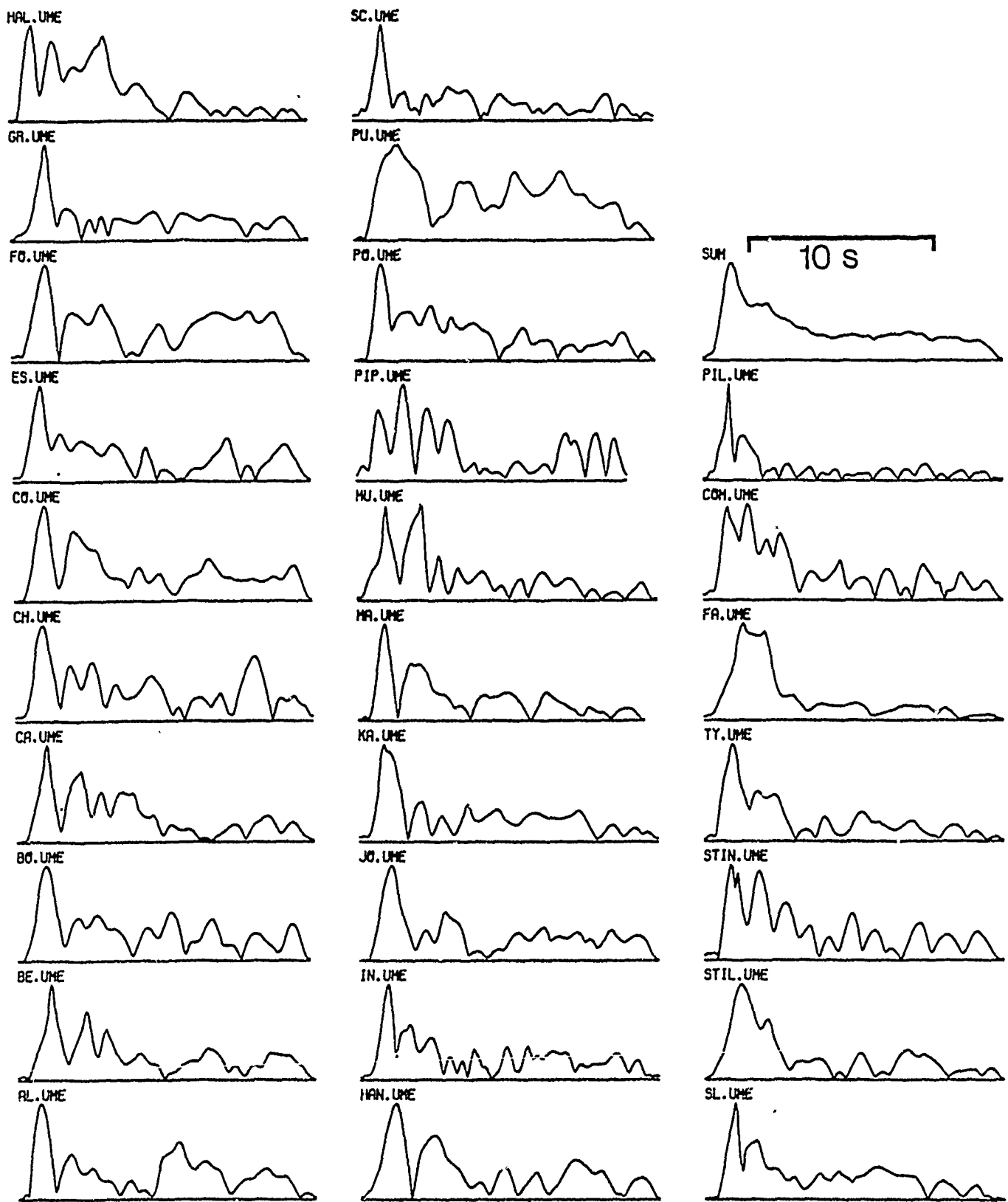
Figure 18b.

Figure 19. a. The envelope of the NTS events recorded at UME. b. The square of the envelopes in part a.

360
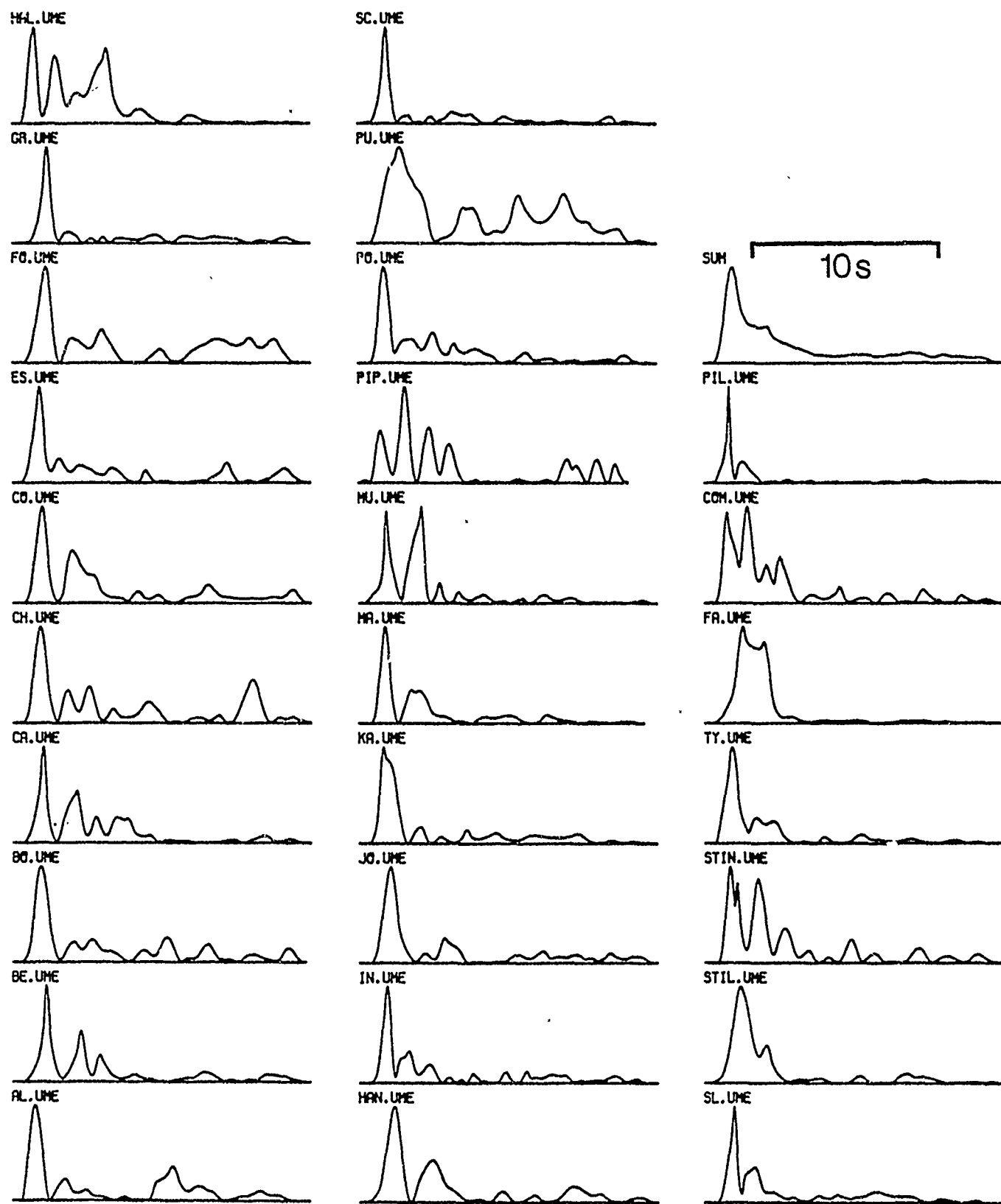
Figure 19b.

DETECTION AND IDENTIFICATION OF COUPLED AND

DECOUPLED UNDERGROUND NUCLEAR EXPLOSIONS

USING VERY HIGH FREQUENCY SEISMIC DATA

by

Charles B. Archambeau

An effective solution to the problem of the detection and identification of low yield decoupled and coupled underground nuclear tests is likely to be found in the use of very high frequency seismic data ranging up to 30 to 40 HZ. In order to evaluate detection-identification capabilities when using such data, it is necessary to consider: (1.) Seismic recording system noise at high frequencies; (2.) Ground noise characteristics over the seismic band to 30-40 HZ; (3.) Signal transmission characteristics over the entire recording band; (4.) Spectral characteristics of both P and S waves from explosions and earthquakes out to very high frequencies.

In this study each of these topics is considered in turn as they relate to event discrimination of low yield coupled and decoupled explosions in the regional and teleseismic distance ranges. This discussion is followed by estimates of the capabilities of specific hypothetical networks to detect explosions within the USSR, with these latter estimates providing a central focus for this study in that they serve to translate diverse and rather complex sets of observational information and theory into concrete predictions of monitoring capability. Following the assessment of detection capability, the identification of small events is considered, with particular emphasis on discrimination at regional distance ranges.

The principal results and conclusions of the study are that: (1.) Seismic system noise can be suppressed to levels well below ground noise at quiet sites out to at least 30-40 HZ using available hardware; (2.) Average ground noise displacement amplitude levels, at carefully selected sites, varies as $f^{-\nu}$ with increasing frequency where $\nu \gtrsim 2$. Further, sites with low levels of high frequency noise are not rare and occur in a number of geologic environments; (3.) Transmission of very high frequency P and S wave signals in the regional distance range is nearly as efficient as in the 1 HZ range, with effective Q factors in shield areas being about 9000 and 4000 for P_n and S_n waves respectively, while in tectonic areas the effective Q for P_n is about 1000; (4.) A network of 25 internal USSR stations and 15 external stations is predicted to be capable of detecting all explosions down to fully decoupled explosions of about 1 kt. located at potential decoupling sites in the USSR; (5.) By inference from event identification using lower frequency data from U.S. and USSR events, identification of all explosions, down to decoupled 5 kt. events, is highly probable using the network of stations for the USSR and spectral body wave (P) magnitude discrimination methods (VFM). Identification below this level (i.e. down to the level of decoupled 1 kt. explosions) appears to require additional discrimination procedures employing S waves, but nevertheless also appears attainable from such a high frequency recording array.

Presentation Title: Detection and Identification of Coupled and Decoupled Underground Nuclear Explosions Using Very High Frequency Seismic Data
Presented By: Charles Archambeau
Contract Number: F19628-85-K-0016

In this study we have attempted to specify the minimum element seismic network for monitoring of the USSR with capability of detection and identification of all underground explosions with compressional wave signal levels equal to or larger than those from 1 kt. decoupled explosions anywhere within the USSR. Thus we have tried to specify a seismic network capable of monitoring a low threshold test ban treaty (LTTBT), with a threshold set at 1 kt.

Our approach has been to specify a network designed to record very high frequency regional seismic data, that is signal data in the frequency band from 3 to about 30 Hz for the distance range from 3° to 20°, as well as the conventional lower frequency data. The use of very high frequency data allows us to take advantage of the rapidly decreasing ground noise levels with increasing frequency and, in principal, to also be able to identify small magnitude coupled and decoupled explosions (down to about $m_b = 2.$) using high frequency spectral discrimination methods.

Figure (1) illustrates the variation of ground noise with increasing frequency which appears to be typical of most sites studied in the US and elsewhere. The decreases in noise levels vary as $f^{-\nu}$, with $\nu \geq 2$. In our study of detection capability we use the three noise levels indicated by the points on the plot ("noisy", "average" and "quiet") as representative of noise levels that can be expected at sites in the USSR.

An important, and certainly critical question, for any estimate of detection and identification capability is whether the efficiency of high frequency signal propagation is sufficient to produce reasonably large signal to noise ratios at regional distances. (In the

NOISE LEVEL VS. FREQUENCY
SELECTED STATIONS
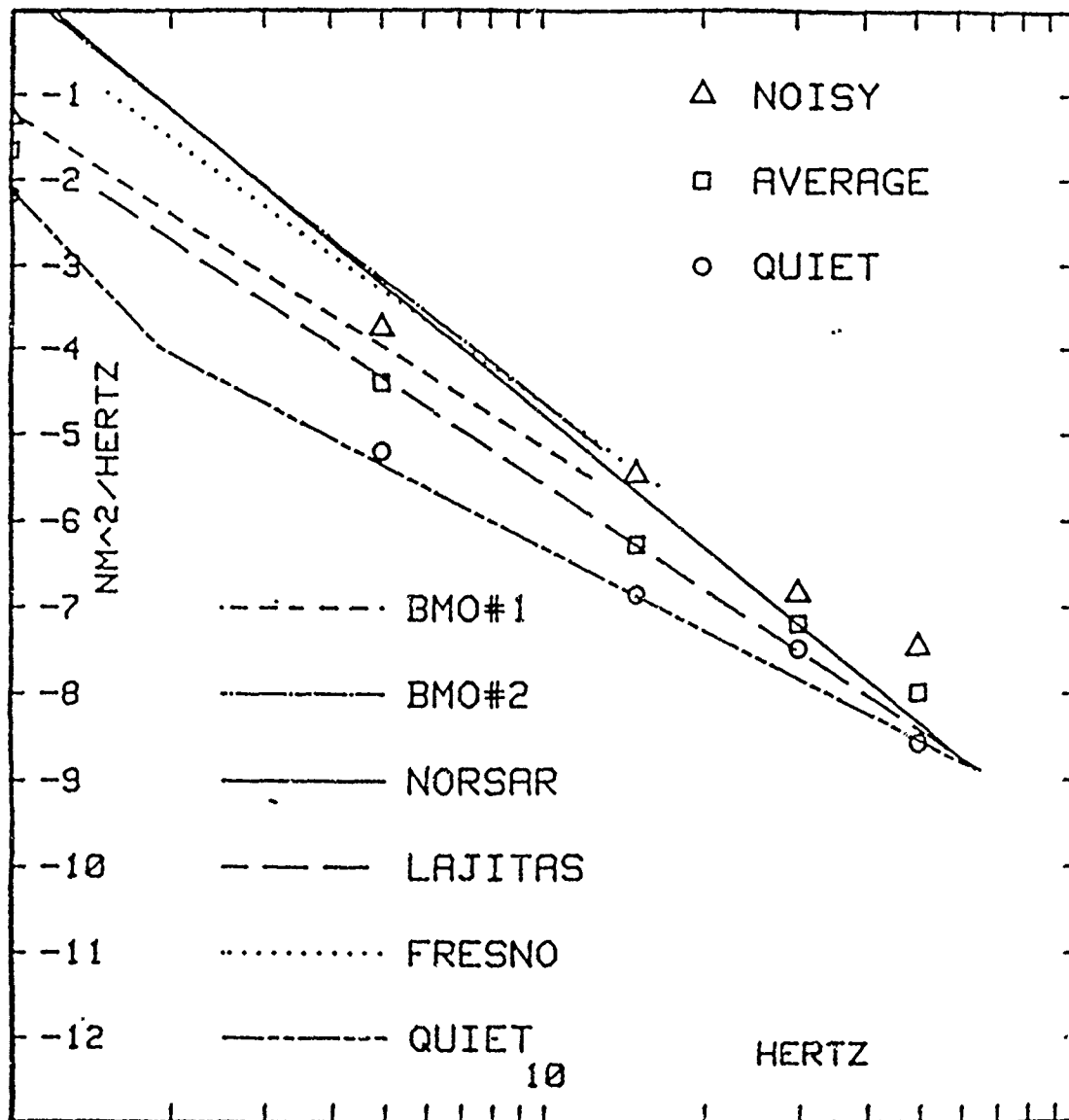
Figure 1 - Observed noise power as a function of frequency. Symbols denote levels adopted in the present study.

364

present analysis we require a predicted signal to noise power ratio of 3 for assured detection.) Figure (2abc) illustrates high frequency signal propagation in the eastern U.S. for a Canadian earthquake recorded in New York at a distance of 190 km. As indicated in this figure, signal data out to about 100 Hz is obtained and the estimated quality factors for P and S waves from the event are $Q_p \simeq 9000$ and $Q_s \simeq 4000$. The event is also well described by a relaxation source theory model, where the different P and S wave corner frequencies, at 5.49 Hz and 2.59 Hz respectively, and the different high frequency spectral slopes varying as f^{-3} and f^{-2} for the P and S waves, respectively, are consistent with the theory. Therefore this event indicates that efficient high frequency propagation can be expected in many or most parts of stable continental regions and that the broad band data observed conforms very well with relaxation source theory predictions. Additional study of more frequently recorded earthquakes and explosions in tectonic provinces in the Western U.S. indicate much lower Q values for P_n wave propagation, with $Q_p \simeq 1000$ being more typical.

Figure (3) illustrates typical observational data from earthquakes and explosions at nearly the same locations in the Western U.S. The figure shows two different types of earthquake P wave spectra, those with f^{-3} high frequency variations above the corner frequency and those with f^{-2} variations, compared with typical explosion spectra, which vary as f^{-2} at high frequencies. As predicted theoretically, earthquakes showing f^{-2} high frequency spectral slopes near their corner frequencies have abnormally low corner frequencies and, when compared to explosions with the same low frequency spectral levels, have much less high frequency content than the explosion due to the differences in corner frequencies between the two event types. Based on theory, these earthquakes are those with low rupture rates and associated low stress drops. On the other hand, the more typical earthquake spectra has a corner frequency somewhat lower than that
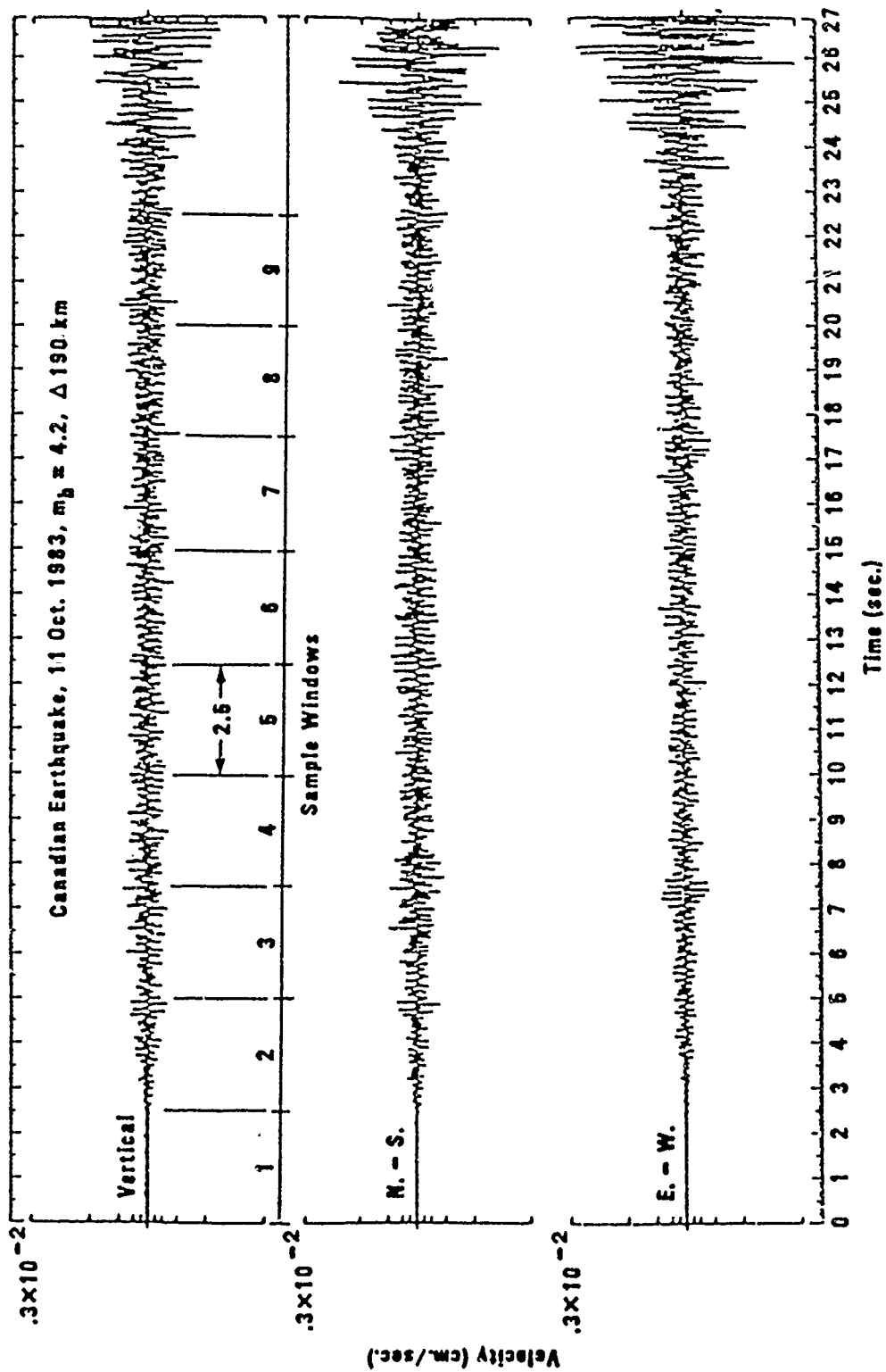
Figure 2a – Canadian earthquake recorded by the USGS in New York using very broad band detectors.

366
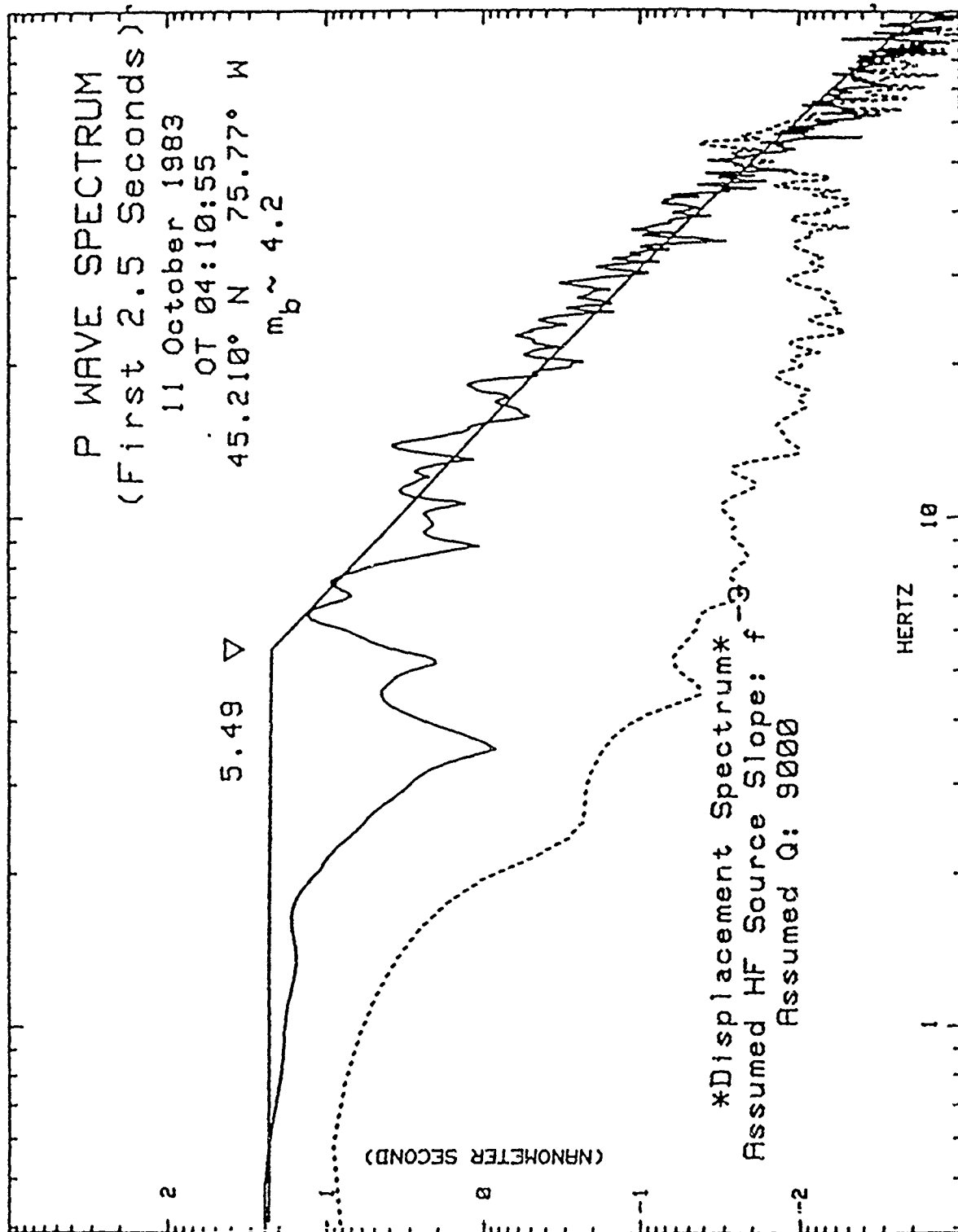
Figure 2b - Spectrum of the P_n wave from the Canadian event of Oct 11, 1983 at a distance of 190 km.

▽ 2.59

S WAVE SPECTRUM
(First 2.5 Seconds)

OT 11 October 1983 04:10:55
45.210° N   75.77° W
$m_b \sim 4.2$

Displacement Spectrum
Assumed HF Source Slope: f^{-2}
Assumed Q: 4000

HERTZ

(NANOMETER SECOND)
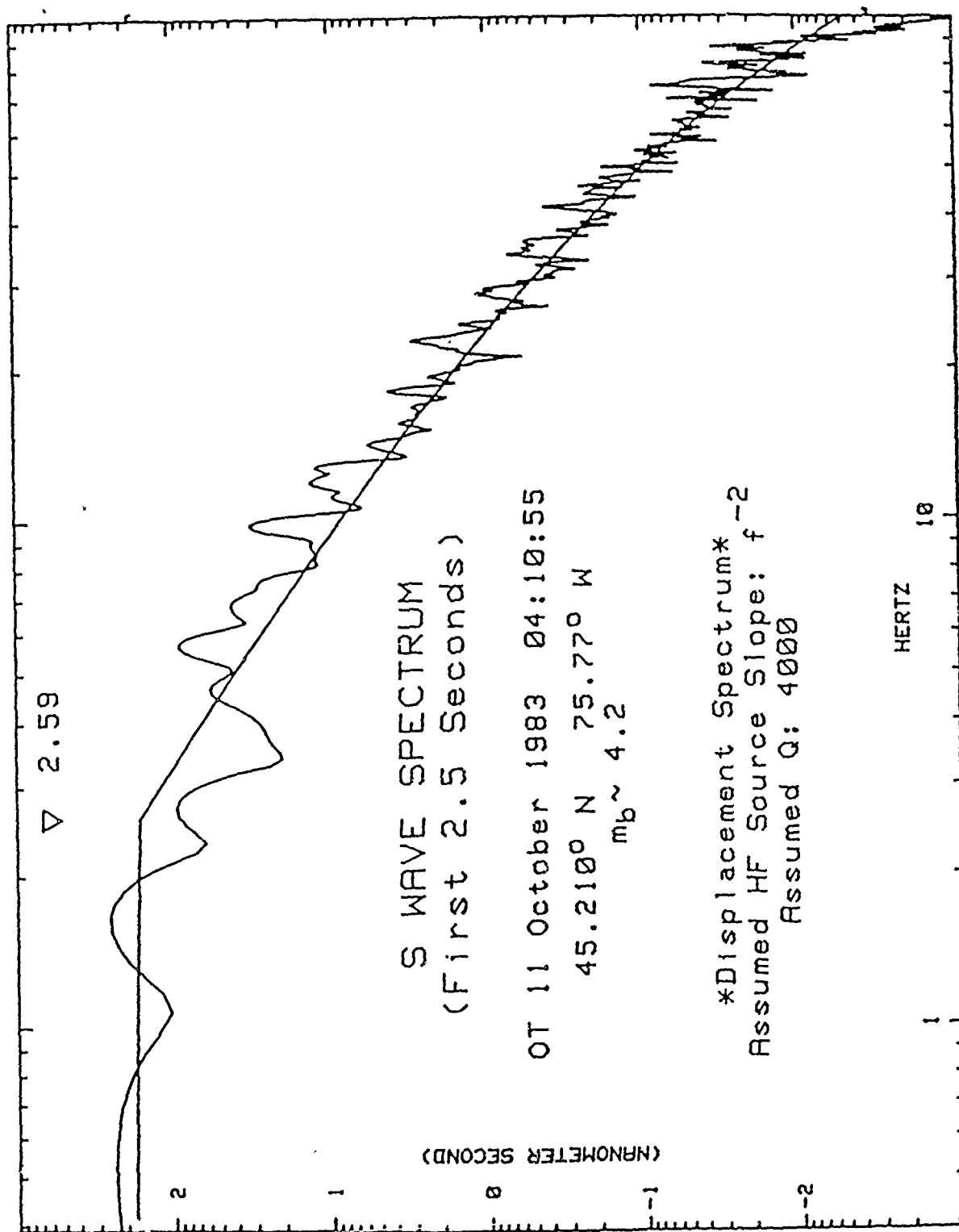
Figure 2c - Spectrum of the S_g wave from the Canadian event of Oct 11, 1983 at a distance of 190 km.

HIGH RUPTURE RATE EQ. VS COMPARABLE EXPLOSION   LOW RUPTURE RATE EQ. VS COMPARABLE EXPLOSIO
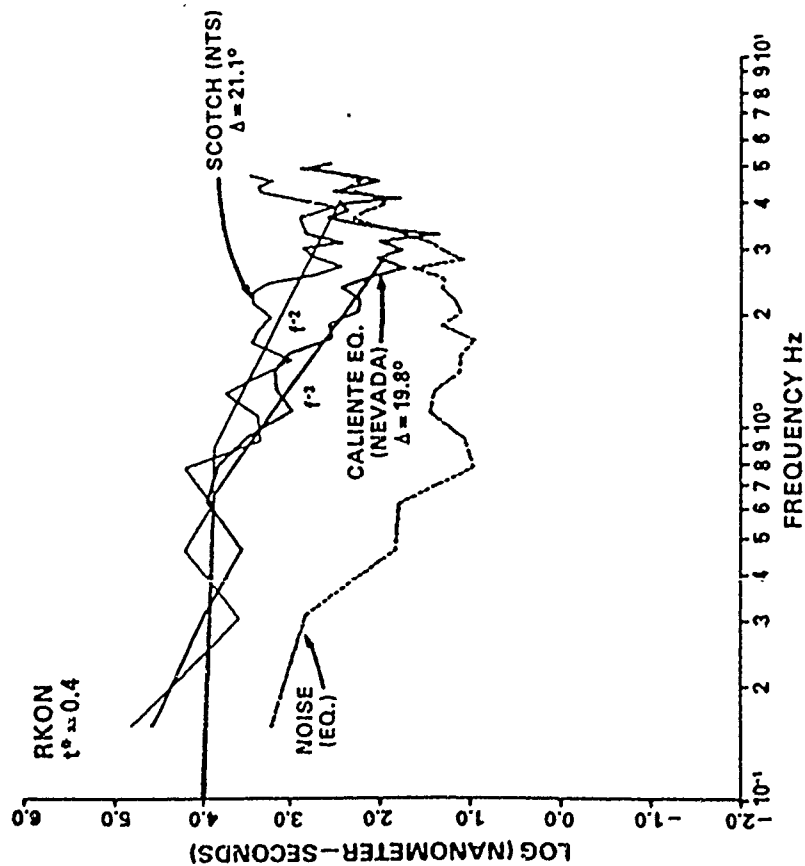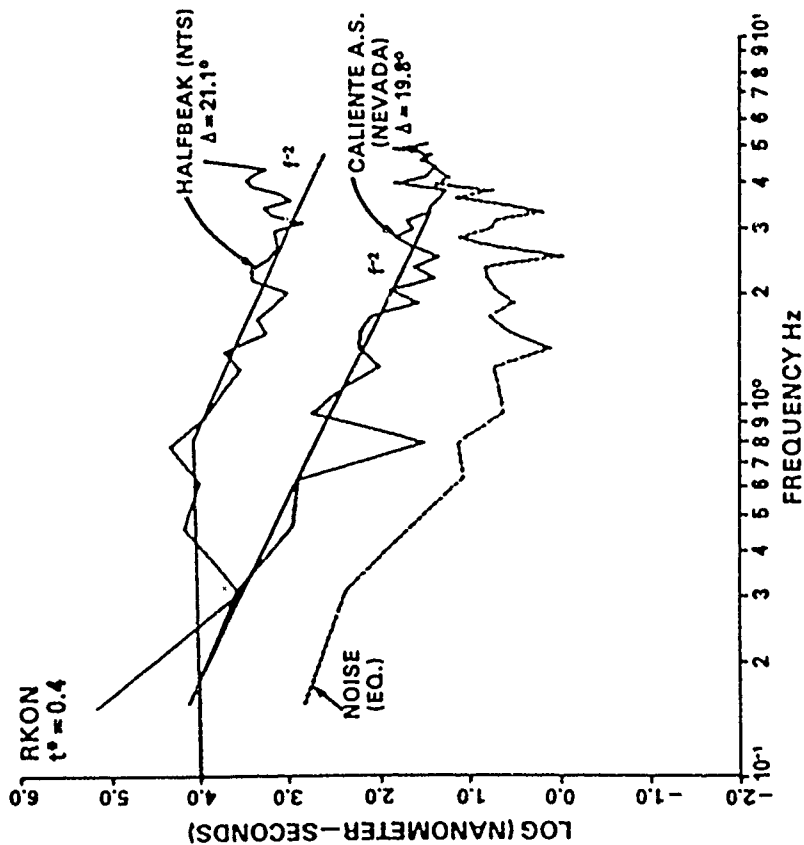
Figure 3 - P wave spectra of comparable earthquakes and explosions from the S.W. United States recorded at Red Lake Ontario.

369

associated with a comparable explosion with the same low frequency spectral level and a f^{-3} spectral decay resulting in reduced high frequency spectral energy compared to the explosion. These earthquakes, as a class, are most nearly like explosions in that their corner frequencies can be near those for comparable explosions and have spectral slopes only modestly different from explosions at high frequencies. Such earthquakes are those with high rupture rates and relatively high stress drops and are those that we consider in our detection and discrimination analysis for the USSR.

Figure (4) shows first order theoretical models used to characterize explosion and earthquake spectra, with both the explosion and earthquake theoretical models in good first order agreement with observations. The dotted lines labeled 25, 100 and 1000 refer to stress drop levels for the earthquake spectra, with the lines themselves denoting the locations of the asymptotic f^{-3} high frequency spectra decay lines for earthquakes with the stress drops indicated. Thus 1 kilobar stress drop earthquakes are expected to have corner frequencies about equal to those of comparable explosions. The discrimination of earthquakes and explosions would, however, involve the distinction between the high frequency spectral content of the typical 25 to 100 bar stress drop earthquakes and explosions with comparable low frequency spectral levels, and so the figure illustrates the frequency range over which spectral information must be acquired in order to distinguish between the events on the basis of high to low frequency spectral content of P wave signals. We observe that data out to 30 to 40 Hz would be required in order to discriminate 1 kt. decoupled explosions from earthquakes with stress drops in the 25 to 100 bar range. Therefore the requirements of a "1 kt. detection-identification system" are that the recording bandwidth extend to such high frequencies, and that the system be dense enough to record P wave signals at acceptable signal to noise ratio levels over the range from near 5 Hz out to 30 or 40 Hz.
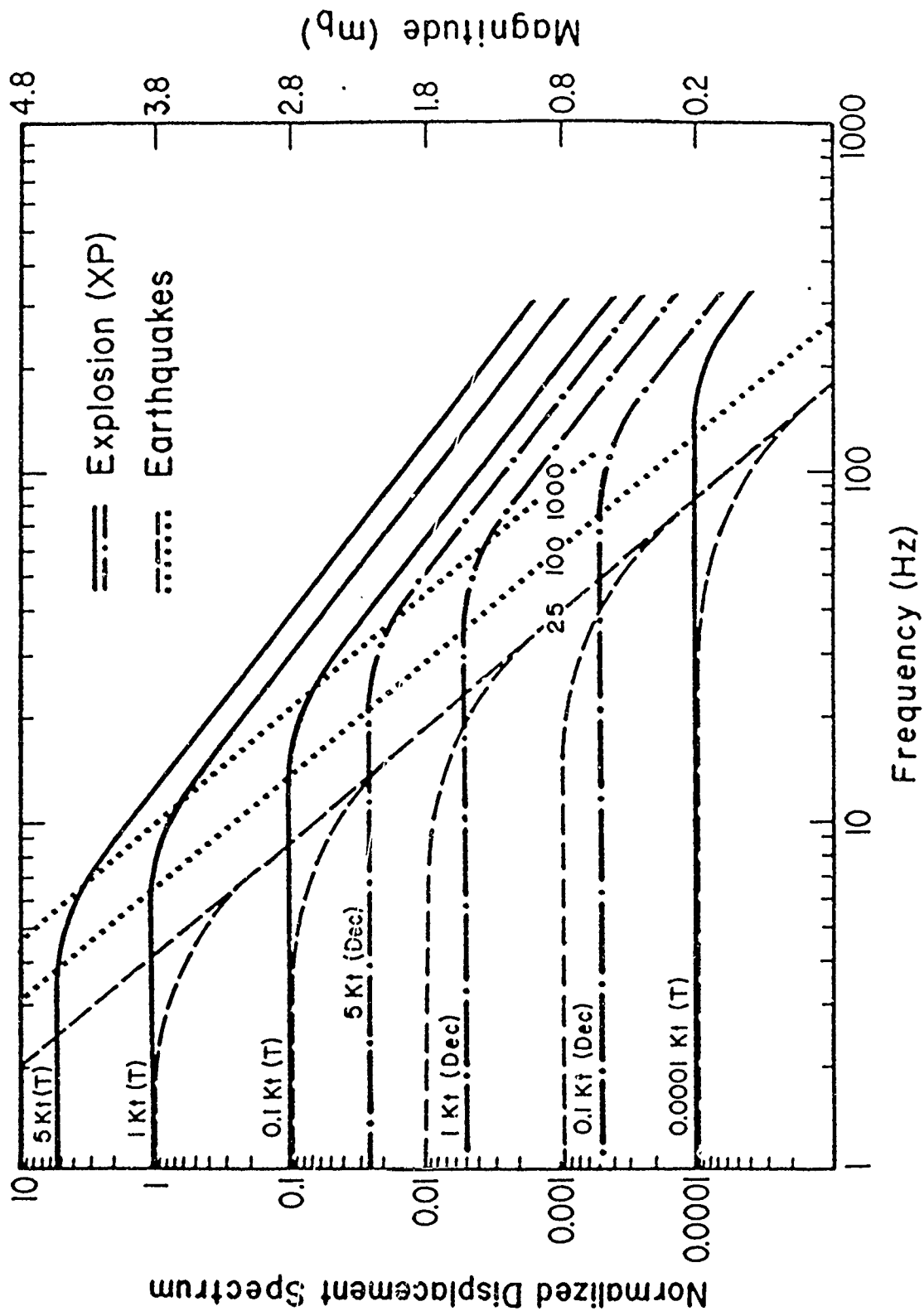
Figure 4 - Theoretical P wave spectra of small comparable earthquakes with 25 bar stress drops and explosions. The notation "DEC" indicates a spectrum for a decoupled explosion of the indicated yield level. The dotted lines labeled "100" and "1000" are corner frequency loci for earthquakes with stress drops of 100 and 1000 bars respectively.

The distance range for such high frequency recording is indicated in Figure (5), which shows "average level" noise curves, multiplied by the inverse of the transfer function for stable continental paths, plotted against the theoretical explosion spectra from the previous figure. Such a plot therefore provides a prediction of signal to noise ratios as a function of distance, with the noise increased with increasing distance as determined by the theoretical-empirical transfer function for P_n signals. Here we have used a $Q_p = 9000$ in the computations of the transfer function.

We observe that large signal to noise ratios are predicted for 1 kt. decoupled explosions at $\Delta = 3°$, with the signal to noise ratio for such an event decreasing to about unity at 30 Hz at a distance of 10°. For the larger P_g wave signal we expect a signal to noise displacement amplitude ratio of about 3 at 10°, in the 30 - 40 Hz range. Thus detection and identification of 1 kt. decoupled explosions using P_g is predicted to be possible out to about 10° in stable continental areas and similar capability is possible using P_n out to 7 or 8 degrees from such a source.

These results have been used to provide estimates of detection-identification capability for Russia. Figure (6) shows the near surface conditions we have used in the analysis. Each symbol indicates the type of medium within which a decoupled or coupled explosion can occur in the USSR, with the symbols, and potential explosion sites, located at 1° grid points. We assume that decoupling is possible in salt, granite and other hard rocks (the latter labeled "other" in the figure). The proposed station distribution is shown by the solid triangles.

Figure (7) shows P_n wave detection capability at 30 Hz for 1 kt. explosions at each of the symbol locations, where full decoupling is assumed if the near surface material is salt, granite or other hard rocks. Here each symbol is at a map location of such an
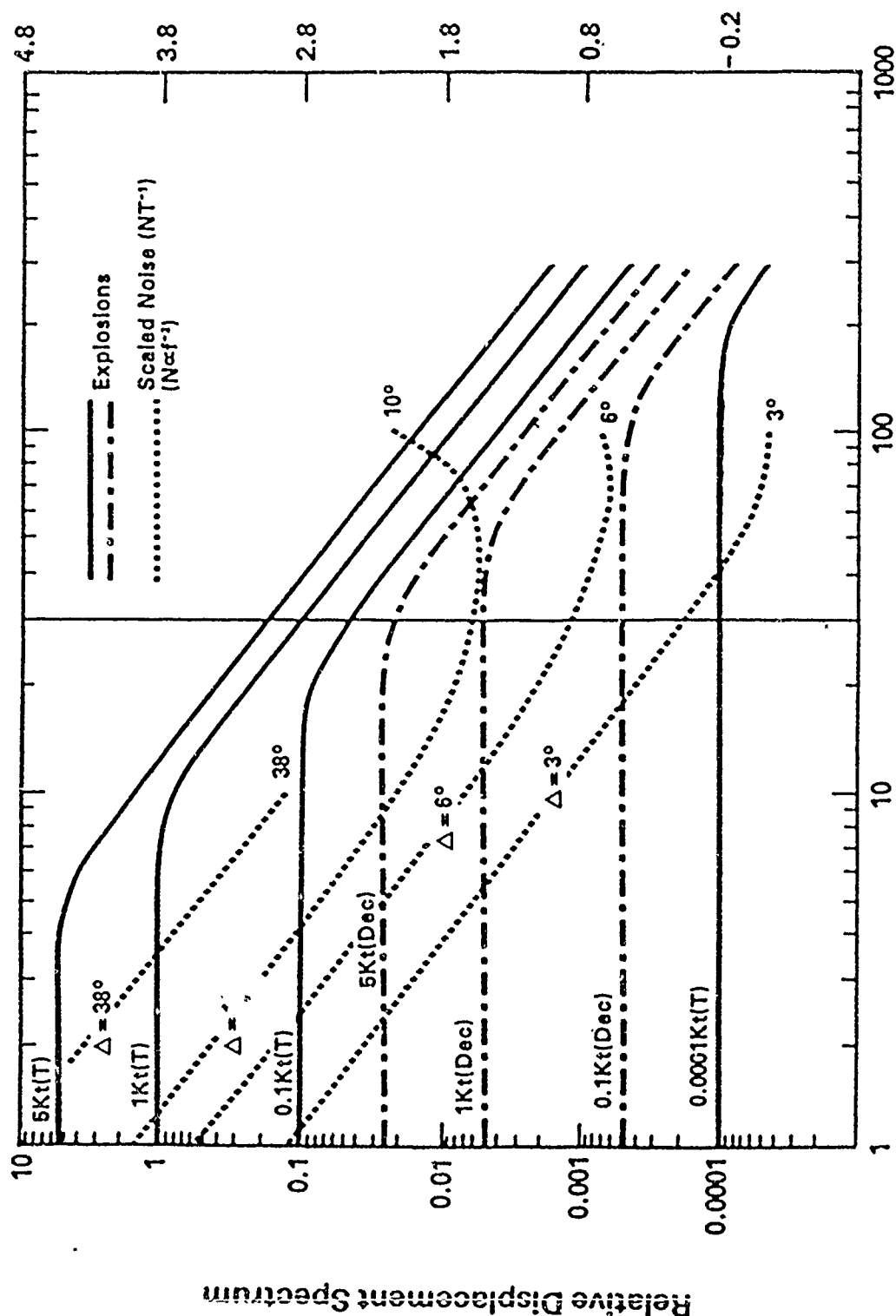
Figure 5 - P wave signal spectra compared to modified average noise levels. Signal to noise ratios can be obtained by taking the ratio of the signal spectral divided by the modified noise curve values at the different distances and frequencies.
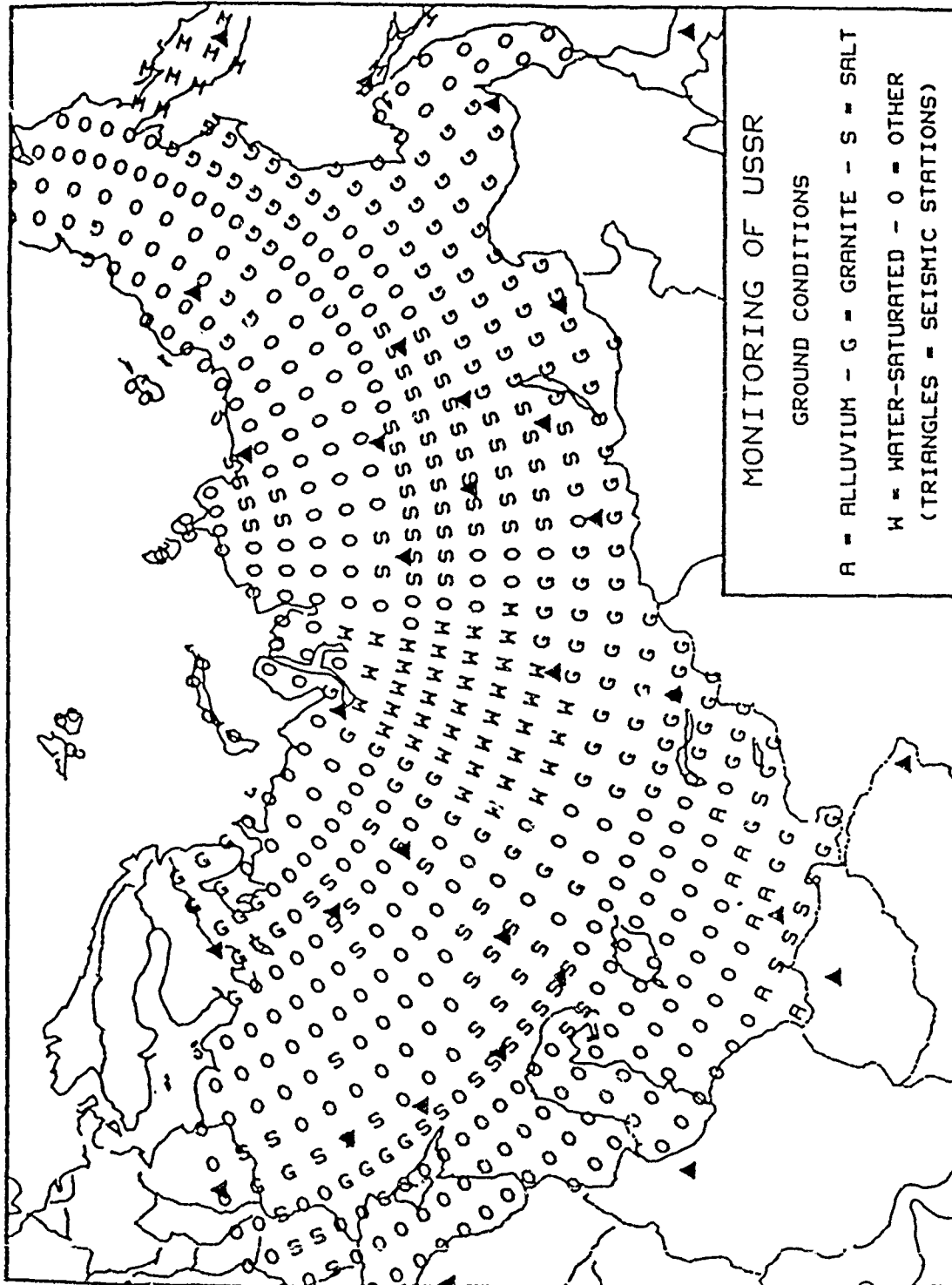
Figure 6 – Near surface material conditions in the USSR. The solid symbols are locations for a network designed to provide monitoring capability down to 1 kt. decoupled explosion signal levels.
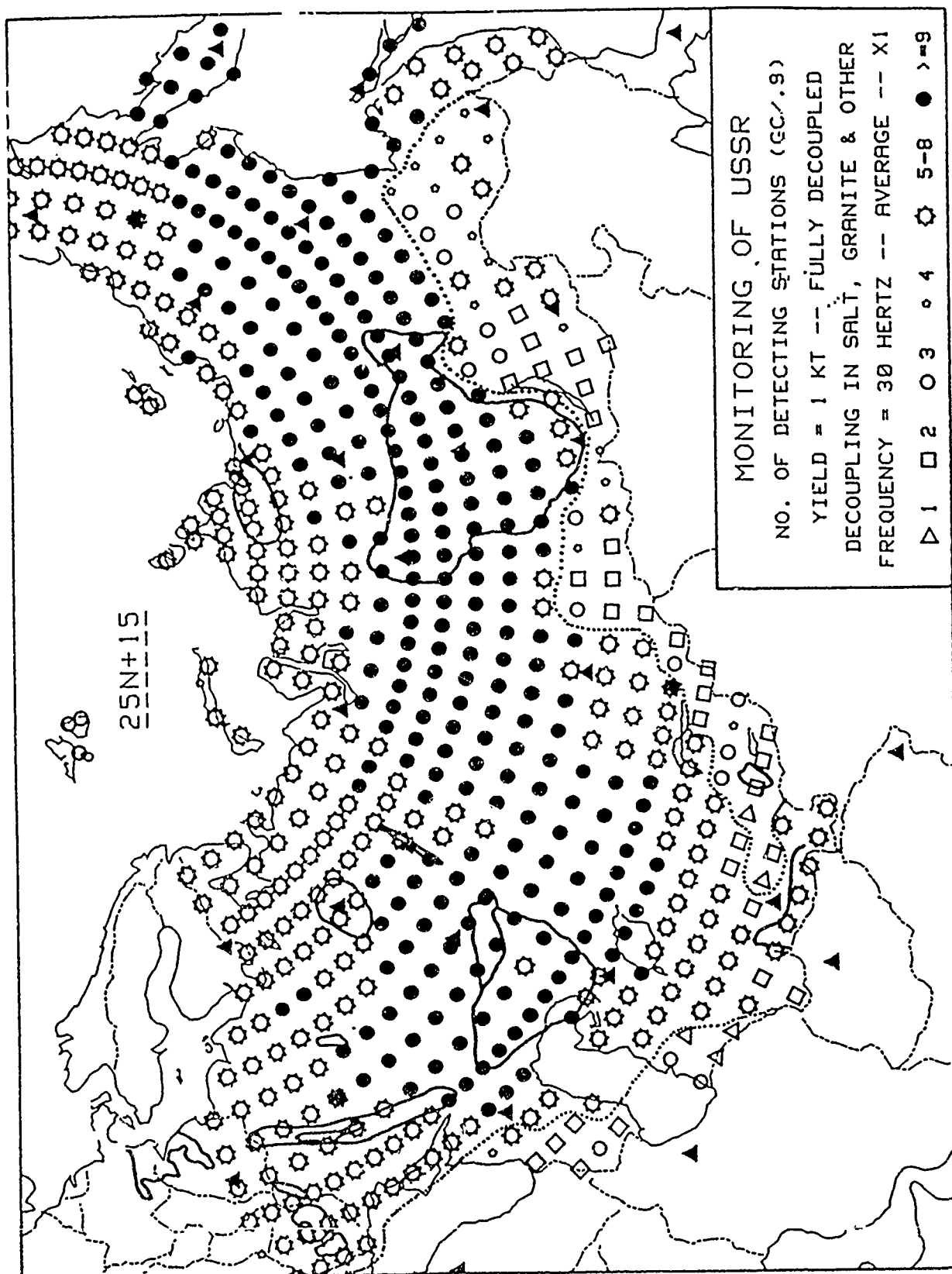
Figure 7 - P_n detection capability of 1 kt. decoupled explosions using a 25 station internal network and a 15 station external network recording at very high frequencies in the USSR. The symbols show the number of stations detecting 30 Hz signal with 90% probability, for an event located at each symbol location. "Average" noise levels assumed at all stations.

explosion, with the symbol type denoting the number of stations predicted to record the event with 90% probability. In this simulation we have used a transfer function incorporating a r^{-2} geometric full-off with distance along with anelastic Q_p of 9000 within the shield and stable continental areas, and a $r^{-7/2}$ fall-off and Q_p of 1000 in the tectonic areas of the USSR. The tectonic zones are shown outlined by the dotted line along the margins of the USSR and there is clearly a reduced detection capability for events occurring within these zones. In general however, the high frequency detection capability is certainly very good within all areas of the USSR using the network shown. In this figure the notation "average" refers to the average background noise curve defined earlier in Figure 1.

Figure (8) shows a similar detection capability map with noise levels assumed to be at the "noisy" level given in Figure (1). A somewhat diminished, yet very good, capability is indicated.

In order to obtain sufficient bandwidth for spectral discrimination of events it is necessary to be able to obtain good P wave spectral data down to around 5 Hz as well as at 30 Hz. Figure (9) shows signal recording capability at 5 Hz for P_g, where it is assumed that the P_g wave is about 3 times as large as P_n in the regional range to about $10°$. A nearly identical, but slightly diminished capability generally applies to P_n waves at 5 Hz, but with only one and often no station detections for these very small events within the bordering tectonic regions. Thus if P_n is to be used exclusively for spectral discrimination, then more of the stations should be placed within the tectonic areas to insure confidence in event identification. If P_g is used when necessary, then the given station distribution appears adequate.
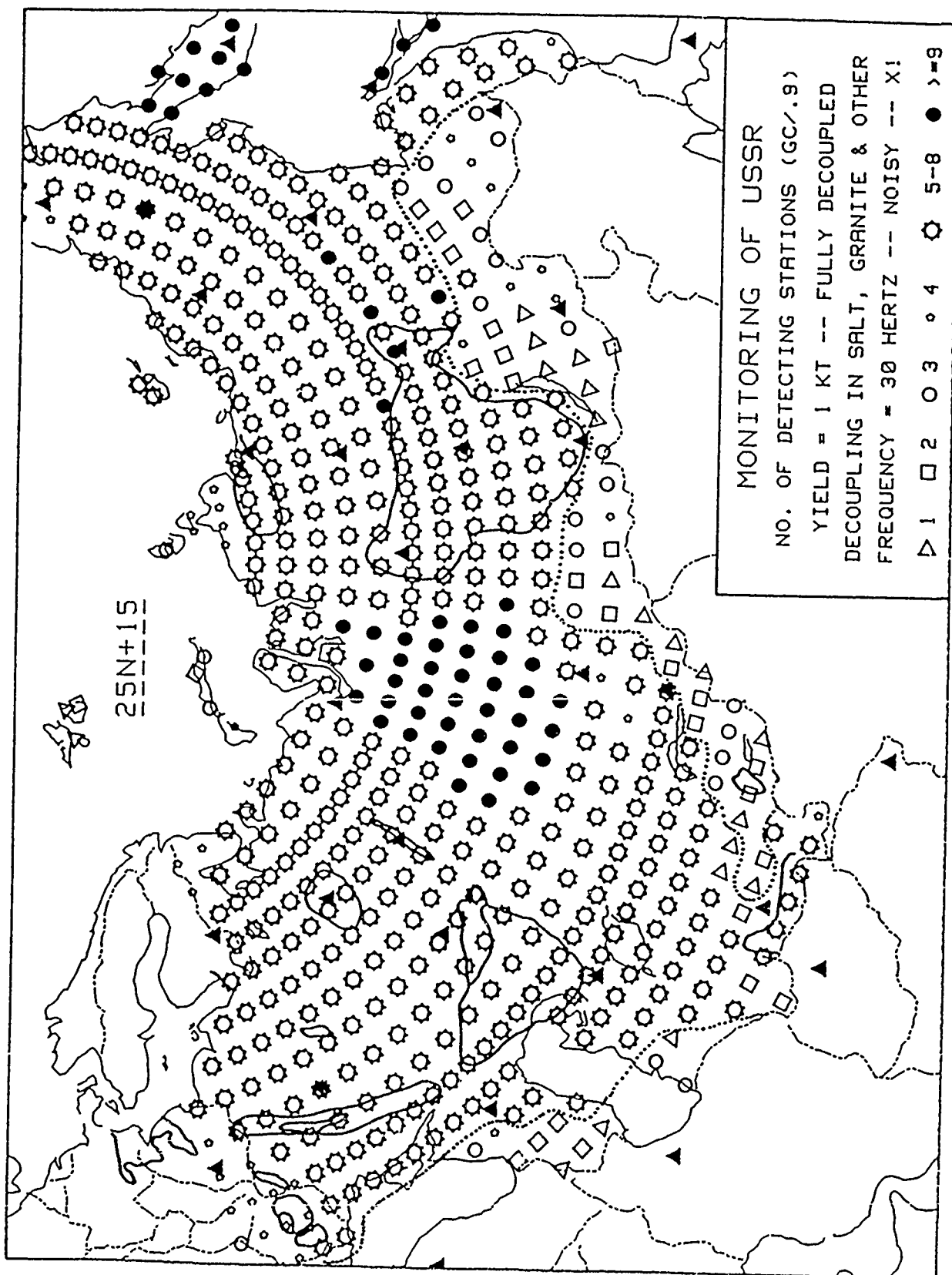
Figure 8 - P_n detection capability at 30 Hz with "noisy" conditions assumed at all stations.
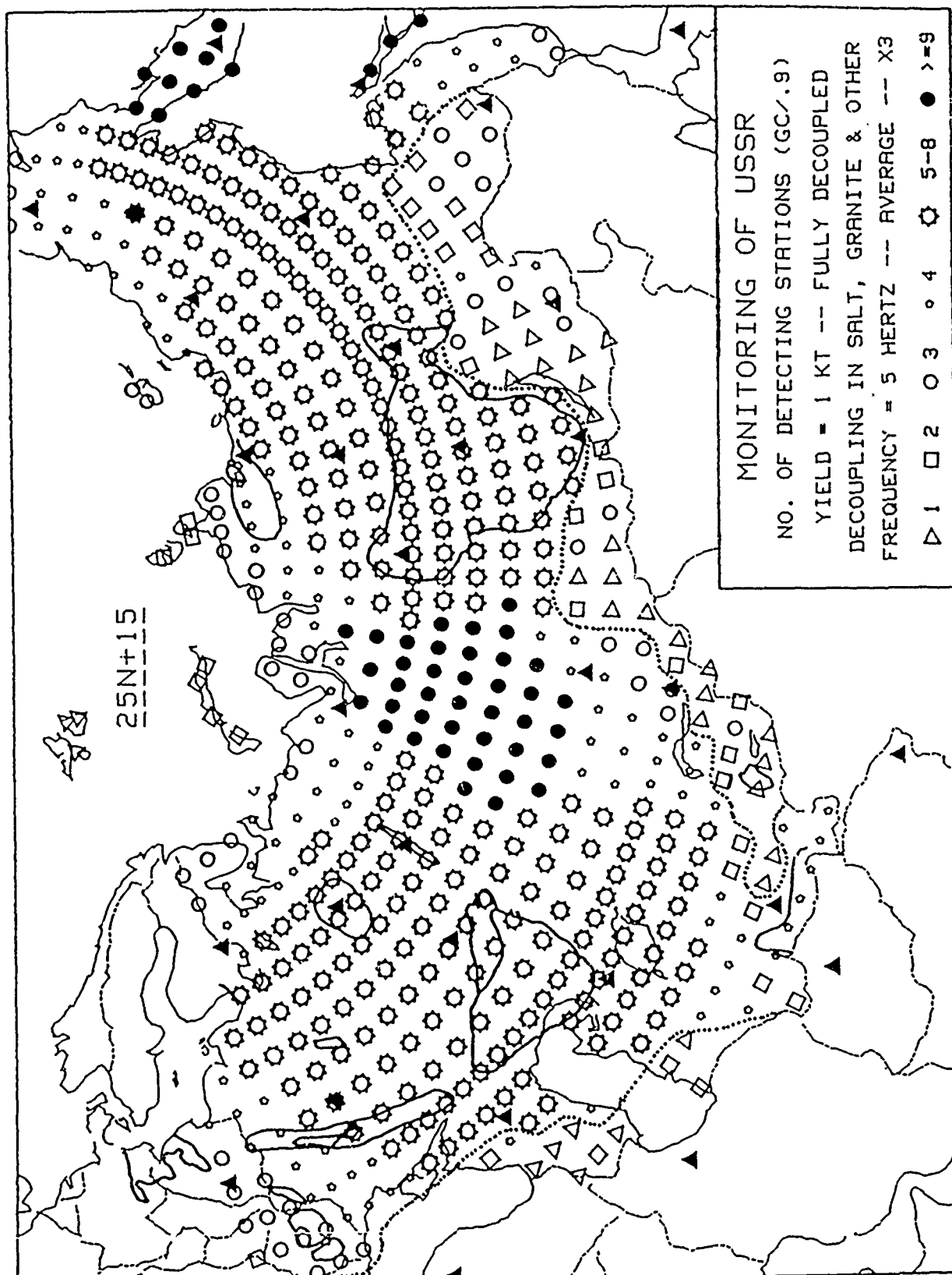
Figure 9 - P_f wave detection capability at 5 Hz with average noise conditions at all stations. (P_f assumed 3 times larger than P_n at all frequencies.)

Figure (10) shows locations of earthquakes and explosions in tectonic provinces of the U.S. that are particularly appropriate for the evaluation of identification capabilities in tectonic regions. Figure (11) shows the results of two station spectral discrimination of the event set. Here the simple Variable Frequency Magnitude (VFM) method is applied, where the body wave magnitude at low frequency (.3 Hz in this example) is plotted against a high frequency magnitude (3 Hz), both magnitudes being obtained from the same seismic phase (P_n in this example). The solid and broken solid lines are the theoretically predicted loci for explosions with two different assumed coupling characteristics. The vertical dashed line is the "boundary line" or high frequency cut-off line for the high frequency m_b of earthquakes, with the earthquakes with stress drops below 100 bars predicted to have m_b values at 3 Hz lying to the left of this line, at lower values. The results show good agreement with the theoretical predictions and indicate a well defined separation between earthquakes and explosions.

As indicated by the results shown in this figure, good discrimination capability is implied for larger magnitude explosions and earthquakes using the lower conventional seismic bandwidth. Similar results for Russian explosions and nearby earthquakes, in the Kazakh test area, have also been obtained. The theory predicts equally good and nearly identical separation of the event populations at lower magnitudes, down to less than $m_b = 2.$, when very high frequency data is used with the high frequency magnitude near 30 Hz and the lower frequency magnitude near 5 Hz. In future studies a direct verification of these latter predictions will be undertaken along with more extensive studies of propagation characteristics for very high frequency P and S waves in the crust and upper mantle in areas of monitoring interest.
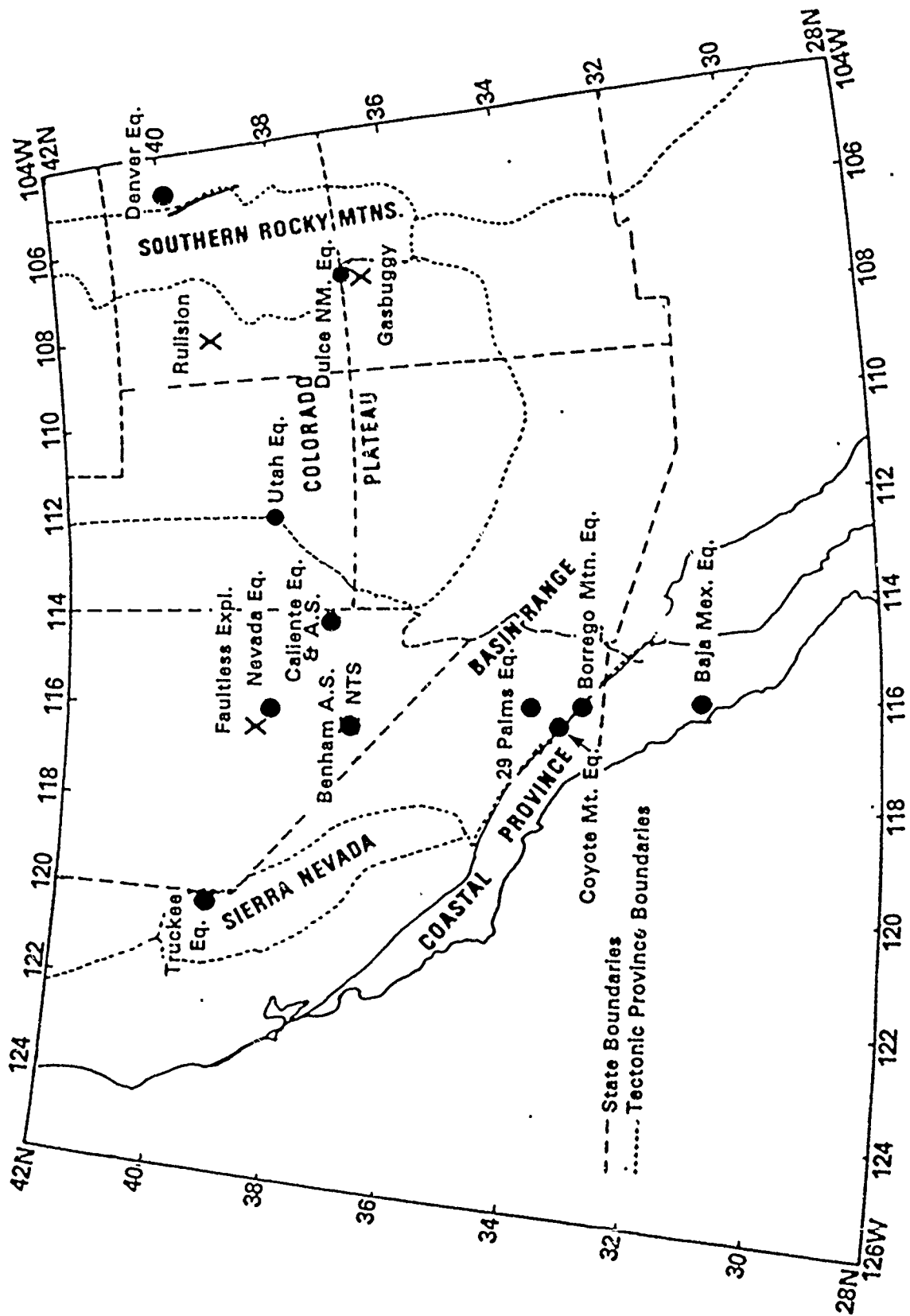
Figure 10 - Locations of comparable explosion and earthquake events in tectonic provinces in the Southwestern U.S.

388
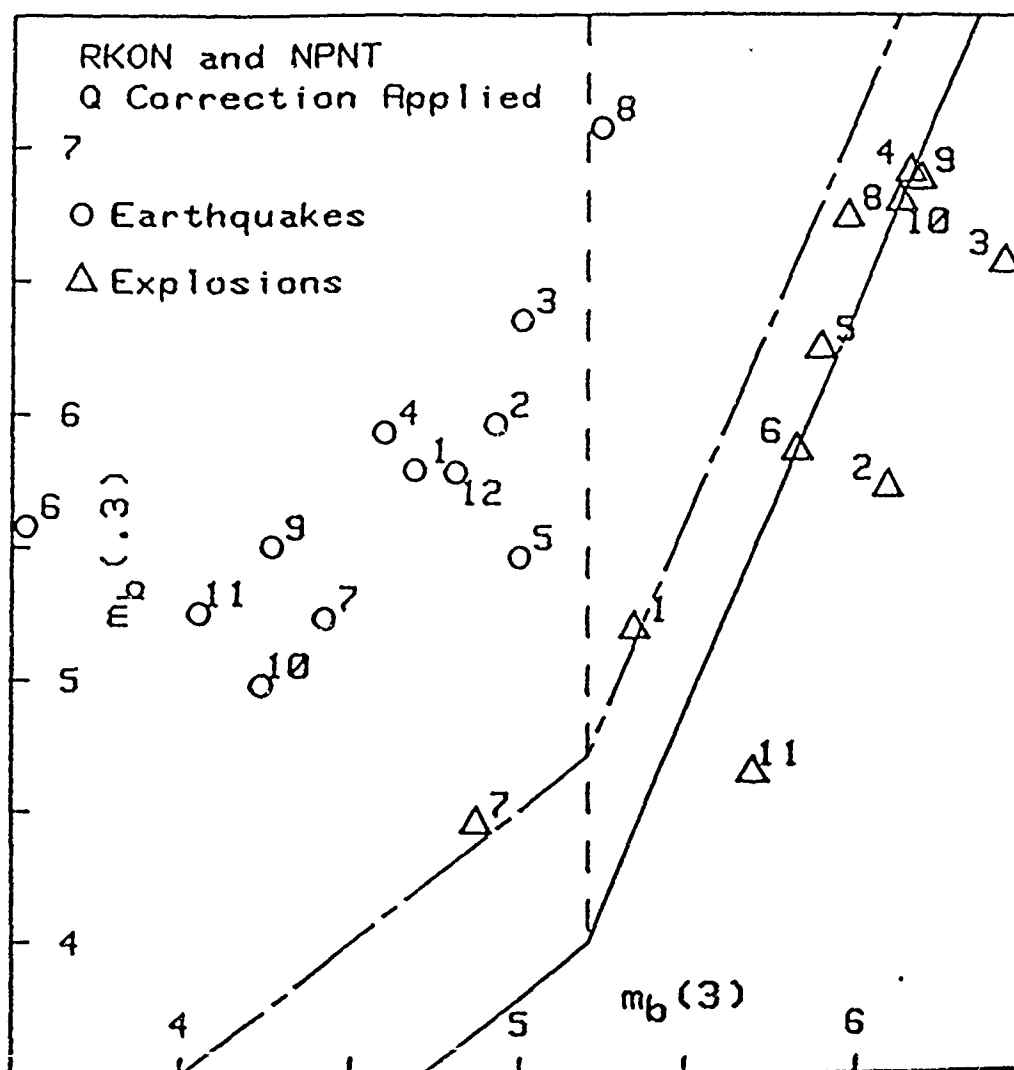
Figure 11 - Variable Frequency Magnitude discrimination results for the P_n wave from the Southwestern U.S. explosion-earthquake event set. The lines are theoretical predictions, with the vertical line denoting a high-frequency magnitude "cut-off" for earthquakes with stress drops less than 100 bars.

AFGL/DARPA REVIEW OF NUCLEAR TEST MONITORING
BASIC RESEARCH
US AIR FORCE ACADEMY, 6-8 MAY 1985

PAPER TITLE: m_b bias in the Great Basin and its implications for the *Faultless* magnitude versus yield anomaly

PAPER AUTHORS: Keith F. Priestley and David E. Chavez

CONTRACT NUMBER: F49620-83-C-0012

SUMMARY: Comparison of teleseismic P-wave delays in the vicinity of the Central Nevada Test Site in Hot Creek Valley, Nevada, with P-delay data over a wider region in the Great Basin, shows that upper mantle speeds under Hot Creek Valley stations are faster than the average for the Great Basin as a whole. However, comparison of the travel times for a nuclear explosion in Hot Creek Valley with explosions at Pahute Mesa and at Yucca Flat shows that the upper mantle speeds under Hot Creek Valley are slower than beneath Pahute Mesa. These observations indicate that the caldera complex in Hot Creek Valley has a high velocity root similar to that proposed to exist beneath the Silent Canyon caldera at Pahute Mesa, although the Hot Creek anomaly is less pronounced. The effect of these upper mantle structures is that they cause a shadow zone at at the distances of the European stations which report to the ISC. The shadow zone is much more pronounced for Pahute Mesa explosions, and consequently amplitudes (and magnitudes) are underestimated for the events at Pahute Mesa. When magnitude versus yield relationships developed using Pahute Mesa data are applied to other areas, such as the Central Nevada Test Site in Hot Creek Valley, they result in an overestimate of yield.

m_b BIAS IN THE GREAT BASIN AND ITS IMPLICATIONS FOR THE *FAULTLESS* MAGNITUDE VERSUS YIELD ANOMALY

Keith F. Priestley and David E. Chavez
Seismological Laboratory, Mackay School of Mines
University of Nevada, Reno, Nevada 89557

INTRODUCTION

The underground nuclear explosion FAULTLESS was detonated at the Central Nevada Test Site (CNTS) in Hot Creek Valley, Nevada, approximately 150 km north-northwest of the Nevada Test Site (NTS). The International Seismological Centre (ISC) body wave magnitude, m_b, of 6.3 is more than 0.3 units (a factor of two in amplitude) greater than that predicted from emperical magnitude-yield curves for NTS explosions given the announced maximum yield of 1000 kilotons. CNTS is physiographically very similar to Pahute Mesa (NTS), so in view of the close proximity of the two test sites it might be expected that the magnitude-yield curves for NTS could also be applied to CNTS.

Spence (1974) used travel-time residuals for NTS explosions recorded at teleseismic distances to infer the presence of a high velocity structure in the mantle beneath the 14 m.y. old Silent Canyon caldera at Pahute Mesa. Geochemical data indicates that most of the basalts of the southern Great Basin region originate in the upper mantle, and in fact, trace and major element studies of the Silent Canyon volcanic center basalts and tuffs indicate an upper mantle magma source. Thus, the high velocity material proposed by Spence may represent upper mantle material largely depleted of its partial melt component by differentiation and associated eruption of the partial melt phase through the Silent Canyon volcanic center.

In order to see if any anomalous structures of a similar nature exist beneath CNTS which could produce the discrepancy in observed m_b for FAULTLESS, we examined teleseismic P-wave residuals from seismic stations in Hot Creek Valley. We conclude that there is only weak evidence for high velocity material beneath CNTS in Hot Creek Valley, and that the anomalous high m_b for the FAULTLESS explosion may result from a bias in the magnitude versus yield curves derived from the NTS data.

DATA and ANALYSIS

Figure 1 is a map giving the generalized geology, station locations, and the FAULTLESS shot point. As seen from the map, the area around Hot Creek Valley is dominated by a series of nested calderas which range in age from 25 to 35 m.y.; these calderas are 10 to 20 m.y. older than Silent Canyon caldera at Pahute Mesa. To the south-east of Hot Creek Valley is the Lunar Craters volcanic field, a site of very recent volcanism.

Data used in the P-delay study consist of recordings of teleseismic P-waves recorded on seven ststions operated by the U. S. Geological Survey in the vicinity of the Hot Creek Valley and on stations of the University of Nevada seismograph network; and travel times from the DUMONT, GREELEY, and FAULTLESS explosions in Yucca Flat, Pahute Mesa, and Hot Creek Valley, respectively.

We first searched for lateral variations in structure of Hot Creek Valley by computing teleseismic P-wave residuals at each station relative to the average residual across the CNTS network. In Figure 2 we present maps which show relative residual as a function of azimuth. Figure 2a shows the residuals at each of the CNTS stations, after the data have been corrected for known variation in sediment thickness and for Moho dip

inferred from seismic refraction and gravity data. Each station location shown in figure 2a is indicated by a circle whose radius is 1.0 second. The circumference represents a zero residual, and lines drawn from the circle are scaled according to the size of the residual. Lines inside the circle are negative residuals (early arrivals) and lines outside the circle are positive residuals (late arrivals). The azimuth of each line corresponds to the azimuth of approach of the wavefront. The data show that the residuals across the whole network are small, but tending to be more negative in the interior of the network and more positive on the network perifery. Residuals relative to event average across the CNTS network will not reveal any large scale velocity anomalies in Hot Creek Valley which are affecting the whole network. Therefore we have also computed P-wave residuals relative to a regional event average using stations throughout the Great Basin. The results shown in Figure 2b indicate that Hot Creek Valley is relatively fast compared to the Great Basin as a whole, suggesting that, as in Silent Canyon, a high velocity vestige of a root to the Hot Creek calderas exits at depth. Finally, we compared travel time residuals for the FAULTLESS explosion in Hot Creek Valley, and the GREELEY explosion at Pahute Mesa, to the DUMONT explosion at Yucca Flat. The result, shown in figure 2c, indicates that compared to DUMONT, travel times from FAULTLESS are slow while travel times from GREELEY are fast. A plausible explanation for these observations is that high velocity mantle roots to the caldera as proposed by Spence (1974) exist beneath both the Silent Canyon caldera and beneath the Hot Creek Valley caldera complex, however the body beneath Hot Creek Valley is older, and thus has had more time to be assimilated into the surrounding mantle.

DISCUSSIONS

Figure 3 compares ray paths for hypothetical explosions in the near surface layers above the proposed upper mantle structures beneath both Pahute Mesa (Fig. 3a) and Hot Creek Valley (Fig. 3b). In our calculations, the high velocity upper mantle anomaly shown by the stippled region in figure 3, was defined by a gradation from a velocity of 7.7 K/S in the "unperturbed" upper mantle to 8.2 K/S in the interior of the high velocity zone. The initial ray parameter in the calculation was let vary to cover the range $\Delta = 20°$ to $180°$.

The density of rays shown in figure 3 is proportional to the expected amplitude. In both figures 3a and 3b, there is a smooth variation in ray density (and hence amplitude) from $\Delta = 20°$ to approximately $\Delta = 45°$. In the region of $\Delta = 50°$ there is a dense concentration of rays resulting in a caustic, i.e., high expected amplitude. The effect of this focusing of energy is much greater for the Pahute Mesa structure than for the Hot Creek Valley structure. At greater distances, $(\Delta > 60°)$, there is a defocusing of the rays, resulting in a shadow zone. Again, this is more severe for the Pahute Mesa structure. Based on these figures, we expect the amplitudes for events of similar size occurring in Hot Creek Valley to be greater in the distance range $\Delta > 60°$, than events occurring at Pahute Mesa.

Most m_b measurements for Nevada explosions are heavily biased by amplitude measurements made at European seismograph stations. From figure 3a, these station fall in the shadow zone for events detonated at Pahute Mesa, while figure 3b suggests that events detonated in Hot Creek Valley will be affected to a much smaller extent. Figure 4 is a comparison of the variation in amplitude of the FAULTLESS and GREELEY explosions with distance, along north-east azimuth. The values plotted in figure 4 are ratios of the FAULTLESS or GREELEY amplitude, to that of the amplitude of the DUMONT explosion at Yucca Flat. These values for the FAULTLESS and GREELEY explosion are similar at near distances. The FAULTLESS amplitude ratio remain close to a constant level with increasing distance. However, at distances of $60°$ to $80°$ (European stations), the FAULTLESS explosion clearly has larger amplitudes than the GREELEY explosion, the GREELEY amplitude ratio having decreased by approximately a factor of 2 to 3.

The variation in amplitude with distance shown in figure 4 supports the hypothesis proposed here that low amplitudes observed at European stations result from defocusing of waves due to anomalous upper mantle structure beneath Pahute Mesa. However, the amplitude variation for the GREELEY explosion might also be the result of tectonic release accompanying the GREELEY explosion. Wallace *et al.* (1984) studied wave forms for a large number of explosions at Pahute Mesa, and find that a number of the large explosions, and GREELEY in particular, show waveform distortion which they attribute to a significant component of tectonic release. In comparison to the 1966 GREELEY explosion, Wallace *et al* (1984) found that the 1975 KASSERI explosion, which was of similar yield to GREELEY, and located less than 2 km from GREELEY, showed simple waveforms which indicate a small component of tectonic release. We have compared the short-period P-wave arrivals of GREELEY and KASSERI at common stations along a northeast azimuth, and find that the amplitudes versus distance relationship for KASSERI is

identical to that shown in figure 4 for GREELEY. Consequently, we feel that the amplitude variation shown for GREELEY in figure 4 is not the result of tectonic release, but rather due to the structural heterogenety.

These results have important implications for the estimation of yields of explosions from teleseismic body-wave magnitude estimates. The majority of magnitude versus yield data are derived from explosions at the Nevada Test Site. Most of the large explosions that have been detonated in the vicinity of Pahute Mesa. The ISC body wave magnitudes for these events are biased by the large number of stations reporting from Europe. If our hypothesis is correct, the anomalous upper mantle structure beneath Pahute Mesa will result in lower amplitude at European stations causing the magnitude versus yield curve to be biased towards low magnitudes for a given yield. Application of the magnitudes versus yield curve derived from NTS explosions to other areas, such as the Central Nevada Test Site, will result in an overestimate of yield, as appears to have been the case for the FAULTLESS explosion.

REFERENCES

Spence, W., P-wave residual differences and inferences on an upper mantle source for the Silent Canyon volcanic centre, southern Great Basin, Nevada, *Geophy. J. R. Astr. Soc.*, *38*, 505-523, 1974.

Wallace, T.C., Helmberger, D.V., and Engen, G.R., Evidence of tectonic release from underground nuclear explosions in long-period P-waves, *Bull. Seismo. Soc Am.*, *74*, 819-842, 1984.
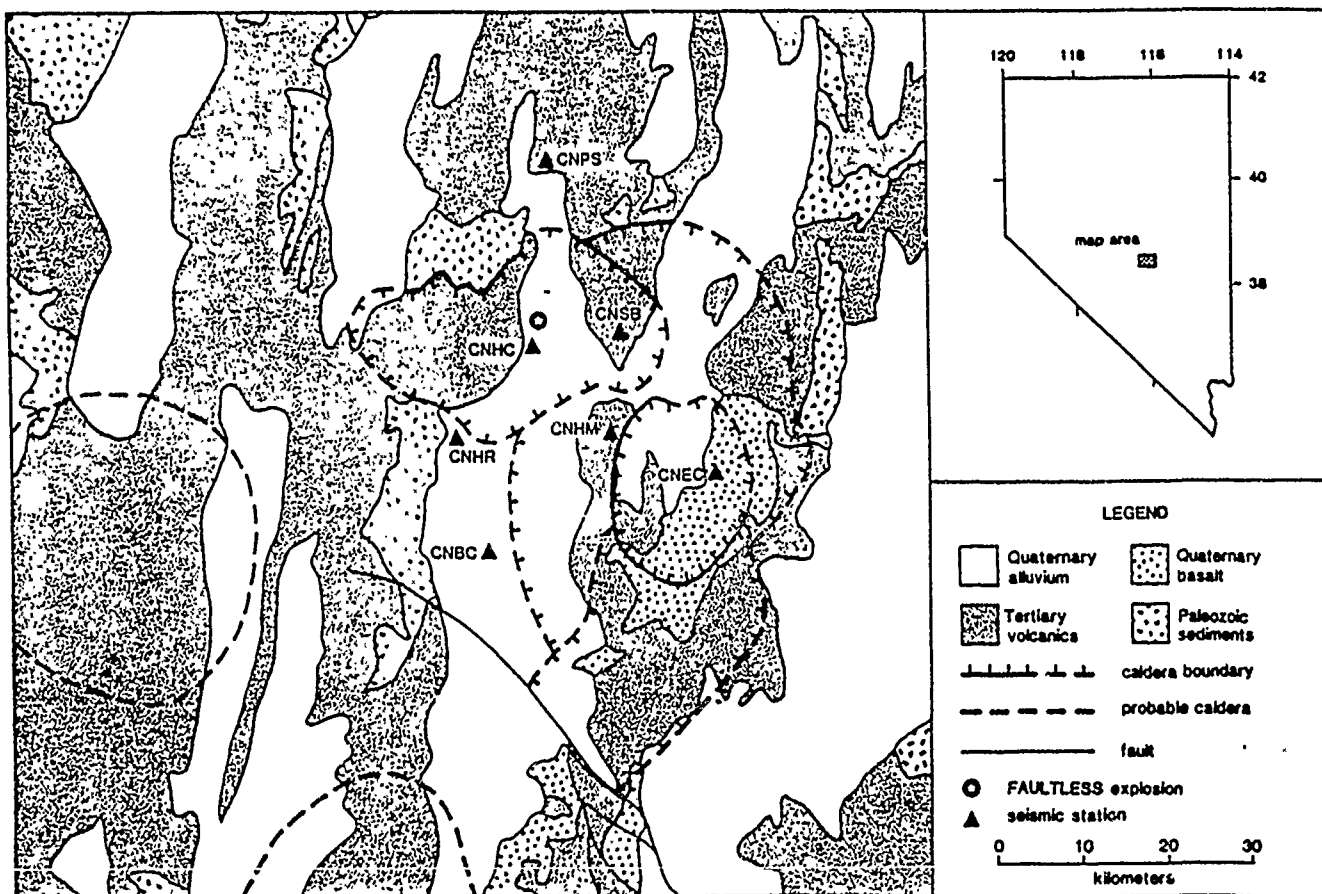
Figure 1. Generalized geologic map of the Hot Creek Valley, Nevada area including station locations and the FAULTLESS shot point.
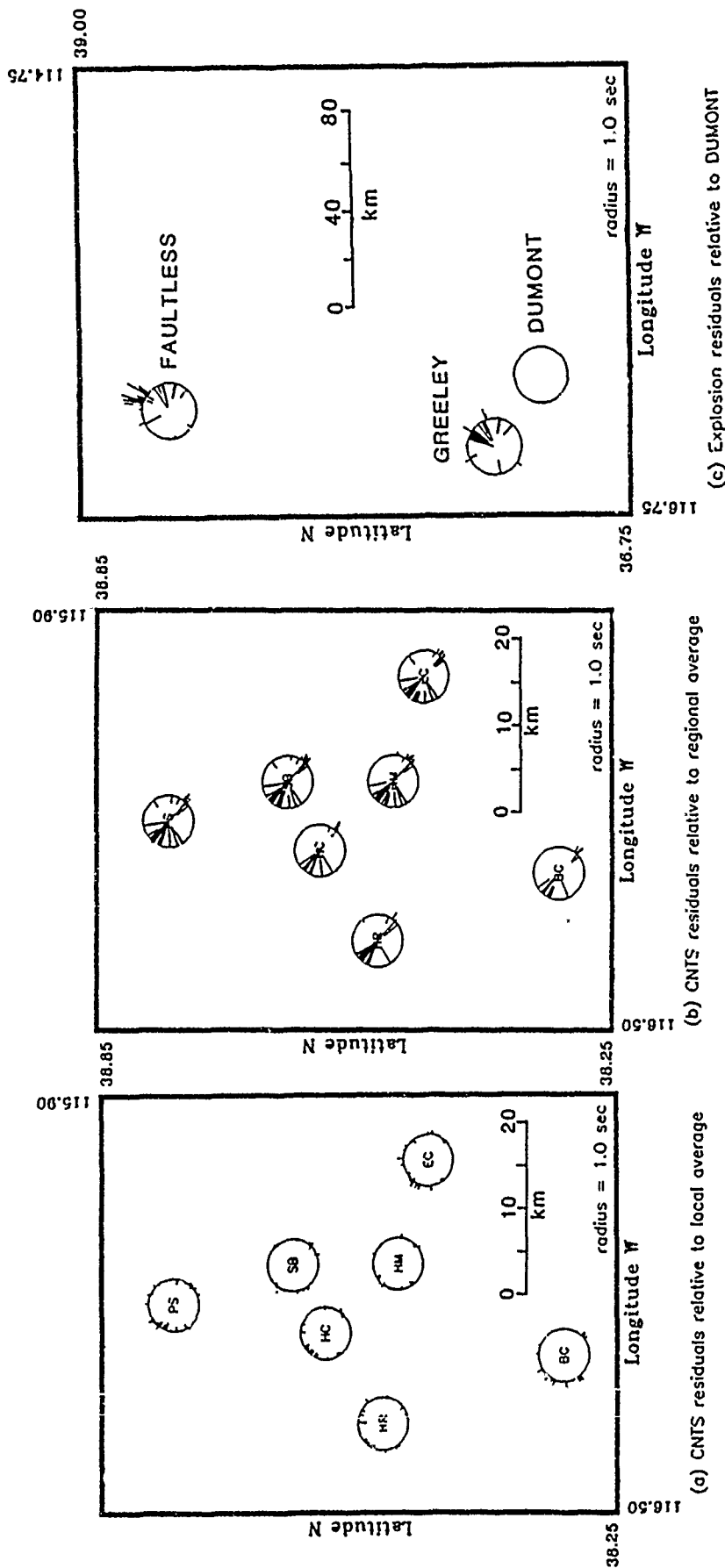
Figure 2. Maps of travel time residuals versus azimuth (format described in the text): a) relative to the event average for all stations after corrections for surface geology and inferred Moho dip have been applied; b) relative to event average which and inferred Moho dip have been applied; b) relative to event average which includes data from Great Basin seismic stations; c) for the FAULTLESS and GREELEY explosions relative to the DUMONT explosion at Hot Creek Valley, Pahute Mesa, and Yucca Flat, respectively.

(a) CNTS residuals relative to local average

(b) CNTS residuals relative to regional average

(c) Explosion residuals relative to DUMONT

radius = 1.0 sec

386
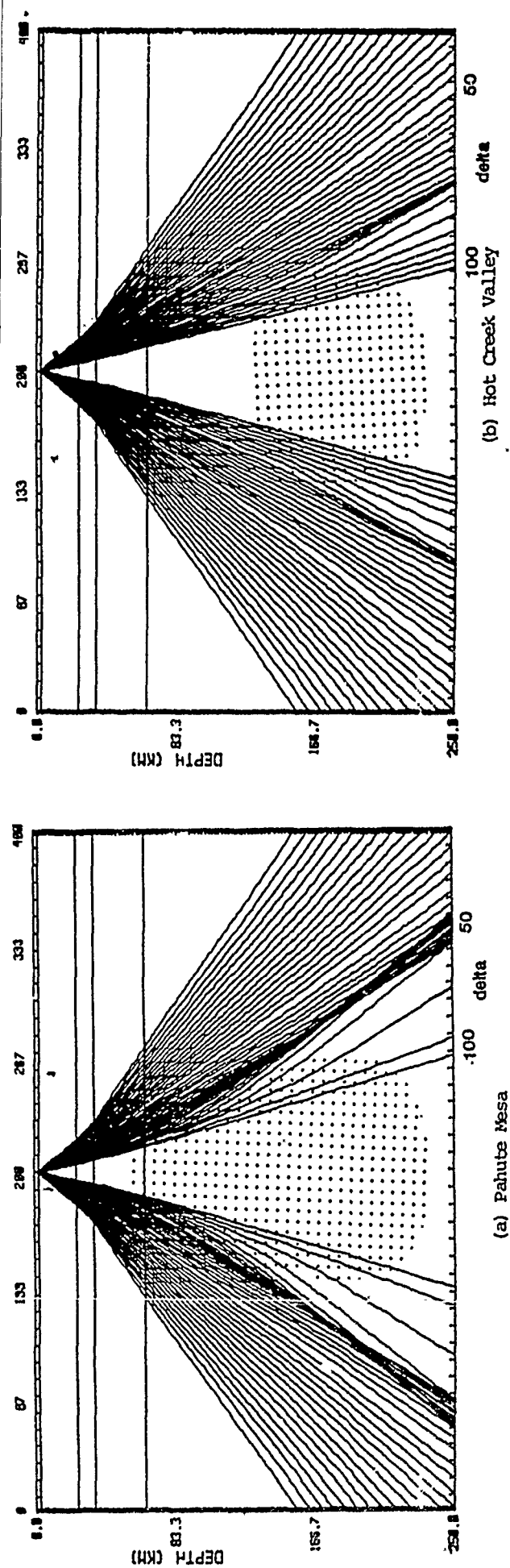
Figure 3. a) Ray paths through the high speed body under Pahute Mesa as postulated by Spence (1974). b) Ray paths through the high speed body under Hot Creek Valley as suggested by our data.

(a) Pahute Mesa

(b) Hot Creek Valley
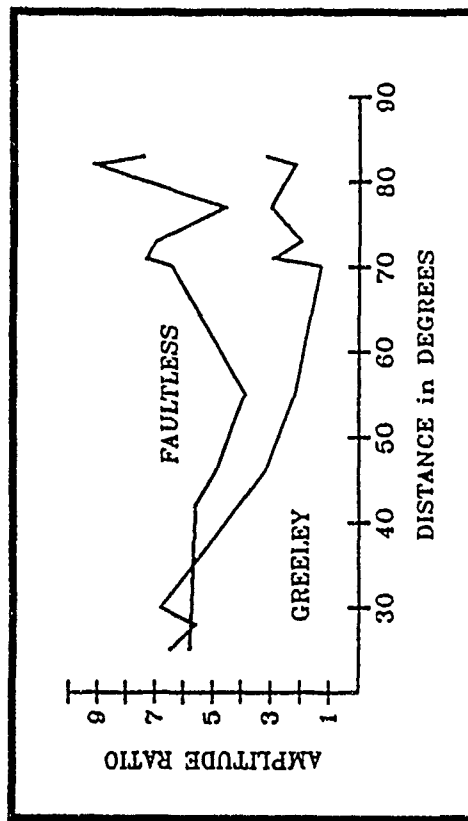
Figure 4. Comparison of the FAULTLESS and GREELEY amplitude ratios to DUMONT, as a function of distance, along a northeast azimuth.

387

PAPER TITLE: L_g attenuation in the northern Great Basin

PAPER AUTHORS: Keith F. Priestley and David E. Chavez

CONTRACT NUMBER: F49620-83-C-0012

SUMMARY: We have determined apparent L_g attenuation in the frequency range $0.3Hz \leq f \leq 3.0Hz$ along two paths in the northern Great Basin by measuring the decay in spectral amplitude with distance. After correction for geometrical spreading, we modeled the spectra as composed of frequency dependent source and Q terms for which we solved using least-squares. We find along both paths a frequency dependent Q with $Q(1Hz)=250\pm50$. These values are comparable to those obtained by other studies in this same region. Our data indicate, however, that the nature of the frequency dependence differs significantly between paths, suggesting strong lateral variations in the apparent attenuation structure. The $Q(f)$ functions along both paths are peaked near 2 Hz. The Q measured at this peak is 800 for a path extending northeast from Mammoth Lakes, California, and is 360 for a path northwest from the Nevada Test Site.

L_g ATTENUATION IN THE NORTHERN GREAT BASIN

Keith F. Priestley and David E. Chavez
Seismological Laboratory, Mackay School of Mines
University of Nevada, Reno, NV 89557

Introduction

L_g waves are short-period (0.3 to 3.0 sec) surface waves which propagate in the continental crust with group velocities of 3.4 ± 0.2 ks^{-1} (Press and Ewing, 1952; Bath, 1954). Knopoff, *et al.* (1973) have identified the transverse component of L_g with higher mode Love waves while Panza and Calcagnille (1975) have shown that the vertical-radial component can be identified with higher mode Rayleigh waves. L_g is commonly the largest phase observed on regional seismograms in the eastern United States, but is a less prominant phase on seismograms of regional earthquakes occurring in the western United States, indicating significant differences in the crustal attenuation between the two regions.

Measurements of L_g amplitude decay with distance have been shown to provide a good means for estimating the average attenuation in the continential crust over regional paths. The reason for this is that as the mode number of surface waves increases, the sampling of the structure becomes more uniform. Moreover, L_g amplitudes appear to be less sensitive to focal mechanism and focal depth than other crustal phases.

Nuttli (1973, 1980, 1981, 1984) exploited these properties of L_g to estimate m_b for earthquakes and explosions, estimate apparent crustal attenuation, discriminate between small earthquakes and explosions, and estimate the yield of nuclear explosions. In the latter case, he found that if L_g amplitudes are to be used to estimate explosion yields to an accuracy of 30%, then average values of spatial attenuation over large areas (such as the western U.S.) are inadequate. Instead, smaller scale regional estimates must be used in order to account for lateral variations in the attenuation structure.

We have begun an investigation into the nature of L_g propagation in the Great Basin in an effort to quantify any small-scale regional variations. In this paper we report on the results of our analysis of L_g attenuation along two paths in the northern Great Basin.

Data and Analysis

Figure 1 shows the locations of the events and stations whose seismograms comprise our data set. The stations are either broad-band (velocity flat from 0.03 to 10 Hz) digital seismographs operated by the University of Nevada-Reno (UNR) (stations MNN, BDE, and WCN in Figure 1) or broad-band (velocity flat from 0.07 to 10 Hz) digital seismographs operated by the Lawrence Livermore National Laboratory (LLNL) (stations MNV, ELK, KNB, and LAC in Figure 1). A typical set of recordings is plotted in Figure 2, which shows the original data after band-pass filtering (to remove the 6 second microseisms and to permit a larger sample interval) and the same data passed through a hypothetical 1-second seismometer. The data in Figure 2a are of an earthquake near Mammoth Lakes,

California and include records along the MNV-ELK path as well as at LLNL stations KNB and LAC which lie to the east and southeast. There is an obvious azimuthal dependence on the character of L_g visible in these seismograms. In the study described here we have analysed only those two on a common azimuth, MNV and ELK. Figure 2b shows recordings of an NTS explosion along the MNN-BDE-WCN path. The explosion source produces simpler looking records.

To determine the L_g attenuation, we computed instrument corrected, displacement amplitude spectra of the vertical component L_g phase. We extracted the $Q(f)$ function using a technique similar to that used by Singh, et al. (1982) for determining the SH Q along the Imperial fault. The observed L_g spectrum was modeled as

$$A(f,R) = \frac{S(f)}{R^{0.5}} e^{\frac{-\pi f t}{Q(f)}} \qquad (1)$$

where $A(f,R)$ is the spectral amplitude observed at a distance R, f is frequency, t is the travel time, $S(f)$ is the source term, and Q is the quality factor. This simple model neglects radiation pattern and scattering effects, therefore it provides a measure of the *apparent* rather than the intrinsic Q. Since L_g has been succesfully modeled as surface wave (Knopoff, et al., 1973; Panza and Calcagnille, 1975) we have assumed that the geometrical spreading scales witn the square root of distance. Taking the logarithim (base 10) of both sides of (1) yields

$$\log_{10}A(f,R) + \log_{10}R^{0.5} = \log_{10}S(f) - \left| \frac{1.364 f}{Q(f)} \right| t \qquad (2)$$

which is the equation for a straight line, where the source term is the intercept and the Q term controls the slope. Fixing f, we know $A(f,R)$, R, and t for each of the stations and we solve for S and Q. By looping over all the frequencies we obtain the source and Q spectra.

In our case, we have only two data points for the MNN-ELK path, and three data points for the MNV-BDE-WCN path, consequently "noise" in any single spectrum strongly influenced the results. We found that we were able to minimize these effects by first low-pass filtering the individual spectra and then averaging the spectra for each source-station pair. Performing the regression on the average spectra yielded more stable results.

We attempted to minimize any spectral distortion introduced by the averaging process by computing the average spectra in the following manner. First, we grouped the data into sets of events with similar S-wave corner frequencies using the spectral source parameters of the 1980 Mammoth Lakes earthquakes given in Archuleta, et al., (1982). Then, assuming that the source spectra in each group were similar except for a constant amplitude value, we corrected for geometrical spreading, normalized to a common reference amplitude and computed the log-average spectrum. Our normalization of the spectral amplitudes is equivalent to the m_b normalization described by Nuttli (1973). This averaging technique assumes that the S-wave source spectrum is in some way related to the L_g spectrum at regional distances, and Street, et al., (1975) have demonstrated that such a relationship does in fact exist. We obtained four sets of events, corresponding to corner frequencies ranging from 1 to 10 Hz. Spectral source paramters for the November 1984 events are not known, however they were of similar magnitude so we assumed they also had similar source spectra. Likewise, we assumed similar source spectra for the nuclear explosions.

In Figure 3 we present the smoothed, average L_g spectra for the two paths. Since these spectra have been corrected for geometrical spreading, the difference in spectral amplitude at any one frequency will, by our technique, be translated into Q. The earthquake spectra shown are for the group of events with corner frequency near 1 Hz and are representative of the earthquake data set.

Figures 4 shows the regression results for each of the two paths. The upper traces are the source terms; note that they have a shape similar to a theoretical source spectrum in that they have a flat, long-period asymptote out to a corner frequency beyond which the amplitudes decay as ω^{-1} for the earthquake data and as ω^{-2} for the explosion data.

The Q spectra obtained are plotted as the lower traces in Figure 4. For both paths we find a frequency dependent Q, however the effect is significantly more pronounced along the MNV-ELK path. Also, both paths show a peak in the Q spectrum near 2 Hz. We expressed the frequency dependence using the relation

$$Q(f) = Q_0 \left(\frac{f}{f_0}\right)^{\eta} \qquad (3)$$

where $Q_0 = Q(f_0)$. Setting $f_0 = 1$ Hz for frequencies below the 2 Hz peak, we find for the MNN-BDE-WCN path a Q_0 of 200 and a fairly constant η value of 0.8. We observe $Q_0 = 300$ for the MNV-ELK path and require two η values same frequency range as above ($f \leq 2$ Hz). For frequencies below 1 Hz, η along the MNV-ELK path is 0.6, however for $1Hz \leq f \leq 2Hz$, we obtain $\eta = 1.4$. Turning our attention to frequencies above 2 Hz, we set $f_0 = 2$ Hz, and find $Q_0 = 360$ for the MNN-BDE-WCN path with $\eta = -0.8$ while for the MNV-ELK path we get $Q_0 = 800$ and $\eta = -0.5$.

Discussion

The $Q(f)$ functions obtained here can be compared to other Q estimates for the Great Basin. Patton (1983) reports a $Q(1Hz)$ of 150 to 350 for L_g, which is in reasonable agreement with our observations. Singh and Herrmann (1983) were able to relate their observations of coda decay to the L_g spatial attenuation coefficient and concluded that the same attenuation mechanism was responsible for both L_g and coda decay. The coda $Q(1Hz)$ values they obtained were between 200 and 300, increasing slightly from west to east. This is in good agreement with our $Q(1Hz)$ values for L_g and with the fact that we observe greater Q along the easternmost path.

As for the frequency dependence, Singh and Herrmann (1983) found η values of 0.4 to 0.5 which are slightly less than our results at the lower frequencies, but significantly less than that at the higher frequencies along the MNV-ELK path. Our observations are in marked contrast with the value of $\eta = -1.8$ which Patton (1983) obtained for the frequency range of 0.5 to 1 Hz.

In summary, our measurments of L_g attenuation yield $Q(1Hz)$ values which are comprable to those obtained in other studies in this same region. Our data suggest, however, that the nature of the frequency dependence of Q is a function of the path, and that significant lateral variations in the apparent L_g attenuation structure exist in the northern Great Basin. A possible explanation for observations of this type has been proposed by Bennet and Murphy (1985). They suggest that the character of L_g propagation in the Great Basin may be a function of the orientation of the path to the regional structural trend.

391

Ruzaikin, *et al.* (1977) have noted such a relationship for paths in central Asia.

References

Archuleta, R. J., E. C. Cranswick, C. Mueller, and P. Spudich (1982). Source paramters of the 1980 Mammoth Lakes, California, earthquake sequence, *J. Geophy. Res.*, *87*, 4595-4607.

Bath, M. (1954). The elastic waves L_g and R_g along Euroasiatic paths, *Arkiv. Geofysik.*, 2, 295-342.

Bennet, T. J., and J. R. Murphy (1985), Source excitation and propagation variability for short-period regional phases in the western U.S., *Earthquake Notes*, 55, p. 21.

Knopoff, L., F. Schwab, and E. Kausel, (1973). Interpretation of L_g, *Geophys. J. R. astr. Soc.*, 33, 389-404. Lateral variations of attenuation in the upper mantle and discontinuities in the lithosphere, *J. Geophys. Res.*, 74, 2648-2682.

Nuttli, O. W., (1973). Seismic wave attenuation and magnitude relations for eastern North America, *J. Geophys. Res.*, 78, 876-885.

Nuttli, O. W., (1980). The excitation and attenuation of seismic crustal phases in Iran, *Bull. Seism. Soc. Amer.*, 70, 469-485.

Nuttli, O. W., (1981). On the attenuation of L_g waves in western and central Asia and their use as a discriminant between earthquakes and explosions, *Bull. Seism. Soc. Amer.*, 71, 249-261.

Nuttli, O. W., (1984). Methodology of using L_g waves for estimating explosion yield and body-wave magnitude bias between test sites, *in* Nuttli, O. W. and B. J. Mitchell, Attenuation of seismic waves at regional distances, Final Report, Saint Louis University, DARPA Contract F49620-83-C-0015.

Panza G. F., and G. Calcagnille, (1975). L_g, L_i, and R_g from Rayleigh modes, *Geophys. J. R. astr. Soc.*, 40, 475-487.

Patton, H. J., (1983). L_g excitation and propagation in the western United States, UCRL-89331, Lawrence Livermore National Laboratory.

Press, F., and M. Ewing (1952). Two slow surface waves across North America, *Bull. Seism. Soc. Amer.*, 42, 219-228.

Ruzaikin, A. I., I. L. Nersesov, V. I. Khalturin, and P. Molnar (1977). Propagation of L_g and lateral variations in crustal structure in Asia, *J. Geophy. Res.*, 82, 307-316.

Singh, S. K., R. J. Apsel, J. Freid, and J. N. Brune (1982). Spectral attenuation of SH waves along the Imperial fault, *Bull. Seism. Soc. Amer.*, 72, 2003-2016.

Singh, S., and R. B. Herrmann, (1983). Regionalization of crustal coda Q in the continental United States, *J. Geophys. Res.*, 88, 527-538.

Street, R. L., R. B. Herrmann, and O. W. Nuttli (1975). Spectral characteristics of the L_g wave generated by central United States earthquakes, *Geophys. J. R. astr. Soc.*, 41, 51-83.

Figure captions

Figure 1. Map showing source regions (stars) and recording sites (triangles) for the data analysed in this study.

Figure 2. Examples of typical seismograms recorded at each of the stations.

Figure 3. Smoothed, averaged L_g spectra for each of the two paths examined.

Figure 4. *Upper traces.* Source terms obtained from the data shown in Figure 3. *Lower traces.* $Q(f)$ functions obtained from the same data.

F I G U R E 1

MNN 108 KM

LAC 414 KM

|—— one minute ——|

ELK 465 KM

KNB 532 KM
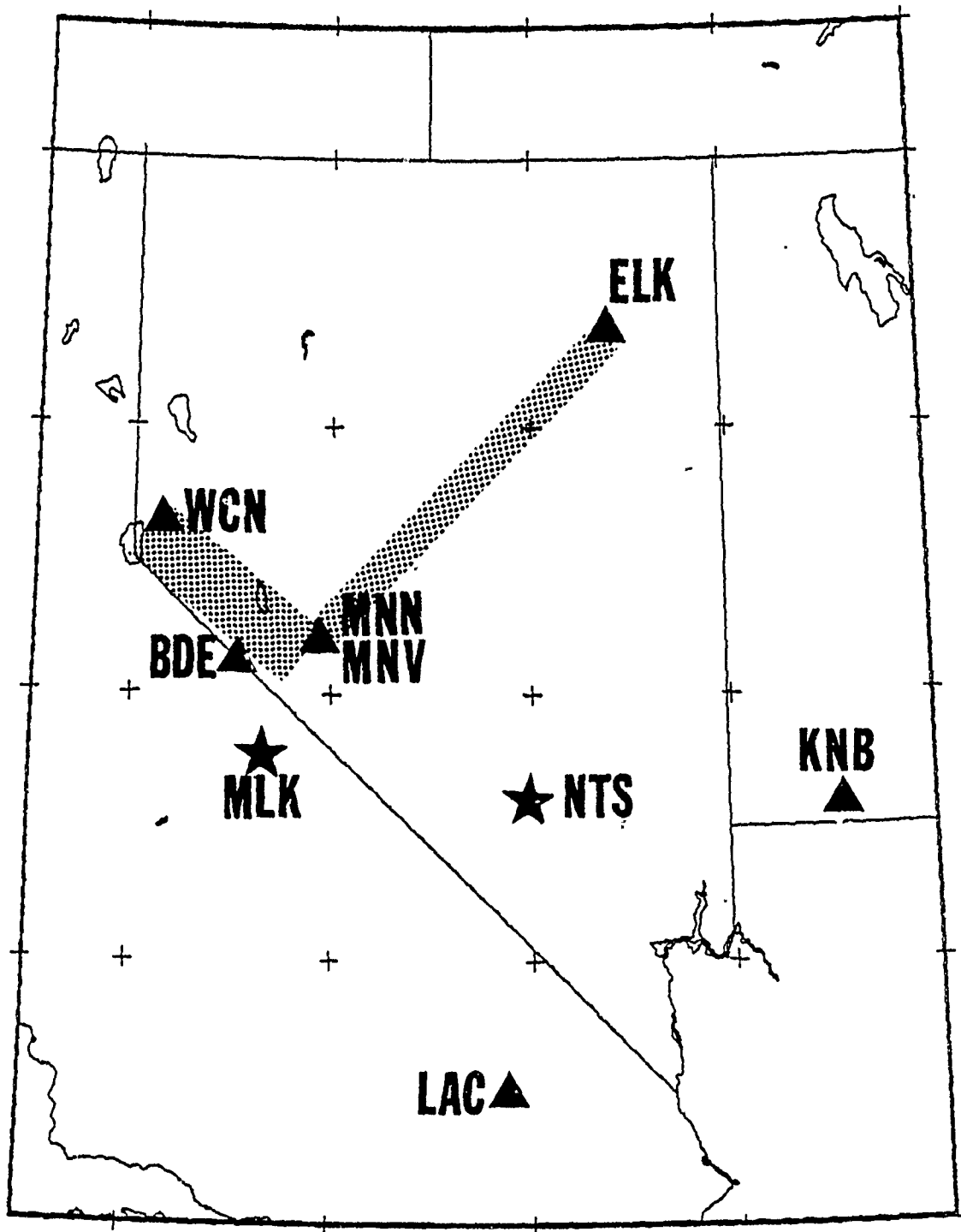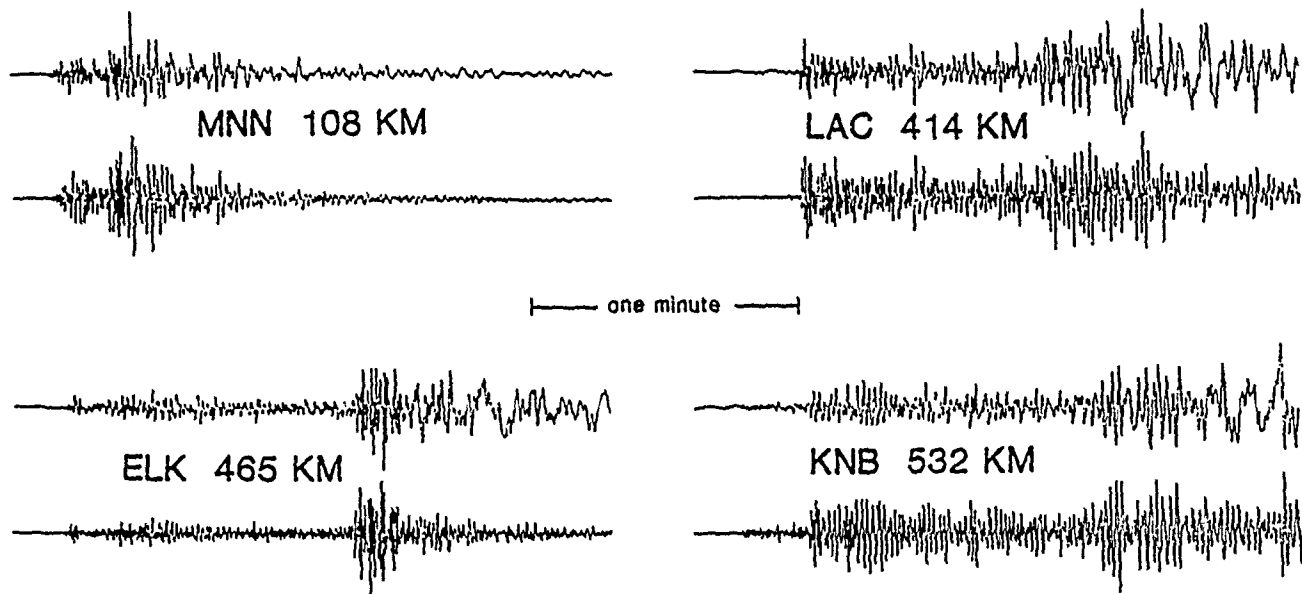
MAMMOTH EARTHQUAKE

- F I G U R E 2 -

MNN 233 KM

BDE 282 KM

|—— one minute ——|

WCN 402 KM
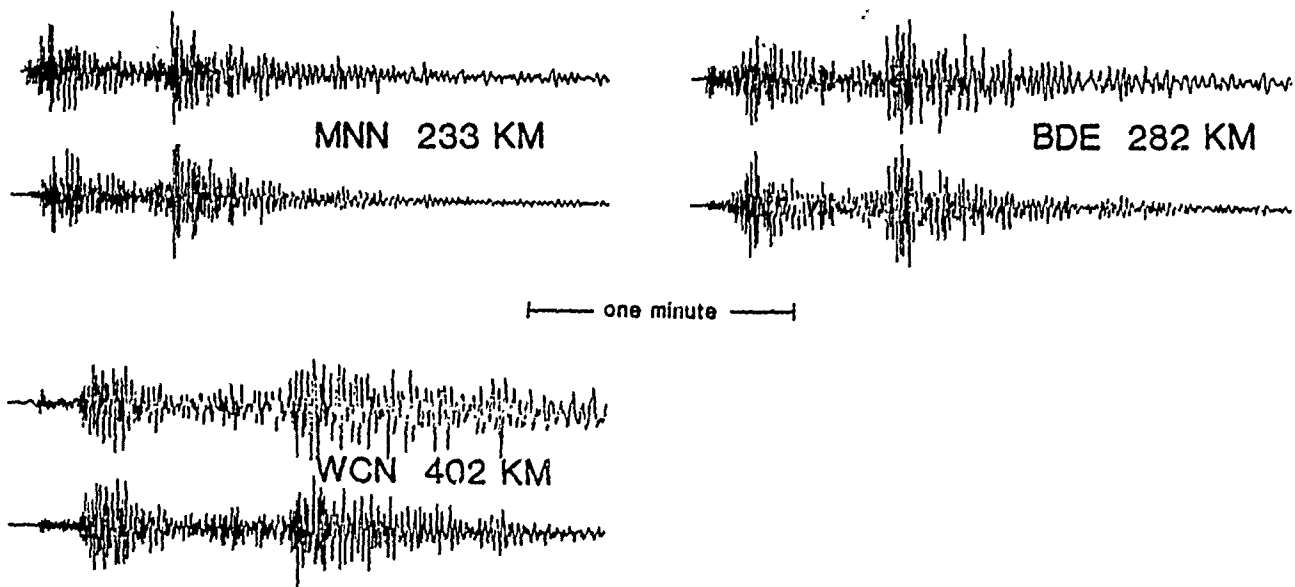
NTS EXPLOSION

AVERAGE SPECTRA: MNN–BDE–WCN PATH
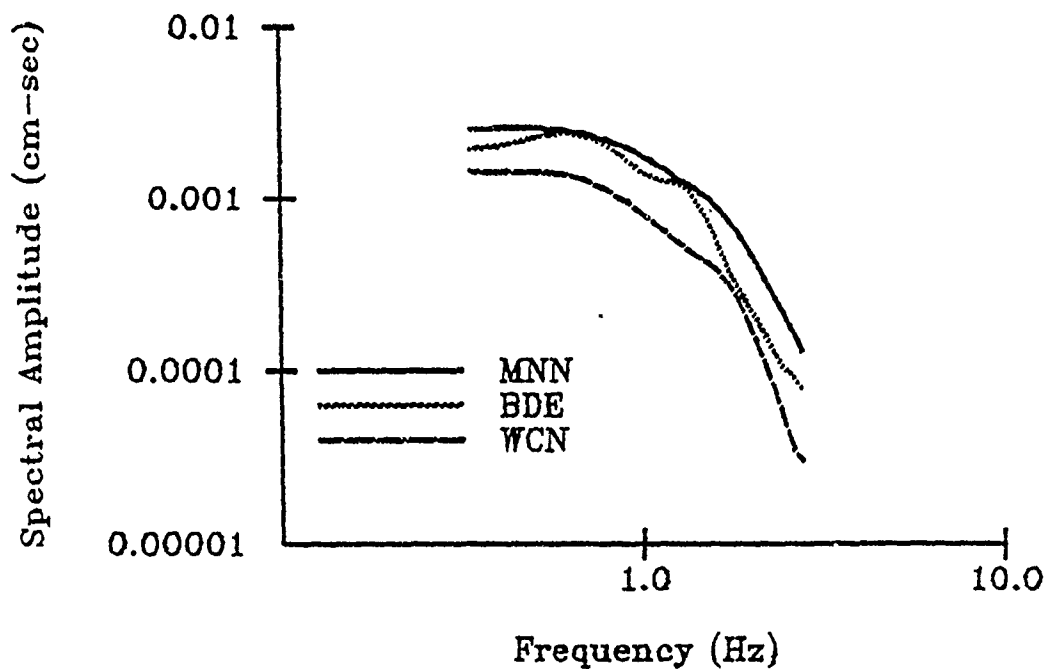
AVERAGE SPECTRA: MNV–ELK PATH
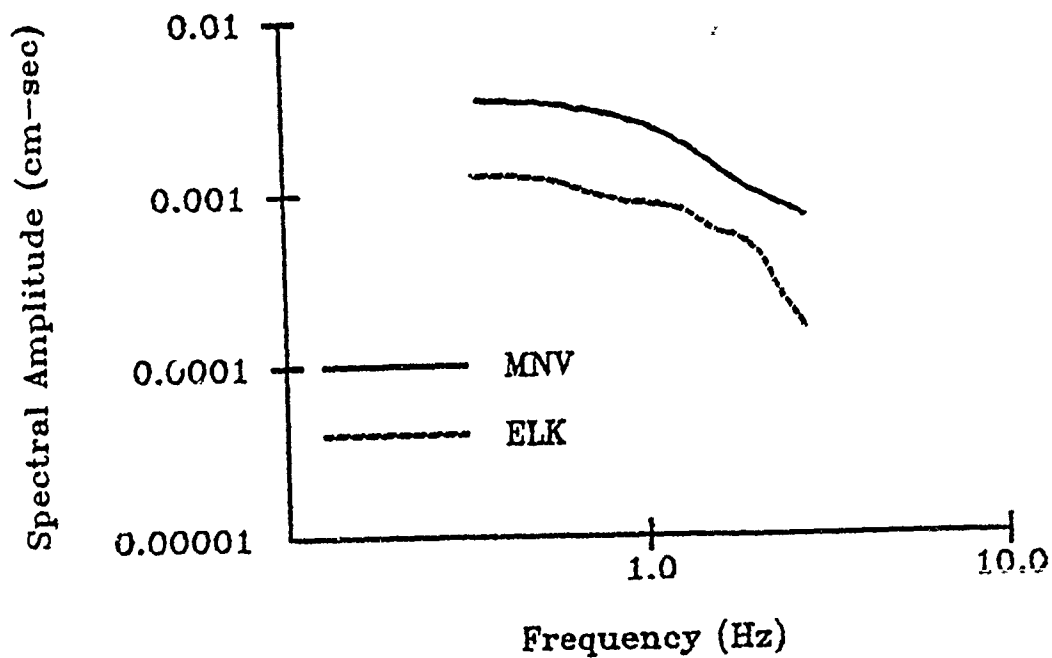
F I G U R E   3
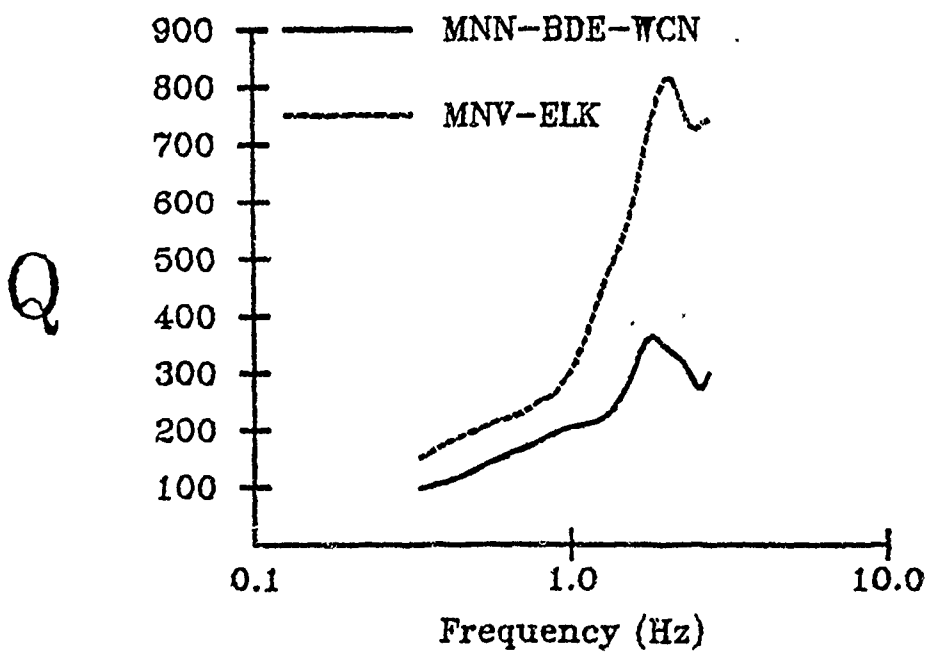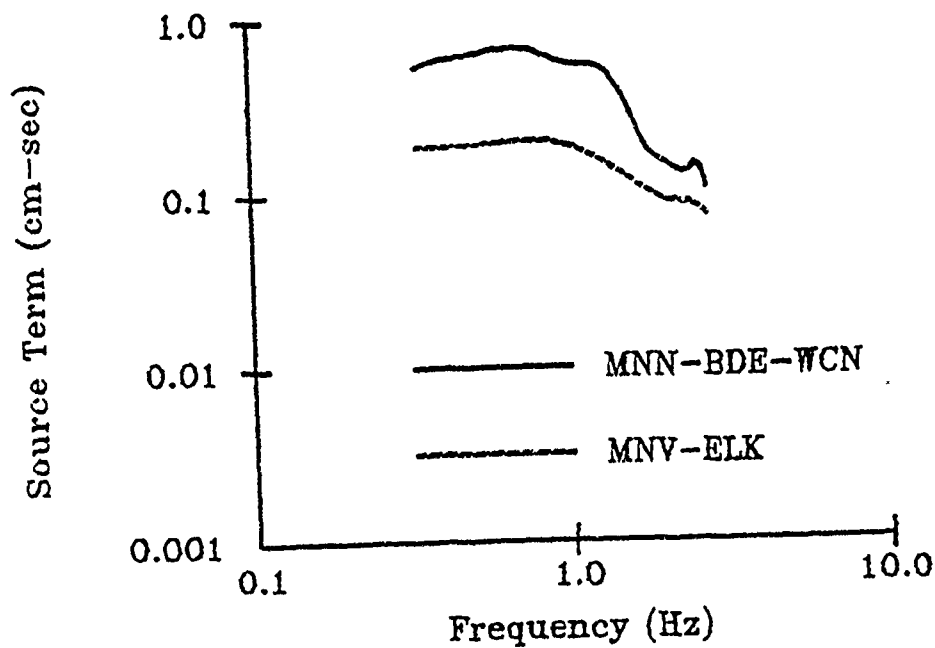
F I G U R E 4
397

PAPER TITLE: Note on m_b Bias at Selected Soviet Seismic Stations

PAPER AUTHOR: Alan S. Ryall, Jr.*

SUMMARY: Magnitude m_b is determined for five earthquakes on 25 and 27 May 1980, from recordings at eight Soviet seismic stations on a 4,300 km-long profile from eastern Kazakh to eastern Siberia. The records were hand-digitized, and magnitudes were determined from traces corrected for instrument response as well as the uncorrected traces. Four of the five earthquakes were at Mammoth Lakes, California, in the western Great Basin; the fifth was at Tonga in the south Pacific. Magnitude residuals with respect to network-averaged m_b's listed in the ISC *Bulletin* were high for stations at Yakutsk and Seymchan in Siberia, low for raypaths through the Baikal rift zone, and intermediate for a station at Semipalatinsk, about 100 km from the East Kazakh test site. A comparison of tabulated magnitude residuals for Soviet seismic stations from previous work of Ringdal (1985), North (1976) and Vanek *et al.* (1978, 1980) shows excellent agreement between these studies. Our results are slightly more scattered but in good agreement with previous work. Recalculation of m_b for 83 events recorded on granite at the Nevada Test Site provided a determination of magnitude bias $(\delta m_b = -0.10 \pm 0.35)$ for the NTS granite site with respect to ISC magnitudes. Comparison of this value with δm_b's for the Soviet stations provides a direct measure of the magnitude bias of the NTS area relative to areas in the USSR in which the stations are located. This bias reflects only differences in attenuation, and does not account for other effects such as differences in coupling, focusing, and tectonic release. The magnitude bias due to attenuation differences between the NTS granite site and the station at Semipalatinsk is -0.20.

Note on mb Bias at Selected Soviet Seismic Stations

Alan S. Ryall

Seismological Laboratory*
University of Nevada
Reno, NV 89557

Introduction

On 25 and 27 May 1980 three M_L 6+ earthquakes occurred in the western Great Basin near Mammoth Lakes, California, about 200 km NW of the Nevada Test Site. As part of our investigation of these earthquakes we requested seismograms from several seismic stations in the Soviet Union, including a station at Semipalatinsk, approximately 100 km NE of the eastern Kazakh test site. This note summarizes m_b determinations for five events on the Soviet records -- the three large Mammoth Lakes events, a smaller (m_b 5.3) Mammoth Lakes shock, plus an earthquake at Tonga (m_b 6.0) that occurred during the time frame of the recordings. The records were searched for eight more events on the ISC list, but none of these were recorded at the Semipalatinsk station and most were not recorded by the other stations. Another strong (m_b 5.4) Mammoth Lakes shock at 16:49 GMT on 25 May and an earthquake in the Kurile Islands (25 May, 23:22 GMT, m_b 4.8) were recorded but not analyzed. Table 1 summarizes information on the events used in this study.

Table 1. List of Events

Date	Time, GMT	Latitude	Longitude	Depth	m_b	M_s
800525	16:33:44.7	37.596°N	118.830°W	6.5	6.1	6.1
800525	19:44:51.1	37.547°N	118.826°W	5.0	5.6	6.0
800525	20:35:48.5	37.616°N	118.847°W	6.1	5.3	5.7
800527	14:50:57.1	37.472°N	118.807°W	10.8	5.7	6.0
800527	13:01:37.9	18.610°S	174.700°E	55	6.0	4.8

Data

The data included recordings from eight seismic stations on a northeast-trending profile from Kzyl-Agach in the southern part of the Kazakh Fold System to Seymchan in the Northeast Siberian Fold System. Table 2 lists the station coordinates and Figure 1 is a polar projection of Asia showing the station locations. Table 3 gives epicentral distances and azimuths for the five events.

Table 2. Station Locations

Code	Name	Coordinates	Region
BOD	Bodaibo	57°51'N,114°11'E	Baikal
ELT	El'tsovka	53°15'N,86°16'E	Altai-Sayan
IK	Irkutsk	52°16'N,104°19'E	Baikal
KZL	Kzyl-Agach	45°25'N,78°45'E	Kazakhstan
SEI	Seymchan	62°53'N,152°26'E	Northeast
SEM	Semipalatinsk	50°24'N,80°15'E	Kazakhstan
UST	Ust'-Kan	50°57'N,84°45'E	Altai-Sayan
YAK	Yakutsk	62°01'N,129°43'N	Yakutiya

Table 3. Distance (Δ°) and Azimuth (Θ°) to the Stations										
Sta	05251633		05251944		05252035		05271450		05271301	
	Δ	Θ	Δ	Θ	Δ	Θ	Δ	Θ	Δ	Θ
BOD	75.09	334	75.14	334	75.07	334	75.21	334	95.95	329
ELT	86.95	345	86.99	345	86.92	345	87.07	345	110.06	321
IRK	82.93	335	82.98	335	82.91	335	83.05	335	99.15	322
KZL	95.86	348	95.91	348	95.84	348	95.99	348	114.54	312
SEI	56.77	327	56.82	327	56.75	327	56.89	327	85.23	346
SEM	90.78	348	90.83	348	90.76	348	90.91	348	113.66	318
UST	89.43	345	89.48	345	89.41	345	89.55	345	110.82	318
YAK	66.51	331	66.55	331	66.48	331	66.63	331	91.54	337

Figure 2 is a polar plot of the world centered on a point (81.5°N, 162.0°W) about halfway between the Mammoth Lakes earthquakes and station SEM, showing the epicenter and recording stations. Figure 3 shows the position of the Soviet stations cn a lower-hemisphere, equal-area projection of the focal sphere for the three largest Mammoth Lakes earthquakes, together with projections of the fault and auxiliary planes for these events from a study of long-period P- and surface-waves (Given *et al.*, 1982). Based on point-source theory (Keilis-Borok, 1950) and the position of the stations on the focal sphere, P-waves to the Soviet stations should have about 80% of the maximum radiated amplitude.

Figure 4 is a polar projection centered on a point (23.0°N, 147.0°E) about halfway between station SEM and the Tonga earthquake. The Kurile event was in a poor distance range (16-47°) for this study, and and had large scatter in m_b values; it will not be considered in the detailed discussions that follow. For the Tonga earthquake a plot similar to Figure 4 indicates that the Soviet stations are close to the null axis on the fault-plane solution, although the latter is not well-constrained.

Table 4 lists instrument parameters for the 86 recordings that were supplied. Values of the maximum magnification V_m and the period range T_m (corresponding to $V = 0.9\ V_m$) were written on the records. For station KZL the period range T_m was not supplied and the range given in the table was taken from the Soviet publication *Earthquakes in the USSR in 1980* (Akademiya Nauk SSSR, 1983). For station BOD the values of V_m marked on the recordings -- "2900" for the NS component and "2700" for the Z and EW -- appeared to be an order of magnitude too low, and the magnification (52,000) for that station was also taken from *Earthquakes in the USSR in 1980*. Use of the larger magnification for BOD is supported by Shishkevish (1974) who lists V_m as 45,000-49,000 for this station in 1970.

For this study only vertical-component recordings from SKM-3 seismographs were used. The SKM-3 system consists of a seismometer and galvanometer with instrument constants designed to produce magnification of ground motion in the range 30,000-100,000 over the period range 0.3-1.5 seconds. According to Aranovich *et al.* (1974) a complete system consists of two SGKM-3 (horizontal) and one SVKM-3 (vertical) seismometers, three GK-VIIM galvanometers and a PS-3M drum recorder. The latter registers the light beams from the three galvanometers on a 29-cm wide by 90-cm long photographic recording. Time marks from a chronometer are printed once per minute. Drum speed was 60 mm/minute for all of the SKM-3 records used in this study except KZL, which recorded at 120 mm/minute. Figure 5 shows relative amplitude response for the eight stations, determined from equations given by Aranovich *et al.* Note that the Soviet short-period seismographs peak at somewhat lower frequency (*ca.* 1 Hz) than systems commonly used in the US, and that for some stations (*i.e.*, SEM and IRK in this study) the system gain is reduced by about a factor of ten at 10 Hz.

Seismometer and galvanometer constants (period, damping) for stations BOD, IRK and SEM were taken from Shishkevish (1974), and the resulting response was checked to insure that the range of T_m was the same as that indicated on the recordings. For ELT the constants given by Shishkevish were modified to give the appropriate upper limit of T_m, and the same constants were used for UST. For YAK Shishkevish lists instrument constants only for the horizontal-component seismographs, and these give a different range of T_m than that specified on the records. For KZL and SEI Shishkevish does not list instrument constants. As a result, for KZL, SEI and YAK various combinations of instrument constants were tried, based on tables of standard setups given by Aranovich *et al.*, until response curves matched the range of T_m marked on the records.

Except for the SKM recordings at station KZL and the long-period recordings at UST all of the records were 12 hours long. The KZL record has twice the time resolution of the other short-period stations and appears to be changed three times a day; the SKD record for UST for 25 May was 24 hours long. Unfortunately the records of primary interest to this analysis -- from station SEM -- were changed at different times than those at other stations and overlap with the latter for only two six-hour periods.

Table 4. Data Received for 25 and 27 May 1980				
Sta	Inst	Comp	V_m	T_m
BOD	SKM-3	NS,Z,EW	52,000	0.2 - 1.2
ELT	SKM-3	NS,Z,EW	50,000	0.2 - 1.4
	SKM-3	EW	5,000	0.2 - 1.4
IRK	SKM-3	NS	17,500	1.1 - 1.6
	SKM-3	Z	17,240	1.1 - 1.6
	SKM-3	EW	17,430	1.1 - 1.6
	SKD	NS,Z,EW	1,200	0.2 - 20
KZL	SKM-3	NS	40,900	0.08 - 1.6
	SKM-3	Z	41,500	0.08 - 1.6
	SKM-3	EW	40,600	0.08 - 1.6
	SKM-3	EW	1,050	0.08 - 1.2
SEI	SKM-3	NS,Z,EW	44,600	0.2 - 1.2
	SKD	NS,Z,EW	1,050	0.2 - 20
SEM	SKM-3	NS,EW	30,050	0.84 - 1.5
	SKM-3	Z	28,400	0.8 - 1.5
	SK	NS,EW	1,700	0.41 - 10.9
	SK	Z	1,100	0.5 - 11
UST	SKM-3	NS,Z,EW	50,000	0.2 - 1.4
	SKM-3	E-W	5,000	0.2 - 1.4
	SKD	NS,Z,EW	1,000	0.2 - 22
YAK	SKM-3	Z	18,800	0.3 - 1.3
	SKM-3	NS	37,600	0.8 - 1.4
	SKM-3	EW	36,800	0.8 - 1.4
	SK-KPCh	NS	140	0.3 - 11
	SK	NS	2,130	0.4 - 11
	SK	Z	680	0.4 - 9.0
	SK	EW	1,930	0.4 - 11

Record Quality. Copies of the records were on 35 mm film of poor-to-good quality. For many of the short-period records the contrast between the trace and the background was poor, and attempts to make enlargements of the waveforms using a reader-printer were not successful. As a result the records had to be projected on a viewing screen and traced by hand; the tracings were then digitized for computer analysis.

Quality of the KZL records was especially poor, and the P-waveform for only one event was traced for that station.

Timing. Two or three time corrections were marked on each of the records, usually corresponding to the beginning and end of the recording period. Clock corrections changed at most stations by less than a second per day. A few records were mislabeled as to sense of the time correction, and in one case the time corrections at the two ends of a recording period were interchanged on different records of the same station. The largest clock drift was 0.5 second/hour for the SEM station, but this rate was constant. Tracings of the P-waves were enlarged such that the average time scale was about 270 mm/minute. Station KZL had a drum speed twice that of the other stations, so the enlarged traces were viewed at a scale of 540 mm/min. For most of the events the beginning of the P-wave (PKP for stations at $\Delta \geqslant 110°$) was identified on records of one of the better stations (SEI, YAK, BOD) and the same point was marked and timed on traces for the other stations by overlaying the recordings.

Traveltime residuals were calculated for the Mammoth Lakes earthquakes using hypocentral coordinates and origin times determined by the University of Nevada from local network recordings and traveltimes calculated from the Herrin et al. (1968) tables. The Soviet stations had average delays of 0.5-2.2 seconds for the Mammoth Lakes events, relative to the Herrin tables. These delays are not considered to be meaningful for the present study, since the larger earthquakes of this sequence appear to have been multiple events, initiated by small ruptures that recorded at regional stations but not at teleseismic distance ranges (e.g., Given et al., 1982). On the other hand, traveltime residuals for individual stations relative to the average delays for all the stations (Table 5) are fairly consistent for the Mammoth Lakes and Tonga earthquakes. Note that the two stations north of Lake Baikal (BOD, IRK) have early arrivals for waves travelling southwest across the Siberian platform from the Mammoth Lakes events, but are late for paths from Tonga that cross the Baikal graben. Station SEM has small traveltime residuals that average to almost zero.

Table 5. Relative P-wave Residuals, Seconds						
Sta	251633	251944	252035	271450	271301	Average
BOD	-1.0	-0.3	-1.2	-0.8	+0.5	-0.6±0.7
ELT				-1.0	-1.5	-1.3±0.4
IRK	-0.7	-0.9	-0.3	-0.9	+0.2	-0.5±0.5
KZL	0.0					0.0
SEI	+0.8	+0.5	+0.6	+1.4	+0.8	+0.8±0.3
SEM	+0.5	-0.5	-0.2	+0.5	+0.5	+0.2±0.5
UST	+0.5	-0.5	-0.2	+0.5	-0.7	-0.1±0.6
YAK	0.0	+0.6	-0.1	+0.6	-0.0	+0.2±0.4

Magnitude Determination

Figure 6 shows an example of the digitized P-waves for the first large Mammoth Lakes event, at 16h 33m on 25 May 1980. All traces are from SVK-M3 instruments, and are normalized; up on the traces corresponds to ground motion up. With the exception of KZL most of the recordings had good signal-to-noise ratios. Stations YAK and BOD appear to have higher frequency content than some of the other stations, including SEM, but this could be a result of differences in instrument response. P-wave spectra for this event, corrected for instrument response, have peaks at about 0.5 and 0.7 Hz; for station BOD the peaks are about equal in amplitude, but for the other stations the amplitude at 0.7 Hz is less than half that at 0.5 Hz. In general the character of the P-wave at the

various stations is similar, consisting of a small first arrival followed 6 seconds later by a larger phase. The time interval between these phases is too consistent for the second arrival to be PcP, since for the distance range of the Soviet stations t(PcP-P) should vary from 60 seconds to zero. The second phase could be another earthquake, but this is unlikely because all of the Mammoth Lakes events have a large second arrival at the Soviet stations. A more likely explanation is that the phase includes the reflected waves pP and and sP. Based on the known crustal structure in the Mammoth Lakes area, a pP-P time of 6 seconds would be consistent with focal depth of about 16 km, and for that depth the sP-P time would be about 8 seconds. For the second and third Mammoth Lakes earthquakes in Table 1, measured X-P times of 4.9 and 2.5 seconds would be consistent with focal depths of about 13 and 6.5 km, respectively, if these arrivals were pP. The fourth Mammoth Lakes event has a complex P-signature and the timing of the second phase is not consistent from one station to another.

Magnitude was determined from computer plots of the digitized P-waves using the standard formula

$$m_b = \log_{10} \frac{A}{T} + B(\Delta),$$

where A is the amplitude of vertical ground motion in nanometers and T is the period corresponding to amplitude A. From the range in m_b values given in the *Bulletin of the International Seismological Centre*, it appears that some observatories measured the amplitude of the initial P-wave for the Mammoth Lakes events, while others measured the amplitude of the second phase. The IASPEI Commission on Practice Concerning Amplitude and Period Measurement recommended in 1979 that "the P wave amplitude measured should be that of the maximum trace deflection, usually within the first 25 seconds of the first onset or before the arrival of the next clear phase." Other workers have recommended measuring A and T within the first few cycles (Zavadil, 1980) or even within the first 3/4 cycle (the "b" amplitude) of the P-wave (Eisenhauer, 1980). Because of the discrepency between maximum amplitude in the P-coda and amplitude of the P onset, we determined m_b for the Mammoth Lakes earthquakes from the maximum amplitude in the first two cycles and from the maximum amplitude in the first 12 seconds -- in both cases taken as one-half the peak-to-peak amplitude. The resulting individual and average m_b values are listed in Tables 6 and 7, together with magnitudes determined by the International Seismological Centre (ISC) and Moscow (MOS), and deviations δm_b from the ISC values.

A third set of magnitudes was determined from measurements of A and T on traces produced by deconvolving the instrument response from the digitized recordings. The deconvolution was accomplished using a program written by W. Peppin to calculate the complex transfer function of a seismograph, given the period and damping of the seismometer and galvanometer, together with the maximum magnification of the system and the period at which the maximum magnification occurs. The records were tapered and bandpass-filtered (0.25-8.0 Hz) before deconvolution, and filtered again (0.1-5.0 Hz bandpass) after deconvolution. Figure 7 gives examples of the P-waves for the first large Mammoth Lakes earthquake after correction for instrument response and filtering. For these records m_b was determined only using the maximum amplitude in the large phase following the initial P-wave. Magnitudes and residuals are listed in Table 8.

Table 6. Magnitudes and Residuals, Uncorrected Data, First Two Cycles

Sta	05251633 m_b	δm_b	05251944 m_b	δm_b	05252035 m_b	δm_b	05271450 m_b	δm_b	Average δm_b
BOD	5.47	-.63	4.97	-.63	4.96	-.34	5.34	-.36	-.49±.16
ELT*							5.78	+.08	+.08±.0
IRK	5.53	-.57	4.98	-.62	4.84	-.46	5.76	+.06	-.40±.31
KZL*	5.58	-.52							-.52±.0
SEI	5.67	-.43	5.17	-.43	5.09	-.21	5.54	-.16	-.31±.14
SEM	5.72	-.38	4.73	-.87	4.89	-.41	5.80	+.10	-.39±.40
UST	5.42	-.68	4.68	-.92	4.92	-.38	5.69	-.01	-.50±.39
YAK	6.16	+.06	5.21	-.39	5.48	+.18	6.38	+.68	+.13±.44
Avg	5.66		4.96		5.03		5.75		
ISC	6.1		5.6		5.3		5.7		
MOS	6.3		5.7		5.5		5.9		

Table 7. Magnitudes and Residuals, Uncorrected Data, First 12 Seconds

Sta	05251633 m_b	δm_b	05251944 m_b	δm_b	05252035 m_b	δm_b	05271450 m_b	δm_b	Average δm_b
BOD	6.04	-.06	5.76	+.16	5.46	+.16	5.66	-.04	+.06±.12
ELT*							5.59	-.11	-.31±.0
IRK	6.16	+.06	5.66	+.06	5.40	+.10	5.58	-.12	+.03±.10
KZL*	6.04	-.06							-.06±.0
SEI	6.48	+.38	5.81	+.21	5.62	+.32	6.03	+.33	+.31±.07
SEM	6.34	+.24	5.63	+.03	5.48	+.18	5.76	+.06	+.13±.10
UST	6.18	+.08	5.52	-.08	5.22	-.08	5.71	+.01	-.02±.08
YAK	6.60	+.50	6.10	+.50	5.90	+.60	6.04	+.34	+.49±.11
Avg	6.30		5.75		5.51		5.80		
ISC	6.1		5.6		5.3		5.7		
MOS	6.3		5.7		5.5		5.9		

Table 8. Magnitudes and Residuals, Corrected Data, First 12 Seconds

Sta	05251633 m_b	δm_b	05251944 m_b	δm_b	05252035 m_b	δm_b	05271450 m_b	δm_b	Average δm_b
BOD	6.12	+.02	5.65	+.05	5.50	+.20	5.70	+.00	+.07±.09
ELT*							5.77	+.07	+.07±.0
IRK	6.20	+.10	5.61	+.01	5.38	+.08	5.64	-.06	+.03±.07
KZL*	6.24	+.14							+.14±.0
SEI	6.47	+.37	5.98	+.38	5.76	+.46	6.00	+.30	+.38±.07
SEM	6.32	+.22	5.71	+.11	5.53	+.23	5.80	+.10	+.17±.07
UST	6.13	+.03	5.60	+.00	5.41	+.11	5.64	-.06	+.02±.07
YAK	6.74	+.64	6.22	+.62	6.10	+.80	6.35	+.65	+.68±.08
Avg	6.33		5.80		5.61		5.86		
ISC	6.1		5.6		5.3		5.7		
MOS	6.3		5.7		5.5		5.9		

* -- ELT and KZL not used in determining average m_b values.

For the Tonga earthquake, values of m_b were determined from the maximum amplitude in the P-wave, from traces uncorrected and corrected for instrument response. Four of the stations for this event were beyond 100° and distance corrections were taken from a curve developed by Ringdal (1985).

Table 9. Magnitudes and Residuals for Tonga Event				
	Uncorrected Data		Corrected Data	
Sta	m_b	δm_b	m_b	δm_b
BOD	5.85	-.14	6.12	+.12
ELT	6.09	+.09	6.22	+.22
IRK	5.38	-.62	5.42	-.58
SEI	6.19	+.19	6.17	+.17
SEM	6.07	+.07	6.06	+.06
UST	5.79	-.21	5.78	-.22
YAK	6.16	+.16	6.15	+.15
Avg	5.93		5.99	
ISC	6.0		6.0	
MOS	5.9		5.9	

Discussion

In this study we have determined magnitude m_b for five earthquakes on 25 and 27 May 1980, from recordings at eight Soviet seismic stations on a 4,300 km-long profile from eastern Kazakh to eastern Siberia. In general, our average magnitudes for the Mammoth Lakes earthquakes (Tables 7 and 8) are about 0.2 m_b unit higher than those determined by the ISC, but for the Tonga event our m_b is close to the ISC value. As might be expected our values are also about the same as magnitudes attributed to Moscow in the ISC *Bulletin*. For the data uncorrected for instrument response our average values differ from the Moscow m_b's by 0.00±0.06 unit; for the corrected data our values are higher than the Moscow m_b's by 0.06±0.06. Magnitudes determined from A and T measured in the first two cycles of the P-wave for the Mammoth Lakes earthquakes (Table 6) averaged 0.33 and 0.50 m_b unit smaller than the ISC and Moscow values, respectively.

The largest positive m_b residuals were for station YAK (average δm_b = 0.33 for the uncorrected data in Tables 7 and 9; 0.42 for the corrected data in Tables 8 and 9). Yakutsk is located on the central Siberian platform in an area where, according to Potap'ev *et al.* (1974), the depth to crystalline basement is shallow, 0.5-1.0 km. About 10 km west of Yakutsk a major north-south fault offsets basement rocks, with the western side downdropped by about 4 km. P-wave velocities in the crust are high, 6.2-6.4 km/sec (Vol'vovsky, 1973), the crust is about 40 km thick, and the P_n velocity is about 8.0 km/sec (Vol'vovsky and Vol'vovsky, 1975; Ryall *et al.*, 1980).

The largest negative m_b residuals were observed for station IRK for the Tonga event (-0.62 uncorrected, -0.58 corrected), for which the raypath crosses the southern part of the Baikal rift zone in a WNW direction. The rift zone is characterized by complex geologic structure, including deep crustal inhomogeneities and velocity anomalies in areas of recent rifting. Within the rift zone P-wave velocity in the crust increases from 5.8 km/sec near the surface to 6.4 km/sec at the crust/mantle interface, crustal thickness is 34-36 km, and the P_n velocity is 7.7-7.8 km/sec (Puzyrev *et al.*, 1975; Ryall *et al.*, 1980). Puzyrev *et al.* (1977) attribute the low P_n velocity to partial melting of upper mantle material, and compare the Baikal region with the East African rift system, the Rhine graben and the Basin and Range province. It is interesting that IRK, which is located on the southern edge of the central Siberian platform just north of the Baikal

rift, has smaller values of δm_b (+0.03±0.10 uncorrected, +0.03±0.07 corrected) for the Mammoth Lakes earthquakes, for which the P-waves approach the station in a SSW direction across the platform and do not appear to be affected by the structure of the rift zone. According to Puzyrev *et al.* (1977) the platform is characterized by uniform layering, with distinct reflecting horizons at depths of 18-21 and 23-27 km, crustal thickness of about 40 km, and "normal" P_n velocity of about 8.1 km/sec.

The m_b residuals for station SEM are intermediate between IRK and YAK. SEM is near the Irtysh River, on the boundary between the west Siberian platform to the north and the Kazakh fold system to the south. In this area the crustal thickness is about 45 km, P_n velocity is 8.2-8.4 km/sec, and P-velocity in the crust is high (Vol'vovsky and Vol'vovsky, 1975). The station is in the Zaysan fold belt, which is relatively simple in terms of stratigraphy and structure. Sediments, principally of Carboniferous age, contain thick limestone deposits and lesser amounts of interbedded volcanics. Folding and faulting are relatively minor in this area, compared with more extensive folding, faulting and intrusion in the Chingiz-Tarbagatai geanticlinal zone to the southwest, in which the eastern Kazakh test site is located (Peyve and Mossakovsky, 1982). For the Mammoth Lakes earthquakes δm_b for this station is +0.13±0.10 for the uncorrected data (Table 7) and +0.17±0.07 for the corrected data (Table 8). For the Tonga earthquake it is +0.07 for the uncorrected, +0.06 for the corrected data. As noted above, SEM is near a maximum on the radiation pattern for the Mammoth Lakes earthquakes, and near the null axis for the Tonga event.

Several published works treat magnitude residuals for stations of the Soviet network, and provide for a comparison with our results (Table 10). First, in a study of magnitude and global network detection capability Ringdal (1985) recomputed m_b for about 70,000 earthquakes, using A and T values given in the ISC *Bulletin* and a maximum-likelihood estimation technique (Ringdal, 1976). In another study, North (1976) calculated mean station magnitude bias from m_b values given in the ISC *Bulletin* for nearly 40,000 events from 1964 to 1973. The biases were computed for the "best" (in terms of events reported) 72 stations with respect to the mean magnitude of observations reported by this set of stations, with the requirement that an event be reported by more than 15 of these stations before a bias was calculated.

In work by Soviet authors Vanek *et al.* (1978, 1980) determined magnitude *corrections* (Δm_b) for 32 reference stations of the Unified System of Seismic Observations (ESSN) of the Soviet Union, following a recommendation of the KAPG Conference at Prague in 1972 to create a uniform system for determining magnitude for the Eurasian continent. The station corrections were determined separately for phases PV, PV_S and PH -- respectively the P-wave recorded on vertical mid-band, vertical short-period and horizontal mid-band seismographs. Calculations were also made separately for five different source regions around the USSR -- Alaska, Japan, the Phillipines, Asia and the Mediterranean. The number of earthquakes in each source region was not given in the 1980 paper, but in the earlier work it ranged from 35 events for Asia and the Mediterranean to 93 events for Japan. The corrections were with respect to one of the reference stations, OBN, selected at least in part for its bias toward large m_b values. Based on a comparison of Δm_b values for the various source regions the reference stations are grouped according to the number of corrections needed for the different source regions. Thus, a station for which Δm_b was the same for all five source regions was classed as a reference station of the *I Kind*, a station with the same correction for four of the five source regions would be a station of the *II Kind, etc.* Of interest to our study, station SEM has the same PV_S correction for all of the source regions, Δm_b = +0.32, making it a station of the *I Kind* and indicating that it has a δm_b *bias* of -0.32 relative to station OBN. Standard deviations are not given by Vanek *et al.* (1980) but in the earlier work they average ±0.05 m_b unit. For comparison with magnitude bias given by other authors, we reversed the sign of Δm_b and increased all of the resulting values by 0.39 --

Ringdal's (1985) bias for station OBN, which Vanek *et al.* use as a base station.

Table 10. Comparison of Station Residuals and δm_b (OB2-NV)						
Sta	Ringdal	North	Vanek*	δm_b^1	δm_b^2	$\delta m_b\,(OB\,2-NV)^3$
BKR	+0.38±0.33		+0.30			-0.44
BOD	-0.02±0.34			-0.05	+0.10	-0.11
CLL	+0.16±0.26	+0.20±0.32	+0.09			-0.25
ELT	+0.15±0.34			-0.01	+0.15	-0.20
FRU	+0.35±0.33		+0.36			-0.46
ILT	+0.08±0.32		+0.03			-0.16
IRK	-0.03±0.31			-0.30	-0.28	+0.10
KHC	+0.03±0.26	+0.10±0.26	+0.08			-0.17
KHE	+0.37±0.31		+0.31			-0.44
KRA	+0.32±0.29	+0.22±0.29	+0.22			-0.35
KZL				-0.06	+0.14	-0.14
MOX	+0.07±0.25	+0.02±0.27	+0.01			-0.13
OBN	+0.39±0.33		+0.39			-0.49
PET	+0.24±0.36		+0.35			-0.40
PRU		+0.04±0.24	-0.06			-0.09
SEI				+0.25	+0.28	-0.37
SEM			+0.07	+0.10	+0.12	-0.20
TIK	+0.03±0.37		+0.00			-0.12
UST				-0.12	-0.10	+0.01
YAK	+0.43±0.34			+0.33	+0.42	-0.49
YSS	+0.20±0.41		+0.02			-0.21
ZAK	-0.11±0.33		-0.03			-0.03

* -- Given by authors as Δm_b corrections relative to base station OBN. Sign reversed and all values increased by 0.39 for comparison with Ringdal (1985).

1 -- Mean of δm_b for Tonga earthquake plus average δm_b for four Mammoth Lakes events from Table 7. Uncorrected data.

2 -- Mean of δm_b for Tonga earthquake plus average δm_b for four Mammoth Lakes events from Table 8. Corrected data.

3 -- Average residual (-0.10±0.35) for OB2-NV with respect to ISC *Bulletin* minus average station residual.

With a couple of exceptions the station residuals listed in Table 10 from the work of Ringdal (1985), North (1976) and Vanek *et al.* (1978, 1980) agree to within a few hundredths of a unit of m_b. Our station residuals are based on a very limited data set and show more scatter when compared to those of the other authors. However, they are in general agreement with the published values, and two of the stations -- SEM and YAK have values of δm_b that are in excellent agreement with those of Vanek *et al.* and Ringdal, respectively.

As a final step we computed the m_b bias between a granite site at the Nevada Test Site and the Soviet stations listed in Table 10. In this calculation we used A and T measurements listed by Der *et al.* (1978) for 83 seismic events for the period September 1976 to March 1977, recorded by a digital seismic system (SDCS) at station OB2-NV (Climax stock at north end of Yucca Valley on NTS). In the Der *et al.* report, the A

values are peak-to-peak amplitudes in nanometers, and magnitudes are computed using distance corrections of Veith and Clawson (1972). For consistency with the work by Ringdal (1985) and North (1976), magnitudes were recomputed using the Gutenberg and Richter (1956) corrections and dividing the peak-to-peak amplitudes by two to obtain zero-to-peak amplitudes. Residuals for the 83 events were calculated as $\delta m_b = m_b (OB\,2-NV)-m_b (ISC)$, and these were averaged to obtain an average δm_b of -0.09±0.39. Five values that fell outside the 2σ limits $(-0.87 \leqslant \delta m_b \leqslant 0.69)$ were dropped and the average δm_b recalculated to obtain -0.10±0.35. This number represents the average bias of the OB2-NV site with respect to network-averaged m_b values listed in the ISC *Bulletin*. To determine the bias of OB2-NV with respect to the Soviet stations, the average residuals in Table 10 for those stations were subtracted from -0.10. The resulting bias values are listed in the right-hand column of Table 10.

Of particular interest to questions of yield verification, the m_b bias of the NTS granite site with respect to station SEM at Semipalatinsk is -0.20, with a range of -0.17 to -0.22. The smaller of these figures (-0.17) is based on the study by Vanek *et al.* (1980), and the larger (-0.20, -0.22) are from our measurements of Soviet records of the Mammoth Lakes and Tonga earthquakes. It should be noted that the bias values in Table 10 represent only the bias due to attenuation in the upper mantle and crust under the respective seismic stations; they do not include other effects such as differences in coupling for explosions at the two test sites, effects due to tectonic release, or those related to focusing and defocusing of seismic waves in the vicinity of a given explosion. The reader should also be reminded that the Semipalatinsk station is about 100 km from the East Kazakh test site, and that, according to Peyve and Mossakovsky (1982), crustal rocks under the test site have been subjected to greater folding, faulting and intrusion than those under the seismic station.

Acknowledgements

References

Akademiya Nauk SSSR (1983). *Zemletryaseniya v SSSR v 1980 godu* (Earthquakes in the USSR in 1980), Nauka Press, Moscow.

Aranovich, Z.I., Ed. and others (1974). *Apparatura i metodika seismometricheskikh nablyudenii v SSSR* (Apparatus and method of seismic observations in the USSR), Nauka Press, Moscow, 240 pp.

Der, Z.A., M. S. Dawkins, T.W. McElfresh, J.H. Goncz, C.E. Gray and M.D. Gillispie (1978). *A Comparison of Teleseismic P Wave Amplitudes and Spectra Observed at Selected Basin and Range Sites and in Eastern North America, Phase 1 Final Report - Volume 2*, Teledyne Geotech Rept. SDAC-TR-77-7, 223 pp.

Eisenhauer, T.D. (1981). Body wave magnitude definitions, in *A Technical Assessment of Seismic Yield Estimation, DARPA-NMR-81-01*, 3 pp.

Given, J.W., T.C. Wallace and H. Kanamori (1982). Teleseismic analysis of the 1980 Mammoth Lakes earthquake sequence, *Bull. Seism. Soc. Am., 4*, 1093-1109.

Gutenberg, B. and C.F. Richter (1956). Magnitude and energy of earthquakes, *Ann. Geof., 9,* 1-15.

Keylis-Borok, V.I. (1950). On the question of determining the dynamic parameters of the focus, *Trudy Geofiz. Inst., Akad. Nauk SSSR, 9,* 3-19.

Peyve, A.V. and A.A. Mossakovsky (1982), Ed., and others. *Tektonika Kazakhstana* (Tectonics of Kazakhstan, explanatory report for the Tectonic Map of Eastern Kazakh), Nauka Press, Moscow, 139 pp.

Potap'ev, S., G. Babayan and I. Podvarkova (1974). *Regional Geophysical Investigations in Almost Inaccessible Regions,* Nauka Press, Novosibirsk.

Puzyrev, N., S. Krylov, B. Mishen'kin, Z. Mishen'kina, G. Petrik and V. Seleznev (1977). *The Structure of the Earth's Crust and Upper Mantle According to Data of Seismic Investigations,* Naukova Dumka Press, Kiev, USSR.

Ringdal, F. (1985). *Study of Magnitudes, Seismicity and Earthquake Detectability Using a Global Network,* Center for Seismic Studies Rept., in press.

Ryall, A.S., V.C. Fryklund and M. Mirkovitch (1980). *DSS Data and Regional Monitoring (Application to the Central Siberian Platform),* R&D Associates Rept. RDA-TR-194206-001, 73 pp.

Shishkevish, C. (1974). *Soviet Seismographic Stations and Seismic Instruments, Part I,* Rand Corp. Rept. R-1204-ARPA, 200 pp.

Vanek, J. and 32 others (1978). Station corrections for longitudinal waves in the Homogeneous Magnitude System of the Eurasian continent, *Akad. Nauk SSSR, Izvestiia Earth Physics, 14,* Amer. Geophys. Un., 169-178.

Vanek, J., N.V. Kondorskaya, I.V. Federova and L. Khristoskov (1980). Optimization of amplitude curves for longitudinal seismic waves for purposes of development of a uniform magnitude system for seismic observations on the Eurasian continent, *Doklady Akad. Nauk SSSR, 250,* 834-838, transl. by Scripta Publ. Co.

Vol'vovsky, I.S. (1973). *Seismic Studies of the Earth's Crust in the USSR,* transl. by Addis Translations International, 289 pp.

Vol'vovsky, I.S. and B.S. Vol'vovsky (1975). *Cross-Sections of the Earth's Crust in the Territory of the USSR, Plotted from Deep Seismic Soundings,* transl. by Addis Translations International, 268 pp.

Zavadil, R.J. (1981). Definitions and estimates of body wave magnitude, in *A Technical Assessment of Seismic Yield Estimation, DARPA-.... -81-01,* 4 pp.

Figure Captions

Figure 1. Polar projection of Eurasia showing stations used in this study. Radius of map is 40°.

Figure 2. Polar projection showing location of Mammoth Lakes earthquakes (solid circle) and stations used in study (triangles). Radius of map is 52°.

Figure 3. Fault-plane solutions for three of the largest Mammoth Lakes earthquakes (from Given *et al.*, 1982). Lower-hemisphere, equal-area projection. Solid circles -- location of raypath to Soviet stations used in study.

Figure 4. Polar projection showing location of Tonga earthquake (solid circle) and stations used in study (triangles). Radius of map is 60°.

Figure 5. Response curves for SVK-M3 short-period vertical instruments for stations used in this study.

Figure 6. P-waves digitized from Soviet recordings for the Mammoth Lakes earthquake on 25 May 1980 at 16:33 GMT.

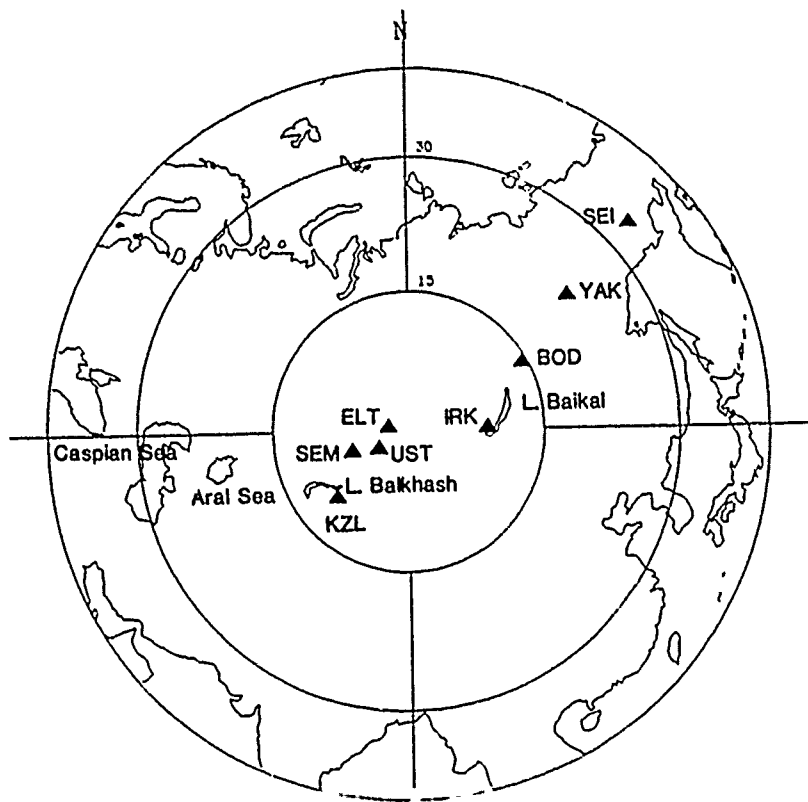Figure 7. P-waves corrected for instrument response for the 25 May 1980, 16:33 GMT, earthquake.
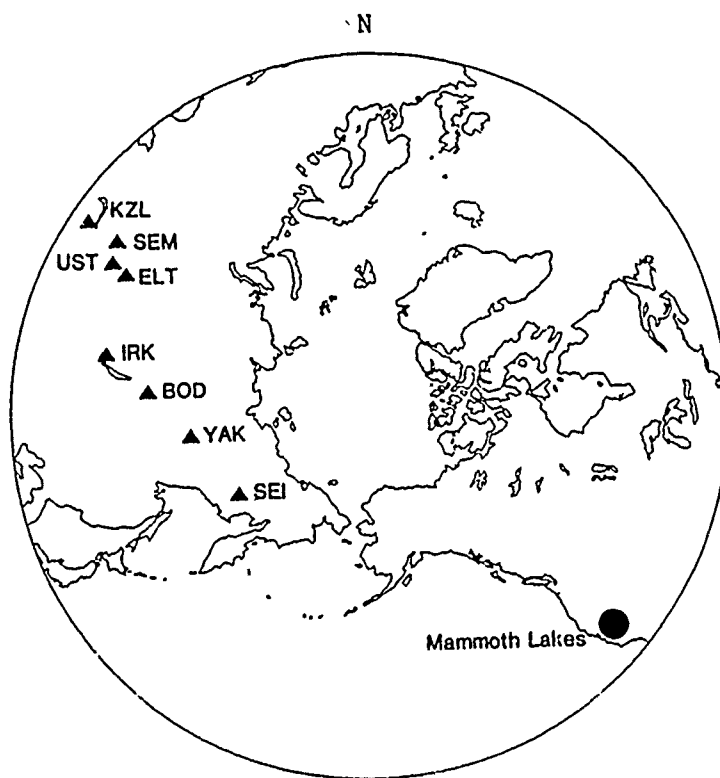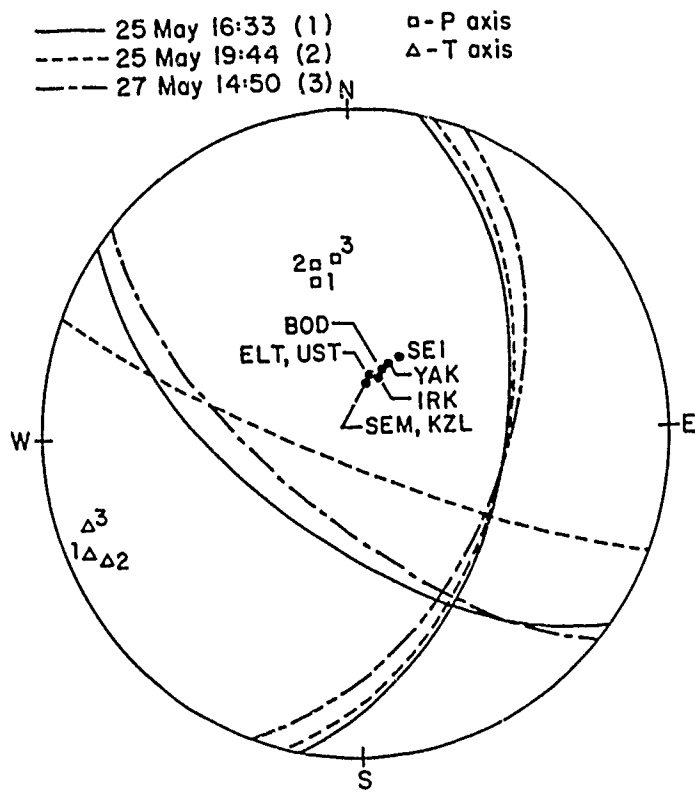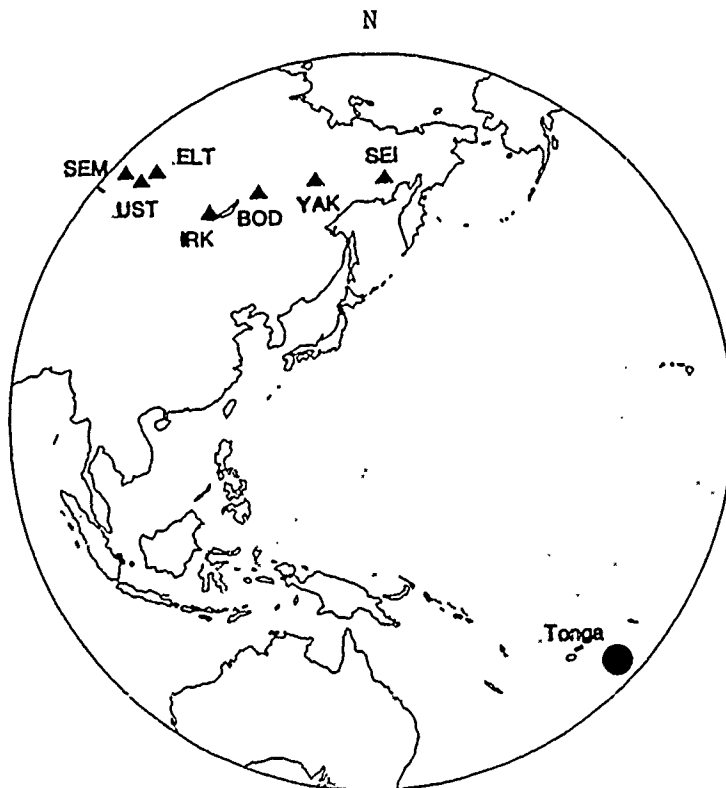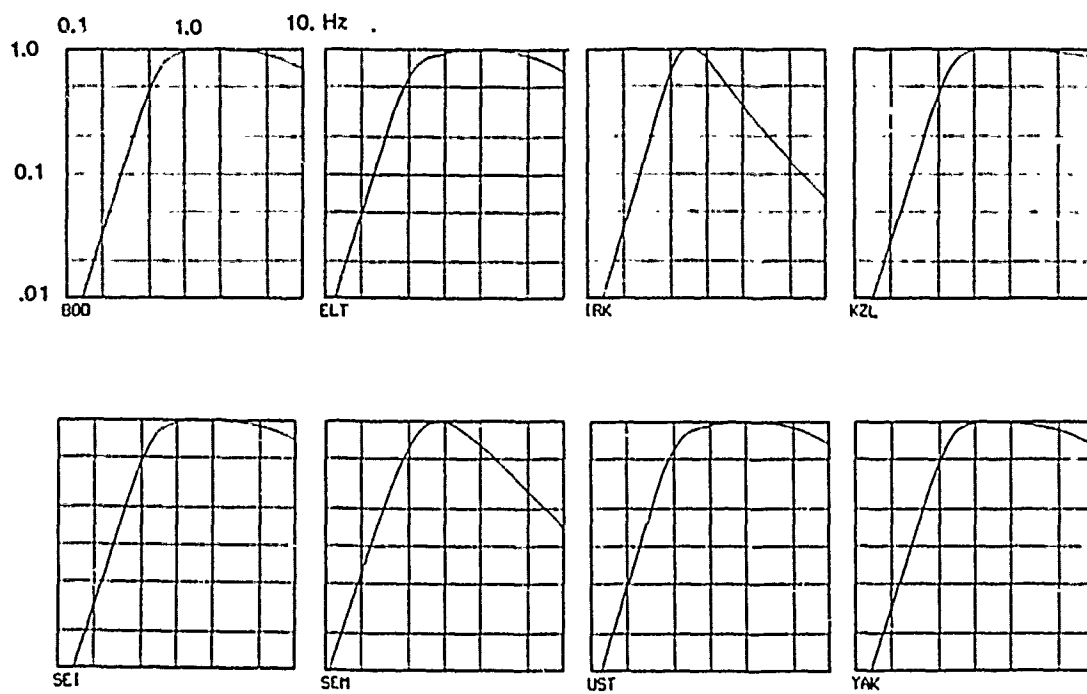
Figure 1

Figure 2
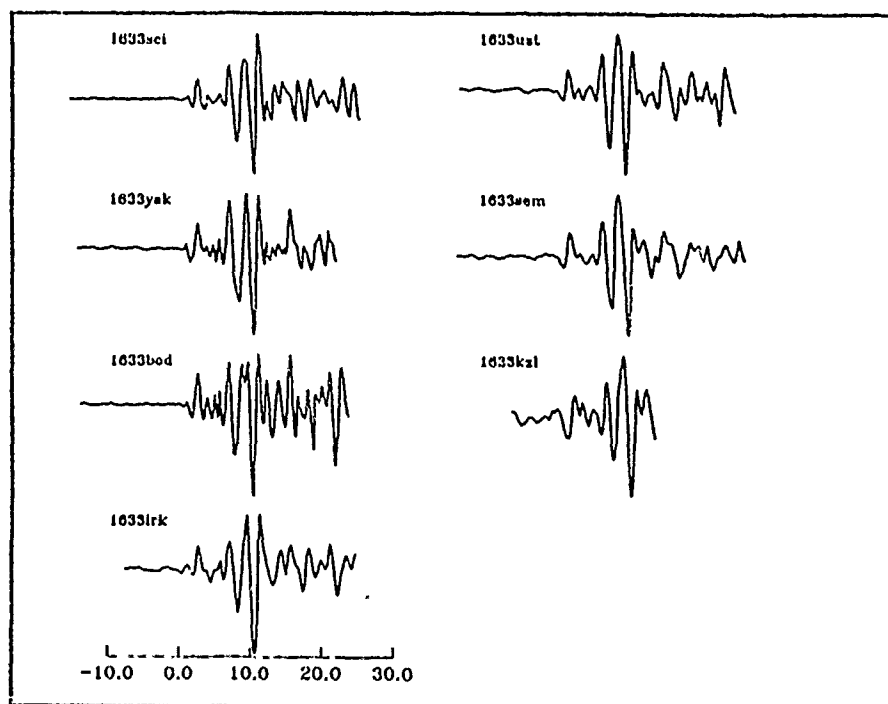
411

Figure 3

Figure 4
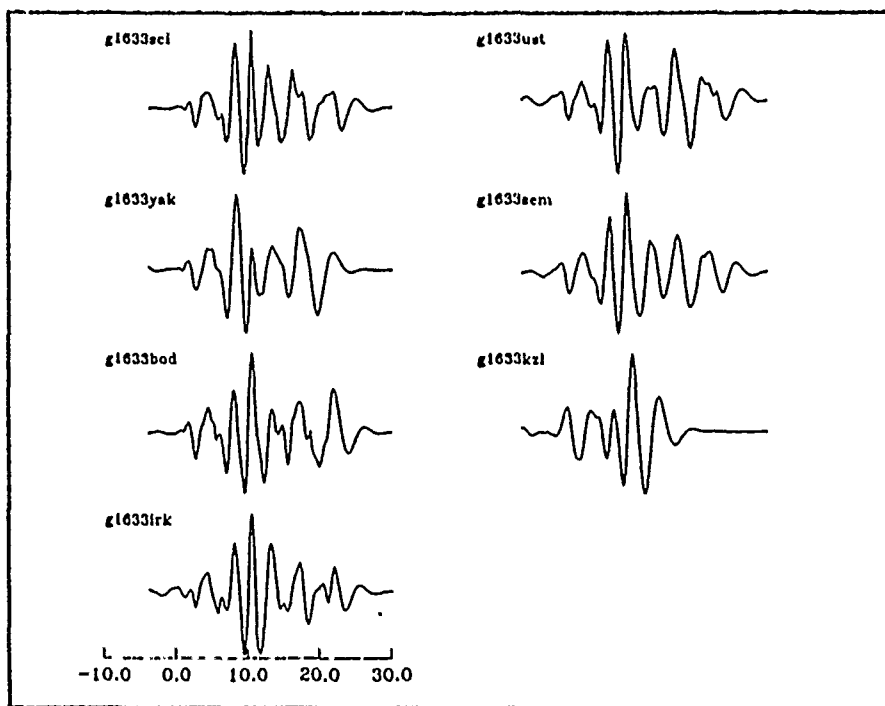
Figure 5

Figure 6

413

Figure 7

REAL TIME EVENT DETECTION USING THE SMALL-APERTURE NORESS ARRAY

by

Frode Ringdal
NTNF/NORSAR, P.O. Box 51, N-2007 Kjeller, Norway

Objective

The objective of the research described in this paper is to develop
and evaluate real time processing methods for the small-aperture
seismic array NORESS, with the aim to detect and locate low-magnitude
seismic events, both at regional and teleseismic distances.

Accomplishments

Since January 1985 data from the new small-aperture array NORESS in
Norway have been proceed in real time at the NORSAR data center at
Kjeller. The data used in the detection processing comprise 25 SPZ
channels, deployed over an area 3 km in aperture and sampled at a
40 Hz rate. The detection algorithm has been described by Mykkeltveit
and Bungum (1984), and briefly consists of

- Digital narrow-band filtering (six filters)

- Beamforming (conventional and incoherent)

- STA/LTA detector applied to each beam

- Frequency-wavenumber analysis of detected signals

- Association of regional phases to aid in locating events.

In the following, initial results from this processing are described,
together with recommendation for future research.

415

Teleseismic events

The P-wave signal-to-noise ratio at NORESS typically peaks in the 2-4 Hz band for teleseismic events in Eurasia, whereas lower dominant frequency is often observed for signals from the western hemisphere and for epicentral distances exceeding 70 degrees. Signal coherency is naturally very good for teleseismic P across NORESS, even at very high frequencies. Depending on signal frequency, the best beam SNR is obtained using various subsets of the array; e.g., at 2 Hz the best subset consists of the center instrument A0 together with the C and D rings (see Fig. 1). Using this subset, the beamforming gain meets or exceeds √N, due to the noise suppression characteristics described in the paper by Mykkeltveit (this volume).

An example of teleseismic processing results from NORESS is given in Fig. 2. The improvement in SNR on the beam relative to the single sensors is quite remarkable.

The on-line procedure uses steered teleseismic beams rather than a single infinite-velocity beam for each filter. The resulting SNR gain is, as an example, 4-5 dB for an apparent velocity of 16 km/s, at 3 Hz frequency. For lower frequencies or higher velocities, the gain is less. Thus, applying only infinte-velocity beamforming for teleseismic detection is a viable alternative, in view of the possibility of operating at a lower detection threshold with the same false alarm rate.

The NORESS array detects many teleseismic signals not observed at the large aperture NORSAR array, which, like NORESS, is located in southeastern Norway; especially from selected regions in Eurasia. On the other hand, the signal focusing effects underneath NORSAR cause some instruments to have up to an order of magnitude stronger signals than NORESS sensors, for regions such as Hindu Kush and the Kuriles. For these regions, NORESS does not match the NORSAR detection capability.

Because of the small aperture of NORESS, only a very coarse automatic estimate of the location of teleseismic events is currently being made. Azimuth errors depend on phase velocity and frequency, and are often around 5-10 degrees for small events. Slowness estimates from the automatic process are typically about 1 sec/deg different from those of NORSAR. Nevertheless, it is clear that location estimates from a small array like NORESS will be very valuable to provide a starting point for association procedures using a seismic network. Regional corrections and more detailed off-line analysis are required to assess the eventual capabilities of the array in this regard.

Local and regional events

At local and regional distances, the best SNR for the P wave varies from 3-5 Hz (at around 1000 km) to more than 8 Hz (local distances). Consequently, either steered beams or incoherent beamforming is necessary to exploit the array capability. P-signal coherency at NORESS is usually good enough to utilize the full array for F-K processing of local and regional P-phases, at least up to about 6-8 Hz.

The Lg phase is usually of slightly lower frequency than P. Conventional beamforming is not very efficient for Lg, since the preceding coda (from Sn) comes in with about the same phase velocity and azimuth. Consequently, little "noise" suppression takes place. A promising approach is that of performing narrow-band filtering at several frequencies for the purpose of Lg detection. It turns out that the SNR is greatly improved in those frequency bands where P and Sn coda energy are low relative to the Lg energy. Combining narrow-band filtering with incoherent beamforming has been found particularly effective.

An example of a complete record from a regional event processed at NORESS is given in Fig. 3. The detection times for P and Lg are marked on the panel of Fig. 3a, whereas Fig. 3b shows F-K solutions for P and Lg together with short plots of each phase in an expanded time scale. The estimated azimuths for P and Lg differ by 2 degrees in this case; and a deviation of 0-5 degrees is common. However, a difference of 10 degrees and more is also fairly often observed in the automatic solution.

The location accuracy of NORESS for regional events is currently being studied. No statistically reliable results are available so far due to the limited data base of known locations. The procedure of locating events by associating P and Lg is applicable only up to about 1200 km distance. At greater distances, the Lg usually is too weak to be detected automatically, but can sometimes be identified by visually inspecting the waveform plots.

In conclusion, the initial results obtained from NORESS are very encouraging, and have met and in some cases exceeded the expectations. Data quality has been excellent, and the operational stability has been very satisfactory, taken into account the complexity of the system. Particularly noteworthy is the excellent P detection in the 2-4 Hz band, which is due to greater than $\sqrt{N}$ noise suppression combined with strong P-wave energy. The automatic detection of secondary phases needs refinement, and in particular the narrow-band filter bank processing should be further investigated.

References

Mykkeltveit, S. and H. Bungum (1984). Processing of regional seismic events using data from small-aperture arrays, Bull. Seis. Soc. Am., 74, 2313-2333.
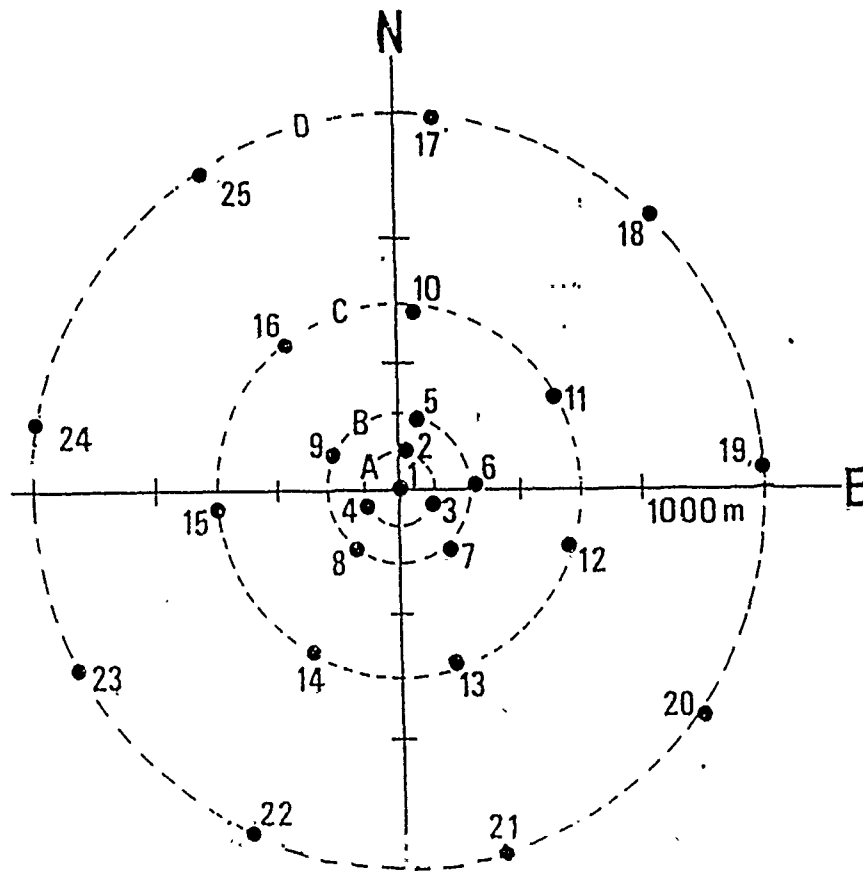
Fig. 1   Geometry of the NORESS array. The array comprises 25 SPZ
seismometers over an area 3 km in diameter. The four rings -
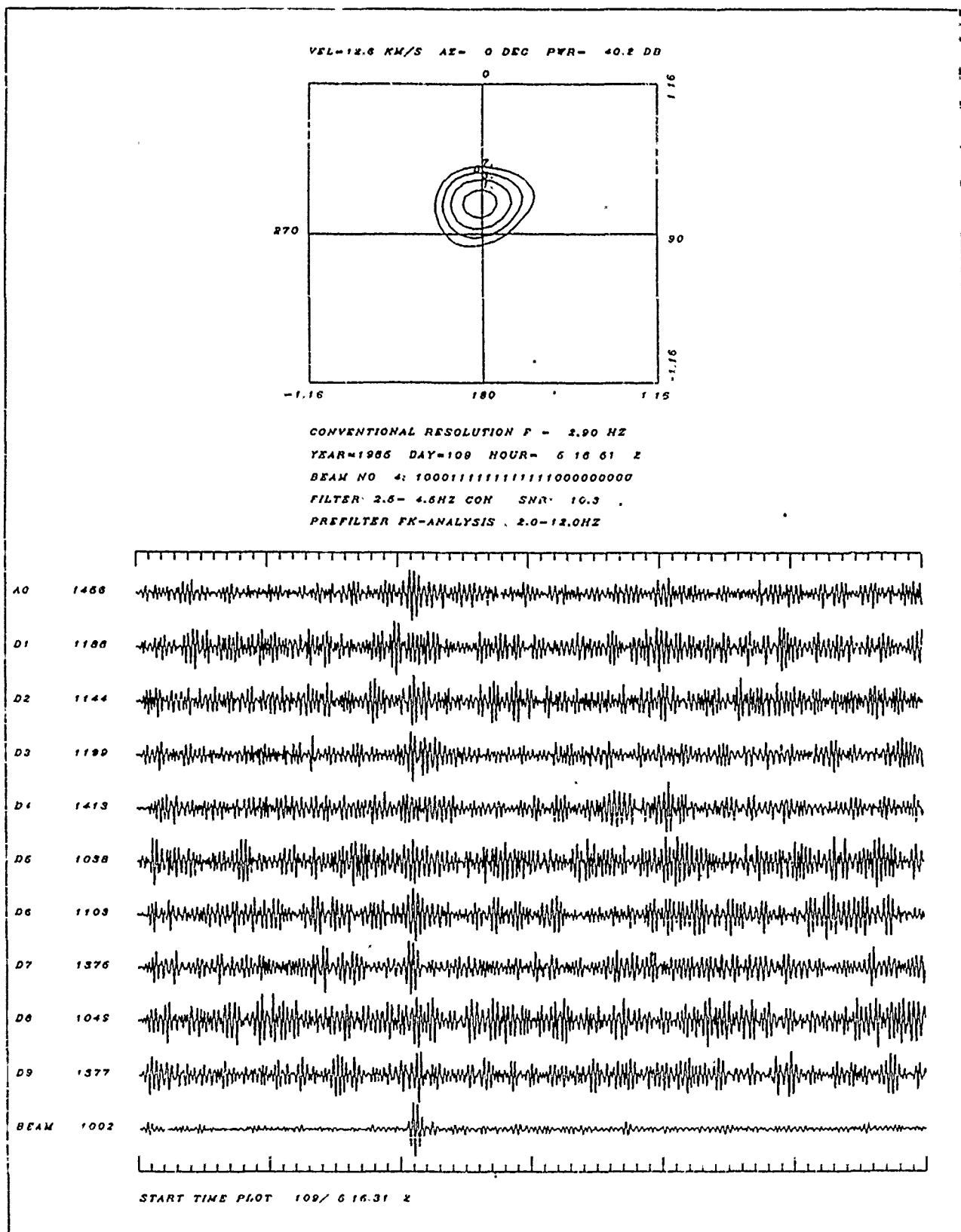A, B, C, D - are marked on the figure.

Fig. 2   Example of automatic processing of a teleseismic event using
         NORESS. The on-line F-K solution is shown at the top,
         together with detection parameters. Ten individual sensor
         traces (filtered 2.5-4.5 Hz) are plotted, together with the
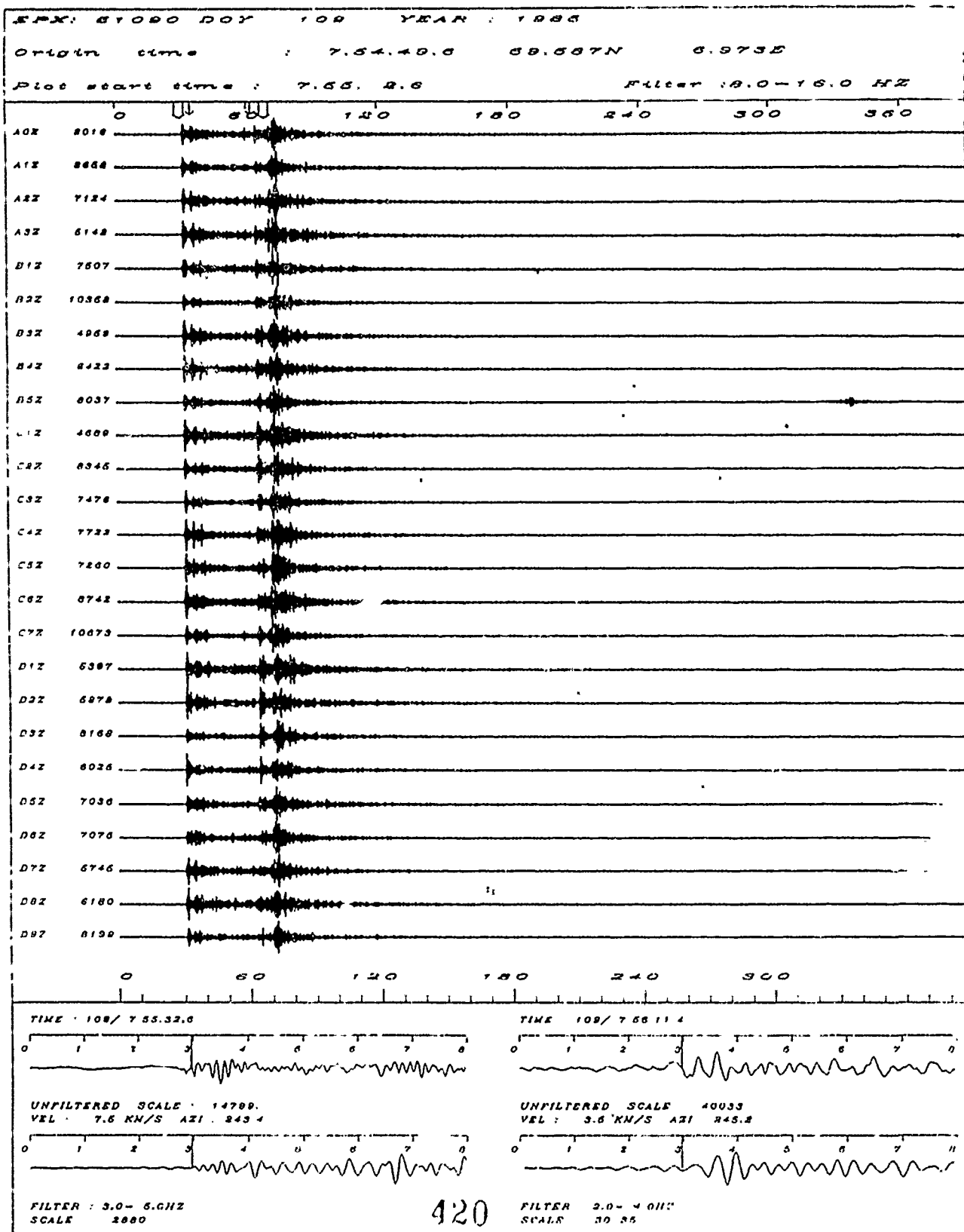   array beam (bottom)

Fig. 3a   Individual NORESS traces for regional event 19 April 1985.
The panel covers 6 minutes of bandpass filtered records
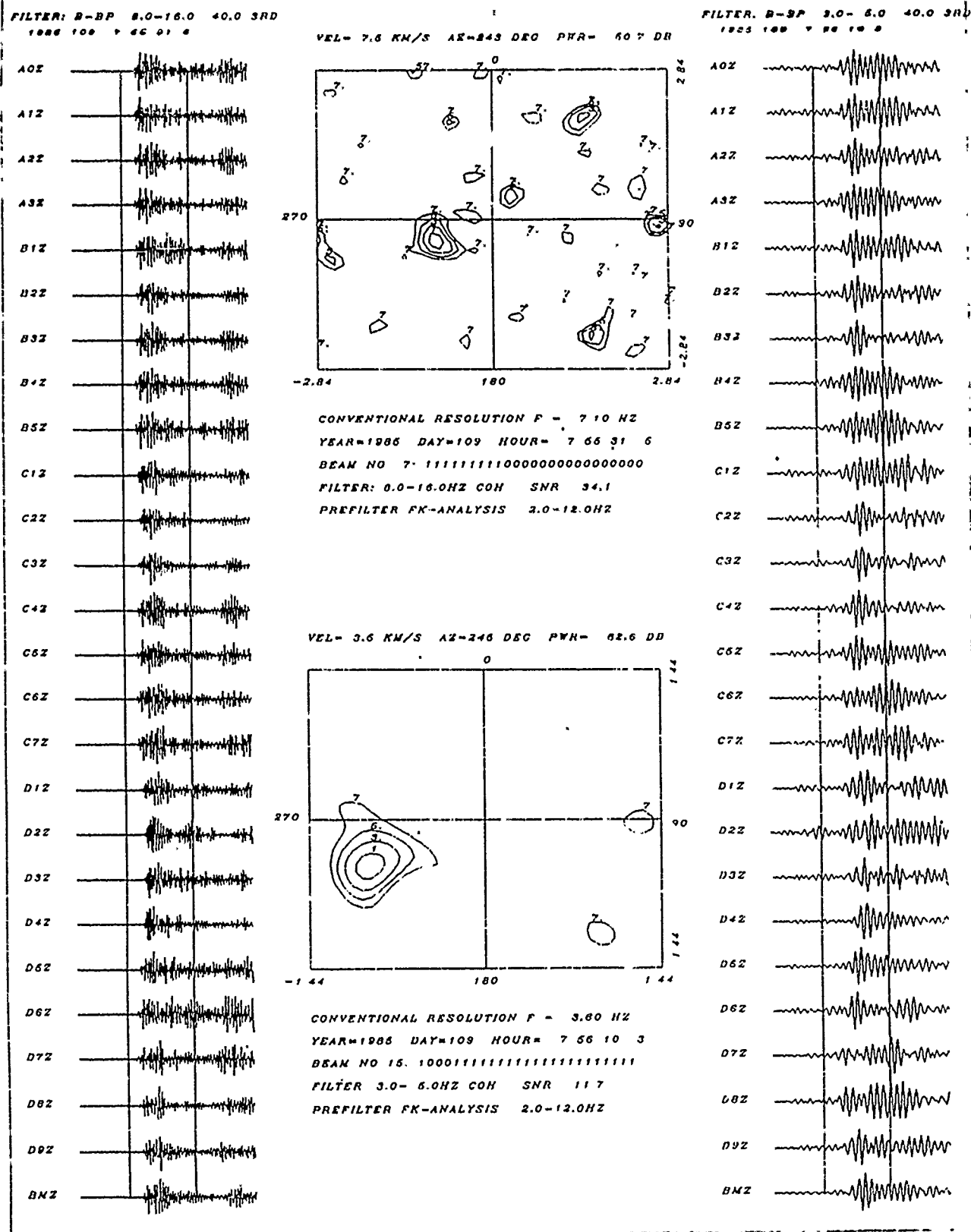(8-16 Hz). P and Lg beams are also shown (bottom part).

Fig. 3b NORESS automatic analysis results for the event of Fig. 3a.
The P-phase (left) and Lg phase (right) are shown for all SPZ
instruments. F-K solutions are shown for P (top) and Lg
(bottom).

PRELIMINARY EVALUATION OF THE EVENT DETECTION AND LOCATION CAPABILITY
OF THE SMALL-APERTURE NORESS ARRAY

by

S. Mykkeltveit*, D.B. Harris** and T. Kværna*

*   NTNF/NORSAR
** Lawrence Livermore National Laboratory

Objectives

Collect a data base of events recorded on the new NORESS array. Evaluate the event detection capability by estimating SNR enhancement by beamforming as a function of frequency for the phases Pn, Sn and Lg and for various subsets of instruments in the array. Also evaluate the location capability of the new array by estimating bearings by FK-analysis for events of known location. Implement results from this investigation in the online processing of NORESS data.

Accomplishments

The new NORESS array in Norway has been in operation since October 1984. The geometry of the array is shown in Fig. 1. The array has 25 short period vertical seismometers, arranged on concentric rings around the central site. Four of the 25 sites are occupied by three-component seismometers.

A data base of local and regional events has been collected, with the purpose of evaluating the event detection and location capability of the new array. As a first approach, we have concentrated our efforts on the study of a data set of 18 seismic events that occurred in the Baltic and Leningrad regions of the U.S.S.R. during the time period January-March 1985. The events are associated with mining activity and are all reported and located by the Finnish network of seismic stations. An example of one such event is shown in Fig. 2. Three distinct phases P, Sn and Lg can be seen for all 18 events. Spectra for noise preceding the P onset, the P phase, the Sn phase and the Lg phase are plotted together in Fig. 3 for one of the events. As can be seen, the P phase is very rich in high frequencies, while Sn and Lg approach the noise level from about 8 Hz. Note also the noise peak at around 6 Hz, which is typical of daytime noise samples.

Now, to assess the detection capability of the array, we have estimated the SNR gain by beamforming for the three phases P, Sn and Lg. This has been done by computing the signal loss and noise suppression and taking the ratio. The signal loss is the spectrum of the beam (with appropriate bearing and velocity depending on the phase type) divided by the average spectrum of all individual channels. Similarly, the noise suppression is the ratio of the spectrum of the noise beam (noise preceding the signal, shifted in the same way as the signal itself for the beamforming) to the average spectrum of all individual channels.

The noise spectra have been estimated using the indirect covariance method. We first estimate the correlation function by splitting a long data record into many windows, calculating a sample correlation function for each window, then averaging the sample correlation functions. Typically, we use 20 windows, each of which is 5 seconds long. Because the earth noise has such a large dynamic range, we prewhiten it prior to estimating the correlation function with a low-order prediction-error filter. The spectrum is then estimated by windowing the correlation function with a 3 second Hamming window, then computing the Fourier Transform. Finally, the spectral estimate obtained this way is compensated for the effects of prewhitening.

The signal spectrum is calculated by windowing the signal with a 10% cosine taper window, 5 seconds long, then calculating the Fourier Transform and finally squaring the transform.

When we do direct comparison of the noise spectrum, which is a power density spectrum, with the signal, which is an energy density spectrum, we divide the signal spectrum by the length of the signal analysis window to convert energy density to power density. The two spectral quantities are then directly comparable. This has been done in Fig. 3.

The signal loss, noise suppression and SNR gain by beamforming have been computed for four different array configurations:

- All elements included ("ALLV" in the figures)
- All elements minus A-ring ("INTERMEDIATE")
- Center instrument, C-ring and D-ring ("TELEV")
- All elements minus D-ring ("HIFREQ").

In Fig. 4, noise suppression curves, representing averaging over the 18 events, are shown for all four array geometries. The horizontal lines represent $\sqrt{N}$ suppression of noise, where N is the number of sensors in the geometry under consideration. This is the expected level for noise that is uncorrelated over the entire array. As can be seen, the "TELEV"-geometry is remarkably good in suppressing the noise in the 1.5-3.5 Hz band, while the other geometries approach the $\sqrt{N}$ level for various frequencies, but do not show better noise suppression than

√N. These results partly reflect on the SNR gains shown in Fig. 5. the signal losses (not shown) tend to be larger for the larger geometries (including outer rings) because of the decaying signal correlation with increasing station separation. The overall effect is to level the gain curves, and we can see from Fig. 5 that only at fairly low and fairly high frequencies do the gain curves for the different geometries deviate substantially.

For the Sn and Lg phases, the "noise suppression" estimates reflect suppression by beamforming of the P and Sn coda, respectively, i.e., we address the problem of detecting a secondary phase in the coda of a preceding phase. Results shown in Fig. 6 are for the Lg phase and correspond to the best SNR result obtained among the four geometries. SNR-gain is now well below √N, essentially because of failure to suppress the Sn coda, which propagates with similar phase velocity and azimuth as the Lg onset. Still, there is a 6 dB gain from beamforming at 1.2 Hz.

Fig. 7 shows the P onset for a Novaya Zemlja explosion (distance approx. 20°) recorded on NORESS, and the SNR gain by beamforming computed as before for the "TELEV" configuration. In the frequency range 1.0-2.7 Hz the gain is better than √N, because of a very modest signal loss in combination with optimum noise rejection, as for the "TELEV"-configuration in Fig. 3. The same result is visualized in the time domain in Fig. 8.

Our approach to the location performance evaluation has been to compute narrow-band FK-spectra for the P, Sn and Lg signals for the events in the data base. FK-spectra have been computed for the array subsets given above and for frequencies corresponding to distinct spectral maxima for each phase. Typical results are given in Table 1 for one event. As can be seen, the analysis frequency is the critical parameter, and more so than the array subgeometry used in the evaluation of the FK-spectra. According to these results, then, the arrival azimuth varies fairly strongly with frequency and due care must be taken in selecting the analysis frequency. To gain more insight into these frequency-dependent lateral refraction effects, we have computed the broad-band maximum likelihood FK-spectra for a number of phases. One example is shown in Fig. 9, where the azimuth's dependency on frequency is given implicitly in the contour plot. The azimuth value of 89.5 serves to illustrate that the broad-band FK tends to give more stable estimates than those derived from narrow-band FK-spectra.

The research effort continues with analysis of events from other regions, in order to obtain the capabilities of the new NORESS array for local and regional events from all source regions of interest. As experience is gained, the results from this study will be utilized directly in the online processing of NORESS data.

424

Table 1

Array	P at 3.40 Hz		P at 6.35 Hz		Sn at 2.20 Hz		Lg at 1.33 Hz		Lg at 1.80 Hz	
	Vel	Az	Vel	Az	Vel	Az	Vel	Az	Vel	Az
HIFREQ	11.71	80.8	9.73	92.3	5.05	86.1	4.55	95.5	4.31	109.0
ALLV	11.58	86.1	10.14	95.8	5.02	84.0	4.29	95.4	4.07	106.9
INTERM	11.52	86.2	10.15	95.9	5.02	84.0	4.29	95.5	4.08	105.7
TELEV	11.51	86.3	10.07	98.1	5.03	84.0	4.28	95.0	4.10	102.3

Table 1   Narrow-band FK-results for one event in the Baltic-Leningrad region data base. According to the location reported by the network of Finnish seismic stations, the true azimuth for NORESS is 91.6°.
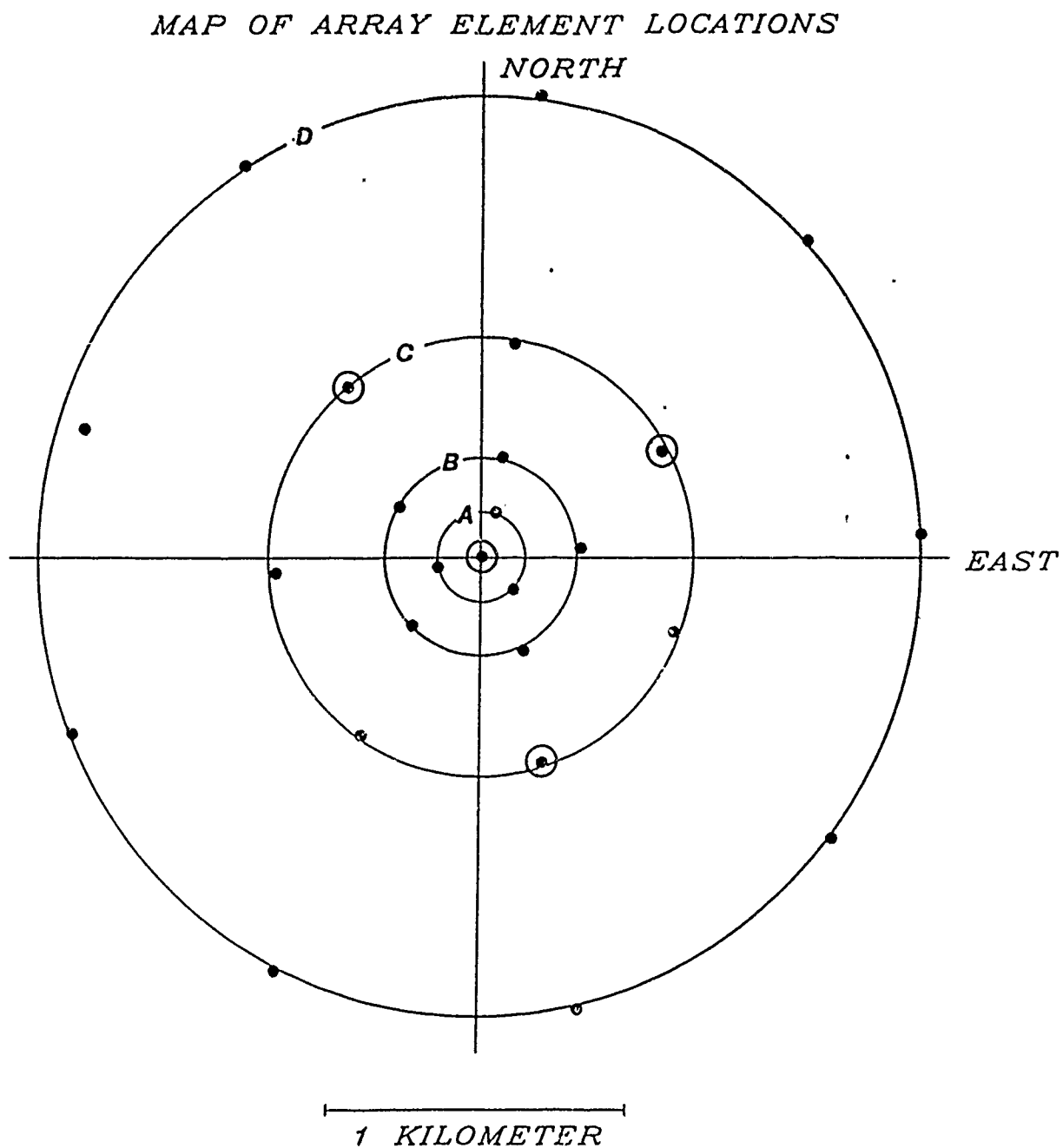
425

MAP OF ARRAY ELEMENT LOCATIONS

Fig. 1   Geometry of the new NORESS array. The four three-component
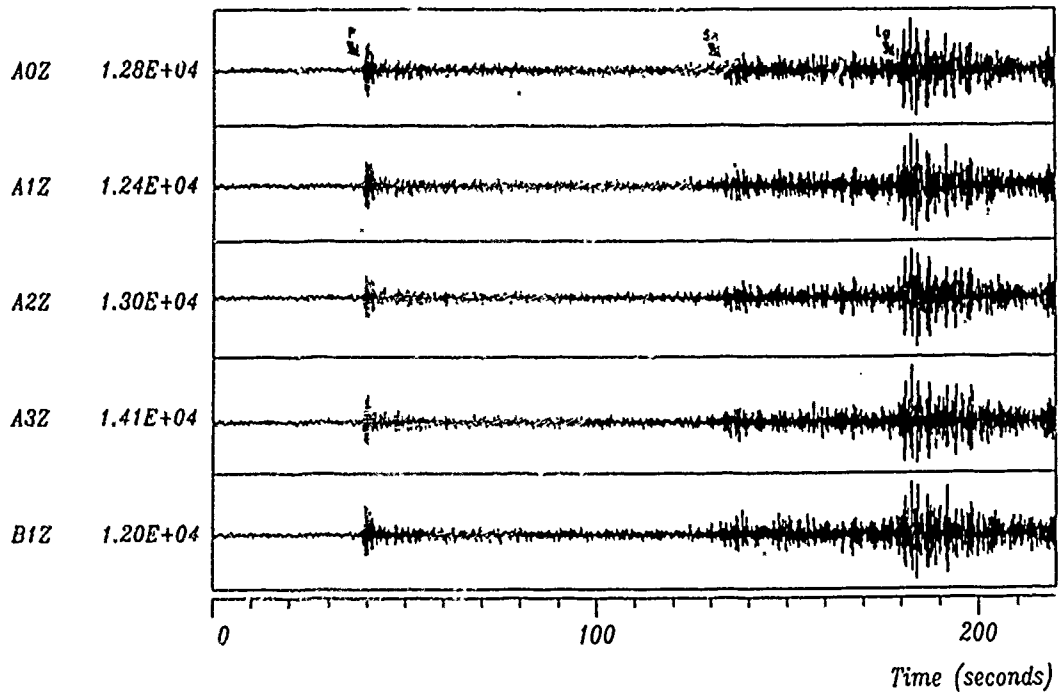stations are marked with special symbols.

Fig. 2   Example of event from the Leningrad region, with P, Sn and Lg phases.
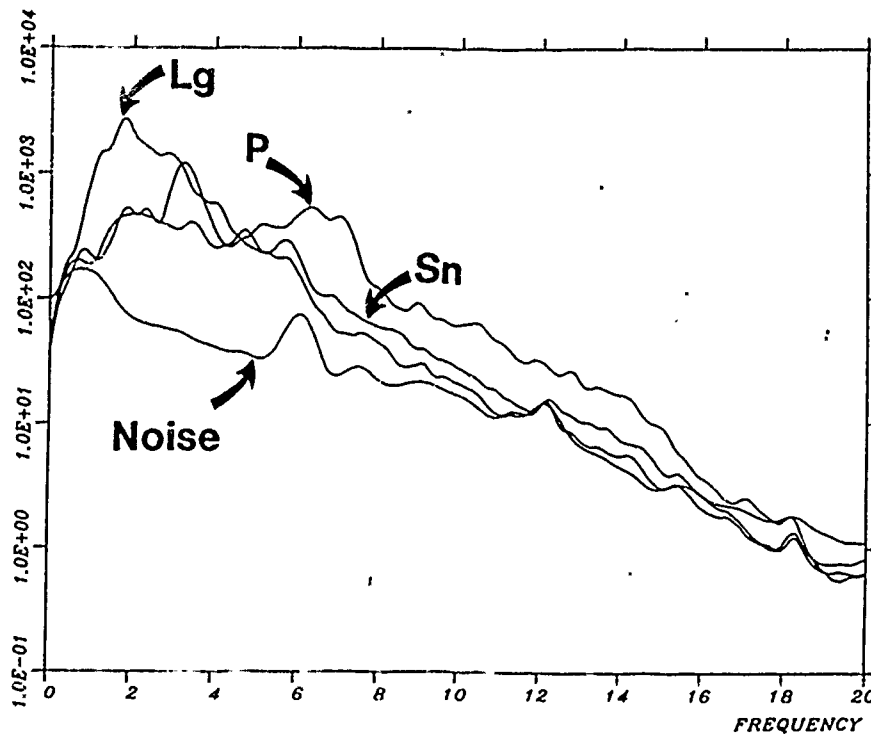

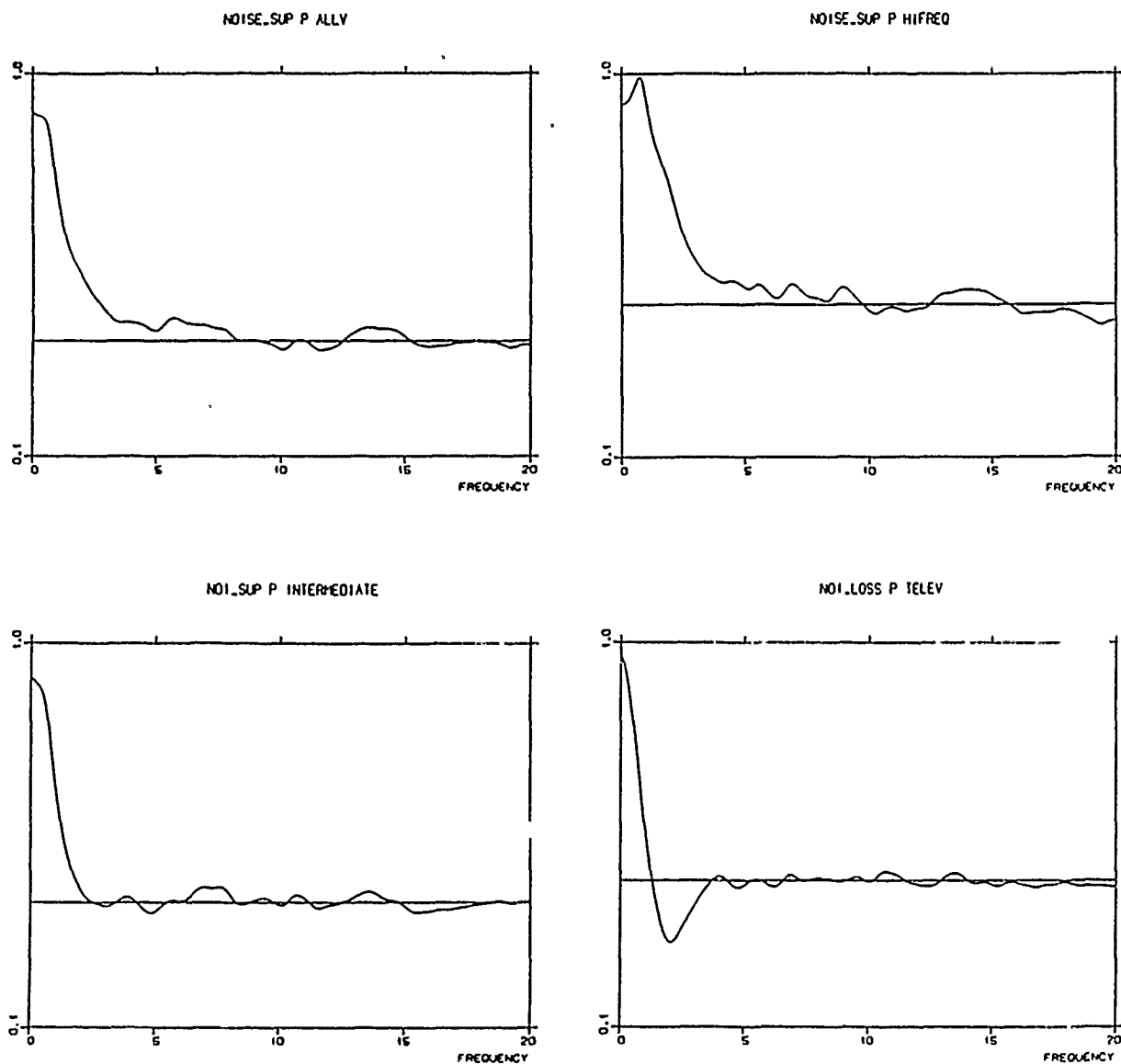Fig. 3   Spectra for the P, Sn and Lg in Fig. 2 and for noise preceding the P arrival.

Fig. 4   Noise suppression for the four array subgeometries. The horizontal
         line represents √N noise rejection, where N is the number of
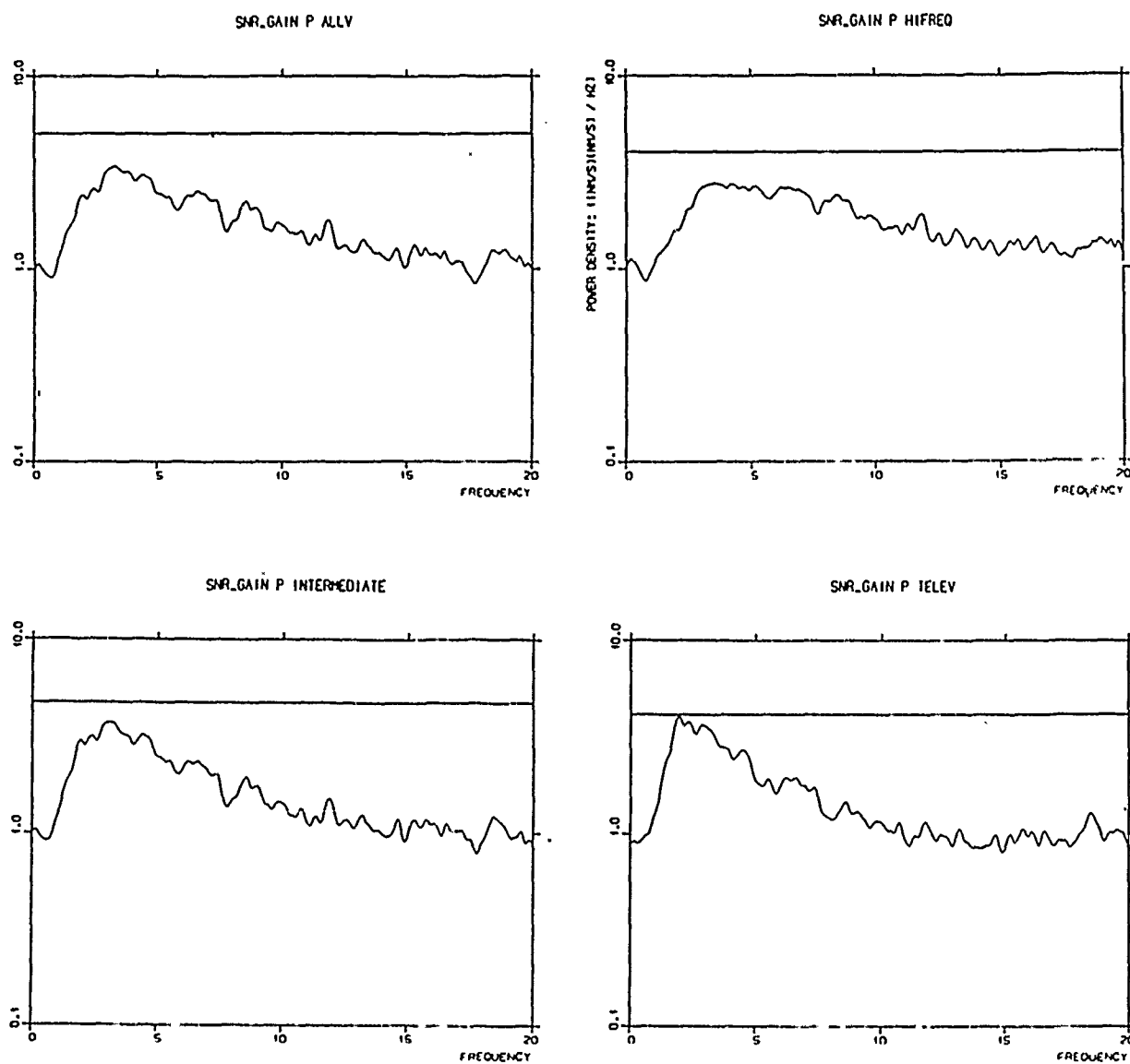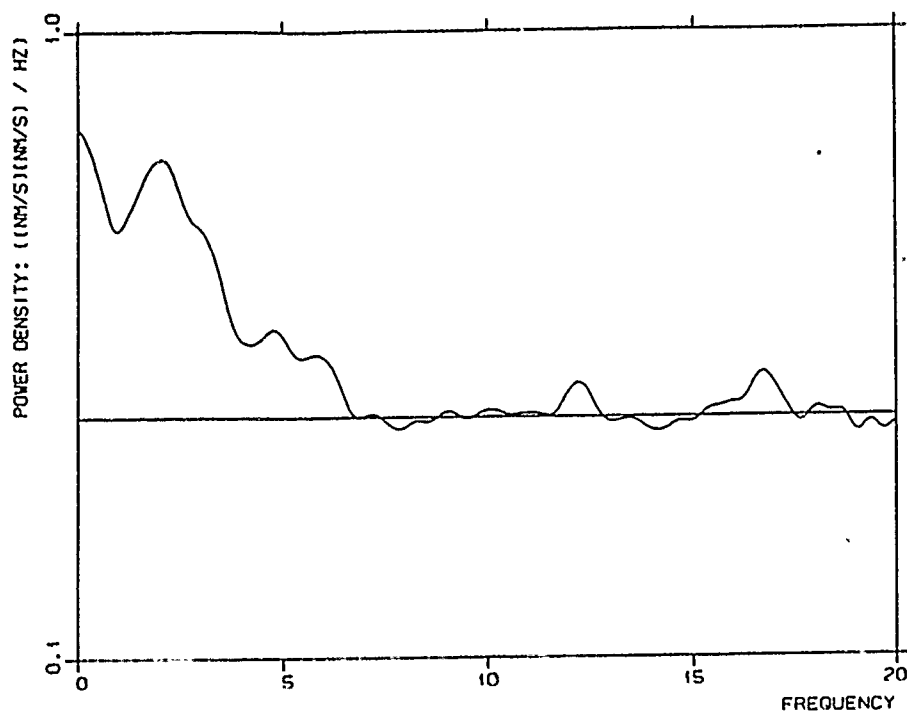   sensors in each subgeometry.   The vertical scale is logarithmic.

428

SNR_GAIN P ALLV

SNR_GAIN P HIFREQ

SNR_GAIN P INTERMEDIATE

SNR_GAIN P TELEV

Fig. 5   SNR gain by beamforming for the four array subgeometries. The
horizontal line represents √N gain, where N is the number of
sensors in each subgeometry. The vertical scale is logarithmic.

429

NOISUP TELEV LG-PHASE
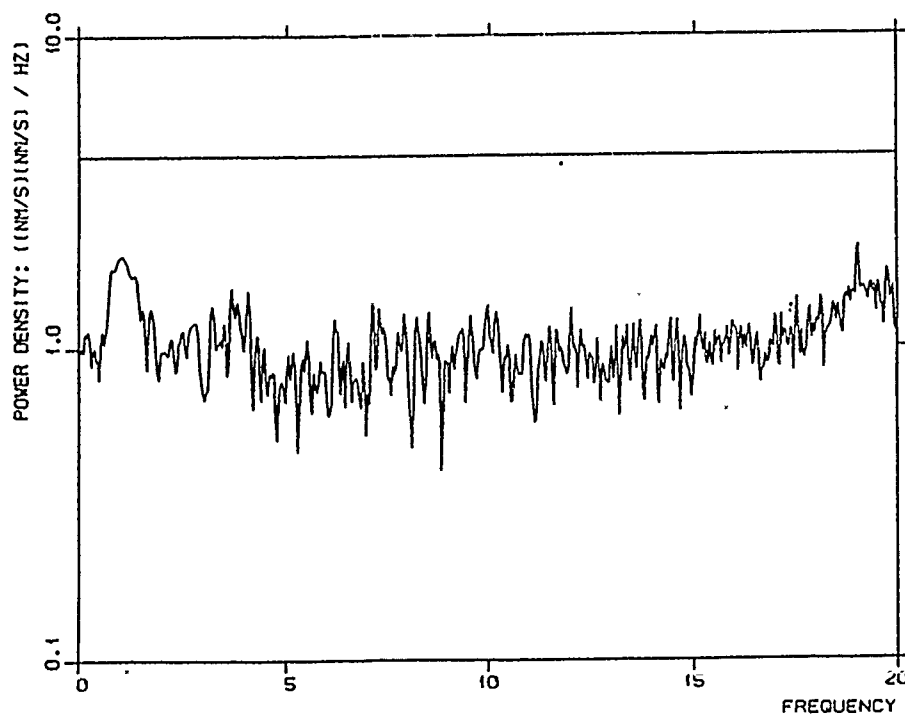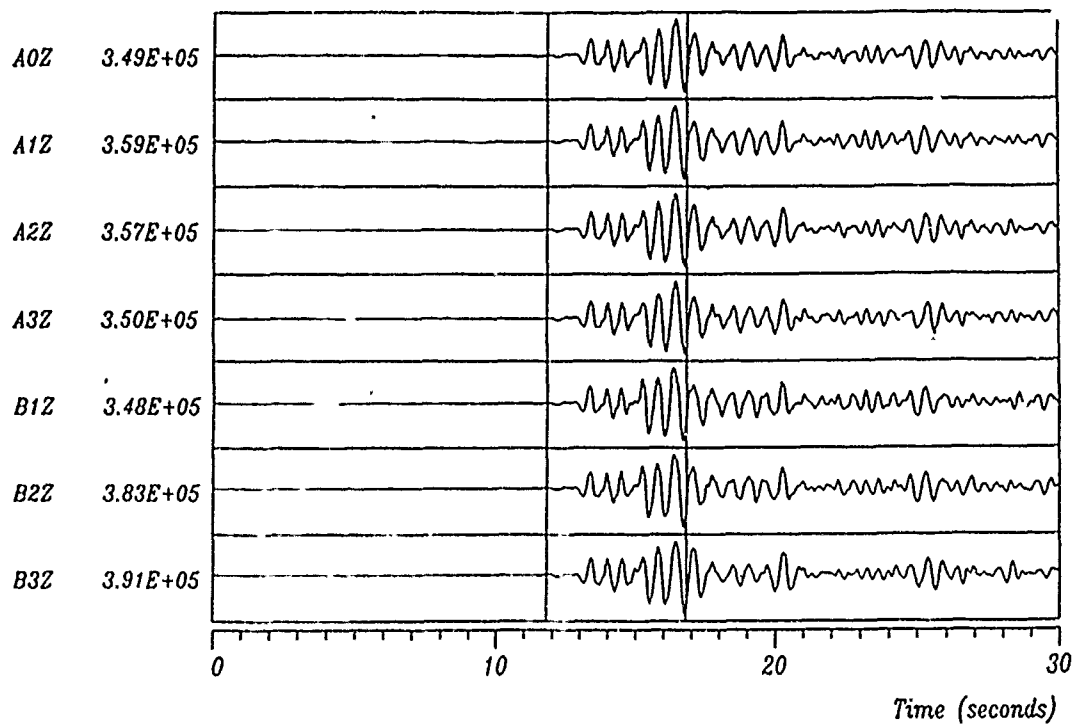

SNR GAIN TELEVLG_PHASE

Fig. 6   Noise suppression and SNR gain for the Lg phase for sub-
          geometry "TELEV". Horizontal lines represent $\sqrt{N}$-noise
          rejection (upper plot) and $\sqrt{N}$-beamforming gain (lower plot),
          with N = 17 for this subgeometry. Vertical scales are
          logarithmic.
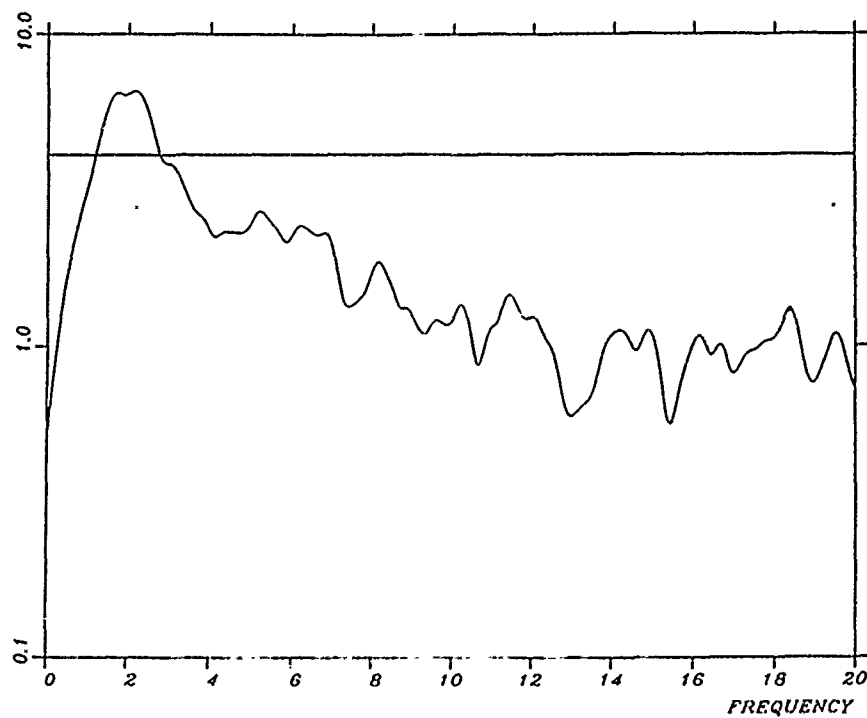
SNR GAIN

Fig. 7   Beamforming gain for array "TELEV" for P-arrival from
              Novaja Zemlja event. P-wave data analysis window on top.
              The horizontal line in the gain plot indicates $\sqrt{N}$ gain,
              with N = 17 for this subgeometry.

NOVAYA ZEMLJA SIGNAL

AOZ   2.84E+05

C1Z   2.96E+05

C2Z   3.20E+05

BEAM   2.66E+05

25 26 27 28 29 30 31 32 33 34 35

Time (seconds)

NOVAYA ZEMLJA NOISE

AOZ   8.00E+02

C1Z   8.00E+02

C2Z   8.00E+02

BEAM   8.00E+02

5 16 17 18 19 20 21 22 23 24 2
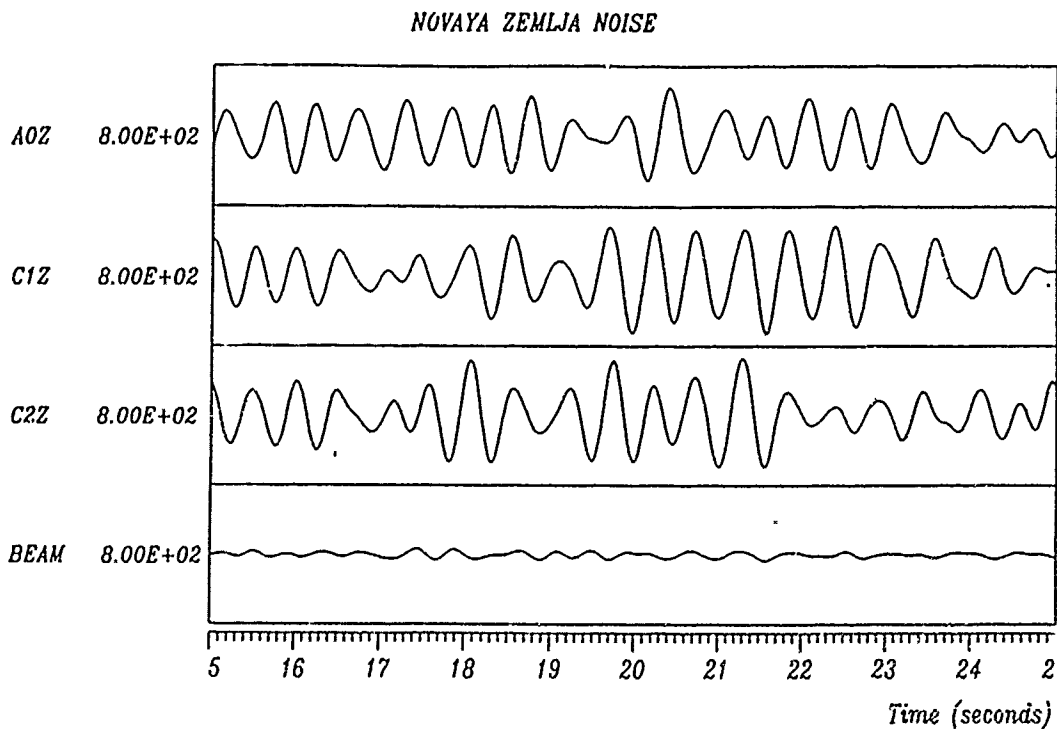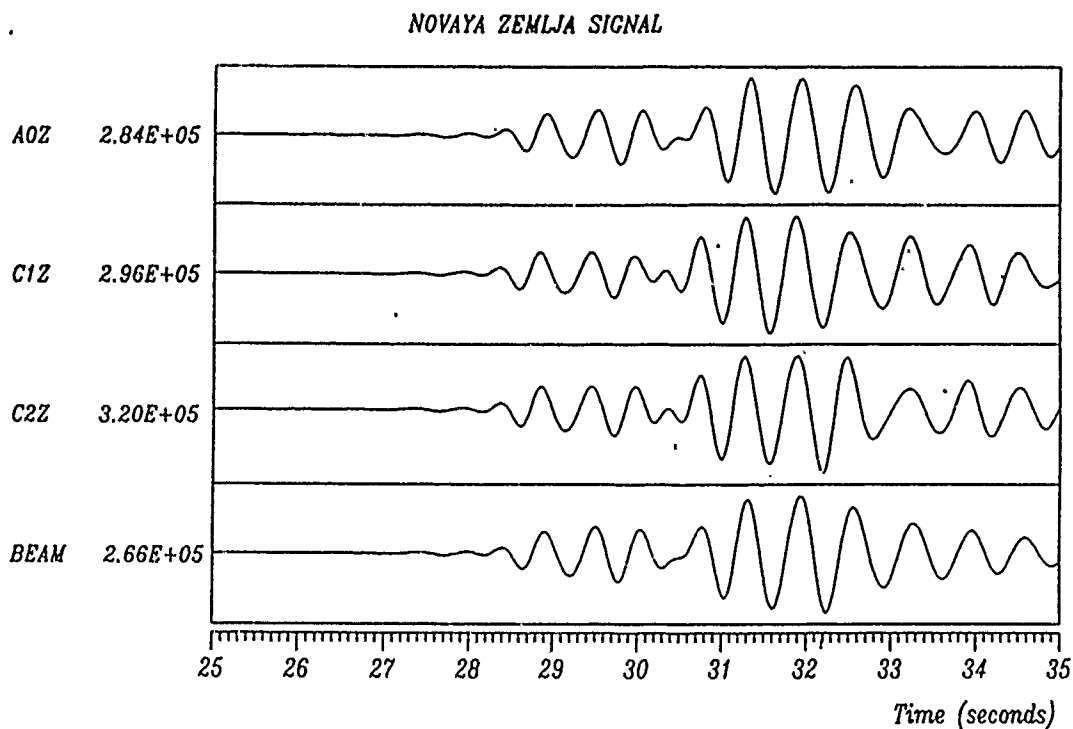
Time (seconds)

Fig. 8   Time domain illustration of the SNR-gain results in Fig. 7.
         Top: Normalized plot of three single channels (out of the 17
         participating in the beam) and the beam, showing a very modest
         signal loss. Bottom: Noise rejection obtained on preceding noise
         (true amplitude plot). The filter bandpass is 1.3-2.5 Hz, cor-
         responding to the peak in the gain curve in Fig. 7.

432

BROAD BAND F-K ANALYSIS

CONTOURS GIVEN IN DECIBEL BELOW MAX. PEAK

VEL = 3.15 KM/S   AZ = 89.5 DEG
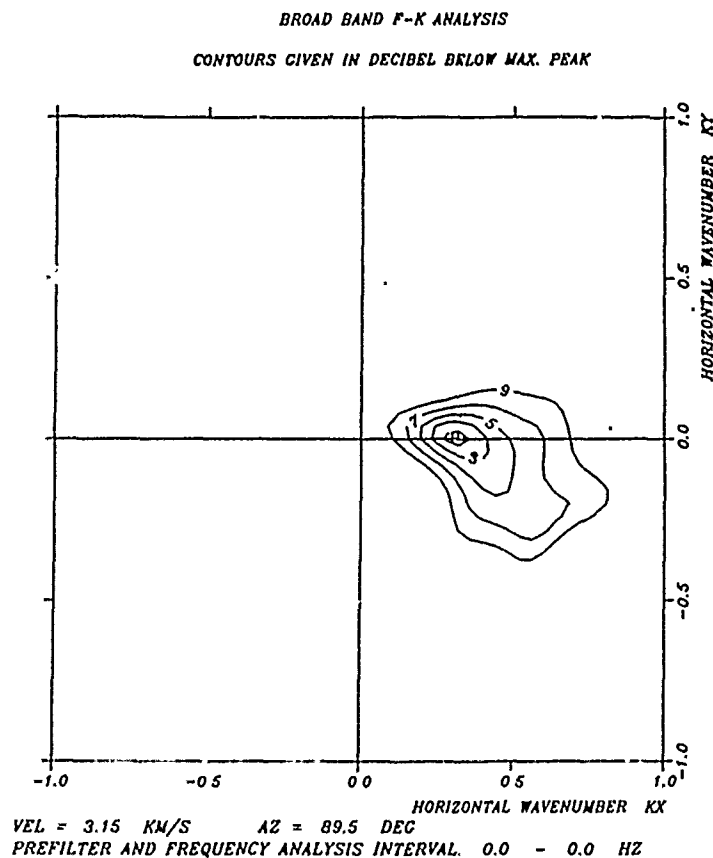PREFILTER AND FREQUENCY ANALYSIS INTERVAL. 0.0 - 0.0 HZ

Fig. 9   Broad-band FK-analysis for the Lg phase of the event used
in Table 1. In order to obtain the velocity corresponding
to the peak, the value of 3.15 km/s must be multiplied by
the dominant frequency of the Lg signal (1.33 Hz) to yield
a phase velocity of 4.19 km/s.

433

PAPER TITLE:

Fingerprinting Mother Earth: 3-Component Seismogram Analysis.

PAPER AUTHORS:

Anders Christoffersson
Dept. of Statistics, Univ. of Uppsala, Sweden
Eystein S. Husebye
NORSAR, Norway
Shane F. Ingate
Department of Earth and Planetary Sciences, MIT, USA

SUMMARY:

In this note we introduce a new technique for analyzing 3-component seismogram records; in essence this implies a comparison of the theoretically expected particle motion covariance matrices with that observed in given time (0.5 to 1 sec) and azimuth (1 to 5 deg) windows. The outcomes are the likelihood or probability of presence of P, S, Love and Rayleigh types of wavelets constituting the signal records. Preliminary results are displayed in terms of likelihood of signal occurrence as a function of time and azimuth, filtered records on the basis of the estimated likelihood functions, and apparent phase velocities of P-wavelets triggered. The events subjected to analysis were recorded by a single 3-component instrument in the new NORESS mini-array in Norway; our analysis results compare not unfavorably with those based on f-k analysis using all vertical instruments in the array.

CONCLUSIONS AND RECOMMENDATIONS:

The preliminary results obtained from our variant of particle motion analysis of high-quality 3-component records from the new NORESS array in Norway are considered very encouraging and thus justify research on a broader scale into this kind of problem. Although currently operational in real-time, methodological problems are a need for more effective estimators (e.g., generalized and unweighted least-squares) and proper parameter settings including shorter updating rates.

The 3-component technique casts a new light on the following research tasks:

(1) Event detection, decomposition of wavetrain into wave-types (P, S, Rayleigh or Love) and identification of modes.

(2) Decomposition of coda into deterministic and random contributions (scattering studies).

(3) Improved signal parameter extraction (for AI, tomography, hypocenter location and source discrimination).

(4) Migration and imaging (arrays of 3-component instruments required).

Perhaps most interesting is the potential for improved capabilities of seismic source identification given that the pattern characterizing signal decomposition via particle motion analysis is diagnostic. The importance of this for expert-system development for use in remote, stand-alone, and "intelligent" seismic data acquisition systems cannot be overemphasized.

FINGERPRINTING MOTHER EARTH: 3-COMPONENT SEISMOGRAM ANALYSIS.

Anders Christoffersson, Dept. of Statistics, Univ. of Uppsala, Sweden.
Eystein S. Husebye, NORSAR, Norway.
Shane F. Ingate, Department of Earth and Planetary Sciences, MIT, USA.

ABSTRACT:

In this note we introduce a new technique for analyzing 3-component seismogram records; in essence this implies a comparison of the theoretically expected particle motion covariance matrices with that observed in given time (0.5 to 1 sec) and azimuth (1 to 5 deg) windows. The outcomes are the likelihood or probability of presence of P, S, Love and Rayleigh types of wavelets constituting the signal records. Preliminary results are displayed in terms of likelihood of signal occurrence as a function of time and azimuth, filtered records on the basis of the estimated likelihood functions, and apparent phase velocities of P-wavelets triggered. The events subjected to analysis were recorded by a single 3-component instrument in the new NORESS mini-array in Norway; our analysis results compare not unfavorably with those based on *f-k* analysis using all vertical instruments in the array.

INTRODUCTION

A properly equipped seismograph station or array always includes 3-component instrumentation for the very simple reason that the seismic wavefield comprises vertical and horizontal ground motions and combinations thereof. Seismologists have for many years successfully exploited the information potential of 3-component records for wave propagation modeling, retrieval of structural information (tomography) and source parameters, but these efforts have mainly been confined to the low frequency part of the wavefield. Likewise, many efforts have been invested in extracting similar information in the high frequency range, say of 1-10 Hz, but in this case less successfully as judged from current literature. The reason for this appears to be twofold; i) high frequency records are rather complex due to scattering, mode conversions, multipathing and similar wave propagation effects and ii) the techniques of analysis fail to produce extracted wavefield parameters in an easily interpretable format. For example, a common procedure is to produce many particle motion plots reflecting the structure in the wavefield, but since such plots generally are messy, the analysis is often left at that.

The problem addressed in this note is that of a new approach to extracting parameter characteristics, the wavefield structure on the basis of *a priori* models for P, S, Love and Rayleigh wave particle motions. Special attention has been given to the problem of presenting results in an easily interpretable manner or extracting signal parameters convenient for a wide variety of research applications. These points will be amply demonstrated in the "Results" section.

3-COMPONENT ANALYSIS TECHNIQUE: WAVEFIELD MODELING

Any approach to extracting signal parameters from a seismc ͐m is based on certain assumptions or models regarding the signals or wavelets constit͐ ͐e records and the background noise. In our case these are; i) noise is orthogonal ͐ the 3-components (vertical, radial, transverse; or Z, E-W, N-S) and ii) particle motior... ͐rived from classical wave theory. The analysing technique, as used in practice, is tied to the theoretically expected particle motion covariance matrix which is compared to that observed in given time and azimuth windows. Then using a maximum likelihood (ML) formulation the primary result is simply the likelihood that a wavelet is either P, S, Love or Rayleigh against the null hypothesis of being noise. Concurrent with the likelihood estimation is that of extracting the axis of the

particle motion ellipse (linear for body waves) which in turn can be converted into angle of approach of the incoming wavefront, that is, angle of incidence (azimuth is already known). To summarize, wavefield information extraction from our 3-component signal analysis procedure is as follows:

(1) Likelihood of presence (> 40%) of P, S, Love and Rayleigh type of wavelets as a function of azimuth (dϑ ~ 1 to 5 deg), and time (dT ~ 1 sec, updating interval 0.5 sec).

(2) Angle of incidence for triggered body wave type of wavelets.

As mentioned, special attention was given to results or extracted wavefield parameter presentations which presently are in the following forms:

(1) Likelihood contouring as a function of azimuth (ranges typically 60-180 degrees) and time (ranges typically 20-50 sec).

(2) Particle motion filtering on the basis of the estimated likelihood function, that is, simply weighting the original records with the likelihood function and confining to an azimuth window of $\pm$ 30 to $\pm$ 40 deg relative "true" azimuth.

(3) Angle of incidence estimates converted to apparent phase velocity (so far for P only) via Herrin tables, and then plotted as a function of time and azimuth.

(4) Azimuth and incident angle of the very first P wavelet transformed to estimates of epicenter coordinates.

We remark that presently our work on 3-component seismogram analysis is just in a rather preliminary stage, the use of other types of estimators has not been explored, nor the use of more complex particle motion models which would include the effects of receiver-structure heterogeneity. Other types of problems are those of better handling interference phenomena typical of the Lg wavetrain and S-wave splitting, but a requirement here seems to be deployment of 5-component instrumentation (1 vertical and 4 horizontal) in order to reduce the degrees of freedom in the statistical tests. On the application side, we have not explored the possibility of coda decomposing in deterministic and random scattering contributions, and perhaps most challenging that of what we term *earth fingerprinting*. With this is meant that the large number of signal parameters extracted may exhibit stationary patterns reflecting structural heterogeneities characteristic of specific site and source regions.

It may also be appropriate to add a few words on how our technique compares with other techniques of 3-component data analysis. The feature in common is that of estimating the axis of the particle motion ellipse, but to our knowledge nobody has tried to include model fit in probabilistic terms nor to use sliding time/azimuth windows permitting a rather comprehensive decomposition of the whole recorded wavetrain. The preliminary results to be presented are an analysis of the 3-component recordings from the new NORESS array, and obviously some comparison has to be made between outcome of our decomposition technique and similar results obtained by f-k analysis using all 24 vertical components of the array. Without going into detail here, it suffices to state that our 3-component results for a single instrument compare favorably with the f-k results; in fact quite often they do better in terms of improved time and azimuth resolutions. The reason for this is that f-k analysis requires longer time windows (a minimum of 2.5 sec is used in the case of NORESS) to account for move-outs across the array, and in case of interfering signals, "averaged" results are produced. Not to forget, the consistency and stationarity of particle ground motion even for short wavelets are at least for us unexpectedly good.

PRELIMINARY RESULTS

As the 3-component technique has only recently become operational, comprehensive analysis of many event recordings has not yet been completed. However, preliminary results from a few rather typical event recordings mostly from the NORESS 3-component station C2 will be presented in the following, so as to illuminate in our opinion the strength and potential of 3-component analysing techniques. Many more events than shown have currently been analysed. Results are presented event-wise (in Figures) using unfiltered data as standard recursive Butterworth filtering produces severe phase distortions. It should be added that so far mostly P-modeling has been attempted.

In the following analysis of six events recorded by the NORESS array, the azimuths were generally taken from the NORESS bulletin (unless otherwise indicated), but locations are as given by PDE and the 3-component analysis as the NORESS bulletin was generally in disagreement with distances in error between 2 to 20 degrees.

Figure 1 shows an event in the Lake Baikal region, event date 10/27/84, NORESS azimuth of 110 degrees, and distance of 24 degrees. Of interest here is the apparent decomposition of the recorded wavetrain into several bursts of P-wave energy. The secondary arrivals are likely associated with triplications due to the upper mantle discontinuities near depths of 400 and 650 km (see Figure 2).

Figure 3 is for a local event to the south of NORESS (accurate location unavailable), event date 11/22/84. Note that the large amplitude Sn and Lg section of the train contains little P-wave motion. Of additional note is the apparent "migration" of P-wave energy that arrives from azimuths to the north of the true event azimuth. This feature has been repeatedly observed in the 3-component and *f-k* analysis (see Mereu *et. al.*, 1983). Figure 4 shows an event in E. Kazakh, event date 11/23/84 and azimuth of approximately 80 degrees.

Figure 5 is a large explosion in the Semipalatinsk region, event date 2/10/85 and azimuth 74 degrees. Again, note the energy migration to northerly azimuths, indicating the possible existence of a deterministic scatterer to the north of the NORESS array. Figure 6 shows a velocity decomposition of the 3-component data as a function of time after first-arrival onset and azimuth.

Figure 7 is an excellent example of interfering events recorded by an array. The first arrival is from a local mining explosion to the south of NORESS, and the second arrival from a mining explosion near Leningrad (the Finnish network was used to locate this event, giving an azimuth of 87 degrees). The interference between the two events is clearly seen at 125 sec. The 3-component analysis has been able to discriminate between the two events, but the NORESS bulletin was in error due largely to the long time-windows used in the *f-k* analysis.

Finally, Figure 8 is a worst case example with exceptionally poor signal-to-noise ratio. The Finnish network located this event on the Finnish/USSR border (event date 3/22/85) and should have an azimuth from NORESS of 71 degrees (NORESS estimated the azimuth to be 90 degrees). The 3-component still seems to work.

CONCLUSIONS:

The preliminary results obtained from our variant of particle motion analysis of high-quality 3-component records from the new NORESS array in Norway are considered very encouraging and thus justify research on a broader scale into this kind f problem. Although currently operational in real-time, methodological problems are a need for more effective estimators (e.g., generalized and unweighted least-squares) and proper parameter settings including shorter updating rates. The good time resolution of signal parameters extracted testifies to the importance of incorporating laterally varying velocity models in synthetic seismogram analysis.

Perhaps most interesting is the potential for improved capabilities of seismic source identification given that the pattern characterizing signal decomposition via particle motion analysis is diagnostic. Surprisingly, epicenter location capabilities appear to be relatively good, azimuth estimates so far seldom exceeded $\pm$ 5 deg (often around $\pm$ 2 deg), while distance is more problematic unless secondary phases (Sn, Lg for regional events or triplications for teleseismic events) are clearly identified. Another interesting aspect here is that of identifying pP and thus significantly improving focal depth estimates.

The 3-component-technique casts a new light on the following research tasks:

(1) Event detection, decomposition of wavetrain into wave-types (P, S, Rayleigh or Love) and identification of modes.

(2) Decomposition of coda into deterministic and random contributions (scattering studies).

(3) Improved signal parameter extraction (for AI, tomography, hypocenter location and source discrimination).

(4) Migration and imaging (arrays of 3-component instruments required).
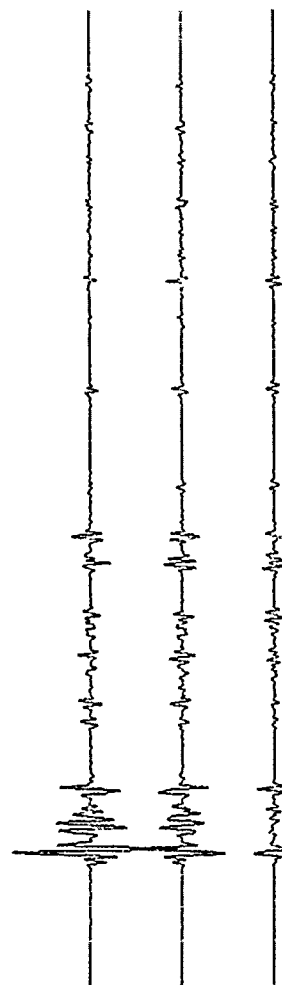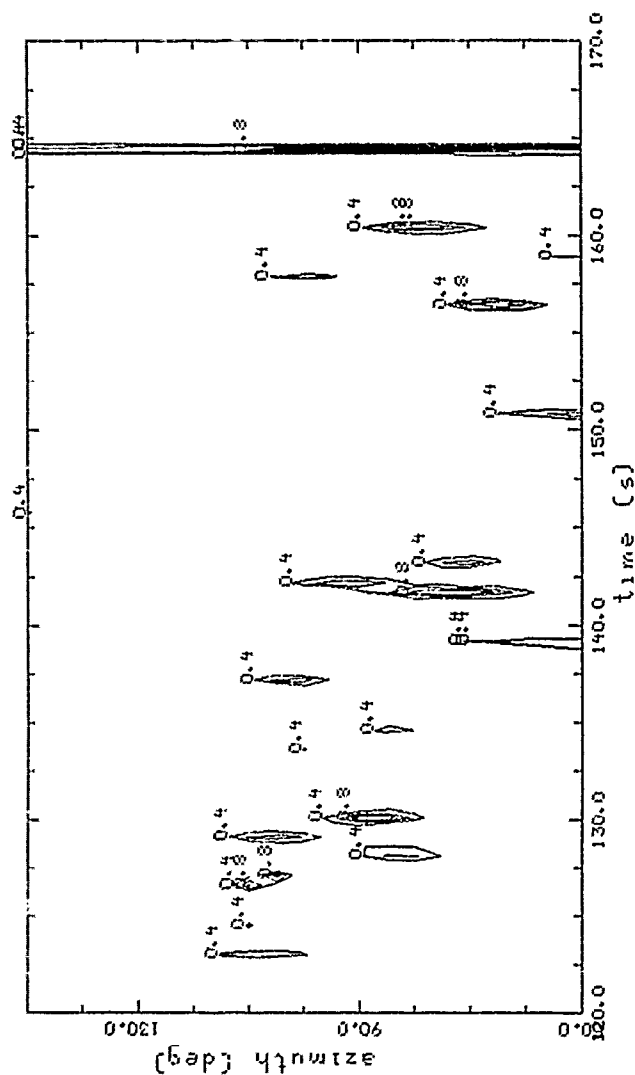
Our final remark is that if the preliminary results presented here are representative of what can be achieved with 3-component instrumentation, this opens up for many new research ventures.

REFERENCES

King, D.W. and G Calcagnile, 1976. P-wave velocities in the upper mantle beneath Fennoscandia and Western Russia. *Geophys. J. R. astr. Soc*, 46, 407-432.

Mereu, R.F., S. Mykkeltveit and E.S. Husebye, 1983. FENNOLORA recordings at NORSAR. *J. Geophys.*, 52, 119-130.

Figure 1. Event date 10/27/84: Lake Baikal. Feature: Travel-time triplication(s). The top three traces are the unfiltered outputs of a single 3-component station in the NORESS array. Instrument and amplitudes are given to the left of the seismograms. The contours represent likelihood of the presence of P-wave motion as a function of time and azimuth. Both seismograms and likelihoods are plotted with the same timing scale. Lowermost traces are the result of weighting the raw seismograms with the computed likelihoods, and thus represent "filtered" data containing only significant P-wave energy.
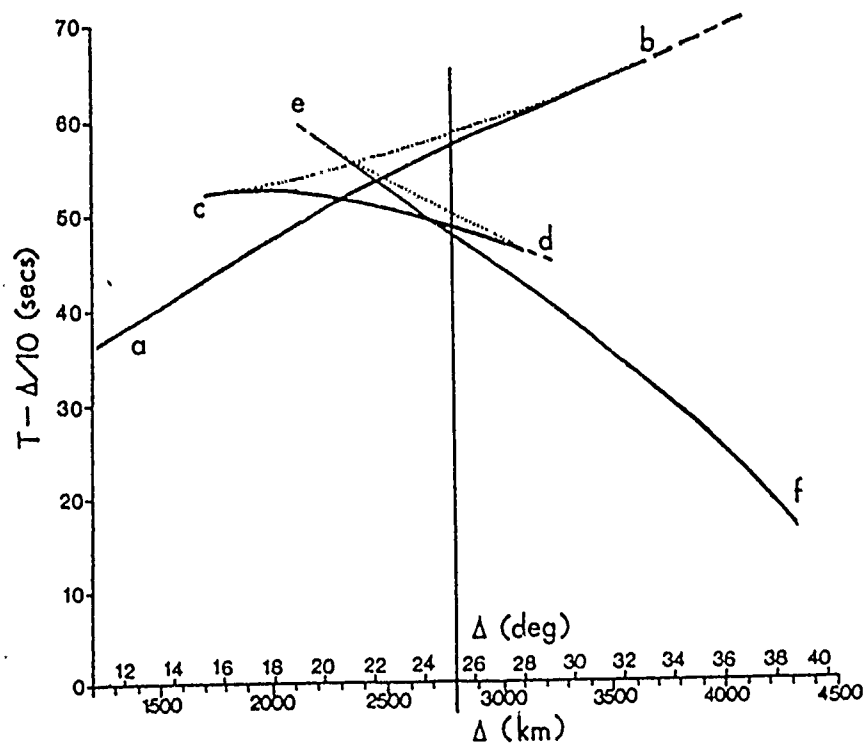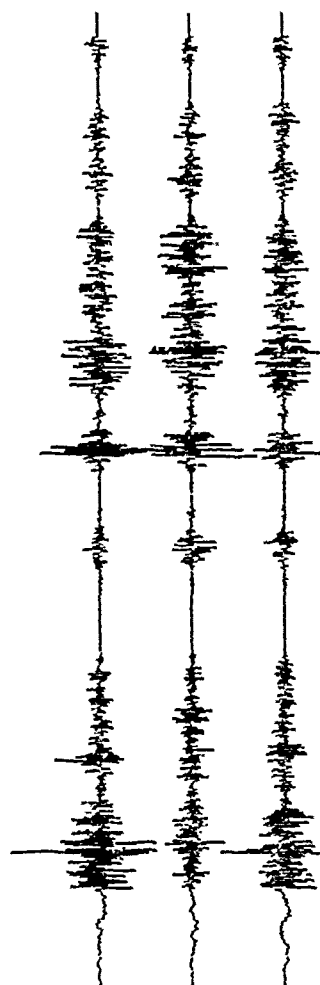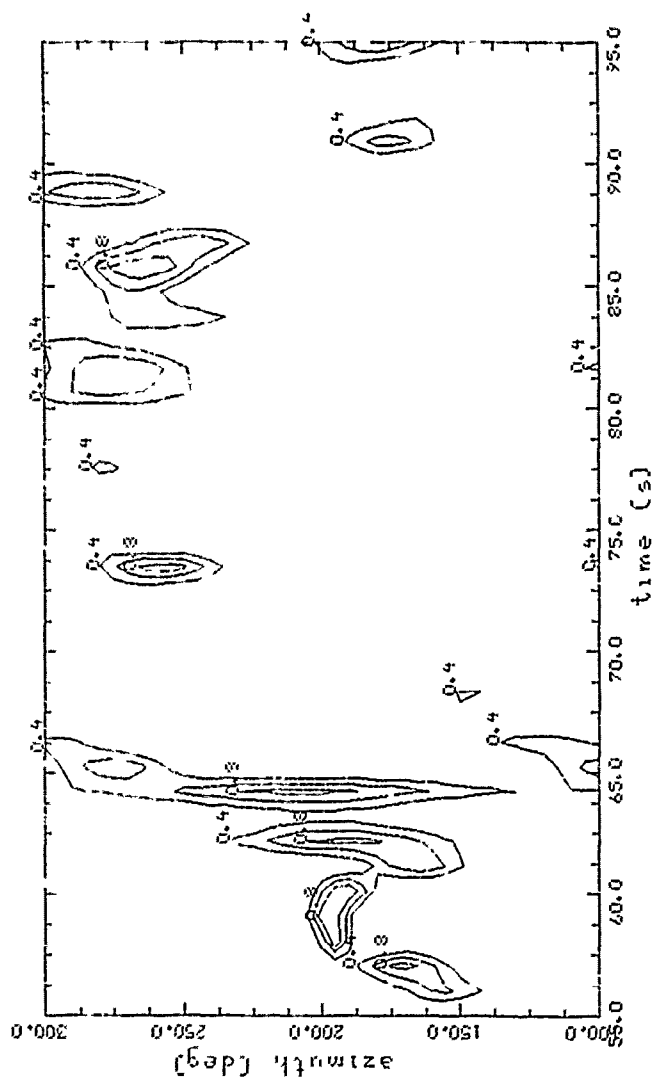
Mon May 27 15:27:02 1985

>>> model=p-wave p(p)#p(po>0) >>>

Event: 84301.06032030

iskip: 4800   scale: 21.0   kfilt: :
lstep: 20   az:100.0   al:50.0   nstep: 5
scale:40.0   iav: 1   ap: 0.   ap1: 0.2
Instrument status: A1 = 1
                   C2 = 0
                   C4 = 0
                   C7 = 0

439

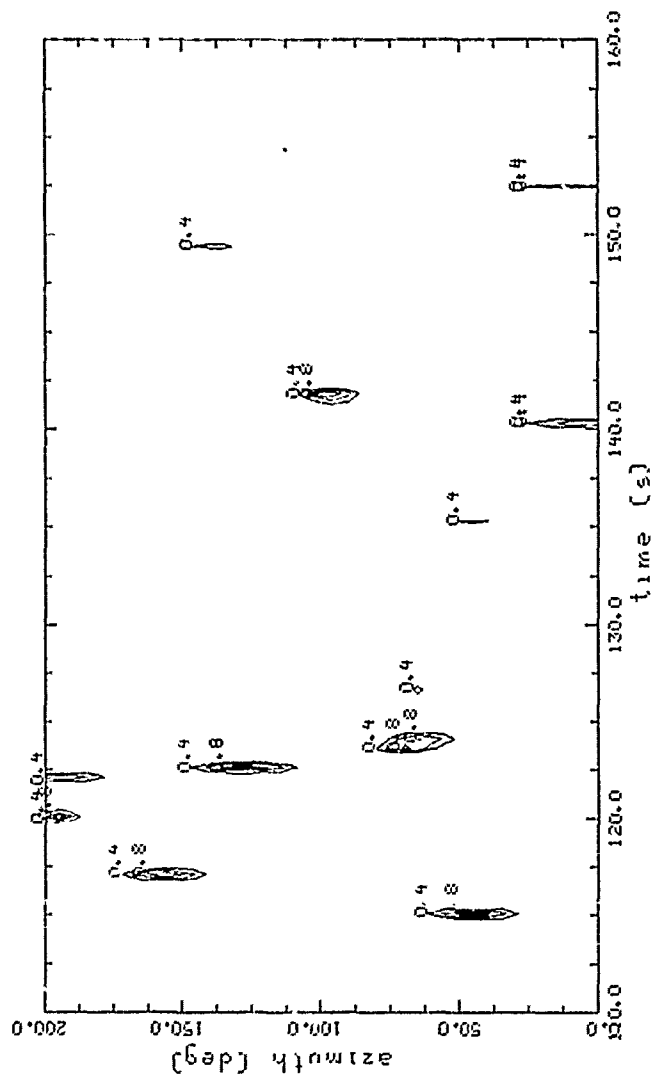*Figure 2.* Travel-time distance curves for the KCA P-velocity model of the upper mantle beneath the Baltic Shield (after King and Calcagnile, 1976).

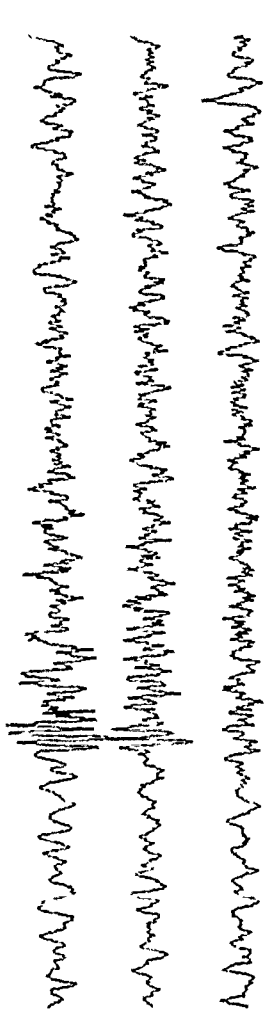*Figure 3.* Event date 11/22/84:
Local explosion. Feature: Complex
local record; energy migration.
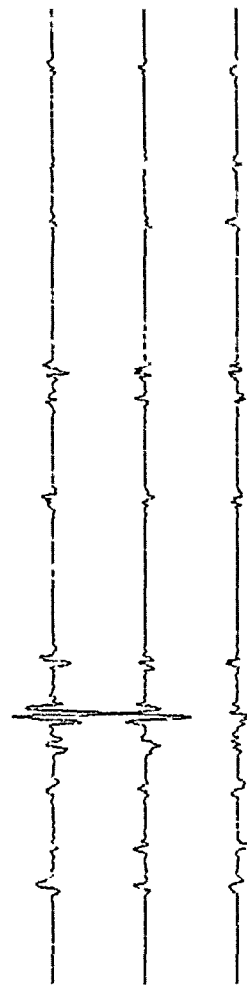
Mon May 27 15:23:35 1985

441

>>> model=p-wave p(p)*p(pp>0) >>>

Event: 84328.04002046

ishift: 4400   scale: 41.0   kfilt: 1

lstep: 20   az:160.0   al: 0.   nstep: 5

scale:40.0   iav: 1   ep: 0.   ap: 0.2

Instrument status: A1 = 1

   C2 = 0

   C4 = 0

   C7 = 0

Figure 4. Event date 11/23/84:
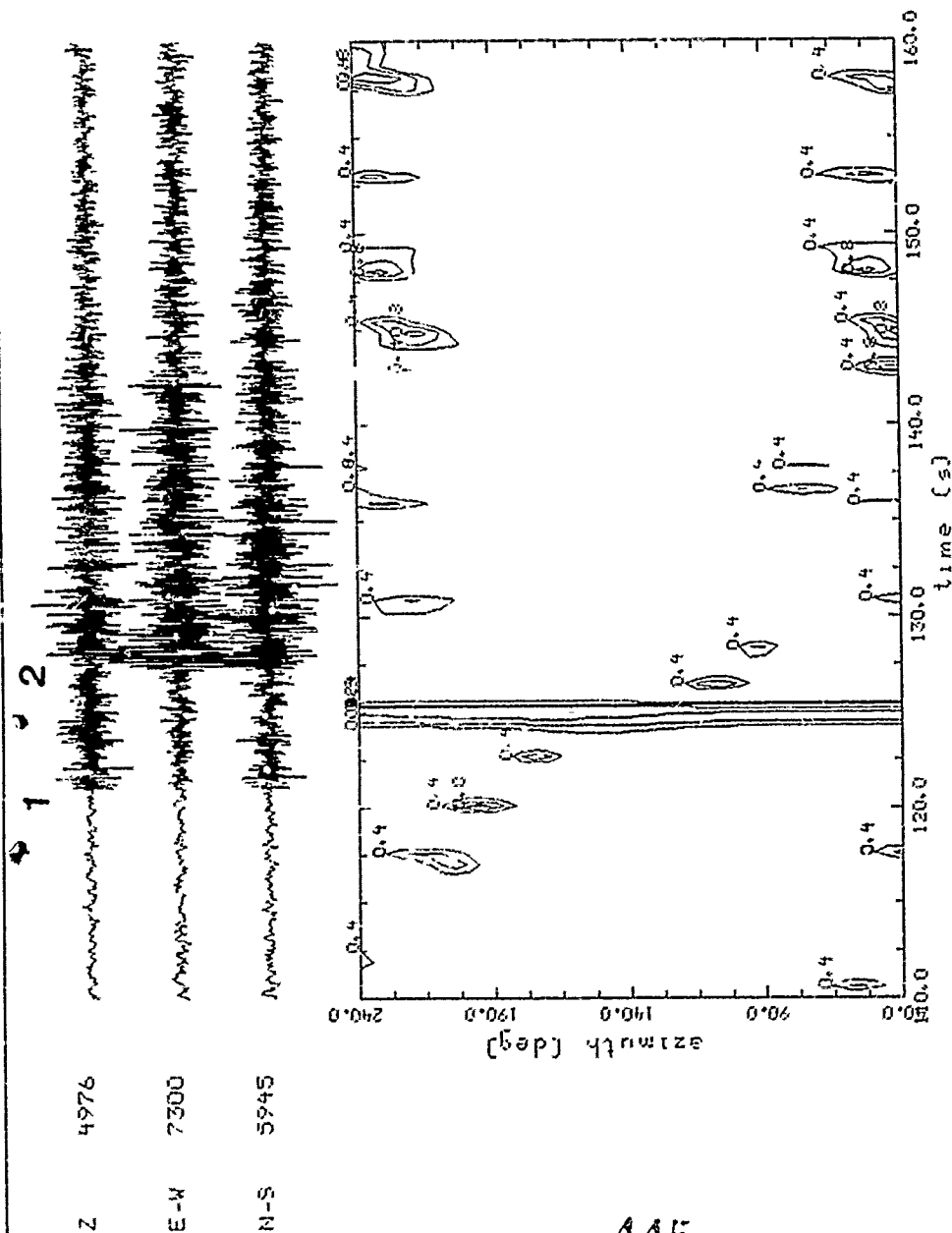E. Kazakh event. Feature: Triplica-
tion of wave train?

Mon May 27 15:31:54 1985

442

>>> model=p-wave p(p)>p(po>0) <<<

Event: 85041.03322506

istp: 4400   srate: 41.0   ifilt: 1

lstep: 20   az:100.0   al: 0.   nstep: 5

scale:40.0   iav: 0   ap: 0.   ap1: 0.2

Instrument status: A1 = 0

C2 = 1

C4 = 0

C7 = 0

Figure 5. Event date 2/10/85: Semipalatinsk event. Feature: Apparent velocity analysis of the first 25 sec of the record.

Z   616960

E-W   273272

N-S   62704

Z   185285

E-W   74389

N-S   41090

azimuth [deg]

200.0   150.0   100.0   50.0   0.0

time (s)

120.0   130.0   140.0   150.0   160.0

443

Figure 6. Velocity analysis as a function of time and azimuth after first P-wave onset of the data in Figure 5.

>>> model=p-wave p(p)>p(po>0) >>>

Event: 85060.1204 1056

iskip: 4400   scale: 41.0   kfilt: 1

lstep: 25   az: 80.0   al:40.0   nstep: 5

scale:40.0   iav: 1   ap: 0.   ap1 0.2

Instrument status: A1 = 1
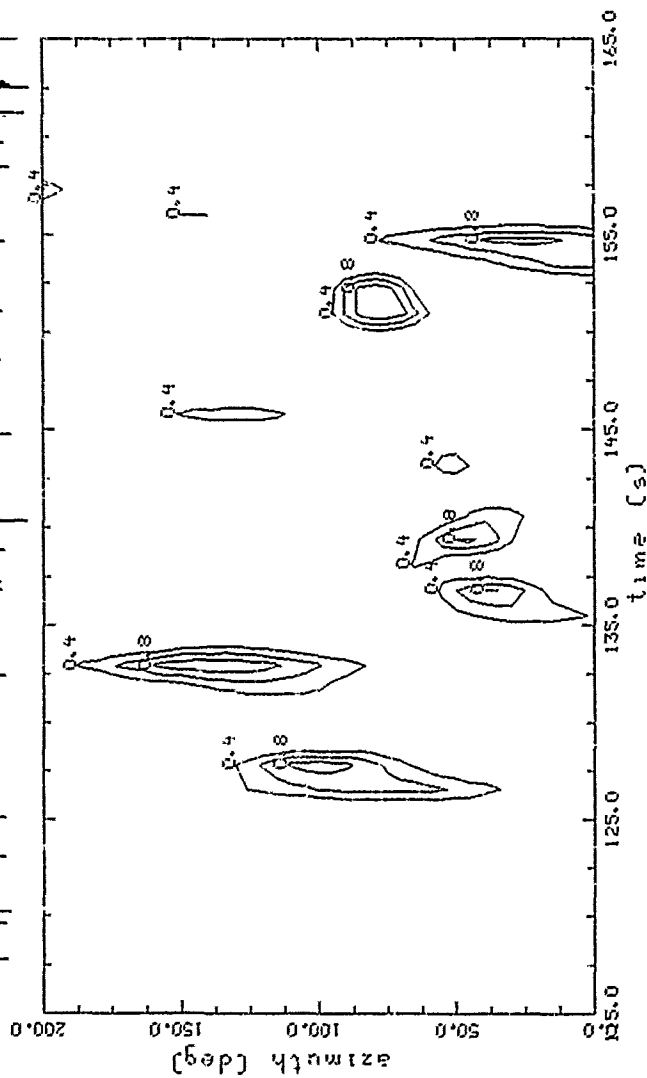 C2 = 0
  C4 = 0
  C7 = 0

Figure 7. Event date 3/1/85: "Leningrad" event. Feature: This is actually a double event easily separated by 3-component analysis. Event labeled "1" is due to a local mining explosion to the south of NORESS, and event labeled "2" is due to a mining explosion in Leningrad.
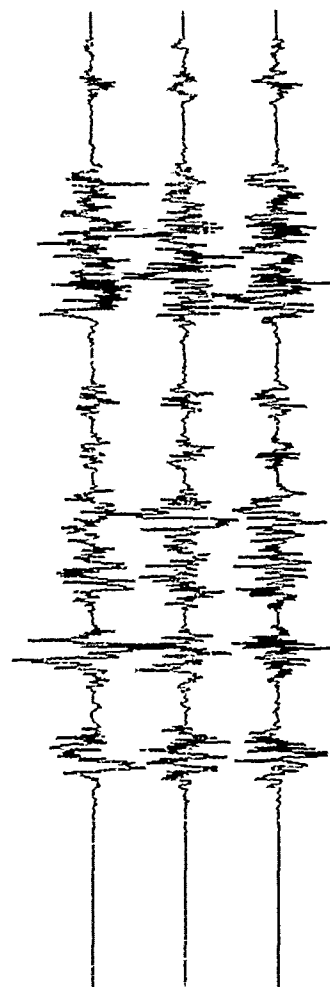
Mon May 27 15:36:44 1985

>>> model=p-wave p(p)*p(pe>0) >>>

Event: 85081.12521067

istip: 4800   srate: 41.0 kfilt: 1

lstep: 50   az: 40.0 el: 0.   nstep: 5

scal=40.0   iav: 2   ap: 0.   ap1: 0.2

Instrument status: Al = 1

C2 = 0

C4 = 0

C7 = 0

Figure 8. Event date 3/22/85: Finland/USSR event. Feature: Worst case event with exceptionally poor SNR, but 3-component analysis still seems to work.

Mon May 27 15:40:00 1985

Z   1532
E-W 1566
N-S 1406

Z   1384
E-W 1079
N-S   936

azimuth (deg)

time (s)

Dr. Monem Abdel-Gawad
Rockwell International Science Center
1049 Camino Dos Rios
Thousand Oaks, CA 91360

Professor Shelton S. Alexander
Geosciences Department
403 Deike Building
The Pennsylvania State University
University Park, PA 16802

Professor Charles B. Archambeau
Cooperative Institute for Research in
   Environmental Sciences
University of Colorado
Boulder, CO 80309

Dr. Thomas A. Bache Jr.
Science Applications Int'l Corp.
1200 Prospect Street
P.O. Box 2351
La Jolla, CA 92038

Dr. James Balau
Rockwell International Science Center
1049 Camino Dos Rios
P.O. Box 1085
Thousand Oaks, CA 91360

Dr. Douglas R. Baumgardt
Signal Analysis and Systems Division
ENSCO, Inc.
5400 Port Royal Road
Springfield, VA 22151

Dr. G. Blake
US Dept of Energy/DP 331
Forrestal Building
1000 Independence Ave.
Washington, DC 20585

Dr. Robert Blandford
Geophysical Sciences Division
Defense Advanced Research Projects Agency
1400 Wilson Boulevard
Arlington, VA 22209-2308

Dr. M. Bouchon
Societe Radioama
27, Rue Claude Bernard
75005, Paris, France

Dr. S. Bratt
Science Applications Int'l Corp.
1200 Prospect Street
P.O. Box 2351
La Jolla, CA 92038

Dr. Hilmar Bungum
NTNF/NORSAR
P.O. Box 51
Norwegian Council of Science,
Industry and Research, NORSAR
N-2007 Kjeller, Norway

Dr. Lawrence J. Burdick
Woodward-Clyde Consultants
P.O. Box 93245
Pasadena, CA 91109-3245

Dr. Roy Burger
Woodward-Clyde Consultants
P.O. Box 93245
Pasadena, CA 91109-3245

Dr. Vernon F. Cormier
Earth Resources Laboratory
Department of Earth, Atmospheric and
        Planetary Sciences
Massachusetts Institute of Technology
42 Carleton Street
Cambridge, MA 02142

Professor Anton M. Dainty
NTNF/NORSAR
P.O. Box 51
Norwegian Council of Science,
Industry and Research, NORSAR
N-2007 Kjeller, Norway

Dr. Zoltan A. Der
Teledyne Geotech
P.O. Box 334
Alexandria, VA 22313

Dr. H. B. Durham
Organization 310
Sandia National Laboratory
Alburquerque, NM 87185

Professor John F. Ferguson
Center for Lithospheric Studies
The University of Texas at Dallas
P.O. Box 830688
Richardson, TX 75083-0688

Dr. Jeffrey W. Given
Sierra Geophysics
15446 Bell-Road, Suite 400
Redmond, WA 98052

Mr. S. Grand
Seismological Laboratory
Division of Geological and Planetary
    Sciences
California Institute of Technology
Pasadena, CA 91125

Professor Roy J. Greenfield
Geosciences Department
403 Deike Building
The Pennsylvania State University
University Park, PA 16802

Professor Peter Harjes
Institute for Geophysik
Rhur University
Bochum
P.O. Box 102148
4630 Bochum 1
Federal Republic of Germany

Professor David G. Harkrider
Seismological Laboratory
Division of Geological and Planetary
    Sciences
California Institute of Technology
Pasadena, CA 91125

Professor Donald V. Helmberger
Seismological Laboratory
Division of Geological and Planetary
    Sciences
California Institute of Technology
Pasadena, CA 91125

Professor Eugene Herrin
Institute for the Study of Earth and Man
Geophysical Laboratory
Southern Methodist University
Dallas, TX 75275

Professor Robert B. Herrmann
Department of Earth and Atmospheric
    Sciences
Saint Louis University
Saint Louis, MO 63156

Dr. E. Husebye
NTNF/NORSAR
P.O. Box 51
Norwegian Council of Science,
Industry and Research, NORSAR
N-2007 Kjeller, Norway

Professor Lane R. Johnson
Seismographic Station
University of California
Berkeley, CA 94720

Professor Thomas H. Jordan
Department of Earth, Atmospheric and
    Planetary Sciences
Massachusetts Institute of Technology
Cambridge, MA 02139

Dr. A. Lerner-Lam
Lamont-Doherty Geological Observatory
    of Columbia University
Palisades, NY 10964

Professor Charles A. Langston
Geosciences Department
403 Deike Building
The Pennsylvania State University
University Park, PA 16802

Professor Thorne Lay
Department of Geological Sciences
1006 C.C. Little Building
University of Michigan
Ann Arbor, MI 48109-1063

Mr. C. Lynnes
Department of Geological Sciences
1006 C.C. Little Building
University of Michigan
Ann Arbor, MI 48109-1063

Dr. Robert Masse
Box 25046
Mail Stop 967
Denver Federal Center
Denver, CO 80225

Dr. B. Massinon
Societe Radioama
27, Rue Claude Bernard
75005, Paris, France

Dr. Pierre Mechler
Societe Radiomana
27, Rue Claude Bernard
75005 Paris, France

Dr. George R. Mellman
Sierra Geophysics
15446 Bell-Road, Suite 400
Redmond, WA 98052

448

Professor Brian J. Mitchell
Department of Earth and Atmospheric
    Sciences
Saint Louis University
Saint Louis, MO 63156

Professor Thomas V. McEvilly
Seismographic Station
University of California
Berkeley, CA 94720

Dr. Keith L. McLaughlin
Teledyne Geotech
P.O. Box 334
Alexandria, VA 22313

Mr. Jack Murphy
S-CUBED
Reston Geophysics Office
11800 Sunrise Valley Drive
Suite 1212
Reston, VA 22091

Dr. Svein Mykkeltveit
NTNF/NORSAR
P.O. Box 51
N-2007 Kjeller, Norway

Dr. Carl Newton
Los Alamos National Laboratory
P.O. Box 1663
Mail Stop C 335
Goup ESS3
Los Alamos, NM 87545

Dr. R. North
Earth Physics Branch
Department of Energy and Mines
1 Observatory Crescent
Ottawa, Ontario
Canada K1A 0Y3

Dr. R. Nowack
Earth Resources Laboratory
Department of Earth, Atmospheric and
    Planetary Sciences
Massachusetts Institute of Technology
42 Carleton Street
Cambridge, MA 02142

Professor Otto W. Nuttli
Department of Earth and Atmospheric
    Sciences
Saint Louis University
Saint Louis, MO 63156

Professor Jack Oliver
3120 Snee Hall
INSTOC
Cornell University
Ithaca, NY 14853

Dr. J. A. Orcutt
Geological Sciences Division
Univ. cf California at San Diego
La Jolla, CA 92038

Dr. Frank F. Pilotte
Chief, Geophysics Division/TGR
Directorate of Science and Technology
Headquarters Air Force Technical
  Applications Center
Patrick AFB, Florida 32925

Professor Keith Priestley
University of Nevada
Mackay School of Mines
Reno, Nevada 89557

Dr. Frode Ringdal
NTNF/NORSAR
P.O. Box 51
Norwegian Council of Science,
Industry and Research, NORSAR
N-2007 Kjeller, Norway

Dr. George Rothe
Chief, Research Branch
Directorate of Science and Technology
Headquarters Air Force Technical
  Applications Center
Patrick AFB, Florida 32925

Professor Larry J. Ruff
Department of Geological Sciences
1006 C.C. Little Building
University of Michigan
Ann Arbor, MI 48109-1063

Professor Alan S. Ryall, Jr.
University of Nevada
MacKay School of Mines
Reno, Nevada 89557

Dr. Jeffrey L. Stevens
S-CUBED,
A Division of Maxwell Laboratory
P.O. Box 1620
La Jolla, CA 92038-1620

Professor Ta-liang Teng
Center for Earth Sciences
University of Southern California
University Park
Los Angeles, CA 90089-0741

Dr. Steve Taylor
Lawrence Livermore National Laboratory
P.O. Box 808
Livermore, CA 99550

Dr. R. B. Tittmann
Rockwell International Science Center
1049 Camino Dos Rios
P.O. Box 1085
Thousand Oaks, CA 91360

Mr. J. Vidale
Seismological Laboratory
Division of Geological and Planetary
        Sciences
California Institute of Technology
Pasadena, CA 91125

Professor Terry C. Wallace
Department of Geosciences
Building #11
University of Arizona
Tucson, AZ 85721

Mr. Gregory Young
ENSCO, Inc.
Signal Analysis and Systems Division
5400 Port Royal Road
Springfield, VA 22151